DEPARTMENT OF GEODESY AND GEOINFORMATION

VIENNA UNIVERSITY OF TECHNOLOGY

OBSERVATOIRE DE PARIS

SYSTÈMES DE RÉFÉRENCE TEMPS-ESPACE

UMR8630 / CNRS

Earth rotation, reference systems, and celestial mechanics:

Synergies of geodesy and astronomy

Rotation de la Terre, systèmes de référence et mécanique céleste: Synergies entre géodésie et astronomie

JOURNÉES 2011 ☆

SYSTÈMES DE RÉFÉRENCE SPATIO - TEMPORELS

☆ VIENNA, 19-21 SEPTEMBER

DEPARTMENT OF GEODESY AND GEOINFORMATION

VIENNA UNIVESITY OF TECHNOLOGY

Gusshausstrasse 27-29, A-1040 Vienna, Austria

OBSERVATOIRE DE PARIS

SYSTÈMES DE RÉFÉRENCE TEMPS-ESPACE

UMR 8630 / CNRS

61 avenue de l'Observatoire, F-75014 Paris, FRANCE

Earth rotation, reference systems, and celestial mechanics:

Synergies of geodesy and astronomy

Rotation de la Terre, systèmes de référence et mécanique céleste: Synergies entre géodésie et astronomie

Edited by

Actes publiés par

H. SCHUH, S. BÖHM, T. NILSSON, and N. CAPITAINE

JOURNÉES 2011 ☆

SYSTÈMES DE RÉFÉRENCE SPATIO - TEMPORELS

☆ **VIENNA, 19-21 SEPTEMBER**

ISBN 978-2-901057-67-3

TABLE OF CONTENTS

PREFACE

The Journées 2011 “Systèmes de référence spatio-temporels”, with the sub-title “Earth rotation, reference systems and celestial mechanics: Synergies of geodesy and astronomy”, were organized from 19th to 21st of September 2011 by the Institute of Geodesy and Geophysics (IGG) of the Vienna University of Technology (TU Vienna), Austria; they were co-sponsored by the International Astronomical Union (IAU) and the International Association of Geodesy (IAG). The venue of the scientific sessions was at Bundesamt für Eich-und Vermessungswesen (BEV). These Journées were the 21st meeting in the Journées conference series, which provide an international forum for advanced discussion in the fields of space and time reference systems, Earth rotation, dynamics of the solar system, astrometry and time. The Journées were organized in Paris each year from 1988 to 1992, and then, since 1994, alternately in Paris (in 1994, 1996, 1998, 2000, 2004, 2007 and 2010) and other European cities, namely Warsaw in 1995 and 2005, Prague in 1997, Dresden in 1999 and 2008, Brussels in 2001, Bucharest in 2002 and St. Petersburg in 2003. Such an organization has been the result of an active and continuing cooperation between the Department “Systèmes de Référence Temps Espace” (SYRTE) of Paris Observatory and other institutions in Europe working in the same field.

The Journées 2011 were focused on issues related to recent developments in fundamental astronomy, time and relativity, plans for the next generation of astronomical space and time reference systems, Earth rotation and global geodynamics, celestial mechanics of solar system bodies, space observations and dedicated missions for geodesy and astronomy. There have been presentations and discussions related to the IAU Division 1 Working Groups, or Division 1 Commissions with potential recommendations to be submitted at the XXVIII General Assembly of the IAU in Beijing (August 2012). These recommendations concerned in particular a redefinition of the astronomical unit, nomenclature for nutation model or Universal Time and standardizing access to ephemerides; they also concerned the establishment of new working groups on pulsar time or on the definition and realization of the future ICRS and the organization of Division 1 within the new IAU structure.

There were 100 participants, coming from 21 different countries. The scientific programme included 10 invited papers, 47 oral communications and 25 posters; it was composed of the five following sessions:
Session 1: Fundamental astronomy, time and relativity;
Session 2: Towards the next generation of space-time reference systems;
Session 3: Modelling, observation and prediction of Earth rotation and global geodynamics;
Session 4: Celestial mechanics of solar system bodies;
Session 5: Space observations and dedicated missions for geodesy and astronomy;
Discussion - On future IAU recommendations and organization

In addition to these scientific activities, the participants met on Monday 19th of September for a welcome drink after the poster session and on Tuesday evening 20th of September for a conference dinner at the restaurant and vineyard-estate ’Fuhrgassl-Huber’ in Neustift am Walde.

The Proceedings are published thanks to a financial support from the IGG of TU Vienna; they are divided into five sections corresponding to the sessions of the meeting. The table of contents is given on pages iii to v, the list of participants on pages vii and viii, the scientific programme and list of posters on pages ix to xiv. The Postface on page 273 gives the first announcement for the “Journées” 2013 that will be held at Paris Observatory (France) on September 16-18, 2013.

We thank here all the participants in the Journées 2011 and all the institutions that supported this meeting. We are very grateful to the Scientific Organizing Committee (SOC) for its active role in the elaboration of the scientific programme and to all the authors of the papers for their valuable contributions. On behalf of the SOC, we thank the Local Organizing Committee for the very efficient preparation of the meeting and the very good local conditions and organization. We are also very grateful to S. Böhm, T. Nilsson and M. Schindelegger for their efficient work for the preparation of these Proceedings.

Harald SCHUH and Nicole CAPITAINE
Co-Chairs of the SOC

30 October 2012

List of Participants

ALJBAAE Safwan, *Observatoire de Paris - SYRTE*, France
ANTON Sonia, *Geo-Space Sciences Research Centre of Faculty of Porto (CICGE - FCUP)*, Portugal
BACHMANN Sabine, *Bundesamt für Kartographie und Geodäsie*, Germany
BAUDISCH Helmut, *University of Vienna*, Austria
BAZSO Akos, *University of Vienna*, Austria
BIANCALE Richard, *CNES/GRGS*, France
BIZE Sébastien, *Observatoire de Paris - SYRTE*, France
BIZOUARD Christian, *Observatoire de Paris*, France
BÖHM Johannes, *Vienna University of Technology*, Austria
BÖHM Sigrid, *Vienna University of Technology*, Austria
BRZEZINSKI Aleksander, *SRC, Polish Academy of Sciences; Warsaw University of Technology*, Poland
BUCCIARELLI Beatrice, *Observatorio Astronomico di Torino/INAF*, Italy
CAPITAINE Nicole, *Observatoire de Paris - SYRTE*, France
CHAPANOV Yavor, *National Institute of Geophysics, Geodesy and Geography at BAS*, Bulgaria
CHARLOT Patrick, *Laboratoire d'Astrophysique de Bordeaux*, France
CHOLIY Vasyl, *Kyiv Shevchenko University*, Ukraine
COELHO Bruno, *FCUP - Faculdade de Cincias da Universidade do Porto*, Portugal
DAMLJANOVIC Goran, *Astronomical Observatory*, Serbia
DE SEIXAS Andréa, *Universidade Federal de Pernambuco*, Brasil
DEHANT Veronique, *Royal Observatory of Belgium*, Belgium
DIMARCQ Noel, *Observatoire de Paris - SYRTE/CNRS*, France
DOBSLAW Henryk, *Geoforschungszentrum Potsdam*, Germany
DVORAK Rudolf, *University of Vienna*, Austria
ESCAPA Alberto, *University of Alicante*, Spain
FIENGA Agnes, *Institut UTINAM*, France
GALIAZZO Mattia, *University of Vienna*, Austria
GARNÉS Silvio, *Universidade Federal de Pernambuco*, Brasil
GOMEZ-GONZALEZ Jesus, *Instituto Geografico Nacional*, Spain
GROSS Richard, *Jet Propulsion Laboratory*, USA
HACKMAN Christine, *U.S. Naval Observatory*, USA
HASE Hayo, *Bundesamt für Kartographie und Geodäsie*, Germany
HILTON James, *U.S. Naval Observatory*, USA
HOBIGER Thomas, *National Institute of Information and Communications Technology*, Japan
HOHENKERK Catherine, *UK Hydrographic Office*, United Kingdom
IVANOVA Tamara, *Institute of Applied Astronomy, Russian Academy of Sciences*, Russia
JACOBS Christopher, *Jet Propulsion Laboratory*, USA
JOHNSTON Kenneth, *U.S. Naval Observatory*, USA
KAUFMAN Mark, *VNIIFTRI*, Russia
KLIONER Sergei, *Lohrmann Observatory, Technical University Dresden*, Germany
KOLACZEK Barbara, *Space Research Centre, Polish Academy of Sciences*, Poland
KOOT Laurence, *Royal Observatory of Belgium*, Belgium
KRYNSKI Jan, *Institute of Geodesy and Cartography*, Poland
KUDRYAVTSEV Sergey, *Sternberg Astronomical Institute, Moscow State University*, Russia
KWAK Younghee, *Korea Astronomy and Space Science Institute*, Rep. of Korea
LAMBERT Sebastien, *Observatoire de Paris - SYRTE*, France
LANOTTE Roberto, *E-GEOS*, Italy
LHOTKA Christoph, *University of Namur*, Belgium
LOVELL Jim, *University of Tasmania*, Australia
LUZUM Brian, *U.S. Naval Observatory*, USA
MA Chopo, *NASA Goddard Space Flight Center*, USA
MALKIN Zinovy, *Central Pulkovo Astronomical Observatory, Russian Academy of Sciences*, Russia
MANCHESTER Richard, *CSIRO Astronomy and Space Science*, Australia
MARCETA Dusan, *Faculty of Mathematics of Belgrade University*, Serbia

MARCO Francisco J., *Universidad Jaume I*, Spain
MAREYEN Maria, *Bundesamt für Kartographie und Geodäsie*, Germany
MARTINEZ Maria J., *Universidad Politecnica de Valencia*, Spain
MCCARTHY Dennis, *U. S. Naval Observatory*, USA
MIGNARD Francois, *Observatory of the Cote d'Azur*, France
MORA DIAZ Julian Andres, *DGFI - German Geodetic Research Institute*, Germany
NAGALSKI Tomasz, *Space Research Centre, Polish Academy of Sciences*, Poland
NASTULA Jolanta, *Space Research Centre, Polish Academy of Sciences*, Poland
NERGE Petra, *German Climate Computing Center*, Germany
NIELL Arthur, *MIT Haystack Observatory*, USA
NILSSON Tobias, *Vienna Univesity of Technology*, Austria
NOTHNAGEL Axel, *University of Bonn*, Germany
PANAFIDINA Natalia, *ETH Zürich*, Switzerland
PASHKEVICH Vladimir, *Central Pulkovo Astronomical Observatory, Russian Academy of Sciences*, Russia
PASYNOK Sergey, *VNIIFTRI*, Russia
PAVLIS Erricos C., *University of Maryland, Baltimore County; NASA Goddard/698*, USA
PITJEVA Elena, *Institute of Applied Astronomy, Russian Academy of Sciences*, Russia
PLANK Lucia, *Vienna University of Technology*, Austria
RICHARD Jean-Yves, *Observatoire de Paris - SYRTE*, France
ROMERO-WOLF Andrew, *Jet Propulsion Laboratory*, USA
RON Cyril, *Astronomical Institute, Academy of Sciences of Czech Republic*, Czech Republic
RUMMEL Reiner, *Technical University of Munich*, Germany
SCHINDELEGGER Michael, *Vienna University of Technology*, Austria
SCHUH Harald, *Vienna University of Technology*, Austria
SEITZ Florian, *ESPACE / Technical University of Munich*, Germany
SHU Fengchun, *Shanghai Astronomical Observatory*, China
SOFFEL Michael, *Lohrmann Observatory, Technical University Dresden*, Germany
SOJA Benedikt, *Vienna University of Technology*, Austria
SOUAMI Damya, *Observatoire de Paris - SYRTE/CNRS/UPMC*, France
SOUCHAY Jean, *Observatoire de Paris - SYRTE*, France
SPICAKOVA Hana, *Vienna University of Technology*, Austria
STAMATAKOS Nick, *U.S. Naval Observatory*, USA
STEWART Susan, *U.S. Naval Observatory*, USA
SUN Jing, *Vienna Univesity of Technology*, Austria
TARIS François, *Observatoire de Paris - SYRTE*, France
TEKE Kamil, *Hacettepe University*, Turkey
TITOV Oleg, *Geoscience Australia*, Australia
TORNATORE Vincenza, *Politecnico di Milano*, Italy
URBAN Sean, *U.S. Naval Observatory*, USA
VONDRÁK Jan, *Astronomical Institute, Academy of Sciences of Czech Republic*, Czech Republic
WEBER Robert, *Vienna University of Technology*, Austria
WERATSCHNIG Julia, *UK Hydrographic Office*, United Kingdom
WHITNEY Alan, *MIT Haystack Observatory*, USA
YAGUDINA Eleonora, *Institute of Applied Astronomy, Russian Academy of Sciences*, Russia
YAO Kunliang, *Observatoire de Paris - SYRTE*, France
YATSKIV Yaroslav, *Main Astronomical Observatory of NAS of Ukraine*, Ukraine
ZHAROV Vladimir, *Sternberg State Astronomical Institute*, Russia

SCIENTIFIC PROGRAMME

Scientific Organising Commitee: N. Capitaine, France (Chair); H. Schuh, Austria (Co-Chair); A. Brzeziński, Poland; V. Dehant, Belgium; C. Hohenkerk, UK; I. Kumkova, Russian Federation; D.D. McCarthy, USA; M. Soffel, Germany; J. Souchay, France; J. Vondrák, Czech Republic; Ya. Yatskiv, Ukraine.
Local Organising Commitee: H. Schuh, J. Böhm, S. Böhm, R. Dvorak, S. Linsmayer, T. Nilsson, M. Schindelegger, R. Weber.

Monday 19 September 2011

9:15–9:30: Opening of the Journées 2011

Welcome from H. Schuh, Vienna University of Technology, Chair of the LOC

Welcome from A. Hochwartner, President of the BEV, Vienna

Introduction to the Journes 2011 by N. Capitaine, Chair of the SOC

9:30–11:00: Session 1 – Fundamental astronomy, time and relativity
(Chair: N. Capitaine and M. Soffel)

Titov O. (invited): *The secular aberration drift and future challenges for VLBI astrometry*

Bucciarelli B., Smart R., Umberto, Dapra M.T., Lattanzi M., Penna J.L., da Silva Neto D.N., Andrei A.H.: *PARSEC's high precision astrometry - the making of*

Coelho B., Anton S., Taris F., da Silva Neto D., Bouquillon S., Souchay J., Andrei A.: *Morphological classification of QSOs in the SDSS DR7 population*

Pitjeva E.: *Values of some astronomical parameters - au, GM, M of the Sun, their possible variations from modern observations, and interrelations between them*

Hohenkerk C.: *SOFA and the algorithms for transformations between scales & between systems*

Vondrák J., Capitaine N., Wallace P.: *New long-term expressions for precession*

Capitaine N.: *Comparison between different forms of variables and parameters used for high accuracy models and observations of the Earth's precession and nutation*

11:00–11:30: Coffee break

11:30–13:00: Session 1 (continuation)
(Chair: N. Capitaine and M. Soffel)

Bize S. (invited): *Highly precise clocks to test fundamental physics*

Hobiger T., Koyama Y., Hanado Y., Ichikawa R., Sekido M., Böhm J. and Sun J.: *On the potential of VLBI2010 for time and frequency transfer*

Dimarcq N.: *High performance time & frequency transfer techniques for remote clocks comparisons*

Soffel M., Tian W.: *Relativity and large ringlaser gyroscopes*

Lambert S.B., le Poncin-Lafitte C.: *On general relativity tests with the VLBI*

Soja B., Plank L., Schuh H.: *General relativistic delays in current and future VLBI*

13:00–14:00: Lunch break

14:00–16:00: Session 2 – Towards the next generation of space-time reference systems
(Chair: J. Vondrk and Y.S. Yatskiv)

Mignard F. (invited): *From the Gaia frame to an ICRF-3?*

Manchester R.N., Hobbs G. (invited): *Pulsar timing and a pulsar-based timescale*

Yatskiv Y.S.: *One possible realization of the ICRF before the Gaia frame*

Malkin Z., Schuh H., Ma C., Lambert S.: *Terrestrial and celestial reference frames: Synergy and mutual impact*

Bourda G., Charlot P.: *Plans for an accurate alignment of the VLBI frame and the future Gaia frame*

Taris F., Andrei A., Klotz A., Vachier F., Côte R., Souchay J.: *Optical monitoring of extragalactic sources for the link between the ICRF and the future Gaia celestial reference frame*

Jacobs C., Majid W., Romero-Wolf A., Sotuela I., Garcia-Miro C., Horiuchi S., Neidhart A., Kronschnabl G., Schreiber U., Porcas R., Kraus A., Gomez-Gonzalez J., Lopez-Fernandez J.A., Colomer F., de Vicente P., Lovell J., Natusch T., Gulyaev S., Zharov V., Takeuchi H., Ichikawa R.: *The Potential for a Ka-band (32 GHz) worldwide VLBI network*

Pavlis E.C., Kuzmicz-Cieslak M., Hinkey P.M.: *Forthcoming improvements in SLR data analysis: Towards the mm SLR*

Romero-Wolf A., Jacobs C.: *Effects of tropospheric spatio-temporal correlated noise on the analysis of space geodetic data*

16:00–18:00: POSTER SESSION

18:00–18:45: Welcome Drink

Tuesday, 20 September 2011

09:00–11:00: Session 3 – Modelling, observation and prediction of Earth rotation and global geodynamics
(Chair: A. Brzezinski and V. Dehant)

Böhm S., Nilsson T., Schindelegger M., Schuh H. (invited): *Atmospheric and oceanic excitation of Earth rotation*

Koot L. (invited): *Constraints on the structure and dynamics of the Earth's deep interior inferred from nutation observations*

Seitz F.: *Simulation, prediction and analysis of Earth rotation parameters with a dynamic Earth system model*

Dehant V., Folgueira M., Puica M.: *Analytical computation of the effects of the core-mantle boundary topography on tidal length-of-day variations*

Gross R.S.: *Improving UT1 predictions using short-term forecasts of atmospheric, oceanic, and hydrologic angular momentum*

Bizouard C.: *Asymmetric excitation of the polar motion*

Stamatakos N., Luzum B., Carter M.S., Stetzler B., Shumate N., Tracey J.: *Recent improvements in the IERS Rapid Service Prediction Center products*

Kaufman M., Pasynok S.: *Rapid EOP calculations using VieVS software*

11:00–11:30: Coffee break

11:30–13:00: Session 3 (continuation)
(Chair: A. Brzezinski and V. Dehant)

Brzezinski A., Böhm S.: *Analysis of the high frequency components of Earth rotation demodulated from VLBI data*

Chapanov Y., Vondrák J., Ron C.: *A model of centennial oscillations of the Earth rotation based on total solar irradiance variations*

Schindelegger M., Böhm J., Salstein D., Schuh H.: *The signature of atmospheric tides in sub-daily variations of Earth rotation as unveiled by globally-gridded atmospheric angular momentum functions*

Dobslaw H., Kadow C., Matthes K., Thomas M.: *Impact of atmospheric tides on subdiurnal length-of-day variations*

Panafidina N., Rothacher M.: *Empirical model of subdaily variations in the Earth rotation from GPS and its stability*

Nilsson T, Böhm J., Schuh H.: *Determination of Earth rotation by combining VLBI and ringlaser observations*

13:00–14:00: Lunch break

14:00–16:00: Session 4 – Celestial mechanics of solar system bodies
(Chair: C. Hohenkerk and J. Souchay)

Escapa A. (invited): *Analytical modeling of the rigid internal motions of a three-layer celestial body through Hamilton's Principle*

Hilton J. (invited): *Progress report of the IAU Commission 4 Working Group on Ephemeris Access and the comparison of high accuracy planetary ephemerides*

Weratschnig J.M., Stewart S.G., Hilton J.L.: *New additions to the astronomical almanac-ephemeris data of dwarf planets*

Kudryavtsev S.M.: *Precision analytical calculation of effect of the solid Earth tides on satellite motion*

Pashkevich V.V., Eroshkin G.I.: *Construction of the numerical and semi-analytical solutions of the Moon rotation*

Ivanova T.V.: *Taking into account the planetary perturbations in the Moon's motion*

Yagudina E.I., Krasinsky G.A., Prokhorenko S.O.: *EPM-ERA 2011 Lunar theory and selenodynamical parameters from LLR data*

Bazso A., Galiazzo M.: *Lunar effects on close encounters of Hungarias with the Earth*

16:00–16:30: Coffee break

16:30–17:00: Session 4 (continuation)
(Chair: C. Hohenkerk and J. Souchay)

Dvorak R., Lhotka Ch., Zhou L.Y.: *On the stability of Earth's Trojans*

Baudisch H., Dvorak R.: *Where are the Saturn Trojans?*

17:00–18:00: Discussion – On future IAU recommendations and organization: Presentation of Topics
(Chair: D.D. McCarthy)

McCarthy D.D.: *Introduction*

Capitaine N.: *Astronomical unit*

Urban S.: *Nomenclature for current precession and nutation models*

Hilton J.: *Standardizing access to ephemerides*

McCarthy D.D.: *IAU structure*

19:00–21:30: CONFERENCE DINNER

Wednesday, 21 September 2011

09:00–10:30: Session 5 – Space observations and dedicated missions for geodesy and astronomy
(Chair: R. Gross and H. Schuh)

Rummel R. (invited): *GOCE: Its principles and science*

Hase H., Behrend D., Ma C., Petrachenko W., Schuh H., Whitney A. (invited): *The future global VLBI2010 network of the IVS*

Biancale R., Gambis D., Richard J.-Y., Seitz M.: *Activity of the Combination at Observation Level Working Group*

Zharov V.E., Girin I.A., Kostenko V.I., Likhachev S.F.: *Estimation of the ground-space interferometer parameters during Radioastron mission*

Pavlis E.C., Ciufolini I., Paolozzi A.: *LARES: A new mission to improve the measurement of lense-thirring effect with Satellite Laser Ranging*

Lovell J., McCallum J., Shabala S., Dickey J., Watson C., Titov O.: *The AuScope VLBI Array*

11:00–11:30: Coffee break

11:00–12:00: Discussion – On future IAU recommendations and organization: Discussion
(Chair: D.D. McCarthy)

Nomenclature
Astronomical unit
Standardizing access to ephemerides
Summary

12:00–12:15: Closing of the Journées 2011

LIST OF POSTERS

Session 1 – Fundamental astronomy, time and relativity

1.1 – Capitaine N., Folgueira M.: *Semi-analytical integration of the Earth's precession-nutation based on the GCRS coordinates of the CIP unit vector*

1.2 – Laloum M.: *Time nature and symmetry: Balance of the Galaxy*

1.3 – Lambert S.B.: *Status of the GLORIA geodetic VLBI analysis software package*

1.4 – Sekowski M., Krynski J.: *Methods of use and presentation of the accurate astrometric data based on the modern terrestrial and celestial reference systems*

Session 2 – Towards the next generation of space-time reference systems

2.1 – Clark J.E., Garcia-Miro C., Horiuchi S., Jacobs C.S., Romero-Wolf A., Sotuela I.: *The contribution of X/Ka-band VLBI to multi-wavelength studies of the Celestial Frame*

2.2 – Damljanovic G., Milic I.S.: *CCD measurements in optical domain and astrometric positions of ICRF2 radio sources*

2.3 – Lambert S.B.: *On the processing of VLBI intensive sessions*

2.4 – Marco F.J., Martinez M.J.: *Statistics and analytic compatibility to joint catalogs with a set of common ICRF defining sources*

2.5 – Mora-Diaz J.A., Heinkelmann R.: *Source structure correction in geodetic VLBI*

Session 3 – Modelling, observation and prediction of Earth rotation and global geodynamics

3.1 – Chapanov Y., Schuh H., Nothnagel A., Böhm J.: *Climatic and solar activity cycles influences on interannual and decadal variations of VLBI stations*

3.2 – Choliy V., Zhaborovsky V.: *KG++ software for processing Satellite Laser Ranging observations*

3.3 – Choliy V.: *On the usage of XML file format in geodynamic calculations*

3.4 – Gambis D., Salstein D., Chapanov Y.: *Some systematic errors in AAM and OAM data*

3.5 – Kaufman M., Pasynok S.: *Tropospheric delays from GPS and VLBI data*

3.6 – Kolaczek B., Pasnicka M., Nastula J.: *Analysis of the geodetic residuals as differences between geodetic and sum of the atmospheric and ocean excitation of polar motion*

3.7 – Krynski J., Zanimonskiy Y.M.: *Geodynamic signals in time series of astrometric observations at Borowa Gora Observatory*

3.8 – Malkin Z.: *On the impact of the galactic aberration on VLBI-derived precession model*

3.9 – Malkin Z., Tissen V.: *Accuracy assessment of the ERP prediction method based on analysis of 100-year ERP series*

3.10 – Marčeta D., Šegan S., Glišović N.: *Detection of the mutual periodical changes in the Earth rate of rotation and the solar activity by singular spectrum analysis*

3.11 – Martinez M.J., Marco F.J.: *Non regular variations in the LOD from European medieval eclipses*

3.12 – Nagalski T.: *Comparison of polar motion excitation function derived from EWT, obtained from filtered Stokes coefficients*

3.13 – Nerge P., Ludwig T., Thomas M., Jungclaus J., Sündermann J., Brosche P.: *GeOGEM - Simulations to the tides of ancient oceans and the evolution of the Earth-Moon-system*

3.14 – Ron C., Vondrák J.: *Comparison of the geophysical excitations with the observed celestial pole offsets*

3.15 – Yao K., Capitaine N., Lambert S.: *Using VLBI and GNSS observations for nutation estimation*

Session 4 – Celestial mechanics of solar system bodies

Session 1:

Fundamental astronomy, time and relativity

Astronomie fondamentale, temps et relativité

THE SECULAR ABERRATION DRIFT AND FUTURE CHALLENGES FOR VLBI ASTROMETRY

O. TITOV
Geoscience Australia
PO Box 378, Canberra, 2601, ACT, Australia
e-mail: oleg.titov@ga.gov.au

ABSTRACT. The centrifugial acceleration of the Solar system, resulting from the gravitational attraction of the Galaxy centre, causes a phenomenon known as 'secular aberration drift'. This acceleration of the Solar system barycentre has been ignored so far in the standard procedures for high-precision astrometry. It turns out that the current definition of the celestial reference frame as epochless and based on the assumption that quasars have no detectable proper motions, needs to be revised. In the future, a realization of the celestial reference system (realized either with VLBI, or GAIA) should correct source coordinates from this effect, possibly by providing source positions together with their proper motions. Alternatively, the galactocentric acceleration may be incorporated into the conventional group delay model applied for VLBI data analysis.

1. SECULAR ABERRATION DRIFT

This barycentre reference system was adopted by the International Astronomical Union as the International Reference System (ICRS). The Very Long Baseline Interferometry (VLBI) technique measures precise group delay differences in arrival times of radio waves at two radio telescopes and produces very accurate coordinates of the reference radio sources. The ICRS is based on a set of theoretical concepts. Practical realization of the ICRS - International Celestial Reference Frame (ICRF) is presented in a form of astrometric catalogue of the reference radio source accurate coordinates.

The second realization of the ICRF (ICRF2) contains 295 "defining" sources (Fey, Gordon and Jacobs, 2009). The floor error of the most observed radio sources among the 295 ICRF2 "defining" is about 41 μas. The median error for 1217 radio sources (295 "defining" and 922 "non-defining") was found to be 174 μas in right ascension and 194 μas in declination.

All the reductions for high-precision VLBI data are done in the reference system with an origin in the barycentre of the Solar system. In this definition, the axes of the ICRS are defined by the adopted positions of a specific set of extragalactic objects (presumably, very distant quasars), which are assumed to have no measurable proper motions. However, the acceleration of the Solar System barycenter would cause a dipole systematic effect in the proper motion described by the first order electric type vector spherical harmonic with magnitude of 4–6 μas/yr. After an early mention by Fanselow (1983), this effect known as secular aberration drift (SAD) was discussed in more detail later (e.g. Bastian, 1995; Gwinn et al., 1997; Sovers et al., 1998; Kovalevsky, 2003; Kopeikin and Makarov, 2006). Finally, it has been confirmed, for the first time, by Titov, Lambert & Gontier (2011) by the least squares adjustment of the apparent proper motion of 555 reference radio sources. Its magnitude, 6.4 ± 1.5 μas/yr, corresponds to the Galactocentric acceleration of $(3.2 \pm 0.7) \times 10^{-13}$ km/s^2, in good agreement with the theoretical predictions.

Figure 1 displays $\mu_\alpha \cos\delta$ versus α for the 40 astrometricaly stable radio sources observed in more than 1,000 sessions. The plot reveals dipole systematic effect even without adjustment by the least squares. Individual proper motions of 555 radio sources are shown in Figure 2. Though, no systematic effect is observed in this plot, the least squares found the dipole as on Figure 3.

Independent analysis of the SAD was done using 328 individual proper motions obtained by Vladimir Zharov using the alternative software ARIADNA (Zharov et al. 2010). The magnitude estimate is 4.8 ± 1.4 μas/yr, and coordinates of the acceleration vector are estimated as $270^\circ \pm 30^\circ$ in right ascension and $-54^\circ \pm 17^\circ$ in declination. The consequences of the secular aberration drift discovery are discussed in this paper.

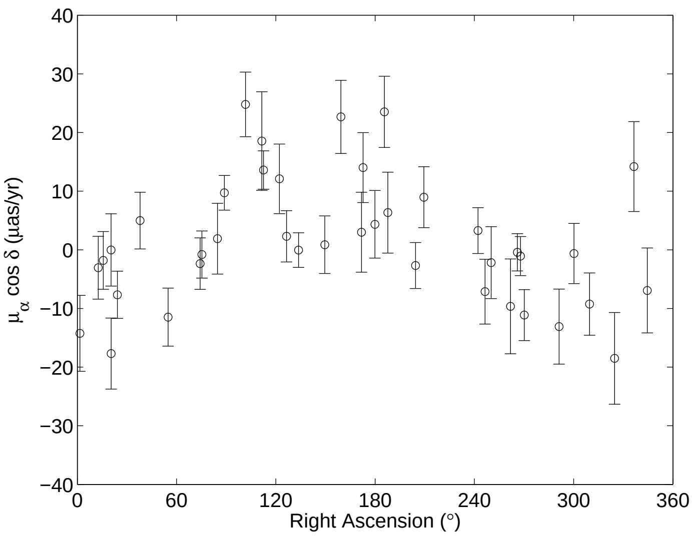

Figure 1: The proper motion in right ascension vs. the right ascension of 40 sources observed in more than 1000 sessions.

2. FUTURE CHALLENGES FOR VLBI ASTROMETRY

In accordance with the IAU Resolutions, the adopted International Celestial Reference System (ICRS) is quasi-inertial, i.e. its fundamental axes do not rotate. However, acceleration of the origin is allowed, in opposition to the definition of the inertial reference system. This theoretical concept of the quasi-inertial system is realised in a form of the catalogue of accurate coordinates of extragalactic radio sources, known as ICRF2 (Fey, Gordon and Jacobs, 2009). Directions of the fundamental axes are fixed by positions of the 295 ICRF2 "defining" radio sources. This theoretical concept of quasi-inertiality as well as practical efforts for production of new catalogues are used to focus on control of the net rotation which may be induced by the variations of the intrinsic structure of the radio sources. All the non-rotational systematic effects in proper motions were considered to be negligibly small and, eventually, ignored. As a result, the No-Net-Rotation constraints which are commonly used to suppress the forbidden rotational systematic also suppress the dipole systematic effect, theoretically allowed. Nonetheless, due to unprecedented improvement of the geodetic VLBI data precision, the dipole systematic effect should not be ignored. Otherwise, the conventional reductional model would become increasingly inadequate. Therefore, the geodetic VLBI faces three challenges which should be solved in near future.

2.1. How To Implement This Effect?

The dipole proper motion induced by the SAD would result in displacement of the actual positions of the reference radio sources from the positions published in catalogues, i.e. ICRF2. This displacement may reach 130 μas over the 20-year period of observations, exceeding the 3-σ level of the ICRF2 floor error (41 μas). If this effect is ignored, estimates of some other parameters may be biased, for instance, corrections to the nutation angles, or the variations UT1-UTC estimated from the Intensive sessions. Therefore, it is reasonable to discuss a possible way to implement the SAD in the conventional procedure of VLBI data reductions.

One possibility is to introduce the dipole proper motion for all reference radio sources as an extension to their ICRF2 coordinates. For a distant body of equatorial coordinates (α, δ), the proper motions are estimated as follows

$$\begin{aligned} \Delta\mu_\alpha \cos\delta &= -d_1 \sin\alpha + d_2 \cos\alpha, \\ \Delta\mu_\delta &= -d_1 \cos\alpha \sin\delta - d_2 \sin\alpha \sin\delta + d_3 \cos\delta, \end{aligned} \tag{1}$$

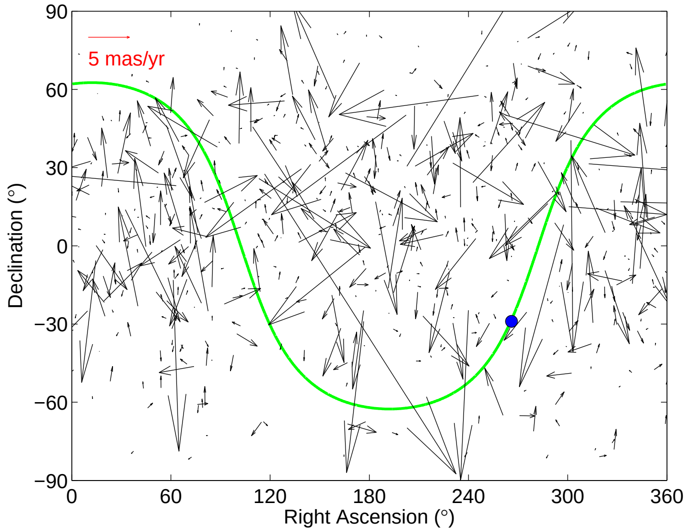

Figure 2: The proper motions of the 555 sources. The green curved line represents the equator of the Milky Way, whose center is indicated by the large blue point.

where the d_i are the components of the acceleration vector in unit of the proper motion calculated as

$$
\begin{aligned}
d_1 &= d\cos\alpha_0\cos\delta_0 \\
d_2 &= d\sin\alpha_0\cos\delta_0 \\
d_3 &= d\sin\delta_0,
\end{aligned} \tag{2}
$$

where d is the magnitude of the SAD, and $(\alpha_0,\ \delta_0)$ — apparent equatorial coordinates of the Galactic centre.

This approach will result to moving away from the attractive idea of the treatment the extragalactic radio sources as fixed fiducial points on the celestial sphere. It may not be appropriate to introduce the systematic proper motion for the radio reference frame only, but keeping in mind the future space astrometric missions (i.e. GAIA, see Perryman et al., 2001; Mignard, 2002), it should be considered as one of the possible options.

Another possibility is to revise the conventional group delay model developed about 20 years ago and recommended by the IERS and IAU (Kopeikin, 1990; Soffel et al. 1991). It was shown (Titov 2010) that SAD may be implemented by the replacement of the barycentric velocity vector $\vec{V}$ by the sum $\vec{V} + \vec{a}\Delta t$, where $\vec{a}$ is the vector of Galactocentric acceleration and Δt is the period of time since an initial epoch. This approach keeps the extragalactic radio sources technically free of the apparent transversal motion. However, it is suitable only for the reduction of the geodetic VLBI data, and it is not clear how to proceed with the data from the space astrometric missions. More detailed analysis of this problem should be initiated to determine the most appropriate solution.

2.2. Are There More Systematic Effects?

Apart from the SAD, more systematic effects may be detected, although with a smaller chance of success. The quadrupole component may come either from the Hubble constant anisotropy or the primordial gravitational waves (i.e. Kristian & Sachs 1966; Eubanks, 1991; Pyne et al., 1996; Gwinn et al. 1997; Book & Flanagan, 2011). Observational results impose constraints on the upper limit of the quadrupole systematic effect (3 μas/yr for a 3-σ standard error (Titov, Lambert & Gontier 2011). The amplitude spherical harmonics were estimated to be very close to the 3-σ level, therefore, it will be useful to check these parameter after collection of more observational data.

The rotational harmonics are unlikely to be separated from the Earth orientation parameters. Although, the differential rotation possible within of a scope of the formula by Kristian and Sachs (1966),

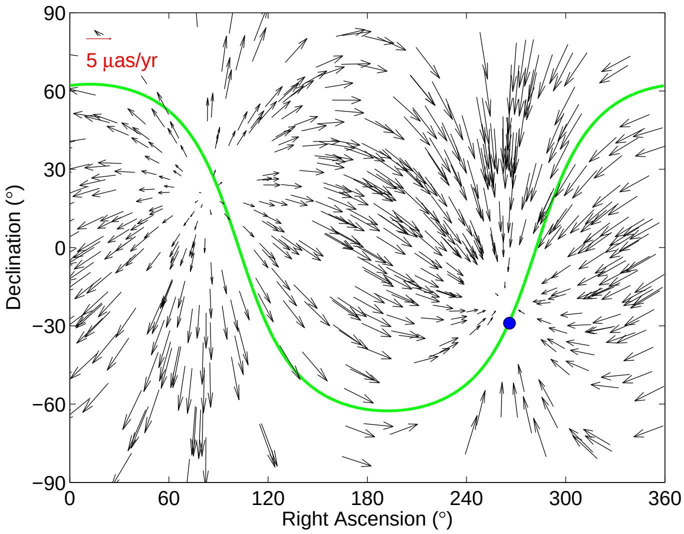

Figure 3: The estimated dipole component of the velocity field.

$$
\begin{aligned}
\frac{de^{\mu}}{dt} =& h^{\mu\nu}\Big\{e^{\beta}(\sigma_{\nu\beta}+\omega_{\nu\beta})+r\Big[e^{\beta}(\sigma_{\nu\beta}+\omega_{\nu\beta})u_{\mu\nu}-e^{\beta}E_{\mu\nu} \\
&+\frac{1}{2}e^{\beta}e^{\gamma}(u_{\nu\beta\gamma}-\epsilon_{\nu\beta\gamma}H_{\mu\nu})+e^{\beta}e^{\gamma}e^{\lambda}(\sigma_{\nu\gamma}+\omega_{\nu\gamma})\sigma_{\beta\lambda}\Big]+...\Big\}
\end{aligned}
\tag{3}
$$

may be disclosed. Where σ - notation for the shear tensor, ω - for the rotation tensor, E, and H - for the tensors describing the electric and magnetic-type gravitational waves, respectively. The distance r before the squared brackets means that if at least one of the tensors in not negligible at level of μas/yr, then the corresponding component will increase for more distant radio sources. Kristian and Sachs (1966) considered the case of gravitational waves with wavelengths of the Universe size $\lambda_{Gr} \sim R_{Un}$. Later papers argued that if $\lambda_{Gr} < R_{Un}$, then the corresponding spherical harmonics are independent of the distance (Pyne, 1996; Gwinn et al., 1997; Book & Flanagan, 2011). So, the first part of Equation (3) should be developed as follows

$$
\frac{de^{\mu}}{dt} = h^{\mu\nu}\left\{e^{\beta}(\sigma_{\nu\beta}+\omega_{\nu\beta})-e^{\beta}E_{\mu\nu}+\frac{1}{2}e^{\beta}e^{\gamma}(u_{\nu\beta\gamma}-\epsilon_{\nu\beta\gamma}H_{\mu\nu})\right\} \tag{4}
$$

The spherical harmonics of order three (octopole) and higher accommodate only 15 % of the total power of the gravitational waves (Gwinn et al., 1997), and we have not found statistically significant harmonics in the proper motion analysis. Nonetheless, these higher harmonics may be still studied in future. To estimate the distance-dependent effects in the spherical harmonics, more proper motions at redshift $z > 2$ are required to be measured.

2.3. Challenge 3. "Observational"

The proper motions of 555 radio sources have been used so far to estimate the SAD components by use of the least squares method, increasing the figure to 2000 will improve the formal accuracy by a factor of two. In fact, several thousand radio sources were observed in one or two VCS sessions (VLBI Calibrator Survey) for the last decade (i.e. Beasley et al., 2002). Therefore, we are able to calculate new proper motions by undertaking regular observations of the VCS sources in further one–two sessions separated from the original epochs by a sufficient time span.

The mutual correlation between different spherical harmonics will vanish for homogeneous coverage of the celestial sphere with observational data. Unfortunately, the shortage of proper motions for the radio sources around the South Pole leads to a correlation between parameters in the matrix of normal equations (Titov & Malkin, 2009). This correlation could be reduced by increasing the data at this zone of the celestial sphere. It is planned to use the Australian VLBI network (AuScope) and New

Zealand station Warkworth (Lovell et al., 2010) for regular observations of those radio sources which have comparatively strong flux (> 0.4 Jy) but are observed only occasionally.

3. CONCLUSION

Appearance of the systematic effects in the apparent proper motion of extragalactic radio sources observed with Very Long Baseline Interferometry requires a revision of some basic assumptions used for many years to establish the fundamental reference frame. The gravitational acceleration of the Solar system barycentre needs to be incorporated to the analytical models for high-precision astrometric data reduction. More work needs to be done in theory, in observations and in data analysis to reveal the small signals with confidence. In particular, observations of the quasars in the southern hemisphere are highly essential.

Acknowledgements. We are thankful to Vladimir Zharov for providing the independent results from the ARIADNA software and Laura Stanford for help in preparation of the manuscript. This paper has been published with permisson of the Geoscience Australia CEO.

4. REFERENCES

Bastian, U. 1995, "Direct detection of the Sun's galactocentric acceleration", In: M. A. C. Perryman & F. Van Leeuwen (Eds.), Proc. RGO-ESA Workshop on Future Possibilities for Astrometry in Space, ESA SP-379, 99.

Beasley, A. J., Gordon, D., Peck, A. B., et al. 2002, "The VLBA Calibrator Survey-VCS1", AJSupp141, pp. 13–21.

Book, L.G., Flanagan, E., 2011, "Astrometric Effects of a Stochastic Gravitational Wave Background", Phys. Rev. D, 83(2).

Eubanks, T. M., 1991, "A consensus model for relativistic effects in geodetic VLBI", In: Proceedings of the U.S. Naval Observatory Workshop on Relativistic Models for use in Space Geodesy, pp. 60–82.

Eubanks, T. M., 1991, "Astrometric Cosmology using Radio Interferometry", In: Proc. of 179th AAS Meeting, Atlanta, Georgia, p. 1465.

Fanselow, J. L. 1983, "Observation Model and Parameter Partials for the JPL VLBI Parameter Estimation Software MASTERFIT-V1.0", JPL Publication 83-39.

Fey, A. L., Gordon, D. G., & Jacobs, C. S. (Eds.) 2009, "The Second Realization of the International Celestial Reference Frame by Very Long Baseline Interferometry", Presented on behalf of the IERS / IVS Working Group, International Earth Rotation and Reference Systems Service (IERS) Technical Note 35, Frankfurt am Main: Verlag des Bundesamts für Kartographie und Geodäsie.

Gwinn, C. R., Eubanks, T. M., Pyne, T., et al., 1997, "Quasar proper motions and low-frequency gravitational waves", ApJ485, pp. 87–91.

Kopeikin, S. M., & Makarov, V. V. 2006, "Astrometric effects of secular aberration", AJ 131, pp. 1471–1478.

Kopeikin, S. M., 1990, "Theory or relativity in observational radio astronomy", Sov. Astron. 34(1), pp. 5–10.

Kovalevsky, J. 2003, "Aberration in proper motions", A&A 404, pp. 743–747.

Kristian, J., & Sachs, R. K. 1966, "Observations in cosmology", ApJ, 143, pp. 379–399.

Lovell, J., Dickey, J., Gulyaev, S., et al. 2010, "The AuScope project and Trans-Tasman VLBI", In: D. Behrend & K. D. Baver (Eds.), Proc. of the 2010 IVS 6th General Meeting, pp. 50–54.

Mignard, F. 2002, "Fundamental Physics with GAIA", In: O. Bienaymé & C. Turon (Eds.), GAIA: A European Space Project, EAS Publication Series, 2, pp. 107–121.

Perryman, M. A. C., de Boer, K. S., Gilmore, G., et al. 2001, "GAIA: Composition, formation and evolution of the Galaxy", A&A 369, pp. 339–363.

Pyne T., Gwinn, C.R., Birkinshaw, M., et al., 1996, "Gravitational radiation and Very Long Baseline Interferometry", ApJ, 465, pp. 566–577.

Soffel, M. H., Muller, J., Wu, X., & Xu. C., 1991, "Consistent Relativistic VLBI Theory with Picosecond Accuracy", AJ 101, pp. 2306–2310.

Sovers, O. J., Fanselow, J. L., Jacobs, C. S. 1998, "Astrometry and geodesy with radio interferometry: experiments, models, results", Rev. Mod. Phys. 70, pp. 1393–1454.

Titov, O., 2009, "Systematic effects in the radio source proper motion", In: G. Bourda et al. (Eds.), Proc. 19th European VLBI for Geodesy and Astrometry (EVGA) Working Meeting, pp. 14–18.

Titov, O., 2010, "Estimation of the Acceleration of the Solar-System Barycenter Relative to a System of Reference Quasars", Astronomy Reports 55, pp. 91–95.

Titov, O., Malkin, Z., 2009, "Effect of asymmetry of the radio source distribution on the apparent proper motion kinematic analysis", A&A 506, pp. 1477–1485.

Titov, O., Lambert, S., & Gontier A.-M., 2011, "VLBI measurement of secular aberration drift", A&A 529, pp. A91–A97.

Zharov, V., Sazhin, M., Sementsov, V., & Sazhina, O. 2010, "Long-term Variations of the EOP and ICRF2", In: D. Behrend & K. D. Baver (Eds.), Proc. of the 2010 IVS 6th General Meeting, pp. 290–294.

PARESC'S HIGH PRECISION ASTROMETRY - THE MAKING OF

B. BUCCIARELLI[1], A.H. ANDREI[1,2,4,5], R.L. SMART[1], U. SCHIROSI[1],
M. DAPRA[1], M.G. LATTANZI[1], J.L. PENNA[2], D.N. DA SILVA NETO[3]

[1] INAF-OATo Osservatorio Astronomico di Torino
Strada Osservatorio 20, 10025 Pino Torinese, TO, Italy
e-mail: bucciarelli@oato.inaf.it

[2] ON/MCT Observatorio Nacional, Brazil

[3] UEZO Universidade Estadual da Zona Oeste, Brazil

[4] SYRTE/OP Observatoire de Paris, France

[5] Observatorio do Valongo/UFRJ, Brazil

ABSTRACT. The core of the PARSEC (Parallaxes of Southern Extremely Cool Objects) program aims at delivering trigonometric parallaxes for over 100 brown dwarfs with an average magnitude of ~ 17.3 in the z band. Stringent observing criteria and careful data treatment, endowed with the current best reference catalogues as calibrators, allow to achieve 5-mas accuracy on position, proper motion and parallactic shift. Astrometric parameters are derived by means of three different approaches, testing in such a way the robustness of the solution. The issues of CCD fringing removal, object matching and choice of the reference observation are addressed. Further observational campaigns recently undertaken to increase the size of the sample and push its average magnitude towards fainter regimes will allow to determine absolute distances of brown dwarfs down to the later T spectral sub-classes, where independent data are mostly needed for understanding their evolution.

1. SCIENCE DRIVERS AND PROGRAM OUTLINE

Understanding extremely low-mass stellar astrophysics is a major goal of current studies of brown dwarfs. Absolute distances are fundamental to determining model-independent temperatures for these sub-stellar objects, hence properly placing them on the color-magnitude diagram. The interpretation of the cooling sequences defined by brown dwarfs in the HR diagram is complicated by an intrinsic mass/age/luminosity degeneracy: older, more massive objects cannot be distinguished from younger, less massive ones. As a consequence, their Luminosity Function is a result of a combination of their Initial Mass Function and their Star Formation History. It appears evident that, while independent methods must be devised in order to constrain the mass/age parameters, trigonometric parallaxes are key quantities to help disentangling such a degeneracy. Ultimately, because of their large number, ubiquity and long-lasting evolution, brown dwarfs represent an especially interesting class of objects for a variety of Galactic studies. More specifically, cold brown dwarf astrophysics is particularly relevant to "hot" science topics such as

- Tests of current atmospheric and evolutionary models of extremely low-mass objects
- Changes of atmospheric processes according to temperature, chemistry, mass and age variations, and their affinity to gas giant planets atmospheres
- Contribution to the Galaxy thin disk, thick disk and halo populations and impact on the history of Galaxy formation

With these objectives in mind, the PARSEC program and its successors, NPARSEC, an ESO Large Program proposal, and IPERCOOL, a Marie Curie FP7 European Community Grant gathering the expertise in the field from Italy, England, China and Brazil, are realizing the largest homogeneous dataset comprising astrometric and astrophysical parameters of L and T dwarfs, which shall be exploited to address some of the above issues.

Until the early 2000's, parallax programs of T dwarfs were operating in a "discovery" mode, by responding to new detections of cooler and cooler temperatures, with the result of becoming biased toward low luminosity objects (Smart 2009). More recently, new available infrared surveys, such as UKIDSS, CFBDS and WISE, have significantly increased the number of known T dwarfs, furthermore extending the spectral range to T9 and beyond. Building on these surveys' assets, our target list has been culled with the goal of providing statistically significant samples in all sub-classes, while still having the potential to rapidly follow up on newly discovered interesting objects. The PARSEC program (Andrei et al. 2011) was executed using the WFI imager (30-arcmin FOV) + z filter (0.964 μm) of the ESO 2.2-m, and was concluded at the beginning of 2011 just when the NPARSEC program, concerning fainter objects, took start at the ESO NTT with the SOFI imager (5-arcmin FOV) + J filter (1.247 μm). In Figures 1 and 2 the distribution of our targets as function of spectral class and magnitude is displayed.

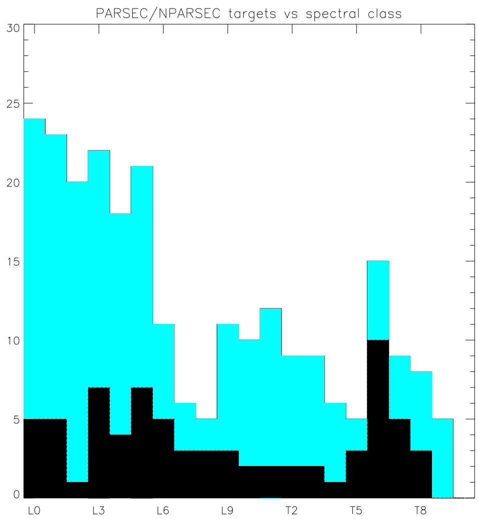

Figure 1: Distribution of PARSEC/NPARSEC targets as function of spectral class (light shadow) and, for comparison, brown dwarf parallaxes from literature data (in black)

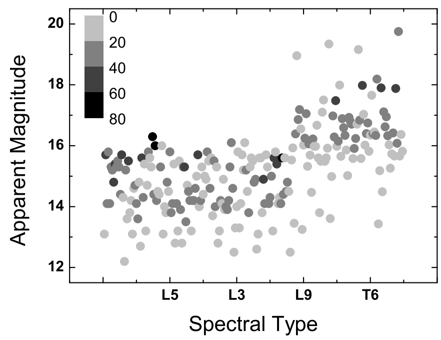

Figure 2: Targets' J magnitude vs spectral type; the gray scale indicates the object's distance in parsecs

2. DATA REDUCTION

We will focus here on the calibration procedures adopted for the WFI camera, since the reduction of SOFI data is still in a preliminary stage. The initial image treatment uses standard IRAF routines for bias and flat subtraction. However, fringing removal required a tailored approach. The interference fringes in the infrared images of the WFI camera are severe: an examination of the counts shows they can vary by up to 10% over the distance of a few pixels. The ideal case would be to make a fringe map for each image: since this was not feasible, our compromise was to make a nightly fringe map whenever possible. The details of our technique are given in Andrei et al. (2011). We emphasize here that a suitable subset of images scaled by their exposure time is selected to make an initial fringe map, removing in such a way most of the fringe patterns; thereafter, the same subset of pre-cleaned images is combined into a final fringe map by adopting the image mean counts as scale factor in order to take into account the sky-dependent intensity of the fringe pattern as well. Figure 3 illustrates a comparison between object centroiding errors using a standard fringe map (as provided by ESO) and ours showing a sensible improvement. All the objects identified on each CCD frame are measured using Robin, a CCD software package developed at OATo (Lanteri 1990), which estimates their centroiding x,y; then, positions from different frames/epochs are cross-matched by means of a low-order polynomial fit, before feeding them to the astrometric model. There are presently several sky surveys that could be combined to our data to provide longer time coverage, when desirable; moreover, multi-band photometry is extremely useful to calibrate our observations, which are limited to one filter only. For this, we intend to exploit catalogs like 2MASS, SDSS, GSC-2, and possibly WISE to extend the astrometric and photometric calibrations to the full field of view, where other objects of interest also appear, with particular attention to the wide WFI CCD field. In order to match observations spanning a long time interval, where usual cone search strategies might fail, we adopt a more sophisticated procedure which assigns higher priority to objects with low proper motion and better positional accuracy, removes matched stars and re-starts the process, also allowing for periodical signatures.

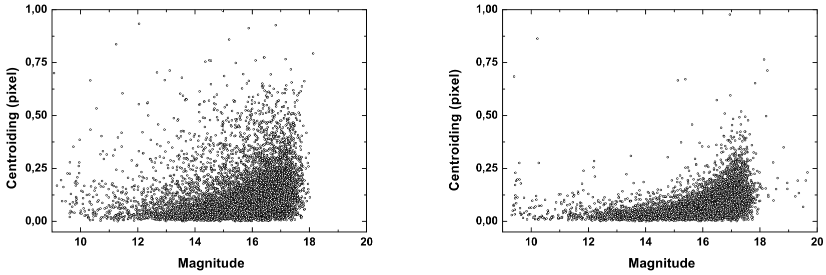

Figure 3: Image centroiding errors (in pixels) vs object magnitude with a standard fringe removal (left) and with our taylored procedure (right)

3. ASTROMETRIC SOLUTION

We have developed three methods for the derivation of the target's parallax, checking in this way the robustness of the solution. The canonical approach is to express the stellar motions in equatorial standard coordinates and to build a system of equations which includes the astrometric parameters of all stars and the instrumental parameters of all frames, the latter suitably modelled by a first order polynomial. In this case, the observation equation for the longitudinal standard coordinate of a generic star on a frame i reads:

$$-x_i = a_i x_i + b_i y_i + c_i - \xi_0 - \mu_\xi (t_i - t_0) - P_{\xi_i} \pi_\xi$$

where (x_i, y_i) are the object's image centroid, t_0 a chosen reference epoch and P_{ξ_i} the parallax factor (Bucciarelli et al. 2010). The parameters to be estimated are ξ_0, μ_ξ, π_ξ, i.e., the star position at t_0, its longitudinal proper motion and its parallax, and the instrumental coefficients a, b, c mapping each frame onto the tangential plane. We have tackled the intrinsic rank deficiency of this problem using two solution techniques: a block iterative one, which is naturally convergent without the need of constraint equations, and a direct one requiring nine additional constraints to fix the solution (Bucciarelli et al. 2010). A different approach consists in using field stars to tie all frames together and then solving for the astrometric parameters of the target star, as detailed in the following. If all frames were equivalent, an equivalent result would be obtained adopting any frame as the reference one, but despite our emphasis on image quality, adequacy and repeatability, the choice is not immaterial; therefore, we have investigated this issue using simulated data. We generated the observations of a typical PARSEC set of a patch of sky imaged twice nightly for 26 nights, with up to 800 stars per image. As we wanted to establish a guideline for the definition of the reference frame in the presence of observational errors, we disregarded systematic effects, so the fake stars have no proper motion, parallax, or movements due to the reference system. Also, the size or time interval of the frames is unimportant. On the other hand, using the outcomes of a Gaussian noise generator, stars could appear and disappear from one frame to another, centroiding errors were assigned, plus terms accounting for tilt and telescope pointing. The fake stars were placed over a regular grid so that their matching in different frames only depended on the repeatability of their position (and not on the performance of a recognition algorithm). The average value resulting from a Monte Carlo simulation of 1,000 runs are shown in Table 1. Results are given for a basis frame corresponding to the first one observed, or the densest one, or yet a fictitious *mean* frame. The poorest choice is to adopt the first frame observed. The densest and the mean frame lead to small differences, although the latter is about 10% better. Additionally, the operation of building a mean frame, though asking for additional computational effort, corresponds to an object matching task, which saves time in the following steps of data reduction.

Solution	Stars Matched	Mean Precision (")
1^{st} frame	257 ± 76	0.0028 ± 0.0001
Densest frame	493 ± 128	0.0026 ± 0.0001
Mean frame	527 ± 134	0.0023 ± 0.0001

Table 1: For each choice of the basis frame, the number of stars found in every frame is given, and the standard deviation of the positional adjustment for those stars.

Once the ensemble of standard coordinates (ξ_{t_i}, η_{t_i}), t_i = epoch of observation, of the target star is on the same reference frame, it can be fitted with an elliptic motion modelling the parallactic effect superimposed to a linear term which accounts for the star's transversal motion. By adopting ecliptic coordinates, and neglecting the eccentricity of the Earth's orbit, the observation equation in ξ takes the simple form (and analogously for the η component)

$$\xi_{t_i}(x, y) = \pi_\xi sin(t_i + \phi_\xi) + \mu_\xi(t_i - t_0)$$

where π_ξ is the object's parallax, ϕ_ξ is a phase term, and t_0 the epoch of the reference frame. We note that, even if the effect of Earth eccentricity can be disregarded given the typical distances of our targets, it can be in principle computed and corrected for being a purely geometrical effect. As an example, we report the reduction of 6 years of observations (93 frames, 54 reference stars) of the high proper motion star LHS3482 (2MASS J19462386+3201021) with the three techniques giving very consistent results, as shown in Table 2. It can ben noted that the quoted errors are sensibily smaller in the case of the direct method. An explanation could lie in the fact the standard deviations coming from the covariance matrix are slightly underestimated, while in the other two cases, the errors are estimated from the residuals of the fit to the target's trajectory and could be more realistic indicators of the true errors.

Method	π (mas)	$\mu_\alpha\ cos\delta$ (mas/y)	μ_δ (mas/y)
Block interative	68.7 ± 4.0	458.8 ± 1.2	−391.2 ± 2.0
Direct LS	68.9 ± 0.8	457.5 ± 0.2	−390.4 ± 0.3
Ellipse fit	70.0 ± 3.2	467.7 ± 0.7	−392.0 ± 1.7

Table 2: The first two methods are variant of the canonical approach: in the first line the one used by the OATo parallax programs, in the second line a solution with all parameters derived at once using a robust least squares (LS) algorithm. The third line shows the results of a direct fit of the target star's trajectory on the ecliptic tangential plane.

Acknowledgements. A.H.A. thanks CNPq grant PQ-307126/2006-0, and the PARSEC International Incoming Fellowship within the Marie Curie FP7 Programme.

4. REFERENCES

Andrei, A.H., Smart, R.L., et al. 2011, "Parallaxes of Southern Extremely Cool Objects. I. Targets, Proper Motions, and First Results", AJ 141 p54.

Bucciarelli, B., Andrei, A.H., Smart, R.L. et al. 2010 "Absolute Parallaxes and Proper Motions from the PARSEC Program", in Journées 2010, Systèmes de Référence Spatio-Temporels, Paris, 22-23 September, pp. 105-108.

Lanteri, L. 1990, Robin Software, Tech. Rep. 16, Osservatorio Astronomico di Torino.

Smart, R.L. 2009, "Bron Dwarf Parallax Programs", in Mem. S.A.It. Vol. 80, pp. 674-677.

MORPHOLOGICAL CLASSIFICATION OF QSOs IN THE SDSS DR7 POPULATION

B. COELHO[1], A. ANDREI[4,6,7,8], S. ANTÓN[2,3], F. TARIS[4], D. DA SILVA NETO[5], J. SOUCHAY[4]

[1]Faculdade de Ciências, Universidade do Porto
Rua do Campo Alegre, 4169-007 Porto, Portugal
e-mail: bruno_coelho@mail.com

[2]CICGE, Faculdade de Ciências, Universidade do Porto, Porto, Portugal

[3]SIM, Faculdade de Ciências da Universidade do Lisboa, Campo Grande, Lisboa, Portugal

[4]SYRTE/OP - Observatoire de Paris, Paris, France

[5]UEZO - Universidade Estadual da Zona Oeste/Rio de Janeiro, Brazil

[6]ON/MCT - Observatorio Nacional, Brazil

[7]OATo/INAF - Osservatorio Astronomico di Torino, Italy

[8]OV/UFRJ - Observatorio do Valongo, Brazil

ABSTRACT. The luminosity of the central part of QSOs may surpass that of the entire host galaxy by two or three orders of magnitude. This is certainly true among the most extreme objects, and for that reason their host galaxy study has been limited to a small number of cases at relatively low redshifts. But even in the case of less luminous objects, and given the point-like scale of the central region, it is possible to pinpoint the host galaxy through the analysis of compound PSF. In the past, we proceeded to the analysis of SDSS QSOs, that clearly showed the signature of the host galaxy of QSOs on a statistical basis. That study validated the method of using redder to bluer multi-color determinations of the QSO PSF relatively to the average PSF of nearby stars. The present study aims to analyse the complete 105783 SDSS DR7 population of QSOs, from their images in the five u, g, r, i, z bands and derived relative PSFs. This is a work in progress, and here we present the results concerning a representative sample of 8874 SDSS QSOs. The main results are that in the five bands there is a steady population of non-point-like objects, and that the targets morphology become less point-like towards the redder bands.

1. INTRODUCTION

Gaia is a mission of the European Space Agency with launch predicted for 2013. The main goal of the Gaia mission is to investigate the origin and evolution of our Galaxy. It will perform spectral and photometric observations and measure the position of $\sim$1 billion objects with an accuracy down to 20 μas, allowing the construction of the most accurate three-dimensional map to date of the Milky Way. Gaia observations will also have impact in research areas such as: solar system, stellar astrophysics, extra-solar planets and AGNs. Along the five years – the predicted duration of the mission – Gaia will detect $\sim$ 500000 QSOs, and the extreme accuracy in their positions will produce a reference frame that will change the future paradigm of the International Celestial Reference Frame–ICRF (Ma et al., 2009). QSOs are among the best objects for the materialization of such a frame, given that they are so distant that do not show proper motions, and look point-like sources (even if they live in galaxies). From the on-board broadband filter detection, and later through variability and peculiar motion confirmation, Gaia is planned to possess the capability of single out QSOs from the contaminant stellar population. At the same time, an Gaia Initial Quasar Catalog (GIQC) is being developed to support the initial matching, enlarging the color comparison template, and to provide a safety minimum of proven, point-like, invariable QSOs for the construction of Gaia's non-rotating, fundamental frame. As referred above, QSOs live in galaxies, as demonstrated by the detailed analysis of nearby objects. Their common point-likeness appearance results on one hand from the fact that the brightness of the central region (ie the AGN) may surpass by orders of magnitude that of the whole galaxy, on the other hand, the far the object is the more difficult it is to detect the fainter extended emission from the stars. Andrei et al. (2009 and 2010) demonstrated that it is possible to pinpoint the host galaxy through the analysis of compound Point Spread Function, that work based on a large sample of 1343 QSOs from DSS and SDSS multiband images. The fact that an extended component may be detected in the QSOs is of extreme relevance for Gaia, as it has an impact on the accuracy of the coordinates of the objects. This is demonstrated in Figure 1, where we compare the light profile of a point-like object that is well described by a PSF, and the light profile of an extended object. It is clear that the existence of an extended component affects the determination of the photocenter position (xc). A significant fraction of the QSOs detected by Gaia will be nearby objects translating in a non negligible fraction of extended objects. In order to model this effect we have embarked in the study of the morphology of the QSOs of the SDSS Quasar Catalogue, that comprises 105 783 objects. This is work in progress, and here we present the results concerning a subsample of 8874 QSOs.

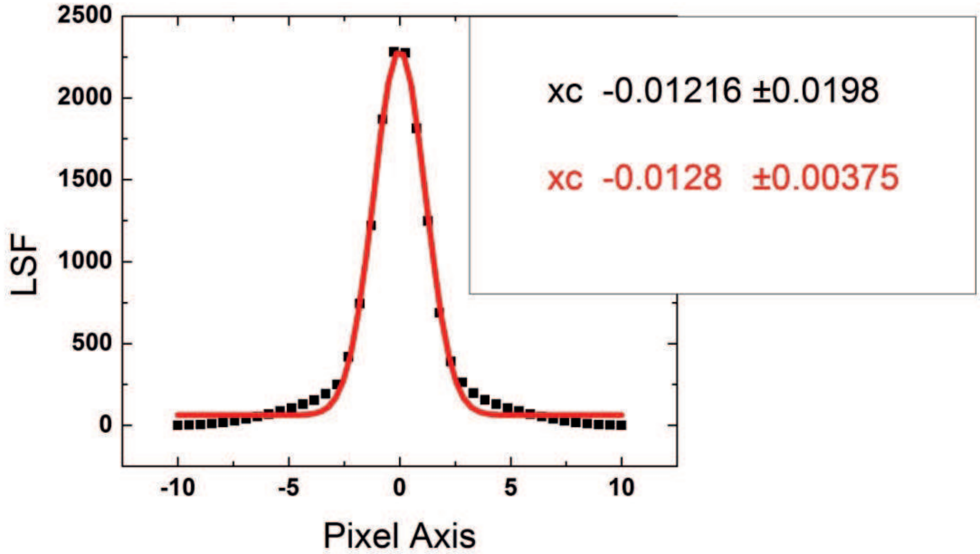

Figure 1: Comparison between the centroid of a profile of an extended object an a point-like source (red).

2. SAMPLE & DATA

This work aims at studying the extended or point-like nature of the QSOs population in Sloan Digital Sky Survey – Data release 7 (SDSS–DR7, Schneider D. et al., 2010). There are 105783 spectroscopically confirmed quasars in SDSS–DR7, covering an sky area $\sim$ 9380 deg^2 and having redshift (z) between 0.065 to 5.46, with a median value of 1.49. We obtained SDSS frames in the in u, g, r, i and z bands for all objects, making in total 528915 frames with 2048x1489 pixels (0.396 arcsec/px). Each frame has approximately 4 MB, so the total amount of data downloaded is $\sim$1.5–2 TB.

3. STRATEGY

We run a IRAF pipeline on the SDSS DR7 frames to issue three PSF parameters: SHARP (skewness), SROUND (circularity) and GROUND (normalness). For each of the frames we obtain a mean PSF. The later are computed firstly based on all the available and suitable field stars, and finally from the combination of the ten objects closest to the QSO, in position and magnitude, which best match the frame's PSF. Stars close to the frames' edges, pack grouped, or saturated are preliminarily excluded. For each QSO in the frame (might happen to exist more than one) we build three morphological indexes as the difference to the frame's local PSF parameters, as normalized by their standard deviation. If any of the morphological indexes differences is larger than two standard deviations of the parameter distribution, then that target is regarded as exhibiting a host galaxy signature. The IRAF pipeline automatically detects and determines the photometric characteristics of the QSOs and field stars.

4. RESULTS

This work is in progress, and by the time of the Journeés 2011 we had u, i, half of the g, r and z frames processed for a subsample of 8784 objects, randomly distributed in the sky (see Figure 2).

Considering the 8784 objects and the frames processed we notice that there are several cases of QSOs present in more than one frame. The actual numbers varied, because of a same detection threshold adopted for all the ugriz bands, and because of unenveness of completion of the analysis for all the frames - nevertheless the samples are always significant, the smallest being the z band with 3725 frames analysed. Table 1 shows that the averages are always close to 1, whereas for an ideal point source the indexes are 0. This indicates the presence of a significant fraction of quasars which strand from point-like. On the other hand the averages of the differences of the indexes of a same quasar imaged in different frames are effectively very close to 0, meaning that the indexes for a same quasar repeat independently of variations of the PSF.

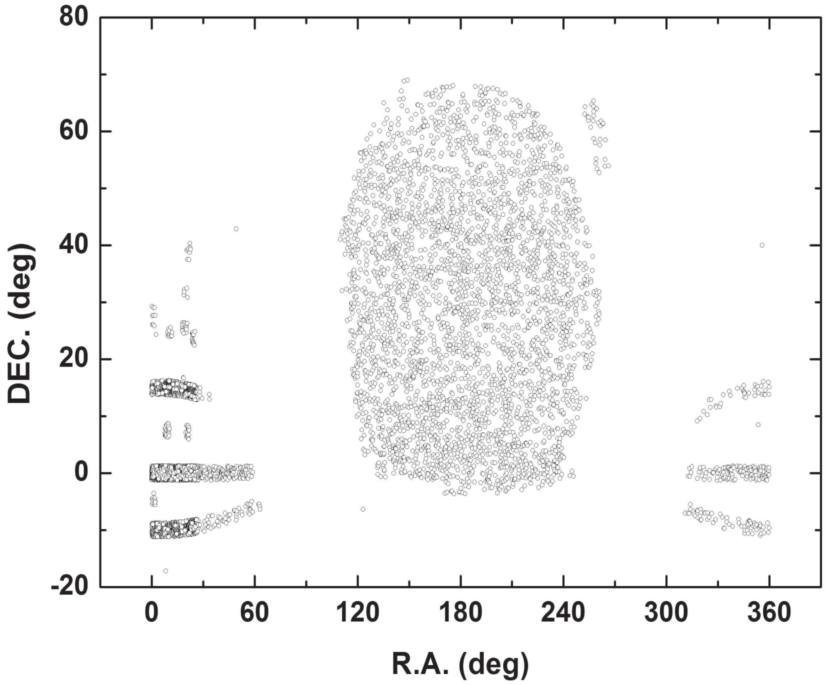

Figure 2: Sky distribution of the 8 784 QSOs.

Band	u		g		r		i		z	
Averages for	Rep.	All	Rep.	All	Rep.	All	Rep.	All	Rep.	All
sharp	0.05	1.13	0.05	0.65	0.01	0.78	0.01	0.88	0.10	1.15
sround	0.03	0.78	0.01	0.71	0.01	0.79	0.02	0.88	0.01	1.02
ground	0.02	0.63	0.04	0.60	0.00	0.73	0.03	0.82	0.03	1.05

Table 1: Average values of the morphological indexes. Under repeated (Rep) are shown the averages for a same quasar found in more than one frame. Under (All) are shown the averages for all the quasars.

Figure 3 presents the distributions of the three PSF parameters, for each ugriz band, of 3114 QSOS (those that were detected in all the bands). That distributions reveal that most of the QSOs have stellar-like morphological indexes (values below 2). However, we also found that in statistically significant number of QSOs, an extended component is present, as demonstrated by their relatively large morphological indexes (i.e. > 2). The extended component is more predominant the redder the band is. We interpret that as the signature of the host galaxy which are mainly redder in comparison with the central (point-like) region. The consistent behaviour revealed by the three distributions illustrate the robustness of the three morphological indexes.

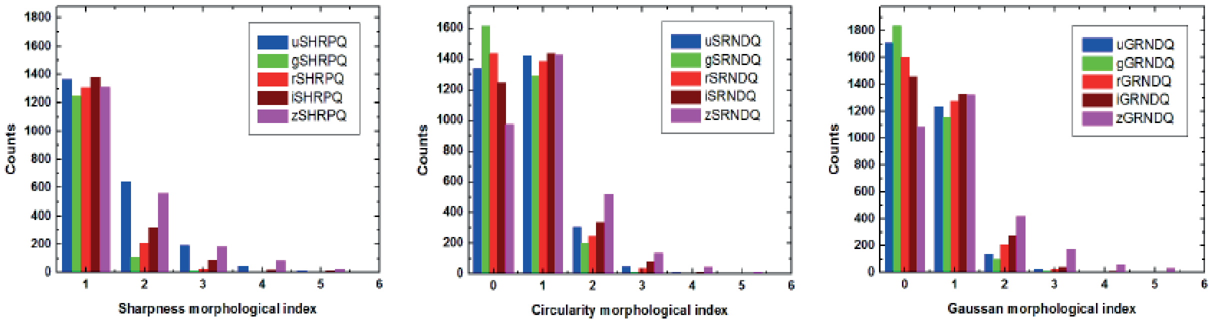

Figure 3: Distributions for 3 114 QSOs with all bands processed. Left–SHARP, center–SROUND, right–GROUND.

Acknowledgements. B. Coelho thanks the Local Organinzing Committee for the travel grant to participate in this meeting. B. Coelho and S. Anton thanks PTDC/CTE-SPA/81711/2003 and PEst-OE/CTE/UI0190/2011 and Program Ciência. A. Andrei thanks CNPq grant PQ-307126/2006-0, and the PARSEC International Incoming Fellowship within the Marie Curie FP7 Programme.

5. REFERENCES

Andrei, A., et al., 2009, A&A, 505,385
Andrei, A., et al.,2009, Gaia CU3 Plenary Meeting, Turin, Italy
Andrei, A., et al., 2010, Journees 2010, Paris, France
Ma, C. et al., 2009, IERS Technical note 35
Schneider, D.,et al., 2010, AJ, 139, 2360

VALUES OF SOME ASTRONOMICAL PARAMETERS (AU, $GM_\odot$, $M_\odot$), THEIR POSSIBLE VARIATIONS FROM MODERN OBSERVATIONS, AND INTERRELATIONS BETWEEN THEM

E.V. PITJEVA
Institute of Applied astronomy RAS
Kutuzov Quay 10, 191187 St.-Petersburg
e-mail: evp@ipa.nw.ru

ABSTRACT. Recent years of high-precision data of spacecraft have given the possibility to estimate the values of the astronomical unit and the heliocentric gravitational constant with great precision. Both estimations have been obtained from more than 635 000 positional observations (1913–2010) of planets and spacecraft. The analysis of the observations was performed on the basis of the numerical Ephemerides of Planets and the Moon (EPM2010) of IAA RAS. The estimation of the change of the $GM_\odot$ heliocentric gravitation constant has also been obtained: $G\dot{M}_\odot/GM_\odot = (-5.0 \pm 4.1) \cdot 10^{-14}$ per year. The obtained decrease of $GM_\odot$ should correspond to the secular decrease of au. However, it has been shown that the present accuracy level of observations does not permit to evaluate the au change. The possibility of finding the $GM_\odot$ change from high-accuracy observations points that fixing the value of au is desirable, as it is highly inconvenient to have the value of the astronomical unit variable.

1. CONNECTION BETWEEN AU AND $GM_\odot$, THEIR ESTIMATIONS

The Astronomical Unit is one of the most basic units of astronomy, it determines the scale of the solar system. Classical measurements in the solar system were angular. Periods (P) or mean motions $n = 2\pi/P$ of celestial bodies were much more easily measured than distances. Thus, in astronomy the adopted units were those of the solar mass (M), a mean solar day (d) and the Gaussian gravitational constant ($k = 0.01720209895$). AU is related to the other three ones by the Kepler third law: $n^2a^3 = k^2M$ and is based upon the Gaussian constant. For a (massless) particle at 1 au from the Sun in keplerian motion, we have $a = 1$, $M = 1$, so the mean motion is $n = k$ and the period $P = 2\pi/k = 365.2568983$ known as a Gaussian year based on the old measurement of the Earth's mean motion.

The term "Astronomical unit" appears at the beginning of the 20-th century, but not until 1976 the International Astronomical Union adopted the following definition of the au "The astronomical unit of length is that length (A) for which the Gaussian gravitational constant (k) takes the value of 0.01720209895 when the units of measurements are the astronomical unit of length, mass and time. The dimensions of k^2 are those of the constant of gravitation (G), i.e., $L^3M^{-1}T^{-2}$".

The value of au is only roughly equal to the mean Earth-Sun distance, however, by its definition it is only connected with the heliocentric gravitation constant: $au^3 = GM_\odot d^2/k^2$.

The distances in the Solar System, measured in au were known quite well from optical observations, however we need the value of au in any metrical units. The first attempt to estimate the au value in metrical units was made by Aristarchus of Samos in the third century BC. In the late 1800's, the accuracy of 0.1% was obtained from asteroid parallaxes. In 1950, Rabe achieved the accuracy of 0.05% (65000 km) from the close approach of Eros. All such determinations were made by optical triangulation methods, with large scatter. Moreover the ranges of the probable errors didn't overlap. Since the beginning of the Venus radar echoes in 1961, the value of the Astronomical Unit, has been determined exclusively from the ranging data of planets and spacecraft. The first ranging to Venus has the accuracy from 2000 km to 130 km. The typical uncertainties in the value of au decreased from many tens of thousands of kilometers to the present level of about a meter.

By its definition the astronomical unit is connected with the heliocentric gravitation constant. Either of these values (au and $GM_\odot$) may be estimated from fitting ephemerides to observations directly or the value of each of them may be obtained from the value of the other one. The modern level of accuracy of observations and dynamical models of planet motions has permitted to determine the heliocentric

	Konopliv et al., 2011 DE423	Fienga et al., 2011 INPOP10a	Pitjeva et al., 2011 EPM2010
$GM_\odot$ [km^3/s^2]	132712440042(10)	132712440055(1)	132712440033(1)
au [m] from $GM_\odot$	149597870700(3)	149597870705(0.3)	149597870696(0.4)

Table 1: The values of $GM_\odot$ obtained while fitting ephemerides to the observations and the value of au deduced from the estimations of the $GM_\odot$

gravitation constant $GM_\odot$ directly from observations. At present, there are the published values of $GM_\odot$ in the physical system of units measured directly and obtained by all three teams (Table 1). One can see that the estimates of $GM_\odot$ obtained by the three independent teams using different ephemerides are close, and the real uncertainties of this parameter and the au value are close to the uncertainty obtained in the paper by Konopliv et al. (2011).

The numerical Ephemerides of Planets and the Moon (EPM2010) of IAA RAS (Pitjeva et al., 2011) have been used for estimating this and all other parameters. These ephemerides originated in the seventies of the last century under the leadership of G.A. Krasinsky to support the Russian space flights, and have been successfully developed since then. More than 635,000 positional observations (Table 2) of planets and spacecraft of various types, mainly radiotechnical (1961–2010), have been used to construct high-precision ephemerides of planets and to determine different parameters.

Radiotechnical measurements began in 1961 and are increasingly continued since, their accuracy became several orders of magnitude better than the accuracy of the optical observations and reaches several meters for today's spacecraft data. It is necessary to say that the ephemerides of the outer planets mainly based on optical measurements have been used since 1913, when at the Naval Observatory of USA the improved micrometer was installed, and the observations become more accurate ($0\overset{''}{.}5$). The most accurate and long-series observations are available for Mars to which spacecraft and landers were repeatedly launched. Radiotechnical observations relating to Venus are much smaller, and the situation for the Mercury observations is much worse. There are a number of radiotechnical observations for Jupiter and Saturn, for Uranus and Neptune there is one 3-D point (α, δ, R), resulting from the encounters of Voyager-2 with these planets.

Observation type	Time interval	Observation number	Accuracy
Optical	1913–2009	57768	$1'' \rightarrow 0\overset{''}{.}05$
Radiotechnical	1961–2010	577763	100 km → 1 m
Total		635531	

Table 2: The observations used

EPM2010 differ from the previous versions by the improved dynamic model of motion of the Solar system bodies with addition of the perturbation from the ring of Trans-Neptunian objects (TNO), by the new value of the Mercury mass, defined from the three encounters of the Messenger spacecraft with Mercury, by the improved reductions of observations with the addition of the relativistic delay effect from Jupiter and Saturn, and by the extended database of observations, including new radiotechnical (2008–2010) and CCD (2009) measurements. Ephemerides were constructed by the simultaneous numerical integration of equations of motion for all the major planets, the Sun, the Moon, the largest 301 asteroids, 21 TNO, the lunar libration, taking into account the perturbations from the oblateness of the Sun and the asteroid belt, lying in the ecliptic plane and consisting of the remaining smaller asteroids, as well as the ring of the TNO rest at the mean distance of 43 au. The equations of motion of the bodies were taken in the post-Newtonian approximation in the n-body metric. Integration in the barycentric system of coordinates for the epoch J2000.0 was performed over 400 years (1800–2200). In the basic version of the improved EPM2010 planetary ephemeris, $\sim$260 parameters are determined: orbital elements of the planets and the 18 satellites of the outer planets, the value of the au or the heliocentric gravitational constant, three angles of orientation with respect to the ICRF frame, and different physical parameters.

2. VARIABILITY OF THE SOLAR MASS

The issue of variability and the possible rate of the change of gravitational constant G or $GM_\odot$ is repeatedly raised and considered. The Sun's mass $M_\odot$, can not be absolutely constant too. On the one hand, it decreases due to continuous thermonuclear reactions and the production of the radiant energy, with the matter carried away by the solar wind. On the other hand, there is a regular drop of interplanetary substances on the Sun, including dust, meteoroids, asteroids and comets.

If we take the average total solar luminosity to be $L_\odot = 3.846 \cdot 10^{33}$ erg/s and the mass of the Sun $M_\odot = 1.9891 \cdot 10^{33}$ g, then the decrease of the mass of the Sun due to radiation as a fraction of the solar mass is equal to $\dot{M}_\odot = -6.789 \cdot 10^{-14} M_\odot$ per year. The mass carried away with the solar wind was also repeatedly evaluated. The flow of the solar wind affects the activity of the Sun and coronal mass ejections. Typically, the average loss per year through the solar wind is estimated as $(2 \div 3) \cdot 10^{-14} M_\odot$, that is, less than a third of the mass loss due to radiation. The total effect of the relative annual decrease of the mass of the Sun due to radiation and the solar wind can be restricted by the inequality $-9.8 \cdot 10^{-14} < \dot{M}_\odot / M_\odot < -8.8 \cdot 10^{-14}$.

The reverse process occurs due to the fall of the matter on the Sun. However, in the solar neighbourhood and in the field of the main asteroid belt there is no sufficient interplanetary matter migrating to the Sun. The upper limit of the possible mass of the Sun drop-down material from this field is less than $10^{-17} \div 10^{-16}$ per year. The mass of the matter that can come from distant regions of the solar system (the Kuiper Belt, a cloud of the Hills, the Oort cloud), mainly in the form of comets, is more uncertain. A large number of comets is detected in the immediate vicinity of the Sun using the LASCO chronograph installed at the SOHO solar space observatory. Statistics of comets discovered by the SOHO observatory gives about $170 \div 200$ comets per year. To obtain the upper limit for falling mass we assume that all the detected comets "vanished" and their masses increased the mass of the Sun. If we take the average value of $d_{com} = 5$ km, the density of 3 g/cm^3 and double the result due to the missing and invisible falling objects, the annual upper bound is $\dot{M}_\odot / M_\odot < +3.2 \cdot 10^{-14}$. Now one can deduce the limits of the change of the solar mass. To obtain the lower limit, let us take the loss estimate due to the solar wind to be maximal, and at the same time, the drop of the material on the Sun to equal zero. To find the upper limit, we use the maximum estimate for the material falling on the Sun and the assumption that there is no mass loss due to the solar wind. Then, we obtain $-9.8 \cdot 10^{-14} < \dot{M}_\odot / M_\odot < -3.6 \cdot 10^{-14}$ per year.

Further, several words should be added concerning the influence of the change of the solar mass or gravitation constant on orbital elements of planets. A small and monotonic change of the solar mass $M_\odot$ or G must lead to the appearance of variations of only certain elements of the planet orbits. It was shown that the possible $GM_\odot$ change in the Solar system should be manifest itself in a systematic, progressive, although very small deviation of the orbital body position (that is its longitude) and the change of the semi-major axes a_i proportional to the $GM_\odot$ change with the opposite sign.

3. ESTIMATIONS OF THE CHANGE OF $GM_\odot$ AND G

In principle, the change of $\dot{G}$ and $G\dot{M}_\odot$ may be estimated. However, it should be noted that for the version of the $\dot{G}$ determination from the planet motions, the main contribution is made by the Sun, since the equations of the planet motions include the products of the masses by the gravitational constant. Among them the term for the Sun ($GM_\odot$) is the main one, several orders of magnitude larger than the others ones. Thus, separation of the change of G from the $GM_\odot$ change (with the dominant term of the $GM_\odot$) is currently impossible. The same is evident by the similarity of the obtained estimates (Pitjeva et al., 2012):

$(G\dot{M}_\odot)/GM_\odot = (-5.04 \pm 4.14) \cdot 10^{-14}$ per year (3σ), $\dot{G}/G = (-4.96 \pm 4.14) \cdot 10^{-14}$ per year (3σ).

Planet	$\dot{a}/a$ (century^{-1})	Correlation coefficients between $\dot{a}$ and a
Mercury	$(3.30 \pm 5.95) \cdot 10^{-12}$	56.5
Venus	$(3.74 \pm 2.90) \cdot 10^{-12}$	95.8
Earth	$(1.35 \pm 0.32) \cdot 10^{-14}$	0.6
Mars	$(2.35 \pm 0.54) \cdot 10^{-14}$	0.4
Jupiter	$(3.63 \pm 2.24) \cdot 10^{-10}$	20.2
Saturn	$(9.44 \pm 1.38) \cdot 10^{-10}$	35.9

Table 3: The secular change values of the semi-major axes for the 6 planets provided by the high-accuracy observations

The parameters $\dot{G}$ and $G\dot{M}_\odot$ were fitted by the least squares method simultaneously with all basic parameters of ephemerides, but separately, i.e. they are considered in different solution versions. Moreover, the secular change values of the semi-major axes for the six planets provided by the high-accuracy observations of spacecraft were simultaneously estimated. Table 3 shows the values obtained for the relative change of semi-major axes of the planet orbits. It is important that all the values obtained for the planets from Mercury to Saturn show positive values of the $\dot{a}/a$ ratio, i.e., indicate the decrease in time of the $GM_\odot$ heliocentric gravitational constant. From the result obtained for $GM_\odot$, it is possible to estimate the restrictions on $\dot{G}$ value using the limits found for the $\dot{M}_\odot/M_\odot$ value. Then, we obtain the $\dot{G}/G$ value with the 95% probability within the interval $-4.2\cdot10^{-14} < \dot{G}/G < +7.5\cdot10^{-14}$ per year.

4. CONSIDERATIONS ON POSSIBLE VARIABILITY OF *AU*

Let us get back to *au*. The change of the astronomical unit is connected with the change of the heliocentric gravitational constant due to the present definition of *au*. In the paper by Krasinsky and Brumberg (2004) based on the raging data 1961–2003, using a numerical theory of planetary motion, nearly coinciding with the EPM2004, the authors obtained the secular increase of the astronomical unit $\dot{au}$ = 15 m per century, which by definition should correspond to the increase of the heliocentric gravitational constant $G\dot{M}_\odot/GM_\odot \simeq 3\cdot10^{-12}$ per year. Such a large positive change of the $GM_\odot$ does not correspond to the estimations of physical processes in the Solar system (the solar radiation and wind, the matter falling on the Sun), as well as to the estimate obtained in present study: $G\dot{M}_\odot/GM_\odot = -5.04\cdot10^{-14}$ per year. However, the authors themselves considered that the increase of *au* is rather matching parameter than the real change of the physical parameters.

The analysis of our results based on a greater number of observations and the EPM2010 ephemerides, shows that the present level of observational accuracy does not permit to evaluate the *au* change. In the paper by Krasinsky and Brumberg the *au* change was determined simultaneously with all other parameters, particularly with the orbital elements of the planets and the value of the *au* astronomical unit. However, it is impossible at present to determine simultaneously the two parameters: the value of the astronomical unit, and its change. In this case, the correlation between *au* and its change $\dot{au}$ reaches 98.1%, and leads to incorrect values of both parameters, in particular, it gives $\dot{au}$ the order of 15 m per century. Without the simultaneous determination of *au* and $\dot{au}$, i.e. if only the change of the astronomical unit is estimated together with other parameters, the $\dot{au}$ value is about 1 m per century, and does not exceed its formal uncertainty, thus it is not determined: $\dot{au} = (1.2 \pm 3.2)$ m/cy (3 σ). Furthermore, including or excluding the $\dot{au}$ value from a number of the solution parameters does not change the observation residuals, the mean error of the unit weight is not also changed ($\Delta\sigma \simeq 0.2\%$), so there is no reason to assume that $\dot{au}$ is the necessary matching parameter, and there is no need to include it in the number of parameters to be estimated. The modern accuracy has approached the level when it is possible to estimate the change of the heliocentric gravitational constant $GM_\odot$, therefore it is desirable to specify the definition of the astronomical unit, for example, by fixing its value, as it is highly inconvenient to have the changing value of the astronomical unit. In future, after obtaining the reliable estimations of $G\dot{M}_\odot$ by different authors, the value of $GM_\odot$ should probably be given on a certain epoch.

5. REFERENCES

Fienga, A., Laskar, J., Kuchynka, P., Manche, H., Desvignes, G., Gastineau, M., Cognard, I., Theureau, G., 2011, "The INPOP10a planetary ephemeris and its applications in fundamental physics", Celest. Mech. Dyn. Astr. 111(3), pp. 363-385, doi: 10.1007/s10569-011-9377-8.

Krasinsky, G.A., Brumberg, V.A., 2004, "Secular increase of Astronomical Unit from analysis of major planet motions, and its interpretation", Celest. Mech. Dyn. Astr. 90(3/4), pp. 267-288, doi: 10.1007/s10569-004-0633-z.

Konopliv, A.S., Asmar, S.W., Folkner, W.M., Karatekin, O., Nunes, D.C., Smrekar, S.E., Yoder, Ch.F., Zuber, M.T., 2011, "Mars high resolution gravity fields from MRO, Mars seasonal gravity, and other dynamical parameters", Icarus 211(1), pp. 401-428, doi: 10.1016/j.icarus.2010.10.004.

Pitjeva, E., Bratseva, O., Panfilov, V., 2011, "EPM - Ephemerides of Planets and the Moon of IAA RAS: their model, accuracy, availability", Proceedings of the "Journees-2010 / Systems de reference spatio-temporels", Capitaine N. (eds.), pp. 49-54.

Pitjeva, E.V., Pitjev, N.P., 2012, "Changes in the Sun's mass and gravitational constant estimated using modern observations of planets and spacecraft", Solar System Research, 46(1), pp. 78-87, doi: 10.1134/S0038094612010054.

SOFA AND THE ALGORITHMS FOR TRANSFORMATIONS BETWEEN TIME SCALES & BETWEEN REFERENCE SYSTEMS

C.Y. HOHENKERK
Chair, IAU SOFA Board
HM Nautical Almanac Office
UK Hydrographic Office, Taunton, TA1 2DN
e-mail: Catherine.Hohenkerk@ukho.gov.uk

ABSTRACT. The SOFA Collection provides users with a myriad of routines. Examples will be given of the various transformations between the time scales TAI, TT, UTC, UT1, TDB, TCB and TCG, which represent the latest set of routines added to the SOFA collection. In particular this paper will also illustrate the combinations of routines that provide transformations between the Geocentric Celestial Reference System (GCRS) and the International Terrestrial Reference System (ITRS). Both the Celestial Intermediate Origin (CIO) and the equinox-based methods are shown, and those supporting International Astronomical Union (IAU) resolutions will be highlighted.

1. SOFA

SOFA, which stands for Standards of Fundamental Astronomy, is a "service" of IAU Division 1, which at present reports through Commission 19. Its task is to establish and maintain an accessible and authoritative set of algorithms and procedures that implement standard models used in fundamental astronomy. To do this, SOFA is made up of three parts: a board of experts (see Section 5), a collection of software, and a web site that makes the routines accessible to all.

The SOFA collection provides libraries of routines in Fortran and ANSI C, which form a basis—the building blocks—that enable users to write their own applications, using authoritative methods. The latest release (2010 December 1), which included 16 time-scale transformations, consists of 59 canonical routines, 72 astronomy support routines, and 55 vector/matrix utility routines; a grand total of 186 routines.

The SOFA Centre is the web site at **www.iausofa.org**. This is the public face of SOFA. From this web site, users may navigate to each routine, then view or copy the source code. Alternatively, a whole library, Fortran or ANSI C, may be downloaded. The Centre is also an archive where previous releases are available. Over the last year and a half, the site has received over 800 unique visitors each month and currently about 600 people have registered to receive news about updates.

SOFA requires continuity, and thus Division I has requested that the IAU Executive Committee consider a change in the IAU by-laws that would recognize this within the IAU structure. If this change is accepted at the 2012 General Assembly, it is proposed that SOFA would be classed as a 'service organization'.

2. SOFA – TIME SCALES

SOFA recognizes seven time scales, namely International Atomic Time (TAI), Coordinated Universal Time (UTC), Universal Time (UT1), Terrestrial Time (TT), Barycentric Dynamical Time (TDB), Geocentric Coordinated Time (TCG) and Barycentric Coordinated Time (TCB). The strategy is to provide routines that link adjacent pairs of time scales. This is the simplest scheme that gives the user most flexibility. Supplementary quantities, such as the variable parameters ΔT and UT1−UTC, must be supplied by the user.

The routines use SOFA's two-argument Julian date convention. Thus, the two routines `DTF2D` and `D2DTF` handle the conversion between civil date and time, i.e., year, month, day, hour, minute and seconds, and the two-part Julian date (or in the case of UTC, quasi-JD) and vice versa. Importantly, all the routines take care to preserve precision by ensuring that the tiny differences are added to (or subtracted from) the smaller of the two-date arguments. In the case of UTC, these routines deal with leap seconds in the rare but crucial cases when it is correct to input or return more than 59 seconds. A cookbook, *Time Scale & Calendar Tools*, with examples in both Fortran and C, may be downloaded.

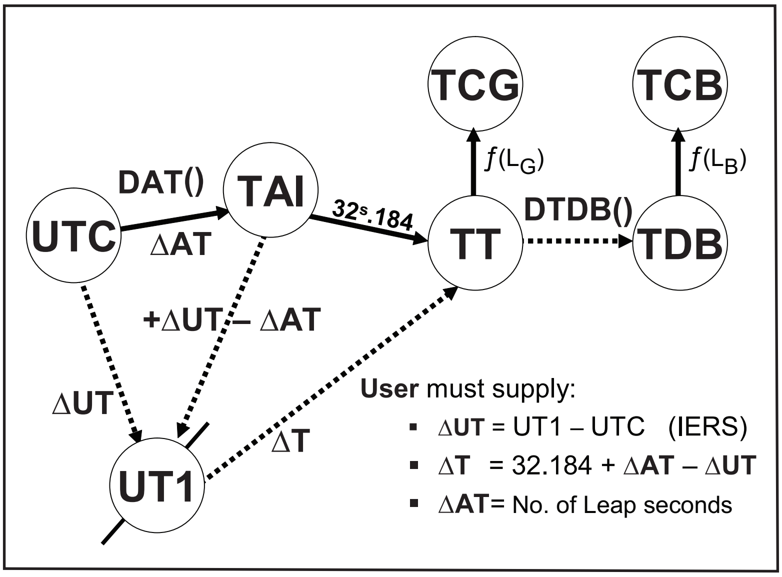

Figure 1: Time Scale Relationships. The dotted lines indicate that the user must supply the difference between the two time scales. The routines `DAT`, which returns the number of leap seconds, and `DTDB`, are part of the SOFA library. Note that the routine `DAT` must be updated whenever a leap second is inserted into UTC.

3. SOFA – TRANSFORMATIONS BETWEEN THE GCRS & THE ITRS

SOFA contains a myriad of routines in order to provide users with various options depending on the application they are writing. Thus, when looking at a whole collection, it can be quite difficult trying to choose the correct routine for the particular purpose. The following is a guide to show how, in general, the routine names are constructed in the context of the transformation between the GCRS and the ITRS, the different paradigms, and various available options. The underlying equations that represent the whole process, in both the Celestial Intermediate Origin (CIO) and equinox based paradigms, respectively, are

$$[\text{ITRS}] = \mathbf{Q}[\text{GCRS}] = \mathbf{W}\ \mathbf{R}_3(\text{ERA})\ \mathbf{C}\ [\text{GCRS}] = \mathbf{W}\ \mathbf{R}_3(\text{GAST})\ \mathbf{NPB}\ [\text{GCRS}]$$

and they also highlight the main reference systems. The matrix **C** or **NPB** transforms from the GCRS to the Celestial Intermediate Reference System or the true equinox and equator of date system, respectively. This is followed by a rotation about the Celestial Intermediate Pole (CIP) for Earth rotation, viz $\mathbf{R}_3$(ERA) or $\mathbf{R}_3$(GAST), i.e. a transformation to the Terrestrial Intermediate Reference System. Finally, **W** (polar motion) completes the rotation to the ITRS.

The names of the SOFA routines are short and give an indication of what the routines do. All valid routines are preceded by `iau_` in Fortran and just `iau` in ANSI C. The SOFA 'free license agreement' requires that users who change the content of any routine must remove the `iau` tag. The usual letters are `M`, `B`, `P`, `N`, `E`, `XY`, `XYS`, `S`, `ERA`, `GST`, `POM`, `C2I` and `C2T`, where the first five stand for matrix, bias, precession, nutation and equinox. The notation `XY`, `XYS` and `S` refer to the CIP and CIO locator, while `ERA` and `GST` deal with Earth rotation, and `POM` stands for polar motion. `C2I` and `PMN` provide matrices for conversion from the GCRS to the Celestial Intermediate Reference System and the true equinox and equator of date system, respectively, and `C2T` produces a matrix that transforms from the GCRS to the ITRS. Some implementations and descriptions (e.g. IERS) may provide the conversion from the ITRS. SOFA's transpose matrix routine `TR` (see Table 2) may be used to transpose a matrix, which in this case is the inverse and gives the transformation between the ITRS and the GCRS. **Note:** always check to ensure that the matrix you generate provides the transformation you require.

A two-digit year implies that there is an associated IAU resolution, but not necessarily a model designation or tag. This is well illustrated by the routine `NUT06A`, which implements the IAU 2000A

CIO-based GCRS to Intermediate	Equinox-based GCRS to Date
Bias, Precession and Nutation	
`C2I06A ( TTA, TTB, C )`	`PNM06A ( TTA, TTB, NPB )`

Table 1: Transformation from the GCRS to either the Celestial Intermediate Reference System or the true equinox and equator of date, respectively. `TTA+TTB` = TT Julian date and fraction.

CIO-based	GCRS to ITRS	Equinox-based
	Input Parameters	
`TTA+TTB` = TT Julian date and fraction; `UT1A+UT1B` = UT1 equivalent date and fraction, required for Earth rotation; x_p, y_p the coordinates of the CIP with respect to the ITRS (IERS).		
	Bias, Precession and Nutation, Earth Rotation and Polar Motion	
		`PNM06A ( TTA, TTB, NPB )`
		`GAST = GST06 ( UT1A,UT1B, TTA,TTB, NPB )`
		`POM00 (` x_p, y_p `SP00(TTA,TTB), W )`
`C2T06A ( TTA,TTB, UT1A,UT1B,` x_p, y_p `Q )`		`C2TEQX ( NPB, GAST, W, Q )`
	ITRS to GCRS	
	`TR ( Q,` Q^{-1} `)`	

Table 2: Transformation between the GCRS and ITRS, excluding the IERS corrections.

nutation after the IAU 2006 resolution dealing with precession, and includes the adjustments that are caused by changes in the obliquity and $\dot{J}_2$ (see Section 4). Lastly, if the final letter is `A` or `B`, then this usually refers to the IAU 2000A or IAU 2000B nutation series (there are no 06B routines). It should be noted that these general rules are only a guide; a few routines do not follow these guidelines.

The three tables illustrate various options. The first table, an 'almanac type' option, shows the routines that produce the matrix—CIO or equinox based—that includes bias, precession and nutation, i.e., the transformation from the CGRS to either the Intermediate Celestial Reference System or the true equinox and equator of date, respectively. Table 2, similar to Table 1, lists the routines for the GCRS to ITRS matrix and thus includes Earth rotation and polar motion. Finally Table 3, which gives the GCRS to ITRS matrix, lists the minimum combination (i.e., no matrices are re-calculated) and allows all the corrections that are supplied by the IERS to be included.

4. SOFA, GCRS TO ITRS & IAU RESOLUTIONS

SOFA routines are consistent between the CIO-based and equinox-based paradigms. Whether you select `XYS06A`, `C2T06A`, `C2I06A`, `PNM06A` or `PFW06`, the same underlying routines are used. These routines all implement the equations that are part of resolution B1 adopted at the IAU 2006 General Assembly. These include using `NUT06A`—whichever paradigm—that implements the additional adjustments that are required to be applied to `NUT00A` when using IAU 2006 precession (see 3 above). The routine `XY06` uses a different approach as it evaluates the series expressions for the X, Y of the CIP directly, and thus requires no adjustments. All these routines were coded and verified by the Board at the time of the resolutions and represent the IAU standard.

Acknowledgements. Following the Journées 2010 the Board were pleased to welcome new members Nicole Capitaine and William Folkner. The work of SOFA gets done by good will and this is an appropriate place to record and thank the Board and their host institutions: John Bangert (US Naval Observatory, USA), Steve Bell (Webmaster, HM Nautical Almanac Office (UKHO), UK), Mark Calabretta (Australia Telescope National Facility, Australia), Nicole Capitaine (Observatoire de Paris, France), William Folkner (Jet Propulsion Laboratory, USA), George Hobbs, (Australia Telescope National Facility, Australia),

CIO-based	Equinox-based
Input Parameters	
TTA+TTB = UTC + ΔAT + 32.184 = TT Julian date and fraction;	
UT1A+UT1B = UT1 equivalent date and fraction, required for Earth rotation;	
x_p, y_p the coordinates of the CIP with respect to the ITRS (IERS);	
ΔUT = UT1−UTC required for calculation of Earth rotation (IERS);	
dX and dY for the CIP (IERS)	dψ and dϵ for nutation (IERS).
GCRS to Intermediate	**GCRS to Date**
Bias, Precession and Nutation	
XYS06A (TTA, TTB, X, Y, s) or	PFW06 (TTA, TTB, γ, ϕ, ψ, ϵ_A)
XY06 (TTA, TTB, X, Y) and	NUT06A (TTA, TTB, $\Delta\psi$, $\Delta\epsilon$)
s = S06 (TTA, TTB, X+dX, Y+dY)	
C2IXYS (X+dX, Y+dY, s, C)	FW2M (γ, ϕ, ψ+$\Delta\psi$+dψ, ϵ_A+$\Delta\epsilon$+dϵ, NPB)
	BPN2XY (NPB, X, Y) & s = S06 (TTA, TTB, X, Y)
Earth Rotation	
ERA = ERA00 (UT1A, UT1B+ΔUT)	GAST = ERA00 (UT1A, UT1B+ΔUT) - EORS (NPB, s)
Polar Motion	
POM00 (x_p, y_p, SP00(TTA, TTB), W)	
GCRS to ITRS	
C2TCIO (C, ERA, W, Q)	C2TEQX (NPB, GAST, W, Q)

Table 3: Transformation from the GCRS to the ITRS, allowing the user to supply all the corrections provided by the IERS, but without duplication of calculation.

Always check the documentation within each routine for the specification, method and arguments so as to ensure that it meets your requirements.

Catherine Hohenkerk (Chair, HM Nautical Almanac Office, UK), Wen-Jing Jin (Shanghai Observatory, China), Brian Luzum (IERS, US Naval Observatory, USA), Zinovy Malkin (Pulkovo Observatory, Russia), Jeffrey Percival (University of Wisconsin, USA) and Patrick Wallace (Rutherford Appleton Laboratory, UK). The Board thanks the UK Hydrographic Office for hosting the SOFA web site.

5. REFERENCES

Hilton, J.L., Capitaine, N., Chapront, J., Ferrandiz, J.M., Fienga, A., Fukushima, T., Getino, J., Mathews, P., Simon, J.-L., Soffel, M., Vondrak, J., Wallace, P., and Williams, J., 2006, "Report of the International Astronomical Union Division I Working Group on Precession and the Ecliptic", Celest. Mech. Dyn. Astron., 94(3), doi:10.1007/s10569-006-0001-2.

Hohenkerk, C.Y., 2011, "SOFA — A Status Report, Review and a Look to the Future", Proceedings of the Journées 2010 Systèmes de référence spatio-temporels.

Petit, G., and Luzum, B., (eds.), 2011, IERS Technical Note 36, "IERS Conventions 2010", Frankfurt am Main: Verlag des Bundesamts für Kartographie und Geodäsie, ISBN 3-89888-989-6.

SOFA Time Scales and Calendar Tools; Fortran edition http://www.iausofa.org/sofa_ts_f.pdf or ANSI C edition http://www.iausofa.org/sofa_ts_c.pdf.

NEW LONG-TERM EXPRESSIONS FOR PRECESSION

J. VONDRÁK[1], N. CAPITAINE[2], P. T. WALLACE[3]

[1] Astronomical Institute, Acad. Sci. Czech Rep.
Boční II, 141 31 Prague 4, Czech Republic
e-mail: vondrak@ig.cas.cz

[2] SYRTE, Observatoire de Paris, CNRS, UPMC
61, avenue de l'Observatoire, 75014 Paris, France
e-mail: n.capitaine@obspm.fr

[3] STFC / Rutherford Appleton Laboratory
Harwell Oxford, Oxon OX11 0QX, UK
e-mail: patrick.wallace@stfc.ac.uk

ABSTRACT. Precession is the secular and long-period component of the motion of the Earth's spin axis in the celestial reference frame. The current precession model, IAU 2006, approximates this motion by polynomial expansions that are valid, with very high accuracy, in the immediate vicinity (a few centuries) of the reference epoch J2000.0. However, for more distant epochs, this approximation quickly deteriorates. Consequently, we recently published new precession expressions (Vondrák et al. 2011b), comprising very long-period terms fitted to a numerical integration of the motion of solar system bodies on scales of several hundreds of millennia. We give a short description of the new expressions, including an assessment of their accuracy and comparisons with other models.

1. INTRODUCTION

All precession models used so far are expressed in terms of polynomial development, no matter which precession parameters are used. Model IAU 2006 is very accurate, but usable only for a limited time interval (several centuries around the epoch J2000); its errors rapidly increase with longer time spans. In reality, precession represents a complicated very long-periodic process, with periods of hundreds of centuries. This can be seen in numerically integrated equations of motion of the Earth in the solar system and its rotation (Vondrák et al. 2009, 2011a).

We define the precession of the equator as being the motion of the equator covering periods longer than 100 centuries; shorter ones are included in the nutation. Similarly, the precession of the ecliptic is assumed to be the part of the motion of the ecliptic covering periods longer than 100 centuries. The goal is to find relatively simple expressions of different precession parameters, with accuracy comparable to the IAU 2006 model near the epoch J2000.0, and lower accuracy outside the interval ±1 millennium (up to several minutes of arc at the extreme epochs ±200 millennia). The paper describing the new model has recently been published (Vondrák et al. 2011b), further referred to as "A&A paper".

2. METHOD USED

We use the numerically integrated values of

- the precession of the ecliptic P_A, Q_A, calculated with the Mercury 6 package by Chambers (1999), which was shown to be consistent with Laskar et al. (1993) values;
- the general precession/obliquity p_A, ε_A (Laskar et al. 1993), ε_A being shown to be consistent with the Laskar et al. (2004) values;

to calculate different precession parameters in the interval ±200 millennia from J2000.0, with 100-year steps. The central part (±1 millennium from the epoch J2000.0) is replaced by IAU 2006 values. These series are then approximated by a cubic polynomial plus up to 14 long-periodic terms, so that the fit is best around J2000.0. This is assured by choosing appropriate weights (equal to 10^4 in the central part and to $1/T$ outside this interval). The periods are found using Vaníček's method (1969), modified by Vondrák (1977) and verified against those found by Laskar et al. (1993, 2004) from much longer time series. Least-squares estimation is then used to determine the sine/cosine amplitudes of individual periodic terms.

3. SOLUTION

We derived the long-term expressions of the following precession parameters, some of them being precession angles, some direction cosines (expressed in terms of certain precession angles):

- precession angles: $p_A, \varepsilon_A, \omega_A, \psi_A, \chi_A, \varphi, \gamma, \psi$;
- direction cosines: $P_A = \sin\pi_A \sin\Pi_A$, $Q_A = \sin\pi_A \cos\Pi_A$, $X_A = \sin\theta_A \cos\zeta_A$, $Y_A = \sin\theta_A \sin\zeta_A$, $V_A = \sin\theta_A \sin z_A$, $W_A = \sin\theta_A \cos z_A$.

The precession angles are depicted in Figure 1. In addition to these, we also derived the expression for the the precession part, s_A, of the CIO locator (i.e., the quantity used to locate the celestial intermediate origin, CIO, in a fixed celestial reference system).

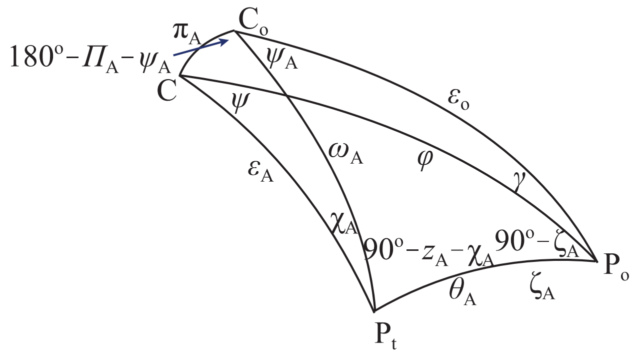

Figure 1: Precession parameters

Long-term expressions of all these parameters are given in a general form

$$a + bT + cT^2 + dT^3 + \sum_{i=1}^{n} (C_i \cos 2\pi T/P_i + S_i \sin 2\pi T/P_i)\,, \qquad (1)$$

in which T is time in centuries from J2000.0, P_i are periods in centuries ($P_i > 100$), and n (between 8 and 14) is the number of periodic terms. Parabolic and cubic coefficients c, d are very small, as they must be for the expression to be usable at large T values.

4. ESTIMATION OF ACCURACY, COMPARISON WITH OTHER MODELS

In the A&A paper, accuracy was estimated using a simple expression based on the average σ for all parameters (estimated from the fit to integrated values) and weights at different epochs; here we use a rigorous formula, based on the full variance-covariance matrix. The result is depicted in Figure 2, where the accuracy of each estimated parameter is given and compared with the one from the A&A paper. It is clear that our previous estimate was too cautious – the rigorous estimate yields much smaller uncertainties for all parameters, in some cases as much as two orders of magnitude lower.

The comparison of the new long-term solution with other models of precession (X_A and Y_A parameters only) is given in Figures 3 and 4. X_A and Y_A values as computed from the values of ζ_A, θ_A by Lieske et al. (1977), Simon et al. (1994) and Capitaine et al. (2003) (denoted as Lieske, Simon and IAU2006$_{\zeta\theta}$, respectively), and computed directly from the X_A, Y_A series of Capitaine et al. (2003) and the A&A paper (denoted as IAU2006$_{XY}$ and LT model, respectively) are compared with the numerically integrated values.

Figure 3 depicts the comparison in the interval ±300 centuries from J2000.0, while Figure 4 shows only the central part (±10 centuries from J2000.0) at an enlarged scale. One can see that, for distant epochs, the direct IAU 2006 series, which are developments of direction cosines of the pole unit vector in the

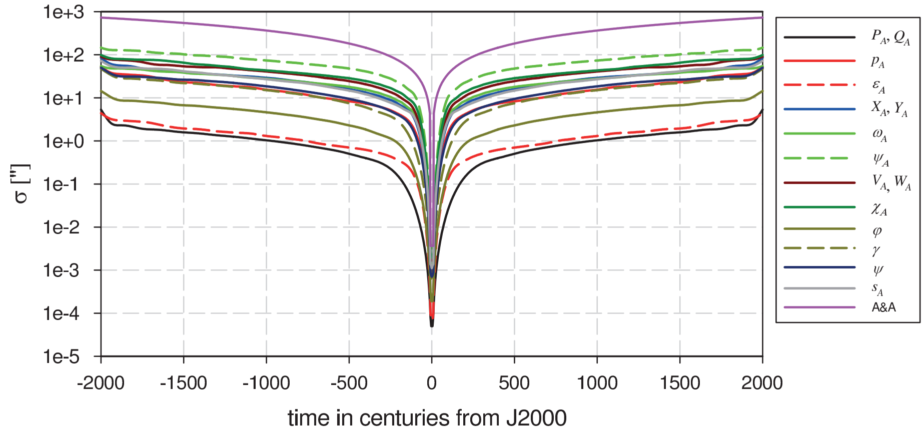

Figure 2: Estimated accuracy of all precession parameters: the line marked 'A&A' shows the overcautious estimate presented in the earlier paper.

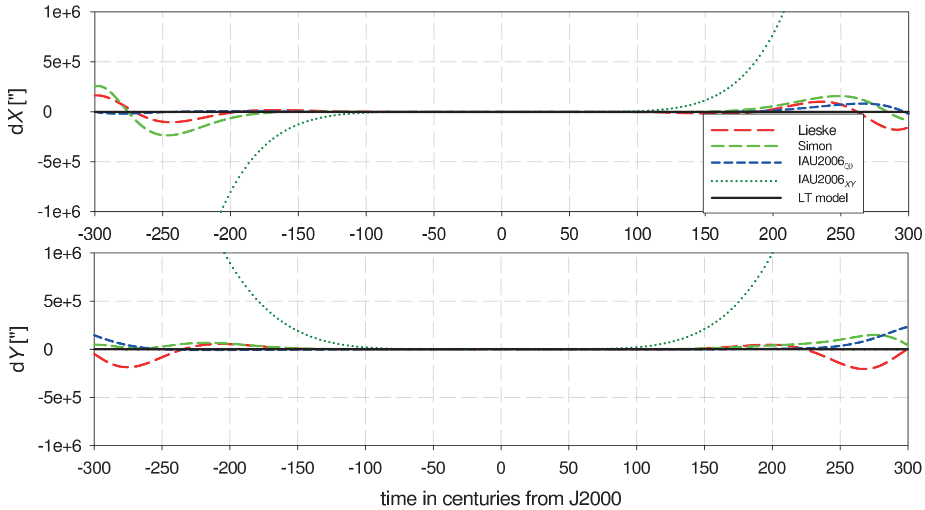

Figure 3: Comparison of different precession models with integrated values

mean frame of epoch as polynomials of time around J2000.0, yield much worse results than the X_A, Y_A expressions based on the 'traditional' precession angles ζ_A, θ_A. The new LT model is indistinguishable from the integration at this scale, whereas all other models display deviations reaching 50 degrees for epochs more distant than 200 centuries. Figure 4 clearly demonstrates the correction of precession rate, and also the quadratic term in obliquity, introduced since the IAU 2000 precession. On the other hand, all models shown are consistent with the numerically integrated precession within one arcsecond or so in the interval ± 10 centuries from J2000.0.

5. CONCLUSIONS

The presently adopted IAU 2006 model provides high accuracy over a few centuries around the epoch J2000.0. For direction cosines X_A, Y_A, using direct IAU 2006 series combines precision and convenience in the modern era; however, for longer periods, expressions based on polynomial development of precession angles ζ_A, θ_A are preferable. The new set of precession expressions, given in our A&A paper and valid over ± 200 millennia, is presented. Its accuracy is comparable to IAU 2006 model in the interval of several centuries around J2000.0, and it fits the numerically integrated position of the pole for longer intervals,

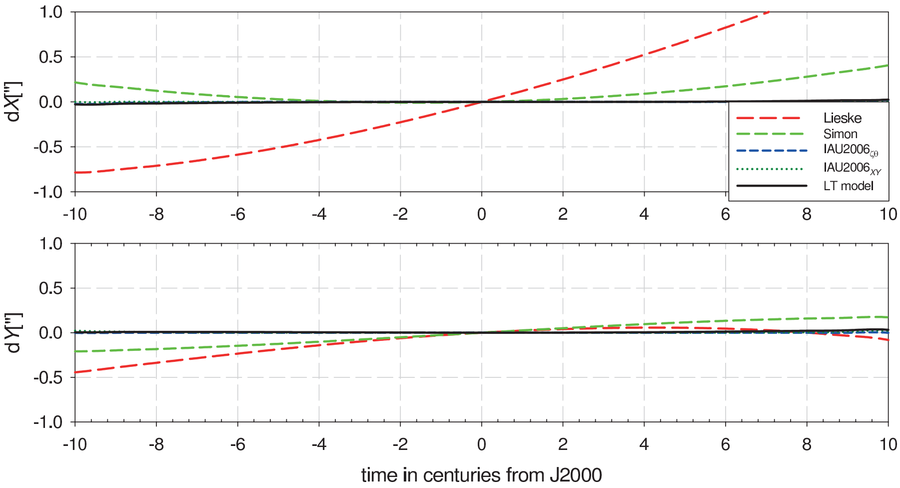

Figure 4: Comparison of different precession models with integrated values: closeup of the central part

with gradually decreasing accuracy (several arcminutes ±200 thousand years away from J2000.0).

Acknowledgments. This study was supported by the grant LC506 awarded by the Ministry of Education, Youth and Sports of the Czech Republic.

6. REFERENCES

Capitaine, N., Wallace, P.T. and Chapront J., 2003, "Expressions for IAU 2000 precession quantities", A&A , 412, pp. 567–586.

Chambers, J.E., 1999, "A hybrid symplectic integrator that permits close encounters between massive bodies", MNRAS , 304, pp. 793–799.

Laskar, J., Joutel, F. and Boudin, F., 1993, "Orbital, precessional, and insolation quantities for the Earth from −20 Myr to +10 Myr", A&A , 270, pp. 522–533.

Laskar, J., Robutel, P., Joutel, F., Gastineau, M., Correia, A.C.M. and Levrard, B., 2004, "A long-term numerical solution for the insolation quantities of the Earth", A&A , 428, pp. 261–285.

Lieske, J.H., Lederle, T., Fricke, W. and Morando, B., 1977, "Expressions for the precession quantities based upon the IAU (1976) system of astronomical constants", A&A , 58, pp. 1–16.

Simon, J.L., Bretagnon, P., Chapront, J., Chapront-Touzé M., Francou G. and Laskar J., 1994, "Numerical expressions for precession formulae and mean elements for the Moon and the planets", A&A , 282, pp. 663–683.

Vaníček, P., 1969, "Approximate spectral analysis by least-squares fit", Astrophys. Sp. Sci., 4, pp. 387–391.

Vondrák, J., 1977, "The rotation of the Earth between 1955.5 and 1976.5", Studia Geophys. Geod. 21, pp. 107–117.

Vondrák, J., Capitaine and N., Wallace, P.T., 2009, "Towards a long-term parametrization of precession", in: M. Soffel, N. Capitaine (eds.) Journées 2008 Systèmes de référence spatio-temporels, Lohrmann Observatorium Dresden and Observatoire de Paris, pp. 23–26.

Vondrák, J., Capitaine, N. and Wallace, P.T., 2011a "Some new thoughts about long-term precession formula", in: N. Capitaine (ed.) Proc. Journées 2010 Systèmes de référence spatio-temporels, Observatoire de Paris, pp. 24–27.

Vondrák, J., Capitaine, N. and Wallace, P.T., 2011b, "New precession expressions, valid for long time intervals", A&A , 534, A22 (2011), doi: 10.1051/0004-6361/201117274.

COMPARISON BETWEEN THE VARIABLES AND PARAMETERS USED FOR HIGH ACCURACY PRECESSION AND NUTATION

N. CAPITAINE
SYRTE, Observatoire de Paris, CNRS, UPMC
61, avenue de l'Observatoire, 75014 – Paris, France
e-mail: n.capitaine@obspm.fr

ABSTRACT. Different forms of variables and parameters, which refer to various celestial reference systems, have been used in the development of high accuracy equations and models for the Earth's precession and nutation, as well as for the estimation of the time-dependent celestial pole offsets from the most accurate astrometric observations. The purpose of this presentation is to compare and relate rigorously those various forms of variables and parameters and recommend the most appropriate ones to be used for providing the best accuracy for the celestial motion of the Celestial intermediate pole.

1. THE PRECESSION-NUTATION PARAMETERS

The CIO based precession-nutation parameters reflect the motion of the Celestial intermediate pole, CIP, in the Geocentric celestial reference system (GCRS); they consist in the coordinates of the CIP unit vector, either in their polar form (E and d), or their rectangular form ($X = \sin d \cos E,\ Y = \sin d \sin E$). These quantities contain precession and nutation of the CIP, frame bias, plus the cross terms; they are directly related to the GCRS and independent of the ecliptic and the equinox (Capitaine et al. 2003).

Figure 1a shows the position of the CIP (P) in the GCRS (of pole $\mathcal{C}_0$ and origin Σ_0 on the GCRS equator) and the celestial intermediate origin, CIO (σ), on the CIP equator (P_0 and σ_0 being the CIP and CIO at epoch t_0). Figure 1b shows the link of the quantities E, d and the Earth rotation angle, ERA, with the corresponding quantities referred to the J2000.0 ecliptic and the equinox. The point Σ is distant from the CIO by the quantity s, called the "CIO locator" (Capitaine & Wallace 2006) and the "equation of the origins", EO, is the difference ERA−GST between ERA and Greenwich sidereal time, GST.

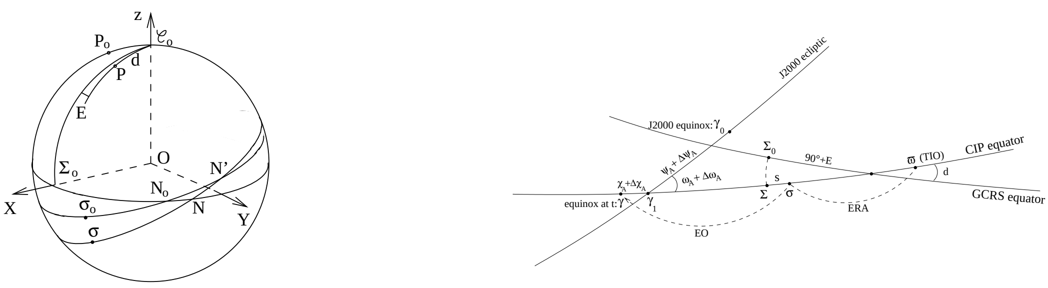

1a 1b

Figure 1: The CIO based precession-nutation parameters and link to the J2000.0 ecliptic and the equinox.

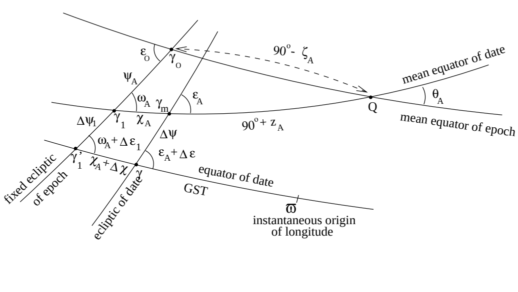

Figure 2: Equinox based precession-nutation parameters referred to the ecliptic (of epoch, or date).

The equinox based precession-nutation parameters refer either to the ecliptic of date, or the ecliptic of epoch (e.g. J2000.0). Figure 2 shows a number of those parameters, e.g. ψ_A, ω_A, which refer to the ecliptic and equinox of epoch, ϵ_A, z_A and the usual nutation angles, $\Delta\psi$, $\Delta\epsilon$, which refer to the ecliptic and (mean or true) equinox of date, and $\chi_A + \Delta\chi_A$ that measures the precession of the ecliptic on the CIP equator (Lieske et al. 1977). It also shows the Euler angles between the J2000 ecliptic system and the terrestrial intermediate reference system, namely $\psi = \psi_A + \Delta\psi_1$, $\omega = \omega_A + \Delta\epsilon_1$, and $\varphi = \mathrm{GST} + \chi_A + \Delta\chi_A$, from γ_1' (intersection of the fixed ecliptic with the CIP equator) to the terrestrial intermediate origin, TIO; γ_1' is distant from the equinox, γ, by the quantity $-\chi_A - \Delta\chi_A$ and from the point Σ, by EO $-\chi_A - \Delta\chi_A - s$.

The rigorous relationship between the CIO and equinox based quantities, are, if ξ_0, η_0 and $d\alpha_0$ are the celestial pole offsets and the frame bias in right ascension, respectively, at J2000.0 (Capitaine 1990):

$$\begin{aligned} X &= \bar{X} + \xi_0 - d\alpha_0\, \bar{Y}, \qquad & Y &= \bar{Y} + \eta_0 + d\alpha_0\, \bar{X} \\ \bar{X} &= \sin\omega\sin\psi, \qquad & \bar{Y} &= -\sin\epsilon_0\cos\omega + \cos\epsilon_0\sin\omega\cos\psi, \end{aligned} \tag{1}$$

and for quantities referred to the ecliptic and equinox of date (developments at the 4th order in ψ_A):

$$\begin{aligned} \bar{X} &= \psi_A \sin\epsilon_0 - (\psi_A^3/6)\sin\epsilon_0 + \psi_A(\omega_A - \epsilon_0)\cos\epsilon_0 + \Delta\psi\sin\epsilon_0 + \Delta\psi\Delta\epsilon\ \cos\epsilon_0 \\ &\quad + (\psi_A\cos\epsilon_0 - \chi_A)\ \Delta\epsilon + (\epsilon_A - \epsilon_0)\ \Delta\psi\cos\epsilon_0 - (\psi_A^2/2)\ \Delta\psi\sin\epsilon_0, \\ \bar{Y} &= (\omega_A - \epsilon_0) - (\psi_A^2/2)\sin\epsilon_0\cos\epsilon_0 + (\psi_A^4/24)\sin\epsilon_0\cos\epsilon_0 + \Delta\epsilon \\ &\quad - (\Delta\psi^2/2)\sin\epsilon_0\cos\epsilon_0 - (\psi_A\cos\epsilon_0 - \chi_A)\ \Delta\psi\sin\epsilon_0 - (\psi_A^2/2)\cos\epsilon_0^2\ \Delta\epsilon. \end{aligned} \tag{2}$$

It should be noted that the equinox of date results from two different phenomena: the precession of the ecliptic, due to planetary perturbations, and the precession-nutation of the equator, due to the effect of the luni-solar and planetary torques on the oblate Earth. Such a reference should therefore be avoided for high accuracy developments. Furthermore, as there is not a unique and clear way to define an ecliptic (of date, or epoch), especially in a geocentric reference system of General relativity, relating equinox based precession-nutation parameters to the GCRS is a complex issue.

Therefore the CIO based precession-nutation parameters, which are related in a direct and rigorous way to the GCRS (the geocentric reference system recommended by the IAU 2000 resolutions for being used for the Earth), are the most appropriate parameters to be used for high accuracy precession-nutation.

2. THE PRECESSION-NUTATION EQUATIONS

The basis for the equations of the rotation of a rigid Earth are the Euler dynamical equations that express the angular momentum balance in the terrestrial reference system as functions of the components of the instantaneous rotation vector and external torque, and the Earth's principal moments of inertia, A, B, C. For an axially symmetric Earth, $A = B$ and the third component of the torque is equal to 0. The precession-nutation equations are obtained from these equations by appropriate transformations. The new variables can be either quantities defined in Section 1 (cf. Capitaine et al. 2006), or the precession and nutation angles referred to the ecliptic and equinox of date (cf. Kinoshita 1977, Williams 1994, Souchay et al. 1999), or the Euler angles ψ, ω, φ, defined in Section 1 (cf. Woolard 1953, Bretagnon et al. 1997). The components of the torque are in an intermediate celestial reference system defined by the CIP, and either the point Σ (cf Figure 1b), or the equinox of date, or the point γ_1' (cf Figure 2).

The precession-nutation equations for a rigid axially symmetric Earth are thus as follows:

(i) CIO based approach (Capitaine et al. 2006):

$$\begin{aligned} -\ddot{Y} + (C/A)\Omega\,\dot{X} &= L_\Sigma/A + F'' \\ \ddot{X} + (C/A)\Omega\,\dot{Y} &= M_\Sigma/A + G'', \end{aligned} \tag{3}$$

Ω being the mean Earth's angular velocity, L_Σ, M_Σ the equatorial components of the torque referred to Σ, and F'', G'' functions of X, Y and of their first and second time derivatives;

(ii) equinox based approach using the Euler angles (Bretagnon et al. 1997):

$$\begin{aligned} -\ddot{\omega} + (C/A)\Omega\,\dot{\psi}\sin\epsilon_0 &= L_{\gamma_1'}/A + F' \\ \sin\epsilon_0\ddot{\psi} + (C/A)\Omega\,\dot{\omega} &= M_{\gamma_1'}/A + G' \\ \ddot{\varphi} &= H', \end{aligned} \tag{4}$$

$L_{\gamma_1'}, M_{\gamma_1'}$ being the equatorial components of the torque referred to γ_1', and F', G', H' functions of ψ, ω, φ and of their first and second time derivatives.

Note that, unlike the Equations (4) based on the ecliptic, Equations (3) using the CIO based paradigm are independent of the variations in the Earth rotation angle. It should also be noted that the CIO based precession-nutation equations provide solutions that are directly expressed in the GCRS.

3. THE IAU PRECESSION-NUTATION MODEL

The IAU 2006/2000A precession-nutation is composed of the IAU 2000A Nutation (Mathews et al. 2002, denoted MHB2000), adopted by IAU 2000 Resolution B1.6 and the IAU 2006 precession (Capitaine et al. 2003, Hilton et al. 2006, denoted P03), adopted by IAU 2006 Resolution B1. The IAU 2000A semi-analytical series for nutation is composed of lunisolar and planetary terms with "in-phase" and "out-of-phase" components of the $\Delta\psi$, $\Delta\epsilon$ angles; they are transformed, from the REN2000 solution (Souchay et al. 1999) of these angles for a rigid Earth model, to nutation of a non-rigid Earth with the MHB2000 "transfer function". The IAU 2006 precession provides P03 polynomial expressions up to the 5th degree in time, both for the precession of the ecliptic and the precession of the equator. The IAU 2006 precession of the equator is based on the expressions of the fundamental quantities ψ_A and ω_A, which have been derived from the dynamical precession equations, using integration constants, such as values for the precession rates of the equator at J2000, the J2000 obliquity and the J_2 rate value.

While the IAU 2006 values for the precession rates of the equator are compatible with the IAU 2000 ones, updates have been applied to the J2000 obliquity, and to the J_2 rate, which was neglected in the IAU 2000 model. Consequently, very small changes, described in the following, are needed in a few of the IAU 2000A nutation amplitudes in order to ensure compatibility with the IAU 2006 precession.

(1) Introducing the IAU 2006 J_2 rate value ($dJ_2/dt = -3.0 \times 10^{-11}$/yr) gives rise to additional Poisson terms in nutation, the coefficients of which are proportional to $\dot{J}_2/J_2$ (*i.e.* -2.7774×10^{-6}/century). The largest corresponding changes (Capitaine and Wallace, 2006) in μas are, in the expressions for X, Y:

$$\begin{aligned} dX_{J2d} &= 18.8\ t \sin\Omega + 1.4\ t \sin 2(F - D + \Omega) \\ dY_{J2d} &= -25.6\ t \cos\Omega - 1.6\ t \cos 2(F - D + \Omega), \end{aligned} \tag{5}$$

and similar changes in the expressions for $\Delta\psi$, $\Delta\epsilon$ (F, D, Ω being fundamental arguments of nutations).

(2) The IAU 2006 obliquity ($84381.406''$) is different from the IAU 2000 obliquity ($84381.448''$) that was used when estimating the IAU 2000A nutation amplitudes. To compensate for this change, it is necessary to multiply the amplitudes of the nutation in longitude by (cf. Section 4) $\sin\epsilon_{\mathrm{IAU2000}}/\sin\epsilon_{\mathrm{IAU2006}}$.

The largest corresponding changes (Capitaine and Wallace, 2006) in μas are:

$$d_\epsilon\psi = \ -8.1\ \sin\Omega - 0.6\ \sin 2(F - D + \Omega). \tag{6}$$

Note that no such adjustment is needed in the case of X, Y. Note also that the periodic terms given by (5) are included in the IAU 2006/2000A version of the X, Y series. This shows that the use of these series ensures the best compatibility between the IAU 2006 precession and the IAU 2000 nutation.

The adjustments above are taken into account in the SOFA implementation of the IAU 2006/2000A precession-nutation as well as in the IERS Conventions 2010, but not in some other implementations. Whenever these corrections are included, a specific label, such as"IAU $2000\mathrm{A}_{\mathrm{R06}}$", or "IAU $2000\mathrm{A}_{\mathrm{R}}$" must be added to specify that the nutation has been revised for use with the IAU 2006 precession.

4. THE OBSERVED PRECESSION-NUTATION

VLBI is the only technique that is currently able to estimate high accuracy corrections to the precession-nutation model on a regular basis, as "celestial pole offsets", with the form of either (δX, δY), or ($\delta\psi$, $\delta\epsilon$). These observations are directly sensitive to the orientation of the Earth's equator (or the CIP) in the GCRS, but they are not sensitive to an ecliptic; therefore, the form used for the "celestial pole offsets" must reflect this property; this is not the case for ($\delta\psi$, $\delta\epsilon$).

The dependence of the precession in longitude, ψ_A (hence $\delta\psi$), on the ecliptic to which it is referred is shown in Figure 3. If such a dependence is ignored and the value for ψ_A is considered as being the "estimated" value, a change from ecliptic 1 (with obliquity at epoch, ϵ_{01}) to ecliptic 2 (with obliquity at epoch, ϵ_{02}) would give a change in the value for $\psi_A \sin\epsilon_0$ to which VLBI is actually sensitive. To compensate for this change, it is necessary to multiply ψ_A by $\sin\epsilon_{\mathrm{IAU2000}}/\sin\epsilon_{\mathrm{IAU2006}}$. For example, the change in the estimated rate in ecliptic longitude corresponding to the change from the IAU 2000 to IAU 2006 ecliptics is 2.37 mas/cy. This clearly shows that the equinox based precession-nutation

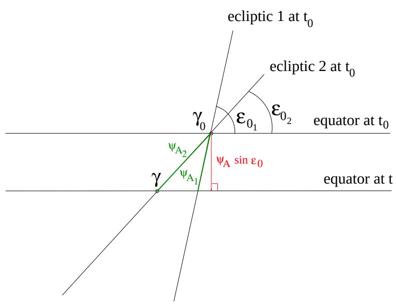

Figure 3: Difference in the precession in longitude referred to two different ecliptics.

parameters are dependent on the conventional ecliptic at epoch. Consequently, there is a big risk, when using such estimated quantities, of introducing inconsistencies between different determinations of nutation offsets. In contrast, the X, Y parameters, and hence (δX, δY), are independent of an ecliptic and are directly related to the motion of the CIP in the GCRS to which VLBI observations are sensitive.

5. CONCLUDING REMARKS

The precision goals for the motion of the CIP in the GCRS are a few μas over a time span of a few centuries. In order to achieve the corresponding accuracy in precession-nutation, it is necessary that the variables used in the equations, the parameters used in the models and the celestial pole offsets estimated from the observations be best compliant with the GCRS and the CIO based paradigm. The coordinates of the CIP unit vector in the GCRS that ensure all these conditions are the appropriate quantities to be used; the general use of the (δX, δY) celestial pole offsets is recommended to avoid various complexities.

In order to ensure the best consistency between the IAU 2006 precession and IAU 2000A nutation, it is necessary to take into account slight adjustments to the IAU 2000A nutation; a label should be given (e.g. "IAU 2006/2000A_{R06}", or "IAU 2006/2000A_R") to the precession-nutation implementations that contain these adjustments in order to clearly distinguish them from those without any adjustment.

6. REFERENCES

Bretagnon, P., Rocher, P., and Simon, J.-L., 1997, "Theory of the rotation of the rigid Earth," A&A 319, 305–317.

Capitaine, N., 1990, "The Celestial Pole Coordinates", Celest. Mech. Dyn. Astr. 48, 127–143.

Capitaine, N., Wallace, P.T., Chapront, J., 2003, "Expressions for IAU 2000 precession quantities", A&A 412, 567–586.

Capitaine, N., Wallace, P.T., 2006, "High precision methods for locating the celestial intermediate pole and origin", A&A 450, 855–872.

Capitaine, N., Folgueira, M. and Souchay, J., 2006, Earth rotation based on the celestial coordinates of the celestial intermediate pole I., The dynamical equations, 2006, A&A 445, 347–360.

Hilton, J., Capitaine, N., Chapront, J., et al., 2006, "Report of the International Astronomical Union Division I Working Group on Precession and the Ecliptic", Celest. Mech. Dyn. Astr. 94, 3, 351–367.

IERS Conventions (2010). G. Petit & B. Luzum (eds.), IERS Technical Note 36, Frankfurt am Main: Verlag des Bundesamts fr Kartographie und Geodsie.

Kinoshita, H., 1977, "Theory of the rotation of the rigid earth", Celest. Mech. 15, 277–326.

Lieske, J. H., Lederle, T., Fricke, W., and Morando, B., 1977, "Expressions for the Precession Quantities Based upon the IAU (1976) System of Astronomical Constants," A&A 58, 1–16.

Mathews, P.M., Herring, T.A. and Buffett B.A., 2002, "Modeling of nutation and precession: New nutation series for nonrigid Earth and insights into the Earth's interior", J. Geophys. Res. , 107(B4).

Souchay, J., Loysel, B., Kinoshita, H., and Folgueira, M., 1999, "Corrections and new developments in rigid Earth nutation theory: III. Final tables REN-2000 including crossed-nutation and spin-orbit coupling effects", A&AS 135, 111–131.

Williams, J. G., 1994, "Contributions to the Earth's obliquity rate, precession, and nutation", A&A 108, 711–724.

Woolard, E.W., 1953, "Theory of the rotation of the earth around its center of mass", Astronomical papers prepared for the use of the American ephemeris and nautical almanac, v. 15, pt. 1.

HIGHLY PRECISE CLOCKS TO TEST FUNDAMENTAL PHYSICS

S. BIZE, P. WOLF
LNE-SYRTE, Observatoire de Paris, UMR 8630 CNRS UPMC
61, avenue de l'Observatoire 75014 Paris, France
e-mail: sebastien.bize@obspm.fr

ABSTRACT. Highly precise atomic clocks and precision oscillators are excellent tools to test founding principles, such as the Equivalence Principle, which are the basis of modern physics. A large variety of tests are possible, including tests of Local Lorentz Invariance, of Local Position Invariance like, for example, tests of the variability of natural constants with time and with gravitation potential, tests of isotropy of space, etc. Over several decades, SYRTE has developed an ensemble of highly accurate atomic clocks and oscillators using a large diversity of atomic species and methods. The SYRTE clock ensemble comprises hydrogen masers, Cs and Rb atomic fountain clocks, Sr and Hg optical lattice clocks, as well as ultra stable oscillators both in the microwave domain (cryogenic sapphire oscillator) and in the optical domain (Fabry-Perot cavity stabilized ultra stable lasers) and means to compare these clocks locally or remotely (fiber links in the RF and the optical domain, femtosecond optical frequency combs, satellite time and frequency transfer methods). In this paper, we list the fundamental physics tests that have been performed over the years with the SYRTE clock ensemble. Several of these tests are done thanks to the collaboration with partner institutes including the University of Western Australia, the Max Planck Institut für Quantenoptik in Germany, and others.

TESTS OF LOCAL POSITION INVARIANCE

M. Niering et al.,
Measurement of the Hydrogen 1S-2S Transition Frequency by Phase Coherent Comparison with a Microwave Cesium Fountain Clock.
Phys. Rev. Lett. 84, 5496 (2000).

H. Marion, et al.,
Search for Variations of Fundamental Constants using Atomic Fountain Clocks.
Phys. Rev. Lett. 90, 150801 (2003).

M. Fischer et al.,
New Limits to the Drift of Fundamental Constants from Laboratory Measurements.
Phys. Rev. Lett. 92, 230802 (2004).

N. Ashby et al.,
Testing Local Position Invariance with Four Cesium-Fountain Primary Frequency Standards and Four NIST Hydrogen Masers.
Phys. Rev. Lett. 98, 070802 (2007).
Note: SYRTE contributed to this test through primary calibrations of the Interntational Atomic Time (TAI).

S. Blatt et al.,
New Limits on Coupling of Fundamental Constants to Gravity Using ^{87}Sr Optical Lattice Clocks.
Phys. Rev. Lett. 100, 140801 (2008).

C. G. Parthey et al.,
Improved Measurement of the Hydrogen 1S-2S Transition Frequency.
Phys. Rev. Lett. 107, 203001 (2011).

TESTS OF LOCAL LORENTZ INVARIANCE

P. Wolf P. et al.,
Tests of Lorentz Invariance using a Microwave Resonator.,
Phys. Rev. Lett. 90, 060402, (2003).

P. Wolf P. et al.,
Whispering Gallery Resonators and Tests of Lorentz Invariance.,
Gen. Rel. and Grav. 36, 2351 (2004).

P. Wolf P. et al.,
Improved test of Lorentz invariance in electrodynamics.,
Phys. Rev. D 70, 051902(R)(2004).

P.L. Stanwix et al.,
Test of Lorentz Invariance in Electrodynamics Using Rotating Cryogenic Sapphire Microwave Oscillators.,
Phys. Rev. Lett. 95, 040404 (2005).

P. Wolf P. et al.,
Cold Atom Clock Test of Lorentz Invariance in the Matter Sector.,
Phys. Rev. Lett. 96, 060801 (2006).

P.L. Stanwix et al.,
Improved test of Lorentz invariance in electrodynamics using rotating cryogenic sapphire oscillators.,
Phys. Rev. D74, 081101(R) (2006).

H. Müller et al.,
Tests of Relativity by Complementary Rotating Michelson-Morley Experiments.,
Phys. Rev. Lett. 99, 050401 (2007).

M. E. Tobar et al.,
Testing local Lorentz and position invariance and variation of fundamental constants by searching the derivative of the comparison frequency between a cryogenic sapphire oscillator and hydrogen maser.,
Phys. Rev. D81, 022003 (2010).

RELATIVITY AND LARGE RING-LASER GYROSCOPES

M.H. SOFFEL, W. TIAN
Lohrmann Observatory,
Dresden Technical University,
01062 Dresden, Germany
e-mail: michael.soffel@mailbox.tu-dresden.de

ABSTRACT. This article deals with a post-Newtonian description of large ring-laser gyroscopes. To this end first two local topocentric reference systems are introduced: a topocentric celestial (ToCRS) and a topocentric terrestrial reference system (ToTRS). The GCRS acts as starting point for these two systems. Whereas the ToCRS is kinematically non-rotating with respect to the GCRS the spatial coordinates of the ToTRS are determined by the ITRS. From the covariant Maxwell-equations a post-Newtonian expression for the Sagnac frequency shift is derived containing contributions from the geodetic-, Lense-Thirring- and Thomas-precession. These relativistic contributions are calculated as a function of some orientation angle α of the Sagnac platform. Conditions for the measurability of these terms by a system of laser-gyros are discussed.

1. CONCEPT OF LARGE RING-LASER GYROSCOPES

A ring-laser gyroscope that we will consider, consists basically of a closed tube filled with He-Ne gas in which laser activity is excited so that TWO laser beams, one traveling in clockwise the other one in counter-clockwise direction, interfere behind a beam splitter where the interference fringes can be analyzed (Figure 1). Such a gyroscope is an inertial device; if it rotates with respect to local inertial one sees a frequency difference between the co-rotating and the counter-rotating beam being proportional to the angular velocity $\mathbf{\Omega}$. This beat frequency or Sagnac frequency Δf is described by the Sagnac formula for active resonators:

$$\delta f = \frac{4A}{\lambda P}\, \mathbf{e}_A \cdot \mathbf{\Omega}\,.$$

Here A is the area enclosed by the laser-beams, λ the effective wavelength of the two beams, P the perimeter of the enclosed area and $\mathbf{e}_A$ is the unit normal vector perpendicular to it. For the 4m x 4m large G-ring at the geodetic fundamental station in Wettzell, Germany, this Sagnac frequency shift is 348.643 Hz.

2. RELATIVISTIC EXPRESSION OF THE SAGNAC FREQUENCY

To theoretically formulate the Sagnac frequency shift we have introduced two new reference systems: a TOpocentric Celestial Reference System (ToCRS) and a Topocentric Terrestrial System (ToTRS). Whereas the ToCRS is assumed to be kinematically non-rotating with respect to the Geocentric Celestial Reference System (GCRS) the spatial coordinates of the ToTRS are determined by the ITRS.

The ToCRS can principally be derived from results in the literature (Klioner & Soffel, 1998); as a check we have re-derived the corresponding metric tensor within the DSX-framework (Damour et al., 1991). We started with the GCRS with coordinates $(cT, \mathbf{X})$ and the metric tensor in the form

$$\begin{aligned} G_{00} &= -1 + \frac{2W}{c^2} - \frac{2W^2}{c^4} + \mathcal{O}(c^{-5}) \\ G_{0a} &= -\frac{4}{c^3} W_a + \mathcal{O}(c^{-5}) \\ G_{ab} &= \delta_{ab}\left(1 + \frac{2}{c^2} W\right) + \mathcal{O}(c^{-4}) \end{aligned}$$

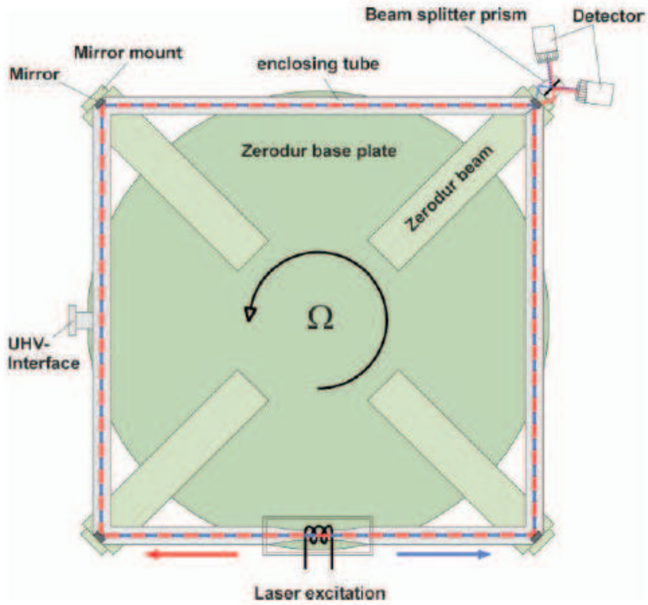

Figure 1: Schematic diagram of a ring-laser gyroscope.

with the geocentric metric potentials W and W_a. From the GCRS we then transformed to ToCRS coordinates $(c\tau, \mathbf{X}_T)$ according to Damour et al. (1991). As expected the local (linearized) metric has potentials

$$W_T = -\mathcal{A}\cdot\mathbf{X}_T\,, \qquad W_T^a = -\frac{c^2}{4}(\mathbf{\Omega}\times\mathbf{X}_T)^a\,.$$

Here $\mathcal{A}$ is the 4-acceleration of the topocenter, i.e, the (non-gravitational) acceleration of the topocenter as seen from a freely falling observer and, in case of the ToCRS, the angular velocity $\mathbf{\Omega} = \mathbf{\Omega}_{\rm iner}$ with

$$\mathbf{\Omega}_{\rm iner} = \mathbf{\Omega}_{\rm GP} + \mathbf{\Omega}_{\rm LT} + \mathbf{\Omega}_T\,.$$

The expressions for $\mathbf{\Omega}_{\rm GP}$ (geodetic precession), $\mathbf{\Omega}_{\rm LT}$ (Lense-Thirring) and $\mathbf{\Omega}_{\rm T}$ (Thomas precession) read

$$\mathbf{\Omega}_{\rm GP} = -\frac{3}{2c^2}\mathbf{V}\times\nabla W\,, \quad \mathbf{\Omega}_{\rm LT} = -\frac{2}{c^2}\nabla\times\mathbf{W}\,, \quad \mathbf{\Omega}_{\rm T} = \frac{1}{2c^2}\mathbf{V}\times\mathcal{A}\,,$$

where $\mathbf{V}$ is the GCRS velocity of the topocenter (a central point of the Sagnac platform), W is basically the Newtonian gravitational potential and the gravito-magnetic potential, $\mathbf{W}$, appearing in the Lense-Thirring part is determined by the Earth's intrinsic angular momentum $\mathbf{S}_{\rm E}$:

$$W_{\rm E}^a = -\frac{G}{2}\frac{(\mathbf{X}\times\mathbf{S}_{\rm E})^a}{R^3}\,.$$

The introduction of a ToTRS generalizes the DSX-framework by allowing for a fast rotation between the GCRS and the ToTRS. We define the ToTRS such that $\Omega_{\rm iner}$ above is replaced by $\mathbf{\Omega}_{\rm E} + \mathbf{\Omega}_{\rm iner}$, where $\Omega_{\rm E}$ is the angular velocity determined by the classical transformation between the GCRS and the ITRS.

From the relativistic Maxwell equations for the laser beams one then finds (e.g., Soffel, 1989)

$$\delta f = S\cdot\Omega^*\,,$$

where $S = (4A/\lambda P)$ is the scale factor and $\Omega^* = (\mathbf{\Omega}_{\rm E} + \mathbf{\Omega}_{\rm iner})\cdot\mathbf{e}_A$. If Φ_0 denotes the nominal latitude of the topocenter and α the tilt angle of $\mathbf{e}_A$ reckoned from the radial direction for Φ_0 towards the equator we get (see also Bosi et al., 2011)

$$\Omega^* = \Omega_{\rm E}\left(\sin(\Phi_0-\alpha) + 2\frac{GM_{\rm E}}{c^2R_{\rm E}}\cos\Phi_0\sin\alpha - \frac{2}{5}\frac{GM_{\rm E}}{c^2R_{\rm E}}(2\sin\Phi_0\cos\alpha + \cos\Phi_0\sin\alpha)\right)\,,$$

where we have used the moment of inertia of a rigid sphere in the expression for $\mathbf{S}_{\rm E}$.

To measure these relativistic effects very high demands must be satisfied (see also Di Virgilio et al., 2010; Bosi et al., 2011)

- sensitivity to rotation of 0.01 prad/s for about 1 hour of integration
- sensor stability of 1 part in 10^{10} over months to years
- sensor orientation to 1 nrad
- Length of Day (LoD) to 0.1 μs.

Obviously no present laser-gyro meets these requirements. The G-ring in Wettzell presently has a sensitivity of about 1 prad/s for one hour of integration time. To increase sensitivity one might, e.g., enlarge the enclosed area A. For the G-ring the required stability might be achievable for a certain period of time due to the Cerodur base plate with thermal expansion of less than 5×10^{-9}/deg, a good thermal isolation and a pressure stabilized enclosure. Also several feedback loops contribute to such a good stability. However, annual temperature variations of some 0.5 deg and internal photon backscatter are still problematic. The orientation of the platform is affected by several local effects, e.g., related with local hydrology (rainfall) that can be reduced significantly by going to larger depths below the ground. It has been suggested to perform such an experiment e.g., in the Gran Sasso laboratory in Italy, 120 km from Rome, with an average rock coverage of some 1400 m (Di Virgilio et al., 2010; Bosi et al., 2011). Finally, to monitor the LoD variations data from geodetic space techniques like VLBI have to be employed. The IERS Bulletin B gives a mean formal error of $4\,\mu$s for LoD-variations so one needs an improvement of about one order of magnitude here. Local contributions to $\mathbf{\Omega}_{\rm E}$, e.g., induced by near surface effects (thermo-elastic, topography, geology, meteorology) are likely to be reduced significantly deeply underground. To have full information of the rotation vector some multi-ring structure, e.g., mounted to the six faces of a cubic monument has been suggested (Bosi et al., 2011).

Acknowledgements. U.Schreiber, T.Klügel and A.Gebauer from Wettzell are thanked for their valuable comments.

3. REFERENCES

Bosi, F., Cella, G., Di Virgilio, A., et al., 2011, arXiv:1106.5072v1
Damour, T., Soffel, M., Xu, C., 1991, Phys.Rev. D **43**, 3273
Di Virgilio, A., et al., 2010, J.Mod.Phys., D **19**, 2331
Klioner, S., Soffel, M., 1998, Phys.Rev.D **58**, 084023
Soffel, M., 1989, Relativity in Astrometry, Celestial Mechanics and Geodesy, Springer, Berlin

ON GENERAL RELATIVITY TESTS WITH THE VLBI

S.B. LAMBERT, C. LE PONCIN-LAFITTE
Observatoire de Paris/SYRTE/CNRS/UPMC
61 av. de l'Observatoire 75014 Paris, France
e-mail: sebastien.lambert@obspm.fr, christophe.leponcin@obspm.fr

ABSTRACT. Relativistic bending in the vicinity of a massive body is characterized only by the post-Newtonian parameter γ within the standard parameterized post-Newtonian formalism, which is unity in General Relativity. To estimate this parameter, we use very long baseline interferometry (VLBI) to measure the gravitational deflection of radio waves by Solar System bodies emitted by distant compact radio sources.

1. ESTIMATING THE PPN PARAMETERS FROM VLBI DELAYS

We recently published two papers (Lambert & Le Poncin-Lafitte 2009, hereafter LL09, and Lambert & Le Poncin-Lafitte 2011, designated as LL11) wherein we estimated the post-Newtonian parameter γ by analyzing group delays recorded by astrometric and geodetic very long baseline interferometry (VLBI) at 8 GHz.

In LL09, we analyzed geodetic VLBI observations recorded between 1979 and 2009 excluding VLBA and RDV sessions. We compared estimates of γ and errors obtained with various analysis schemes, including global estimations over several time spans and with various Sun elongation cut-off angles, and with analysis of radio source coordinate time series. We arrived at the conclusion that the relativistic parameter γ cannot be estimated at better than 2×10^{-4}. The main factor of limitation is the uncertainty in determining of (global or session-wise) radio source coordinates. A sum of various instrumental and modeling errors and analysis strategy defects, which cannot be decorrelated and corrected yet, is at the origin of the limiting noise.

2. A POSSIBLE IMPROVEMENT USING SPECIALLY DESIGNED SESSIONS

With respect to LL09, the latest paper included additional sessions of the IVS regular geodetic monitoring program (IVS rapid turn around sessions R1 and R4) in 2009–2010, as well as a relatively small number of additional sessions after 1994 used of the 10-station North American Very Long Baseline Array (VLBA). The observing configuration of the VLBA network allows one to image sources and determine highly accurate station and source positions (see, e.g., Petrov et al. 2009). The VLBA can be used either alone (these sessions will be referred to as VLBA sessions in the following) or together with additional overseas antennas (denoted by VLBA+ sessions in the following) that push baseline lengths to more than 10,000 km. The former category includes the VLBA Calibrator Survey (VCS) programs 1 to 6 (Beasley et al. 2002, Fomalont et al. 2003, Petrov et al. 2005, 2006, Kovalev et al. 2007, Petrov et al. 2008) that were scheduled between 1994 and 2007. They contain observations as close as 1.4° to the Sun, which are indicated as green, vertical bands in Figure 1. In the latter category, one finds the sessions known as RDV experiments using the VLBA plus up to ten additional geodetic stations located worldwide (in blue in Figure 1). It appears that VLBA+ sessions stopped observing at less than 15° from the Sun after 2002, like all other routine VLBI experiments. VLBA and VLBA+ sessions usually have a number of observations larger than 10,000 and a postfit rms delay in the range 5–30 ps.

The most complete solution in LL09 processed 5,055 sessions between 3 August 1979 and 30 August 2010, totaling more than 7.3 millions ionosphere-free group delay measurements at 8 GHz. The analysis configuration is detailed in the relevant paper. Including both VLBA+ and VLBA sessions in our analysis, we obtained $\gamma = 0.99992 \pm 0.00012$. Note that adding VLBA+ and VLBA sessions increases the number of delays by 30% and the number of sources by a factor of four. Our results show that the VLBA experiments, although scheduled sparsely, have a good potential for General Relativity tests.

Although we do not challenge the results of Bertotti et al. (2003) from Cassini spacecraft measurements

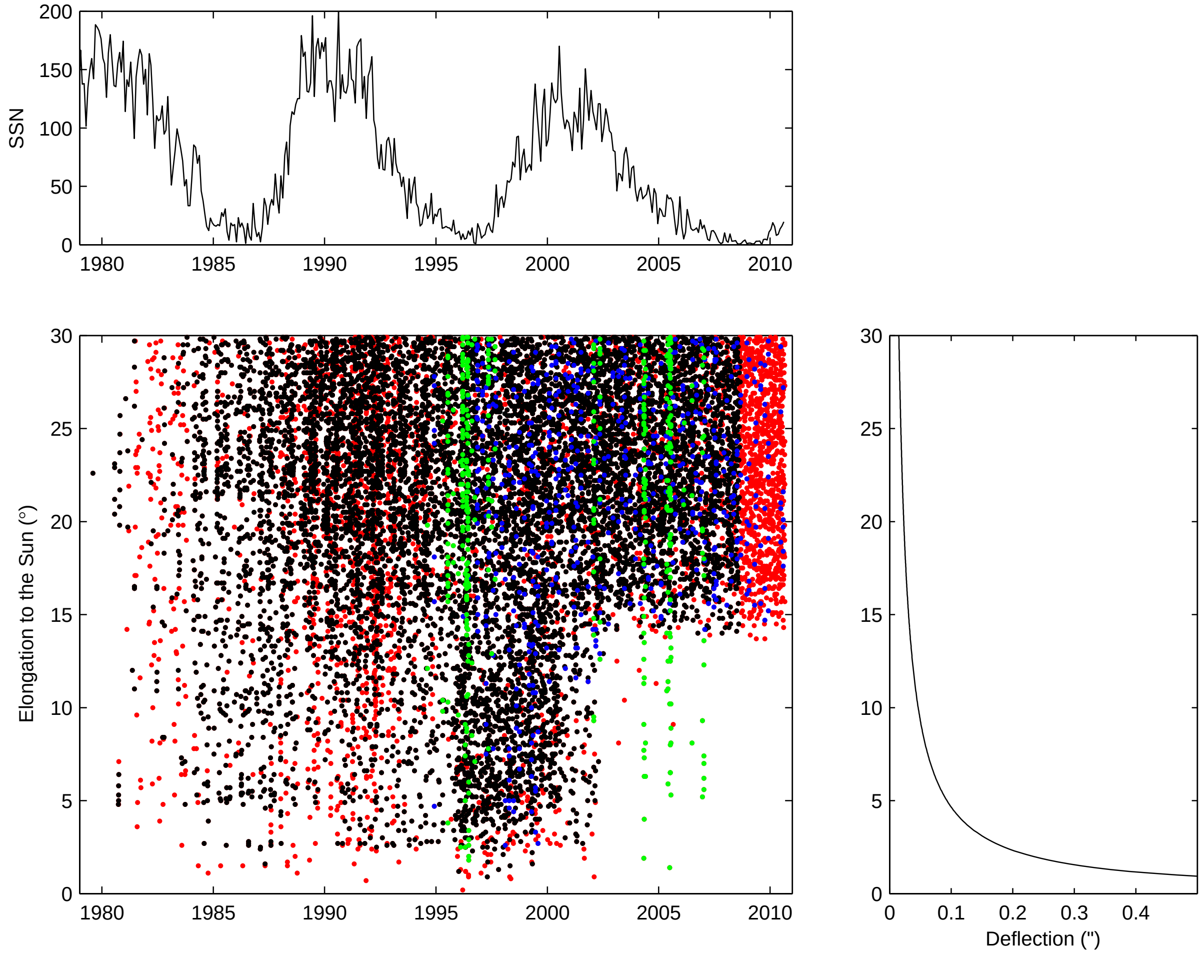

Figure 1: The main plot displays the observational history of the sources at less than 30° from the Sun (black: observations treated in LL09; red: additional observations of routine experiments not processed in LL09 excluding VLBA+ and VLBA; blue: VLBA+; green: VLBA). The upper plot gives the Sun spot number. The right plot displays the deflection angle predicted by General Relativity.

($\gamma = 1.00002 \pm 0.00002$), the results presented in this study are notable because they illustrate the capability of certain geodetic/astrometric VLBI networks and observing configurations to increase the sensitivity to γ. The VLBI observational data base provides a very flexible way to test General Relativity in the Solar System at the level of 10^{-4} thanks to the public availability of the data and the low CPU time taken by the solutions.

This data base is still increasing with new observations of very good quality thanks to a great, joint effort of worldwide radio astronomical observatories and space agencies. The upcoming VLBI 2010 will be designed in particular to reduce systematic errors, including possible source structure corrections thanks to faster antennas, larger networks, and higher data rates resulting in a *uv* coverage that is much better than in the current geodetic experiments (Petrachenko et al. 2008). This new VLBI network will likely lead to improved ground-based tests of General Relativity (Heinkelmann & Schuh 2010). We therefore encourage VLBI observing program committees to schedule observations of sources close to the Sun as in the VLBA calibrator survey sessions.

3. REFERENCES

Beasley, A. J., Gordon, D., Peck, A. B., et al. 2002, ApJSS, 141, 13

Bertotti, B., Iess, L., & Tortora, P. 2003, Nature, 425, 374
Fomalont, E. B., Petrov, L., MacMillan, D. S., et al. 2003, AJ, 126, 2562
Heinkelmann, R., & Schuh, H. 2010, In: S. A. Klioner et al. (Eds.), Proc. International Astronomical Union (IAU), 261, 286
Lambert, S. B., & Le Poncin-Lafitte, C. 2009, A&A, 499, 331
Lambert, S. B., & Le Poncin-Lafitte, C. 2011, A&A, 529, A70
Lambert, S. B., Dehant, V., & Gontier, A.-M. 2008, A&A, 481, 535
Petrachenko, W. T., Charlot, P., Collioud, A., et al. 2008, In: N. Capitaine (Ed.), Proc. Journées 2007 Systèmes de Référence Spatio-Temporels, Observatoire de Paris, France
Petrov, L., & Boy, J.-P. 2004, J. Geophys. Res., 109, 3405
Petrov, L., Kovalev, Y. Y., Fomalont, E. B., & Gordon, D. 2005, AJ, 129, 1163
Petrov, L., Kovalev, Y. Y., Fomalont, E. B., & Gordon, D. 2006, AJ, 131, 1872
Kovalev, Y. Y., Petrov, L., Fomalont, E. B., & Gordon, D. 2007, AJ, 133, 1236
Petrov, L., Kovalev, Y. Y., Fomalont, E. B., & Gordon, D. 2008, AJ, 136, 580
Petrov, L., Gordon, D., Gipson, J., et al. 2009, J. Geod., 83, 859

GENERAL RELATIVISTIC DELAYS IN CURRENT AND FUTURE VLBI

B. SOJA, L. PLANK, H. SCHUH
Institute of Geodesy and Geophysics, Vienna University of Technology
27-29 Gußhausstraße, A-1040 Wien, Austria
e-mail: b.soja@gmx.at, lucia.plank@tuwien.ac.at
harald.schuh@tuwien.ac.at

ABSTRACT. The effect of gravitational time delay due to general relativity is clearly visible in VLBI measurements. While the Sun and the Earth cause gravitational delays up to some nanoseconds respectively picoseconds in geodetic VLBI observables, standard delay models also recommend the inclusion of Jupiter, the Earth's Moon and some of the other planets on the modeling side.

Using the IERS Conventions model, we have calculated the gravitational time delay of standard VLBI observation constellations of the past years. The influences due to the Sun, the Earth, the Moon, Jupiter, Saturn and Venus were large enough to justify their consideration in routine VLBI data analysis (based on the accuracy of the upcoming VLBI2010 system). For VLBI data before 2002, the higher order term of the Sun should also be taken into account. Additionally, the relation between the gravitational delay of the Earth and the estimated tropospheric parameters (e.g. zenith wet delays) was investigated.

1. INTRODUCTION

From General Relativity we know that electromagnetic waves are affected by gravity in terms of bending and dilation. This is also the case for the signals coming from the extragalactic radio sources which are observed by VLBI. As both ray paths in VLBI usually do not pass a gravity source at the same distance, the individual rays are bent and delayed in a different way. VLBI observes the relative time delay τ of the signals' arrival time at the two stations and therefore only the relative gravitational delay ΔT_{grav} between the two rays is of interest. This delay, also called Shapiro delay, is included in the IERS Conventions model for VLBI (Petit and Luzum, 2010). The calculation is based on the so-called consensus model from the beginning of the 90s. The main term can be computed as follows:

$$\Delta T_{grav} = 2\frac{GM}{c^3} \ln \frac{|\vec{R}_1| + \vec{K} \cdot \vec{R}_1}{|\vec{R}_2| + \vec{K} \cdot \vec{R}_2} \tag{1}$$

with G being the gravitation constant, M the mass of the gravitating body, c the speed of light, $\vec{K}$ the barycentric unit vector towards the radio source and $\vec{R}_i$ the vectors between the gravitating body's center of mass and the two telescopes. The factor 2 comes from $1+\gamma$, γ being the PPN parameter describing the curvature of space due to the existence of mass. In general relativity $\gamma = 1$ (Soffel, 1989). The model of the IERS Conventions is designed to assure an accuracy of 1 ps and therefore includes all terms of the order of 0.1 ps. It recommends to include the gravitational effects of the Sun, the Earth, the Moon, and most other planets.

2. AIMS

In the next decade, with the upcoming VLBI2010 system, new VLBI technology, new types of antennas (small dishes, fast slew rates), and new observing strategies will be used (Petrachenko et al., 2009). The number of observations will increase significantly. The aim is to reach a position accuracy of 1 mm. On this basis, the theoretical model should at least include all terms of the order of 0.1 mm or 0.3 ps (Heinkelmann and Schuh, 2009). Compared to the accuracy level of the current IERS model, the level derived from VLBI2010 is less rigorous, but based on realistic prospects. Currently, the influence of some of the recommended bodies is not yet crucial since there are error sources of much greater magnitude. In the following chapter we will describe which terms and celestial bodies should be included when considering the VLBI2010 accuracy limits.

3. THEORETICAL DELAYS

Based on the observation constellations of the past years, theoretical delays according to the IERS Conventions were computed. They were split up into several terms of interest. Basically, for every observation and every important celestial body equation (1) was evaluated. The constellations of the R1 and R4 sessions by the International VLBI Service for Geodesy and Astrometry (IVS; Schlüter and Behrend, 2007) between 2002 and 2009 were used. These are sessions observed twice a week to determine Earth orientation parameters. In total, about 1.5 million observation constellations were processed. The Vienna VLBI Software (VieVS) (Böhm et al., 2011) was used for the computations.

For several observations, the delay caused by the Sun reached values >1 m when multiplied with the speed of light and 99.9% were above the 0.1 mm/0.3 ps limit (Table 1). In the case of the gravitational influence of the Earth, this ratio was 96.0% with maximum values of 5-6 mm. The left plot of Figure 1 shows the computed delays caused by Jupiter. Roughly 1 out of 50 observations had a gravitational delay due to Jupiter larger than 0.3 ps. Jupiter is therefore a very important body to consider. Next important was the influence of Saturn (Figure 1, right plot) with 0.1% of 1.5 million delays above the limit. The Moon's impact was still lower (0.02%). The least important celestial body to have gravitational delays above the 0.3 ps level was Venus (for nine observations in total the limit was surpassed). Neptune and Uranus reached delays of 0.1 ps. The inclusion of these two planets is recommended by the IERS Conventions model but they are not necessary if we base our limits on the 1 mm accuracy of VLBI2010. Mercury and Mars can be neglected in any case.

	Sun	Earth	Jupiter	Saturn	Moon	Venus	Neptune	Uranus
abs. > 1 ps	1515853	1322912	2923	73	5	0	0	0
rel. [%]	99.70	87.01	0.19	0.00	0.00	0	0	0
abs. > 0.3 ps	1519034	1459686	29674	1327	274	9	0	0
rel. [%]	99.91	96.01	1.95	0.09	0.02	0.00	0	0
abs. > 0.1 ps	1519964	1500156	242522	10189	2150	117	33	5
rel. [%]	99.97	98.67	15.95	0.67	0.14	0.01	0.00	0.00

Table 1: Number of observation constellations with gravitational delays larger than 1 ps, 0.3 ps and 0.1 ps and their percentage compared to the 1520401 constellations of the IVS-R1 and IVS-R4 sessions between 2002 and 2009.

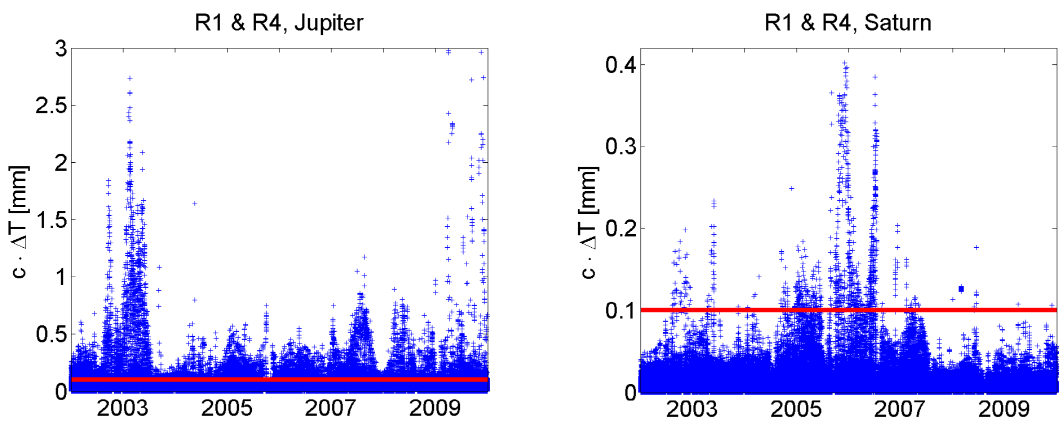

Figure 1: Gravitational delays for IVS-R1 and IVS-R4 sessions between 2002 and 2009 due to Jupiter (left) and Saturn (right) with respect to 0.3 ps/0.1 mm (red line). Every symbol represents the delay for one observation constellation.

4. SUN'S TERM OF HIGHER ORDER

The term depicted in Equation (1) is only the main term to describe the gravitational influence. There are also terms of higher order, with the next most important being caused by the bending of the ray path (Petit and Luzum, 2010):

$$\delta \Delta T_{grav} = 4 \frac{G^2 M^2}{c^5} \frac{\vec{b} \cdot (\hat{R}_1 + \vec{K})}{(|\vec{R}_1| + \vec{R}_1 \cdot \vec{K})^2} \tag{2}$$

This correction is significantly smaller and recommended to apply for observations close to the Sun. However, such observations are also strongly influenced by the Sun's radiation that reduces the coherence of the signals. To avoid measurements of low quality (especially during periods of high solar activity), in the mid of 2002 a stringent cut-off elongation angle of about 15° towards the Sun was introduced by the IVS. In analogy to the main terms of the gravitational delay of the different celestial bodies, the question arises with respect to this term of higher order for the Sun whether an inclusion in theoretical models is justified. The considered limit is again 0.1 mm/0.3 ps.

For analysing the effect of the cut-off elongation angle introduced in 2002, VLBI data from the begin of 1998 to the end of 2003 were processed. For all observation constellations during this period (roughly 1.9 million) the term of higher order of the Sun was computed according to Equation (2). Figure 2 (left plot) shows the theoretical delays for all of these constellations. It can be recognized that before 2002 there are a few observations with gravitational delays >0.3 ps and after 2002 there are none.

5. EARTH'S INFLUENCE ON STATION COORDINATES

In Chapter 3 we have shown that the influence of the Earth on VLBI delays can reach up to 6 mm, indicating the role of the Earth as the second most important body to consider after the Sun. In this chapter we want to show the influence of the Earth on the estimated station coordinates.

The gravitational delay of the Earth is calculated using Equation (1) with R_i as the geocentric coordinate vectors of the stations. For the Earth, Schuh (1987) states that this equation can be written in dependence of the elevation angles E_i of both radio telescopes:

$$\Delta T_{grav,E} = 2 \frac{GM_E}{c^3} \ln \frac{1 + \sin(E_1)}{1 + \sin(E_2)} \tag{3}$$

In this representation it becomes evident that the difference of the elevation angles and the gravitational delay due to the Earth are positively correlated. In this respect the gravitational influence of the Earth is closely related to that of the troposphere. Here the mapping functions of the different stations are strongly dependent on the elevation angles (in the simplest case $\frac{1}{\sin E}$). Since the tropospheric influence on the delay τ is calculated as the difference between the influences of the respective stations, this effect is also larger with big elevation angle differences between the stations. Because of this correlation between troposphere and Earth gravitation we supposed that there is a difference if you estimate station coordinates including an estimation of troposphere parameters like zenith wet delays and gradients or if these parameters are not considered.

For these investigations, we created artificial observation files with VieVS based on the schedule of the R1 and R4 sessions between 2002 and 2009. The observables in these files are identical to the calculated time delays for the respective observation constellations. Solving for the station coordinates using these artificial files combined with a slightly modified theoretical model (in our case: exclusion of the gravitational influence of the Earth) provides corrections that show solely the effect of the modified parameters. The corrections for the coordinates of the 19 VLBI sites involved in the sessions were estimated for each session and then averaged over the whole time span. The same procedure was repeated including the estimation of the tropospheric parameters.

The gravitational influence of the Earth without estimating the troposphere was 2–7 mm for the radial components / station heights (Figure 2, right plot) with an average of 4.0 mm corresponding to $\sim$0.6 ppb in the scale of the corresponding TRF from VLBI. The amount of this effect was dependent on the station distribution: stations on the southern hemisphere or in Japan usually are part of longer baselines and therefore have been more affected than stations located in or near Europe. When comparing these results with those including troposphere estimation it became evident that the gravitational influence declined. This effect was up to 1 mm for the radial components. This means that there was in fact a noticeable correlation between the gravitational and tropospheric influences. Some of the model error caused by disregarding the Earth influence was soaked up by the tropospheric parameters.

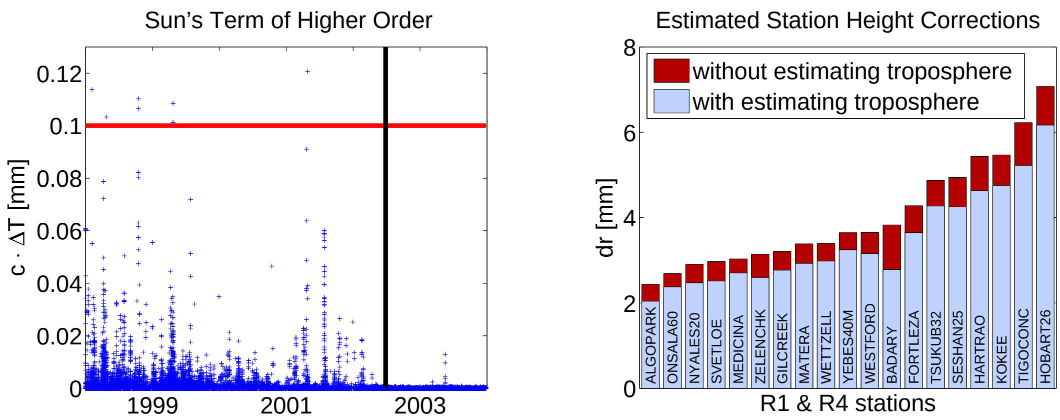

Figure 2: Left: Gravitational delays of higher order for sessions between 1998 and 2003 due to the Sun with respect to 0.3 ps/0.1 mm (red line). Cut-off elongation angle was changed from 5° to 15° since mid of 2002 (black line). Right: Mean influence of Earth gravitation on station heights for IVS-R1 and IVS-R4 sessions between 2002 and 2009 with/without estimating tropospheric parameters.

6. CONCLUSION

In this paper it is shown that there have been observation constellations in the past in which the theoretical gravitational influence of certain celestial bodies of our solar system are of a magnitude which cannot be neglected when aiming to achieve a positional accuracy of 1 mm (VLBI2010). These bodies include the Sun, the Earth, Jupiter, Saturn, the Earth's Moon and Venus. It is suggested that in new versions of software packages for VLBI computations these findings are considered by adapting the implementation of the gravitational delay model accordingly.

The influence of Earth's gravitation on the estimated station coordinates was also investigated by calculating this effect on the radial components with 2–7 mm. The size of this effect was dependent on the geometric station distribution. When additionally estimating tropospheric parameters it becomes evident that there is a correlation between the gravitational influence of the Earth and the troposphere: zenith wet delays and gradients absorb up to 1 mm of the gravitational influence.

7. REFERENCES

Böhm, J., et al., 2011, "The new Vienna VLBI Software VieVS", In: S. Kenyon, M. C. Pacino, U. Marti (eds), Proceedings of the 2009 IAG Symposium, Buenos Aires, Series: International Association of Geodesy Symposia Series, Vol. 136 in press, Springer, 2011, ISBN 978-3-642-20337-4.

Heinkelmann, R., Schuh, H., 2009, "Very Long Baseline Interferometry: Accuracy limits and relativistic tests", In: S. Klioner, P. K. Seidelmann und M. Soffel (eds), Proceedings IAU Symposium No. 261, doi: 10.1017/S1743921309990524.

Petit, G., Luzum, B., 2010, "IERS Conventions 2010, IERS Technical Note No. 36, Chapter 11: General relativistic models for propagation", Frankfurt am Main: Verlag des Bundesamts für Kartographie und Geodäsie, ISBN 3-89888-989-6, pp. 159-165.

Petrachenko, B., et al., 2009, "Design Aspects of the VLBI2010 System", Prog. Rep. of the IVS VLBI2010 Comm., NASA/TM-2009-214180, ftp://ivscc.gsfc.nasa.gov/pub/misc/V2C/TM-2009-214180.pdf.

Schlüter, W., Behrend, D., 2007, "The International VLBI Service for Geodesy and Astrometry (IVS): current capabilities and future prospects", Journal of Geodesy, Vol. 81, Nos. 6-8, pp. 379-387, doi: 10.1007/s00190-006-0131-z.

Schuh, H., 1987, "Die Radiointerferometrie auf langen Basen zur Bestimmung von Punktverschiebungen und Erdrotationsparametern", Verlag der Bayrischen Akademie der Wissenschaften, Reihe C, Dissertationen, Heft Nr. 328, ISBN 3 7696 9378 7 {german}.

Soffel, M. H., 1989, "Relativity in Astrometry, Celestial Mechanics and Geodesy", Springer, Berlin, Heidelberg, New York, A&A library, ISBN 3-540-18906-8.

SEMI-ANALYTICAL INTEGRATION OF PRECESSION-NUTATION BASED ON THE GCRS COORDINATES OF THE CIP UNIT VECTOR

N. CAPITAINE[1], M. FOLGUEIRA[2,1]

[1] SYRTE, Observatoire de Paris, CNRS, UPMC
61, avenue de l'Observatoire, 75014 – Paris, France
e-mail: n.capitaine@obspm.fr

[2] Sección departamental de Astronomía y Geodesia, Facultad de Ciencias Matemáticas
Universidad Complutense de Madrid, Spain
email: martafl@mat.ucm.es

ABSTRACT. In a previous paper (Capitaine et al. 2006), referred here as Paper I, we demonstrated the possibility of integrating the Earth's rotational motion in terms of the coordinates (X, Y) of the celestial intermediate pole (CIP) unit vector in the Geocentric celestial reference system (GCRS). Here, we report on the approach that has been followed for solving the equations in the case of an axially symmetric rigid Earth and the semi-analytical (X, Y) solution obtained from the expression of the external torque acting on the Earth derived from the most complete semi-analytical solutions for the Earth, Moon and planets.

1. THE EQUATIONS AND INTEGRATION METHOD

In the axially symmetric case, the rigorous form of the precession-nutation equations of a rigid Earth model in terms of the GCRS coordinates (X, Y) of the CIP unit vector established in Paper I are:

$$\begin{aligned} -\ddot{Y} + \sigma \dot{X} &= \frac{L}{A} + F'', \\ \ddot{X} + \sigma \dot{Y} &= \frac{M}{A} + G'', \end{aligned} \tag{1}$$

where $\sigma = \frac{C\omega}{A}$ is the frequency of the Euler free motion in the celestial system, A and C being the Earth's principal moments of inertia and ω the mean angular velocity of the Earth.

L and M are the first two components of the external torque acting of the Earth in the geocentric celestial reference system denoted CIRS' (defined by the CIP and the point Σ on the CIP equator such that $\Sigma\mathrm{M} = \Sigma_0\mathrm{M}$, M being the node of the CIP equator on the GCRS equator and Σ_0 the origin on the GCRS equator). F'' and G'' are functions of the (X, Y) quantities and their first and second time derivatives; their rigorous expressions have been provided in Paper I (Equations 25 and 44).

The (X, Y) solutions are obtained by integration of Equation (1) by the method of variations of parameters.

2. SEMI-ANALYTICAL COMPUTATIONS

The external torque considered in this study is that caused by the solar system objects on the non-spherical Earth, supposed to be rigid and axially symmetric. The largest contribution is the torque exerted by the Moon for which it is necessary to take into account the contributions produced by the Earth's zonal coefficients J_2, J_3 and J_4. The CIRS' components $(L_\mathrm{M}, M_\mathrm{M})$ of the lunar torque are:

$$\begin{pmatrix} L_\mathrm{M} \\ M_\mathrm{M} \end{pmatrix} = k'_{J_2}\left(\frac{a}{r}\right)^3 \begin{pmatrix} v'\,w' \\ -u'\,w' \end{pmatrix} k'_{J_3}\left(\frac{a}{r}\right)^4 \begin{pmatrix} v'\,(1-5w'^2) \\ -u'\,(1-5w'^2) \end{pmatrix} + k'_{J_4}\left(\frac{a}{r}\right)^5 \begin{pmatrix} \frac{1}{3}v'w'\,(3-7w'^2) \\ -\frac{1}{3}u'w'\,(3-7w'^2) \end{pmatrix}, \tag{2}$$

where r is the geocentric distance of the Moon, a is the semi-major axis of the lunar orbit, u', v', w', are the CIRS' components of the geocentric unit vector toward the Moon, and:

$$k'_{J_2} = \frac{3Gm}{a^3} MR^2\, J_2; \quad k'_{J_3} = \frac{1}{2}\left(\frac{R}{a}\right) \frac{3Gm}{a^3}\, MR^2\, J_3; \quad k'_{J_4} = \frac{5}{2}\left(\frac{R}{a}\right)^2 \frac{3Gm}{a^3}\, MR^2\, J_4\,, \tag{3}$$

G being the gravitational constant, R the mean radius of the Earth, M the mass of the Earth and m the mass of the Moon.

The development of the torque exerted on the Earth by the Sun and the planets can be obtained with the same approach as for the case of the Moon. Due to the distance of these bodies to the Earth as compared to that of the Moon to the Earth, only the effects related to the zonal coefficients J_2 and J_3 for the Sun, and the zonal coefficient J_2 for the planets, have to be considered for ensuring consistent accuracies. In the case of the planets, additional computations have been performed in order to obtain the analytical expressions for $(a_P/r)^3$ (a_P being the semi-major axis of the planet and r its geocentric distance) for both inner and outer planets.

The semi-analytical computations that have been performed for obtaining the expressions of (i) the components of the torque acting on the Earth and (ii) the solutions of the differential Equation (1), include polynomial forms of time and periodic components with several hundreds or thousands of Fourier and Poisson terms (up to the 5th order in time). The computations are based on the lunar theory ELP2000 (Chapront-Touzé & Chapront 1998) and the planetary theory VSOP87 (Bretagnon & Francou 1988) as well as on the use of the software package GREGOIRE (Chapront 2003) devoted to Fourier and Poisson series manipulations. The fundamental nutation arguments are referred to the J2000 ecliptic and equinox (cf. Bretagnon et al. 1998); the numerical values for the constants relative to the dynamics of the Earth, Moon and planets are from the IAU 2009 System of astronomical constants (Luzum et al. 2011). Table 1 provides the number of Fourier and Poisson terms considered for the different parts (due to the Moon, the Sun and the planets, respectively) of the L and M components of the torque in order to obtain the (X, Y) solution with a microarcsecond accuracy.

External torque due to	the Moon	the Sun	the planets
number of terms in the (L, M) components			
	$\boldsymbol{J_2}$	$\boldsymbol{J_2}$	$\boldsymbol{J_2}$
	(2386, 2060) Fourier	(244, 228) Fourier	(70, 70) Fourier
	(375, 474) Poisson 1st order	(36, 49) Poisson 1st order	(10, 10) Poisson 1st order
	(90, 81) Poisson 2nd order	(5, 5) Poisson 2nd order	
	(5, 8) Poisson 3rd order	(2, 3) Poisson 3rd order	
	$\boldsymbol{J_3}$	$\boldsymbol{J_3}$	
	(435, 391) Fourier	(5, 4) Fourier	
	(76, 100 Poisson 1st order	(2, 2) Poisson 1st order	
	(13, 14) Poisson 2nd order		
	$\boldsymbol{J_4}$		
	(86, 85) Fourier		
	(10, 21) Poisson 1st order		

Table 1: Number of terms considered in the expression of the external torque acting on the Earth.

3. PRELIMINARY RESULTS

The precession-nutation solutions for a rigid Earth obtained directly in the (X, Y) variables by this new method, show an agreement at the 10–100 μas level (depending on the frequency of the term) with those that we have derived indirectly in those variables from the most accurate nutation series (Bretagnon et al. 1998, Souchay et al. 1999), expressed originally in the classical variables $(\Delta\psi, \Delta\epsilon)$.

4. REFERENCES

Bretagnon, P. and Francou, G., 1988, A&A 202, 309.
Bretagnon, P., Francou, G., Rocher, P., Simon, J.L., 1998, A&A 329, 329.
Capitaine, N., Folgueira, M. and Souchay, J., 2006, A&A 445, 347 (denoted Paper I).
Chapront, J., 2003, Notice, Paris Observatory (January 2003).
Chapront-Touzé M. and Chapront J., 1998, A&A 190, 342.
Luzum, B., Capitaine, N., Fienga, A., Folkner, W. et al., 2011, Celest. Mech. Dyn. Astr. 110, 4, 293.
Souchay, J., Loysel, B., Kinoshita, H. and Folgueira, M., 1999, A&AS 135, 111.

STATUS OF THE GLORIA GEODETIC VLBI ANALYSIS SOFTWARE PACKAGE

S.B. LAMBERT
Observatoire de Paris/SYRTE/CNRS/UPMC
61 av. de l'Observatoire 75014 Paris

ABSTRACT. Initiated in the 1990s in and around the Paris Observatory, GLORIA (GLObal Radio Interferometric Analysis) has been used several times in the past for O–C comparisons (e.g., during the test phase of the IAU 2000 models) and was operational for the analysis of intensive sessions. Late 2010, I proposed to develop the software with the objective of being operational in a near future. Here is a short report on the current status of this software package.

1. GENERAL STRUCTURE

GLORIA allows one to compute the theoretical, build up observation equations, and solve for the parameters. It looks for the relevant information in the GSFC data base files as submitted to the IVS data centers. Note that the current version treats single frequency observations only: the ionosphere calibration is not handled yet and taken from the database. Observations with DELUFLAG=2 are eliminated. As well, in the current version, observations with missing meteorological data are eliminated.

It returns partials with respect to the five EOP (polar motion, UT1, and X, Y coordinates of the celestial pole), baseline and source coordinates, wet and dry zenith troposphere delays, wet and dry East and North troposphere gradients, and the post-Newtonian relativistic parameter. The theoretical delay and delay rate are computed using the most recent astronomical and geophysical models (see Table). Especially, GLORIA implements the non-rotating origin based transformation between celestial and terrestrial reference frames.

2. PARAMETERIZATION AND SOLUTION SCHEME

GLORIA implements various constraints: minimal constraints (no-net rotation and translation for the stations, no-net rotation for the sources), absolute and relative constraints for EOP, clocks, and atmosphere parameters. Source and station coordinates, and the post-Newtonian parameters can be estimated as offsets. EOP and troposphere (ZTD and gradients) time behavior can be modeled as piecewise linear functions. Clock drift can be modeled as degree-2 polynomials. The time interval on which each parameter is estimated is chosen by the user.

For the analysis, SHELL scripts successively call various routines. First, an O–C file is created, containing observed and theoretical delays, as well as partials. Second, after a preliminary solution with a standard parameterization, the residuals are investigated so that big outliers are eliminated. Data are iteratively reweighted so that the χ^2 converges reasonably close to unity. Finally, the system is inverted again with reweighted data and using the desired parameterization to get the final estimates.

An operational-like solution has been set up with a classical parameterization: session-wise EOP, rates and station coordinates, 3-hr ZTD and 6-hr gradient estimates, and up-to-date modeling and mapping. Figure 1 compares the pole coordinates, UT1–UTC, and celestial pole coordinates with the a priori data. Rms of the difference is of ~ 1 mas for the pole and 0.34 ms for UT1. The figure shows no systematics. However, the reweighting and/or inversion scheme, as well as the constraint weights, should be further investigated to improve these results.

Plate motion	NNR-NUVEL1A
Ephemerides	DE 405/ELP 2000
Tidal displacement	IERS Conv. 2003
Nutation and precession	IAU 2000A/IAU 2006
Ocean loading	FES 2004
Atmospheric loading	APL (Wijaya et al. 2011)
Mapping functions	VMF1 (Böhm & Schuh 2007)
Antenna thermal deformation	Nothnagel (2009)
Antenna axis offsets	IVS Analysis Coordinator's office
Troposphere gradients	Chen & Herring (1997)
A priori EOP	IERS EOP 08 C 04
A priori station positions/velocities	VTRF 2008A
A priori source coordinates	ICRF2

Table 1: Most recent astronomical and geophysical models available in GLORIA.

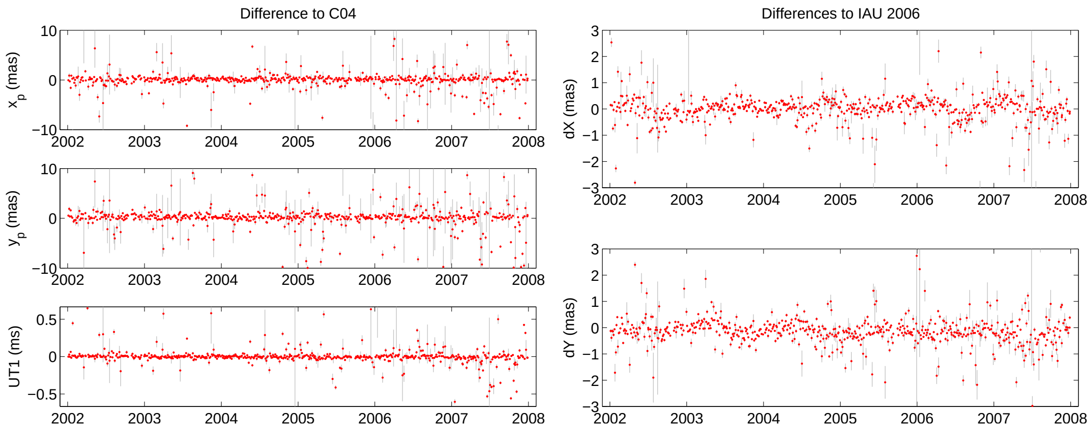

Figure 1: Session-wise estimates of EOP using IVS rapid sessions between 2002 and 2008.

3. REFERENCES

Böhm, J., & Schuh, H. 2007, J. Geod., doi:10.1007/s00190-007-0144-2
Chen, G., & Herring, T. A. 1997, J. Geophys. Res., doi:10.1029/97JB01739
Nothnagel, A. 2009, J. Geod., doi:10.1007/s00190-008-0284-z
Wijaya, D. D., Böhm, J., Schindelegger, M., et al. 2011, submitted to J. Geophys. Res.

METHODS OF USE AND PRESENTATION OF THE ACCURATE ASTROMETRIC DATA BASED ON THE MODERN TERRESTRIAL AND CELESTIAL REFERENCE SYSTEMS

M. SEKOWSKI, J. KRYNSKI
Institute of Geodesy and Cartography
27 Modzelewskiego St., 02-679 Warsaw, Poland
e-mail: msek@igik.edu.pl, krynski@igik.edu.pl

ABSTRACT. The increasing precision of the modern astrometric data as well as changes from the introduction of a new paradigm for the relations of terrestrial and celestial systems, forces the changes in methods of the usage and presentation of the data. The paper presents the efforts undertaken to satisfy these needs in the “Rocznik Astronomiczny”. Among the issues under consideration are: 1) identification and analysis of the sources of problems with interpolation of the high accuracy data; 2) reviewing the used interpolation methods; 3) development of the new methods of presenting of the high accuracy data, allowing their proper interpolation; 4) research on the need and the possibility to redefine the ”Besselian Numbers” algorithm in calculations of the ”apparent places”, to the form in which it could be used in the new paradigm (CIP/CIO).

1. INTERPOLATION OF APPARENT POSITIONS OF STARS

Apparent positions of stars are usually published with an interval of 1 or 10 days (Krynski, Sekowski, 2003–2010). For interpolation the most important are the factors which cause the highest amplitude changes of apparent position of a star in a short time.

Annual aberration of light — the effect within a single day slightly differs from a linear one. In the extreme case, the linear interpolation errors for 24 hours interval shall not exceed 1 mas. In the case of 10-days intervals, linear interpolation errors can reach values of 70÷80 mas; in this case a quadratic interpolation gives compliance at 1 mas (Sekowski, 2006).

Precession and nutation — nutation of the pole of the Intermediate Reference System is the major factor affecting the variability of the apparent position of stars (Krynski, 2004a, 2004b). All nutation theories IAU80, IAU2000 and IAU2006 are represented by the series of periodic terms (sine, cosine) of fundamental arguments. Quality of interpolation of the tabulated apparent position of stars is mostly affected by the amplitudes of short-periodic terms of the series. Among the long-periodic nutation terms, both in longitude and obliquity, the most dynamic variability shows the terms of periods of 186.2, 6798.4, 121.7 and 365.3 days. The dynamics of their variability, reaches in longitude/obliquity: 45.3/19.7, 15.9/8.5, 2.7/1.2, and 2.5/0.1 mas/day, respectively (Sekowski, 2006). Amplitudes of short-periodic terms achieve much smaller absolute values. They show, however, much higher dynamic variability. The short-periodic nutation component exhibiting highest dynamics that determines its practical potential in the context of interpolation, is a term of the period of 13.7 days. Its dynamics of variability reaches 104.7 mas/day and 45.0 mas/day in longitude and obliquity, respectively (Sekowski, 2006).

Interpolation methods — there are three basic methods typically used for interpolation of the astrometric data: 1) Stirling interpolation — giving good results in the nearest vicinity of the main node u_0 (not further then 30% of the interpolation interval), its linear variant is spanned on three nodes (one backward and one forward; 2) Newton interpolation — giving good results on both ends of the interpolation interval, identical with the Bessel method in their linear variants; 3) Bessel interpolation — giving the best results in the middle of interpolation interval, in its second order variant symmetrical with respect to the interval, constructed on two backward and two forward nodes.

In case of linear interpolation Newton and Bessel methods give identical results, which are much better then those from Stirling scheme everywhere within the interpolation interval. In case of second order interpolation Bessel interpolation method shows much less errors then two other methods investigated.

2. TABULATION OF THE INCREASED PRECISION DATA

Data published in the astronomical almanacs are presented in tabulated form. This refers to the majority of data being published as they are time dependent. These are, in particular, solar and lunar ephemerides, sidereal time data, the apparent positions of stars, and all other data related with them, e.g. Besselian Numbers, precession-nutation matrix coefficients etc.

The increasing precision of the fundamental catalogue data, the accuracy of modelling of location and movement of the Earth and Solar System bodies, and the contemporary definitions of the reference systems cause, that the data published in astronomical almanacs could potentially reach much higher quality. In many cases, however, the accuracy is lost as a result of inappropriate form of presentation.

The manner in which data appear in the data tables is closely associated with the terms of their interpolation. The appropriate step of the data tabulation as well as the interpolation algorithm used are strongly associated with the potential to achieve the expected accuracy. There is data, e.g. precession-nutation matrix coefficients, which accuracy is far higher then it is possible to be achieved from interpolation between the exact values, with even as short as 1-day interpolation step. In such cases completely new ways of tabulation are needed (e.g. based on Tchebyshev polynomials) in order to maintain the current non-electronic forms of data publishing.

3. RIGOROUS AND SIMPLIFIED APPARENT POSITION ALGORITHMS

Precession-nutation matrix — today's algorithm for calculating apparent positions of the celestial bodies is based on a rigorous vector algebra and the precession-nutation is given in a form of the rotation matrix. Therefore astronomical almanacs usually contain the tables listing a sequence of nine element sets of precession-nutation matrix. The matrix elements are numbers from 0 to 1, having up to 12 significant digits. A large number of matrix elements and their significant digits makes the use of precession-nutation data in this form inconvenient. The presentation of data also poses problems with the interpolation, since the matrix elements contain all components of short-periodic nutation terms. Thus the search for alternative ways of presenting precession-nutation data, without loss of accuracy of interpolated data, under the largest possible interpolation interval is required.

Besselian Numbers — current, simplified algorithm for calculating an apparent position on the basis of the Besselian Numbers does not meet the criterion of possible to achieve nowadays accuracy. Developing a new algorithm that uses the current theory of nutation, with increased accuracy, is furthermore hampered by the apparent lack of separation between long- and short-periodic terms of nutation. The new simplified algorithm should also be in line with the new paradigm of astronomy, in which the sidereal time is replaced by the Earth Rotation Angle.

4. FINAL REMARKS

Examination of the presented problems will be a methodological basis for practical solutions, the development of a modernized form of data presentation in printed form, and finally sharing the almanac data via the Internet.

Creation of the web version of the almanac is a further objective of this project, significant for a practical applications in geodetic astronomy as well as for education and popularization.

Acknowledgements. The work presented is a subject of research grant N526 154737 awarded to the Institute Geodesy and Cartography, Warsaw by the Ministry of Science and Higher Education of Poland.

5. REFERENCES

Krynski, J., Sekowski, M., 2003 – 2010, "Rocznik Astronomiczny", Institute of Geodesy and Cartography.

Krynski, J., 2004a, "Relacje pomiedzy systemami niebieskimi i systemem ziemskim", Monographic series of the Institute of Geodesy and Cartography, No 10.

Krynski, J., 2004b, "Nowe skale czasu i idea posredniego systemu odniesienia", Monographic series of the Institute of Geodesy and Cartography, No 10.

Sekowski, M., 2006, "Wplyw wyboru katalogu fundamentalnego na wartosci obliczanych pozycji pozornych gwiazd", Monographic series of the Institute of Geodesy and Cartography, No 11.

Session 2:

Towards the next generation of space-time reference systems

Vers la prochaine génération de systèmes de référence spatio-temporels

FROM GAIA FRAME TO ICRF3 ?

F. MIGNARD
University of Nice Sophia-Antipolis
CNRS, UMR Lagrange
Observatoire de la Côte d'Azur
Le Mont Gros, BP4229 , 06304 Nice cedex 4
e-mail: francois.mignard@oca.eu

ABSTRACT. The Astrometric solution of Gaia will come with an internally built Celestial Reference Frame, based on the observation of extragalactic sources. This frame must be constructed in agreement with the ICRS overall principles to ensure that it is kinematically non-rotating and that its orientation is consistent with the ICRF. The general methods used within the Gaia community to build this solution are outlined together with the main properties of the Gaia Celestial Reference Frame. It is proposed to form an IAU-Division I-level working group to deal with the issues relating the Gaia CRF and the future realisation of the ICRF in the visible.

1. INTRODUCTION

The ESA space astrometry mission, due for launch in late 2013, will survey the sky down to the 20th magnitude with an unprecedented astrometric accuracy of 25 μas at 15 mag, carrying out simultaneously multi-epoch photometry and spectroscopy. The mission is optimised to observe stellar sources to produce a stereoscopic and kinematic census of about one billion stars in our Galaxy enabling to probe the formation and evolution of the Milky Way. The expected astrometric accuracy is shown in Figure 1 as a function of the G magnitude (very similar to R band).

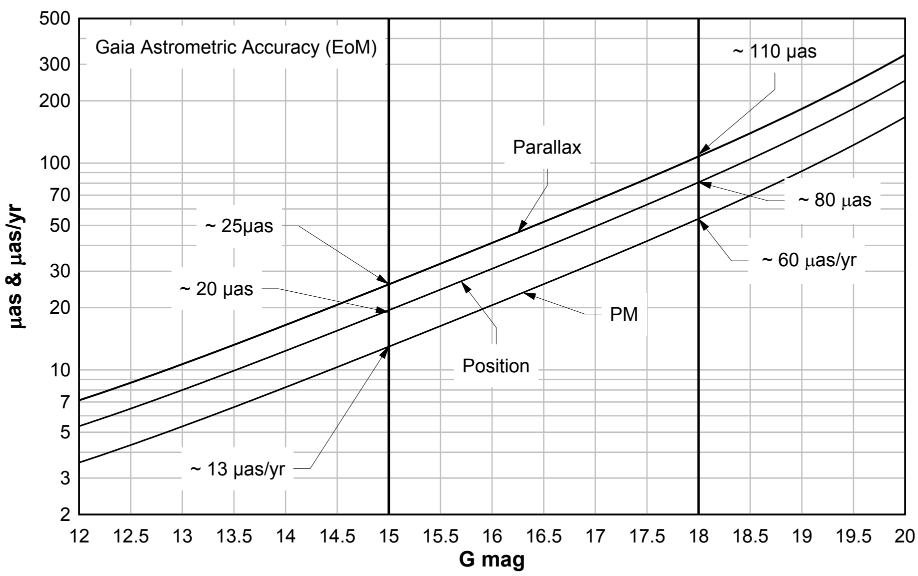

Figure 1: End-of-Mission astrometric accuracy expected with Gaia for the position, proper-motion and parallaxes, for point like sources (stars or QSOs).

While the core of the mission is dedicated to stellar and galactic physics, the sensitivity limited internal detection system will allow also to observe and astrometrically measure several 100,000s quasars, but also the fast moving objects from the solar system and other extended objects, like unresolved galaxies. These consistent and repeated observations will lead to the realisation of a kinematically defined inertial frame in the optical wavelengths. To achieve this goal one must first recognize the QSOs from the stars in an automatic and efficient way and select a clean sample of sources to serve as defining source for the frame. Then the astrometric solution for these point-like sources would not depart too much from the standard iterative process detailed in Lindegren et al. [3].

The internal photometric detection has been shown, on simulated data, very efficient to get rid of the traditional contaminants like the white dwarfs or very red stars. Final filtering with astrometry (parallaxes and proper-motions of these stars will be large and not compatible with extragalactic sources) will end up with a clean set containing virtually only point-like extragalactic sources (unresolved galaxies will fall in another box). Simultaneously photometric redshift measurements will be feasible without additional effort for most of the detected sources. Thus one may reasonably expect a census of several hundreds thousands quasars at galactic latitudes $|b| > 25^\circ - 30^\circ$, although these limits are not precisely known today. Closer to galactic plane, Gaia faces two difficulties: (i) the galactic extinction and reddening that will block off the light of these distant and rather faint sources, (ii) the difficulty to discriminate between the stars as their relative density to that of the quasars increases drastically at low galactic latitudes (this ratio is about 10,000 at $b = 10^\circ$ and $G = 19$). Multi-images formed by lensing of intervening galaxies could be detected at separation as small as ~ 0.2 arcsec, a significant improvement to the resolution of current ground based investigations with nice inferences in the distribution of distant galaxies.

Finally the extensive zero-proper motion survey of extragalactic sources will provide a direct realization of the quasi-inertial celestial reference frame in optics with a residual rotation less than 0.3 μas per year and an easy access for the user given the space density achievable. Many more secondary sources (stellar or extragalactic) will also facilitate the access to this frame over a wide range of magnitudes.

2. THE GAIA REFERENCE FRAMES

The astrometric solution resulting from the Gaia data processing carried out by the DPAC (Data Processing and Analysis Consortium) will be referred to a kinematically non-rotating frame thanks to the global zero-proper motion constraint set on the clean subset of quasars detected by Gaia. The positional accuracy of the individual sources will depend on their magnitude, but at least for the $\sim 30,000$ QSOs brighter than $G = 18$ this would be better than 80 μas and 60 μas/yr. This astrometric solution both for the stars and the quasars will be made available through the different releases of the Gaia products, culminating with the final solution to be published around 2020. From its very principle, Gaia is designed to carry out absolute astrometry from space observations and the Gaia releases will include simultaneously a set of extragalactic sources used to build its internal non-rotating frame, and a large stellar catalogue down to the 20th magnitude referred to the same frame. To fix the terminology I refer to the whole set at the Gaia-CRF (Gaia Celestial Reference Frame) which comprises:

- A set of defining sources from the clean subset of QSOs used to fix the frame spin
- A larger set of secondary QSOs not used to remove the residual rotation
- A very small set of QSOs common to Gaia and ICRF2 used to tie the orientation
- The Gaia-SRF (for Stellar Reference Frame)

  a- About one billion stars with positions, proper motions and parallaxes

  b- An average density of 25000 stars per square degree, highly variable with galactic latitude

  c- This positional catalogue will degrade with time as shown in Figure 2.

The current realization of the International Celestial Reference Frame (ICRF2) is based on Very Long Baseline Interferometry (VLBI) positions of radio sources with accuracies or the order of 100 μas for the best sources. While the spin of the Gaia frame will come out naturally from the application of the ICRS paradigm to the quasars, it goes differently for the orientation (origin of right ascension and position of the pole) which is a free parameter. As always in metrology, Gaia scientists will endeavour to maintain the best continuity with the ICRF by ensuring that the orientation of the Gaia-CRF triad is the same as the ICRF, within the uncertainties of either realisation or their combination. A set of extragalactic

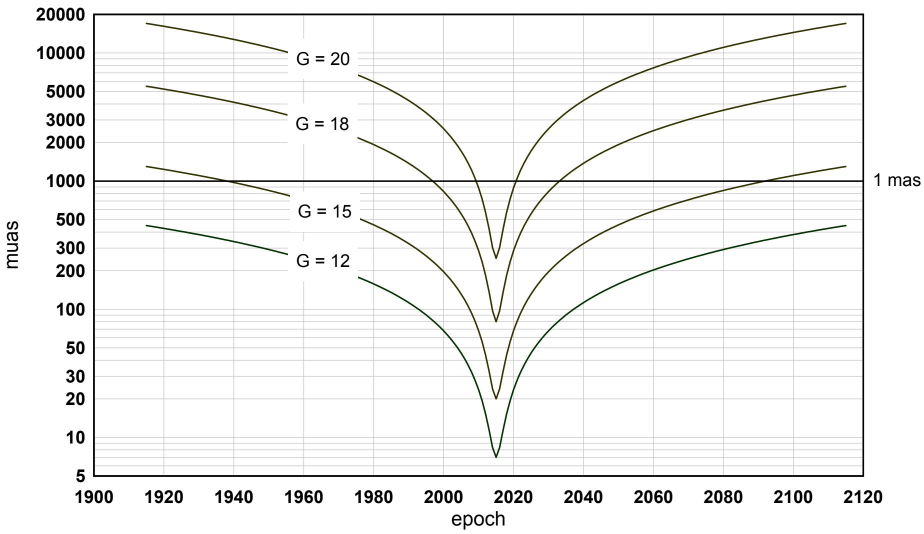

Figure 2: Evolution of the accuracy of the Gaia positional stellar catalogue with time due to the uncertainty in the annual proper motions of stars. The diagram refers only to the stars, not to the QSO-tied reference frame.

sources with good astrometry in the ICRF (not necessarily ICRF sources) and observed by Gaia will be selected to align the two frames (see [1], [2]).

However it is important to notice that Gaia will observe the optical counterparts of the extragalactic sources detected and measured in radio bands in the ICRF frame, and that for a given source, they are not necessarily coincident. Quasar optical emission may originate from three potential sources for which the detailed physics remains largely unknown: thermal emission from the accretion disk surrounding the black hole, non-thermal coronal disk emission, and for a sub-set of the extreme radio-loud quasars non-thermal emission from knots in the relativistic jet. For radio-loud quasars part of the emission very likely takes place in the jets aligned with the axis of the accretion disk. Therefore one cannot exclude an offset between the two centres of emission. The comparison of the pos-alignment residuals in the common sources will provide valuable insight into the physical processes responsible from the light or radio emission. By directly aligning the two frames through quasar astrometry one will be able to investigate the relationship between the radio core and optical photocentre at unprecedented accuracies.

The spin, or residual rotation, has much more physical significance since it is the way the Gaia-CRF will be turned into a kinematically non-rotating reference system. The ICRF paradigm is based on the fact there is a frame in which very distant extragalactic sources have no global rotation. By definition this frame is considered to be kinematically non-rotating. Its link to the inertial frame realised by applying the equations of motion to solar system objects has so far shown than the two have no relative rotation. Using the direct observation in the visible of $10^4 - 10^5$ quasars or point-like galactic nuclei, and applying the constraint of non global rotation to their astrometric solution, will allow to determine the rotation ω and put the Gaia astrometric solution into this non-rotating frame. The expected accuracy of the residual rotation, or equivalently the default of inertiality of the final Gaia frame, is shown in Figure 3, as a function of the G magnitude of the faintest sources that might be selected. One sees that with the assumption that these extragalactic sources have no astrometric instability over short timescale, one could achieve a final accuracy in the frame rotation of the order of 0.2 μas yr^{-1}. Being more conservative by considering just a core of bright defining sources and allowing for a loss of 50% of unsuitable sources (anomalous residuals due to internal motions affecting the photocentre direction over short timescales), we can safely say that the inertiality should be as good as 0.5 μas yr^{-1} as illustrated in Figure 3. The plot is based on a realistic simulation of the distribution of QSOs on the sky, including a no-observation zone around the galactic plane. The luminosity function has been scaled with local surveys, providing a complete census of QSOs beyond the detection limit of Gaia. Then this density has been used to generate a full-sky catalogue.

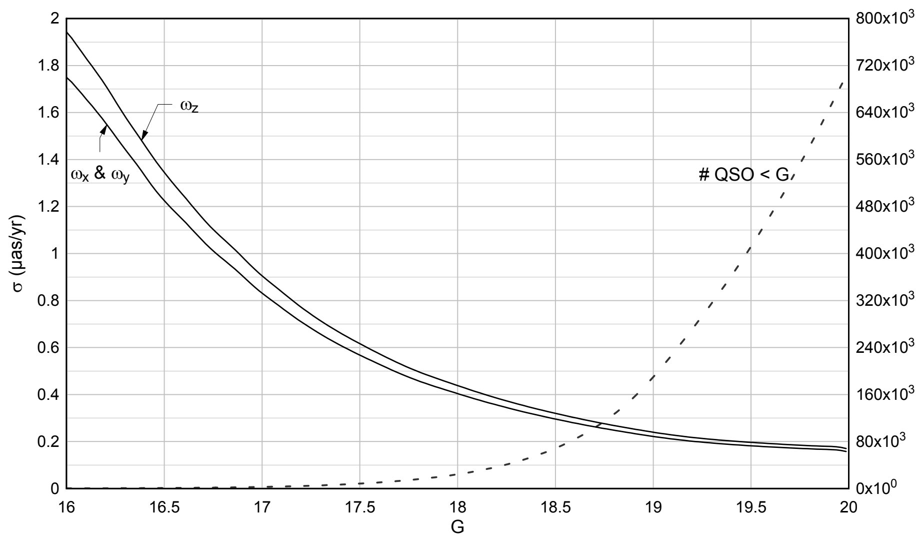

Figure 3: Inertiality of the final Gaia Celestial Reference Frame based on the QSO observations, expressed by the accuracy of the residual rotation. The precision for a G magnitude is computed with only sources brighter than G. Here galactic coordinates have been used and the random instability has been taken equal to 20 μas yr^{-1} and quadratically added to the single star noise. The asymmetry between the three axes comes from the Galactic plane screening. The right scale gives the number of sources found brighter than G.

3. THE EPOCH OF THE GAIA CRF

Once the global rotation of the defining QSOs has been removed, each source will still show some residual proper motion. Although the magnitude of these proper motion components will be dominated by the random noise, a global pattern is expected resulting from the acceleration of the solar system with respect to the distant extragalactic sources. This is a well known effect widely documented for its theoretical principles. The acceleration of the Solar System barycentre translates into a systematic proper motion of the extragalactic source, with a well defined pattern: a regular dipolar-like field directed towards the galactic centre. The amplitude a can be estimated to be of about 4 μas yr^{-1} from the Galactic rotation parameters. An actual measurement has been reported recently by Titov et al, ([4]) from the VLBI observations of radio sources at 6.4 ± 1.5 μas yr^{-1}. Gaia will be able to determine this parameter to an accuracy of about $0.2 - 0.3$ μas yr^{-1}. The whole pattern of proper motion is fully determined by only three parameters (the direction of the drift axis and its magnitude) and enables us to update the position of the QSOs at any epoch before or after the mean Gaia epoch of observations. This means that the Gaia-CRF will come with an epoch attached to it, even though the annual corrections (typically of 4 μas yr^{-1}) will be much smaller than the individual random error in position (typically 80 μas for the core of the defining sources). The associated degradation of the frame will be very slow if the dipole is really determined with the expected accuracy of $0.2 - 0.3$ μas yr^{-1}.

4. THE GAIA CRF AND IAU

The final Gaia solution will be fully consistent with the ICRS overall principles and given the easy access to this frame through the Gaia stellar catalogue, one may anticipate that the Gaia-CRF will be widely used in numerous astronomical research works. The set of defining QSOs with their astrometric solution, including the dipolar drift, will materialise the realisation of the axes. The system will be aligned to the ICRF version available at the time of Gaia completion. We hope to provide also at this time some preliminary assessment of the difference between the centre of emission of the radio signal and the photocentre for the sources used to perform the alignment.

Clearly a further step is needed to have this frame recognised by the IAU as being an optical realisation

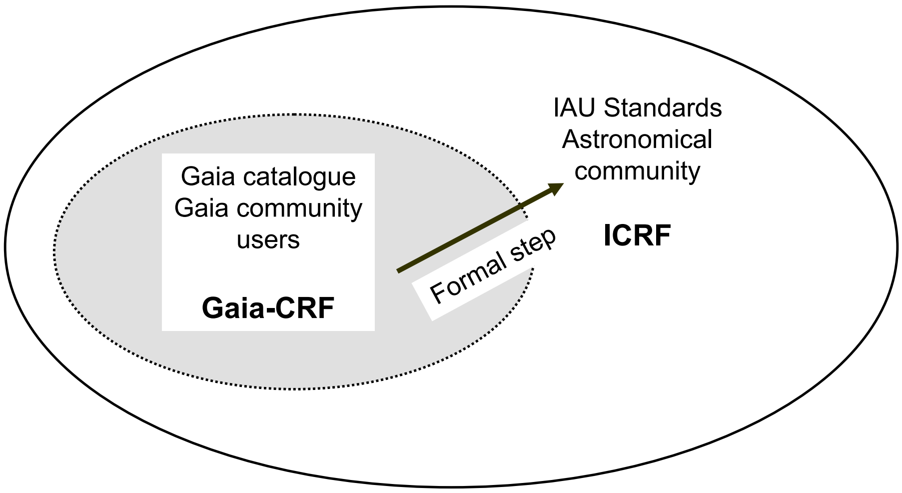

Figure 4: Schematic relationship between a Gaia-defined reference frame and an IAU-endorsed version of an ICRF.

of the ICRF, to be used by every astronomers in needs of accurate astrometry. This step is sketched in Figure 4. A formal contact must be established between the Gaia community in charge of producing the intermediate and final Gaia solutions and the astronomical community, as this was done during the Hipparcos mission to ensure a good communication between the Hipparcos scientists and the international group building the first realisation of the ICRF with VLBI. Something similar should be established at the IAU Division I level between the radio ICRF and the Gaia astrometrists. The main topics that should appear in the Terms of Reference will comprise at least,

- Construction of the Optical ICRF with Gaia
- Qualification of the Gaia frame at the international level
- Relationship between the Radio and optical frames
- Extension to fainter magnitudes

The qualification of the intermediate and final realisations of the Gaia frame should involve a wider group than the Gaia subgroup performing the astrometric solution, with expertise on ICRF (radio or optical), QSO physics, high accurate astrometric modelling to guarantee the adherence to ICRS principles and the use of standardized theoretical and numerical models identical in Radio and Optics. This is also essential to prepare the final adoption of the Gaia-CRF as a new realisation of the ICRF. The same group should also advise IAU on how to deal with two realisations, one in optical, one in radio serving different purposes. The long term consistency between these two solutions would require careful thinking. The WG should report at the 2015 IAU General Assembly and make proposals on how to realise an ICRF in the optical wavelength, in parallel to the Radio realisation.

5. REFERENCES

[1] Bourda, G., Charlot, P. et al., 2010, VLBI observations of optically-bright extragalactic radio sources for the alignment of the radio frame with the future Gaia frame I, A&A vol. 520.

[2] Bourda, G., Collioud, A. et al., 2011, VLBI observations of optically-bright extragalactic radio sources for the alignment of the radio frame with the future Gaia frame II, A&A vol. 526.

[3] Lindegren, L., Lammers, U. et al., 2012, The astrometric core solution for the Gaia mission. Overview of models, algorithms, and software implementation, A&A vol. 538.

[4] Titov, O., Lambert, S.B., Gontier A.M, et al., 2011, VLBI measurement of the secular aberration drift A&A vol. 529, A91.

PULSAR TIMING AND A PULSAR-BASED TIMESCALE

R.N. MANCHESTER and G. HOBBS
CSIRO Astronomy and Space Science
P.O. Box 76, Epping NSW 2121, Australia
e-mail: dick.manchester@csiro.au; george.hobbs@csiro.au

ABSTRACT Pulsar Timing Arrays in which precise timing observations are made for a large number of pulsars spread across the celestial sphere have many applications, including the direct detection of gravitational waves. They can be used to detect irregularities in the atomic timescale used as a reference for the timing observations, thereby establishing a pulsar-based timescale which is independent of the reference timescale. The Parkes Pulsar Timing Array (PPTA) project has been timing 20 millisecond pulsars at 2 – 3 week intervals using the Parkes 64-m radio telescope since 2005. The PPTA data set has been analysed together with earlier timing data from Parkes using TT(TAI) as the reference timescale. The resulting timescale which we call PT(PPTA10) has deviations from TT(TAI) which closely match the differences between TT(BIPM10) and TT(TAI). This both demonstrates the practicality of a pulsar-based timescale and verifies that TT(BIPM10) is an improvement on TT(TAI).

1. PULSAR TIMING BASICS

Pulsars are highly stable celestial clocks. They are identified by their broad-band and periodic pulse emission. The basic pulse periodicity P is typically between 100 ms and 1 s but a very important class known as millisecond pulsars (MSPs) have much shorter periods, mostly between 1.5 and 20 ms. Pulsars are identified as rotating neutron stars. Almost all of the ~ 2000 known pulsars are located within our Galaxy with typical distances of a few kpc (1 kpc = 1000 pc = 3.085×10^{19} m). Although other formation routes are possible, most neutron stars are believed to be formed in the core collapse of a massive star, resulting in a supernova explosion and the formation of a highly magnetised and rapidly rotating stellar remnant – the neutron star. This combination of rapid rotation and strong magnetic fields means that huge voltages are generated within the magnetosphere of the star, accelerating charged particles to ultra-relativistic energies. By mechanisms that are not fully understood, these ultra-relativistic particles radiate beams of electromagnetic radiation which rotate with the star. We see a pulse when one of these beams sweeps across the Earth.

Since pulsars are powered by their rotation, they slow down as they lose energy. The rate of slowdown is very small however, with $\dot{P}$ typically about 10^{-15} for "normal" (non-millisecond) pulsars; for MSPs it is even smaller, typically about 10^{-20}. Precise parameters for a pulsar are obtained by measuring a series of pulse times of arrival (ToAs) and then fitting a timing model to them. In practice, ToAs are obtained by synchronously averaging data for intervals typically between a few minutes and an hour to form a mean pulse profile. The averaging reduces the effects of both random receiver noise and pulse-to-pulse shape variations. The resulting mean pulse profile is then cross-correlated with a standard template to determine the effective arrival time at the telescope of a reference phase on the mean profile (normally at or near the profile peak). Observed pulse ToAs are initially with reference to the observatory time standard. At most observatories, GPS systems and published timescale offsets[1] are used to reference the ToAs to an international timescale, e.g., TT(TAI), giving observatory pulse arrival times $t_{\rm o}$.

Observed ToAs must also be corrected for the motion and varying gravitational potential of the observatory by referring them to an inertial frame, that is, one which is unaccelerated with respect to the distant Universe; in practice, the barycentre of the Solar system (SSB) is normally used. Pulse ToAs at the SSB are given by

$$t_{\rm o,b} = t_{\rm o} - \Delta_{\rm R} - \Delta_{\rm E} - \Delta_{\rm a} - \Delta_{\rm p} \tag{1}$$

where $\Delta_{\rm R}$ is the Roemer delay or propagation time of a plane wavefront from the SSB to the observatory, $\Delta_{\rm E}$ is the "Einstein" delay resulting from the relativistic transformation from the observatory frame to

[1]Circular T from http://www.bipm.org/en/scientific/tai/

the SSB, Δ_a is the additional propagation delay in the Earth's atmosphere and ionosphere and Δ_p is the effective "parallax" delay resulting from the curvature in the wavefront due to a finite source distance.

In the reference frame of the pulsar, the pulse phase may be described by a truncated Taylor series

$$\phi = \phi_0 + \nu t_p + \frac{1}{2}\dot{\nu} t_p^2 \tag{2}$$

where the pulse frequency $\nu = 1/P$ and t_p is the proper time at the pulsar (ignoring the effect of the pulsar's gravitational field). The reference phase ϕ_0 is chosen so that $\phi = 0$ for emission times which correspond to the reference phase of the observed ToAs. For comparison with the observed ToAs, the pulse emission times must also be transformed to the SSB:

$$t_{p,b} = t_p + \Delta_{IS} + \Delta_B \tag{3}$$

where Δ_{IS} is the "interstellar" delay, primarily the dispersive delay in the interstellar medium and in the Solar system (the vacuum propagation delay and its first time derivative are unmeasurable and are ignored) and Δ_B is the relativistic transformation from the pulsar-centred frame to the barycentre frame of the binary system. See Edwards et al. (2006) for a full description of all of the terms in Equations (1) and (3).

The differences $t_{o,b} - t_{p,b}$ are known as timing residuals. A series of timing residuals will have systematic variations related to errors in the terms in Equations (1) – (3) together with any perturbations which are not included in these equations. A least-squares fit of functions describing the effect of errors in these terms using a program such as Tempo2 (Hobbs et al. 2006) can determine improved values and uncertainties for the various parameters, including the pulsar position and proper motion through the term Δ_R. Unmodelled terms such as higher-order variations in the intrinsic pulse frequency ν, perturbations due to gravitational waves (GWs) passing over the pulsar and the Earth, errors in Solar-system ephemeris used to compute Δ_R and irregularities in the reference timescale will remain after such a least-squares fit. However, because of the fitting of Equation (2), any perturbations which are linear or quadratic in time will be absorbed into ν and $\dot{\nu}$.

2. PULSAR TIMING ARRAYS

With observations of just a single pulsar it is not possible to separate the unmodelled perturbations described above. However, with observations of many pulsars spread across the sky, a so-called "pulsar timing array" (PTA), it is possible to separate these effects. Irregularities in the reference timescale affect all pulsars equally, in effect a monopole term with reference to position on the sky. Errors in Solar-system ephemeris correspond to a displacement of the SSB from its true position and so introduce a dipole term, whereas GWs passing over the Earth result in residuals which have a quadrupolar dependence on sky position. Therefore, in principle, these three sources of perturbation can be separated from intrinsic pulse frequency variations and the effect of GWs passing over each pulsar; these are of course different for every pulsar. Our ability to achieve this separation in practice is limited by the precision with which we can measure pulse ToAs, the number and sky distribution of pulsars for which sufficiently accurate ToAs can be obtained and the cadence and total data span of the ToA measurements.

Because GWs induce a frequency perturbation but pulsar timing is essentially a phase measurement, PTAs are most sensitive to long-period GWs. Furthermore, since linear and quadratic phase perturbations are not detectable, PTAs are most sensitive to GWs with periods comparable to the data span. Estimates of the strength of GWs in the Galaxy from likely astrophysical sources (e.g., Sesana et al. 2008) show that weekly ToAs with precision of order 100 ns for about 20 pulsars over a 5-year data span are necessary to make a significant detection of astrophysical GWs (Jenet et al. 2005). Possible errors in the Solar-system ephemeris arise from uncertainties in the mass of planets relative to the Sun, especially those in the outer Solar system, and the presence of Solar-system objects not included in the ephemeris. Recent ephemerides from the Jet Propulsion Laboratory, for example, DE421 (Folkner et al. 2008), include more than 300 of the largest asteroids in their model. Errors and omissions in the ephemeris may induce timing residuals of order 100 ns in observed ToAs (see, e.g., Champion et al. 2010). The most accurate timescales based on atomic frequency standards are those produced by the BIPM by retroactive reweighting of the various atomic clocks that are used to form TAI (Arias et al. 2011). Successive revisions of the TT(BIPMYY) timescale[2] result in timescale differences of order 50 ns. It is clear that significant detections of any of

[2]Obtainable from ftp://tai.bipm.org/TFG/TT(BIPM)

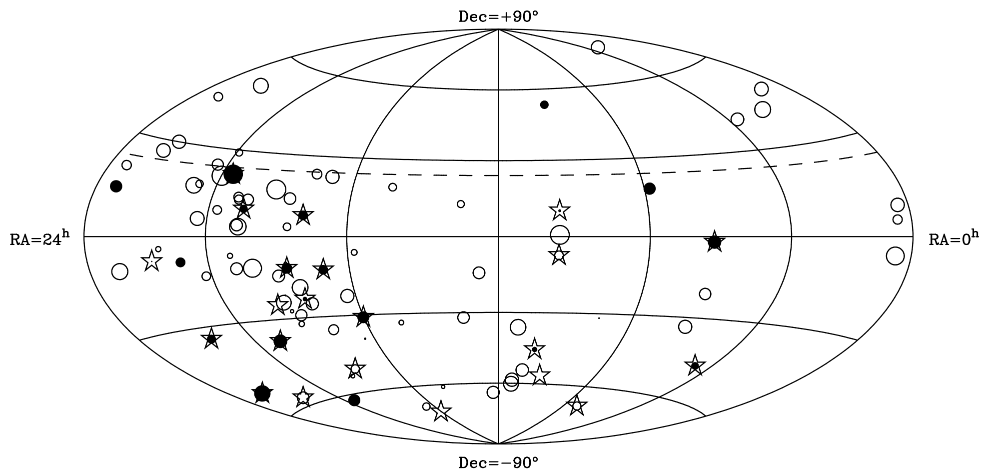

Figure 1: Distribution on the celestial sphere of pulsars suitable for PTA projects. The size of the circle is inversely related to the pulsar period and circles are filled if the pulsar mean flux density is greater than 2 mJy. The dashed line marks the northern limit for the Parkes radio telescope. Pulsars observed by the PPTA project are marked with stars.

these effects require observations of a large sample of pulsars for which ToA precisions are of order 100 ns. With current instrumentation, this is possible only for MSPs and indeed only for a subset of the known MSPs that have relatively narrow pulse features and relatively large flux densities. Since all of the expected signals are very "red", i.e., the signal spectrum is dominated by low frequencies, detection is aided by long data sets.

There are currently three main PTA projects world-wide. The European Pulsar Timing Array (EPTA) is based on the large radio telescopes in Europe: the Effelsberg 100-m telescope in Germany, the Nançay radio telescope in France, the Westerbork Synthesis Radio Telescope in the Netherlands and the Jodrell Bank radio telescope in England (Ferdman et al. 2010). The EPTA currently has high quality observations (rms residuals $< 2.5\ \mu$s) for nine MSPs. The NANOGrav project is based in North America and makes use of data from the 100-m Green Bank Telescope in West Virginia and the 300-m Arecibo radio telescope in Puerto Rico (Jenet et al. 2009). NANOGrav has high quality observations for 17 MSPs. The third main PTA is the Parkes Pulsar Timing Array (PPTA) which uses data from the Parkes 64-m radio telescope in New South Wales, Australia (Manchester 2008; Hobbs et al. 2009). Each of these PTAs is timing about 20 MSPs, with some overlap between the samples. The main goal of these projects is to detect nanoHertz GWs but they have many secondary goals. One of the most important of these is to establish a pulsar-based timescale (Hobbs et al. 2011; Rodin 2011).

3. THE PARKES PULSAR TIMING ARRAY

The PPTA project uses the Parkes 64-m radio telescope to make precise timing measurements of 20 MSPs. The project is a collaboration primarily between CSIRO Astronomy and Space Science and Swinburne University of Technology, with important contributions from colleagues based in North America, China and Europe. Observations commenced in 2004 and regularly-sampled high-quality data have been obtained since 2005 March. Observations are made in three radio-frequency bands, 50 cm ($\sim$ 700 MHz), 20 cm ($\sim$ 1400 MHz) and 10 cm ($\sim$ 3000 MHz), typically at 2 – 3 week intervals. On-line signal processors use 8-bit digitisation to Nyquist-sample the full bandwidth for each band, 64 MHz at 50 cm, 256 MHz at 20 cm and 1024 MHz at 10 cm. Two types of dedispersion are used. The Parkes digital filterbank systems use polyphase digital filters to split the data into many (typically 1024) frequency channels which are incoherently summed off-line to provide dedispersed profiles. For the 50 cm band and high DM/P pulsars (DM is dispersion measure) at 20 cm, baseband recording systems and quasi-real-time coherent dedispersion give superior results. Off-line signal processing uses the PSRCHIVE suite of programs (Hotan et al. 2004)[3] and TEMPO2 (Hobbs et al. 2006)[4]. Figure 1 shows the sky distribution of MSPs suitable for

[3]See http://psrchive.sourceforge.net
[4]See http://tempo2.sourceforge.net

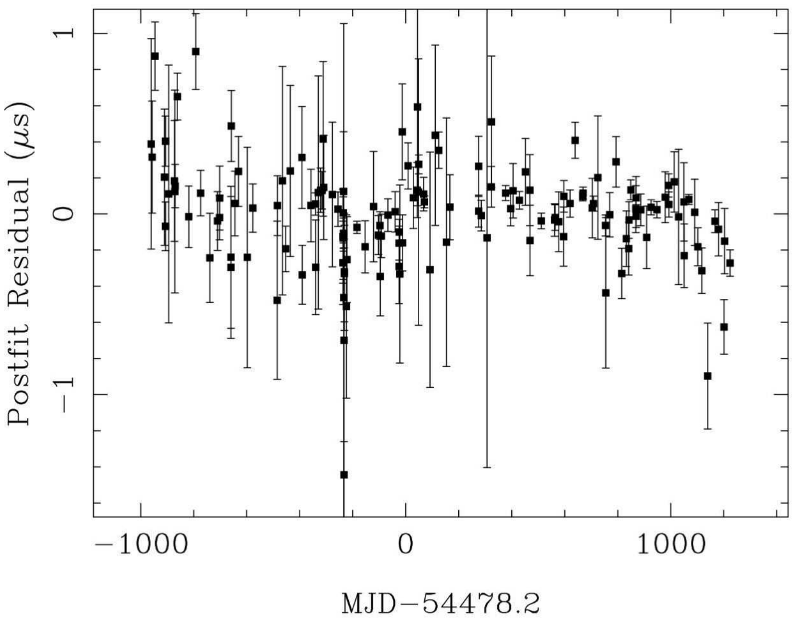

Figure 2: Timing residuals over a six-year data span for PSR J1909−3744. The ToAs were obtained using data from the 10 cm system and have been corrected for variations in interstellar dispersion using ToAs from the 20 cm and 50 cm systems.

PTA observations and the PPTA sample. While not fully isotropic, the PPTA pulsars do sample nearly two thirds of the celestial sphere.

After correction for variations in interstellar dispersion and fitting for parameters in Equations (1) – (3), 19 of the 20 PPTA pulsars have rms timing residuals of less than 2.5 μs over a six-year data span. However, for more than half of the pulsars, the post-fit residuals are dominated by a cubic term. Figure 2 shows the post-fit timing residuals for one of our best-performing pulsars, PSR J1909−3744, which has a pulse period of 2.95 ms and a pulse width of just 43 μs (Jacoby et al. 2003). It is clear that the rms timing residual, 137 ns, is dominated by a cubic term. Fitting to a 1-year span of recent data gives a "white" rms timing residual of just 61 ns. Similar fits to the other PPTA pulsars show that all have rms residuals of less than 1.5 μs and for more than half, the rms residual is less than 500 ns. These results are approaching those needed to achieve the PPTA goals. We can expect some reduction in these rms residuals from further improvements in signal processing algorithms and the development of new and more sensitive receiving systems.

4. A PULSAR-BASED TIMESCALE

We have combined the PPTA data sets for 13 pulsars with earlier Parkes data from Verbiest et al. (2008, 2009) to give data sets covering about 16 years from mid-1994 to mid-2011. The upper part of Figure 3 shows the distribution of ToAs over this interval for the 13 pulsars. To extract the timescale offsets or "common-mode signal" from the observed residuals, the standard TEMPO2 analysis was extended to simultaneously process ToA data from multiple pulsars, solving for the optimal parameters for each pulsar as well as for the common-mode signal. The Cholesky method (Coles et al. 2011) was used to properly deal with the red noise in the residual spectrum of each pulsar. The timescale offset signal was sampled at intervals of 300 days and constrained to have zero mean and no linear or quadratic components. The resulting offsets and their uncertainties are shown in the lower part of the plot. These define a pulsar-based timescale which we name PT(PPTA11). Also plotted is the difference between TT(BIPM10) (extended) and TT(TAI) after subtraction of a second-order polynomial to mimic the effect of fitting Equation (2) to the pulsar data.

It is striking that the variations of PT(PPTA11) relative to TT(TAI) closely match the deviations of TT(BIPM10) relative to TT(TAI). This demonstrates both that it is possible to define a pulsar-based timescale of comparable accuracy to the best available atomic timescale and that the revisions used to

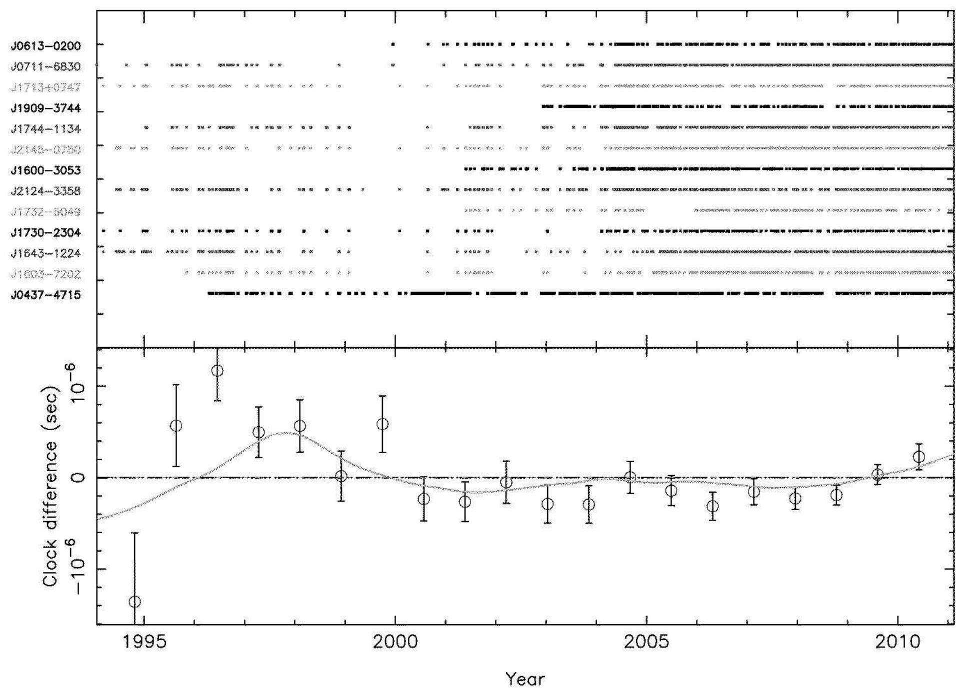

Figure 3: The upper part of the figure shows the distribution of ToAs for 16-year data sets for 13 PPTA pulsars. Timescale offsets relative to TT(TAI) derived from the pulsar timing data are shown in the lower part of the figure. The curved line is the deviation of TT(BIPM10) from TT(TAI) after subtraction of a second-order polynomial.

form TT(BIPM10) do result in a more stable timescale. There are some marginally significant deviations of PT(PPTA11) relative to TT(BIPM10) in the late 1990s. Definition of the pulsar timescale will be enhanced by combining the PPTA and earlier Parkes data sets with those from other PTAs. A collaborative project between the three main PTAs, known as the International Pulsar Timing Array (IPTA), has been established (Hobbs et al. 2010) and this will facilitate progress toward the common goals. In the more distant future, the Square Kilometre Array (Kramer et al. 2004) will provide enormously increased sensitivity for PTA observations, resulting in much improved results for all of the PTA objectives.

Acknowledgements. We acknowledge the contributions of our colleagues in the PPTA project and the staff of Parkes Observatory to the results presented here. The Parkes radio telescope is part of the Australia Telescope which is funded by the Commonwealth Government for operation as a National Facility operated by CSIRO.

5. REFERENCES

Arias, E. F., Panfilo, G., & Petit, G. 2011. "Timescales at the BIPM", Metrologia, 48, S145–S153.

Champion, D. J. Hobbs, G. B., Manchester, R. N., Edwards, R. T., Backer, D. C., Bailes, M., Bhat, N. D. R., Burke-Spolaor, S., et al. 2010. "Measuring the Mass of Solar System Planets Using Pulsar Timing", ApJ, 720, L201–L205.

Coles, W., Hobbs, G., Champion, D. J., Manchester, R. N., & Verbiest, J. P. W. 2011. "Pulsar timing analysis in the presence of correlated noise", MNRAS, 418, 561–570.

Edwards, R. T., Hobbs, G. B., & Manchester, R. N. 2006. "TEMPO2, a new pulsar timing package - II. The timing model and precision estimates", MNRAS, 372, 1549–1574.

Ferdman, R. D. van Haasteren, R., Bassa, C. G., Burgay, M., Cognard, I., Corongiu, A., D'Amico, N., Desvignes, G., et al. 2010. “The European Pulsar Timing Array: current efforts and a LEAP toward the future”, Class. Quant Grav., 27(8), 084014.

Folkner, W. M., Williams, J. G., & Boggs, D. H. 2008, “JPL Planetary and Lunar Ephemeris DE421”, Tech. Rep. IOM 343R-08-003, NASA Jet Propulsion Laboratory.

Hobbs, G., Archibald, A., Arzoumanian, Z., Backer, D., Bailes, M., Bhat, N. D. R., Burgay, M., et al. 2010. “The International Pulsar Timing Array project: using pulsars as a gravitational wave detector”, Classical and Quantum Gravity, 27(8), 084013.

Hobbs, G., Coles, W., Manchester, R., & Chen, D. 2011. “Developing a pulsar-based timescale”, in Proceedings of the Journées 2010 Systèmes de Référence Spatio-Temporels, 237–242.

Hobbs, G. B., Bailes, M., Bhat, N. D. R., Burke-Spolaor, S., Champion, D. J., Coles, W., Hotan, A., Jenet, F., et al. 2009. “Gravitational-Wave Detection Using Pulsars: Status of the Parkes Pulsar Timing Array Project”, PASA, 26, 103–109.

Hobbs, G. B., Edwards, R. T., & Manchester, R. N. 2006. “TEMPO2, a new pulsar-timing package - I. An overview”, MNRAS, 369, 655–672.

Hotan, A. W., van Straten, W., & Manchester, R. N. 2004. “PSRCHIVE and PSRFITS: An Open Approach to Radio Pulsar Data Storage and Analysis”, PASA, 21, 302–309.

Jacoby, B. A., Bailes, M., van Kerkwijk, M. H., Ord, S., Hotan, A., Kulkarni, S. R., & Anderson, S. B. 2003. “PSR J1909−3744: A Binary Millisecond Pulsar with a Very Small Duty Cycle”, ApJ, 599, L99–L102.

Jenet, F. Finn, L. S., Lazio, J., Lommen, A., McLaughlin, M., Stairs, I., Stinebring, D., Verbiest, J., et al. 2009. “The North American Nanohertz Observatory for Gravitational Waves”, ArXiv:0909.1058.

Jenet, F. A., Hobbs, G. B., Lee, K. J., & Manchester, R. N. 2005. “Detecting the Stochastic Gravitational Wave Background Using Pulsar Timing”, ApJ, 625, L123–L126.

Kramer, M., Backer, D. C., Cordes, J. M., Lazio, T. J. W., Stappers, B. W., & Johnston, S. 2004. “Strong-field tests of gravity using pulsars and black holes”, New Astr., 48, 993–1002.

Manchester, R. N. 2008. “The Parkes Pulsar Timing Array Project”, in 40 Years of Pulsars: Millisecond Pulsars, Magnetars and More, ed. C. Bassa, Z. Wang, A. Cumming, & V. M. Kaspi, Vol. 983 (New York: American Institute of Physics), 584–592.

Rodin, A. E. 2011. “Ensemble Pulsar Time Scale”, in Proceedings of the Journées 2010 Systèmes de Référence Spatio-Temporels, 243–246.

Sesana, A., Vecchio, A., & Colacino, C. N. 2008. “The stochastic gravitational-wave background from massive black hole binary systems: implications for observations with Pulsar Timing Arrays”, MNRAS, 390, 192–209.

Verbiest, J. P. W. Bailes, M., Coles, W. A., Hobbs, G. B., van Straten, W., Champion, D. J., Jenet, F. A., Manchester, R. N., et al. 2009. “Timing stability of millisecond pulsars and prospects for gravitational-wave detection”, MNRAS, 400, 951–968.

Verbiest, J. P. W. Bailes, M., van Straten, W., Hobbs, G. B., Edwards, R. T., Manchester, R. N., Bhat, N. D. R., Sarkissian, J. M., et al. 2008. “Precision timing of PSR J0437-4715: an accurate pulsar distance, a high pulsar mass and a limit on the variation of Newton’s gravitational constant”, ApJ, 679, 675–680.

ONE POSSIBLE REALIZATION OF THE ICRF BEFORE THE GAIA FRAME

Ya.S. YATSKIV[1], P.N. FEDOROV[2],
[1]Main Astronomical Observatory NAS of Ukraine
Akademika Zabolotnogo 27, 03680 MSP Kiev, Ukraine
e-mail: yatskiv@mao.kiev.ua
[2] Institute of Astronomy of Kharkiv National University
Sumska 35, 61022 Kharkiv, Ukraine
e-mail: pnfedorov@gmail.com

ABSTRACT. A brief overview of current state of densification and extension of the HCRF (Hipparcos Celestial Reference Frame) is given. For a first step in this matter the XPM catalogue could be used. The XPM system of proper motions has been obtained by direct link of about 300 millions of stars to extragalactic sources. This catalogue has no significant magnitude equation. As a result of the comparison of the XPM with catalogues compiled in the HCRF system, a residual rotation of the HCRF system was derived. The parameters of this residual rotation could be used for combining the catalogues computed in the HCRF system and the XPM catalogue for creation of a new optical realization of the ICRF.

1. INTRODUCTION

An overview of current state and future ground and space-based projects for realization of the ICRS is given in the IERS Technical Note No. 36 (pp. 21–27), see IERS (2010). The 24^{th} IAU General Assembly adopted Resolution B 1.2, which defines the Hipparcos Celestial Reference Frame (HCRF) for the optical realization of the ICRS. The Resolution B3 of the 27^{th} IAU General Assambly resolved that from 1 January 2010 the realization of the ICRS is the ICRF2. The alignment of the HCRF to the ICRF was realized with an error of about 0.6 mas for the orientation and 0.25 mas/yr for the spin. For practical use, it is necessary to bridge the large gaps between the ICRF sources, i.e. to densify the HCRF and ICRF2. All current optical densification catalogs rely on a set of the HCRF stars (see Table 1).

Name of catalogue	Number of stars (in million)	Ranges of δ and m	Uncertainties at epoch 2000.0	
			Position (in mas)	Proper motion (in mas/yr)
Tycho-2	2.5	$-90^\circ < \delta < +90^\circ$ $B < 13.5$; $V+$	~ 60	~ 2.5
UCAC-3	100.8	$-90^\circ < \delta < +90^\circ$ $R < 16$	15-100	1-10
PPMXL	910	$-90^\circ < \delta < +90^\circ$ $V < 20$; $R+$; $I+$	80-300	7-15 (N) 15-30(S)
SPM-4	103.3	$-90^\circ < \delta < -20^\circ$ $V < 17.5$	30-150	2-10
USNO-B1.0	1042.6	$-90^\circ < \delta < +90^\circ$ $B < 22$; $R+$; $I+$	200	unknown

Table 1: Overview of some densification catalogues based on the HCRF

2. THE XPM CATALOGUE

The XPM catalogue of positions and absolute proper motions of about 300 million objects distributed over the whole celestial sphere without gaps in the magnitude range 10 m < B < 22 m was created at the

Institute of Astronomy of Kharkiv National University in Ukraine. It was shown that the uncertainties of absolute proper motions of the XPM stars are equal to about 5 mas/yr and about 8 mas/yr for the northern and southern hemispheres, respectively (Fedorov et al., 2009). Using positions of about 1 million galaxies taken from the 2MASS and the USNO-A2.0 catalogues, the zero-point of the XPM absolute proper motions was derived with a mean formal error of about 1 mas/yr. Based on comparisons of the proper motions of stars in the XPM and the Tycho-2, PPMXL and UCAC3, we concluded that the relative rotation of the HCRF system around the Z axis is about -1.8 ± 0.16 mas/yr (Fedorov et al., 2011). The residual rotation vectors (ω) are different for the catalogues mentioned above (see ω_z component in Figure 1).

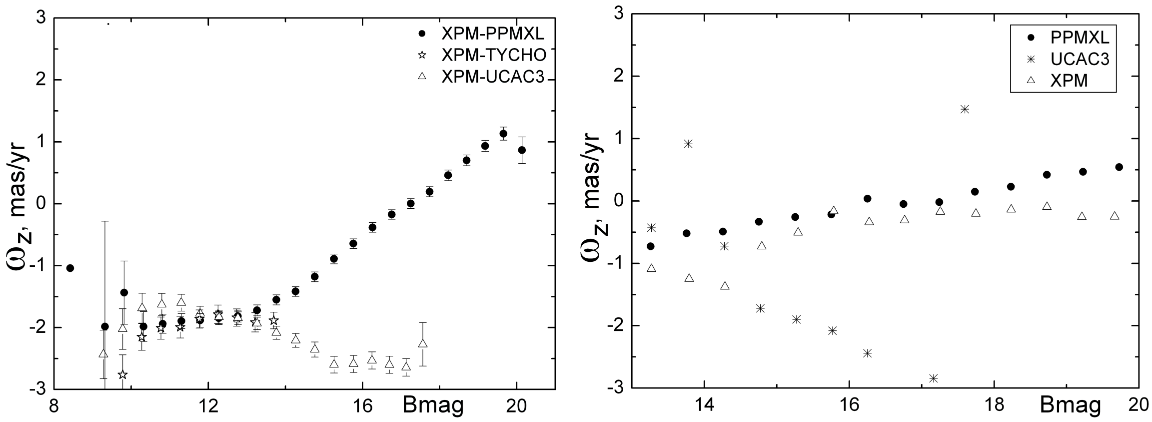

Figure 1: Component ω_z derived from the comparison of stellar proper motions of XPM with those of PPMXL, Tycho-2 and UCAC3 (left panel) and from the determination of formal proper motions of extragalactic objects of XPM, PPMXL and UCAC3 (right panel)

3. CONCLUSION

There are several densification catalogues at optical and near-IR wavelengths derived from the HCRF. The comparison of these catalogues with the XPM resulted in a determination of residual rotation components of catalogue coordinate systems with respect to an inertial system. The values of these residual rotation components could be used for combining the catalogues under considerations and making further steps with regard to the densification of the optical reference frame.

4. REFERENCES

Fedorov P.N., Myznikov A.A., Akmetov V.S., 2009, The XPM Catalogue: absolute proper motions of 280 million stars, MNRAS , 393, pp. 133–138.

Fedorov P.N., Akmetov V.S., Yatskiv Ya.S., 2011, The XPM Catalogue as a realisation of the extragalactic reference system in optical and infrared wavelengths, in Proceedings of the Journées 2010 "Systèmes de référence spatio-temporels", N. Capitaine (ed). pp. 117–120.

IERS, 2010, "IERS Conventions (2010)", Petit, G. and Luzum, B. (Editors), Verlag des Bundesamts für Kartographie und Geodäsie, Frankfurt am Main.

INTERACTION BETWEEN CELESTIAL AND TERRESTRIAL REFERENCE FRAMES AND SOME CONSIDERATIONS FOR THE NEXT VLBI-BASED ICRF

Z. MALKIN[1], H. SCHUH[2], C. MA[3], S. LAMBERT[4]

[1]Pulkovo Observatory, St. Petersburg 196140, Russia

[2]Institute of Geodesy and Geophysics, TU Vienna, 1040 Vienna, Austria

[3]NASA Goddard Space Flight Center, Greenbelt MD 20771-0001, USA

[4]Paris Observatory, SYRTE, CNRS/UMR8630, 75014 Paris, France

e-mail: malkin@gao.spb.ru, harald.schuh@tuwien.ac.at
chopo.ma@nasa.gov, sebastien.lambert@obspm.fr

ABSTRACT. In this paper we outline several problems related to the realization of the international celestial and terrestrial reference frames ICRF and ITRF at the millimeter level of accuracy, with emphasis on ICRF issues. The main topics considered are: analysis of the current status of the ICRF, mutual impact of ICRF and ITRF, and some considerations for future ICRF realizations.

1. INTRODUCTION

International terrestrial and celestial reference frames, ITRF and ICRF, respectively, as well as the tie between them expressed by the Earth Orientation parameters (EOP) are key products of geodesy and astrometry. The requirements to all the components of this triad grows steadily and a mm and/or μas level of accuracy is the current goal of the astronomic and geodetic community.

The current computation procedures for ITRF and ICRF are based on multi-stage processing of observations made with several space geodetic techniques: VLBI, SLR, GNSS, and DORIS. Not all of them provide equal contributions to the final products. The latest ITRF realizations have been derived from combination of normal equations obtained from all four techniques, whereas the ICRF is a result of a single global VLBI solution. The latter is tied to the ITRF using an arbitrary set of reference stations. But VLBI relies on the ITRF origin provided by satellite techniques and shares responsibility with SLR for the ITRF scale. And all the techniques contribute to positions and velocities of ITRF stations.

This situation causes complicated mutual impact of ITRF and ICRF, which should be carefully investigated in order to improve the accuracy of both reference systems and the consistency between each other and EOP. The subject becomes more and more complicated when moving to millimeter accuracy in all components of this fundamental triad. As a result, we have systematic errors in reference frames and inconsistency between them.

Due to its limited extent, this paper will deal only with the VLBI-derived ICRF errors and its dependence on the interaction with the ITRF.

2. CURRENT ICRF STATUS

The latest ICRF realization, ICRF2, was created in 2009 (Ma et al. 2009). It provides much improvement as compared to the first ICRF (Ma et al. 1998, Fey et al. 2004) by:

- increasing the total number of sources from 717 to 3414;
- increasing the number of defining sources from 212 to 295;
- improving the distribution of the defining sources over the sky;
- improving the source position uncertainties (error floor) from 250 μas to 40 μas;
- elimination of large systematic error at the level of about 0.2 mas (see Figure 1);
- improving the axis stability from about 30 μas to about 10 μas.

However, there are severe problems preventing further ICRF improvement, especially with respect to systematic errors. Here is a list of some of them to be solved or mitigated in the next ICRF realizations:

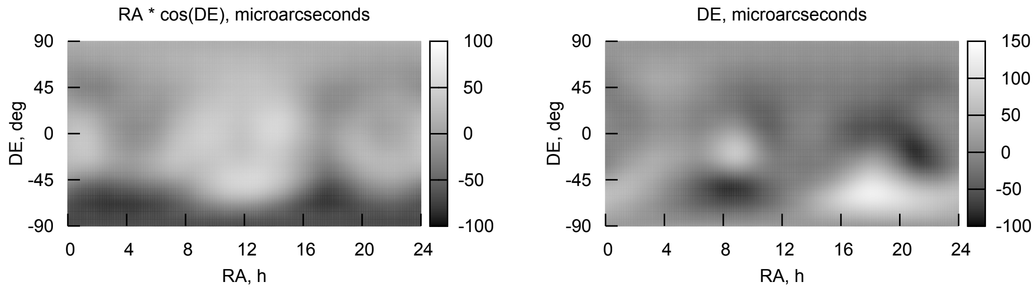

Figure 1: Smoothed differences ICRF2 - ICRF in μas. One can see large (up to 200-250 μas depending on the smoothing) peak-to-peak differences normally attributed to the ICRF systematic errors.

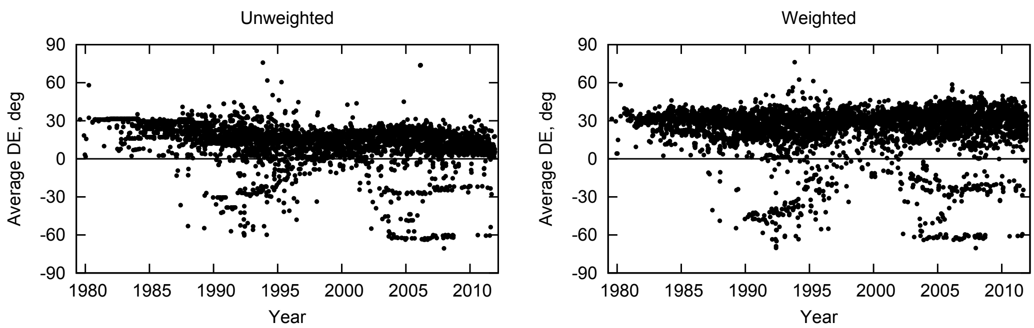

Figure 2: Average declination obtained from 24h sessions: unweighted (left, simple averaging source declination for all observations) and weighted (right, averaging declination with weights equal to the number of observations). One can see that the situation does not much improve during the history of VLBI.

- the ICRS definition may need refinement;
- the distribution of ICRF sources over the sky is rather uneven (weight on Northern sources, which is caused by the large number of Northern stations (see Figure 2);
- the distribution of the errors in ICRF source positions over the sky is rather uneven;
- proper (physical, coming from variable source structure) and apparent (coming from instrumental and analysis errors) source motions are complicated and poorly predictable;
- source positions depend on the wavelength (analogous to the color equation in optical astrometry);
- computed source positions depend on the analysis options and observing network.

3. MUTUAL IMPACT OF ICRF AND ITRF

CRF results obtained from global VLBI solutions depend on the tie to the ITRF. There are several problems that affect the source position catalog:

- Dependence on the ITRF datum.
- Dependence on the set of reference stations used.
- Dependence on the modeling of non-linear station motion.

The first problem seems to be not significant at the cm-level, but needs further investigation at the mm-level. Selection of the set of reference (minimally constrained) stations that is used to tie VLBI global solutions to ITRF varies between different analysis centers and between different solutions obtained at the same center.

Non-linear station movement represents a more serious problem that cannot be modeled properly in the ITRF. ITRF describes station displacements only using a linear model with eventual jumps. However, many stations show significant non-linear terms in position time series. The most common are exponential movement of stations due to post-seismic relaxation and seasonal signals. Two examples of such behavior

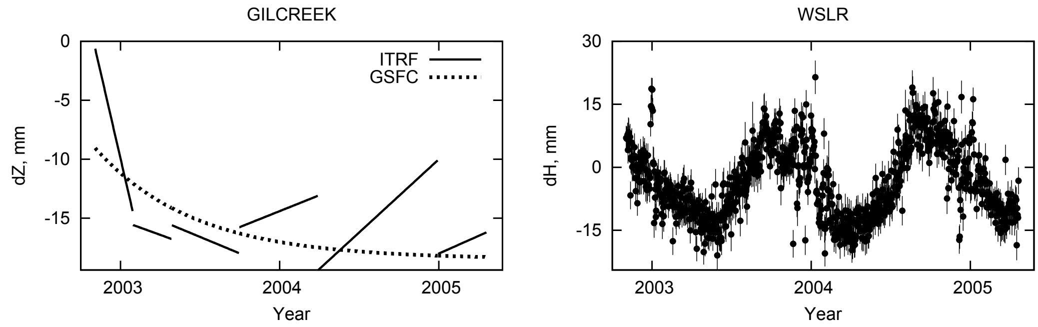

Figure 3: Two examples of non-linear station movement. The plot on the left shows post-seismic displacements of VLBI station GILCREEK, AL, USA, computed using the ITRF2008 model (solid line) and exponential model by MacMillan & Cohen (2004). The plot on the right shows seasonal height variations for IGS station WSLR, BC Canada as an example of large annual displacements.

are given in Figure 3. For the WSLR station position, computed at SOPAC[1], one can see that using a linear IERS model is by no means satisfactory because this can lead to errors in station position modeling exceeding 1 cm.

This has two consequences. First, using these stations may disturb the ICRF orientation. Secondly, if the actual station position for a given epoch differs substantially from the ITRF model, this increases both systematic errors and scatter of the EOP solution, which is obtained for this epoch from the daily set of observations involving the station concerned. Both effects seem to be not carefully investigated yet.

Our goal is modeling station daily-averaged positions at mm-accuracy for any arbitrary epoch inside the operational period, and for extrapolation to the real time and near future. Several options are used in practice for this purpose:

1. ITRF model: linear drift + jumps
   — not generally suitable
2. SOPAC model (Nikolaidis 2002): linear drift + jumps + seasonal term + exponential relaxation
   — performs much better
   — model parameters must be provided as a part of ITRF
3. GSFC model (Petrov 2005): B-splines
   — the best approximation to the computed movement
   — physical meaning is questionable
   — problems with dissemination, reproduction and extrapolation

The second option is perhaps the most reasonable compromise between accuracy, predictability, and complexity.

4. CONSIDERATIONS FOR FUTURE VLBI ICRF REALIZATIONS

If one takes a look at the ICRF history, one can mention that the successive versions were issued with interval of about five years, see Table . Following this sequence, we can set a goal to complete the next ICRF versions in 2014, and 2019. It should be mentioned that the ICRF, ICRF-Ext.1, ICRF-Ext.2 represent, in fact, the same system based on unchanged coordinates of 212 defining sources. Such long-time preserving of the positions of defining (and, as a rule, most observed) sources computed in 1995 may be the main reason of the ICRF systematic errors discussed above (Sokolova & Malkin 2007). On the contrary, all the ICRF2 source positions were adjusted in a single global solution independently, and are tied to the ICRF only by orientation (NNR constraint). One out of several options would be to keep this strategy for the next realizations too, and name them ICRF3 and ICRF4. In this connection, perhaps it would be better to use the term 'core' sources instead of 'defining'. Other options for the calculation of the next ICRF realizations exist and will be examined thoroughly.

[1] http://sopac.ucsd.edu/

ICRF version	ICRF	ICRF-Ext.1	ICRF-Ext.2	ICRF2	(ICRF3)	(ICRF4)
Year	1995	1999	2004	2009	(2014)	(2019)
Observations, mln	1.6	2.2	3.4	6.5	(9–9.5)	(12–13)
Epoch difference, yr		4	5	5	(5)	(5)

Table 1: Realized (1995–2009) and prospective (2014, 2019) ICRF versions. For the latter, foreseen values are given in parentheses as a conservative guess.

The primary goals of ICRF3 would be to incorporate new observations and enrich the set of core sources in the southern hemisphere. It will be based on about 50% more observations, and can help us to reach the following goals:

- increase the total number of sources to > 4100 (one source per 10 sq. deg.) mostly by southern sources;
- increase number of the core sources to > 410 (one source per 100 sq. deg.);
- achieve a more uniform sky distribution of all and in particular core sources and position errors;
- improve the source position errors, especially, in the Southern hemisphere.

It is advisable to develop, simultaneously with the preparation of the ICRF3, new procedures of observation planning and an advanced strategy of station usage, which shall allow us to reach the following goals with ICRF4 in 2019:

- substantially increase the number of all multi-session and core sources;
- achieve a near-uniform distribution of all and in particular core sources over the sky;
- substantially improve the source position uncertainties and accuracy;
- achieve a near-uniform distribution of source position errors over the sky.

It is expected that these goals will be achieved in the framework of regular VLBI2010 operations. Active participation of the Southern stations is a key point in this plan.

Finally, an ICRF4 catalog with near-uniform distribution of both sources and position errors can be used for the GAIA catalog orientation.

5. SUMMARY

The following proposals can be made towards actively improving the VLBI-based ICRF and its consistency with ITRF: Up to now, a decision on a list selection of defining sources was made, in fact, during ICRF computation. A good practice would be the creation of a preliminary list of the next ICRF core (defining) sources simultaneously with a ICRF realization. Active observation of the prospective core sources for ICRF3 should be started as soon as possible. More such sources should be included in the regular IVS multi-baseline observing sessions like R1, R4, and T2. Special CRF-dedicated sessions should be observed by a global network with good latitudinal and longitudinal coverage. Secondly, an agreement on a standard set of VTRF core stations should be reached, which can be used in VLBI global solutions to tie to the ITRF. Finally, a method for the uniform description of non-linear station movement should be developed, which allows a better description, reproduction and prediction of the actual motion.

6. REFERENCES

Fey, A.L., Ma, C., Arias, E.F., et al., 2004, AJ, 127(6), 3587–3608.

Ma, C., Arias, E.F., Eubanks, T.M., et al., 1998, AJ, 116(1), 516–546.

Ma, C., Arias, E., Bianko, G., et al., 2009, IERS Technical Note 35, A.Fey, D.Gordon, C.S.Jacobs (eds.).

MacMillan, D., Cohen, S., 2004, In: IVS 2004 General Meeting Proc., N.R.Vandenberg, K.D.Baver (eds), 491–495.

Nikolaidis, R., 2002, Ph.D. Thesis, University of California, San Diego.

Petrov, L, 2005, In: Proc. 17th Working Meeting of EVGA, M.Vennebusch, A.Nothnagel (eds), 113-117.

Sokolova, J. and Malkin Z., 2007, A&A, 474(2), 665–670.

PLANS FOR AN ACCURATE ALIGNMENT OF THE VLBI FRAME AND THE FUTURE GAIA FRAME

G. BOURDA[1,2], P. CHARLOT[1,2]
[1] Univ. Bordeaux, LAB, UMR5804, F-33270, Floirac, France
[2] CNRS, LAB, UMR5804, F-33270, Floirac, France
e-mail: bourda@obs.u-bordeaux1.fr

ABSTRACT. The European space astrometry mission Gaia will construct a dense optical QSO-based celestial reference frame. For consistency between optical and radio positions, it will be fundamental to align the Gaia and VLBI frames with the highest accuracy. A proper alignment is also important in the framework of astrophysics, for example to probe properly the AGN jets properties and the physics of these objects. The VLBI-Gaia frame alignment requires quasars that are bright at optical wavelength, that have a compact radio core, and that do not exhibit complex structures. In this paper, we draw prospects for this alignment, based on the ICRF2 catalogue and an ongoing dedicated VLBI project designed to observe additional weaker extragalactic radio sources for this purpose. The list of suitable sources will have to be monitored to check the relevance of the sources for the alignment, especially in terms of position stability and structures. Accordingly, we present the observations we envision in the framework of the IVS and other VLBI networks, before and during the Gaia mission.

1. THE IMPORTANCE AND CHALLENGES OF ALIGNING FRAMES

During the past decade, the IAU (International Astronomical Union) fundamental celestial reference frame was the ICRF (International Celestial Reference Frame; Ma et al. 1998, Fey et al. 2004), composed of the VLBI (Very Long Baseline Interferometry) positions of 717 extragalactic radio sources, measured from dual-frequency S/X observations (2.3 and 8.4 GHz). Since 1 January 2010, the IAU fundamental celestial reference frame has been the ICRF2 (IERS Technical Note 35, 2009), successor of the ICRF. It includes VLBI coordinates for 3 414 extragalactic radio sources, with a floor in position accuracy of 60 μas and an axis stability of 10 μas.

The European space astrometry mission Gaia, to be launched in June 2013, will survey all stars and QSOs (Quasi Stellar Objects) brighter than apparent optical magnitude 20 (Perryman et al. 2001). Using Gaia, optical positions will be determined with an unprecedented accuracy, ranging from a few tens of μas at magnitude 15–18 to about 200 μas at magnitude 20 (Lindegren et al. 2008). Unlike Hipparcos, Gaia will permit the realization of the extragalactic celestial reference frame directly at optical bands, based on the QSOs that have the most accurate positions. A preliminary Gaia catalog is expected to be available by 2015 with the final version released by 2020.

The alignment between the VLBI and Gaia frames will be important not only for guaranteeing a proper transition if the fundamental reference frame is moved from the radio to the optical domain, but also for registering the radio and optical images of any celestial target with the highest accuracy. Such a registration will allow one, for example, to pinpoint the relative location of the optical and radio emission in active galactic nuclei (AGN) to a few tens of μas, placing constraints on the overall AGN geometry. Estimates of this optical-radio core shift indicate that it may amount to $\sim$100 μas on average at X-band (Kovalev et al. 2008), significantly larger than Gaia and VLBI position accuracies. It should thus be directly measurable. Conversely, these shifts will also affect the accuracy of the link between the two frames. For this reason a large number of objects is desirable in order to average out such effects.

2. STATUS AND PLANS TO ALIGN FRAMES

The alignment between the VLBI and Gaia frames, to be determined with the highest accuracy, requires several hundreds of common sources, with a uniform sky coverage and very accurate radio and optical positions. Obtaining such accurate positions implies that the link sources must be brighter than optical magnitude 18 (Mignard 2003), and must not show extended VLBI structures in order to ensure the highest VLBI astrometric accuracy (Fey & Charlot 2000).

In a previous study, we investigated the potential of the ICRF for this alignment and found that only 70 sources (10% of the catalog) are appropriate for this purpose (Bourda et al. 2008). This highlighted the need to identify additional suitable radio sources, which is the goal of a VLBI program that we initiated four years ago. This program has been devised to observe 447 optically-bright extragalactic radio sources, on average 20 times weaker than the ICRF sources, selected from the NRAO VLA Sky Survey, a dense catalog of weak radio sources (Condon et al. 1998). The observing strategy to detect, image, and measure accurate VLBI positions for these sources is described in Bourda et al. (2010). From the pilot imaging experiment conducted in March 2008, about half of the sources observed were found to be point-like (Bourda et al. 2011). Assuming similar statistics for the subsequent experiments, this would lead finally to a sample of about 200 sources suitable for the alignment of the frames.

3. ICRF2 SUITABILITY

With the advent of the ICRF2, which comprises 4–5 times more sources than the ICRF, one may wonder how many additional suitable link sources one would get. We hence investigated the optical counterparts of the ICRF2 sources within the LQAC (Large Quasar Astrometric Catalogue; Souchay et al. 2009). By cross-correlating these two catalogues (with a cut-off value of 3″; see Table 1 for the results), we found 1 128 ICRF2 sources with a proper optical counterpart (i.e. magnitudes V or R or I $\leq$ 18 from LQAC).

In order to estimate the astrometric quality of these sources, we then calculated the X-band continuous structure index from the VLBI images available (see Bourda et al. 2011 for more details; see Figure 1 for the distribution plot). In all, structure indices were derived for 34% of the 1 128 optically-suitable ICRF2 sources. Among these, 201 sources were found to have an appropriate X-band structure index (i.e. < 3.0), corresponding to 6% of the catalogue. Figures 2 and 3, respectively, show the X-band flux density distribution for these 201 sources, and their dissemination on the sky. This latter appears quite homogeneous.

Magnitude	mag > 0	$0 <$ mag ≤ 20	$0 <$ mag ≤ 18
V	1 220	1 184	511
R	2 076	1 938	755
I	1 806	1 800	1 013

Table 1: Number of ICRF2 sources cross-identified within LQAC, depending on the value and the type of the magnitude (cross-identification cut-off value of 3″).

4. VLBI OBSERVATIONAL PLANS

Based on the current list of VLBI sources suitable for the alignment with the Gaia frame, plans are being devised for VLBI observations prior the launch of the satellite and during the mission. First, we need highly accurate VLBI positions for these sources (i.e. $\sigma < 100$ μas). Accordingly, we need to measure source positions before Gaia launch, for those sources which VLBI position accuracy is not yet sufficient. For this purpose, specific VLBI astrometric observations will be planned from 2012. Then, we need to monitor sources during the Gaia mission, in order to control source position stability and accuracy, as well as potential variations in VLBI structures. To this end, the Gaia scanning law should allow us to carry out quasi-simultaneous VLBI and Gaia observations. This might be also of high interest for astrophysical purposes (e.g. optical-radio comparisons for constraining AGN jets properties).

In order to achieve these plans, we will use several VLBI networks, because they are complementary. The IVS (International VLBI Service for Geodesy and Astrometry) network would be used for the stronger sources, while the EVN, VLBA and DSN networks could be of high interest for weaker sources (European VLBI Network; Very Long Baseline Array; Deep Space Network). Finally, one might think also about higher frequency observations in order to reduce core-shift effects, as the higher you observe in radio frequency the closer you get from the base of the radio jet and hence from the optical emission region.

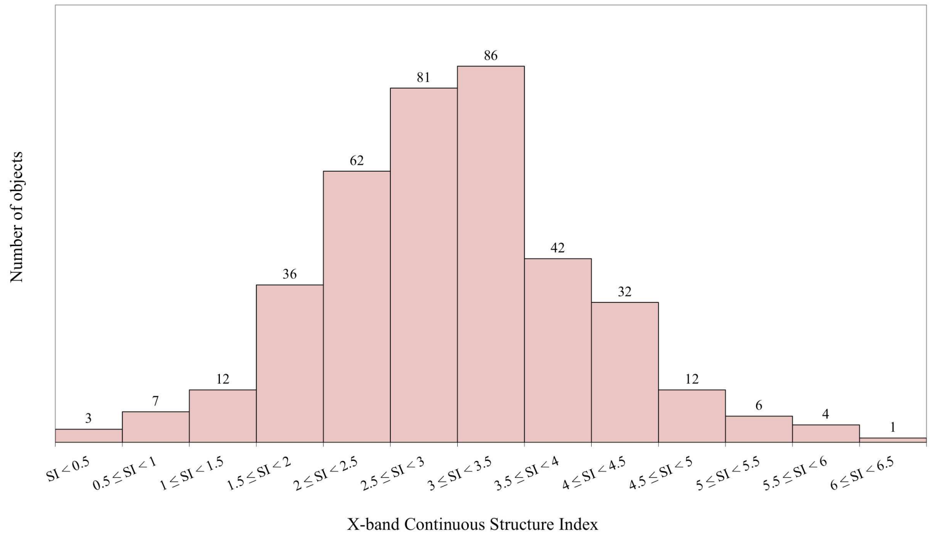

Figure 1: Distribution of the X-band continuous structure index determined for the 1 128 ICRF2 sources with a proper optical counterpart within LQAC.

5. REFERENCES

Bourda, G., Charlot, C., Le Campion, J.-F., 2008, "Astrometric suitability of optically-bright ICRF sources for the alignment with the future Gaia celestial reference frame", A&A 490, pp. 403–408.

Bourda, G., Charlot, P., Porcas, R., Garrington, S., 2010, "VLBI observations of optically-bright extragalactic radio sources for the alignment of the radio frame with the future Gaia frame. I. Source detection", A&A 520, A113.

Bourda, G., Collioud, A., Charlot, P., et al., 2011, "VLBI observations of optically-bright extragalactic radio sources for the alignment of the radio frame with the future Gaia frame. II. Imaging candidate sources", A&A 526, A102.

Condon, J., Cotton, W., Greisen, E., et al., 1998, "The NRAO VLA Sky Survey", AJ 115, pp. 1693–1716.

Fey, A., Charlot, P., 2000, "VLBA Observations of Radio Reference Frame Sources. III. Astrometric Suitability of an Additional 225 Sources", ApJS 128, pp. 17–83.

Fey, A., Ma, C., Arias, E., et al., 2004, "The Second Extension of the International Celestial Reference Frame: ICRF-EXT.1", AJ 127, pp. 3587–3608.

IERS Technical Note 35, 2009, "The Second Realization of the International Celestial Reference Frame by Very Long Baseline Interferometry", A. Fey, D. Gordon & C. Jacobs (eds.), Frankfurt am Main: Verlag des Bundesamts für Kartographie und Geodäsie.

Kovalev, Y., Lobanov, A., Pushkarev, A., Zensus, J., 2008, "Opacity in compact extragalactic radio sources and its effect on astrophysical and astrometric studies", A&A 483, pp. 759-768.

Lindegren, L., Babusiaux, C., Bailer-Jones, C., et al., 2008, "The Gaia mission: science, organization and present status", In: Proceedings of IAU Symposium 248, "A Giant Step: from Milli- to Micro-arcsecond Astrometry", W. Wenjin, I. Platais & M. Perryman (eds.), Cambridge University Press, pp. 217–223.

Ma, C., Arias, E., Eubanks, T., et al., 1998, "The International Celestial Reference Frame as Realized by Very Long Baseline Interferometry", AJ 116, pp. 516–546.

Mignard, F., 2003, "Future Space-Based Celestial Reference Frame", In: Proceedings of IAU General Assembly XXV, Joint Discussion 16: "The International Celestial Reference System: Maintenance and Future Realization", R. Gaume, D. McCarthy & J. Souchay (eds.), pp. 133–140.

Perryman, M., de Boer, K., Gilmore, G., et al., 2001, "GAIA: Composition, formation and evolution of the Galaxy", A&A 369, pp. 339–363.

Souchay, J., Andrei, A., Barache, C., et al., 2009, "The construction of the large quasar astrometric catalogue (LQAC)", A&A 994, pp. 799-815.

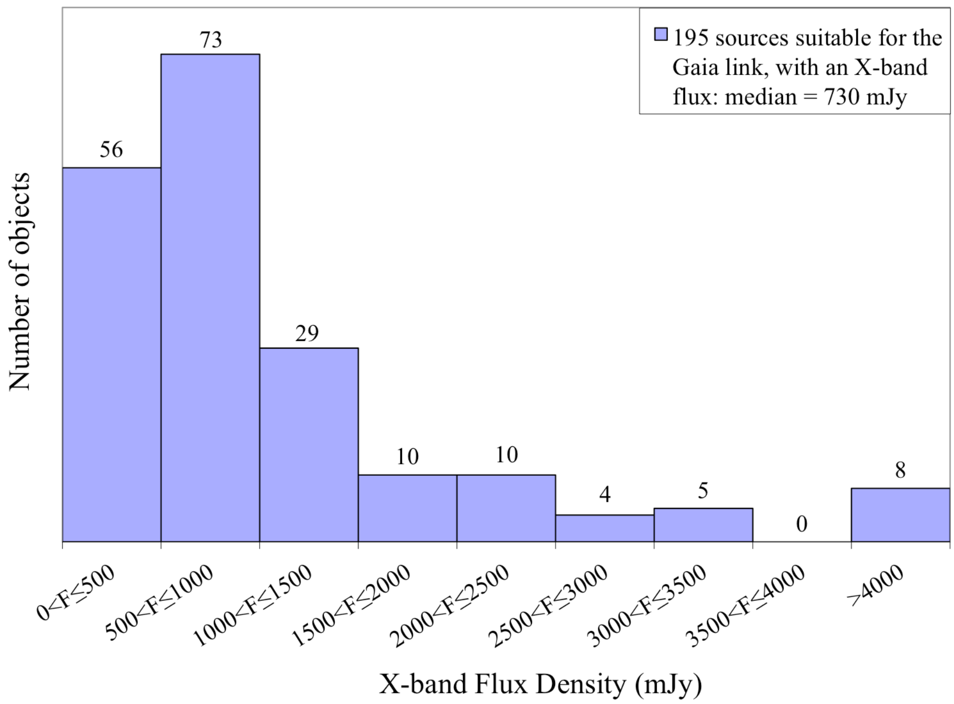

Figure 2: Distribution of the X-band flux density for the 201 ICRF2 sources suitable for the alignment with the Gaia frame (units in mJy).

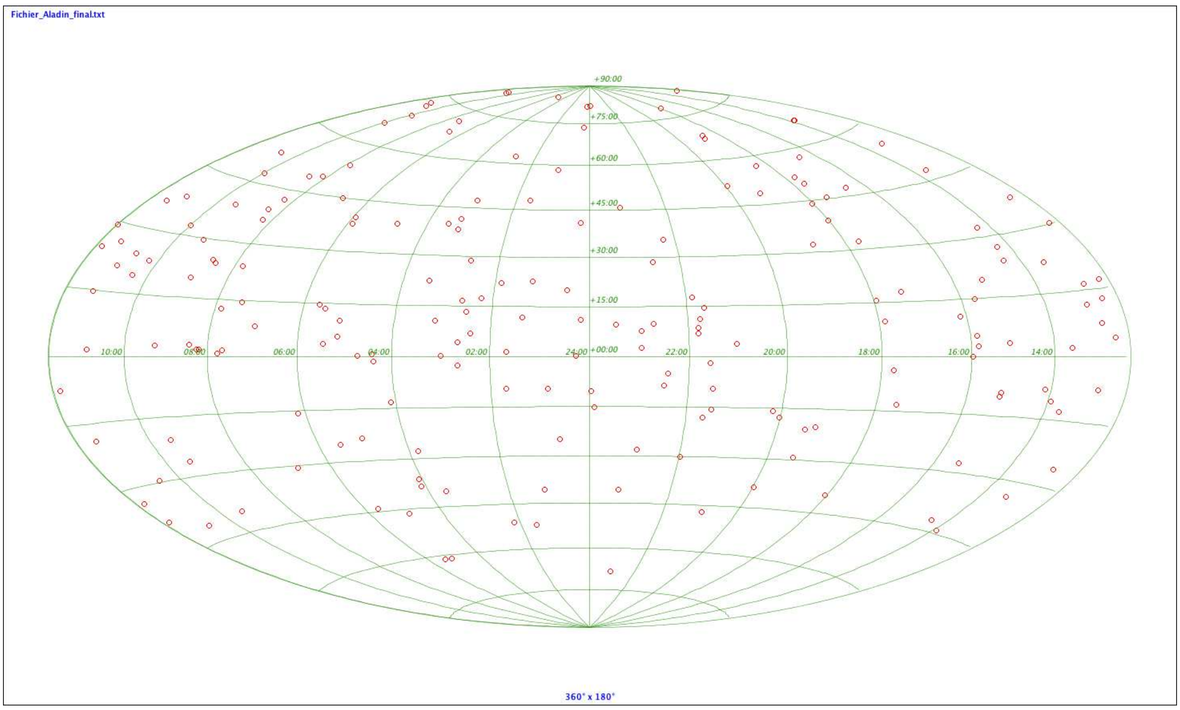

Figure 3: Sky distribution of the 201 ICRF2 sources suitable for the alignment with the Gaia frame.

OPTICAL MONITORING OF EXTRAGALACTIC SOURCES FOR THE LINK BETWEEN THE ICRF SOURCES AND THE FUTURE GAIA EXTRAGALACTIC REFERENCE FRAME

F. TARIS[1], A. ANDREI[2,3,4,1], A. KLOTZ[5], F. VACHIER[6], R. COTE[1], J. SOUCHAY[1], S. ANTON[7]

[1] Observatoire de Paris, SYRTE, CNRS/UMR8630, Paris, France
61, Av. de L'observatoire 75014 Paris, FRANCE
e-mail: francois.taris@obspm.fr

[2] INAF, Osservatorio Astronomico di Torino, Italy

[3] Observatorio Nacional, MCT, Rio De Janeiro, Brasil

[4] Observatorio do Valongo, UFRJ, Rio De Janeiro, Brasil

[5] CESR, Toulouse, France

[6] Observatoire de Paris, IMCCE, Paris, France

[7] CICGE, Fac. Sciences Univ. Porto, Porto, Portugal

ABSTRACT. This work presents AGN observations with small and medium size aperture telescopes (0.25 m to 1 m). One goal of these observations is to provide a list of suitable targets that could be used to establish the link between the ICRF and the future Gaia celestial reference frame.

1. INTRODUCTION

Optical telescopes involved in this experiment and reference frames are presented in the two following sections. Some results about individual targets in terms of observability, light curve, compacity index and morphology are given as examples.

2. OPTICAL TELESCOPES INVOLVED IN THIS WORK

The observations were carried out with four telescopes located in France, Chile and Australia. This section is dedicated to the presentation of these telescopes.

The telescope of 1.2 m of the OHP (Observatoire de Haute Provence[1], IAU code 511) is located in the south east of France. It was used form March 2010 to February 2011 during 17 nights. It is equipped with a 1.2 m mirror of 7.2 m focal length. It uses a 1024x1024 px^2 CCD camera with a pixel scale in the focal plane of 0.69 arcsec/px given a field of view of 10 arcmin^2. The seeing during the observations was relatively poor, with a mean value of 3.4 arcsec. The filters used were the V and R Cousins filters.

TAROT (Klotz et al. 2008) is a french acronym which stands for "Télescope à Action Rapide pour l'Observation des phénomènes Transitoires". There are two telescopes located for the first one in the south east of France (OCA, Observatoire de la Côte d'Azur[2] and for the second one in Chile (ESO). TAROT are robotic observatories that observe with no human interaction. TAROT are two identical 25 cm telescopes $F/D = 3.4$ that cover 1.86°x1.86° field of view on the Andor CCD cameras (Marconi 4240 back illuminated). Spatial sampling is 3.3 arcsec/px. Six filters are available : BVRI, a clear filter and a 2.7 density coupled to V (for Moon and planets). Detection limit is about $V = 17$ in 1 minute exposure. These two telescopes are used since February 2011.

Zadko[3] is a one meter robotic telescope funded by a donation from James Zadko to the University of Western Australia (UWA). It is a 1-meter $f/4$ Cassegrain telescope located in the state of Western Australia about 67 km north of Perth. It is equipped with an Andor 2048x2048 backilluminated CCD. The field of view is 23.5 arcmin^2 and the filters used for this study are g and r Gunn filters. Zadko

[1]see http://www.obs-hp.fr
[2]see http://tarot.obs-hp.fr/tarot
[3]see http://www.zt.science.uwa.edu.au

and TAROT are part of the same robotic telescope network for space debris identification and tracking (Laas-Bourez et al. 2010). Currently, five robotic observatories are linked to a central observatories coordinator CADOR (Coordination et Analyse des Données des Observatoires Robotiques).

3. REFERENCE SYSTEMS

The current conventional realization of the ICRS (International Celestial Reference System) is the second version of the International Celestial Reference Frame (ICRF) called ICRF2. In the optical domain, the Hipparcos Catalogue is the current international conventional realization but in the future (around 2020) the Gaia catalogue should be the basis of the optical realization of the ICRS. The link between these reference frames, in the radio and in the optical domain, is of course of primary significance. In this section, we present, in a didactic way, all of these fundamental concepts.

The construction of the ICRF2 used almost 30 years of geodetic very long baseline interferometry (VLBI) observations at 3.6 cm and 13 cm wavelengths. The ICRF2 catalogue contains positions of 3 414 compact radio sources. The formal errors σ in source coordinates increased according to $((1.5\sigma)^2+\sigma_0^2)^{1/2}$ where σ_0 is a noise floor set to 40 μas. The median error in the position of sources observed in more than two sessions is 175 μas. The frame axes are defined by the coordinates of 295 "defining" sources with a stability of $\sim$10 μas. The defining sources were chosen on the basis of their high positional stability and low structure index. A subset of 138 defining sources was used to align the ICRF2 catalogue onto the ICRS. The ICRF2 currently represents the most accurate realization of the celestial system with respect to which the position of any object in the celestial sphere should be measured. We note that the ICRF is epochless and independent of the dynamical frame (ecliptic) and reference point (equinox), but is consistent with previous realizations of the ICRS, including the FK5 J2000.0 optical system.

The European astrometric space mission Gaia will be launched in 2012. It will provide positions and proper motions of around one billion of stars and about 500 000 QSOs with unprecedented uncertainty between the 6th and the 20th magnitude. The predicted accuracy is a few hundred of μas at 20th magnitude. To prepare the future Gaia extragalactic reference frame, a clean sample of at least 10 000 QSOs must be implemented (Gaia initial quasar list). This work is being performed in the framework of the Gaia work-package GWP-S-335-13000 with the aim of giving an initial QSO catalogue.

Two catalogues are at the basis of this work, the LQAC (Souchay et al. 2009) and the LQRF (Andrei et al. 2009). Relating the ICRF2 to the Gaia extragalactic reference frame will be a very important task in the near future and some works are currently underway to achieve this.

Bourda et al. (2008) evaluated the suitability of the current individual ICRF-Ext2 (the ICRF catalogue that preceded the ICRF2) extragalactic radio sources for the alignment with the future Gaia frame. They identify 243 candidates among the ICRF-Ext2 sources used to align with the Gaia frame, with an optical counterpart brighter than the apparent magnitude $V = 18$. Among these 243 candidates, only 70 have data of excellent or good astrometric quality (i.e, an X-band structure index value of either 1 or 2) for determining the Gaia link with the highest accuracy. Nevertheless, this index value is perhaps not well suited to determining the best sources in the optical domain in the sense that several sources given by these authors are not point-like sources (for example NGC3031 or Messier81, MARK421, NGC4374 or Messier84).

An investigation of the correlation between long-term optical variability and what is dubbed the random walk of the astrometric centroid of QSOs is being pursued at the ESO Max Planck 2.2-meter telescope in Chile (Andrei et al. 2008). A sample of quasars has been selected in term of their large amplitude and long-term optical variability. The observations are typically performed every two months. The analysis procedure is completely differential: the quasar positions and brightness are determined starting from a set of selected stars for which the average relative distances and magnitudes remain clearly constant. The preliminary results for four objects bring strong support to the hypothesis of a relationship between astrometric and photometric variability. If verified, the relationship could indicate that high photometric variation would make a given quasar less apt to materialize a stable extragalactic reference frame such as the one provided by the GAIA mission.

It is a matter of fact that variations of the radiostructure of QSOs degrades the positional accuracy of the radiocenter's position. It can be also postulated that variations of the photocenter's position could be correlated with magnitude variations. Roughly speaking, for a quasar at the distance of 1 Gpc and for an emission region with a size of 1 pc (in that case the magnitude variations occurs in some years) the corresponding angular size in the sky would be 200 μas. This value must be compared to the uncertainty of the coordinates in the future Gaia catalogue (few hundred of μas at 20th magnitude).

4. PROPERTIES OF THE TARGETS

Among the 67 targets (the 70 initial targets minus 3), 24 of them have been observed elsewhere for a long time and some light curves have been found in referred papers. For 36 targets (54% of the initial list), the light curves obtained during this work bring new informations to our knowledge about them. Among these 36 targets, three (QSO B1508-055, QSO B1725+044, QSO B1954-388) have only one measure of magnitude reported in the literature, one (QSO B2126-158) has only one measure of magnitude plus no variations and two (QSO B0955+326 and QSO B1749+096) have only intranight variability. Seven of the 67 targets remain unobserved in the frame of this work.

Some targets (10 among the 67) were difficult to observe with our small telescopes due to their magnitudes. One other is very near to a bright star. Consequently these 11 targets will remain difficult to observe with other telescopes.

Figure 1 gives an example of a light curve for a well observed target (Katajainen et al. 2000). Our light curve shows a 1.5 magnitude variation (both in R and V band) during one month. Due to the distance of this target ($z = 0.3$) it means that the emission region has an angular (maximum) size of roughly 5 μas. Other curves (Katajainen et al. 2000) show the same kind of events but during three months (15 μas). Other targets from our work show magnitude variation during three months (1147+245, $z = 0.2$, 25 μas).

Compacity index has been computed from DSS images for 55 targets of the initial list. For 21 of them, values lower than 0.5 (compact sources) have been found, and for 20 of them, the compacity index is greater than 1 (not compact sources). Compacity index with the images obtained during this experiment is currently under computation and will be published very soon elsewhere.

About the morphology of the targets, 14 (always among the 67) have a host galaxy in the optical band as 14 have not and 39 targets have an unknown morphology. Among these 39 interesting targets, 17 are the subject of data mining in the HST MAST archive and the remaining 22 are the subject of observation proposals with the CFH Telescope (3.6-meter Canada France Hawaii Telescope), the ESO MPG2.2 Telescope (2.2-meter telescope in Chile) and the SOAR Telescope (4.1-meter telescope in Chile).

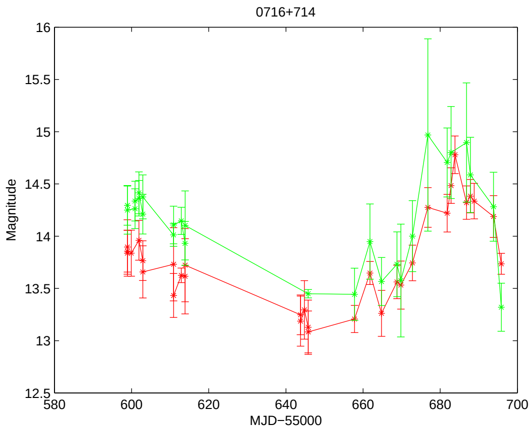

Figure 1: Light curves (R and V filters) of QSO 0716+714 obtained by Tarot telescope

5. CONCLUSION

This work presents optical observations of suitable extragalactic targets used for the link between the ICRF and the future Gaia celestial reference frame. Among the 70 targets of the initial list, 55 have been observed easily in the optical wavelength and 11 remain difficult due to the size of the telescope used or to their relative position to bright stars. A large amount of the targets seem to be variable (0.1 to 1.5 mag) both in R and V with time scales from few days to some months. The astrometric uncertainty due to the emission region is then of the same order than the Gaia astrometric uncertainty. For 36 targets (54%

of the initial list), the light curves obtained during this work bring new informations to our knowledge about them.

Compacity index has been computed from DSS images for 55 targets of the initial list. The same work is under progress with the images obtained during this experimentation.

Morphology studies with high angular resolution are currently under progress to characterize the host galaxies and to evaluate the corresponding shift of the photocenter with respect to the quasi stellar object one. Detailed results about the work presented during the Journées will be soon published elsewhere.

6. REFERENCES

Andrei, A., Bouquillon, S., Camargo, S., et al., 2008, Astrometric and photometric variability in quasars, Proc. JSR2008, M. Soffel and N. Capitaine (eds), Lohrmann Observatorium and Observatoire de Paris

Andrei, A., Souchay, J., Zacharias, N., et al., 2009, The large quasar reference frame (LQRF). An optical representation of the ICRS, A&A , 505, 385

Bourda, G., Charlot, P., Le Campion, J. F., 2008, Astrometric suitability of optically bright ICRF sources for the alignement with the future Gaia celestial reference frame, A&A , 490, 403

Katajainen, S., Takalo, L., Sillanpaa, A., et al., 2000, Tuorla quasar monitoring, A&A Suppl. Ser., 143, 357

Klotz., A., Boër, M., Eysseric, J., et al., 2008, Robotic oservations of the sky with TAROT. 2004-2007, PASP, 120, 1298

Laas-Bourez, M., Coward, D., Klotz., A., et al., 2010, A robotic telescope network for space debris identification and tracking, AdSpR, 47, 402

Souchay, J., Andrei, A., Barache, C., et al., 2009, The construction of the large quasar astrometric catalogue (LQAC), A&A , 494, 799

A POTENTIAL Ka-BAND (32 GHz) WORLDWIDE VLBI NETWORK

C.S. JACOBS[1], U. BACH[6], F. COLOMER[7], C. GARCÍA-MIRÓ[2], J. GÓMEZ-GONZÁLEZ[7], S. GULYAEV[9], S. HORIUCHI[3], R. ICHIKAWA[12], A. KRAUS[6], G. KRONSCHNABL[5], J.A. LÓPEZ-FERNÁNDEZ[7], J. LOVELL[8], W. MAJID[1], T. NATUSCH[9], A. NEIDHARDT[4], C. PHILIPS[13], R. PORCAS[6], A. ROMERO-WOLF[1], L. SALDANA[14], U. SCHREIBER[5], I. SOTUELA[3], H. TAKEUCHI[11], J. TRINH[1], A. TZIOUMIS[13], P. DE VINCENTE[7], V. ZHAROV[10]

[1]Jet Propulsion Laboratory, California Institute of Technology
4800 Ok Grove Dr., Pasadena CA, USA
e-mail: Christopher.S.Jacobs@jpl.nasa.gov

[2] Madrid Deep Space Communications Complex/NASA, INTA, Madrid, Spain

[3] Canberra Deep Space Communications Complex/NASA, CSIRO, Canberra, Australia

[4] Technische Universität München, Munich, Germany

[5] Bundesamt für Kartographie und Geodäsie, Bad Kötzting, Germany

[6] Max-Planck-Institut fuer Radioastronomie, Bonn, Germany

[7] Instituto Geográfico Nacional, Madrid, Spain

[8] University of Tasmania, Hobart, Tasmania, Australia

[9] Institute for Radio Astronomy and Space Research, Auckland University of Technology Auckland, New Zealand

[10] Sternberg State Astronomical Institute, Moscow, Russia

[11] ISAS/JAXA, Sagamihara, Japan

[12] Kashima Space Research Center, NICT, Kashima, Japan

[13] C.S.I.R.O. Astronomy and Space Science, Australia

[14] ITT Exelis, 1400 Shamrock, Monrovia, CA, U.S.A.

ABSTRACT. Ka-band VLBI capability now exists, is under development or is being considered at 22 sites around the world. Thus, there is now an opportunity to create a worldwide Ka-band VLBI network. This paper will examine the potential for a cooperative network capable of high resolution imaging and astrometry. Initial fringe tests on a few individual baselines have been successful and more tests are planned. With baselines approaching a Giga-lambda, a Ka-band network would be able to probe source structure at the nano-radian (200 μas) level and thus gain insight into astrophysics of the most compact regions of emission in active galactic nuclei.

1. INTRODUCTION

There are 22 VLBI antennas worldwide that either have, are planning, or are considering Ka-band capability (Table 1). Ka-band is around 32 GHz or 9 mm wavelength. It is found between the 22 GHz water line and the 60 GHz O_2 line. At Ka-band sources tend to be more core dominated because the extended structure in the jets tends to fade away with increasing frequency.

Advantages of Ka: There are several advantages of Ka-band. The short 9 mm wavelength and long baselines approaching a Giga-λ allow for resolution approaching 200 μas. The sources are more compact than at X-band which should reduce source structure effects and core shifts. Ka-band allows for higher telemetry rates for spacecraft communications by +5 to +8 dB as well as smaller lighter RF spacecraft systems. Ka-band avoids S-band RFI issues. Ionosphere and solar plasma effects are reduced by a factor of 15 compared to X-band, thus allowing observations closer to the Sun or the Galactic center.

Disadvantages of Ka: Because Ka-band is near the 22-GHz water line, Ka-band is more weather sensitive and has higher system temperatures than comparable systems at X-band. Because Ka-band has a shorter wavelength than X-band, coherence times are shorter thus limiting the potential for longer integrations on source. Some sources are weaker or resolved. Antenna pointing is more difficult. The net effect is to reduce system sensitivity. Our intent is to compensate by increasing data rates.

X/Ka-band radio catalog: A catalog of ∼470 Ka-band sources already exists. Based on comparisons to the S/X-based ICRF2 (Ma et al., 2009), Ka-band accuracy is 200 to 300 μas (Jacobs et al., 2011). The south polar cap is not yet covered, but a pilot project is now underway using 144 of the 498 candidates identified by Sotuela et al. (2011). So sufficient sources exist to provide geodetic reference sources and calibrators for phase referencing.

2. NETWORK GEOMETRY AND UV COVERAGE

How strong is the potential for imaging? Using AIPS software, we simulated the set of projected baseline lengths generated as the Earth rotates (uv coverage). The European sub-net (1st 11 stations of Table 1) covers out to 600 Mλ and gives excellent coverage for circumpolar sources (Figure 2a). Likewise, the south Pacific sub-net has good circumpolar coverage to 500 Mλ. Adding Japanese "outriggers" gives ∼Gλ North-South resolution, but with a sacrifice in the uniformity of coverage (Figure 2b).

Figure 1: Ka-band Station Distribution. Note clusters in Europe and Australia. *Credit: Google maps*

In summary, there is potential for imaging at the few 100 μas level which corresponds to the inner few parsecs of a typical active galactic nucleus where the most energetic processes are thought to occur.

3. Ka-BAND FEEDS

Ka-band capable feeds are a key element required for a functioning Ka network. NASA's Deep Space Network (DSN) has had X/Ka feeds for over a decade in its 34-m antennas (e.g. Chen et al., 1993 and 1996; Stanton et al., 2001). More recently, several designs have appeared for 12-m class antennas intended for geodesy in the IVS-2010 era. Hoppe & Reilly (2004) designed an X/Ka feed for the (then) Patriot 12-m antenna. Twin Telescopes Wettzell (TTW) is designing an S/X/Ka feed (Göldi, 2009). The RAEGE project is also designing an S/X/Ka feed. Thus there are sufficient feed designs to equip antennas at Ka-band. We have achieved our first Ka-band fringes outside the DSN on a baseline from

marker	Station	Location	Size (m)	bands	date
A	Robledo	Spain	34	S/X/Ka	now
B	Cebreros	Spain	35	X/Ka	now
G	Effelsberg	Germany	100	Ka	now
H	Wettzell	Germany	13	S/X/Ka	2012
	RAEGE Net				
C	Yebes	Spain	13	S/X/Ka	2012
F	Flores	Azores	13	S/X/Ka	2014
E	Santa Maria	Azores	13	S/X/Ka	2013
D	Canaries	Canaries	13	S/X/Ka	2014
C	Yebes	Spain	40	S/X/Ka	2013/4
	Russian Net				
I	Kazan	Russia	12	S/X/Ka	TBD
J	Kislovodsk	Russia	12	S/X/Ka	TBD
	S. Pacific Net				
K	Tidbinbilla	Australia	34	X/Ka	now
L	Narrabri	Australia	22	Ka	now
M	Mopra	Australia	22	Ka	now
N	Parkes	Australia	12	S/X/Ka	TBD
O	Hobart	Tasmania	12	S/X/Ka	TBD
P	Katherine	Australia	12	S/X/Ka	TBD
Q	Yaragadee	Australia	12	S/X/Ka	TBD
R	Warkworth	New Zealand	12	S/X/Ka	TBD
	N. Pacific Net				
S	Kashima	Japan	34	Ka	now
T	Usuda	Japan	45	X/Ka	2018
	E. Pacific				
U	Goldstone	U.S.A.	34	X/Ka	now

Table 1: Status of existing and potential Ka-band stations

DSS-55 to Effelsberg on day-of-year 223 of 2011 with source OT 081 recording at 448 Mbps.

4. CONCLUSIONS

Ka-band (32 GHz, 9 mm) Very Long Baseline Interferometric (VLBI) global networking is feasible within the next few years. Ka-band VLBI astrometry from NASA's Deep Space Network has already developed a catalog of observable sources with highly accurate positions. Now, a number of antennas worldwide are planning or are considering adding Ka-band VLBI capability. Thus, there is now an opportunity to create a worldwide Ka-band network capable of high resolution imaging and astrometry. With baselines approaching a Giga-lambda, a Ka-band network would be able to probe source structure at the nano-radian (200 μas) level and thus gain insight into the astrophysics of the most compact regions of emission in active galactic nuclei. We have discussed the advantages of Ka-band, shown $\sim$470 known sources and $\sim$500 candidate sources, simulated uv coverage, and discussed potential RF feeds. First Ka fringes have been demonstrated! All these things demonstrate that a worldwide Ka-band network is feasible within the next few years!

Acknowledgements. This research done in part under contract with NASA. U.S. Government sponsorship and sponsorship of our respective institutions and funding agencies acknowledged.

5. REFERENCES

Chen, et al., 'Performance of the X-/Ka-/KABLE-Band Dichroic Plate in DSS-13 Beam Waveguide Antenna,' TDA PR 42-115, pp. 54-64, 1993.
http://tmo.jpl.nasa.gov/progress_report/42-115/115e.pdf

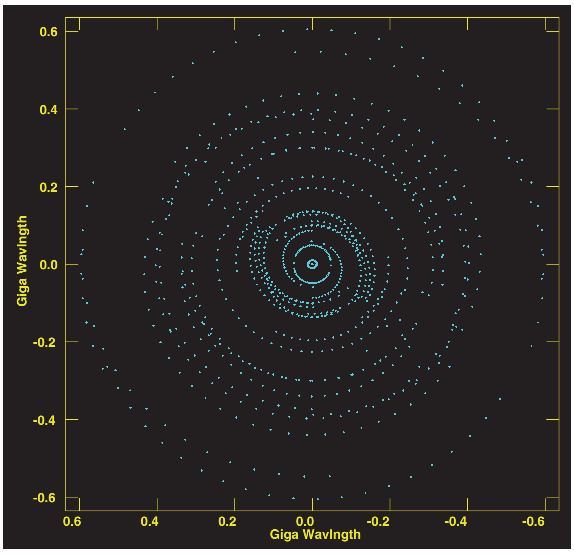

a. European network: source at Dec +75°.

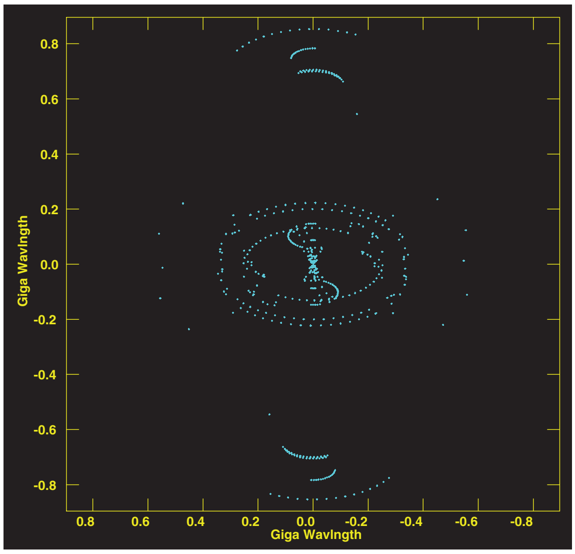

b. S. Pacific net + Japan outrigger: Dec −30°

Figure 2: Ka-band Network UV coverage examples.

Chen, et al., 'Prototype Ka-/Ka-Band Dichroic Plate With Stepped Rectangular Apertures,' TDA PR 42-124, pp. 143-152, 1996. http://tmo.jpl.nasa.gov/progress_report/42-124/124C.pdf

Göldi, W., 'TTW Tri-band feed,' Mirad; FRFF-Workshop, Wettzell, 2009.

Hoppe, D.J., & H. Reilly, '8–9 GHz & 30–40 GHz Feed for DSN,' JPL IPN Prog. Rept. 42-157, 2004. http://tmo.jpl.nasa.gov/progress_report/42-157/157B.pdf

Jacobs, C.S., et al., 'The Celestial Frame at X/Ka-band,' 20^{th} EVGA, Bonn, Germany, 2011. http://www.mpifr-bonn.mpg.de/div/meetings/20thEVGA/EVGA-Talks/Jacobs_XKa_110330.pdf

Ma, et al., IERS Technical Note No. 35: '2^{nd} Realization of ICRF by VLBI,' Eds. A. Fey, D. Gordon, and C.S. Jacobs, IERS, BKG, Frankfurt am Main, Germany, 2009. www.iers.org/documents/publications/tn/tn35/tn35.pdf

RAEGE, http://www.raege.net/

Sotuela, I., et al., 'Contribution of X/Ka VLBI to Multi-wavelength CRF studies,' GREAT-ESF workshop, Porto, Portugal, 2011. http://www.fc.up.pt/great-ws-porto/Ioana_Sotuela.pdf

Stanton, P. H., D. J. Hoppe, and H. Reilly, 'Development of 7.2-, 8.4-, 32-Gigahertz (X-/X-/Ka-Band) 3-Frequency Feed for DSN,' TMO PR 42-145, pp. 1-20, 2001. http://tmo.jpl.nasa.gov/progress_report/42-145/145D.pdf

FORTHCOMING IMPROVEMENTS IN SLR DATA ANALYSIS: TOWARDS THE mm-SLR

E.C. PAVLIS, M. KUZMICZ-CIESLAK, P.M. HINKEY

Goddard Earth Science and Technology Center, University of Maryland, BC
e-mail: epavlis@umbc.edu

ABSTRACT. Accuracy requirements for the International Terrestrial Reference Frame (ITRF) are becoming increasingly more stringent, especially with regards to its origin definition and its scale stability. Satellite Laser Ranging (SLR) contributes unique information on the origin, and along with VLBI, for its absolute scale. Advances in our understanding of the coupling between the sub-components of system Earth require that we revisit our current modeling used in the reduction of SLR data. With the recent release of numerous products from global circulation models and satellite and terrestrial observations, we are now able to examine the effect of improved modeling in the analysis of several years of SLR data. We present results from such analyses and compare them to our nominal results, based on the currently accepted ILRS standards. Depending on the outcome of these tests, we anticipate that in the near future, ILRS will formulate a proposal to IERS for modification of the analysis standards related to the products contributing to the establishment of the future ITRFxx.

1. INTRODUCTION

The International Terrestrial Reference Frame (ITRF) accuracy requirements are becoming increasingly more stringent, driven primarily by those dictated by the Global Geodetic Observing SystemGGOS. It is now commonly accepted that the future ITRF should exhibit 1 mm accuracy in the origin of the reference frame at epoch and 0.1 mm/y stability over time (Wilson et al., 2010). SLR determines uniquely the origin of the ITRF and along with VLBI, its scale. For many years now SLR has also observed mass redistribution in the Earth system (Pavlis, 2002), providing unique estimates prior to the launch of GRACE (Tapley et al., 2004). With the proliferation of GRACE products and the availability of global fields of atmospheric, oceanic, and hydrological circulation, it is now high time to consider the forward modeling of these processes in the analysis of SLR data for the establishment of the TRF. Although at present we focus on the analysis of LAGEOS data only, in subsequent stages we will extend these model improvements to LEO targets to make their contribution useful and of acceptable accuracy for inclusion in the development process of the ITRF.

2. CURRENT STATUS OF SLR MODELING

The improvement of the gravitational models, the static as well as time-varying components, thanks to the launch of GRACE, has removed a major source of error in Precise Orbit Determination (POD) for all missions in recent years. As these errors are suppressed, errors that we previously considered insignificant, are now taking central role and limit our ability to fit the SLR data to their inherent 1 mm accuracy. The components that contribute to the total error in the SLR analysis vary with regard to the tracking station, spacecraft target, geophysical model, local survey, etc. from between a few mm to few cm, as it is shown in Figure 1. It is clear that there a lot of areas where improvement by an order of magnitude is required, if we want to reach our goal of a 1 mm accurate technique.

3. FUTURE IMPROVEMENTS IN SLR

Even if the modeling improves with the adoption of state-of-the-art models, SLR is still suffering from two other shortcomings: the unbalanced global distribution of its tracking network and the limited number of suitable targets in orbit.

The first limitation is now addressed within the GGOS initiative, with the international community agreeing to reestablish the geodetic networks in general, using the latest hardware and software available,

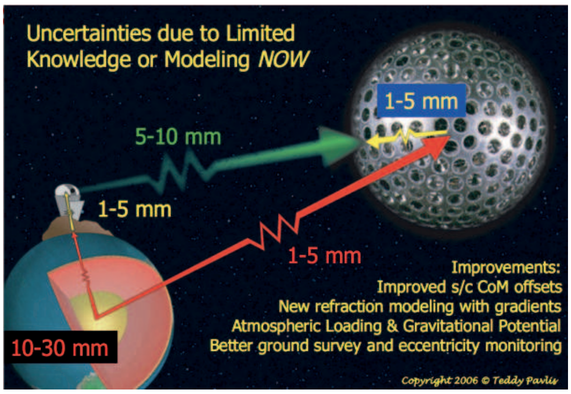

Figure 1: Current state of modeling SLR data to geodetic targets (LAGEOS, ETALON, etc.)

and making every effort to co-locate all space techniques in an as balanced global network as physical limitations permit (Figure 2).

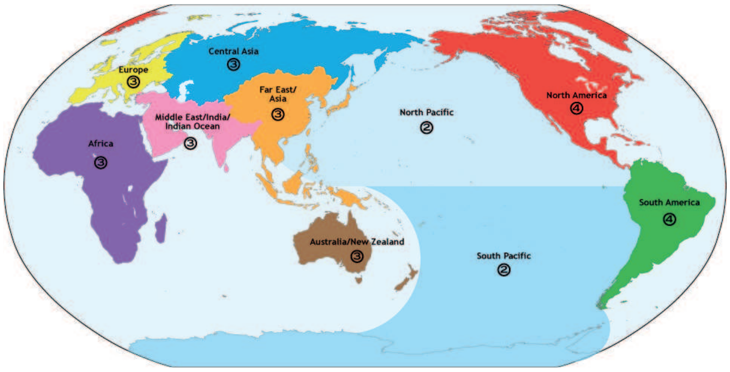

Figure 2: Envisioned space geodetic techniques station distribution for the future GGOS 2020 network)

The second issue, the limited number of targets in orbit is also addressed in more than one ways. First of all the improved modeling is expected to allow us to make use of targets in significantly lower orbits, previously thought prohibited for ITRF work (e.g. Starlette, Stella, LARETS, etc.). New designs of novel approaches for new targets that can in principle support the 1 mm accuracy goal. One example already in orbit is the "Ball Lens In The SpaceBLITS" satellite (Figure 3) designed by the IPIE group under the Federal Space Program of Russia. It is a double Luneburg sphere that acts as a single retroreflector when ranged from the one hemisphere, with a very precisely measured aspect-independent signature. Unlike our other targets that return a signal that is the convolution of multiple reflections from several retroreflectors, BLITS' return signal is distorted only by the propagation media.

The initial results from the reduction of BLITS SLR ranges indicate that there is potential in the development of such targets if the quality of the material can be improved for a much longer life in space and the size of the spacecraft increased so that it can be used in higher, more stable orbits.

A second project that will also enhance our dedicated target collection is the imminent launch of the ASI mission LARES (see Pavlis et al., in these proceedings).

From the purely modeling point of view, one of the first improvements to be considered is of course the time varying gravitational signals that GRACE observes at monthly intervals. With several years of GRACE data accumulated by now, it is even possible to derive sufficiently high-resolution models that can be used even during the time period prior to GRACE's launch, in order to describe at least the dominant signals (secular, annual, semi-annual, seasonal, Figure 4). In this fashion we can benefit and improve the results from reanalysis of historical SLR data collected long before the GRACE era.

Other less obvious improvements can come from the adoption of new and improved models for atmospheric loading (from NCEP or ECMWF), hydrological loading (e.g. from GLDAS), new ocean tides

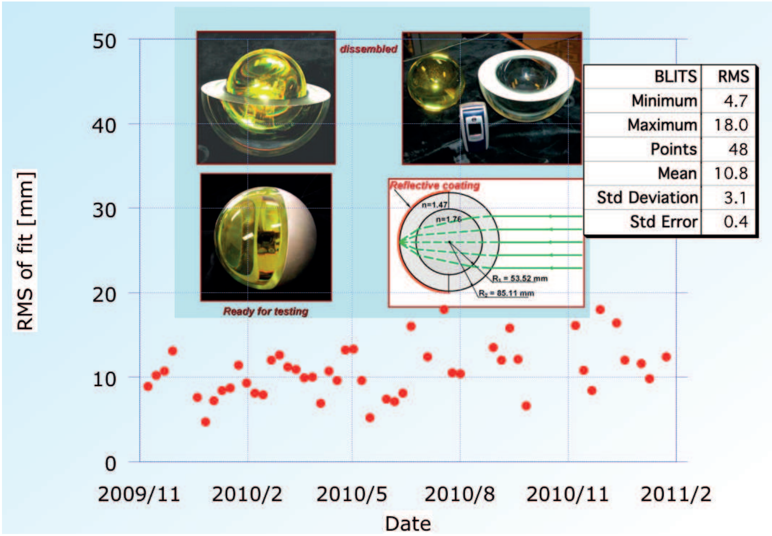

Figure 3: Retroreflector spacecraft BLITS and the RMS of fit for a preliminary analysis of its SLR data)

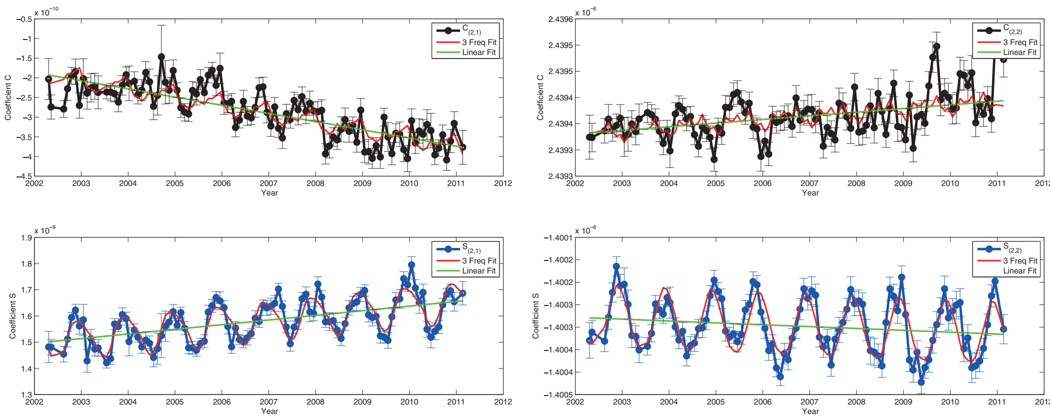

Figure 4: Temporal variations in the degree two harmonics for orders 1 and 2 observed by GRACE, and the linear (green) and harmonic (red) analytical model fitted to them. Note the significantly better fit for the sine terms (S_{2m})

models (e.g. GOT04.7 or more recent) with proper treatment for the atmospheric tides, upgrading our atmospheric refraction modeling from an analytic model (Mendes and Pavlis, 2004) to using 3-D atmospheric ray tracing (ART) that will include atmospheric gradients (Hulley and Pavlis, 2007), albedo models from global satellite-based fields, etc.

The effect of atmospheric circulation (mass redistribution) to each station's position due to its loading of the crust can be modeled with corrections derived from global atmospheric fields such as NCEP or ECMWF. A service providing such corrections was pioneered a few years ago by Petrov and Boy (2004), and results are available for various operational and experimental fields from ECMWF, as well as from NCEP.

We chose to test these in 2001 and 2006, so that we can investigate the maximum possible number of versions of these fields. The results were compared to those obtained without atmospheric modeling, and indicate an average reduction in the overall RMS of fit of the order of 3 mm in the mean and a similar level scatter over the test period.

SLR unlike other space geodetic techniques is marginally affected by atmospheric refraction. Nevertheless, when we strive for mm-level accuracy, even the otherwise small effects of horizontal gradients in the lower atmosphere must be accounted for. Hulley and Pavlis (2007) demonstrated how to compute refraction corrections along the laser beam path directly from three-dimensional ray tracing through the meteorological fields, now routinely available. The SLR data for 2004–2005 were corrected using using the 3D ART approach, based on three different global fields: ECWMF, NCEP and the satellite observations from the AIRS instrument on board NASA's AQUA platform.

The results indicated that 3D ART with AIRS-observed fields is the best approach, explaining almost 25% of the residual variance versus an alternate approach, where the isotropic delay is modeled through the analytical model of (Mendes and Pavlis, 2004) and the gradients are obtained from 3D ART, which only accounts for 14% of the variance for the same data.

4. CONCLUSIONS AND FUTURE PLANS

The stringent accuracy requirements of GGOS are a strong incentive for the improvement of the models underlying the reduction of space geodetic data. One of the most significant errors in techniques sensitive to gravitational variations are the temporal signals caused by the continuous mass redistribution in the Earth system. Using the available GRACE monthly fields we can generate models for these variations that can be used in orbital modeling along with consistent improved tidal models, to significantly reduce the residual variance. Similarly, the use of meteorological fields to derive the corresponding loading effects at the tracking stations can further explain part of the remaining variance. Additional improvement comes from the computation of the entire atmospheric delay using meteorological fields, especially those obtained from global satellite observations, in order to properly account for the horizontal gradients which are otherwise ignored. Implementing these changes in the future reduction of SLR data will result in significantly improved products with emphasis on consistency over time. Other improvements specific to SLR are the new network to be established in support of GGOS and the use of additional well-designed targets, either already in orbit or soon to be launched. These enhancements will allow us to meet the GGOS requirements and reach our millimeter SLR goal.

Acknowledgements. Erricos Pavlis gratefully acknowledges the support of NASA Grant NNX11AI44G.

5. REFERENCES

Hulley, G. C. and E. C. Pavlis, (2007), A ray-tracing technique for improving Satellite Laser Ranging atmospheric delay corrections, including the effects of horizontal refractivity gradients, J. Geophys. Res., 112, B06417, doi:10.1029/2006JB004834.

Mendes, V. and E. C. Pavlis, (2004), "High-Accuracy Zenith Delay Prediction at Optical Wavelengths", Geophys. Res. Lett., 31, L14602, doi:10.1029/2004GL020308.

Pavlis, E. C., (2002), Dynamical Determination of Origin and Scale in the Earth System from Satellite Laser Ranging, in Vistas for Geodesy in the New Millennium, Proceedings of the 2001 International Association of Geodesy Scientific Assembly, Budapest, Hungary, September 2-7, 2001, J. Adam and K.-P. Schwarz (eds.), Springer-Verlag, New York, pp. 36-41.

Wilson, S., W. Abdalati, D. Alsdorf, J. Benveniste, H. Bonekamp, G. Cogley, M. Drinkwater, L. Fu, R. Gross, B. Haines, E. Harrison, G. Johnson, M. Johnson, J. LaBrecque, E. Lindstrom, M. Merrifield, L. Miller, E. C. Pavlis, S. Piotrowicz, D. Roemmich, D. Stammer, R. Thomas, E. Thouvenot, and P. Woodworth, (2010), "Observing Systems Needed to Address Sea-level Rise and Variability", Ch. 12 in Understanding Sea-level Rise and Variability, Church., J., P. Woodworth, T. Aarup, and S. Wilson, (eds.), ISBN: 978-1-4443-3452-4, Wiley-Blackwell, (September 2010).

Petrov, L., and J.-P. Boy, (2004), Study of the atmospheric pressure loading signal in VLBI observations, J. Geophys. Res., 109, B03405, doi:10.1029/ 2003JB002500.

Tapley, B. D., S. Bettadpur, M. Watkins and Ch. Reigber, (2004), "The gravity recovery and climate experiment: Mission overview and early results", Geophys. Res. Lett. 31 (9).

EFFECTS OF TROPOSPHERIC SPATIO-TEMPORAL CORRELATED NOISE ON THE ANALYSIS OF SPACE GEODETIC DATA

A.F. ROMERO-WOLF[1] and C.S. JACOBS[2]

Jet Propulsion Laboratory, California Institute of Technology
4800 Oak Grove Drive, Pasadena, CA 91109

[1] e-mail: Andrew.Romero-Wolf@jpl.nasa.gov

[2] e-mail: Christopher.S.Jacobs@jpl.nasa.gov

ABSTRACT. The standard VLBI analysis models measurement noise as purely thermal errors modeled according to uncorrelated Gaussian distributions. As the price of recording bits steadily decreases, thermal errors will soon no longer dominate. It is therefore expected that troposphere and instrumentation/clock errors will increasingly become more dominant. Given that both of these errors have correlated spectra, properly modeling the error distributions will become more relevant for optimal analysis. This paper will discuss the advantages of including the correlations between tropospheric delays using a Kolmogorov spectrum and the frozen flow model pioneered by Treuhaft and Lanyi. We will show examples of applying these correlated noise spectra to the weighting of VLBI data analysis.

1. INTRODUCTION

Errors in VLBI data have, until recently, been somewhat dominated by thermal noise, which is characterized by Gaussian uncorrelated random distributions. It is expected that as the cost of recording bits goes down data rates will increase. This means that there will be up to a factor of ten reduction in thermal errors in the near future. As thermal noise contributions drop correlated noise sources will begin to dominate the error budget. Until now, the correlated nature of error sources such as those induced by clocks and troposphere fluctuations have not been given much consideration given that their contribution was small compared to thermal errors. In this paper we will briefly review the correlated delay error model of the troposphere developed by Treuhaft and Lanyi (1987) and present a simplified application to a set of VLBA catalogue runs.

For about the last ten years VLBI systems have been recording at a rate of 128 Mbps. Recent research and development runs with the VLBA have been recording at 256 Mbps giving a $\sqrt{2}$ improvement in signal to noise ratio. The VLBA currently provides the option to record at 512 Mbps giving a factor of two improvement. There have also been research and development VLBA fringes recorded at 2 Gbps per second with the Mark-5C giving a factor of 4 improvement. NASA Deep Space Network (DSN) can achieve recording rates of 2 Gbps with a Mark-5C and 4 Gbps if running with two disk packs at a time. Finally, the Haystack Mark-6 recorder can achieve 16 Gbps recording with short term 32 Gbps rates. The fast improvement in recording data rates means that there will be factors 10 improvement in the near future. In addition, sampling the data near the front end means that thermal variations in filters and cables may be greatly reduced. All of these technology improvements will yield a factor of 10 improvement in the thermal error contribution in the near future.

The impact of tropospheric turbulence on VLBI data has been probed with water vapor radiometers (WVRs). An experiment was performed with the DSN 8000 km Goldstone-Madrid baseline where each station had a JPL advanced water vapor radiometer (A-WVR) (Bar-Sever et al. 2007) monitoring the brightness temperature of the 22 GHz water line along the line of site. The antennas were observing a very strong source and measuring phase delay to reduce the thermal error contribution to negligible levels. The results of the experiment showed that including the observations of the A-WVR reduces the scatter of the delay residuals from 3mm to 1mm.

Unfortunately water vapor radiometers cost about a half million dollars and they are not available at every station. However, we can understand something about the correlation of troposphere fluctuation errors based on the Kolmogorov (1941) theory of turbulence. Essentially, density fluctuations in the water vapor content of the troposphere lead to fluctuations in observed delays. The spatial and temporal scales of these density fluctuations will determine the degree of troposphere induced correlation between delay errors at different stations.

In VLBI the observing unit is not a single antenna but rather an antenna pair or baseline. The error models currently applied to VLBI data analysis do not include common sources of error to both stations in a baseline but rather treat station errors individually. The inclusion of correlated error models in the analysis of VLBI data is expected to improve results by properly treating common sources such as large scale troposphere fluctuations. We attempt to estimate the impact of applying correlated error models with VLBA K-band catalogue data (Lanyi et al. 2010; Charlot et al. 2010). Seeing improvements with current thermal error levels provides an indication of the importance of developing and applying correlated error models for future analysis of VLBI.

This paper is organized as follows. In Section 2 we review the correlated troposphere delay error model by Treuhaft and Lanyi (1987). In Section 3 we present the results of an application of the Treuhaft-Lanyi model on archival VLBA data and DSN X/Ka data. The results are compared to analysis with uncorrelated errors. We discuss the results and future analysis.

2. CORRELATED TROPOSPHERE ERROR MODEL

Kolmogorov's theory of turbulence provides a handle on the spatial scales of troposphere fluctuations. The structure function of a turbulent velocity $\mathbf{u}$ is defined as $D_{\mathbf{u}}(R) = \left\langle |\mathbf{u}(\mathbf{r}+\mathbf{R}) - \mathbf{u}(\mathbf{r})|^2 \right\rangle$ where $\mathbf{r}$ is a position in the sky and $\mathbf{R}$ is an offset vector. Kolmogorov (1941) used dimensional arguments to determine that the structure function is given by a power law $D_{\mathbf{u}}(R) = C\epsilon^{2/3}R^{2/3}$ where ϵ is the average energy dissipation of the medium and C is a medium independent constant. This result assumes only that the turbulence is locally isotropic and that $R > (\nu^3/\epsilon)^{1/4}$ where ν is the viscosity of the medium.

In Tatarskii (1961) the structure function for spatial variations of the refractivity χ = (index of refraction - 1) are determined based on the Kolmogorov (1941) theory of turbulence. This is given by $D_\chi(R) = C^2R^{2/3}$ where the constant C is independent of spatial coordinates $\mathbf{r}$ and $\mathbf{R}$. Starting from this point Treuhaft and Lanyi (1987) translated the turbulent refractivity structure function into radio signal delay and delay rate structure functions. The electromagnetic wave delay (τ) observed at an antenna is obtained by integrating the refractivity along the path of propagation.This relation naturally connects the structure function in refractivity D_χ to the structure function in delay D_τ. The covariance of delays measured at different stations due to troposphere fluctuations on VLBI data are determined directly from the structure function.

The delay structure function (Figure 1) behaves as a broken power law whose exponent depends on the antenna separation ρ relative to the effective height of the troposphere ($h \sim 2$ km). The break can be intuitively understood as the difference between delay fluctuations being influenced by many small scale scatterers when $\rho/h < 1$ rather then being influenced by a few large scale scatterers $\rho/h > 1$. The magnitude of the structure function depends on the elevation angle since this determines the amount of troposphere the electromagnetic wave has traversed.

The spatial dependence of the delay structure function can be translated to a temporal dependence via the frozen flow model. This assumes that the overall turbulent structure of the troposphere is shifted in time with the direction of the wind. The wind speed scales relevant to the frozen flow model are typically ~ 10 m/s. For all the mathematical details for the calculation of structure functions, variances, and covariances as well as examples with DSN data see Treuhaft and Lanyi (1987).

3. TESTS OF TROPOSPHERE COVARIANCE ON VLBA K-BAND

We performed a simplified test of the effects of correlated troposphere errors on a data set obtained with the VLBA. The VLBA consists of an array of ten antennas giving a total of 45 baselines. The longest baseline is from the Mauna Kea station in Hawaii to St. Croix in the U.S. Virgin Islands. The shortest baseline in the array is 240 km between the Los Alamos and Pie Town stations in New Mexico.

As thermal errors are reduced with increasing recording rates the data error models cannot be treated as 45 independent instruments. Tropospheric and instrumental correlated errors begin to affect the ability to average down random errors from 45 baselines. Our goal in this study is to see if, in the current state of bit recording capabilities and thermal error levels, the inclusion of correlated troposphere errors make a difference in the data analysis.

The data used in this study consists of twelve sessions of 24 hour source catalog runs in K-band dating from 2002 to 2008. For details on the data see (Lanyi et al. 2010; Charlot et al. 2010). The data is recorded at 128 Mbit/s and have median thermal error levels of 23 ps in delay and 5 fs/s in delay rate. With future recorders a factor of 10 improvements means that delay errors will be reduced to 2 ps. This is equivalent to position errors going down from 1 cm to 1 mm. The question we try to address with these data is whether we can begin to see the effects of correlated errors with thermal delay errors of $\sim$ 23 ps. Troposphere turbulence alone is expected to introduce errors of 20-40 ps which is comparable to the thermal error contribution.

The inclusion of troposphere covariance error models on large data sets involving many baselines has not been thoroughly tested in software. For this reason we have chosen to simplify the setup by using only 9 of the 45 baselines. The 9 baselines all have the Mauna Kea station in Hawaii in common. Mauna Kea is chosen due to the fact that it is the most distant station from the rest of the VLBA network so its troposphere is expected to be the least correlated to the other 9 stations. All inter-station correlations were ignored. We modeled only the intra-station correlations between ray paths of scan i with scan j.

Rather than following the standard practice of introducing troposphere breaks every 20 minutes we use only one troposphere parameter estimate for each station over a 24 hour period. Station clock parameter estimates are included in three hour periods. The advantage of including troposphere covariance is the it re-defines χ^2 such that drifts are not penalized nearly as much. Also the number of free parameters is reduced from what would typically be 1200 troposphere and clock breaks to 74.

As a figure of merit for the quality of reconstruction we compare the catalog solution of our reduced 9-baseline test to the ICRF2 catalog (Fey et al. 2009). In particular we look at the difference in reconstructed source declination ($\Delta\delta$) versus declination (dec) since we expect this to be most affected by the troposphere. Figure 2 shows the results of $\Delta\delta$ vs. dec for twelve catalog runs each lasting 24 hours with and without troposphere covariance. Both cases include a daily troposphere break and 3 hour clock parameter breaks. A small improvement was found in the slope and offset of the $\Delta\delta$ vs. dec relation. The results are summarized in Table 1.

We begin to see some improvement in the difference in declination between the catalog solution to ICRF2. The weighted RMS of the difference is decreased. Also note the the plots have a small slope which is expected to be due to the fact that low declinations mean that observations are made through thicker atmosphere profiles. Both the slope and the offset of the linear fits are reduced with the introduction of troposphere covariance error models.

4. OUTLOOK AND CONCLUSIONS

In this study we have shown that the inclusion of troposphere covariance provides improved results. However, the improvements have not been shown to be statistically significant. It is expected that as thermal error levels decrease the inclusion of troposphere covariance error models will show more significant improvements in the results. The implementation of troposphere covariance in the full VLBA 45 baseline solution is still pending. It also remains to be conclusively shown that using correlated error models is a better approach than introducing frequent troposphere and clock parameter estimation rates. Our preliminary results introducing covariant error models and physical reasoning indicate that there is promise in this approach.

Acknowledgements. This research was carried out at the Jet Propulsion Laboratory, California Institute of Technology, under contract with the National Aeronautics and Space Administration.

5. REFERENCES

Bar-Sever, Y.E. et al, 2007 “Atmospheric Media Calibration for the Deep Space Network”, Proc. IEEE, vol. 95, No. 11, pp. 2180-2192.

Charlot, P. et al. 2010. “The Celestial Reference Frame at 24 and 43 GHz. II. Imaging”, *The Astronomical Journal* , **139**, 1713-1770.

Fey, A. L., et al. 2009, “The Second Realization of the International Celestial Reference Frame by Very Long Baseline Interferometry”, Frankfurt am Main: Verlag des Bundesamts für Kartographie und Geodäsie.

Kolmogorov, A.N. 1941, “Dissipation of energy in locally isotropic turbulence”, *Doklady Acad. Nauk USSR*, **32**, 16.

Lanyi, G.E. et al. 2010. "The Celestial Reference Frame at 24 and 43 GHz. I. Astrometry", *The Astronomical Journal* , **139**, 1695-1712.
Tatarskii, V.I. 1961, *Wave Propagation in a Trubulent Medium* , Dover, New York.
Treuhaft R.N. and Lanyi, G.E. 1987, "The effect of the dynamic wet troposphere on radio interferometric measurements", *Radio Science*, **22**, 251-265.

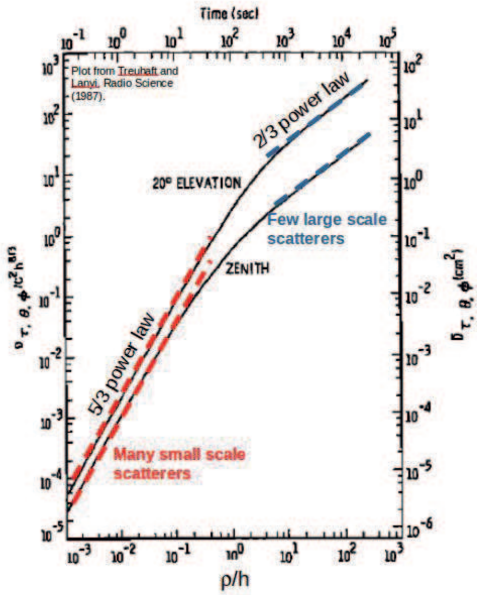

Figure 1: Delay structure function from Treuhaft and Lanyi (1987) is given by a broken power law whose exponent depends on the antenna separation ρ relative to the troposphere effective height ($\sim$ 1 km). See text for details.

$\Delta\delta$ vs dec	No Trop. Cov.	With Trop. Cov.
wRMS (μas)	436	350
Y0 (μas)	178 $\pm$ 57	135 $\pm$ 71
Slope (μas/deg)	-2.6 $\pm$ 1.0	-2.0 $\pm$ 1.2
χ^2	1.91 $\pm$ 0.17	0.81 $\pm$ 0.07

Table 1: Comparison of VLBA catalog positions with ICRF2 for analysis with and without implementation of troposphere covariance error modeling.

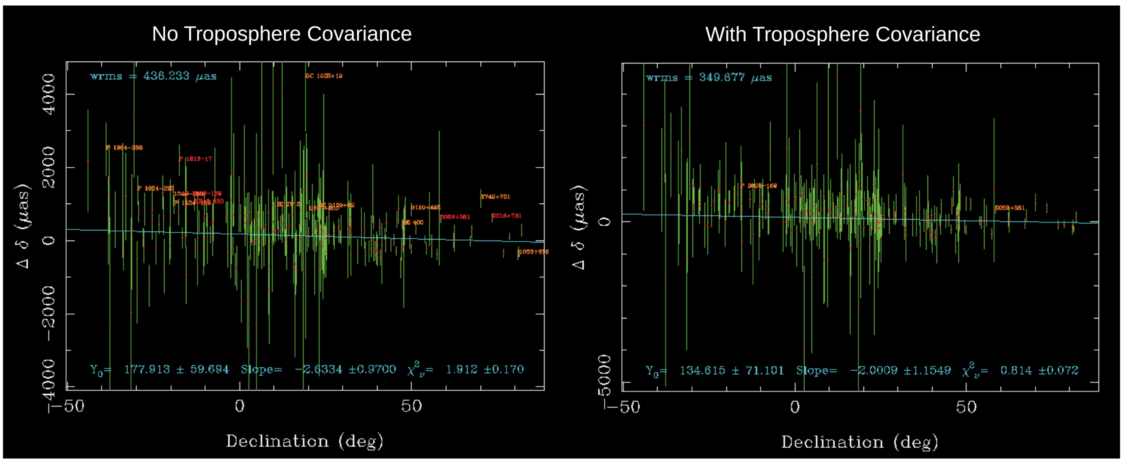

Figure 2: Comparison of VLBA K-band catalog reconstruction vs. ICRF2 with and without the inclusion of troposphere covariance. See text for details.

X/Ka VLBI FRAME'S ROLE IN MULTI-WAVELENGTH STUDIES

C.S. JACOBS[1], J.E. CLARK[1], C. GARCÍA-MIRÓ[2], S. HORIUCHI[3], I. SOTUELA[2]

[1]Jet Propulsion Laboratory, California Institute of Technology/NASA
4800 Oak Grove Dr., Pasadena CA, 91109, USA
e-mail: Christopher.S.Jacobs@jpl.nasa.gov

[2] Ingenieria y Servicios Aeroespaciales, Instituto Nacional de Técnica Aeroespacial/NASA
Madrid Deep Space Com. Complex, Paseo del Pintor Rosales, 34 bajo, E-28008, Spain

[3] C.S.I.R.O. Astronomy and Space Science/NASA
Canberra Deep Space Com. Complex, PO Box 1035, AU Tuggeranong ACT 2901, Australia

ABSTRACT. This paper is an update of Sotuela et al. (2011) which improves their simulated Gaia frame tie precision by ∼10% by adding three additional VLBI observing sessions. Astrometry at X/Ka-band (8.4/32 GHz) using NASAs Deep Space Network has detected 466 quasars with accuracies of 200–300 μas. A program is underway to reduce errors by a factor of 2–3. From our sample, 345 sources have optical magnitudes $V < 20$ and should also be detectable by Gaia. A covariance study using existing X/Ka data and simulated Gaia uncertainties for the 345 objects yields a frame tie precision of 10–15 μas (1-σ). The characterization of wavelength dependent systematics from extended source morphology and core shift should benefit greatly from adding X/Ka-band measurements to S/X-band (2.3/8.4 GHz) measurements thus helping to constrain astrophysical models of the wavelength dependence of positions.

1. INTRODUCTION

Our X/Ka celestial frame is best understood in the context of the ICRF2 and the planned Gaia frame. The ICRF2 (Ma et al., 2009) based on 8.4 GHz VLBI observations of 3414 extragalactic radio sources is the current IAU fundamental frame. Its position noise floor is ∼40 μas; ∼10 μas in axes. The Gaia extragalactic optical frame (Lindegren et al., 2008) will be based on 10^9 objects down to $V = 20$ magnitude with accuracy of 25 μas at $V = 16$ and ∼200 μas at $V = 20$. The catalog is expected in 2021.

2. ALIGNING VLBI AND GAIA FRAMES

Quasars being at great distances (∼Gpc) have no measurable proper motion or parallax making them ideal for both VLBI and Gaia quasi-inertial frames. However, the absolute orientation is poorly constrained. Thus frames are first aligned by estimating a 3-D rotational offset ("frame tie") using common objects before doing multi-wavelength studies such as the relative offsets of optical-radio emissions.

There are challenges in making an accurate frame tie: detecting common objects, uniformity of sky coverage, wavelength dependence of emission centroids, and non-point-like morphology (source structure).

Detecting common objects: Most quasars don't produce both strong optical and radio detections. Our X/Ka sources have a median optical magnitude of $V = 18.6$ which is at the weak end of Gaia's detection range. There are few sources which are ideal in both the optical and radio. The Bourda et al. (2011) solution is to seek weaker radio objects which are optically bright (V<18) and compensate by leveraging improvements in ground-based radio detection which allow going to 30 mJy.

Simulated frame tie precision: Our current X/Ka data has 345 sources with V<20 including 132 with V<18. X/Ka positions have ∼200 μas precision. Corresponding predicted Gaia precisions are ∼100 μas. A frame tie covariance study using these precisions estimated that 3-D rotational alignment could be determined to ±14, ±11, and ±10 μas in Rx, Ry, and Rz, respectively (1-σ). Because radio precision is the limiting factor, anticipated radio improvements have potential to improve the tie to 5–10 μas by the end of Gaia's mission. However, tie accuracy may be limited not by precision, but by systematic errors.

Extending uniform sky coverage south: VLBI has weak coverage in the south due to the small number of southern stations. X/Ka coverage (Figure 1) is weak in the mid-south and totally lacking in the south polar cap. However, simulations (Bourda et al., 2010) show that a very small data set of 1000 delay measurements on a 9000 km "all-southern" baseline could dramatically improve the X/Ka frame.

We have now gone beyond simulation by identifying 498 candidates (Figure 2) which have strong, very compact X-band VLBI detections thus making them excellent candidates for VLBI at Ka-band. In particular, Figure 2, shows numerous well distributed candidates in the south polar cap. Thus prospects for uniform sky coverage at X/Ka-band are very positive with potential for 900+ sources.

Compactness and core shift: VLBI frames now exist at 24 and 43 GHz (Lanyi et al., 2010; Charlot et al., 2010), and 32 GHz (Jacobs et al., 2011). These intermediate frequencies between the 8-GHz ICRF2 and Gaia's optical enable frequency dependent systematic error studies: chiefly, extended structure from emissions out in the jet and shifts in the radio core's position. Because we observe mostly blazars which are characterized by jets pointing near the line of sight, we observe down the 'throat' of the jets thus bringing into consideration opacity effects. Higher frequency observations may see farther into the jets thus changing the observed position. However, Porcas (2009) notes that group delay observations such as our X/Ka data may greatly reduce this core shift effect.

On average systematic errors from non-point-like source structure are reduced as extended emissions tend to fade with increasing radio frequency. In our core dominated sources, the radio core position is thought to occur at a point near where the optical depth becomes unity. The frequency dependence of the jet's opacity is suspected to move the core closer to the central engine as frequency increases. Thus moving to higher frequencies may reduce both systematic errors thereby improving the radio-optical tie.

Outlook: Our goal is to improve 32-GHz VLBI to the 70 μas accuracy achieved by the 8-GHz ICRF2 and projected for Gaia (18^{th} mag). Accuracy improvements focus on three items:

1. We have increased our data rate by 4x and expect another 4x. The total 16x improves precision 4x.
2. We are building phase-cal tone generators in order to reduce instrumental errors by a factor of 10.
3. We are seeking improved southern geometry. Simulations (Bourda et al., 2010) show that adding an all-southern baseline from our existing Australian antenna to either S. Africa or S. America allows 200 μas accuracy over the south polar cap. If we are successful in all three areas, the X/Ka frame has potential for 70 μas accuracy over the full sky. Thus we would have X/Ka precision comparable to Gaia at 18^{th} mag while greatly reducing radio systematic errors from source structure and core shift.

Acknowledgements. This research done under NASA contract. Government sponsorship acknowledged.

3. REFERENCES

Bourda, et al., 2010, 'Future Radio Ref. Frames & Implications for Gaia Link,' ELSA, Sevres, France.
Bourda, G., et al., 2011, 'Alignment of VLBI & Gaia,' Proc. GREAT-ESF workshop, Porto, Portugal.
Charlot, P., et al., 2010, 'CRF at 24 & 43 GHz II.,' AJ, 139, 5, 1713. doi: 10.1088/0004-6256/139/5/1713
Jacobs, C.S., et al., 2011, 'X/Ka CRF,' Proc. 20th EVGA, Alef, Bernhart, Nothnagel (eds.), 166.
Lanyi, G.E., et al., 2010, AJ, 139, 5, 1695. 'CRF at 24 & 43 GHz I.,' doi: 10.1088/0004-6256/139/5/1695
Lindegren, L. et al., 2008, 'Gaia Mission: Science, Organiz., Status,' IAU 248, Wenjin et al. (eds.), 217.
Ma, C., et al., 2009, 'Realization of ICRF2 by VLBI,' IERS Tech. Note 35. Fey, Gordon & Jacobs (eds.)
Porcas, R., 2009, 'Astrometry, Chromatic AGN Cores,' A&A Let., 505, 1, doi: 10.1051/0004-6361/200912846
Sotuela, I., et al., 2011, 'Contribution of X/Ka VLBI to Multi-λ Cel. Frame Studies,' Mem. S.A.It., 83.

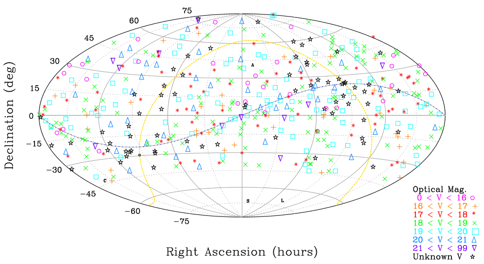

Figure 1: Distribution of 466 X/Ka sources. Optical counterpart V magnitude defined in legend. $(\alpha, \delta) = (0, 0)$ is at the center. The ecliptic is indicated by the sinusoidal curve. The galactic plane is indicated by the Ω-shaped yellow curve. Note the large number of sources lacking optical identifications near the galactic plane, especially near its center and anti-center.

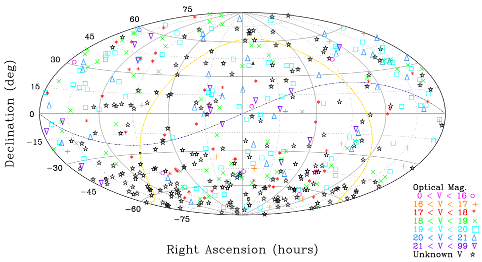

Figure 2: Distribution of 498 X/Ka candidates. Color code is same as Fig. 1. Selection is based on unresolved X-band flux ≥ 200 mJy and $\geq 70\%$ of the total flux in the unresolved core. [input list: L. Petrov, astrogeo.org, rfc2011a]. South polar cap is well covered, but lacks optical identifications for many candidates. 2^{nd} southern station will be needed to observe cap.

CCD MEASUREMENTS IN OPTICAL DOMAIN AND ASTROMETRIC POSITIONS OF ICRF2 RADIO SOURCES

G. DAMLJANOVIC, I. MILIC
Astronomical Observatory
Volgina 7, 11060 Belgrade 38, Serbia
e-mail: gdamljanovic@aob.bg.ac.rs; ivana@aob.bg.ac.rs

ABSTRACT. At the IAU XXIIIth GA in 1997, the International Celestial Reference Frame (ICRF) was adopted; hereafter referred to as ICRF1. After the original list of radio objects there were two extensions, ICRF-ext1 and ICRF-ext2. All together, there were 717 sources: 212 defining ones, 109 new ones, 294 candidate ones, and 102 additional ones. At the IAU XXVIIth GA in 2009, the second realization of the ICRF (the ICRF2) was adopted with the list of precise positions for 3414 compact radio astronomical sources. At that moment there were nearly 30 years of VLBI observations. The ICRF2 has a noise floor of about 0.04 mas (near six times better than ICRF1) and an axis stability of about 0.01 mas (nearly twice as stable as ICRF1). Also, it is of importance to make the observations of some ICRF2 extragalactic radio sources (ERS) which are visible in the optical domain, and to compare their optical (calculated via the reference stars) and radio positions (VLBI ones). We started to do it by using the CCD camera VersArray 1300B and the RCC telescope[1] ($D/F = 2\mathrm{m}/16\mathrm{m}$) of Rozhen National Astronomical Observatory (Bulgarian Academy of Sciences). About 30 frames were observed at the end of March 2011. The main steps of our calculations and some preliminary results (comparison between the measured optical positions and the radio ones) for a few ERS from ICRF2 list were presented here.

1. CALCULATION AND RESULTS

Regular maintenance of the system and improvement of the frame is necessary. The ERS coordinates are continuously improving via VLBI observations (a large number of observations of defining ERS over a long data span). The frame's stability is based upon the assumption that there is no global rotation of the universe. The compact ERS are mostly quasars (quasi stellar objects – QSO), BL Lacertae (BL Lac) sources and a few active galactic nuclei (AGNs); they are far away and with negligibly small proper motions. The ERS positions are known to better than 1 mas, and the ultimate accuracy is limited because of the structure instability of ERS in radio wavelengths. The alignment of ICRF2 with the ICRS was made using 138 common ICRF2/ICRF-Ext.2 stable ERS. The two largest weaknesses of ICRF1 were eliminated (more uniform sky distribution of ERS and the position stability of the 295 ICRF2 defining sources). From 1 January 2010, the realization of the ICRS is the ICRF2.

The Hipparcos Celestial Reference Frame – HCRF (ESA, 1997) is the optical realization of the ICRS, and it was linked to the radio ICRF1 with an accuracy of ± 0.6 mas in position for the epoch 1991.25 and ± 0.25 mas/yr in rotation. That accuracy degrades over time because of the error in proper motions of stars, and it is necessary to verify and refine the relation between the HCRF and the ICRF2. It can be done via different telescopes and methods. Also, the proper motions of many double or multiple stars are unreliable due to the short epoch span of Hipparcos observations, and van Leeuwen (2007) did a new reduction (with some significant improvements, mainly for the parallaxes) of the Hipparcos data. Some of densification catalogues are: Tycho-2, UCAC3, 2MASS (near-IR), PPMXL, XPM, etc. The Tycho-2 was the first step of densification. Here, we used the XPM (Fedorov et al., 2010) one. It contains the positions and proper motions for 314 million stars for the epoch 2000.0.

The main characteristics of CCD camera are: 1340x1300 pixels, the pixel size is 20x20 mkm, one pixel is $0''.258$. The AIP4WIN image processing package (Berry and Burnell, 2002) was used. All frames were reduced individually. A total of five optical counterparts of ERS from the ICRF2 list were observed: Q 1252+119 (ICRF J125438.2+114105), L 1215+303 (ICRF J121752.0+300700), Q 1240+381 (ICRF

[1]Based on observations with the 2 m RCC telescope of the Rozhen National Astronomical Observatory operated by the Institute of Astronomy, Bulgarian Academy of Sciences.

J124251.3+375100), Q 1219+044 (ICRF J122222.5+041315) and L 1221+809 (ICRF J122340.4+804004).

We made six frames per source (three at R filter and three at V one). Figure 1 shows an example. To transform the measured CCD coordinates (x, y) to tangential ones (ξ, η) the standard astrometric "plate" reduction ($\xi = ax + by + c$, $\eta = dx + ey + f$) with the available reference stars was used. Also, the unweighted Least-Squares Method was applied. The corrections for apparent displacements (as differential refraction one) were not applied (Aslan et al., 2010; Kiselev, 1989) because of the small field of view (FOV is $5'.5$x$5'.5$).

We compared the ERS optical positions and the radio ones to determine $(O-R)_\alpha$ and $(O-R)_\delta$, and the unweighted mean offsets relative to the XPM catalogue are: $-0''.06$ in α and $-0''.05$ in δ.

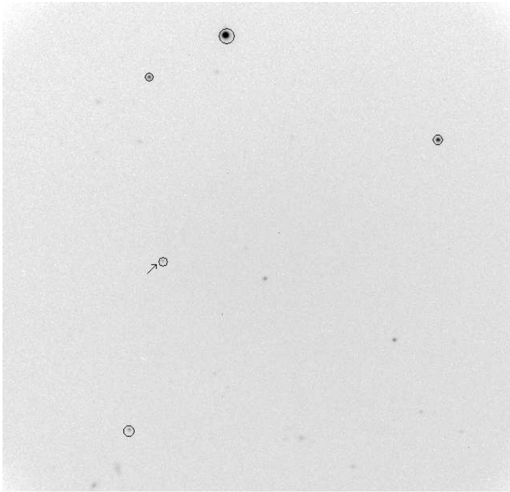

Figure 1: The observation of ERS Q 1219+044 at R filter (the ERS is marked with direction arrow and circle) and reference stars (circles); $exp = 20^s$, $mag_V = 18.0$, $mag_R = 16.8$

2. CONCLUSIONS

The optical observations of ERS are possible by using a 2-meter Rozhen telescope and a good CCD camera. The positions of ERS were calibrated with respect to the XPM catalogue, and it is possible to use XPM as the reference catalogue for astrometric reduction in small FOV of CCD observations. The XPM is with high star density and a good densification of HCRF, but a higher accuracy catalogue of higher star density is required. Even a few ERS, our calculated offsets (in α and in δ) are small. So, the link between HCRF and ICRF2 is good enough at the mean epoch of our observations; the XPM is a similar frame. Also, some problems during the calculation of ERS optical positions can be caused by: faintness of the optical counterparts to ERS, atmospheric influences and technical problems.

Acknowledgements. The Authors performed this work as a part of the Projects No 176011 "Dynamics and kinematics of celestial bodies and systems" supported by the Ministry of Education and Science of R. Serbia. Also, the authors gratefully acknowledge the observing grant support from the Institute of Astronomy and Rozhen National Astronomical Observatory, Bulgarian Academy of Sciences.

3. REFERENCES

Aslan, Z., Gumerov, R., Jin, W., Khamitov, I., Maigurova, N., Pinigin, G., Tang, Z., Wang, S., 2010, "Optical counterpart positions of extragalactic radio sources and connecting optical and radio reference frame", A&A, 510, A10.

Berry, R., Burnell, J., 2002, "The Handbook of Astronomical Image Processing, Includes AIP4WIN Software", Willmann-Bell, Inc., Richmond, USA.

ESA, 1997, "The Hipparcos and Tycho Catalogues", ESA SP-1200,ESA Publications Division,Noordwijk.

Fedorov, P. N., Akhmetov, V. S., Bobylev, V. V., Bajkova, A. T., 2010, "An investigation of the absolute proper motions of the XPM catalogue", MNRAS, 406, pp. 1734-1744.

Kiselev, A. A., 1989, "Theoretical foundations of photographic astrometry", Nauka, Moskva.

van Leeuwen, F., 2007, "Hipparcos, the new reduction of the raw data", Dordrecht: Springer.

ON THE PROCESSING OF VLBI INTENSIVE SESSIONS

S.B. LAMBERT
Observatoire de Paris/SYRTE/CNRS/UPMC
61 av. de l'Observatoire 75014 Paris

ABSTRACT. Operated every day, intensive VLBI sessions are designed for providing near real-time estimates of UT1. Due to the weak network geometry, nuisance parameters associated with troposphere path delay are generally considered as constant over the full duration of the session. All other quantities are fixed to a priori values, including site coordinates and velocities, source positions, polar motion and nutation. It appears that the analyses of intensives differ from corresponding results obtained with multi-baseline 24-hour VLBI sessions in two major points. First, the postfit rms delays of intensives are significantly higher (40 ps in average) than for larger networks (20 ps in average). Second, the scatter of UT1 is larger by a factor of two. Is there a way of improving these two points? Studies have been undertaken in various directions: using a GNSS-derived polar motion to map the Earth orientation (Ray et al. 2005), improving the nutation by adding an empirical modeling of the nutation offsets to the current nutation model (Malkin 2009, 2011), and modeling the troposphere delay by using 3D troposphere models and direct ray tracing for each observation (Böhm et al. 2010). In the present study, I revisit the results of Malkin by trying a slightly different modeling of the nutation offsets and assessing differently the quality of the results. As well, I investigate the possibility to estimate other parameters, that are traditionally fixed to a priori values in the operational analysis. This study is detailed in an unpublished research note available on request to the author. I will briefly summarize the results here.

1. IMPROVING UT1 BY MAPPING NUTATION

The IAU 2000A nutation model is not perfect. The nutation offsets contain a non negligible signal arising from unmodeled or mismodeled tidal terms or other geophysical contribution including the atmosphere and the free core nutation (FCN). An empirical modeling of the nutation can be achieved by (i) adjusting the FCN term, and (ii) fitting a number of tidal terms to the nutation offsets, like those listed in the Table 1 of Herring et al. (2002). The atmospheric contribution to the nutation remains unpredictable due to strong inconsistencies in the global circulation models at diurnal frequencies and will therefore not be considered here.

To test the efficiency of mapping nutation offsets, I run several solutions in which the nutation offsets are alternatively (i) unmapped (i.e., the nutation series are entirely given by the IAU 2000A model), or mapped by (ii) a variable FCN term plus 42 tidal waves. Efficiency of the solutions in terms of reproducing the length-of-day (LOD) as predicted by the combined NCEP and ECCO excitations are reported in Table where S is the rms of the difference to C04, and C the correlation coefficient between the geophysical LOD and the one derived from the estimated UT1. The improvement is about 0.07 % and 0.004 %, respectively for the averaged postfit rms delay and the correlation coefficient.

2. OVERPARAMETERIZATION OF INTENSIVE SOLUTIONS

Can I use an analysis configuration closer to the one used in the processing of multi-baseline diurnal VLBI sessions? Instead of estimating the ZTD as a constant offset over the full duration of the session, one can estimate it over shorter intervals, say 30 min or even 10 min, if the number of scans within the interval is sufficient. In addition, one can free the station positions and apply a loose constraint of $\sigma \sim 100$ m to tie them to the terrestrial reference frame and avoid degeneracy of the system of equations. I run a number of solutions to illustrate these options. In all the solutions below, the polar motion is mapped by the C04 series, but the nutation offsets are unmapped. Characteristics of the solutions and averaged postfit rms delay together with S, C, and length repeatability (LR) for Kokee–Wettzell (Kk–Wz) and Tsukuba–Wettzell (Ts–Wz) baselines are reported in Table . It appears that the postfit rms have values comparable to those obtained with routine VLBI experiments (i.e., of the order of 20 ps) when a

	Averaged postfit rms delay (ps)	S (mas)	C
(i)	38.133	0.12450	0.940564
(ii)	38.127	0.12447	0.940593

Table 1: Characteristics of the solutions comparing mappings of nutation offsets.

ZTD interval (min)	Station status	Average postfit rms delay (ps)	S (mas)	C	Kk–Wz LR (mm)	Ts–Wz LR (mm)
Full duration	Not estimated	38.134	0.12450	0.940564		
Full duration	Estimated	35.789	0.12453	0.940549	73	25
30 min	Not estimated	30.992	0.12444	0.940614		
30 min	Estimated	28.902	0.12452	0.940550	79	26
10 min	Not estimated	22.721	0.12428	0.940629		
10 min	Estimated	20.902	0.12451	0.940562	87	27

Table 2: Characteristics of the solutions.

maximum number of parameters including ZTD over 10-min intervals and site coordinates are estimated. However, the lowest rms is obtained when ZTD is estimated over 10-min intervals with fixed stations (as much as 40 % smaller than for S0). This solution also provides the highest correlation coefficient with the geophysical excitation, and, therefore, the UT1 closest to the reality. Again, the differences between the various strategies are of about 0.2 % for S and 0.007 % for C.

3. CONCLUSIONS

Using independent modeling and analyses and a different method to assess the quality of the UT1 estimates, I confirm the results of Malkin (2009, 2011). Mapping the nutation offsets by a simple model of variable FCN and a small number of tidal terms slightly improves the determination of UT1. The overparameterization of the solution, consisting of estimating station positions and/or troposphere zenith time delays over intervals of a few minutes, considerably reduces the postfit rms delay to values comparable to those obtained from the analysis of routine VLBI experiments. However, the quality of UT1 estimates is only marginally improved.

This study addresses the usefulness of providing an empirical model for the nutation offsets. Currently, the Chapter 5 of the IERS Conventions recommends a FCN model adjusted to the C04 data. Completing this model by the fit of a few tidal waves to the same data could be useful. Nevertheless, the improvement in UT1 estimates from intensive sessions will remain marginal.

4. REFERENCES

Böhm, J., Hobiger, T., Ichikawa, R., et al. 2010, J. Geod., 84, 319

Herring, T. A., Mathews, P. M., & Buffett, B. A. 2002, J. Geophys. Res., 107, 2069

Malkin, Z. 2009, Presented at the IERS Workshop on EOP Combination and Prediction, Warsaw, 19–21 October 2009

Malkin, Z. 2011, In: D. Behrend, K. D. Baver (Eds.), International VLBI Service for Geodesy and Astrometry (IVS) 2010 General Meeting Proc., NASA/CP-2010-215864, 261

Ray, J., Kouba, J., & Altamimi, Z. 2005, J. Geod., 79, 505

STATISTIC AND ANALYTIC COMPATIBILITY TO JOINT CATALOGUES WITH A SET OF COMMON ICRF DEFINING SOURCES

F.J. MARCO[1], M.J. MARTINEZ[2]

[1] Universidad Jaume I
Dept. Matematicas, Institut de Matematiques I Aplicacions de Castello, Castellon, Spain
e-mail: marco@mat.uji.es

[2] Universidad Politecnica de Valencia
Dept. Matematica Aplicada, Valencia, Spain
e-mail: mjmartin@mat.upv.es

ABSTRACT. The construction of quasar catalogs from other catalogs containing few reference points but including a significant number of ICRF defining sources represents an interesting way to obtain an increasingly extended and accurate catalog (see [1], [3] and [5]). There are several questions that should be taken into account to reach this aim. For example, each catalogue should have its residuals normally distributed and this property should be also transferred to the final catalog. In addition, after the correction, the defining sources from each individual catalog should be related with the ones belonging to the other catalogs only by means of infinitesimal rotations, as usual. Also, the total residuals in the final catalog should not decrease while the variance increases too much, in order to avoid the introduction of excessive deformations.

There are several ways to correct catalogs. Roughly speaking we can classify the different methods in parametric and non-parametric. The parametric methods subdivide in geometrical (including corrections for rotation or rotation+deformation) and analytical (which consider developments in different sets of functions, such as spherical harmonics or Legendre-Fourier functions). All the parametrical methods make apriori suppositions about the function of residuals, in order to assure that this function belongs to a certain functional space. On the other hand, non-parametrical methods do not need to make any supposition about the functional expression of the function of residual, because they build on the statistical properties of the data. Our method uses both techniques (parametrical and non-parametrical) in order to obtain the best possible properties because some problems arise when we improperly apply the parametrical methods. We would like to remark that the application of the usual discrete least squares method, in order to obtain a functional continuous representation of the residuals, might provide erroneous results due to different causes (more details in [2]), such as:

1. Analytical causes: a lack of homogeneity in the data causes that the functional orthogonality of the set of functions employed in the adjustment is not necessarily preserved and thus the coefficients in the development would not be accurate.
2. Statistical causes: The hypothesis of the Gauss-Markov theorem should be fulfilled in order to assure that the least squares method provides the least variance estimator in the class of unbiased estimators.

All the former problems could be avoided if we use a non-parametrical method as an intermediary. In this case, a good method is to compute a estimation of the function over fiducial points homogeneously distributed over the celestial sphere. This procedure has additional advantages: each coefficient of a harmonic development can be computed independently as a quotient of the integral inner products from the Hilbert functional space. Such integrals can be approximated with precision as high as required. In these integrals each function has been approximated using a kernel non-parametrical method that requires the use of a bandwidth [4] whose length is very important in order to obtain the required accuracy. Altogether there is an additional advantage, because we can select a different bandwidth according to the order of each one of the coefficients which is being calculated and to the statistical properties of the data.

1. CONDITIONS TO BE FULFILLED TO OBTAIN A CATALOG FROM INPUT CATALOGS WITH COMMON ICRF DEFINING SOURCES

We propose two main conditions in order to assure the compilation of an improved catalogue from other source catalogs:

1. First Condition (for each individual input catalog): previous study of the properties of each catalogue that is going to be used in the improvement process. We demand that the distribution of the residuals obtained through the comparison with the ICRF2 acts as a normal random variable before and after the correction.
2. Second Condition (for the combined final catalog): the differences between the final positions (after the correction) and the initial ones (before the correction) must behave as a normal random variable and not as a sum of Gaussians, in order to avoid the introduction of deformations.

It is possible that we should previously remove those positions clearly bad determined in order to fulfill these conditions. The inclusion of these positions could have a negative influence in the adjustment.

2. STEPS TO BUILD AN IMPROVED CATALOG

STEP 1: Selection of each individual catalogue to be used in the adjustment, taking into account that they should verify the First Condition. Then, we will make a non-parametrical adjustment over the defining sources of each selected catalog and then we obtain the geometrical transformation rotation+deformation for each one. At this stage, we will consider only the rotation computed using the catalog whose residuals have the minimum variance and we will disregard the deformation, which will be absorbed in the next step. Each catalog will provide a different rotation, thus all of them should be transformed into the same system. To this aim, we should apply to each catalog its own rotation and the inverse of the selected rotation (the one from the catalog with minimum variance). Notice that at the end of the first step, we have removed the geometric systematics.

STEP 2: We apply to the remaining individual residuals of each catalog a new non-parametrical adjustment to obtain the approximations over the selected fiducial points (over the whole sphere) and over all the sources selected for the adjustment. The inverse of the obtained variances are used as weights to built the final catalogue.

STEP 3: Test of the Second Condition given in the 1st section. This is to verify that the final errors are Gaussian, but do not form a Gaussian mixture distribution. This property should be seriously taken into account, because there is the risk of inhomogeneities in the final catalog if it is not fulfilled. A particular case is the sum of two Gaussians with the same (or nearly the same) centers and different variances. To detect this undesirable case, we have a developed a special method, out of the scope of this extended abstract and which is now under review.

Acknowledgements: Part of this work was supported by grant P1-1B2009-07 from Fundacio Caixa Castello BANCAIXA.

REFERENCES

[1] Malkin, Z. A&A. 474, 665-670. 2007
[2] Marco F.J., Martinez M.J. and Lopez J.A. A&A. 418. 1159-1170. 2004.
[3] Sokolova, Ju & Malkin, Z. A&A. 474, 665-670. 2007
[4] Wand M.P. & Jones M.C. Kernel Smoothing. Ed. Chapman & Hall.1995.
[5] Yatskiv, Y. & Malkin, Z. Journes systmes de rference spatio- temporels. 2007

Session 3:

Modelling, observation and prediction of Earth rotation and global geodynamics

Modèle, observation et prédiction de la rotation de la Terre et géodynamique globale

ATMOSPHERIC AND OCEANIC EXCITATION OF EARTH ROTATION

S. BÖHM, T. NILSSON, M. SCHINDELEGGER, H. SCHUH
Institute of Geodesy and Geophysics, Advanced Geodesy
Vienna University of Technology
Gußhausstraße 27-29, 1040 Vienna, Austria
e-mail: sigrid.boehm@tuwien.ac.at

ABSTRACT. All kinds of mass variations in the Earth's surface fluids accordingly change the tensor of inertia, while moving particles in wind or current flows induce relative angular momentum. Via interaction with the solid Earth, both matter and motion effects cause fluctuations in the direction of the Earth's rotation axis, signified as polar motion, as well as changes in the angular velocity, expressed, e.g. in terms of length of day (LOD). This paper gives an overview of the most important atmospheric and oceanic effects on polar motion and LOD from subdaily to multi-annual time scales and discusses the variable agreement between the observational evidence of excitation effects and their corresponding geophysical models. Special emphasis, including a brief synopsis of recent results, is placed on tidal phenomena and in particular on those caused by short period ocean tides.

1. EARTH ROTATION OBSERVATION AND MODELING

Variations in the magnitude and orientation of the Earth rotation vector are conventionally quantified as Earth orientation parameters (EOP). These EOP comprise the length of day (LOD) or dUT1 (UT1-UTC), representing irregularities in the Earth rotation speed, the pole coordinates x_p and y_p, determining the orientation of the reference axis w.r.t. the terrestrial reference system, and X and Y, which are the coordinates of the CIP (Celestial Intermediate Pole) in the celestial reference system. Strictly speaking, the EOP do not represent the Earth rotation axis, but the observed axis of reference, which is the axis of the CIP by convention. The subset of parameters referring to the terrestrial motion of the CIP, the pole coordinates and LOD or dUT1 is often denoted as Earth rotation parameters (ERP).

The EOP are regularly monitored by means of space geodetic techniques and published by the IERS (International Earth Rotation and Reference Systems Service) as continuous time series, combined from the results of different measurement techniques. The measurements of Earth rotation provide only the purely geometric information about the deviation of the rotation axis from a mean state, without permitting the distinction between different causes of the observed effects.

The most prominent and common formulation to investigate the driving mechanisms of Earth rotation variations is the angular momentum approach. In this approach, the Earth with oceans and atmosphere is considered as one closed system, the total angular momentum of which is conserved. If one of the subsystems, such as the atmosphere, undergoes a change of its associated angular momentum, the solid Earth experiences a coincident variation of its proper angular momentum, leading to a corresponding variation of the Earth rotation vector. Such variations of angular momentum of single subsystems are expressed using so-called angular momentum functions (AMF). The AMF are composed of two parts, a mass term containing changes of the tensor of inertia due to mass redistribution and a motion term representing relative angular momentum caused by relative particle motion where one mass element is immediately replaced by another after its dislocation.

Atmospheric and oceanic excitation of Earth rotation are studied on the basis of numerical models, which provide certain state variables of the respective fluid for distinct points in time on a global grid. The quantities of special interest are vertical density or surface pressure, respectively, and wind velocities in case of the atmosphere and ocean bottom pressure as well as current velocities in case of the oceans. Yet in oceanic excitation there is usually a distinction between non-tidal effects and tidal effects, which are mostly treated separately. The parameters of ocean tide models relevant to Earth rotation are tidal height variations and tidal current velocities. Atmospheric, oceanic and ocean tidal angular momentum functions are derived from the mentioned model outputs by global integration.

2. OBSERVED VS. MODELED EARTH ROTATION VARIATIONS - FORMALISM

Basically there are two ways to compare ERP observed with space geodetic techniques to Earth rotation variations predicted from geophysical modeling. One option is to transform the ERP to so-called geodetic excitation and then compare them to the geophysical excitation given in terms of AMF. The second possibility is to express the AMF in terms of Earth rotation parameters. At least regarding polar motion this is a somewhat more sophisticated procedure because it involves the solution of a convolution integral. The most important formulae describing both methods are provided below. The AMF as they are quoted here are actually called effective angular momentum functions (EAMF), since they consider the non-rigidity of the Earth. The components of polar motion are in the following equations denominated p_x and p_y (equivalent to x_p and y_p). They represent the polar motion of the CIP, while the Earth rotation vector is composed of $\Omega \cdot (m_1, m_2, 1 + m_3)$, with the nominal angular velocity of the Earth Ω. $\hat{\sigma}_{CW}$ is the complex angular frequency of the Chandler Wobble. LOD_0 stands for the nominal length of the solar day of 86400 s. $\hat{\chi}(t) = \chi_1 + \mathrm{i}\chi_2$ represents equatorial excitation.

Polar motion of the CIP:

$$\hat{p}(t) = p_x(t) - \mathrm{i}p_y(t) \tag{1}$$

Polar motion of the rotation pole:

$$\hat{m}(t) = \hat{p}(t) - \frac{\mathrm{i}}{\Omega}\frac{\mathrm{d}\hat{p}(t)}{\mathrm{d}t} \tag{2}$$

Excess length of day:

$$\frac{\delta\mathrm{LOD}(t)}{\mathrm{LOD}_0} = -\frac{\mathrm{d}}{\mathrm{d}t}\mathrm{dUT1}(t) = -m_3 \tag{3}$$

Geodetic excitation:

$$\hat{\chi}(t) = \hat{p}(t) + \frac{\mathrm{i}}{\hat{\sigma}_{CW}}\frac{\mathrm{d}\hat{p}(t)}{\mathrm{d}t} \tag{4}$$

$$\chi_3(t) = \frac{\delta\mathrm{LOD}(t)}{\mathrm{LOD}_0} \tag{5}$$

The variable components of the tensor of inertia are $\hat{c} = c_{13} + \mathrm{i}c_{23}$ and c_{33}. The vector of relative angular momentum is called h with the elements $\hat{h} = h_1 + \mathrm{i}h_2$ and h_3. C signifies the polar moment of inertia and A' the average of the equatorial moments of inertia. C_m is the polar moment of inertia of the mantle only. The numerical factors in the EAMF are taken from Gross (2007).

Equatorial EAMF:

$$\hat{\chi}(t) = \frac{1.100 \cdot \hat{c}(t)}{(C - A')} + \frac{1.608 \cdot \hat{h}(t)}{\Omega \cdot (C - A')} = \hat{\chi}^{mass} + \hat{\chi}^{motion} \tag{6}$$

Axial EAMF:

$$\chi_3(t) = 0.748\frac{c_{33}(t)}{C_m} + 0.998\frac{h_3(t)}{C_m\Omega} = \chi_3^{mass} + \chi_3^{motion} \tag{7}$$

Geophysical excitation in terms of ERP:

$$\hat{p}(t) = e^{\mathrm{i}\hat{\sigma}_{CW}t}\left(\hat{p}(0) - \mathrm{i}\hat{\sigma}_{CW}\int_0^t \hat{\chi}(\tau)e^{-\mathrm{i}\hat{\sigma}_{CW}t}d\tau\right) \tag{8}$$

$$\delta\mathrm{LOD}(t) = \chi_3(t) \cdot \mathrm{LOD}_0 \tag{9}$$

The prevailing procedure of comparison is to express atmospheric and oceanic effects as well as ERP observations in terms of excitation, i.e. using Equations (4)–(7).

3. NON-TIDAL EFFECTS OF ATMOSPHERE AND OCEANS

The following paragraph provides a chiefly graphical overview of the most important non-tidal atmospheric and oceanic effects in polar motion and LOD on seasonal and intraseasonal time scales. The numbers shown in the figures were extracted from Gross et al. (2003, 2004). The geophysical excitation investigated therein is derived from atmospheric angular momentum based on data from the NCEP/NCAR (National Centers for Environmental Prediction/National Center for Atmospheric Research) reanalysis project and from oceanic angular momentum calculated from the ECCO (Estimating the Circulation and Climate of the Ocean) consortium's simulation of the general circulation of the oceans. The observed ERP variations are the COMB2000 series, which stem from a combination of Earth rotation measurements taken by the techniques of optical astrometry, Lunar and Satellite Laser Ranging, Very Long Baseline Interferometry and Global Navigation Satellite Systems.

Seasonal variations are subdivided into annual, semiannual and terannual periods. The term intraseasonal covers all periodic and irregular phenomena from four days to one year, except seasonal fluctuations. Seasonal effects are plotted in terms of excitation amplitudes, whereas intraseasonal effects are given in percent of variance explained (10).

$$\text{variance explained} = 100\% \times \frac{var(obs) - var(obs - model)}{var(obs)} \tag{10}$$

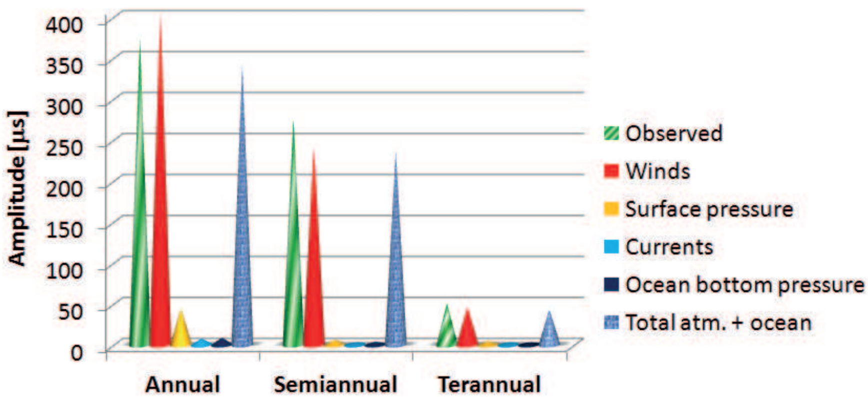

Figure 1: Seasonal excitation of LOD

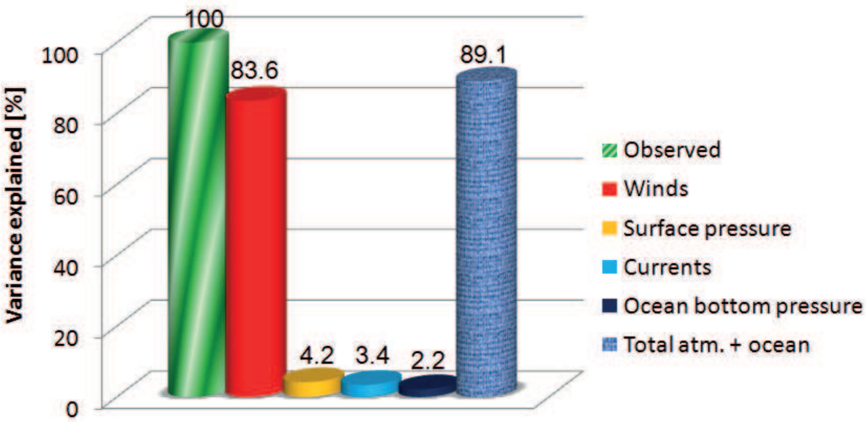

Figure 2: Intraseasonal excitation of LOD

Figures 1 and 2 display diagrams of seasonal and intraseasonal excitation in the axial component or in LOD, respectively. The plots show the magnitude and variance explained of the geodetic excitation (observed) and of atmospheric excitation, split into a wind and surface pressure portion, and oceanic excitation, divided into a current and ocean bottom pressure term. Figures 3 and 4 contain the same effects for the equatorial components or polar motion excitation, respectively.

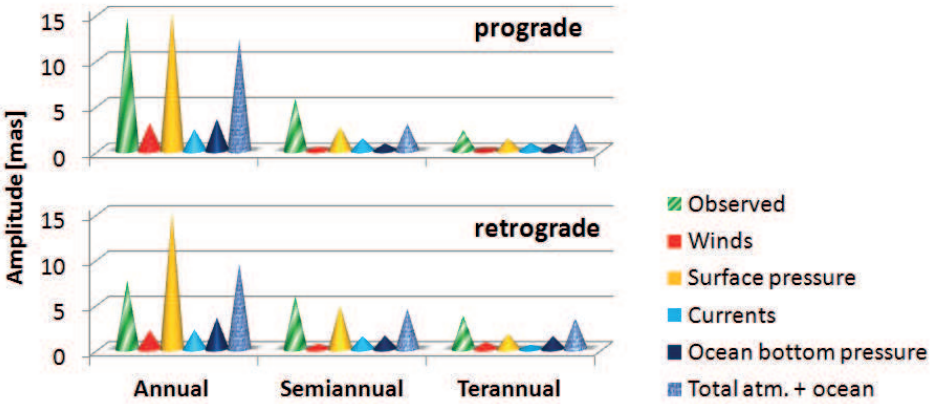

Figure 3: Seasonal polar motion excitation

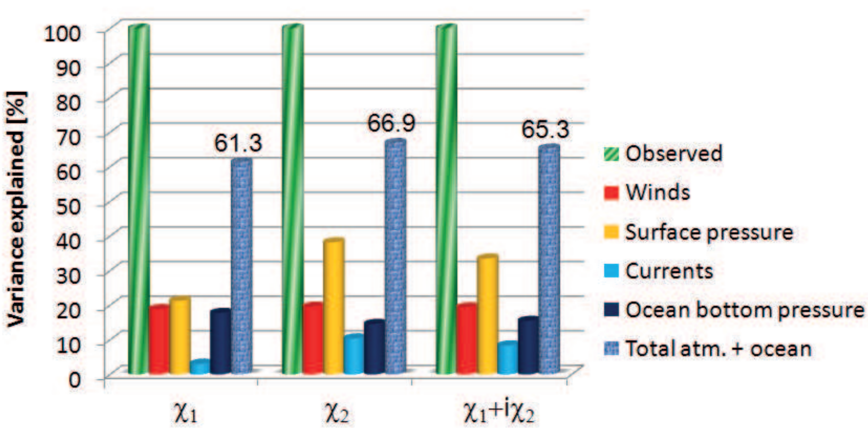

Figure 4: Intraseasonal polar motion excitation

4. TIDAL EFFECTS OF ATMOSPHERE AND OCEANS

As a completion to Section 3, where only non-tidal atmospheric and oceanic effects were treated, this section deals with the influence of tides of the atmosphere and the oceans on Earth rotation. Generally, the term "tidal" implies phenomena which are caused by the tidal forces exerted on solid Earth, oceans and atmosphere by the Moon and the Sun. More specifically, these effects are called gravitational tides in contrast to so-called radiational tides. The latter are caused by the diurnal and annual solar heating cycle of the atmosphere and oceans. In the case of Earth rotation excitation the impact of the radiational atmospheric tides is much more dominant than the effect of gravitational tides in the atmosphere. Concerning the oceans the size of the radiational tides is almost negligible compared to the gravitational ocean tides.

The following Figures 5 and 6 provide a compilation of tidal effects in universal time and polar motion broken down into period groups. Tides of the atmosphere occur at diurnal and semidiurnal periods with the smallest amplitudes. Ocean tides are present in the high as well as in the low-frequency range with periods up to 18.6 years. Solid Earth tides affect LOD or dUT1, respectively, at the same periods as the long-period ocean tides. The body tides also cause retrograde diurnal polar motion, which however is considered as nutation according to the definition of the CIP, just as well as the retrograde diurnal part of the ocean tidal polar motion.

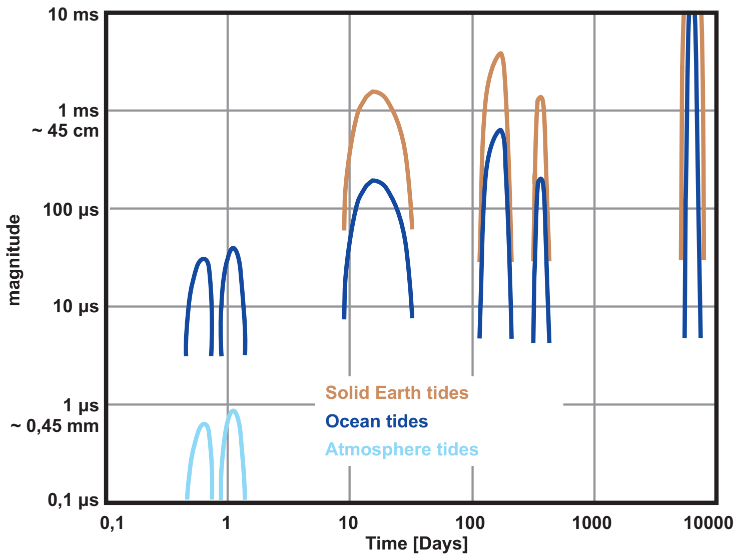

Figure 5: Tidal effects in UT

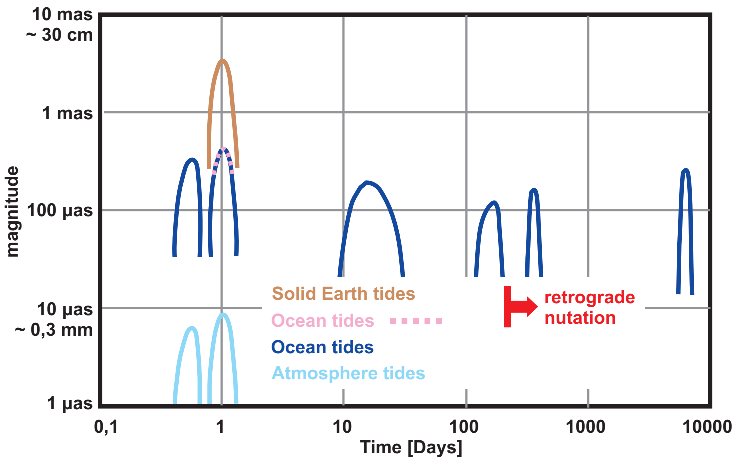

Figure 6: Tidal effects in polar motion

4.1 Diurnal and subdiurnal ocean tidal effects

A still ongoing and somewhat open issue is the budget of diurnal and subdiurnal ERP variations, which are predominantly of tidal origin. High-frequency Earth rotation variations are mainly composed of ocean tidal effects, atmospheric effects and libration. Libration which stands for the effect of the lunisolar torque on the triaxial figure of the Earth, is conventionally accounted for within the processing of space geodetic techniques. The IERS Conventions (2010) also provide a model for ocean tidal ERP variations. However, different studies have shown that there are small but, due to their harmonic nature, detectable and significant discrepancies between the predictions of the IERS model and the observations of the space geodetic techniques. In fact, the IERS model is based on a rather old ocean tide model, wherein data from only a few years of satellite altimetry was assimilated. Since then the accuracy of ocean tide models has increased notably, not least because a much longer time span of altimetry measurements has become available. In the last part of this paper we present the results of a study the aim of which was to probe the performance of new ocean tide models in the prediction of high-frequency ERP. The performance was tested by comparing the root mean square differences of time series calculated from different sources according to the following list: (1) IERS2010: conventions model; (2) TPXO7.2: calculated from TPXO7.2 ocean tide model (Egbert and Erofeeva, 2002); (3) HAM11a: calculated from HAMTIDE11a ocean tide model (Taguchi et al., 2011); (4) VLBI: time series (26 years) derived with Vienna VLBI Software VieVS (Böhm et al., 2011); (5) GPS: time series (13 years) derived with Bernese GPS Software (by courtesy of N. Panafidina, ETH Zürich). The resulting values are assembled in Figure 7.

Model	IERS2010	TPXO7.2	HAM11a	GPS	VLBI	ERP
IERS2010		29.4	26.0	30.0	36.0	Δx [µas]
TPXO7.2	34.2		20.6	**24.3**	**34.2**	
HAM11a	27.9	27.0		28.4	41.6	
GPS	33.4	**25.3**	34.6		35.4	
VLBI	42.4	**39.8**	50.0	41.1		
ERP	Δy [µas]					

Model	IERS2010	TPXO7.2	HAM11a	GPS
IERS2010				
TPXO7.2	2.3			
HAM11a	3.1	2.1		
GPS	**2.7**	2.9	3.8	
VLBI	3.1	**2.8**	3.1	3.2
ERP	ΔUT1 [µs]			

Figure 7: RMS differences in terms of polar motion (left) and dUT1 (right) time series

By purely looking at the numbers we can state that the ERP variations based on TPXO7.2 fit best to the GPS and VLBI values, except for GPS dUT1. Nevertheless, the improvement w.r.t. the IERS2010 model is not really significant.

5. CONCLUDING REMARKS

As to Section 4.1, we conclude that taking most recent ocean tide models alone is not sufficient to close the gap between observed and modeled high-frequency ERP variations. Additionally a careful reassessment of the whole model development procedure will be necessary.

In the area of non-tidal atmospheric and oceanic effects, the excitation budget is closed neither for LOD nor for polar motion as can be deduced from the respective figures. Yet, the observed LOD variations can be explained considerably better with present geophysical models than polar motion. At least in case of seasonal and also intraseasonal LOD variations the pictures reveal clearly that the atmospheric winds are the most important driving agents. For polar motion the surface pressure can be explicitly identified as the major excitation mechanism only w.r.t. seasonal time scales.

6. REFERENCES

Böhm S., Brzeziński A., Schuh H., 2011, "Complex demodulation in VLBI estimation of high frequency Earth rotation components", J. Geodyn., available online, doi:10.1016/j.jog.2011.10.002.

Egbert G. D., Erofeeva S. Y., 2002, "Efficient inverse modeling of barotropic ocean tides", J. Atmos. Oceanic Technol., 19, pp. 183-204.

Gross, R. S., Fukumori, I., Menemenlis, D., 2003, "Atmospheric and oceanic excitation of the Earth's wobbles during 1980-2000", J. Geophys. Res. 108, NO. B8, 2370, doi:10.1029/2002JB002143.

Gross, R. S., Fukumori, I., Menemenlis, D., 2004, "Atmospheric and oceanic excitation of length-of-day variations during 1980-2000", J. Geophys. Res. 109, B01406, doi:10.1029/2003JB002432.

Gross, R. S., 2007, "Earth rotation variations – long period", In Herring, T. A. (ed.), Physical Geodesy. Amsterdam: Elsevier, Treatise on Geophysics, Vol. 3.

IERS Conventions (2010), G. Petit and B. Luzum (eds.), IERS Technical Note 36, Frankfurt am Main: Verlag des Bundesamts für Kartographie und Geodäsie, 2010, ISBN 3-89888-989-6.

Taguchi E., Stammer D., Zahel W., 2011, "Inferring deep ocean tidal energy dissipation from the global high-resolution dataassimilative HAMTIDE model", submitted to J. Geophys. Res..

CONSTRAINTS ON THE STRUCTURE AND DYNAMICS OF THE EARTH'S DEEP INTERIOR INFERRED FROM NUTATION OBSERVATIONS

L. KOOT
Royal Observatory of Belgium
3 avenue circulaire, B-1180 Brussels, Belgium
e-mail: laurence.koot@observatoire.be

ABSTRACT. The gravitational torque applied on the Earth by the other celestial bodies generates periodic variations in the orientation of the Earth's rotation axis in space which are called nutations. This motion has two normal modes, the Free Core Nutation (FCN) and the Free Inner Core Nutation (FICN), of which the frequencies and dampings depend directly on the Earth's interior structure and dynamics (e.g. Mathews et al. 1991a, 1991b, Mathews & Shapiro 1992). Both normal modes are characterized by differential rotations of the inner core, the outer core, and the mantle. Their natural frequencies are thus directly affected both by the strength of the mechanical coupling at the outer core boundaries and by the way the three regions deform due to the action of centrifugal forces. Similarly, the damping of the modes reflects the energy dissipated both through the couplings at the outer core boundaries and through anelastic deformation. The mechanical coupling can be of several physical origins such as gravitational, electromagnetic, viscous, or pressure/topographic couplings. Due to the high precision of the nutation observations, obtained from the Very Long Baseline Interferometry (VLBI) technique, the frequency and damping of the normal modes can be estimated from the resonance effect they induce on the forced nutations (Mathews et al. 2002, Koot et al. 2008, 2010). Interpretation of these estimated natural frequencies and dampings allows then for insights into the deep Earth's physical properties. In this talk, we review the constraints that have been inferred from nutation observations on deep Earth's properties such as the intensity of the magnetic field at the outer core boundaries (Buffett et al. 2002, Koot et al. 2010, Buffett 2010a), the viscosity of the core fluid close to those boundaries (Mathews & Guo 2005, Deleplace & Cardin 2006, Koot et al. 2010), the chemical stratification at the top of the core (Buffett 2010b), and the viscosity of the inner core (Koot & Dumberry 2011). We also present an estimation of the atmospheric contributions to nutations and their implications for the estimation of deep Earth's properties from nutation observations (Koot & de Viron 2011).

REFERENCES

Buffett, B.A., Mathews, P.M., Herring, T.A., 2002. Modeling of nutation and precession: effects of electromagnetic coupling. J. Geophys. Res. 107, 2070.

Buffett, B.A., 2010a. Tidal dissipation and the strength of the Earth's internal magnetic field. Nature 468, 952955.

Buffett, B.A., 2010b. Chemical stratification at the top of Earth's core: Constraints from observations of nutations. Earth and Planetary Science Letters 296, 367-372

Deleplace, B., Cardin, P., 2006. Viscomagnetic torque at the core mantle boundary. Geophys. J. Int. 167, 557566.

Koot, L., Rivoldini, A., de Viron, O., Dehant, V., 2008. Estimation of Earth interior parameters from a Bayesian inversion of very long baseline interferometry nutation time series. J. Geophys. Res. (Solid Earth) 113, 8414.

Koot, L., Dumberry, M., Rivoldini, A., de Viron, O., Dehant, V., 2010. Constraints on the coupling at the core-mantle and inner core boundaries inferred from nutation observations. Geophys. J. Int. 182, 12791294.

Koot, L., de Viron, O., 2011. Atmospheric contributions to nutations and implications for the estimation of deep Earth's properties from nutation observations, Geophys. J. Int. 185, 1255-1265.

Koot, L., Dumberry, M., 2011. Viscosity of the Earth's inner core: Constraints from nutation observations, Earth and Planetary Science Letters 308, 343-349.

Mathews, P.M., Guo, J.Y., 2005. Viscoelectromagnetic coupling in precession-nutation theory. J. Geophys. Res. 110, 2402.

Mathews, P.M., Shapiro, I.I., 1992. Nutations of the earth. Annu. Rev. Earth Planet. Sci. 20, 469500.

Mathews, P.M., Buffett, B.A., Herring, T.A., Shapiro, I.I., 1991a. Forced nutations of the earth: influence of inner core dynamics. 1. Theory. J. Geophys. Res. 96, 82198242.

Mathews, P.M., Buffett, B.A., Herring, T.A., Shapiro, I.I., 1991b. Forced nutations of the Earth: influence of inner core dynamics. 2. Numerical results and comparisons. J. Geophys. Res. 96, 82438258.

Mathews, P.M., Herring, T.A., Buffett, B.A., 2002. Modeling of nutation and precession: new nutation series for nonrigid Earth and insights into the Earth's interior. J. Geophys. Res. 107, 2068.

SIMULATION, PREDICTION AND ANALYSIS OF EARTH ROTATION PARAMETERS WITH A DYNAMIC EARTH SYSTEM MODEL

F. SEITZ[1], M. THOMAS[2]

[1] Earth Oriented Space Science and Technology (ESPACE), Technische Universität München
Arcisstr. 21, D-80333 Munich, Germany;
e-mail: seitz@bv.tum.de

[2] Deutsches GeoForschungsZentrum GFZ, Potsdam

ABSTRACT. Dynamic processes in the Earth system involving mass transports in the subsystems atmosphere and ocean are known to be the prominent sources for changes of Earth rotation on sub-seasonal to interannual time scales. Since respective geodetic observations of polar motion and variations of length-of-day are integral quantities, numerical model approaches are required in order to assess individual contributions from underlying processes in different subsystems. This paper discusses simulations of polar motion from the dynamic Earth system model DyMEG. Results for two different model set-ups are presented: First, realistic forcing based on reanalysis data is applied. Second, DyMEG is forced by scenario runs over 200 years (1860-2060) based on a fully coupled atmosphere-hydrosphere model. Special attention is drawn to the long-term development of the modelled Chandler oscillation and its excitation mechanisms. It is shown that simulated and observed patterns of amplitude variations of the Chandler oscillation agree very well. Various experiments reveal that wind is its most important driving mechanism.

1. INTRODUCTION

The rotation of the Earth and its temporal variation are monitored by geodetic and astrometric observation systems since decades with very high accuracy. Observations of the orientation of the Earth axis and the angular velocity of the rotation are transformed into time series of Earth rotation parameters (ERP) polar motion and length-of-day respectively. Precise knowledge of temporal variations of the ERP is essential for various applications, such as the realisation of time systems, the highly precise computation of geodetic reference frames, the relation of Earth-fixed and space-fixed coordinate systems, and precise navigation on Earth and in space. In addition, ERP are interesting quantities for various disciplines of geosciences since dynamic processes in the Earth system are reflected in their temporal variations.

The analysis of ERP time series allows for conclusions with respect to processes and changes in the Earth system on various temporal scales. But since ERP are integral quantities of the Earth system whose variations are caused by a multitude of superposed effects, additional information from physical modelling is indispensable. In the following, results of the geophysical forward model DyMEG (Dynamic Model for Earth Rotation and Gravity) are presented which has been developed in order to simulate variations of rotation, gravity field and surface deformations of the Earth in a physically consistent way (Seitz 2004). The focus of this presentation is put on inter-annual variations of polar motion that are caused by processes in the coupled atmosphere-hydrosphere system.

This paper is a direct follow-up of the article of Seitz and Drewes (2009). Therefore the description of both the set-up of DyMEG and the atmospheric-hydrospheric forcing is kept very short intentionally in order to provide room for the discussion of numerical results of extended experiments.

2. SIMULATIONS OF POLAR MOTION

DyMEG is based on the Euler-Liouville Equation that describes the balance of angular momentum in an Earth-fixed coordinate system. External gravitational torques from Sun, Moon and planets are balanced with variations of angular momentum in the Earth system. Those are caused by mass transports (i.e. the redistribution and motion of mass elements) and changes of the Earth rotation vector. By solving the Euler-Liouville Equation for the latter, variations of ERP are determined.

In order to obtain meaningful results various forcings and parameters need to be introduced into

DyMEG. Beside ephemerides of external celestial bodies that are required for the computation of gravitational torques and tidal deformations of the Earth, information about mass transports in the (relevant components of the) Earth system must be available. Respective mass redistributions and motions are converted into temporal variations of the Earth's tensor of inertia and so-called relative angular momenta. Furthermore the model requires a number of geometrical, physical and rheological parameters of the Earth. Naturally the model result is highly dependent on the completeness of the considered effects as well as on the quality and consistency of applied forcing and model parameters.

2.1. Experiment 1: Realistic Forcing

In a first experiment numerical values for variations of the tensor of inertia and relative angular momenta are deduced from the atmospheric reanalyses of NCEP and the unconstrained version c20010701 of the global ocean circulation model ECCO. ECCO is forced by NCEP fields of wind stress, heat and freshwater fluxes. Consequently the combination of those two models allows for a consistent description of mass transport processes in the subsystems atmosphere and ocean. Water storage variations and related mass redistributions in the continental hydrology are derived from the global hydrological model LaD. Minor effects (e.g., earthquakes, volcanic eruptions, postglacial uplift, core/mantle interactions) are neglected. The results from DyMEG are displayed in Figure 1. The modelled curves for polar motion and the geodetic observations (series C04 of the International Earth Rotation and Reference Systems Service, IERS) agree very well. The correlation coefficients amount to 0.98 (x-component) and 0.99 (y-component), and the respective RMS differences are 29.5 and 23.3 mas. This result can be seen as a proof that DyMEG is suitable of producing a result for polar motion which highly corresponds to observations when the model is forced with realistic forcing based on reanalysis data.

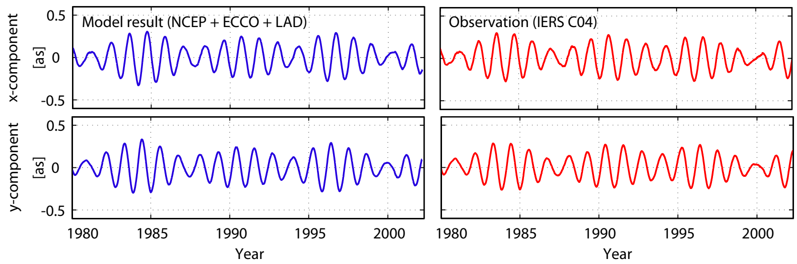

Figure 1: Model result for polar motion from DyMEG with realistic forcing (left) in comparison with geodetic observations (right)

2.2. Experiment 2: ERP predictions with scenario runs over 200 years

In a second experiment DyMEG is forced by the fully and self-consistently coupled atmosphere-hydrosphere model ECOCTH. ECOCTH is based on atmosphere-ocean model combination ECHAM5-T63/MPI-OM (Jungclaus et al., 2006) that has been extended by a land surface hydrology model. The model simulates fluxes of momentum, energy and mass between atmosphere, ocean and continental hydrosphere. Five equiprobable scenario runs were produced for a period of 200 years between 1860 and 2060. The runs differ solely with respect to the initial conditions for the atmospheric-hydrospheric state of 1860. ECOCTH simulations until 1999 were performed under observed climate forcing taking into account anthropogenic and natural influences. Climate prediction simulations for the 21st century were performed under the A1B scenario for future man-made climate forcing (see Sündermann and Hense, 2009, for details). Since the coupled model is absolutely free, only statistical conclusions can be drawn from the results, i.e. an analysis with respect to real time is not possible.

ECOCTH predictions of mass transports are introduced as forcing into DyMEG. A run with DyMEG is performed for each of the five ensemble members. The respective results for polar motion are displayed in Figure 2 of the article by Seitz and Drewes (2009) together with astrometric/geodetic observations from the C01 series of the IERS. Even though identical climate forcing is applied to all five ensemble members of ECOCTH the resulting curves for polar motion from DyMEG are very different. This implies that the excitation of polar motion depends largely on random processes in the atmosphere-hydrosphere system. A decomposition of the curves into the two largest signal components, the Chandler and the annual oscillation, is performed by means of wavelet filtering (Seitz and Schmidt, 2005). Figure 2 displays the results for two of the runs (runs 1 and 4) together with respective curves determined from observations.

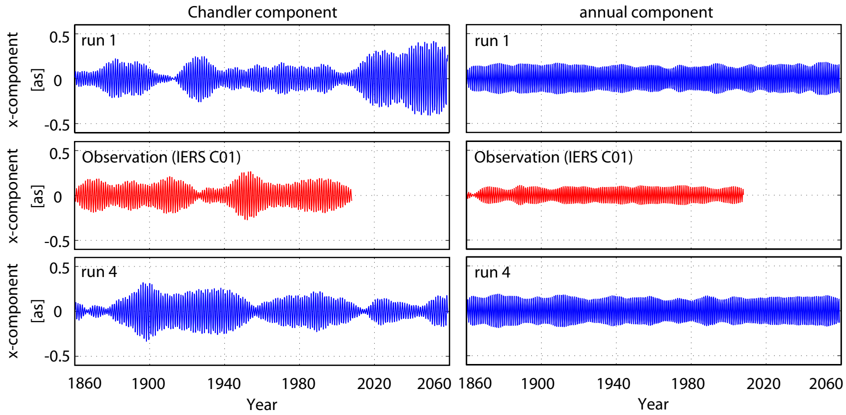

Figure 2: Chandler and annual oscillations of model results from DyMEG (ECOCTH forcing; runs 1 and 4) in comparison with respective signal components from geodetic observations (x-components).

As discussed by Seitz and Drewes (2009) the annual components are similar and feature rather stable amplitudes in all runs. However, the annual amplitudes are nearly twice as large as observed which indicates an overestimation of the annual variability by ECOCTH. The Chandler components differ significantly between the runs (cf. also Figure 3 of Seitz and Drewes, 2009). But the overall signal characteristic showing increasing and decreasing amplitudes corresponds well with the observations.

By taking a closer look at the time series of the Chandler oscillation pieces of the curves can be identified that look very similar in the model results and the observations (Figure 3). For the two displayed runs these pieces cover almost 100 years (run 1) and 90 years (run 4). Shifting the pieces by +26 and +54 years respectively leads to remarkable correlation coefficients of 0.74 and 0.92. As stated above the simulated dynamics of ECOCTH are not related to real time. Therefore a time shift between the curves is irrelevant for the analysis of the results.

The Chandler oscillation is a free rotational mode of the Earth. Due to the anelastic response of the Earth's mantle to polar motion its amplitude is damped and would diminish within a few decades if no counteracting mechanism would excite it. Broad consensus has been reached in the scientific community that the Chandler oscillation is excited by dynamical processes in atmosphere and hydrosphere. Forced polar motion caused by mass transports in these subsystems is coupled back to so-called rotational deformations. Those deformations involve mass redistributions in the solid Earth and in the oceans that are known to influence the Chandler amplitude. The results of DyMEG indicate that ECOCTH is very well suited for analysing the relevant dynamical processes. In this context the long time period of ECOCTH is of special interest since it allows for studying the mechanisms of excitation and damping of the Chandler oscillation over many decades.

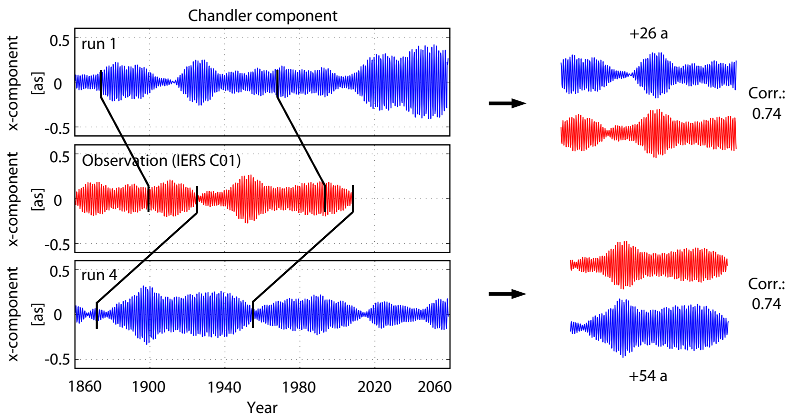

Figure 3: Analysis of the Chandler oscillations from DyMEG (runs 1 and 4) w.r.t. geodetic observations.

3. EXCITATION OF THE CHANDLER OSCILLATION

In order to identify the strongest contributors to the excitation of the Chandler oscillation additional experiments with DyMEG are performed. Exemplarily ECOCTH forcing of run 4 is applied. First, the joint effect of redistributions and motions of mass elements is studied separately for the two subsystems atmosphere and ocean. Respective variations of the tensor of inertia (mass effect) and relative angular momenta (motion effect) are deduced from the model components ECHAM5-T63 and MPI-OM. Mass transports in the continental hydrology are not considered here since their effect on the Chandler oscillation is very small (Seitz and Schmidt, 2005). The results of this experiment are displayed in Figure 4 (first column). For either case DyMEG produces an oscillation that shows increasing and decreasing amplitudes. Thus both subsystems atmosphere and ocean clearly contribute to the excitation of the Chandler oscillation. The atmospheric contribution is a bit stronger, and maxima and minima of both curves are not necessarily synchronous. In a second experiment mass and motion effects are separated (Fig 4; second column). Now atmosphere and ocean are introduced into DyMEG simultaneously, but either only mass redistributions (i.e. tensor variations) or only mass motions (i.e. relative angular momenta) are considered. The motion effect on the excitation of the Chandler oscillation turns out to be significantly stronger than the mass effect. In further experiments mass and motion effects are studied separately for atmosphere and ocean (Figure 4; third and fourth column). All model results are linear, i.e. the sum of the curves obtained for individual effects is equal to the curve obtained for the respective joint effect. In sum the experiments indicate that (1) the atmosphere is the strongest contributor, and that (2) in particular the atmospheric motion component (that is related to equatorial winds) is a very important excitation mechanism of the Chandler amplitude.

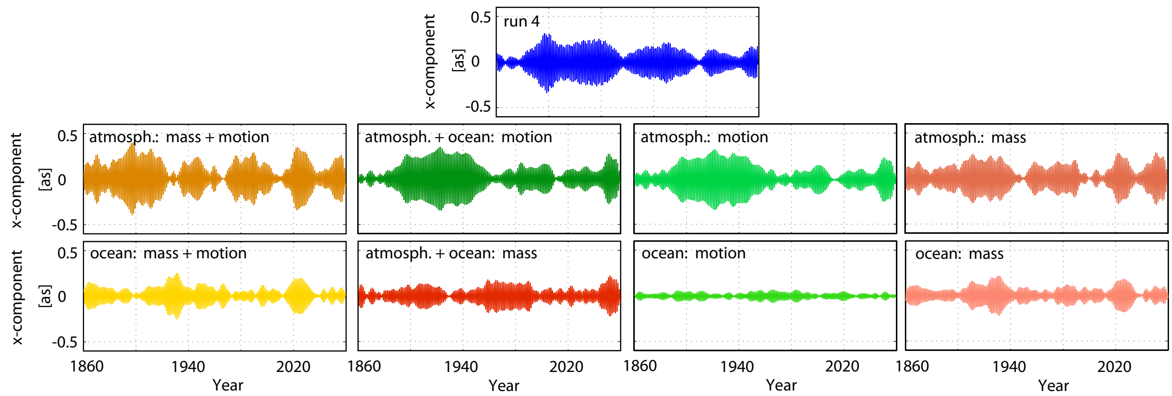

Figure 4: Top panel: Chandler oscillation from DyMEG for run 4 (full forcing, cf. Figure 2). Lower panels: Chandler oscillations from various experiments with partial forcing.

4. RÉSUMÉ

The Dynamic Model for Earth Rotation and Gravity (DyMEG) has been applied for simulations of polar motion. An experiment with realistic forcing demonstrated the model's ability for producing meaningful results for polar motion. The fully coupled atmosphere-hydrosphere model ECOCTH provides an ideal data basis for studies of the dynamical mechanisms of the excitation of polar motion and in particular of the Chandler oscillation over many decades. Future investigations will be directed towards the identification of specific dynamical states of the atmosphere-hydrosphere system and processes of mass transports that are responsible for the amplitude variations of the Chandler oscillation.

5. REFERENCES

Jungclaus, J.H., M. Botzet, et al., 2006. J. Climate 19 (16), pp. 3952-3972.
Seitz, F., 2004. Deutsche Geodätische Kommission, C 578, Munich (in German).
Seitz F., H. Drewes, 2009. Proc. Journées 2008, Lohrmann-Observatorium and Obs. Paris.
Seitz, F., M. Schmidt, 2005. J. Geophys. Res., 110, B11406, doi: 10.1029/2005JB003826.
Sündermann, J., A. Hense, 2009. Proc. Journées 2008, Lohrmann-Observatorium and Obs. Paris.

ANALYTICAL COMPUTATION OF THE EFFECTS OF THE CORE-MANTLE BOUNDARY TOPOGRAPHY ON TIDAL LENGTH-OF-DAY VARIATIONS

V. DEHANT[1], M. FOLGUEIRA[2], M. PUICA[2]

[1] Royal Observatory of Belgium
avenue Circulaire 3, B1180 Brussels, Belgium
e-mail: v.dehant@oma.be

[2] Universidad Complutense de Madrid, Spain

ABSTRACT. We have computed coupling mechanisms at the core-mantle boundaries of terrestrial bodies of the Solar system, and in particular, the pressure torque on the topography at the core-mantle boundary. The philosophy of the computation follows Wu and Wahr (1997), which allows to solve for the velocity field coefficients in terms of the topography coefficients. The velocity in the fluid core is decomposed into a global classical velocity and an incremental velocity related to the topography. We have used an analytical approach to compute this last part as well as the incremental changes in the periodic variations of the length-of-day (LOD) and in the librations, i.e. oscillating motions in space. We have found that there are topography coefficients that are enhanced due to resonances at particular frequencies. For the Earth the tidal forcing frequencies are compared to those resonance frequencies. The total torque on the core-mantle boundary is demonstrated to be dependent on particular amplitudes of the topography.

1. MOTIVATION

The length-of-day variations are usually computed from angular momentum equations of the whole Earth and of the different layers (inner core, outer core and mantle). Coupling mechanisms must be considered at the CMB and ICB (Inner Core Boundary). The torque considered in the classical approach is the gravitational and pressure torques related to the flattening of the core. In a more sophisticated approach and for the nutations, one considered the electromagnetic torque (e.g. Mathews et al., 1991) or even the viscous torque (e.g. Mathews and Guo, 2005). The topographic torque related to the non-hydrostatic part of the CMB shape is not considered, while the problem has been addressed by Wu and Wahr (1997) in a numerical approach. These

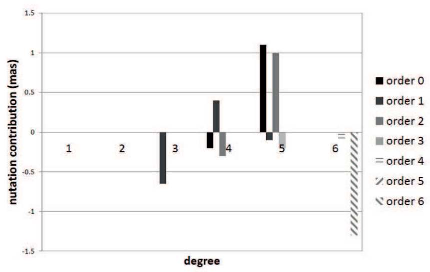

Figure 1: Results concerning nutations, from Wu and Wahr, 1997

authors have shown that the topographic torque, often disregarded, may be important at CMB. Wu and Wahr (1997) have computed numerically the topographic torque using topography expanded in Spherical Harmonics and have shown that some harmonics of the topography have important contributions to nutations. From the approach and from the results, it is difficult to understand if the enhancement of some topography components is due to the topography amplitudes or due to something else, such as the geometry of the core topography itself. We may suspect some resonance effects with inertial waves as when perturbing a rotating fluid, the particle motion is characterized by a low-frequency oscillation called inertial wave. We may thus wander if the enhancements seen in the topographic torque would be related to enhancements of the inertial waves. For that reason we have considered to use an analytical approach in order to study the results in more detail. In this paper we consider the approach in the frame of length-of-day variations. Nutations are computed elsewhere (see Dehant and Folgueira, 2011).

2. EQUATIONS

The total pressure torque on the whole topography can be decomposed into two parts: $\Gamma^0 + \Gamma^{\phi}_{topo}$, where (1) Γ^0 the constant classical part of the torque for an ellipsoidal topography at equilibrium, and (2) Γ^{ϕ}_{topo} due to the inertial rotation pressure $(P - P_0 - \rho_f \phi^f)$ related for the global relative rotation of the fluid on the topography, where P is the pressure and $\phi^f = \phi^e + \phi^1$ is the gravitational potential consisting of the sum of the external potential (ϕ^e) and the incremental potential due to the deformation (ϕ^1). Only the second part of the torque is of importance when computing the effects of a perturbing potential and related additional rotations of the core and the mantle on a topography different with respect to the ellipsoidal hydrostatic shape.

In order to be able to evaluate this torque, one considers the expression $\vec{\Gamma}^{\phi}_{topo} = -\int\int_{CMB} \vec{r}\times \vec{n}\rho_f\, \phi\, dS$ related to ϕ $(= \frac{(P-P_0)}{\rho_f} - \phi^f)$. In order to integrate the torque, one needs then to consider the Navier-Stokes equation. The philosophy for solving the equations is to separate the velocity into a global part $(\vec{v})$ and an additional part ($\vec{u}$ or $\vec{q}$ if normalized) and to separate the equation into two equations of which the solutions are $\vec{v}$ and $\vec{q}$ and can be computed analytically. $\vec{v}$ is the global relative velocity of the fluid and $\vec{q}$ is the incremental one, function of the coefficients a_l^k in the expression of ϕ, both being incompressible.

The boundary conditions at the CMB are imposed on the total velocity and yield thus a relation between $\vec{v}$ (and thus components of the relative global fluid rotation m_1^f and m_2^f), $\vec{q}$ (and thus the a_l^k coefficients), and the topography coefficients ϵ_n^m. This allows to solve for the a_l^k in terms of the relative global relative fluid rotation.

The basic dynamical equations are the linearized Navier-Stokes equation. If one considered that the equilibrium corresponds to the hydrostatic case, they become:

$$\frac{\partial \vec{V}}{\partial t} + 2\vec{\Omega}\times\vec{V} + \frac{1}{\rho_f}\nabla p - \nabla\phi_m + \Omega\frac{\partial \vec{m}}{\partial t}\times\vec{r} = 0 \tag{1}$$

where $\vec{\Omega}$ is the uniform equilibrium angular rotation of amplitude Ω, $\vec{m}$ is the scaled additional mantle angular velocity, $\vec{m} = \begin{pmatrix} m_1 \\ m_2 \\ m_3 \end{pmatrix}$, $\vec{r} = \begin{pmatrix} x \\ y \\ z \end{pmatrix}$ is the position of the fluid particle in the reference frame, $\vec{V}$ is the velocity of the fluid particle in the reference frame, ρ_f is the fluid density and p is the incremental effective pressure computed by $p = P - P_0 - \rho_f\phi_1 - \rho_f\phi_e$ as expressed before. Note that the angular velocity vector of the reference frame attached to the mantle $\vec{\omega} = \vec{\Omega} + \Omega\vec{m}$.

The first boundary condition at the core-mantle boundary (CMB): $\vec{\hat{n}}\cdot\vec{V} = 0$ ($\vec{\hat{n}}$ is the normal to the surface); it is expressed as a function of the boundary topography; the boundary surface (hydrostatic + non-hydrostatic parts) is expressed using:

$$r = r_0\left[1 + \sum_{n=1}\sum_{m=-n}^{n} \varepsilon_n^m Y_n^m(\theta,\lambda)\right] \tag{2}$$

where r_0 is the surface mean radius, $Y_n^m(\theta, \lambda)$ are the Legendre Associated Functions as a function of the colatitude θ and the longitude λ, and ε_n^m are small dimensionless numbers related to the existence of the topography. The largest contribution is ε_2^0 due to the flattening (hydrostatic + non-hydrostatic parts) of the CMB. It must be noted that the ϵ_2^0 in a topography development in spherical harmonics usually contains the hydrostatic part and the non-hydrostatic contribution to the topography; these must be separated. Here it is separated into a hydrostatic part $\epsilon_2^{0\,hydr}$ and an additional one noted confusingly ϵ_2^0 as well from now on and for writing simplicity.

The second boundary condition is the condition of incompressibility: $\nabla \cdot \vec{V} = 0$. We now decompose the velocity: $\vec{V} = \vec{u} + \vec{v} = \Omega\, L\, \vec{q} + \vec{v}$, where L is the maximum radius of the core and $\vec{q}$ is a non-dimensional velocity. One imposes that $\vec{u} << \vec{v}$.
The equation and condition for $\vec{v}$ are:

$$\begin{cases} \frac{\partial \vec{v}}{\partial t} + 2\vec{\Omega} \times \vec{v} + \; + \Omega \frac{\partial \vec{m}}{\partial t} \times \vec{r} - \nabla \phi_m \; = \; 0 \\ \nabla \cdot \vec{v} = 0 \end{cases} \tag{3}$$

The equation and condition for $\vec{q}$ are:

$$\begin{cases} i\,\sigma_m\,\vec{q} + 2\vec{\hat{z}} \times \vec{q} + \nabla\Phi \; = \; 0 \\ \nabla \cdot \vec{q} \; = \; 0 \\ \vec{n} \cdot \vec{q} + \Omega^{-1}\, L^{-1} \vec{n} \cdot \vec{v} \; = \; 0 \end{cases} \tag{4}$$

where $\Phi = \frac{\phi}{\Omega^2\, L^2}$ and $\phi = \frac{p}{\rho_f}$, Φ being called the non-dimensional dynamic pressure. The time dependence of the variables is considered as $e^{i\sigma t}$ where σ is the nutation frequency in the reference frame attached to the mantle. When used in non-dimensional equations as above, the frequency to be used is σ_m instead of σ, where $\sigma = \Omega\sigma_m$. In the case of computing the Length-of-day variations, the velocity $\vec{v}$ can be expressed by$\vec{v} = -\Omega m_3 \vec{\hat{z}} \times \vec{r}$.

After some algebra on the first line of Equation (4), one can obtain the following expression for $\vec{q}$ as a function of $\nabla\Phi$:

$$\vec{q} \;=\; \frac{-i\,\sigma_m}{4 - \sigma_m^2} \left[\nabla\Phi - \frac{2}{i\,\sigma_m}\, \vec{\hat{z}} \times \nabla\Phi - \frac{4}{\sigma_m^2}\, (\vec{\hat{z}} \cdot \nabla\Phi)\, \vec{\hat{z}} \right] \tag{5}$$

where $\vec{\hat{z}}$ is the normalized vector in the direction of $\vec{\Omega}$.

Using the above equation for $\vec{q}$ and the incompressibility condition for this fluid velocity (second line of Equation 4), one obtains the following equation for Φ: $\nabla^2\Phi - \frac{4}{\sigma_m^2} \frac{\partial^2 \Phi}{\partial Z^2} \; = \; 0$ where Z is a particular coordinate (related to the cylindrical coordinates involving the colatitude θ), which is equal to $\sqrt{\frac{\sigma_m}{2}} \cos\theta$. The factor $(1 - \frac{4}{\sigma_m^2})$ being negative, this mixed differential equation is an hyperbolic differential equation has the typical form of a wave propagation equations. It expresses that small perturbations of an equilibrium configuration can propagate in the fluid in the form of waves which are the so-called inertial waves because they are controlled by the Coriolis force as a restoring force.

The solution of this equation for Φ must be proportional to the associated Legendre functions of the first kind; it has the following form:

$$\Phi \;=\; \sum_{l=1} a_l^k\, P_{lk}(\frac{\sigma_m}{2})\, Y_l^k(\theta, \lambda). \tag{6}$$

where $P_{lk}(\frac{\sigma_m}{2})$ are the fully normalized associated Legendre polynomials, and the $Y_l^k(\theta, \lambda)$, the fully normalized associated Legendre functions as introduced before, and the a_l^k are coefficients that will be determined in the next step using the boundary conditions (third line of Equation 4). Using the boundary condition for $\vec{q}$ (third line of Equation 4) and the expression of $\vec{q}$ in function of Φ (Equation 5), substituting the above solution for Φ (Equation 6), after a lot of algebra, one obtains for the first order in the small quantities such as ϵ_n^m:

$$\sum_{l,k} Y_l^k \left[k P_{lk}(\frac{\sigma_m}{2}) - \left(1 - \frac{\sigma_m^2}{4}\right) P'_{lk}(\frac{\sigma_m}{2}) \right] a_l^k - 2\left(1 - \frac{\sigma_m^2}{4}\right) \sum_{n=1} m \epsilon_n^m Y_n^m m_3 = 0 \tag{7}$$

where $Y_l^k \equiv Y_l^k(\theta, \lambda)$. Equation (7) allows us to solve for the a_l^k as a function of the ϵ_n^m and σ_m; because we have only kept first order in ϵ_n^m, the a_l^k coefficients are linear functions of ϵ_n^m. It must be noted that this equation can be considered component per component by projection on each $Y_{l'}^{m'}$ and that we can solve as well for each ϵ_n^m separately and then sum over all the contributions.

3. RESULTS

Substituting the solution for Φ, provided in Equation (6) as a function of the coefficients a_l^k, in the expression for $\vec{q}$ provided by Equation (5), and computing the contribution to the torque, one gets the $\vec{q}$-contribution to topographic torque $\vec{\Gamma}_{topo}^{\phi}$ as a function of a_l^k (or equivalently ϵ_n^m by means of Equation 7). The results are shown in Figure 2.

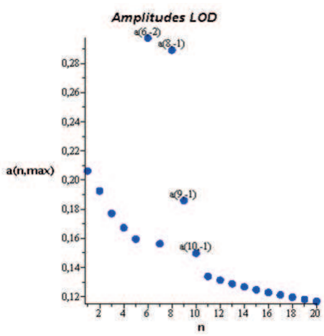

Figure 2: Amplitude of the a_l^k for a_l^k being the maximum values for each n.

4. CONCLUSIONS

From our computation we have seen that some topography coefficients provide larger contributions to LOD than others and that there are some differences with respect to Wu and Wahr (1997), even when using the same CMB topography. But the main features such as the degree 6 being larger than the others, has been recovered.

With this computation, we have understood that the degrees and orders of these amplifications do not depend on the geometry/dimension/topography amplitudes of core but rather on the degrees and orders of the excitation and topography expressed in spherical harmonics.

We must note however that our computations/conclusions may change with an inner core.

5. REFERENCES

Dehant V., and Folgueira M., 2011, “Analytical expression of the topographic torque on the CMB”, Proceedings of EGU General Assembly 2011 (submitted).

Mathews P.M., Buffett B.A., Herring T.A. and Shapiro I.I., 1991a, “Forced nutations of the Earth: Influence of inner core Dynamics. I. Theory”, J. Geophys. Res., 96, B5, pp 8219-8242.

Mathews P.M., Buffett B.A., Herring T.A. and Shapiro I.I., 1991b, “Forced nutations of the Earth: Influence of inner core Dynamics. II. Numerical results and comparisons”, J. Geophys. Res., 96, B5, pp 8243-8258.

Mathews P.M. and Guo J.Y., 2005, “Visco-electromagnetic coupling in precession-nutation theory”, J. Geophys. Res., 110, B02402, DOI: 10.1029/2003JB002915.

Wu X. and Wahr J.M., 1997, “Effects of non-hydrostatic core-mantle boundary topography and core dynamics on Earth rotation”, Geophys. J. Int., 128, pp 18-42.

IMPROVING UT1 PREDICTIONS USING SHORT-TERM FORECASTS OF ATMOSPHERIC, OCEANIC, AND HYDROLOGIC ANGULAR MOMENTUM

R.S. GROSS
Jet Propulsion Laboratory, California Institute of Technology
4800 Oak Grove Drive, Pasadena, CA 91109, USA
e-mail: Richard.Gross@jpl.nasa.gov

ABSTRACT. Predictions of UT1 are greatly improved when dynamical model-based forecasts of the axial component of AAM are used as proxy length-of-day forecasts. Here, the impact on short-term UT1 predictions of additionally incorporating forecasts of oceanic and hydrologic angular momentum is evaluated.

1. INTRODUCTION

Accurate, short-term predictions of the variations in the Earth's rotation are needed for a number of reasons including precise tracking and navigation of interplanetary spacecraft. Short-term Universal Time (UT1) variations are particularly difficult to predict because, apart from largely predictable tidal variations, they are caused mainly by torques associated with changes in atmospheric circulation, making their prediction as challenging as predicting the weather.

Atmospheric effects on the Earth's rotation are generally studied by examining changes in atmospheric angular momentum (AAM). In the absence of external torques, and neglecting other effects like those due to the oceans and hydrology, the angular momentum of the Earth-atmosphere system is conserved. So when the angular momentum of the atmosphere changes, the angular momentum of the solid Earth must change by an equal but opposite amount, leading to changes in the Earth's rotation.

The angular momentum of the atmosphere, computed from the wind and pressure fields of numerical weather forecast models such as those operated by the US National Centers for Environmental Prediction (NCEP) and the European Centre for Medium-Range Weather Forecasts (ECMWF), is available from the International Earth Rotation and Reference Systems Service (IERS) Global Geophysical Fluids Center (GGFC) Special Bureau for the Atmosphere (SBA; http://www.aer.com/scienceResearch/diag/sb.html) and the IERS Associated Product Center at the GFZ German Research Centre for Geosciences in Potsdam (http://www.gfz-potsdam.de/portal/gfz/Struktur/Departments/Department+1/sec13/services). In addition to computing the angular momentum of the atmosphere at regularized epochs of the observations, forecasts of the AAM are also computed from these numerical weather forecast models.

A number of studies have shown that predictions of UT1 are greatly improved when forecasts of the axial component of AAM from numerical weather prediction models are used as proxy length-of-day (LOD) forecasts (Freedman et al. 1994; Johnson et al. 2005). For example, and as shown below, the accuracy of JPL's 7-day predictions of UT1 are improved by about a factor of 1.7 when AAM forecasts from NCEP are used. Here, AAM forecasts from both the NCEP and the ECMWF numerical weather prediction models are used to predict UT1 and the results compared and contrasted. The impact of additionally incorporating forecasts of oceanic angular momentum (OAM) and hydrologic angular momentum (HAM) on short-term UT1 predictions is also evaluated.

2. APPROACH

The impact of AAM, OAM, and HAM forecasts on the accuracy of short-term UT1 predictions is evaluated using JPL's Kalman filter-based approach to combining and predicting Earth orientation

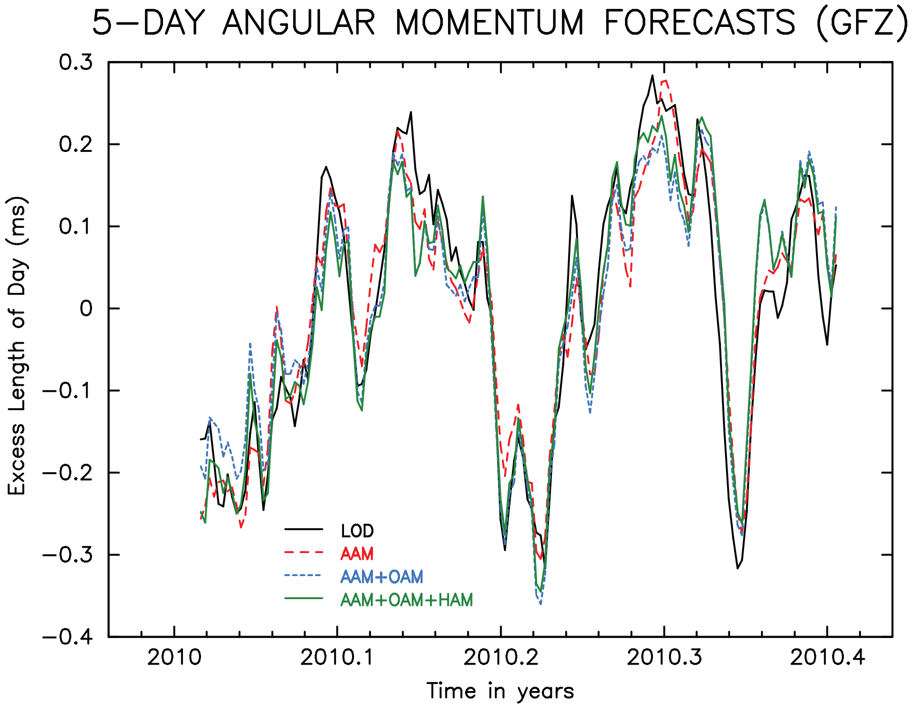

Figure 1: Comparison of observed LOD variations in milliseconds (ms, solid black line) during 06 January 2010 to 02 June 2010 with variations caused by 5-day forecasted ECMWF/GFZ AAM (long dashed red line), sum of 5-day forecasted ECMWF/GFZ AAM and OMCT OAM (short dashed blue line), and sum of 5-day forecasted ECMWF/GFZ AAM, OMCT OAM, and LSDM HAM (solid gray or green line). The AAM is the sum of the wind and inverted barometer pressure terms, the OAM is the sum of the current and bottom pressure terms, and the HAM is the sum of the motion and mass terms, although the motion term is negligibly small. A mean has been removed from each displayed time series. Note that the comparison is being done at the forecasted epoch, not at the epoch 5 days earlier when the forecasts were generated.

parameters (Gross et al. 1998). For nearly three decades, the Kalman Earth Orientation Filter (KEOF) has been used at JPL to combine and predict Earth orientation parameters in support of interplanetary spacecraft tracking and navigation. Kalman filters are commonly used to estimate parameters of some system when a stochastic model of the system is available and when the data contain noise. For the purpose of combining Earth orientation series, the system consists of the usual Universal Time and polar motion (UTPM) parameters, their excitations, and full covariance matrices. The data consist of observed Earth orientation parameters (EOPs) and covariance matrices. KEOF not only estimates all three UTPM parameters along with their excitations but also predicts them out to 78 days in advance. Since the early 1990s, KEOF has included AAM forecasts from NCEP, obtained through the IERS SBA (Salstein et al. 1993), in order to improve the accuracy of the UT1 predictions.

KEOF is run operationally once-a-day to generate the combined and predicted EOP files that are delivered to the spacecraft navigation teams. Here, 143 of the operational runs done between 01 January 2010 and 28 May 2010 have been re-done using AAM forecasts from ECMWF instead of the NCEP forecasts that were used operationally. The ECMWF AAM forecasts were obtained from the GFZ German Research Centre for Geosciences in Potsdam (Dill and Dobslaw 2010). Since the angular momentum of only the 5-day wind forecasts from NCEP are used at JPL to improve the UT1 predictions, only the 5-day wind forecasts from ECMWF/GFZ have been used here. In order to study the impact of forecasted pressure variations on the accuracy of UT1 predictions, the respective 5-day inverted barometer (ib) pressure AAM forecasts have been added to the wind forecasts.

The ECMWF forecast fields are used at GFZ to force the Ocean Model for Circulation and Tides (OMCT; Dobslaw and Thomas 2007) in order to generate forecasted OAM and are also used to force the Land Surface Discharge Model (LSDM; Dill 2008) in order to generate forecasted HAM. These models

Forecast Series	LOD Variance Explained	Correlation with LOD
ECMWF/GFZ 5-day wind forecasts	84.311%	0.9215
ECMWF/GFZ 5-day wind+ib forecasts	88.566%	0.9426
GFZ 5-day AAM+OAM (mass+motion)	86.093%	0.9294
GFZ 5-day AAM+OAM+HAM (mass+motion)	87.625%	0.9361

Table 1: Comparison of 5-day AAM, OAM, and HAM Forecasts with Observed LOD

are run in such a manner that global freshwater mass conservation is enforced (Dobslaw et al. 2010). The resulting 5-day forecasted OAM and HAM (sum of mass and motion terms) have been added to the total 5-day forecasted ECMWF/GFZ AAM (sum of wind and ib pressure terms) in order to study their impact on UT1 predictions.

3. RESULTS

Figure 1 compares the observed LOD variations (solid black line) from the COMB2009 combined EOP series (Ratcliff and Gross 2010) with those caused by the total 5-day forecasted ECMWF/GFZ AAM (long dashed red line), those caused by the sum of the total 5-day forecasted ECMWF/GFZ AAM and OMCT OAM (short dashed blue line), and the sum of the total 5-day forecasted ECMWF/GFZ AAM, OMCT OAM, and LSDM HAM (solid gray or green line). Note that the comparison is done at the epoch of the forecast, not at the epoch 5 days earlier when the forecasts were generated. As can be seen, the 5-day forecasted AAM, AAM+OAM, and AAM+OAM+HAM series are all in good agreement with the LOD observations.

Table 1 gives the percentage of the observed LOD variance explained by different combinations of the angular momentum series. It also gives their correlation with the LOD observations. Adding the 5-day forecasted ib pressure term to the 5-day forecasted wind term increases the agreement with the LOD observations with both the LOD variance explained and the correlation becoming greater. Adding the total 5-day forecasted OAM to the total AAM causes the agreement with LOD to get worse. Adding the total HAM to the total AAM+OAM improves the agreement, although the best agreement with the LOD observations is obtained with just the total AAM.

Table 2 gives the error in the predictions of UT1 out to 7 days in the future when different combinations of the angular momentum series are used. If no AAM forecasts are used to predict UT1 then the error in the predictions grows rapidly, becoming 34.9 centimeters (cm) after just 7 days. But when AAM forecasts are used, the error is dramatically reduced, becoming only 20.3 cm after 7 days when the total NCEP forecasts are used, and 19.9 cm when the total ECMWF forecasts are used. For both the NCEP and ECMWF forecasts, adding the respective 5-day forecasted ib pressure terms to the wind terms improves the UT1 prediction accuracy only slightly. The accuracy of the UT1 predictions is no better when the NCEP and ECMWF forecasts are averaged than it is when just the ECMWF forecasts are used (either wind term alone or the sum of the wind and ib pressure terms).

Adding the total OMCT OAM forecasts to the total ECMWF/GFZ AAM forecasts improves the UT1 predictions, reducing the error of the 7-day prediction from 19.9 cm to 17.6 cm. However, additionally adding the total LSDM HAM forecasts slightly degrades the UT1 prediction error.

4. DISCUSSION AND SUMMARY

All of the 5-day forecasted angular momentum series studied here agree quite well with the observed LOD during 06 January 2010 to 02 June 2010 (see Figure 1 and Table 1). This high degree of agreement allows AAM forecasts to be used as proxy LOD forecasts when predicting UT1. However, the forecasted angular momentum series that agreed best with the LOD observations, the total AAM forecasts, does not lead to the best UT1 predictions. The best UT1 predictions are obtained when the sum of the total ECMWF/GFZ AAM and OMCT OAM forecasts are used.

Adding OAM to AAM forecasts improves the accuracy of the UT1 predictions by about 12%. This relatively small degree of improvement is to be expected given the high degree of agreement that already exists between LOD and AAM. But adding OAM to AAM forecasts should greatly improve polar motion

Forecast Series	Prediction Interval, days							
	0	1	2	3	4	5	6	7
No forecasts	1.2	2.6	5.7	10.1	15.5	21.5	28.0	34.9
NCEP 5-day wind forecasts	1.2	2.2	4.3	7.0	10.1	13.3	16.7	20.7
NCEP 5-day wind+ib forecasts	1.2	2.2	4.1	6.7	9.7	12.8	16.2	20.3
ECMWF/GFZ 5-day wind forecasts	1.2	2.2	4.2	6.8	9.7	12.8	16.2	20.2
ECMWF/GFZ 5-day wind+ib forecasts	1.2	2.1	4.1	6.5	9.4	12.4	15.9	19.9
Average NCEP+ECMWF/GFZ 5-day wind	1.2	2.2	4.2	6.9	9.8	12.9	16.3	20.2
Average NCEP+ECMWF/GFZ 5-day wind+ib	1.2	2.1	4.1	6.6	9.4	12.5	15.9	19.9
ECMWF/GFZ AAM+OAM (mass+motion)	1.2	2.0	3.6	5.7	8.1	10.7	13.8	17.6
ECMWF AAM+OAM+HAM (mass+motion)	1.2	2.0	3.7	5.8	8.2	11.0	14.1	18.0

Table 2: UT1 Prediction Error. Prediction day 0 is the epoch of the last LOD measurement. The epoch of the last UT1 measurement is typically a few days earlier. Units of UT1 prediction error are cm. A change in rotation equivalent to a 1 ms change in UT1 corresponds to a 46.3 cm displacement of the Earth's surface at the equator.

predictions since the oceans are known to be a major source of polar motion excitation.

In summary, it is found that by reprocessing operational runs done during 01 January 2010 to 28 May 2010, the 7-day UT1 prediction accuracy is about 2% better when the 5-day wind AAM forecasts from ECMWF/GFZ are used instead of those from NCEP. Including the respective 5-day ib pressure AAM forecasts with the wind forecasts improves the UT1 predictions by about 2%. Averaging the 5-day NCEP and ECMWF/GFZ AAM forecasts does not improve the UT1 predictions. Finally, we find that adding the total 5-day OMCT OAM forecasts to the total ECMWF/GFZ AAM forecasts improves the accuracy of the UT1 predictions by about 12%, but additionally adding the total 5-day LSDM HAM forecasts is found to slightly degrade the accuracy of the UT1 predictions.

Acknowledgements. The work described in this paper was performed at the Jet Propulsion Laboratory, California Institute of Technology, under contract with the National Aeronautics and Space Administration.

5. REFERENCES

Dill, R., 2008, "Hydrological model LSDM for operational Earth rotation and gravity field variations", Scientific Technical Report STR08/09, GFZ Potsdam, Germany, 35p.

Dill, R. and Dobslaw, H., 2010, "Short-term polar motion forecasts from Earth system modeling data", J. Geodesy, 84, pp. 529-536.

Dobslaw, H. and Thomas, M., 2007, "Simulation and observation of global ocean mass anomalies", J. Geophys. Res., 112, C05040, doi:10.1029/2006JC004035.

Dobslaw, H., Dill, R., Groetzsch, A., Brzezinski, A., Thomas, M., 2010, "Seasonal polar motion excitation from numerical models of atmosphere, ocean, and continental hydrosphere", J. Geophys. Res., doi:10.1029/2009JB007127.

Freedman, A.P., Steppe, J.A., Dickey, J.O., Eubanks, T.M., Sung, L.-Y., 1994, "The short-term prediction of universal time and length of day using atmospheric angular momentum", J. Geophys. Res. (Solid Earth), 99(B4), pp. 6981–6996.

Gross, R.S., Eubanks, T.M., Steppe, J.A., Freedman, A.P., Dickey, J.O., Runge, T.F., 1998, "A Kalman filter-based approach to combining independent Earth orientation series", J. Geodesy, 72, pp. 215-235.

Johnson, T.J., Luzum, B.J., Ray, J.R., 2005, "Improved near-term Earth rotation predictions using atmospheric angular momentum analysis and forecasts", J. Geodyn., 39, pp. 209–221.

Ratcliff, J.T. and Gross, R.S., 2010, "Combinations of Earth orientation measurements: SPACE2009, COMB 2009, and POLE2009", JPL Publ. 10-22, Pasadena, Calif., 29 pp.

Salstein, D.A., Kann, D.M., Miller, A.J., Rosen, R.D., 1993, "The Sub-bureau for Atmospheric Angular Momentum of the International Earth Rotation Service: A meteorological data center with geodetic applications", Bull. Amer. Meteor. Soc., 74, pp. 67-80.

ASYMMETRIC EXCITATION OF THE POLAR MOTION

C. BIZOUARD
Observatoire de Paris, 61 av. de l'Observatoire
e-mail: christian.bizouard@obspm.fr

ABSTRACT. Polar motion analysis is commonly based upon symmetric linearised Euler-Liouville equations. Then, in absence of forcing, the rotation pole coordinates evolve in the same way. Actually, expressing thoroughly the pole tide and taking into account the triaxiality, the equations become asymmetric with respect to the pole coordinates. This leads to the formulation of the generalised Euler-Liouville equation, for which we derive a general solution. We discuss possible observational consequences.

1. INTRODUCTION

The geophysical analysis of the polar motion is generally accomplished thanks to the *symmetric* linearised Euler-Liouville equations in the Terrestrial Reference Frame (TRF):

$$m + \frac{i}{\tilde{\sigma}_c}\dot{m} = \Psi \tag{1}$$

where $m = m_1 + im_2$ is the complex equatorial coordinate of the instantaneous rotation pole and $\tilde{\sigma}_c = \sigma_c(1 + \frac{i}{2Q})$ the complex Chandler angular frequency of which the quality factor Q (within the range $40 - 200$) accounts for dissipation. There Ψ means the modelled equatorial excitation, produced by mass transports within the Earth or its hydro-atmospheric layers. In this equation m_1 and m_2 are driven in the same way by geophysical excitation. Actually it neglects any asymmetric effects resulting from triaxiality and rotational deformation. Whereas triaxiality has been investigated by many studies (see e.g. Chen and Shen 2010), the asymmetry brought by ocean pole tide is oddly overlooked. The consistent analysis of both effects is done. This leads to an extended form of equatorial Euler-Liouville equation, for which we propose a general solution.

2. ASYMMETRIC EFFECTS

We start from the Euler-Liouville equation for a triaxial Earth expressed in the frame of the mean principal axes $Gx'y'z'$ associated with inertia moment $A < B < C$ (Munk and Mac Donald 1960):

$$m'_1 - \frac{B}{(C-A)\Omega}\dot{m}'_2 = \Psi'_1 \qquad m'_2 + \frac{A}{(C-B)\Omega}\dot{m}'_1 = \Psi'_2 \tag{2}$$

where m'_1 and m'_2 are rotation pole coordinates related to $Gx'y'z'$, and Ψ'_1 and Ψ'_2 are the components of the equatorial excitation function in $Gx'y'z'$. We adopt the values $A = 8.010083(9)\,10^{37}$ kg m^2, $B = 8.010260(9)\,10^{37}$ kg m^2, $C = 8.036481(9)\,10^{37}$ kg m^2 derived by Chen and Shen (2010) from EGM08 gravity model. Note that $(B-A)/A \approx 2,5\,10^{-5}$ whereas $(A-C)/A \approx (B-C)/B \approx 3\,10^{-3}$. The equatorial excitation function is given by:

$$\Psi'_1 = \frac{\Omega c'_{13} + h_1}{\Omega(C-A)} + \frac{\Omega\dot{c}'_{23} + \dot{h}'_2}{\Omega^2(C-A)} - \frac{L'_2}{\Omega^2(C-A)}\ ; \quad \Psi'_2 = \frac{\Omega c'_{23} + h_2}{\Omega(C-B)} - \frac{\Omega\dot{c}'_{13} + \dot{h}'_1}{\Omega^2(C-B)} + \frac{L'_1}{\Omega^2(C-B)} \tag{3}$$

where $c_{1/2,3}$ are the off-diagonal inertia moment increments, $h_{1/2}$ the components of the relative angular momentum and $L_{1/2}$ the external torque. The triaxiality affects the geophysical function at the level of 1%. Insofar as the modelling of the latter effect has a much larger relative uncertainty, the difference between $C-A$ and $C-B$ can be cast aside. Let $\bar{A}$ be the mean equatorial moment given by:

$$\bar{A} = (A+B)/2 \tag{4}$$

then, the equatorial geophysical function is approximated by:

$$\Psi' = \Psi'_1 + i\Psi'_2 = \frac{\Omega c' + h'}{\Omega(C-\bar{A})} - \frac{i}{\Omega}\frac{\Omega\dot{c}' + \dot{h}'}{(C-\bar{A})\Omega} + i\frac{L}{\Omega^2(C-\bar{A})} \tag{5}$$

After having introduced the *triaxial coefficients*:

$$r = \sqrt{\frac{(C-A)A}{(C-B)B}} = 1.00379 \ , \ \ \Delta r = r - 1 \approx 3.8\,10^{-3} \tag{6}$$

the equations (2) can be shortened into the form:

$$m_1' - \frac{1-\Delta r}{\sigma_e}\dot m_2' = \Psi_1' \qquad\qquad m_2' + \frac{1+\Delta r}{\sigma_e}\dot m_1' = \Psi_2' \tag{7}$$

with $\sigma_e = \sqrt{\frac{(C-A)(C-B)}{AB}}\Omega = e\ \Omega$ (second order terms in Δr are neglected). For practical purpose we have to go back to the Terrestrial Reference Frame $Gxyz$. In a first approximation the triaxial frame can be deduced from the TRF by the axial rotation of angle $\lambda_A = -14.92851(8) \pm 0.0010°$ (Chen and Shen 2010). So for going back to TRF, we apply the complex coordinate change $m = m'e^{i\lambda_A}$ (correspond to the axial rotation of angle $-\lambda_A$ which brings inertia axis Gx' in coincidence with Gx). In the TRF we have also $c = c'e^{i\lambda_A}$. Finally we obtain:

$$m_1 - \frac{1-\Delta r\cos 2\lambda_A}{\sigma_e}\dot m_2 - \frac{\Delta r \sin 2\lambda_A}{\sigma_e}\dot m_1 = \Psi_1; \quad m_2 + \frac{1+\Delta r\cos 2\lambda_A}{\sigma_e}\dot m_1 + \frac{\Delta r\sin 2\lambda_A}{\sigma_e}\dot m_2 = \Psi_2 \tag{8}$$

with λ_A the longitude of the first principal inertia axis and $\Psi = \Psi_1 + i\Psi_2$ the geophysical excitation expressed in TRF:

$$\Psi = \Psi_1 + i\Psi_2 = \frac{\Omega c + h}{\Omega(C-\bar A)} - \frac{i}{\Omega}\frac{\Omega\dot c + \dot h}{(C-\bar A)\Omega} + i\frac{L}{\Omega^2(C-\bar A)} \tag{9}$$

In a first approach we neglect the influence of the fluid core. Let $\tilde k_2 = k_2 + i\Bbbk_2 \approx 0.3(1+i0.01)$ be the solid Earth Love number, the rotational excitation associated with the solid Earth is expressed by:

$$\chi^r = \frac{\tilde k_2}{k_s} m \tag{10a}$$

By analogy the rotational angular momentum function caused by ocean pole tide is

$$\chi_o^r = \frac{\tilde k_o}{k_s}\left[A_1 m_1 + A_2 m_2 + i(A_2 m_1 + B_2 m_2)\right] \tag{10b}$$

where we have introduced the equivalent oceanic Love number $\tilde k_o = k_o + i\Bbbk_o$ with the real part

$$k_o = \frac{3}{5}(1 + k_2 - h_2)\frac{\rho_o}{\rho_\oplus}(1 + k_2') \approx 0.05 \tag{11}$$

There $k_2 = 0.3$, $h_2 = 0.6$ and $k_2' = -0.3$, $\rho_o \sim 1035$ kg/m^3 is the ocean density, and $\rho_\oplus = 5500$ kg/m^3 the Earth density. According to this notation, the Desai's model of equilibrium ocean pole tide (Desai 2002, Eq. 24) is associated with the coefficients $A_1 = 0.942 \quad B_1 = -0.021 \quad B_2 = 0.746$.

3. GENERALIZED EULER-LIOUVILLE EQUATIONS

Removing the rotational excitations (10a) and (10b) from the right hand side of (8) and putting them into the left hand side, the equatorial Euler-Liouville equations take the generalised form:

$$\begin{array}{l} (1+\alpha_1)m_1 - \frac{1+\beta_1}{\sigma_e}\dot m_2 + \gamma_1 m_2 + \frac{\delta_1}{\sigma_e}\dot m_1 = \Psi_1^{(pure)} \\ (1+\alpha_2)m_2 + \frac{1+\beta_2}{\sigma_e}\dot m_1 + \gamma_2 m_1 + \frac{\delta_2}{\sigma_e}\dot m_2 = \Psi_2^{(pure)} \end{array} \tag{12a}$$

with the particular coefficients

$$\begin{array}{lll} e' = \frac{\sigma_e}{\Omega} & \alpha_1 = -\frac{k_2 + k_o A_1 - \Bbbk_o B_1}{k_s} & \alpha_2 = -\frac{k_2 + k_o B_2 + \Bbbk_o B_1}{k_s} \\ & \beta_1 = -\Delta r\cos 2\lambda_A + e'\frac{k_2 + k_o B_2 + \Bbbk_o B_1}{k_s} & \beta_2 = \Delta r\cos 2\lambda_A + e'\frac{k_2 + k_o A_1 - \Bbbk_o B_1}{k_s} \\ & \gamma_1 = \frac{\Bbbk_2 - k_o B_1 + \Bbbk_o B_2}{k_s} & \gamma_2 = -\frac{\Bbbk_2 + k_o B_1 + \Bbbk_o A_1}{k_s} \\ & \delta_1 = -(\Delta r\sin 2\lambda_A + e'\frac{\Bbbk_2 + k_o B_1 + \Bbbk_o A_1}{k_s}) & \delta_2 = \Delta r\sin 2\lambda_A + e'\frac{-\Bbbk_2 + k_o B_1 - \Bbbk_o B_2}{k_s} \end{array} \tag{12b}$$

By contrast to (1) these equations exhibit an asymmetry with respect to m_1 and m_2 and cannot be reduced to a complex form. The generic form (12a) define the *Generalised Linearised Euler-Liouville*

Equations. In the considered case here-above, the coefficients of these equations respect the following orders of magnitude $|\alpha_i| \lesssim 0.3 \quad |\beta_i|, |\gamma_i|, |\delta_i| \lesssim e \quad$ (e= flattening).

Solution in frequency domain (12a) gives two eigenfrequencies. The positive one is associated with the Chandler angular frequency including the damping:

$$\tilde{\sigma}_c \approx \sigma_e \left[\sqrt{(1+\alpha_1)(1+\alpha_2)} + i\frac{1}{2}\left(\gamma_2 - \gamma_1 + \delta_1(1+\alpha_2) + \delta_2(1+\alpha_1)\right) \right] \tag{13}$$

The second eigenfrequency is the complex conjugate of $\tilde{\sigma}_c$:

$$\tilde{\sigma}_c^- = -\sigma_c^* \tag{14}$$

In frequency domain the solution is given by:

$$\left| \begin{array}{l} m_1(\sigma) \\ m_2(\sigma) \end{array} \right. \approx -\frac{\sigma_e^2}{(\sigma - \tilde{\sigma}_c)(\sigma - \tilde{\sigma}_c^-)} \left| \begin{array}{l} (1+\alpha_2 + i\frac{\sigma}{\sigma_e}\delta_2)\Psi_1(\sigma) + \left(i\frac{\sigma}{\sigma_e}(1+\beta_1) - \gamma_1\right)\Psi_2(\sigma) \\ (1+\alpha_1 + i\frac{\sigma}{\sigma_e}\delta_1)\Psi_2(\sigma) - \left(i\frac{\sigma}{\sigma_e}(1+\beta_2) + \gamma_2\right)\Psi_1(\sigma) \end{array} \right. \tag{15}$$

Let $\Psi(t) = \Psi_0 e^{i\sigma_0 t}$ be a circular excitation at angular frequency σ_0. From (15) its effect on on polar motion is:

$$\begin{aligned} m(t) = &-\frac{\Psi_0 \sigma_e^2}{(\sigma_0 - \tilde{\sigma}_c)(\sigma_0 - \tilde{\sigma}_c^-)} \left[\left(2 + \alpha_1 + \alpha_2 + i(\gamma_1 - \gamma_2) + \frac{\sigma_0}{\sigma_e}(2 + \beta_1 + \beta_2) + i\frac{\sigma_0}{\sigma_e}(\delta_1 + \delta_2) \right) \frac{e^{i\sigma_0 t}}{2} \right. \\ &\left. + \left(\alpha_2 - \alpha_1 - i(\gamma_1 + \gamma_2) - \frac{\sigma_0}{\sigma_e}(\beta_2 - \beta_1) - i\frac{\sigma_0}{\sigma_e}(\delta_2 - \delta_1) \right) \frac{e^{-i\sigma_0 t}}{2} \right] \end{aligned} \tag{16a}$$

where we identify the quantities A^+, A^-, m_0^+ and m_0^- by:

$$m(t) = -\frac{\Psi_0 \sigma_e^2}{(\sigma_0 - \tilde{\sigma}_c)(\sigma_0 - \tilde{\sigma}_c^-)} \left(A^+ e^{i\sigma_0 t} + A^- e^{-i\sigma_0 t} \right) = m_0^+ e^{i\sigma_0 t} + m_0^- e^{-i\sigma_0 t} \tag{16b}$$

4. POSSIBLE OBSERVATIONAL CONSEQUENCE

We apply the previous formalism to the case of a triaxial Earth partially covered by the oceans. Putting the corresponding coefficients (12b) into (13), the Chandler angular frequency is:

$$\tilde{\sigma}_c \approx \sigma_e \left(1 - \frac{\tilde{k}_2}{k_s} - \frac{\tilde{k}_o}{k_s}\frac{A_1 + B_2}{2} \right) \tag{17}$$

After having introduced the *effective Love number* $\tilde{k} = \tilde{k}_2 + \tilde{k}_o\frac{A_1+B_2}{2}$ the Chandler frequency takes the classic form $\tilde{\sigma}_c \approx \sigma_e\left(1 - \frac{\tilde{k}}{k_s}\right)$. According to (16) a circular excitation at frequency σ_0 produces two circular components in polar motion with opposite frequencies, that is an elliptical motion. The term circling in the same direction as the excitation has the complex amplitude:

$$m_0^+ = -\frac{\Psi_0 \sigma_e^2}{(\sigma_0 - \tilde{\sigma}_c)(\sigma_0 - \tilde{\sigma}_c^-)} A^+ \tag{18}$$

with

$$A^+ \approx \left(1 - \frac{\tilde{k}_2}{k_s} - \frac{\tilde{k}_o}{k_s}\frac{A_1 + B_2}{2} \right)^* + \frac{\sigma_0}{\sigma_e} = \frac{\sigma_c^* + \sigma_0}{\sigma_e} = \frac{\sigma_0 - \tilde{\sigma}_c^-}{\sigma_e} \tag{19}$$

Thus:

$$m_0^+ = -\frac{\Psi_0 \sigma_e}{(\sigma_0 - \tilde{\sigma}_c)} \tag{20}$$

and we recognise the classic term (or symmetric), exhibiting the unique resonance at Chandler angular frequency $\tilde{\sigma}_c$. But there appears also an exotic term of opposite frequency $-\sigma_0$ given by the complex amplitude:

$$m_0^- = -\frac{\Psi_0 \sigma_e^2}{(\sigma_0 - \tilde{\sigma}_c)(\sigma_0 - \tilde{\sigma}_c^-)} A^- \tag{21}$$

with

$$A^{-} \approx \frac{k_o}{k_s}\frac{A_1 - B_2}{2} + i\frac{k_o}{k_s}B_1 - \frac{\sigma_0}{\sigma_e}\left(\Delta r e^{i\lambda_A} + e'\frac{k_o}{k_s}\frac{A_1 - B_2}{2} + ie'\frac{k_o}{k_s}B_1\right) \tag{22}$$

Although the term m_0^- presents a double resonance, both at Chandler frequency and its opposite, it is strongly reduced by the smallness of the coefficient A^- (same order than e). We compute the ratio m_0^-/Ψ_0 in two cases: i) oceans and triaxiality are considered together ii) triaxiality is neglected. Results, displayed in Figure 1a, show that m_0^-/Ψ_0 reaches about 3 mas at the resonance frequencies, and mostly results from the oceans alone (biaxiality). The relative impact of m_0^- with respect to the classical effect m_0^+ is quantified by the ratio m_0^-/m_0^+, represented in Figure 1b, and completed by the corresponding ellipticity of the induced polar motion, given by the relative difference between small and great axes:

$$\frac{|m_0^+| + |m_0^-| - (|m_0^+| - |m_0^-|)}{|m_0^+| + |m_0^-|} = \frac{2|m_0^-|}{|m_0^+| + |m_0^-|} \tag{23}$$

The ratio m_0^-/m_0^+ reaches a maximum of 3 at $-\sigma_c$ (1 for ellipticity). Far from this frequency it remains less than 0.05 (0.01 for ellipticity). Considering the retrograde annual term of the polar motion (10 mas),

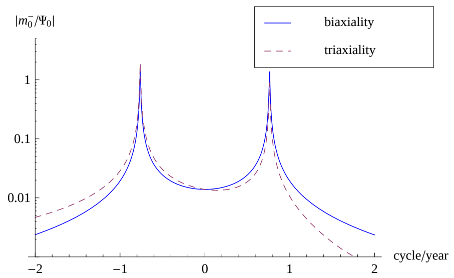

(a)

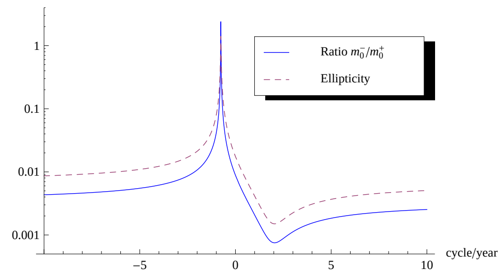

(b)

Figure 1: (a) Complex ratio m_0^-/Ψ_0 (amplitude) in function of the excitation frequency, exhibiting the double resonance at Chandler frequency and its opposite. (b) Amplitude of the ratio m_0^-/m_0^+ and corresponding ellipticity as function of the frequency.

we see that the asymmetric effect can reach 0.5 mas. On the other hand the geodetic excitation function is radically modified in the vicinity of the Chandler frequency, as we havw shown in Bizouard (2012).

5. CONCLUSION

Pole tide excitation and Earth triaxiality introduce asymmetry which cannot be neglected in light of the contemporaneous pole coordinates accuracy (0.1 mas). Their consistent handling leads to an extended form of the linearised Euler-Liouville equation, for which we propose a general solution. Casting aside the influence of the fluid core, we analyse possible observational consequence of the asymmetric effect. A given circular excitation gives an elliptical polar motion, the ellipticity reaching 1 in the vicinity of the negative Chandler frequency. Quantification of these effects strongly rely on ocean pole tide modelling. A complete derivation and the consequence on geodetic excitation can be found in Bizouard (2012).

6. REFERENCES

Bizouard C., 2012, *Interprétation géophysique du mouvement du pôle de l'heure au siècle*, Mémoire d'Habilitation à diriger des recherches, 260 p., ftp://syrte.obspm.fr/pub/bizouard/habil.pdf, Observatoire de Paris, in press.

Chen W. and Shen W., 2010, New estimates of the inertia tensor and rotation of the triaxial nonrigid Earth *J. Geophys; Res.* 115, B12419, doi:10.1029/2009JB007094

Desai, 2002, Observing the pole tide with satellite altimetry, *J. Geophys. Res. (Oceans)* 107 (C11):7-1. DOI 10.1029/2001JC001224

Munk W. H. et Mac Donald G., 1960, *The rotation of the Earth*, Cambridge University Press.

RECENT IMPROVEMENTS IN THE IERS RAPID SERVICE PREDICTION CENTER PRODUCTS FOR 2010 AND 2011

N. STAMATAKOS[1], B. LUZUM[1], B. STETZLER[1], N. SHUMATE[1],
M.S. CARTER[2], J. TRACEY[1]

[1] USNO, 3450 Massachusetts Avenue, N. W., Washington, D. C. 20392
e-mail: nick.stamatakos@usno.navy.mil

[2] NOFS, 10391 West Naval Observatory Road, Flagstaff, Arizona 86001-8521

ABSTRACT. The International Earth Rotation and Reference Systems Service (IERS) Rapid Service/Prediction Center (RS/PC) has made improvements to its products and has also updated a web-based Earth Rotation matrix calculator to be compliant with IERS Tech Note (TN) 36 equinox-based theory. The improvements to the Earth Orientation Parameters (EOP) products include updating the RS/PC EOP system to the 08C04 from the 05C04 system (the official long-term IERS EOP series), using the Geospatial Information Authority of Japan (GSI) Intensives in generating operational EOPs, and making the 2x daily EOPs available publicly. Also, being investigated on beta test software development systems is generating a 4x daily EOP solution, using new Universal Time-like GPS (UTGPS) updates based on more recent IGS (International GNSS Service) Ultras, and using a Kalman Filter (KF) in place of a cubic spline for generating EOPs.

1. OVERVIEW OF RS/PC SOLUTION

The daily EOP combination and prediction (CP) solution (finals.daily) is produced at approximately 17:00 UTC each day; the weekly version (Bulletin A) is produced on Thursdays at approximately 17:30 UTC. Both provide EOP values which include polar motion, UT1-UTC, and celestial pole offsets (CPO), with results located at `http://maia.usno.navy.mil`. These EOP values are used in determining the terrestrial to celestial transformation matrix. Data from Very Long Baseline Interferometry (VLBI), the Global Positioning System (GPS), Satellite Laser Ranging (SLR), and Atmospheric Angular Momentum (AAM) are used in these solutions. Further details about inputs, processes, numbers of users, and results can be obtained in Stamatakos et al. (2011) and references provided therein.

2. CHANGE OF REFERENCE SYSTEM FROM 05C04 to 08C04

To maintain consistency with the official IERS long-term EOP solution, which was officially changed on February 1, 2011, adjustments were made to the RS/PC EOP products by early February 2011. The IERS long-term EOP solution, called the C04, is produced by the IERS Earth Orientation Center, Observatoire de Paris (OP), and on February 1, 2011, they made changes to Polar Motion and UT1-UTC portions of the EOP set, and renamed the series from 05C04 to 08C04.

Prior to the official February 1, 2011 switch-over, OP had provided the new C04 series to the RS/PC. New systematic corrections (a bias and/or slope) were computed relative to the new 08C04 for each input data series and for the weekly, updated RS/PC EOP solution, finals.data. During this period before February 1, several test combination solutions were run, wherein the input data series weights and smoothing parameters were adjusted to attempt to improve the RS/PC root mean squared RMS residuals in Polar Motion and UT1-UTC relative to the new 08C04 series. Once the systematic corrections, weights, and smoothing parameters were determined, a new weekly solution file (finals.data) was produced, which contained a new combination solution based on these new parameters, going back to February, 2010.

The RS/PC made a new updated daily (finals.daily) and updated weekly (Bulletin A and finals.data) solution available to users on Tuesday, February 1, and Thursday February 3, respectively, both adjusted to the new C04 system. However, based on user comments after February 3, it was shown that the Polar Motion Y solution could be improved further, and the entire process for Polar Motion Y was repeated, with a better resulting RS/PC daily and weekly solution produced on February, 10, 2011.

3. ADDITION OF GSI VLBI INTENSIVES TO THE RS/PC EOP SOLUTION

In August 2010, UT1-UTC results produced by GSI, from VLBI Intensives observed on the weekends, were added as inputs to the operational RS/PC EOP solution. (The term, VLBI Intensives, is discussed in Kronschnabl, 2009.) Each of these weekend observations are made well before noon UTC, and the GSI process is automated and can generate an EOP solution within an hour of the observation; thus making the input available to the 17:00 UTC RS/PC solution.

GSI is not always able to produce a UT1-UTC result on the same day as the observations. For instance, from early May to the end of October 2011, GSI produced same day results 65% of the time. In the earlier months of GSI EOP generation, the automated analysis process caused some failures to produce a same day result, but lately, the automated process has improved – the last reported automated analysis failure was on June 11, 2011; lately, any failures have been due to other reasons, such as data transfer problems.

To show the improvement in UT1-UTC 1-day predictions when using GSI Intensives in the RS/PC solution, daily EOP results were regenerated on a test computer for several past months. For each Saturday and Sunday from February to October, 2011 when a GSI Intensive was available, the EOPs were regenerated on a test computer with that Saturday or Sunday GSI Intensives removed. The results shown in Figure 1 indicate that with the GSI Intensives (shown with blue "X" symbols), the UT1-UTC RMS error was 52 μseconds (μs), and without (shown with green "O" symbols), the error was 65 μs.

4. TWICE-DAILY EOP SOLUTION

A second RS/PC EOP solution, computed at 03:10 UTC, is available at `http://maia.usno.navy.mil/2xdaily`. Normally, the integrated IGS length-of-day (LOD) and Polar Motion inputs produced from "18-hour" and "0-hour" IGS Ultra-Rapid orbit solutions (IGS Ultras) – which contain the LOD and Polar Motion results reported for 06:00 and 12:00 UTC, respectively – are the only additional inputs beyond those inputs used in the 17:00 UTC daily solution; however, when VLBI Intensives processing is occasionally late and misses the 17:00 UTC daily solution it will be added to the next 03:10 UTC solution. Also, this solution is not as closely monitored by RS/PC personnel as the 17:00 UTC daily solution. Users who notice problems with the solution may contact the RS/PC at ser7@maia.usno.navy.mil.

5. IMPROVEMENTS OF UT1-UTC PREDICTIONS IN RECENT YEARS

The UT1-UTC 1 to 10 day prediction errors have been decreasing over the last decade, as shown in Figure 2. Prediction errors are the differences between the daily produced EOP predictions and the combination solution computed several weeks later for the same epochs; e.g., a 1-day UT1-UTC prediction error (of -0.0188 seconds) produced at MJD 55700 is the difference between UT1-UTC at MJD 55701 in finals.daily (-0.286607) and the combination value at MJD 55701 produced several weeks later in finals.data (-0.2677922). The 1-day RMS prediction errors for UT1-UTC were 110 μs in 2009, 75 μs in 2010, and, for the first 10 months of 2011, it was 57 μs. The reduced latency of Int1 and Int2 VLBI Intensives (Stamatakos et al., 2008), the removal of AAM LOD from the EOP combination (but not from the prediction) (Stamatakos et al., 2011), and the addition of the integrated IGS Ultras in April 2011 have decreased the short term UT1-UTC errors. In 2009, latencies of 1 day or less, between observation to inclusion of VLBI inputs in the EOP solution, occurred only 30% of the time; by 2011, the percentage had increased to 70%. The 5 and 10 day prediction errors for 2011 have been slightly worse than for 2009 and 2010, and the reasons are still under investigation.

6. A NEW UTGPS SOLUTION BASED ON IGS ULTRAS

The USNO GPS Analysis Division has produced a new UTGPS Ultras solution, a UT1-like solution based on IGS Ultras orbits. The solution is produced daily around 09:00 UTC, just after the "6-hour" IGS Ultra solution becomes available. A special EOP solution is being generated around 09:15 UTC each day on a test computer using this new input. From February to the end of October, 2011, a 15% improvement in the "0-day prediction" of UT1-UTC has been observed when using this new input versus the operational solution produced at 17:00 UTC on the previous day. Figure 3 contains a plot of the 0-day prediction error for both the new UTGPS Ultras solution and for the operational solution since February, 2011. The new UTGPS Ultras solution had an rms error of 24.8 μs, versus 29.4 μs for the operational solution. It is hoped that with new changes to the filtering of the provided UTGPS Ultras solution (Stamatakos et al., 2009), the error can be further decreased.

7. UPGRADE OF EO MATRIX CALCULATOR TO TN 36 EQUINOX-BASED

The terrestrial to celestial (T2C) transformation matrix calculator was upgraded on the USNO EOP server at `http://maia.usno.navy.mil/t2c36e/t2c36e.html`. The T2C transformation relates the orientation of the International Terrestrial Reference Frame (ITRF) to the Geocentric Celestial Reference System (GCRS). An earlier version of the T2C calculator based on TN 32 is described in Stamatakos et al. (2011), and the upgraded version (which is slightly more accurate) is based on TN 36 using the equinox-based equations listed therein. The reference, just listed, provides details about the user-interface, observable inputs, optional intermediate outputs, and output formats for the TN 32 option. Many details between the two versions are similar, and Table 1 provides a list of changes made.

Item	TN 32	TN 36
User Interface:		
Input option for librations	NO	YES
Intermediate outputs option for Greenwich Apparent Sideral Time (GAST) and Bias matrix	NO	YES
Special user-requested output format	YES	NO
Tidal models:		
Long period tides	DS_ZONT.F	RG_ZONT2.F
Subdiurnal/diurnal tides	ORTHO_EOP.F	ORTHO_EOP.F
SOFA software at `http://www.iausofa.org/`	`2007_0810_F.html`	`2010_1201.html`

Table 1: Summary of changes from TN 32 to TN 36 T2C transformation matrix calculator.

8. FUTURE DIRECTIONS

Four EOP solutions will be produced each day starting in 2012, and sometime in the next several years, an EOP solution will be regenerated any time a new input data series is available. Also, an EOP combination based on a Kalman Filter approach is under study – results for UT1-UTC are similar to those obtained from the USNO EOP operational solution. More testing and development of this Kalman Filter approach will be done in the future. Finally, improvements in Polar Motion predictions using combined AAM plus Ocean Angular Momentum (OAM) are under investigation by RS/PC personnel.

9. REFERENCES

Kronschnabl G., "Experiences with regular e-transer of geodetic INTENSIVE data at Wettzell", Proceedings of Science, 2009, The 8th International e-VLBI Workshop, EXPReS09, June 22-26, 2009, Madrid, Spain, pp. 1-5; (`http://pos.sissa.it/archive/conferences/082/034/EXPReS09_034.pdf`)

Stamatakos N., Luzum B., Stetzler B., Shumate, N., Carter, M. S., (2011) "Recent improvements in the IERS Rapid Service/Prediction Center Products", *Journées Systèmes de Référence Spatio-Temporels* 2010, pp. 184-187

Stamatakos N., Luzum B., Stetzler B., Wooden W., Shultz E., (2009) "Recent improvements in the IERS Rapid Service/Prediction Center Products", *Journées Systèmes de Référence Spatio-Temporels* 2008, pp. 160-163

Stamatakos N., Luzum B., Wooden W., (2008) "Recent improvements in the IERS Rapid Service/Prediction Center Products", *Journées Systèmes de Référence Spatio-Temporels* 2007, pp 163-166.

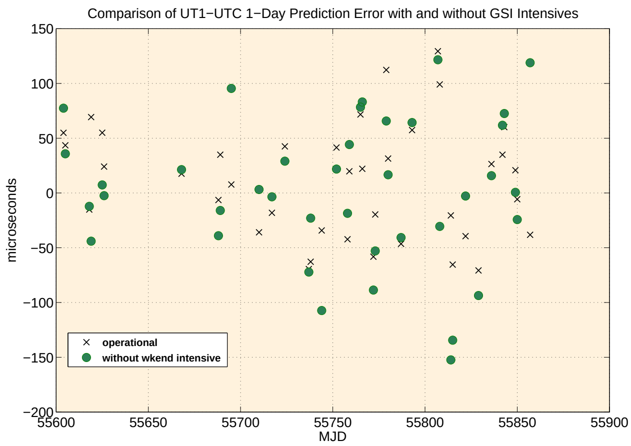

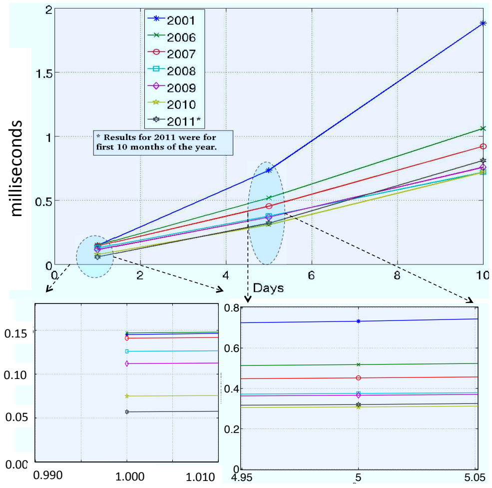

Figure 1 (left): Comparison of UT1-UTC 1-day prediction error with and without GSI Intensives.
Figure 2 (right): UT1-UTC 1 to 10 day prediction error from 2001 to 2011.

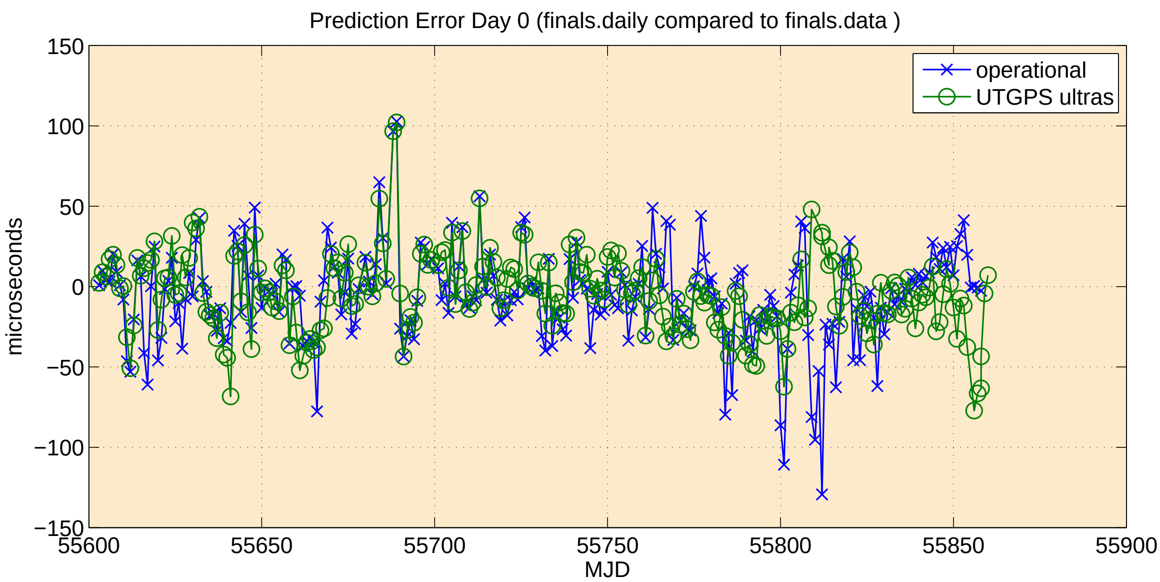

Figure 3: Comparison of last combination epoch errors using UTGPS-Ultras input and the current operational EOP solution. RMS error for UTGPS Ultras solution was 24.8 μseconds. RMS error for the operational solution was 29.4 μseconds.

RAPID EOP CALCULATION USING VIEVS SOFTWARE

M.B. KAUFMAN, S.L. PASYNOK
National Research Institute for Physical and Radio-technical Measurements (VNIIFTRI)
141570, VNIIFTRI, Mendeleevo, Moscow Reg., RUSSIA
e-mail: mark@vniiftri.ru, pasynok@vniiftri.ru

ABSTRACT. For many years the Main Metrological Center of Russian Time, Frequencies and Earth Rotation Service has carried out rapid EOP processing based on GNSS, VLBI, and SLR observations. In 2011 we began a new processing with the production of VLBI EOP series using VieVS (Vienna VLBI Software) developed at the Institute of Geodesy and Geophysics (IGG), Vienna University of Technology. According to requirements of rapid calculations (quick automatic processing without participation of operator), the special control program *eop_start.m* was written. No changes were made in VieVS blocks when developing the control program. Its task is receiving, processing and sending data without manual interaction. The structure and advantages of the control program, and results of EOP calculations are shown.

1. INTRODUCTION

State Time, Frequency and Earth Rotation Service (RTE) is a permanently functioning system. Many Russian facilities and organizations are incorporated and/or related to this common scientific, technical and metrological activity, which includes continuous reproduction, keeping and dissemination of the national time scale and also the determination of Earth's orientation parameters (EOP).

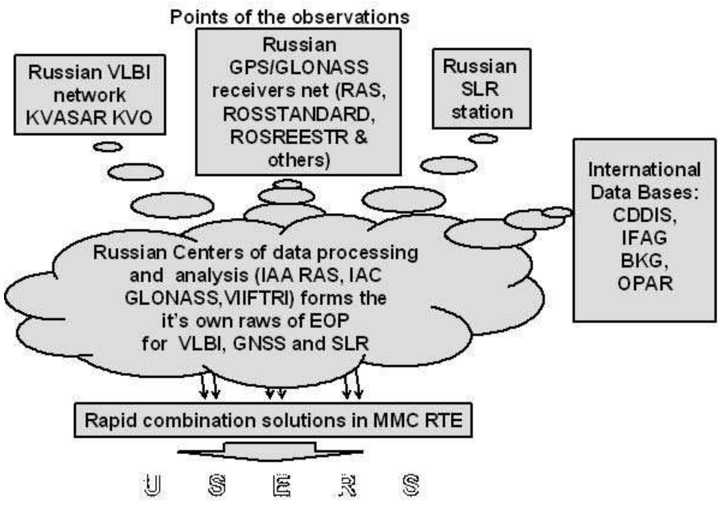

Figure 1: The information streams at RTE

The Main Metrological Center (MMC) of the Service is located at the National Research Institute for Physical and Radio-technical Measurements (VNIIFTRI). The information streams in RTE are represented in Figure 1. For many years, MMC has carried out operational EOP evaluation by combination and processing of the VLBI, GNSS and SLR observations (Kaufman M., Pasynok S., 2010). VLBI observations processing has been started at MMC in 2004 using the software package OCCAM5.0. The actual MMC processing program of EOP evaluations from VLBI observations is now obsolete and requires replacement with more modern and precise programs. There are some modern packages of VLBI

data processing: CALC/SOLVE, MODEST, OCCAM, GLORIA, SteelBreeze, GEOSAT, VieVS, c5 ++, ARIADNA, and others. After careful analysis we have chosen program VieVS developed at the Institute of the Geodesy and Geophysics (IGG) of the Vienna Technical University (Boehm J. et al.,2009). Why did we choose this program? Because it has the following attractive properties.
Firstly, VieVS - the multisystem program, can practically work in any operation system. Secondly, it was written in Matlab language. This program language makes it easy to describe the most complicated mathematical operations and allows to make changes into an initial code of the program if necessary. Besides MMC researchers have a long-term experience with Matlab programming. Thirdly, in the program the graphic representation of results is provided, which considerably facilitates the analysis of results in case of problems with VLBI session processing.

2. MOTIVATION

For operational EOP estimation it was necessary to automate the following operations: collecting new VLBI observations files, detecting VLBI session type and setting processing parameters, launching the VieVS program, analysis of intermediate results, detecting outliers and bad stations, and starting of repeated calculations if necessary, converting results into standard IVS format and saving on the ftp server.
As result, the special managing program *eop_start.m* has been developed at VNIIFTRI. This program executes the operations mentioned above. No changes were made in VieVS blocks when developing the managing program.

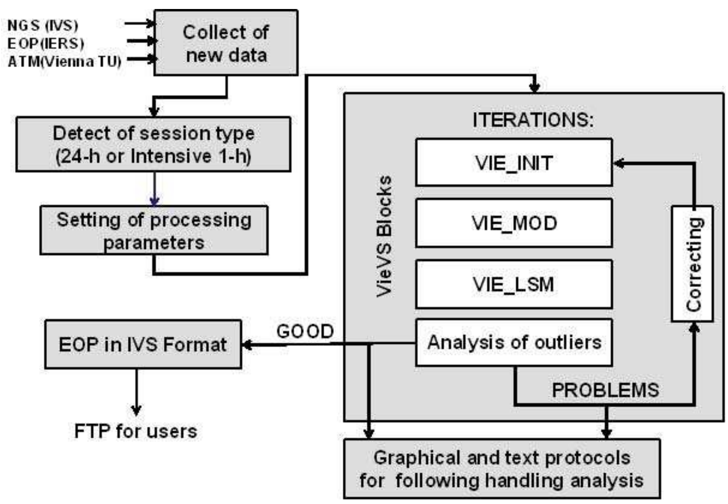

Figure 2: Algorithm of the managing program *eop_start.m*

3. ALGORITHM OF THE MANAGING PROGRAM

Schematically the algorithm of the managing program *eop_start.m* is represented in Figure 2. As a whole, it consists of consecutive operations listed in section 2. The explanations are following with some details.
For 1-hour sessions, UT1-UTC and zenith wet delay parameters are estimated. For daily 24-hour sessions all 5 EOP and also parameters of the troposphere are estimated. Outliers are identified if $O - C > 5\ \sigma_0$. However, we do not use the RMS as σ_0, but the inter quartile range (IQR). For the data containing the big outliers, IQR is more representative than RMS. Problematic stations are found with the following simple condition. The station is considered as problematic if less then 10 % from an average of all observations for given stations are remaining after rejection of outliers for the given station. The information about outliers and problematic stations is kept in OUTLIERS and OPT files of the program VieVS. Results of processing of each session are interpolated for a mean epoch of observations and the string of results in IVS EOP format is formed. This string contains modified Julian date (MJD), Earth's orientation parameters ($x, y, UT1, dX, dY$) and their uncertainties; weighed root-mean-square errors (WRMS) of divergences in

delays in picoseconds, correlation coefficients: $k(x, y); k(x, UT1); k(y, UT1); k(dX/dY)$, velocities of EOP changes and their uncertainty, and also other data (IVS-code of stations, etc.). Strings are inserted into result files in the chronological order. Later, the operator carries out analysis of results of automatic processing mode. He might process observations again in standard interactive mode if it is needed.

4. RESULTS

For experimental tests we carried out EOP evaluations for the time span from January 2010 to September 2011. The EOP discrepancies between evaluated values and EOPC04 series are represented in Figure 3. RMS are 19 and 11 microseconds for 1-hour and daily sessions, respectively. Using the VieVS program with our module for operative EOP evaluations from VLBI observations will start on January 2012.

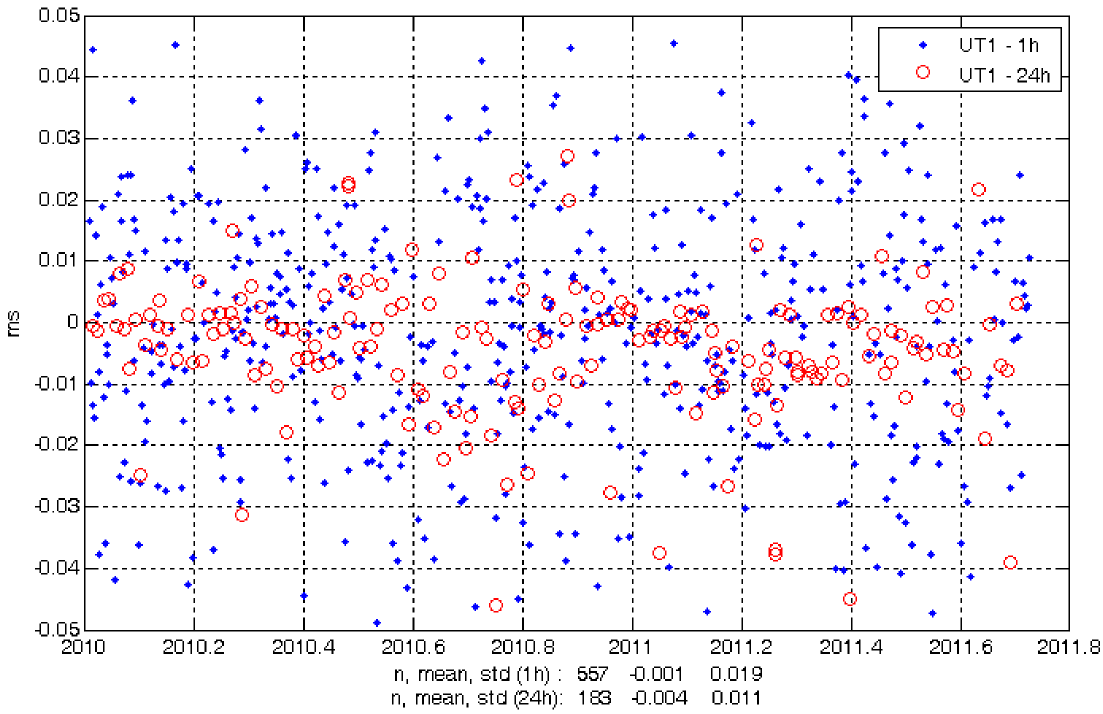

Figure 3: Results (the discrepancies between observables and EOP_C04) of UT1-UTC with VieVS and the managing program for automatic processing *eop_start.m*

5. REFERENCES

Kaufman, M., Pasynok, S., 2010, "Russian state time and Earth rotation service: observation, EOP series, prediction", Artificial Satellites, Vol. 45, No. 2, pp. 81-86.

Boehm, J.,Spicakova, H., Plank, L., Teke, K., Pany, A., Wresnik, J., Englich, S., Nilsson, T., Schuh, H., Hobiger, T., Ichikawa, R., Koyama, Y., Gotoh, T., Kubooka, T., Otsubo, T., "Plans for the Vienna VLBI Software VieVS $http:\backslash\backslash www.u-bordeaux1.fr/vlbi2009/proceedgs/36\_Boehm.pdf>$", Proceedings of the 19th European VLBI for Geodesy and Astrometry Working Meeting, 24-25 March 2009, Bordeaux, edited by G. Bourda, P. Charlot, and A. Collioud, 2009.

ANALYSIS OF THE HIGH FREQUENCY COMPONENTS OF EARTH ROTATION DEMODULATED FROM VLBI DATA

A. BRZEZIŃSKI[1,2] and S. BÖHM[3]
[1] Faculty of Geodesy and Cartography, Warsaw University of Technology, Warsaw, Poland
[2] Space Research Centre, Polish Academy of Sciences, Warsaw, Poland
e-mail: alek@cbk.waw.pl
[3] Institute of Geodesy and Geophysics, Vienna University of Technology, Vienna, Austria

ABSTRACT. In the recent work (Böhm et al., 2011) we demonstrated the application of the complex demodulation technique to Very Long Baseline Interferometry (VLBI) parameter estimation for the determination of high frequency signals in Earth rotation. Here we present preliminary results of the analysis of diurnal, semidiurnal, terdiurnal and quarterdiurnal components of polar motion and UT1, demodulated from VLBI data.

1. INTRODUCTION

Polar motion and universal time UT1 contain high frequency signals (diurnal and subdiurnal) which are predicted by physics. This is not the case for precession-nutation which, by definition, does not contain variations with periods shorter than 2 days. Note, however, that when precession-nutation is expressed in the Earth-fixed reference system it becomes a nearly diurnal phenomenon.

The high frequency signals in Earth rotation are relatively small, not exceeding the level of 1 milliarcsecond (mas), nevertheless already well measurable and important for understanding the high frequency dynamics of the Earth and its fluid layers. The main contributions are from diurnal and semidiurnal ocean tides. Significantly smaller (< 0.1 mas) are the so-called librations in polar motion and UT1 caused by direct influence of the tidal gravitation upon the triaxial figure of the Earth, and less regular signals associated with the atmospheric thermal tides.

Early attempts to estimate high frequency signals in Earth rotation were concentrated on the determination of the parameters of strictly harmonic models with known tidal arguments. However, this approach is not adequate for the investigation of atmospheric and nontidal oceanic effects which are irregular to a certain extent and thus should be expressed by time series. One method to describe high frequency variations is to shorten the sampling interval of polar motion coordinates and UT1 to the hourly level. An alternative method is to introduce as additional parameters, the instantaneous amplitudes and phases of the sinusoidal terms with frequencies of exactly 1 and 2 cycle per sidereal day – cpsd (with possible extension to 3, 4, ..., N cpsd), while keeping the basic sampling interval of 1 day. The last method, originally proposed by Herring and Dong (1994), is an application of the so-called complex demodulation method; see (Brzeziński, 2012) for a detailed description of the theoretical background of complex demodulation and its application for the analysis of Earth rotation and corresponding geophysical excitation data. Recently, the algorithm of complex demodulation was implemented by Böhm et al. (2011) into a dedicated version of the Vienna VLBI Software VieVS. They processed all VLBI sessions over 1984.0-2010.5 and estimated simultaneously the time series of the celestial pole offsets and of diurnal, semidiurnal, terdiurnal and quarterdiurnal components of polar motion and UT1. We will discuss here preliminary results of the analysis of those high frequency signals demodulated from VLBI data.

2. COMPLEX DEMODULATION IN VLBI DATA ANALYSIS

The following parametrization of polar motion (PM) and universal time (UT1) has been applied for complex demodulation of VLBI data

$$\begin{bmatrix} x(t) \\ y(t) \end{bmatrix} = \sum_{\substack{\ell=-N \\ \ell\neq -1}}^{N} \left\{ \begin{bmatrix} x_\ell(t) \\ y_\ell(t) \end{bmatrix} \cos(\ell\Phi) + \begin{bmatrix} y_\ell(t) \\ -x_\ell(t) \end{bmatrix} \sin(\ell\Phi) \right\}, \tag{1}$$

$$\Delta \mathrm{UT1}(t) = \sum_{\ell=0}^{N} \left[u_\ell^c(t)\cos(\ell\Phi) + u_\ell^s(t)\sin(\ell\Phi)\right], \tag{2}$$

where x, y are the reported coordinates of polar motion, ΔUT1=UT1$-$UTC is the difference of UT1 and the uniform time scale UTC, Φ =GMST+π, GMST stands for Greenwich Mean Sidereal Time and $x_\ell(t)$, $y_\ell(t)$, $u_\ell^s(t)$, $u_\ell^c(t)$ are assumed to be slowly varying functions of time t. When estimated from VLBI data, these time dependent amplitudes are treated as constant during one 24-hour session. We also assume that the argument Φ is a linear function of time $\Phi = \Omega t + \Phi_\circ$, where Ω denotes the mean angular velocity of diurnal sidereal rotation (equal 2π rad/sidereal day = $7\,292\,115 \times 10^{-11}$ rad/s) and $\Phi_\circ$ is a constant phase referred to the initial epoch $t = 0$. Let us make the following remarks:

- the terms $\ell = 0$ of the expansion in Equations (1)–(2) are the long periodic components of PM and UT1 estimated in standard adjustment;
- the terms $\ell = \pm 1, \pm 2, \pm 3, \pm 4, \ldots$, express quasi diurnal, semidiurnal, terdiurnal, quarterdiurnal, ..., variations in PM (retrograde/prograde for $-/+$) and in UT1;
- adding the $\ell = -1$ term to the expansion (1) gives an equivalent representation of the celestial pole offsets δX, δY, in a sense that $[x_{-1}(t), -y_{-1}(t)] = [\delta X(t), \delta Y(t)]$ in the first order approximation;
- the high frequency components ($\ell \neq 0$) of UT1 are expressed by two parameters, the time dependent cosine and sine amplitudes $u_\ell^c(t)$, $u_\ell^s(t)$.

The complex parameters

$$p_n(t) = x_n(t) - iy_n(t); \qquad \Delta \mathrm{UT1}_n(t) = \left[u_n^c(t) - iu_n^s(t)\right]/2, \tag{3}$$

are designated as complex demodulate of polar motion and UT1, respectively, at frequency $\ell\Omega$.

3. DATA ANALYSIS

Böhm et al. (2011) performed several runs of VLBI data processing over 1984.0–2010.5 based on the complex demodulation model described by Equations (1)–(2) with $N = 4$ and adopting different additional assumptions. In the following analysis we will use the high frequency components of polar motion and UT1 demodulated by applying the modified VLBI Software VieVS under the following assumptions:
– Equation (1) includes the $\ell = -1$ term of PM while the celestial pole offsets δX, δY are not estimated;
– the estimation incorporates all a priori models recommended by the IERS Conventions 2010 (Petit and Luzum, 2010), including the IAU 2006/2000A precession-nutation model, the model of diurnal and semidiurnal variations due to ocean tides and the model of libration in UT1 and PM.

The output comprises 12 complex-valued time series expressing diurnal, semidiurnal, terdiurnal and quarterdiurnal components of retrograde PM, prograde PM, and UT1. Each series contains about 3500 data points with irregular sampling. At first we apply a least-squares algorithm with weighting to estimate corrections to the main tidal constituents, including the S_1, S_2 and S_3 terms associated with the atmospheric thermal tides. Further analysis includes both the original demodulated series and their reduced version derived by removal of the estimated corrections to the tidal terms. The next step is the application of a Gaussian low-pass filter with full width at half-maximum (FWHM)=10 days to simultaneously smooth and interpolate the time series at 5-days intervals. Finally we perform the maximum entropy method (MEM) spectral analysis (Brzeziński, 1995) of the smoothed original and reduced time series. The spectral analysis has been done over the entire time interval 1984.0–2010.5, as well as over different sub-intervals obtained by removal of certain parts of early data.

The demodulated components of polar motion and UT1, raw original data with the error bars and smoothed values, are shown in Figure 1. A first simple observation is that the time series are not homogeneous in time. There are much higher errors in early data. Moreover, the smoothed signals contain in the first years some variability which is not confirmed by more recent data. The last conclusion is also confirmed by the MEM analysis which produces very complicated power spectra (not shown here) when computed over the entire interval, and more and more smooth spectra after removal of early data. Our conclusion is that an acceptable homogeneity of data is reached after rejection of all data prior to 1990.0. Table 1 shows that for the smoothed signals the sample standard deviations computed over 1984.0–2010.5 and over 1990.0–2010.5 differ by the factor of two to three.

Based on the above conclusion we show in Figure 2 the MEM power spectra estimated only over the reduced time interval 1990.0–2010.5. We compare in the plots the spectra of the original series and after removal of the estimated correction model.

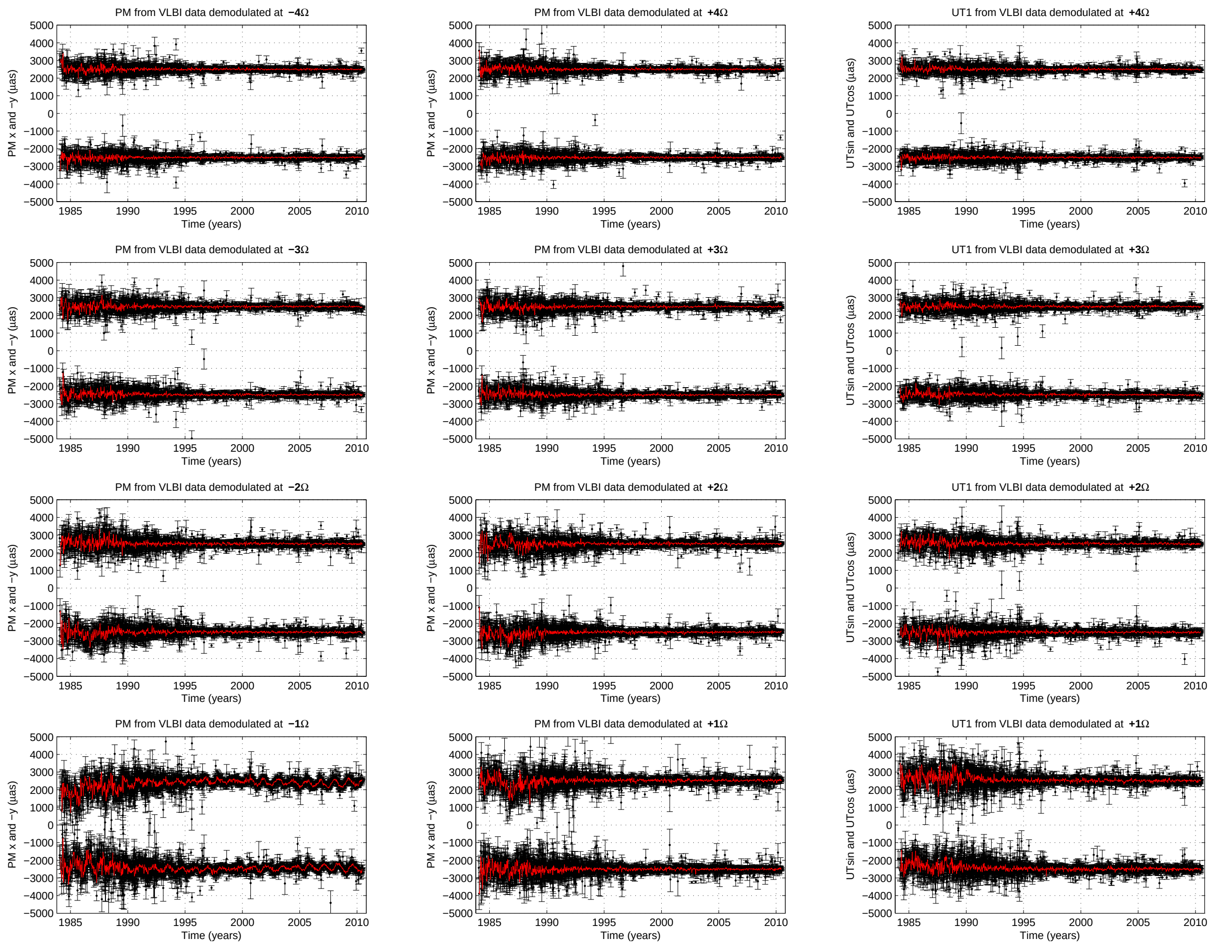

Figure 1: Demodulated high frequency components of retrograde (left) and prograde (middle) polar motion, and UT1 (right). Shown are raw values with 1-σ error bars and smoothed values. Analysis has been done over 1984.0–2010.5 with the a priori IERS models applied.

Another observation from Figure 1 and Table 1 is that the signals demodulated at $\ell\Omega$ decrease in size with increasing ℓ. The retrograde diurnal component of polar motion, which expresses the residual precession-nutation including the free core nutation signal, exceeds in size all other signals considered here by the factor of at least two. The corresponding power spectrum shown in Figure 2 does not differ from earlier results based on the analysis of the celestial pole offsets.

The MEM power spectra of all series representing the terdiurnal and quarterdiurnal components of PM and UT1 and the prograde semidiurnal component of PM, do not show any significant spectral feature. Moreover, removal of the empirical correction model does not introduce any important change to the spectral plots. Hence, our analysis does not confirm earlier claims based on Earth rotation data from the CONT campaigns about the existence of the 8-hour oscillation in polar motion and/or in UT1.

The most important change introduced by removal of the empirical correction model is in case of prograde diurnal and retrograde semidiurnal components of PM and in diurnal and semidiurnal components of UT1. It consists in smoothing the spectrum and reduction of its power.

4. SUMMARY AND CONCLUSIONS

The high frequency components of polar motion and UT1, diurnal, semidiurnal, terdiurnal and quarterdiurnal, have been demodulated from VLBI data using the modified Vienna VLBI Software VieVS. Our analysis of demodulated data sets shows

– data prior 1990 is too noisy and, therefore, should not be used for the time domain analysis and geophysical interpretation;

Series	Demodulation frequency -4Ω	-3Ω	-2Ω	-1Ω	Ω	2Ω	3Ω	4Ω
PM (1984.0–2010.5)	114	142	189	336	236	189	135	114
PM (1990.0–2010.5)	47	59	73	174	84	66	56	46
UT1 (1984.0–2010.5)					86	54	38	32
UT1 (1990.0–2010.5)					37	25	21	17

Table 1: Standard deviation of the smoothed high frequency components of polar motion and UT1 (μas)

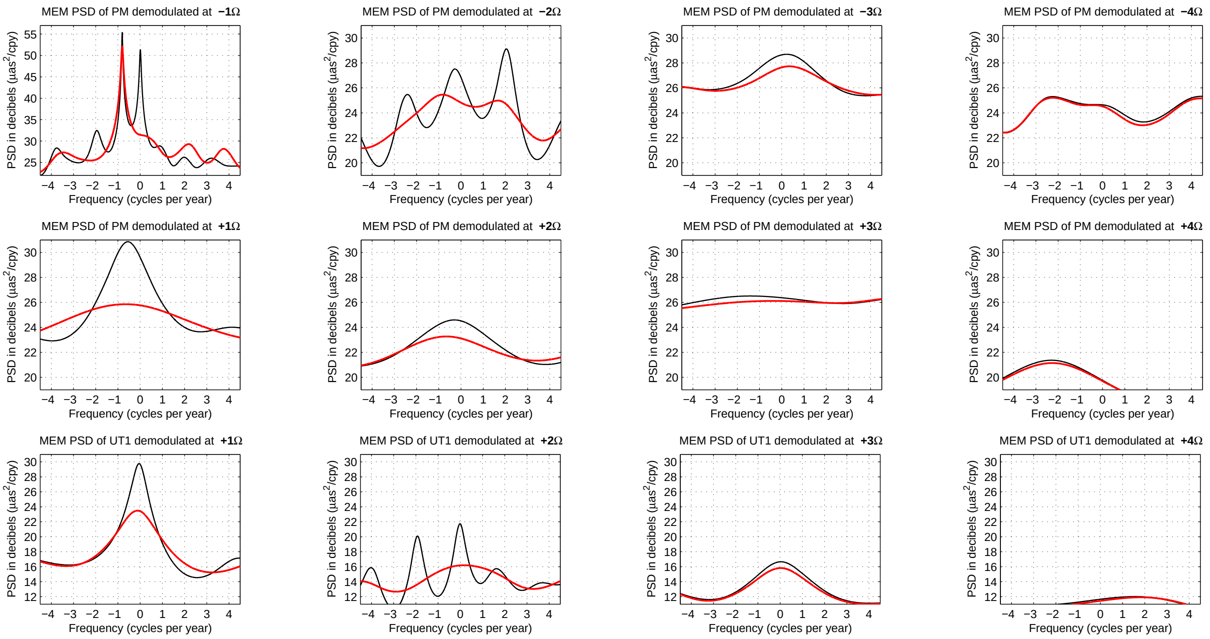

Figure 2: Maximum entropy power spectra of demodulated high frequency components of Earth rotation, thin black – with the a priori IERS models applied, thick red – after additional removal of the residual tidal terms. Period of analysis 1990.0 – 2010.5.

– spectral analysis of terdiurnal and quarterdiurnal terms does not reveal any sharp spectral line; hence, our analysis does not confirm the existence of 8-hour oscillation either in PM or in UT1.

A future task is the comparison of demodulated PM and UT1 series to the corresponding components demodulated from atmospheric and nontidal oceanic angular momentum data.

Acknowledgments. Participation of A.B. in the Journées 2011 has been supported by the Polish National Science Centre under grant No. 1570/B/T02/2011/40.

5. REFERENCES

Böhm, S., Brzeziński, A., and Schuh, H., 2011, "Complex demodulation in VLBI estimation of high frequency Earth rotation components", J. Geodynamics, doi: 10.1016/j.jog.2011.10.002.

Brzeziński, A., 2012, "On estimation of high frequency geophysical signals in Earth rotation by complex demodulation", J. Geodynamics, doi: 10.1016/j.jog.2012.01.008.

Brzeziński, A., 1995, "On the interpretation of maximum entropy power spectrum and cross-power spectrum in earth rotation investigations", manuscripta geodaetica, 20, pp. 248–264.

Herring, T. A., and Dong, D., 1994, "Measurement of diurnal and semidiurnal rotational variations and tidal parameters of Earth", J. Geophys. Res., 99(B9), pp. 18,051–18,071.

Petit, G., and Luzum, B. (eds.), 2010, "IERS Conventions (2010)", IERS Tech. Note no. 36, Bundesamts für Kartographie und Geodäsie, Frankfurt, Germany, 179 pp.

A MODEL OF CENTENNIAL OSCILLATIONS OF EARTH ROTATION BASED ON TOTAL SOLAR IRRADIANCE VARIATIONS

Ya. CHAPANOV[1], J. VONDRÁK[2], C. RON[2]

[1] National Institute of Geophysics, Geodesy and Geography of Bulgarian Academy of Sciences
Acad. G. Bonchev Str., Bl.1, Sofia 1113, Bulgaria,
e-mail: chapanov@clg.bas.bg

[2] Astronomical Institute, Academy of Sciences of Czech Republic
Boční II, 141 31 Prague, Czech Republic
email: vondrak@ig.cas.cz, ron@ig.cas.cz

ABSTRACT. The centennial variations of Earth rotation are driven by the solar cycles which affect climatic variations, followed by global environmental changes. The centennial solar cycles consist of several oscillations with most known periods 178.7 a (Jose cycle), 210 a and 230 a (de Vries cycle). These periods are close to the harmonics of the millennial Hallstatt cycle (2300 a), so the proper separation between the centennial cycles needs a model with main period 2300 a. The centennial variations of the Universal Time UT1 and Length of Day LOD are investigated by means of reconstructed time series of the Total Solar Irradiance TSI for the last 9300 years. The parameters of the centennial TSI variations are estimated in 2300-year running windows; time variations of the phases and amplitudes of the centennial cycles are determined. A linear regression model of the TSI influence on UT1 centennial variations is created. The parameters and time series of the centennial UT1 and LOD oscillations for the last 9.3 Ka are determined.

1. INTRODUCTION

The irregular and long-term variations of Earth rotation are mainly caused by the displacements of matter in different parts of the planet with the initial excitation mechanism being the influence of the Sun and the solar activity cycles. The existing long climatic and astronomical time series with centennial and millennial time spans are useful to study interconnection between the centennial cycles of the solar activity and Earth rotation. In Chapanov et al. (2011) the centennial cycles of the solar activity and Earth rotation are investigated by means of the available data of Earth rotation, solar activity and climatic parameters. The used data consist of time series with duration from centuries to several millennia: UT1-TT and LOD for the period 1623–2005; total solar irradiance TSI for the period 843–1961 (Bard et al., 2000); 2.2 Ka time series of North America temperature (Salzer and Kipfmueller, 2005); Mean sea level at Stockholm for the period 1770-2001 (Ekman, 2003); 8 Ka time series of North America precipitation (Hughes and Graumlich, 2000). It has been determined that the centennial cycles of Earth rotation consist of at least three oscillations with significant amplitudes and periods from the interval 171–230 years (Chapanov et al., 2011). The 210-year oscillation has a dominating amplitude, and strong correlation between the 210-year cycles of the UT1, MSL and TSI (Figure 2a,b) exists (Chapanov et al., 2011). The detailed study and separation of the UT1 centennial cycles need data covering more than 2300 a intervals, so time series of TSI with duration 9.3 Ka (Steinhilber et al., 2009) and 11 Ka series of sunspot numbers SSN (Solanki et al., 2004) are used in this work (Figure 1).

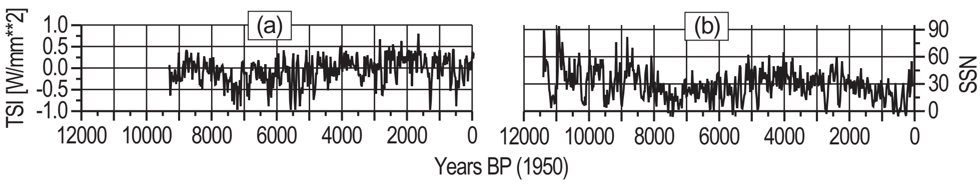

Figure 1: Millennial time series of Total Solar Irradiance TSI (a) and Sunspot numbers SSN (b).

2. LINEAR REGRESSIONS BETWEEN UT1, MSL AND TSI CENTENNIAL VARIATIONS

Real and reliable UT1 observations are available since 1623. The data of Earth rotation variations before 1623 during the Holocene is possible to reconstruct by means of TSI time series. So, the linear regression between UT1 and TSI (Equation 1), based on the real UT1 data, will be used to transform the TSI variations into UT1 variations and the linear regression between MSL and TSI variations (Equation 2) will prove the centennial model of solar-terrestrial energy transfer:

$$\mathrm{UT1} = -15.47\mathrm{TSI} + 0.05, \tag{1}$$

$$\mathrm{MSL} = 2.2\mathrm{TSI} + 0.07, \tag{2}$$

where the universal time UT1 is expressed in seconds, the mean sea level MSL in centimeters and the total solar irradiance in W/m^2.

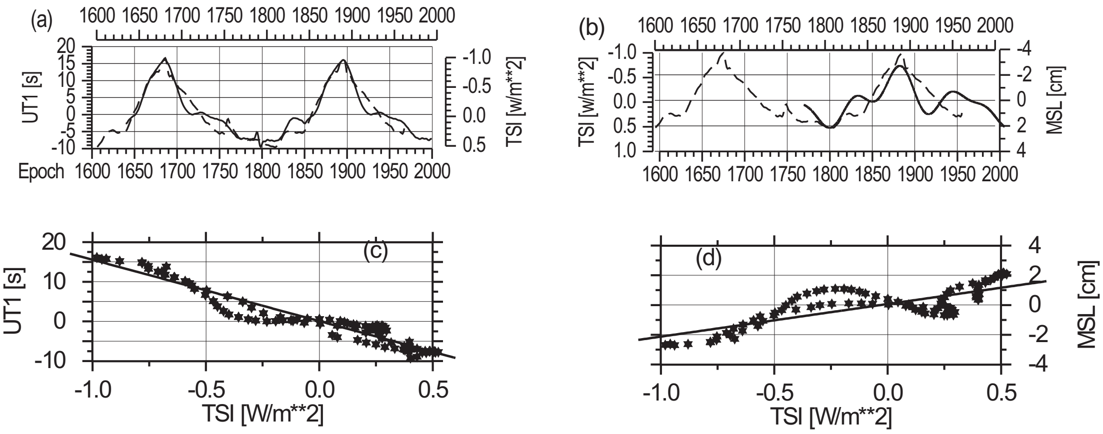

Figure 2: Comparison between UT1 (solid line) and TSI (dashed line) centennial cycles (a) and MSL (solid line) and TSI (dashed line) cycles (b), according to Chapanov et al. (2011). Linear regressions UT1-TSI (c) and MSL -TSI (d).

3. MODELS OF UT1, AND TSI CENTENNIAL VARIATIONS

The simplest model of UT1 and TSI centennial variations is based on Fourier approximation of all data with a main period of 2300 a (Hallstatt cycle) and the first 13 harmonics. This model includes the following harmonics: 10-th with 230 a period (Suess cycle); 11-th with 209 a period (de Vries cycle) and 13-th with shifted Jose cycle (176 a). A more precise model is based on Fourier approximation of all data with a main period of 9200 a and the first 55 harmonics. The centennial oscillations from this model are composed out of the harmonics 39-55 and the periods from the interval 167 a – 235 a.

The values of the periods of Hallstatt, de Vries and Suess cycles are rather rounded. Even the planetary periods may appear in the observed data with shifted values, due to their superposition with high-frequency terms. The proper values of the centennial cycles of the TSI are determined by varying the main period from 2280 a to 2400 a with 10-year steps, where the period of the corresponding j-th harmonics of the Fourier approximation also varies with steps equal to 10/j years (Figure 3). The amplitudes of the Fourier harmonics have maxima when the periods are close to their real values.

The amplitudes of de Vries and Sues cycles have common maxima for TSI and SSN data, while their periods are 208 a and 231 a. The planetary terms and Jose cycle are represented by a common maximum at 183-year period and a few non-matching maxima. So, the base model of centennial UT1 and TSI oscillations includes three oscillations with periods 231 a (Suess cycle), 208 a (de Vries cycle) and 183 a (Jose cycle, 1965). This model have 2100-year maximal beat period between the frequencies. An extended

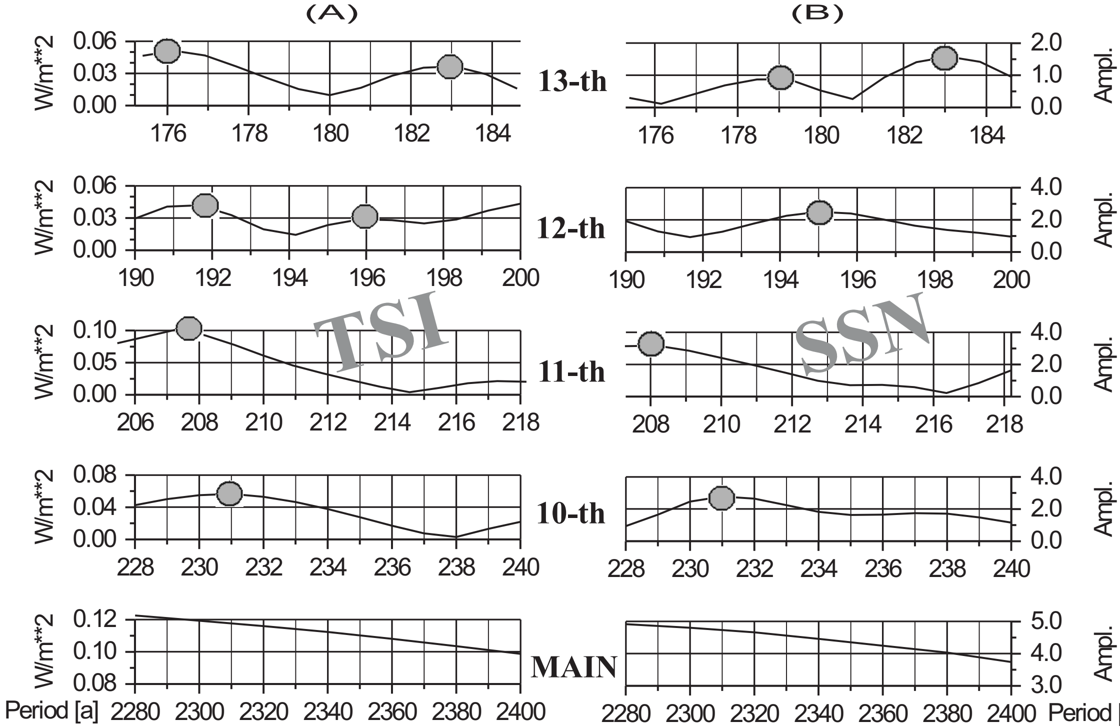

Figure 3: Amplitude maxima of the main oscillation and harmonics 10-13 of the Fourier approximations, determined by varying the main period from 2280 a to 2400 a with 10-year steps from total solar irradiance data (A) and sunspot numbers (B).

model, including six oscillations of centennial UT1 and TSI variations is proposed by adding three terms with periods 171.4 a, 178.8 a and 196 a to the base model. The extended model represents better the variations of the parameters of the centennial UT1 and TSI cycles. This model has 7800-year maximal beat period between the frequencies.

The TSI variations with periods between 170 a and 2300 a, determined by the 2300 a model (Figure 4a), have a significant cooling effect every 2300 years, when the TSI decrease by 0.4 W/m^2, modulated by three centennial cycles. These variations do not represent the real cooling events, which are non-evenly spaced in time.

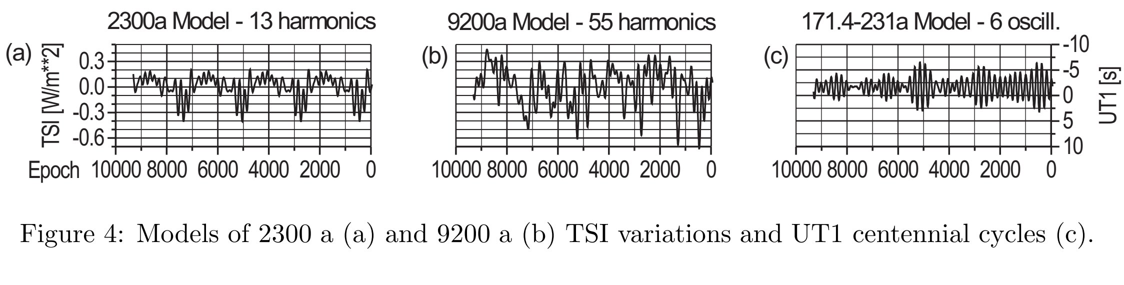

Figure 4: Models of 2300 a (a) and 9200 a (b) TSI variations and UT1 centennial cycles (c).

The TSI variations determined by the 9200 a model (Figure 4b) have significant cooling effects, whose minima are in good agreement with the real cool events, when the TSI decrease by 0.2-0.7 W/m^2, modulated by the centennial cycles. The centennial UT1 variations, determined by the extended six-oscillation model, have variable amplitudes with some amplification during the cool minima (Figure 4c). The UT1 cycles have more stable amplitude after 3000 a BP.

4. TIME VARIATIONS OF THE PHASES AND AMPLITUDES OF THE CENTENNIAL CYCLES IN A 2300-YEAR RUNNING WINDOW

The centennial oscillations of Earth rotation and solar activity have variable amplitudes in time. The variations of the phases and amplitudes of the 231-, 208- and 183-year oscillations from the base model are determined in a 2300-year running window (Figure 5). The amplitude of the 208-year oscillation is dominating during the last 4000 years. For the time interval 4000-8000 a before present the amplitudes of the 208-year and 231-year cycles have almost similar behavior and equal values. The 208- and 231-year cycles have almost opposite phases for the interval 2000–6000 years before present. The amplitudes of the 183-year and 208-year cycles are anticorrelated, so these three oscillations probably have a common excitation source.

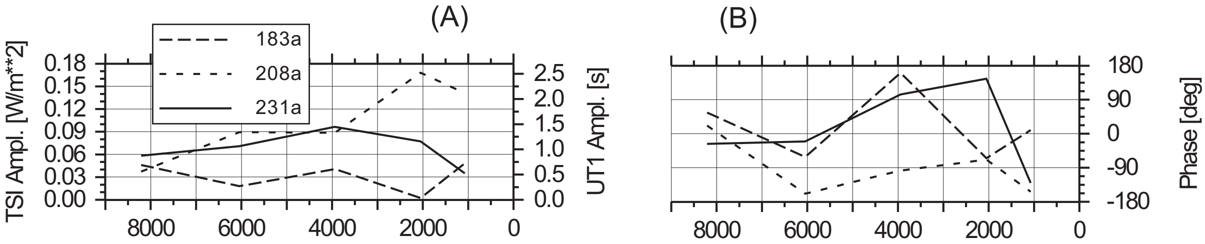

Figure 5: Variations of the amplitudes of the oscillations with periods 183 a, 208 a and 231 a (A) and corresponding phases (B), determined in a 2300-year running window.

5. CONCLUSIONS

The centennial cycles of the solar activity strongly affect Earth's climatic variations, providing a significant cooling effect especially over the polar ice, leading to decreasing the MSL and the principal moment of inertia C during the solar grand minima (acceleration of the Earth's rotation). The cooling effect is amplified significantly by the millennial cycles.

The frequencies of TSI centennial oscillations with maxima of amplitudes are different from the frequencies of 2300-year harmonics. So, the Suess, de Vries and Jose cycles appear to be independent from the 2300-year harmonics and their close frequencies lead to a complex oscillating system with millennial periods.

The time variations of the phases and amplitudes of the centennial cycles in a 2300-year running window show a dominating amplitude of a 208-year oscillation for the last 4000 a and equal 208-year and 231-year amplitudes before, with mostly opposite phases. The amplitudes of the 183-year and 208-year cycles are anticorrelated.

Acknowledgements. The paper was supported by the contract DO02-275 with the Bulgarian NSF and by the grant No. 205/08/0908 awarded by the Grant Agency of the Czech Republic.

REFERENCES

Bard, E., G. Raisbeck, F. Yiou, and J. Jouzel, 2000, "Solar irradiance during the last 1200 years based on cosmogenic nuclides", TELLUS B, vol. 52 (3), pp. 985-992.

Chapanov Ya., Vondrák J., Ron C., 2011, "Centennial cycles of the solar activity and Earth rotation", Journées 2010 "Systèmes de référence spatio-temporels", Paris, 149-152.

Ekman, M, 2003, "The world's longest sea level series and a winter oscillation index for northern Europe 1774 - 2000", Small Publications in Historical Geophysics, 12, 31 pp.

Hughes, M.K. and L.J. Graumlich, 2000, "Multi-Millennial Nevada Precipitation Reconstruction". International Tree-Ring Data Bank. IGBP PAGES/World Data Center-A for Paleoclimatology Data Contribution Series #2000-049. NOAA/NGDC Paleoclimatology Program, Boulder CO, USA.

Jose, P., 1965, "Sun's motion and sunspots", Astronomical Journal, 70, pp. 193 - 200.

Salzer, M.W. and K.F. Kipfmueller, 2005, "Reconstructed Temperature and Precipitation on a Millennial Timescale from Tree-Rings in the Southern Colorado Plateau", U.S.A. Climatic Change, 70, No 3, pp. 465 - 487

Solanki, S.K., I.G. Usoskin, B. Kromer, M. Schüssler and J. Beer. 2004. "An unusually active Sun during recent decades compared to the previous 11,000 years". Nature, Vol. 431, No. 7012, pp.1084-1087

Steinhilber, F., J. Beer, and C. Fröhlich. 2009. "Total solar irradiance during the Holocene". Geophys. Res. Lett., 36, L19704, doi:10.1029/2009GL040142.

THE SIGNATURE OF ATMOSPHERIC TIDES IN SUB-DAILY VARIATIONS OF EARTH ROTATION AS UNVEILED BY GLOBALLY-GRIDDED ATMOSPHERIC ANGULAR MOMENTUM FUNCTIONS

M. SCHINDELEGGER[1], J. BÖHM[1], D.A. SALSTEIN[2], H. SCHUH[1]

[1] Institute of Geodesy and Geophysics, Vienna University of Technology
27-29 Gußhausstraße, A-1040 Wien, Austria
e-mail: michael.schindelegger@tuwien.ac.at, johannes.boehm@tuwien.ac.at, harald.schuh@tuwien.ac.at

[2] Atmospheric and Environmental Research, Inc.
131, Hartwell Avenue, Lexington, MA 02421-3126, USA
e-mail: salstein@aer.com

ABSTRACT. Thermally-driven atmospheric tides provide a small but distinct contribution to short-period variations of Earth rotation parameters (ERP). The effect of diurnal and semi-diurnal tides, commonly denoted as S_1 and S_2, respectively, is in the range of 2 - 10 μas for polar motion and 2 - 10 μs for changes in length-of-day (LOD). Even though ocean tides represent a much more dominant driving agent for ERP fluctuations at short time scales, high-frequency atmospheric effects are non-negligible, particularly given the prospective measurement accuracy of space geodetic techniques. However, previous studies, such as Brzeziński et al. (2002), de Viron et al. (2005) or Schindelegger et al. (2011), have been noticeably inconclusive on the exact amplitude and phase values of S_1 and S_2 atmospheric excitation signals.

This study aims at shedding light on the origin of these uncertainties with respect to the axial component of Earth's rotation vector by investigating times series of atmospheric angular momentum (AAM) functions that are given on global grids and computed from three-hourly meteorological data of the European Centre for Medium-Range Weather Forecasts (ECMWF). The signature of diurnal and semi-diurnal atmospheric tides is clearly visible in the gridded axial AAM functions, revealing a distinct spatial and temporal phase difference between pressure and wind tidal constituents of about $\pm\pi$. It is shown that due to this counterbalance and the explicit axisymmetric spatial structure of S_1 and S_2, the net effect in sub-diurnal AAM (which is calculated from the global sum of gridded AAM functions) is always a small quantity, particularly sensitive to minor differences between the analysis fields of numerical weather models.

1. DATA AND METHODOLOGY

The three-hourly meteorological data of this paper originated from the so-called *Atmospheric model delayed cut-off (DCDA)* analysis, which was introduced as a part of a recent re-organization of the ECMWF assimilation system on 29 June 2004. Geopotential, temperature and specific humidity values as well as wind velocities were downloaded as pressure level data at 1° horizontal resolution for the time span 1 January 2010 to 1 July 2010. The preprocessing of the data involved interpolation of all meteorological parameters onto a topography-based reference surface and an appropriate georeferencing of the discrete atmospheric grid.

Based on such a dataset, routine calculation of AAM, which is conventionally split up into pressure and wind terms, requires full spatial integration over pressure p, co-latitude θ and longitude λ. In this study though, we solely performed vertical integration (from the top of the atmospheric model down to the surface pressure p_s) for every 1° by 1° atmospheric column, arriving at the area-weighted grid point-wise contributions to the axial pressure and wind AAM functions χ_3^p and χ_3^w (Schindelegger et al., 2011):

$$\chi_3{}^p(\theta,\lambda) = \frac{0.757}{C_m}\int_0^{p_s}\frac{r^4}{g}\sin^2\theta\ [\sin\theta d\lambda d\theta]\, dp \tag{1}$$

$$\chi_3{}^w(\theta,\lambda) = \frac{0.999}{C_m\Omega}\int_0^{p_s}\frac{r^3}{g}u\sin\theta\ [\sin\theta d\lambda d\theta]\, dp \tag{2}$$

Herein, C_m is the mantle's polar moment of inertia, Ω denotes the Earth's mean angular velocity and g is the gravity acceleration at geocentric radius r. The decisive quantity for the wind term is the field of zonal wind speed u. Equations (1) and (2) are valid at any single epoch. Hence, considering the entire time span accordingly produced two three-dimensional arrays $\chi_3{}^p(t,\theta,\lambda)$ and $\chi_3{}^w(t,\theta,\lambda)$, which were signified as *gridded AAM functions* (pressure and wind terms).

In order to access the contribution of diurnal and semi-diurnal atmospheric tides to the gridded AAM functions, we applied a suitable bandpass filter on the time series of each grid-point at the frequencies of interest, i.e. 1 and 2 cyc/day. As a result, four three-dimensional grids were obtained, featuring the global and regional contributions of the S_1 and S_2 pressure and wind tides to atmospheric excitation of LOD. In a final step, we transformed the half-yearly record of those grids onto a mean day by averaging all fields with common integer hour. The gridded and filtered AAM functions were thus stacked to $\overline{\chi}_3{}^{p,w}(t,\theta,\lambda)$, with the time vector being reduced to $t = (0,3,6,9,12,15,18,21)$ UTC. The mean day grids of $\overline{\chi}_3{}^{p,w}$ provided the backbone of our analysis and are further examined in the next section.

2. ATMOSPHERIC TIDES IN GRIDDED AAM FUNCTIONS

Figure 1 gives an idea of how the S_1 and S_2 pressure and wind tides are represented in the gridded AAM functions at the very first epoch (0 UTC) of the daily mean cycle. A distinct pattern of alternating highs and lows is evident for the semi-diurnal cycle (left part of Figure 1) and one would recognize a westward movement of those signals if further epochs are considered. More importantly, we found a distinct spatial phase difference of $\pm\pi$ between the pressure and zonal wind contributions of S_2. The right part of Figure 1 reveals a less harmonic and regular structure of the S_1 constituents, and thus no clear spatial phase shift is discernable between the gridded pressure and wind terms. These qualitative findings are in agreement with the predicted behavior of atmospheric tides from simple dynamical models, e.g. the pioneering work of Chapman and Lindzen (1970).

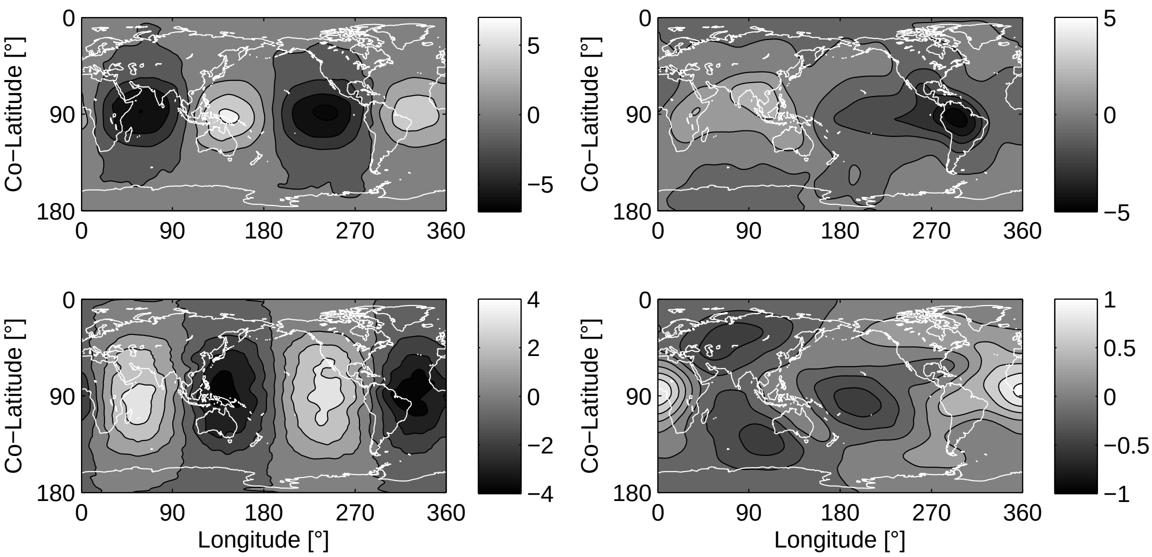

Figure 1: Semi-diurnal and diurnal atmospheric tides as represented by axial gridded AAM functions at 0 UTC. Left part of figure: S_2 pressure term (top half) and S_2 wind term (bottom half). Right part of figure: S_1 pressure term (top half) and S_2 wind term (bottom half). Units are [μs]$\cdot 10^{-3}$.

It proved interesting to perform summation over longitude and latitude for each field of $\overline{\chi}_3{}^{p,w}(t,\theta,\lambda)$, thus looking at the epoch-wise net effect of the gridded and filtered AAM functions. The resulting mean day variations of S_1 and S_2 are displayed in Figure 2, split up into a pressure portion, a wind portion and the total effect on excitation of LOD. For both tidal bands, the wind term shows a phase lag of about 6 hours with respect to the pressure term. This phenomenon prompts the semi-diurnal wind term to largely balance the respective contribution of the pressure term, so that the total net effect at S_2 remains a smaller quantity throughout.

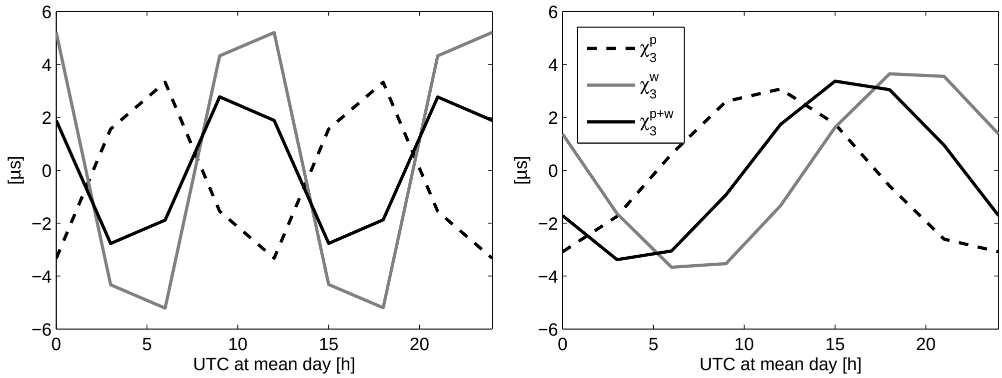

Figure 2: Daily mean variations of the S_2 (left figure) and S_1 (right figure) signals in atmospheric excitation of LOD, calculated from three-hourly gridded AAM functions. Pressure term (*dashed black line*) and wind term (*gray line*) add up to the total excitation signal (*solid black line*).

We tried to address the nature of signals depicted in Figure 2 by focusing on the gridded AAM functions in the semi-diurnal band. In detail, the origin of the epoch-wise net effect and the prevailing counterbalance of pressure and wind effects as illustrated in Figure 2 were investigated. At first, we discerned that the first-order approximation of the global grids of $\overline{\chi}_3{}^{p,w}\,(t,\theta,\lambda)$ is an axisymmetric structure corresponding to a spherical harmonic of degree and order $n = m = 2$. However, precisely due to its axisymmetry, this $n = m = 2$ component possesses a vanishing net effect, and it was therefore removed from the gridded pressure and wind terms at each epoch by means of a least squares fit and subsequent subtraction. The resulting pressure term at 0 UTC (Figure 3) reveals regionally distributed residuals, most notably over the Pacific and the Indian Ocean. Both anomalies are negative and therefore amplify the associated semi-diurnal pressure lows in Figure 1, so that the net effect at 0 UTC is negative, cf. the pressure term values in the left part of Figure 2. This assertion is supported by a dominating negative bulge in the cumulated meridional profile, which was obtained from $\overline{\chi}_3{}^{p}\,(t,\theta,\lambda)$ after summation over longitude.

An equivalent analysis was carried out for the gridded wind term at 0 UTC, see Figure 4. Removal of the symmetric $n = m = 2$ component again revealed notable residuals in the Pacific band from $\lambda = 150°$ to about 300°, which account for a positive value in the global net effect, cf. the wind term values in the left part of Figure 2. The associated meridional profile of $\overline{\chi}_3{}^{w}\,(t,\theta,\lambda)$ shows two main positive bulges located at temperate latitudes.

3. DISCUSSION AND CONCLUSION

By investigating gridded AAM functions at three-hourly resolution for the time period 1 January 2010 to 1 July 2010, we found that the primary diurnal and semi-diurnal pressure and wind signals of atmospheric tides, which are associated with harmonic coefficients of degree and order 1 and degree and order 2, respectively, do not contribute to excitation of LOD. Instead, small secondary pressure and wind effects are decisive for changes in the axial component of AAM. It is highly likely that those residuals are represented differently in the analysis fields of each atmospheric model. In particular for the semi-diurnal cycle, the relevant anomalies can be interpreted as amplifications of the pressure and wind highs and lows over the same latitude band, located in the Pacific region. Considering this and the fact that the barometric S_2 tide features a distinct spatial phase difference of $\pm\pi$ with respect to the S_2 wind tide, it is understandable that the resulting excitation time series of pressure and wind terms are almost exactly out-of-phase and thus largely counterbalance each other.

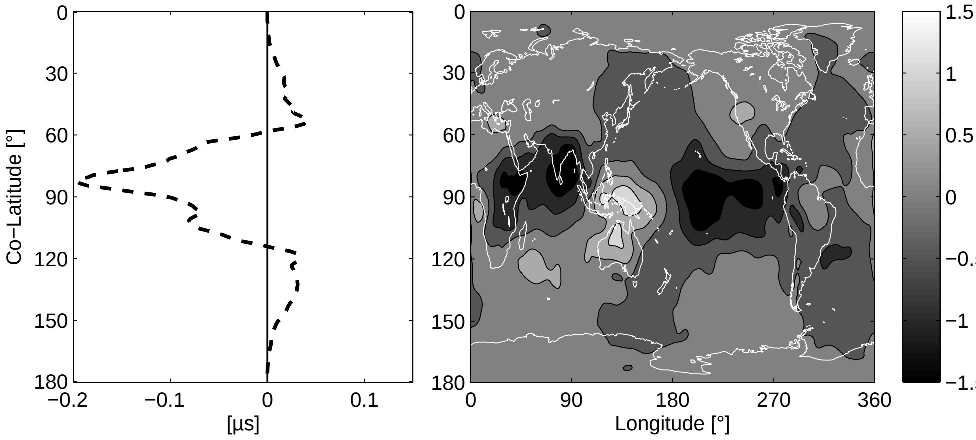

Figure 3: Right figure: gridded pressure term at 0 UTC after removal of the symmetric tidal signal of degree and order 2. Units are [μs]$\cdot 10^{-3}$. Left figure: corresponding longitudinal sum of the pressure term at 0 UTC.

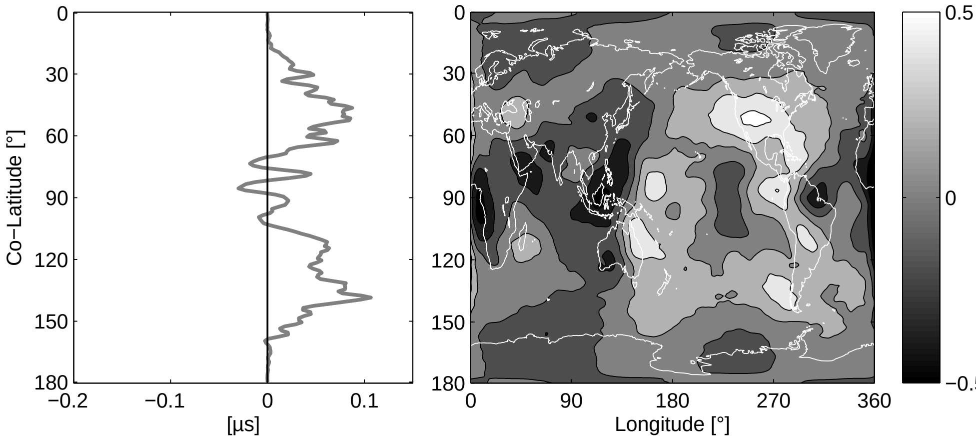

Figure 4: Right figure: gridded wind term at 0 UTC after removal of the symmetric tidal signal of degree and order 2. Units are [μs]$\cdot 10^{-3}$. Left figure: corresponding longitudinal sum of the wind term at 0 UTC.

Acknowledgements. This study was carried out within project P20902-N10 of the Austrian Science Fund. David Salstein was also supported by the US National Science Foundation under Grant ATM-0913780.

4. REFERENCES

Brzeziński, A., Bizouard, C., Petrov, S.D. Influence of the atmosphere on Earth rotation: What new can be learned from the recent atmospheric angular momentum estimates? *Surveys in Geophysics*, 23:33-69, 2002.

Chapman, S. and Lindzen, R.S. *Atmospheric Tides: Thermal and Gravitational.* Reidel, Dordrecht, The Netherlands, 1970.

de Viron, O., Schwarzbaum, G., Lott, F., Dehant, V. Diurnal and semi-diurnal effects of the atmosphere on the Earth rotation and geocenter motion. *J. Geophys. Res.*, 110(B11404), 2005.

Schindelegger M., Böhm J., Salstein D., Schuh H. High-resolution atmospheric angular momentum functions related to Earth rotation parameters during CONT08. *J. Geod.*, 85(7), pp. 425-433, 2011.

IMPACT OF ATMOSPHERIC TIDES SIMULATED IN A CHEMISTRY-CLIMATE MODEL ON SUB-DIURNAL VARIATIONS IN UT1

C. KADOW[1], H. DOBSLAW[2], K. MATTHES[3], M. THOMAS[1,2]

[1] Freie Universität Berlin, Institute of Meteorology
12165 Berlin, Germany
e-mail: christopher.kadow@met.fu-berlin.de

[2] Deutsches GeoForschungsZentrum, Department 1: Geodesy and Remote Sensing
14473 Potsdam, Germany
e-mail: dobslaw@gfz-potsdam.de, mthomas@gfz-potsdam.de

[3] Helmholtz-Zentrum für Ozeanforschung Kiel - GEOMAR
24148 Kiel, Germany
e-mail: kmatthes@geomar.de

ABSTRACT. Sub-diurnal variations in Earth rotation parameters as obtained from time-series of space geodetic observations contain substantial variability even after correcting for the effects of oceanic tides. These residuals are in particular apparent at frequencies of 1, 2 and 3 cycles per solar day, where atmospheric tides, principally excited by water vapor absorption and ozone heating in the middle atmosphere, are known to occur. By means of hourly data of the chemistry-climate model WACCM, the potential of atmospheric tides on the excitation of UT1 variations is re-assessed. Tidal signals are separated into migrating and non-migrating zonal waves for individual height levels. Only standing waves of wavenumber zero are found to be effective in exciting UT1 variations, which are subsequently discussed in terms of their characteristic surface pressure and vertically varying wind amplitudes.

1. INTRODUCTION

The Earth's atmosphere exhibits periodic variations in its global temperature, pressure and wind fields that are principally induced by the diurnal cycle of solar energy absorption. Those variations, commonly referred to as thermal or atmospheric tides, are by a factor of 20 larger than the gravitational lunisolar tides in the atmosphere (Volland, 1988), and cover also variations due to the absorption of solar energy at the surface and corresponding radiative or convective vertical transfer processes. Since these tides are primarily excited by the daily variation of solar irradiation, signals at periods of 24 h and corresponding higher harmonics occur, that are additionally slightly altered by seasonal modulations.

Analyses of continuous VLBI campaigns designed to observe sub-diurnal tidal variability in Earth rotation parameters revealed substantial residuals at periods of 8, 12, and 24 h for example in UT1-TAI on the order of a few μs, even after correcting for the effects of ocean tides (Artz et al., 2010). Those residuals, although eventually affected by sun-synchronous systematic errors like thermal deformations of the antennas or temperature dependent delays in the receiving electronics (see Sovers et al., 1993), are often hypothesized to be related to atmospheric tides (e.g. Brzezinski, 2008).

Atmospheric data considered for analyzing the atmospheric contributions to rotational changes of the Earth are usually obtained from numerical weather prediction models. The most recent reanalysis from ECMWF, ERA-Interim, for example, is limited in its vertical extend to a level of 1 hPa. Thus, processes relevant for the excitation of tides in the middle atmosphere, where peak heating per unit mass via absorption of solar ultraviolet radiation by ozone occurs (Covey et al., 2011), are not adequately resolved in such models.

We therefore analyze a recent experiment from the Whole Atmosphere Community Climate Model (WACCM; Garcia et al., 2007) that is discretized on a regular horizontal grid with 1.9° x 2.5° and extends well into the thermosphere up to an altitude of 140 km. The simulation was performed within the SPARC-CCMVal activity under the REFB1 scenario and has been forced by observed sea surface temperatures, solar irradiances, greenhouse gas concentrations and ozone depleting substances as well as the observed, nudged Quasi-Biennial Oscillation (Matthes et al., 2010). For the year 2002, hourly

		wave number						
		s=3	s=2	s=1	s=0	s=-1	s=-2	s=-3
diurnal	$n = 1$	DW3	DW2	DW1	D0	DE1	DE2	DE3
semi-diurnal	$n = 2$	SW3	SW2	SW1	S0	SE1	SE2	SE3
ter-diurnal	$n = 3$	TW3	TW2	TW1	T0	TE1	TE2	TE3

Table 1: Naming convention for individual zonal waves contributing to the atmospheric tides. Waves with $s = n$ and zonal phase speeds $C_\phi = -\omega$ (i.e., DW1, SW2 and TW3) are called migrating tides to distinguish them from the remaining non-migrating components with $s \neq n$ (after Forbes, 2003).

three-dimensional fields of temperature, zonal and meridional wind, geopotential, and surface pressure are available, allowing us to assess the regional contributions to variations in UT1.

2. ZONAL WAVES RELEVANT FOR UT1 VARIATIONS

Periodic variations with n cycles per solar day of length $1/\omega = 24$ h can be described for an atmospheric state variable G at any location given by latitude φ, longitude λ, and pressure p from locally analyzed amplitudes A and phases ϕ as

$$G_n(\varphi, \lambda, p, t) = A_n(\varphi, \lambda, p) \cos(n\omega t - \phi_n(\varphi, \lambda, p). \tag{1}$$

However, tidal motions are generally not excited locally, but originate from a resonant motion of the laterally unbounded atmosphere. Given that the primary energy source is varying with the incidence angle of solar insulation, it is straightforward to represent tidal motions as a sum of zonal waves with different wave numbers s which include travelling waves towards east ($s < 0$) and west ($s > 0$), as well as standing waves ($s = 0$) (Forbes, 2003):

$$G_n(\varphi, \lambda, p, t) = \sum_{s=-\infty}^{s=\infty} A_{n,s}(\varphi, p) \cos(n\omega t + s\lambda - \phi_{n,s}(\varphi, p)). \tag{2}$$

Rewriting Equation (2) in terms of local time $t_{LT} = t + \lambda/2\pi$, we obtain

$$G_n(\varphi, \lambda, p, t) = \sum_{s=-\infty}^{s=\infty} A_{n,s}(\varphi, p) \cos(n\omega t_{LT} + (s-n)\lambda - \phi_{n,s}(\varphi, p)). \tag{3}$$

For wave numbers $s = n$, variations for any given local time are independent of longitude. Those components correspond to a zonal phase speed of $C_\phi = d\lambda/dt = -n\omega/s = -\omega$, implying a westward propagation of the signal at the same angular velocity as the apparent motion of the sun with respect to a ground-based observer. Those sun-synchronous components that dominate their spectra are referred to as migrating tides in order to distinguish them from the non-migrating tides with $s \neq n$ (Table 1).

Variations in Universal Time $\mathrm{UT1_{p,w}}$ are proportional to changes in the axial component of the angular momentum due to atmospheric surface pressure variations p_s, and the relative angular momentum caused by variations in the zonal wind u, respectively (Gross, 2009):

$$\frac{\partial(\mathrm{UT1_p} - \mathrm{TAI})}{\partial t} \sim \iint p_s(\varphi, \lambda) \cos^2\varphi \; d\lambda \; d\varphi \tag{4}$$

$$\frac{\partial(\mathrm{UT1_w} - \mathrm{TAI})}{\partial t} \sim \iiint u(\varphi, \lambda, p) \cos\varphi \; dp \; d\lambda \; d\varphi. \tag{5}$$

By considering the de-composition of atmospheric tides into zonal waves it follows that only a sub-set of waves is contributing to UT1 variations. By inserting Equation (3) into Equations (4) and (5), it is clear that contributions from all wavenumbers $s \neq 0$ vanish when integrated over the globe, leaving only standing waves $s = 0$ to contribute to changes in UT1. Those waves will be subsequently discussed in more detail.

3. STANDING WAVES FROM WACCM

Hourly WACCM output of the relevant quantities surface pressure and zonal wind were Fourier de-composed for wave numbers $|s| \leq 8$ (Figure 1). Note that the migrating tides DW1 and SW2 who dominate all other waves in amplitude (see, e.g., Figures 5 and 6 of Covey et al., 2011, for an idea) have been excluded here since they do not contribute to UT1 variations. Non-migrating tides ($s \neq n$) arrive from a wide range of processes including deep convective activity leading to variations in rain fall and corresponding latent heating, or longitudinally varying insolation absorption due to changing water vapor content at different altitudes, that is closely related to the orography and land-sea distribution (Forbes, 2003). Amplitudes for D0 reach 12 Pa in the tropics with accompanying variations in the zonal winds. Since winds are more effective in exciting UT1 variations when they occur closer to both the surface and the equator, jet-like structures seen at subtropical latitudes that extend well down into the troposphere are in particular relevant, suggesting further analysis of the simulated strong zonal winds centered at 35° N on tropopause level.

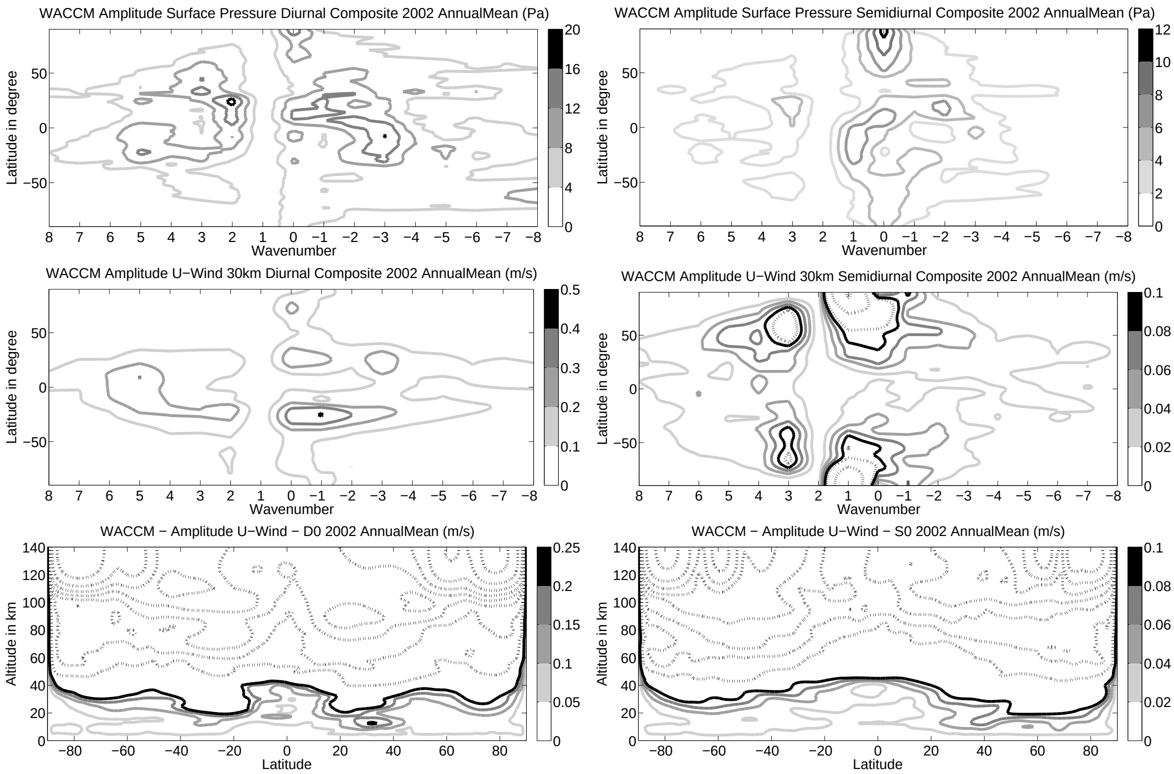

Figure 1: Wave number de-composition of diurnal (left) and semi-diurnal (right) oscillations in the mean atmospheric surface pressure (top) and the zonal wind at 30 km altitude (middle), as well as the vertical distribution of standing wave amplitudes D0 and S0 in the zonal wind (bottom), all obtained from one year of hourly WACCM data. Values out of range of the greyscale are marked by dashed lines that represent doubled amplitudes for each increment.

For the semidiurnal standing wave S0, surface pressure amplitudes are around 8 Pa in the tropics and even higher at the North Pole, where, however, the potential to excite UT1 variations is very small. For the same reason, strong wind amplitudes simulated in the polar vortex are of limited effect only. However, hemispheric assymmetries in the S0 wind amplitudes are more pronounced than for D0, calling for further analyses of the simulated low-level wind amplitudes at moderate latitudes in WACCM.

Amplitudes and phases of the standing waves D0, S0, and T0 are subsequently integrated into UT1 contributions and compared to estimates from WACCM data that has not been Fourier de-composed (Table 2). Apart from the semi-diurnal band, where the migrating component SW2 is particularly strong and affects the de-composition, standing waves indeed dominate the changes in UT1 due to variability in both wind, and surface pressure. Variability is generally decreasing with increasing frequency, consistent with energy distribution considerations. For all frequencies, wind and pressure contributions partly

		$UT1_p$ (μs)		$UT1_w$ (μs)		$UT1_{p+w}$ (μs)	
		sin	cos	sin	cos	sin	cos
diurnal	D0 only	0.092	0.25	-0.30	-0.56	-0.21	-0.31
diurnal	not decomposed	0.088	0.19	-0.27	-0.54	-0.18	-0.35
semi-diurnal	S0 only	0.17	0.013	-0.14	-0.021	0.034	-0.0085
semi-diurnal	not decomposed	0.22	0.040	-0.18	-0.023	0.041	0.017
ter-diurnal	T0 only	0.00083	-0.0032	0.0024	0.0066	0.0032	0.0034
ter-diurnal	not decomposed	0.00058	-0.0032	0.0030	0.0073	0.0036	0.0041

Table 2: Annual mean contributions of atmospheric tides at diurnal, semi-diurnal and ter-diurnal frequencies to variations in UT1, as separated into contributions from wind and atmospheric surface pressure from both the standing waves D0, S0 and T0 as obtained from a Fourier de-composition, as well as from the original wind and pressure distributions as simulated by WACCM.

compensate each other, which is in line with earlier studies based on data from numerical weather prediction models (Schindelegger, 2011).

4. SUMMARY AND CONCLUSIONS

Wind and pressure distributions available for one year of a simulation with the chemistry-climate model WACCM were used to calculate the annual mean contribution of atmospheric tides to variations in UT1. Although processes relevant for the excitation of tides are more complete in WACCM than in numerical weather prediction models, amplitudes are, however, substantially lower than current residuals from space geodetic techniques and also previously analyzed numerical models (Artz et al., 2010), suggesting that atmospheric tides even from modern chemistry-climate models are not able to fully account for this gap between theory and observation. However, since standing zonal waves were shown to be primarily responsible for the atmospheric contribution to UT1 variations, it is possible to focus now on the validation of these waves by means of auxiliary observations. Besides utilizing in-situ records from weather stations and radiosondes that are always afflicted by sampling limitations, different satellite instruments provide valuable data-sets on high altitudes tidal variations. In addition, seasonal modulations of atmospheric tides need to be considered in more detail, in particular when UT1 residuals calculated from observations of a limited time period are to be interpreted.

5. REFERENCES

Artz, T., S. Böckmann, A. Nothnagel, P. Steigenberger, 2010, "Subdiurnal variations in the Earth's rotation from continuous Very Long Baseline Interferometry campaigns", J. Geophys. Res., 115, B05404.

Brzezinski, A., 2008, "On the Influence of diurnal atmospheric tides on Earth rotation", in: Proc. Journees Systemes de Reference Spatio-Temporels 2007, edited by N. Capitaine, pp. 180–183.

Covey, C., A. Dai, D. Marsh, R. S. Lindzen, 2011, "The Surface-Pressure Signature of Atmospheric Tides in Modern Climate Models", J. Atmos. Sci., 68(3), pp. 495–514.

Forbes, J. M., 2003, "Nonmigrating diurnal tides in the thermosphere", J. Geophys. Res., 108(A1), 1033.

Garcia, R. R., D. R. Marsh, D. E. Kinnison, B. A. Boville, F. Sassi, 2007, "Simulation of secular trends in the middle atmosphere, 1950–2003", J. Geophys. Res., 112, D09301.

Gross, R. S., 2009, "Earth Rotation Variations - Long Period", in: Treatise on Geophysics: Geodesy, edited by T. Herring, pp. 239–294, Elsevier, Amsterdam.

Matthes, K., et al. 2010, "Role of the QBO in modulating the influence of the 11 year solar cycle on the atmosphere using constant forcings", J. Geophys. Res., 115(D18), D18110.

Schindelegger, M., J. Böhm, D. Salstein, H. Schuh, 2011, "High-resolution atmospheric angular momentum functions related to Earth rotation parameters during CONT08", J. Geodesy, 85(7), pp. 425–433.

Sovers, O. J., C. S. Jacobs, R. S. Gross, 1993, "Measuring Rapid Ocean Tidal Earth Orientation Variations With Very Long Baseline Interferometry", J. Geophys. Res., 98(B11), pp. 19,959–19,971.

Volland, H., 1988, "Atmospheric Tidal and Planetary Waves", 348 pp., Kluwer Academic Publishers, Dordrecht.

EMPIRICAL MODEL OF SUBDAILY VARIATIONS IN THE EARTH ROTATION FROM GPS AND ITS STABILITY

N. PANAFIDINA[1], S. KURDUBOV[2], M. ROTHACHER[1]
[1] Institute of Geodesy and Photogrammetry, ETH Zurich
Schafmattstr. 34, CH-8093 Zurich, Switzerland
e-mail: panatali@ethz.ch
[2] Institute of Applied Astronomy, nab. Kutuzova 10, St. Petersburg, Russia

ABSTRACT. The model recommended by the IERS for these variations at diurnal and semidiurnal periods has been computed from an ocean tide model and comprises 71 terms in polar motion and Universal Time. In the present study we compute an empirical model of variations in the Earth rotation on tidal frequencies from homogeneously re-processed GPS-observations over 1994–2007 available as free daily normal equations. We discuss the reliability of the obtained amplitudes of the ERP variations and compare results from GPS and VLBI data to identify technique-specific problems and instabilities of the empirical tidal models.

1. INTRODUCTION

External gravitational torques and internal processes causing mass redistributions in the system Earth lead to variations in Earth rotation, both in polar motion (PM) describing the position of the rotational axis and the speed of rotation (UT1). On the periods of 1 day and shorter the main mass redistribution in the Earth system is caused by the ocean tides, what allows to derive theoretically from an ocean tidal model the amplitudes of the variations in the Earth rotation on the tidal frequencies. The International Earth Rotation Service (IERS) has adopted a model derived in Ray et al. (1994) as an official sub-diurnal model for the Earth rotation parameters (ERPs). We will refer to it as to IERS2003 tidal model.

Additional variations taking place on the same frequencies as tidal variations are caused by the external torques acting on the flattened equator of the Earth. This interaction leads to a high-frequency nutation of the rotational axis, which is called libration. In accordance with the convention these nutation terms are not included in the model for precession and nutation, they are taken into account in the terrestrial reference frame as a part of polar motion. The values of these variations are well computed theoretically and can be found in the IERS Conventions. Also non-tidal oceanic and atmospheric variations driven by the solar heating cycles and atmospheric and ocean normal modes lead to additional changes in the ERPs partly on the same tidal frequencies.

The present study is devoted to the derivation of an empirical model of subdaily variations in the Earth rotation as observed by the GPS. Since space geodetic techniques observe the variations in the Earth rotation caused by all the geophysical excitations together, we can partly interpret the differences in amplitudes between the tidal model IERS2003 and the obtained empirical models as the effects caused by other phenomena than ocean tides, e.g. by libration and radiational atmospheric tides. Other possible reasons for the differences are the uncertainties of the models, both the IERS2003 tidal model and the computed empirical models.

Here we consider the question of reliability and stability of the GPS-derived empirical tidal models. A comparison with two tidal models estimated from the VLBI observations is done to identify technique-specific deficiencies of the estimated values.

2. EMPIRICAL TIDAL MODELS

The variations in the ERP can be estimated on the observation level (i.e. set up as parameters in the processing of the observations), or a posteriori from a time series of the ERPs, or the estimation can be done on the normal equation (NEQ) level when the ERPs are transformed into the amplitudes of the variations on given frequencies. The first and the third methods have the advantage of taking into account the full variance-covariance information. We used here the third method for the estimation of empirical tidal models.

As input data we used free normal equation systems (NEQ) obtained from processing GPS and VLBI data. From GPS-observations we had free daily NEQs covering the time span 1994-2007 and obtained within the GGOS-D project (Rothacher et al., 2011). The parameters included in the daily NEQs contained station coordinates, orbits (6 osculating elements, 9 radiation pressure parameters, 3 stochastic pulses at 12 o'clock), tropospheric zenith delays and gradients, Earth rotation parameters with time resolution of 1 hour and corrections to the nutation angles with time resolution of 24 h. From VLBI-observations we had free NEQs for 24 h VLBI-sessions covering the time span 1984-2010, these normal equations were provided by the Institute of Geodesy and Geophysics (IGG), TU Vienna. The parameters included in the NEQs contained station coordinates, radiosources coordinates, ERPs with 1 hour resolution and nutation corrections with 24 h resolution.

The GPS and VLBI IGG tidal models were estimated with a modified Bernese GPS Software. The transformation between the ERPs and tidal terms is a linear transformation, the general theory concerning changes in the NEQ system caused by linear transformations of parameters can be found in (Thaller, 2008). More specific the changes in the NEQ system needed to transform the ERPs into tidal terms are described in (Artz et al., 2011).

Also for comparison with our GPS and VLBI tidal models computed on the NEQ level, we used a VLBI tidal model computed in the Institute of Applied Astronomy (IAA, St. Petersburg, Russia) with the software package QUASAR. In this case the tidal terms were computed on the observational level. Comparison of 2 VLBI tidal models computed fully independently with different software and different approaches should provide a better understanding of the results.

2.1 GPS empirical tidal model

The GPS solution was computed as a multiyear solution for station coordinates, i.e. for each station one set of coordinates and velocities was estimated for the whole time span covered by the NEQs, allowing for jumps for stations showing a non-linear behaviour. To align the solutions to the ITRF05 a No-Net-Rotation condition was applied over a set of stable IGS stations, in this case the origin of the reference frame (geocenter) is defined dynamically by the satellite orbits. Tropospheric zenith delays and gradients were pre-eliminated on daily basis. Nutation corrections were kept fixed to zero and ERPs were transformed into amplitudes of the tidal terms. For the empirical tidal model all the terms from the IERS2003 model were estimated except one term with the period of 24.000 h, because of its full correlation with the term S1. The amplitudes of some tidal terms are not constant, but vary together with the changes in the Moon's declination with the period of revolution of the lunar nodes (Ray, 2007), it is taken into account by the estimation of sidebands of the affected terms. Since the time span covered by the available re-processed GPS NEQs (13 years) is shorter than is needed for the separation of the sidebands (18.6 years), all the sidebands were constrained using the respective heights of the tidal potential, the exact procedure and tidal potential values are the same as described in (Artz et al., 2011).

GPS orbits are modelled by a set of 6 osculating elements for the middle of the arc and a set of additional parameters to account for not well enough known force field. These parameters include the radiation pressure parameters (RPRs: empirical accelerations in 3 directions containing a permanent and a periodic (sine and cosine) term), and stochastic pulses which allow a satellite a sudden change in velocity in 3 directions at a given epoch. We used orbital arc length of 7-days with stochastic pulses set up also on the days' boundaries. A tight constraint was applied on the out-of-plane component for the stochastic pulses; for the RPRs periodic terms in D- (direct to the Sun) and Y- (along solar panels) directions were constrained. This way of orbit modeling was proposed and studied in detail in (Springer et al. 1999).

2.2 VLBI empirical tidal models

The way of computing the VLBI tidal model from the NEQs provided by the IGG TU Vienna was the same as in the case of GPS. Here also a multi-year solution was computed for the station coordinates. In this case No-Net-Translation condition was applied over a set of stable stations in addition to the No-Net-Rotation condition, because VLBI observations do not provide information about the position of the geocenter. ERPs were transformed into tidal terms, all the terms from the model IERS2003 were estimated. Sideband constraints were considered specially, because in case of VLBI the time span covered by the observations (1984-2010) is long enough to estimate the sidebands independently of the main term. But on the other hand most sidebands have very small amplitudes and the differences between amplitudes of freely estimated sidebands and constrained sidebands can give an idea about the real accuracy of the empirical model (the formal errors are about the same for all terms without constraints and is ~0.8 μas for PM and ~0.04 μs for UT1). We made such a test and found that the mean differences in the amplitudes of sidebands are about 2-4 μas in PM and 0.2-0.4 μs in UT1. So we considered the real accuracy of the model to be not enough to reliably estimate most of the sidebands and they were constrained the same way as in the case of GPS solution. Nutation corrections were estimated as one offset and rate each 4 weeks. Radiosource positions were estimated once over the whole time span with a NNR-condition applied over a set of 20 stable sources.

The VLBI solution provided by the IAA was computed on the observation level as a multi-year solution for the station coordinates, the radiosource positions were kept fixed to the a priori. Amplitudes of tidal terms in PM were set up as parameters in such a way that for each frequency the sum of prograde and retrograde variations was estimated. That implies that some nutation terms corresponding to the retrograde diurnal terms in PM were set up and estimated. For that reason the nutation corrections were fixed to aprioris. Sidebands in this case were estimated freely.

3. STABILITY OF EMPIRICAL TIDAL MODELS

To give a general impression about the agreement of the computed models we show in Figure 1 the differences in tidal amplitudes in PM between the 3 empirical tidal models. Since the IAA solution was computed without constraints on the sidebands and the other two models with the constraints we used for the comparison only the not constrained terms. As can be seen the two VLBI solutions agree with each other a bit better than with the GPS solution. The biggest differences show the terms on the periods very close to 24 and 12 hours, also the amplitudes for the term M2 (12.42h) disagree noticeably.

To estimate the stability of the tidal amplitudes we computed several tidal models using not all the timespan, but only some years of data: for GPS 8 models were computed over 6 years each with a shift of 1 year (1994-1999, 1995-2000,..), for both VLBI solutions we computed 9 models over 19 years each with a shift of 1 year (1984-2001, 1985-2002,..). The timespan of 19 years for VLBI allows the estimation of sidebands without constraints by the IAA. Then for each tidal term the root mean square (RMS) values of the estimated amplitudes were computed. The resulting RMS for all 3 solutions are shown in Figure 2 for PM and Figure 3 for UT1. As can be seen the GPS tidal model shows a high RMS for the terms N1 (24.132h), K1 (23.934h), P1 (24.066h), S1 (24.000h) and Ψ1 (23.869h) in daily part, and the terms S2 (12.00h) and K2 (11.967h) in the semidaily part. All these terms should be strongly affected by any errors in the GPS orbits, and probably we can make a conclusion that these terms cannot be reliably estimated from the GPS data. Terms in PM show also a high RMS for periods of about 28 and 13 hours, but these terms are stable in a GPS solution with 1-day orbit (which we do not show here). Terms in UT1 show in addition a high RMS for term O1 (25.819h) which remains unstable in GPS solutions with different orbital arc lengths. All the terms in VLBI IGG solution have a good stability on the level of 2-4 μas in PM. The IAA solution shows a higher RMS for terms in PM around 24 and 12 hours, we attribute it to the influence of not constrained sidebands. In UT1 both VLBI solutions show a noticeably high RMS for terms S1 and K1, IAA solution having bigger variations also seen in semidaily part.

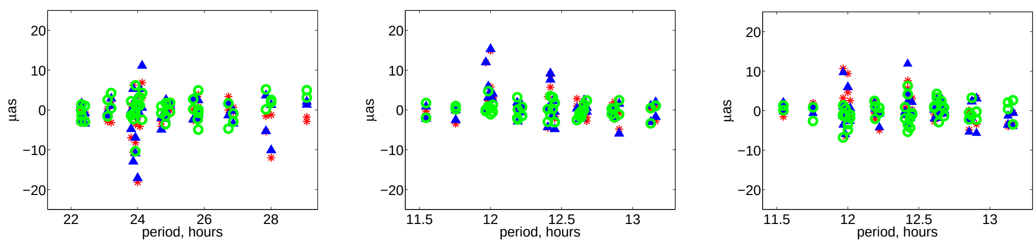

Figure 1: Differences in tidal amplitudes in PM for 3 solutions: (left) prograde daily PM; (middle) prograde semidaily PM; (right) retrograde semidaily PM. GPS minus VLBI IGG (red asterisk), GPS minus VLBI IAA (blue triangle), VLBI IGG minus VLBI IAA (green circle)

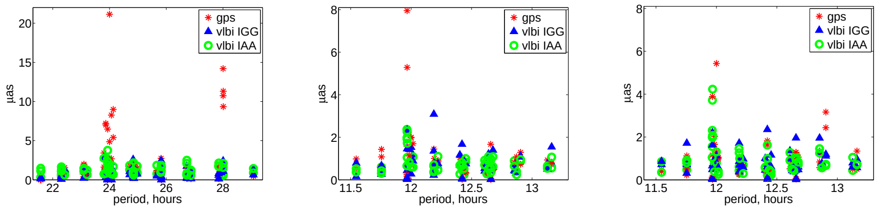

Figure 2: RMS of tidal terms in PM for 3 solutions: (left) prograde daily PM; (middle) prograde semidaily PM; (right) retrograde semidaily PM. GPS (red asterisk), VLBI IGG (blue triangle), VLBI IAA (green circle)

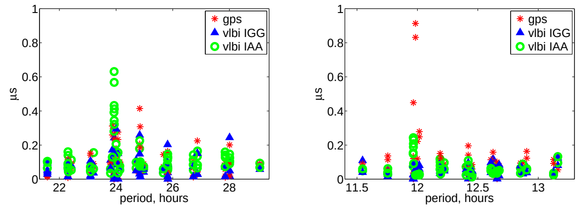

Figure 3: RMS of tidal terms in UT1 for 3 solutions: (left) daily UT1; (right) semidaily UT1. GPS (red asterisk), VLBI IGG (blue triangle), VLBI IAA (green circle)

4. CONCLUSIONS

The tidal models computed over different timespans show that the terms with periods very close to 24 and 12 hours cannot be reliably estimated from GPS. We attribute it to deficiencies in orbit modeling. This instability makes it impossible to compare the affected terms from GPS with the same terms from VLBI. The geophysical interpretation of the unstable terms is also problematic, e.g. the estimated GPS S1 term cannot be used for comparisons with the expected influences of the atmospheric tide and non-tidal angular momentum, because this term changes strongly (within ~30 μas) depending on the used timespan and the orbit modeling. VLBI tidal models on the contrary have a good stability for all terms. The independent VLBI tidal models from IGG and IAA agree well for most of the terms. The real accuracy of the VLBI estimates is on the level of 2-4 μas for PM and ~0.2-0.4 μs for UT1.

5. REFERENCES

Artz T., Tesmer S. nee Boeckmann, Nothnagel A., 2011, "Assessment of periodic sub-diurnal Earth rotation variations at tidal frequencies through transformation of VLBI normal equation systems", Journal of Geodesy, Vol. 85, Nr. 10, pp. 565-584, DOI: 10.1007/s00190-011-0457-z.

Ray R., 2007, "Decadal Climate Variability: Is there a tidal connection?", Journal of Climate, Vol. 20, pp. 3542-3560, DOI: 10.1175/JCLI4193.1.

Ray R., Steinberg D., Chao B., Cartwright D., 1994, "Diurnal and semidiurnal variations in the Earth's rotation rate induced by oceanic tides", Science 264(5160):830-832. DOI: 10.1126/science.264.5160.830.

Thaller D., 2008, "Inter-technique combination based on homogeneous normal equation systems including station coordinates, Earth orientation and troposphere parameters", Dissertation, Scientific Technical Report STR 08/15, Deutsches GeoForschungsZentrum, ISSN 1610-0956, DOI: 10.2312/GFZ.b103-08153.

Rothacher M., Angermann D., Artz T., Bosch W., Drewes H., Gerstl M., Kelm R., Koenig D., Koenig R., Meisel B., Mueller H., Nothnagel A., Panafidina N., Richter B., Rudenko S., Schwegmann W., Seitz M., Steigenberger P., Tesmer S., Tesmer V., Thaller D., 2011, "GGOS-D: homogeneous reprocessing and rigorous combination of space geodetic observations", Journal of Geodesy, Vol. 85, Nr. 10, pp. 679-705, DOI: 10.1007/s00190-011-0475-x.

Springer T., Beutler G., Rothacher M., 1999, "Improving the orbit estimates of GPS satellites", Journal of Geodesy, Vol. 73, Nr. 3, pp. 147-157, DOI: 10.1007/s001900050230.

DETERMINATION OF EARTH ROTATION BY COMBINING VLBI AND RING LASER OBSERVATIONS

T. NILSSON, J. BÖHM, H. SCHUH
Institute of Geodesy and Geophysics
Vienna University of Technology, Vienna, Austria
e-mail: tobias.nilsson@tuwien.ac.at

ABSTRACT. We investigate the potential of combining VLBI data with ring laser gyroscope measurements. The formal errors of polar motion and UT1-UTC obtained from such a combination are estimated as function of the ring laser measurement accuracy. The possible improvements obtained by using data from three globally distributed ring lasers, instead of only one, is also investigated. It is shown that if three globally distributed ring lasers are used – all being one order of magnitude more accurate than the current Wettzell ring laser – the formal errors of the estimated Earth rotation parameters are reduced by more than 50%, compared to a VLBI only solution.

1. INTRODUCTION

In recent years large and very sensitive ring laser gyroscopes have been constructed which are able to measure the rotation of the Earth (Schreiber et al., 2009, 2011). Presently the ring laser accuracy is about one order of magnitude worse compared to space geodetic techniques such as Very Long Baseline Interferometry (VLBI) (Nilsson et al., 2012), but the accuracy is increasing rapidly (Schreiber et al., 2011). Common problems in ring lasers observations are however unknown offsets and drifts, making it difficult to obtain the absolute Earth rotation vector and its long term variations. The strength of the ring laser data is mainly to observe the high frequency variations, e.g. at sub-daily periods. Furthermore, since one single ring laser is only sensitive to one component of the Earth rotation vector, at least three ring lasers (with different orientation) would be needed in order to get all Earth rotation parameters.

In order to make the best use of the ring laser data it should be combined with another technique. In such a combination ring laser data will mainly help in resolving the high frequency Earth rotation variations. A first attempt was done by Nilsson et al. (2012), who combined data from the "G" ring laser in Wettzell, Germany, with simultaneous VLBI observations. It was found that the impact of the ring laser data in the combination was normally very low, which is not surprising given that VLBI is about one order of magnitude more accurate. Only for those VLBI sessions which have a low sensitivity to Earth rotation did the inclusion of ring laser data significantly affect the results. However, if the accuracy of the ring laser is improved – or more than one ring laser is used in the combination – its impact could be expected to be larger also for normal VLBI sessions. In this work we investigate the potential improvement obtained by using more accurate data from several globally distributed ring lasers.

2. THEORY

Here the ring laser measurements and the combination with VLBI are briefly described. For more details, see Nilsson et al. (2012).

In a ring laser gyroscope, two laser beams are transmitted in opposite directions in a ring. At the point where to two laser beams meet the Sagnac (beat) frequency f between the signals is measured. This frequency will depend on the rotation of the ring laser, i.e. the rotation of the Earth if the ring laser is fixed to the Earth's surface. The Sagnac frequency f is given by (Schreiber et al., 2009):

$$S_{rlg} = \frac{\delta f}{f_0} = \frac{\vec{\Omega}^T \hat{n}}{\vec{\Omega}_0^T \hat{n}_0} - 1 \tag{1}$$

S_{rlg} is called the relative Sagnac frequency, $\delta f = f - f_0$, $\vec{\Omega}$ the rotation vector of the Earth, and $\hat{n}$ the normal unit vector of the ring laser. $\vec{\Omega}_0$, $\hat{n}_0$, and f_0 are the nominal values of $\vec{\Omega}$, $\hat{n}$, and f, respectively.

The Earth rotation vector can be expressed as $\vec{\Omega} = \Omega_0 [m_1, m_2, 1 + m_3]^T$, where m_1, m_2, and m_3 are related to the polar motion (x_p and y_p) and DUT1 (UT1-UTC) normally measured by space geodetic techniques such as VLBI (Brzezinski and Capitaine, 1993):

$$m = p - \frac{\mathrm{i}}{\Omega}\frac{\partial p}{\partial t} \quad (2)$$

$$m_3 = \frac{\partial DUT1}{\partial t} \quad (3)$$

Here $m = m_1 + \mathrm{i}\, m_2$ and $p = x_p - \mathrm{i}\, y_p$.

The combination of the ring laser and VLBI data was performed at the normal equation level. First, the normal equation matrices for the VLBI data (N_{vlbi} and b_{vlbi}) were set up using the Vienna VLBI Software (VieVS, Böhm et al., 2011). Polar motion and DUT1 were modelled as piece-wise linear offsets in one hour intervals. Additionally, clock errors, tropospheric parameters, and station coordinates were estimated. Using exactly the same parametrisation for polar motion and DUT1 as in the VLBI analysis, normal equation matrices for the ring laser data acquired during the VLBI session were set up (N_{rlg} and b_{rlg}). Additionally for the ring laser data, one offset and one rate were estimated. Finally the normal equation matrices from VLBI and ring laser were stacked to obtain a common normal equation system:

$$N_{tot} = N_{vlbi} + N_{rlg} \quad (4)$$

$$b_{tot} = b_{vlbi} + b_{rlg} \quad (5)$$

By inverting the system, the unknown parameters (polar motion, DUT1, and additional parmaeters) are obtained. The variance-covariance matrix for the estimates, C_x, can be calculated by:

$$C_x = N_{tot}^{-1} \quad (6)$$

3. RESULTS

As shown by Nilsson et al. (2012) the impact of the ring laser data in the combination is presently very low. With future improvements of the ring laser technique and/or with more ring lasers being available the impact of the ring laser observations is expected to grow. One way of investigating the possible improvements is to look at the formal errors obtained from the variance-covariance matrix C_x (Equation 6). Since C_x does not depend on the observations, we can obtain the expected formal errors without having access to any actual observed data.

In these investigations we consider the combination of VLBI data from the session R1431 (17–18 May, 2010) with ring laser data. Figure 1 shows the median formal errors of polar motion and DUT1 as function of the ring laser accuracy, when one ring laser located in Wettzell (longitude: 12.9°, latitude: 49.1°) is used. The present accuracy of the relative Sagnac frequency S_{rlg} (Equation 1) is about 10^{-8} (Nilsson et al. 2012, Schreiber et al., 2011). We can note that the ring laser data only have a minor impact on the formal errors at this accuracy. However, as the accuracy increases the formal errors are reducing. It is interesting to note that when the accuracy of S_{rlg} is below 10^{-9} mainly the formal errors in y_p and DUT1 are affected, while for very accurate ring laser data (10^{-11}) the biggest reduction in formal error is in x_p. The reason for this is that a ring laser located in Wettzell will mainly be sensitive to the m_1 and m_3 components of the Earth rotation vector but not as much to m_2 (due to the small longitude of Wettzell). From Equation 2 we find that $m_1 = x_p - \frac{1}{\Omega}\frac{\partial y_p}{\partial t}$. When the accuracy is low the ring laser data mainly constrain the very high frequency (e.g. hourly) variations in m_1 which is mainly due to high frequncy variations in y_p. By more accurate ring laser data also the variations over relatively longer periods can be constrained, and these are more affected by the variations in x_p.

Figure 2 shows the effect of having data from more ring lasers in the combination. The formal errors of the hourly polar motion and DUT1 offsets are shown. One ring laser is assumed to be in Wettzell, one in East Brazil (longitude: 45.0°W, latitude: 23.5°S), and one in West Mexico (longitude: 115°W, latitude: 29.7°N). Having the ring lasers placed in these locations their normals will be almost perpendicular to each other, thus together they should have a good sensitivity to the full Earth rotation vector. We can see that when three ring lasers are used, similar reductions in formal errors are found for all three Earth rotation parameters. Two cases are shown, one with the accuracy of the ring lasers being equal to the current accuracy of the Wettzell ring laser, and one with accuracies being one order of magnitude better.

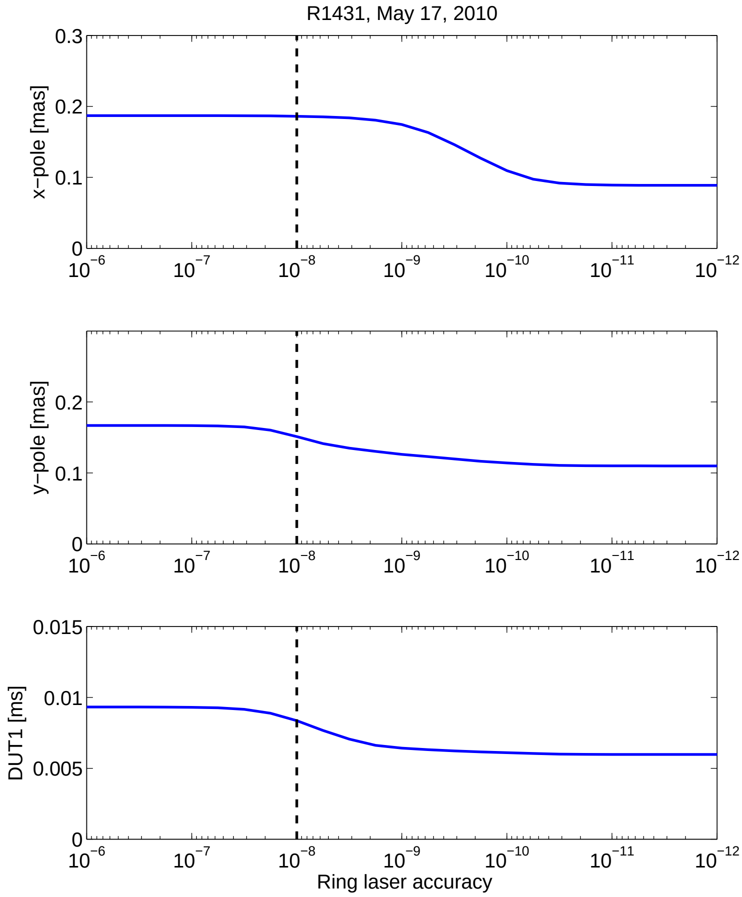

Figure 1: Median formal errors of polar motion and DUT1 estimated from combination of VLBI and ring laser data, as function of the accuracy of the ring laser measurements. The current accuracy of the Wettzell "G" ring laser is marked.

With three accurate ring lasers the formal errors are reduced by about 50% in both polar motion and DUT1, compared to using only VLBI data.

4. CONCLUSIONS

Currently, the Earth rotation parameters estimated in a VLBI – ring laser combination is only slightly more accurate than what is obtained by using only VLBI data. However, if the accuracy of the ring laser measurements can be improved by one order of magnitude or more, the improvement would be more significant, especially if data from several ring lasers distributed over the world is used. Over the last couple of years there has been a significant improvement in the ring laser accuracy (Schreiber et al., 2011). If the accuracy continues to improve at the current rate, the improvement by one order of magnitude will be reached in the not too distant future.

Acknowledgements. This work was funded by the German Science Foundation (DFG, Deutsche Forschungsgemeinschaft) within the Research Unit FOR584 Earth Rotation and Global Dynamic Processes, project number SCHU 1103/3-2.

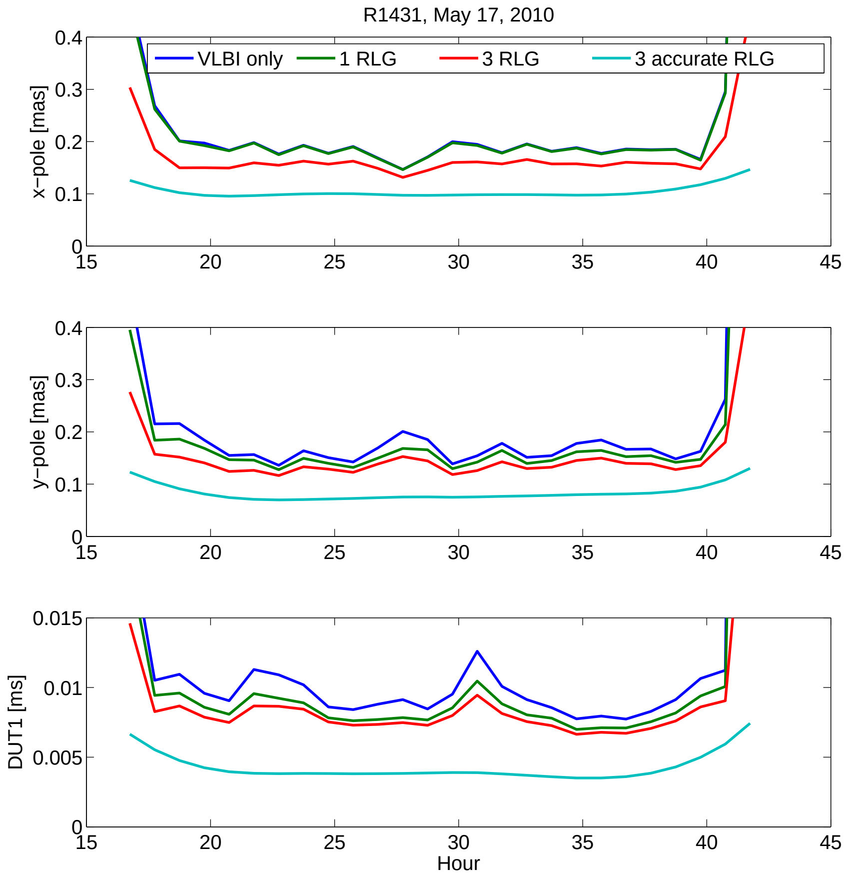

Figure 2: Formal errors of polar motion and DUT1 obtained using VLBI data, as well as from combining VLBI with data from one ring laser (Wettzell) or three globally distributed ring lasers. For the combination using three ring lasers two cases are considered: one case with the ring lasers all having the same accuracy as the current Wettzell ring laser, and one case with one order of magnitude more accurate ring laser data.

5. REFERENCES

Böhm, J., Böhm, S., Nilsson, T., Pany, A., Plank, L., Spicakova, H., Teke, K., Schuh, H., 2011, "The New Vienna VLBI Software VieVS", in Kenyon, S., Pacino, M. C., Marti, U. (Eds.): "Geodesy for the Planet Earth": Proceedings of the 2009 IAG Symposium, Buenos Aires, Argentina, IAG Symposia Vol. 136, Springer, pp. 1007-1012.

Brzeziński, A., Capitaine, N., 1993, "The use of the precise observations of the celestial ephemeris pole in the analysis of geophysical excitation of earth rotation", J. Geophy. Res., 98(B4), pp. 6667-6675.

Nilsson, T., Böhm, J., Schuh, H., Schreiber, U., Gebauer, A., Klügel, T., 2012, "Combining VLBI and ringlaser observations for determination of high frequency Earth rotation variation", J. Geodynamics, in press, doi: 10.1016/j.jog.2012.02.002.

Schreiber, K. U., Klügel, Velikoseltsev, A., Schlüter, W., Stedman, G. E., Wells, J.-P. R., 2009, "The Large Ring Laser G for Continuous Earth Rotation Monitoring", Pure Appl. Geophys., 166, pp. 1485-1498 doi: 10.1007/s00024-004-0490-4.

Schreiber, K. U., Klügel, T., Wells, J.-P. R., Hurst, R. B., Gebauer, A., 2011, "How to Detect the Chandler and the Annual Wobble of the Earth with a Large Ring Laser Gyroscope", Phys. Rev. Lett, 107, 173904, doi: 10.1103/PhysRevLett.107.173904.

CLIMATIC AND SOLAR ACTIVITY INFLUENCES ON INTERANNUAL AND DECADAL VARIATIONS OF VLBI STATIONS

Ya. CHAPANOV[1], H. SCHUH[2], A. NOTHNAGEL[3], J. BÖHM[2]

[1] National Institute of Geophysics, Geodesy and Geography of Bulgarian Academy of Sciences
Acad. G. Bonchev Str., Bl.1, Sofia 1113, Bulgaria
e-mail: chapanov@clg.bas.bg

[2] Institute of Geodesy and Geophysics, Vienna University of Technology, Gußhausstr. 27-29, 1040 Vienna, Austria

[3] Institute of Geodesy and Geoinformation, University of Bonn,
Nußallee 17, 53115 Bonn, Germany

ABSTRACT. The time series of the VLBI station coordinates and baselines contain significant interannual and decadal variations for the period 1983-2010. These variations are highly correlated with the climatic indices and solar activity cycles. The variations of the smoothed time series of several VLBI sites (Wettzell, Westford and Fortaleza in East, North and Up directions) and the baseline Wettzell - Westford are analyzed. The 11-year and 22-year oscillations of the VLBI station coordinates exactly match Wolf's numbers (W_n and W_{n22a}) variations with a time delay of 0.5 to 1.5 years. The interannual site displacements are in good agreement with the smoothed time series of the equatorial solar asymmetry (SA) and the geomagnetic index AA with a time delay of about 1.5 years. The interannual site oscillations are strongly affected by climatic variations, represented by the Palomar Drought Severity Index (PDSI) with irregular phase reverses in 5- to 8-year intervals.

1. VLBI STATION TIME SERIES

The individual solutions for VLBI station coordinates provide time series of site displacements with high accuracy for a time span of more than 25 years for some stations (Figure 1). These time series contain wide-spectrum signals from various local and global sources as well as some systematic errors and uncertainties of the used mathematical models. Böckmann et al. (2007) show that some colocated VLBI, GPS, or SLR station motions are highly correlated.

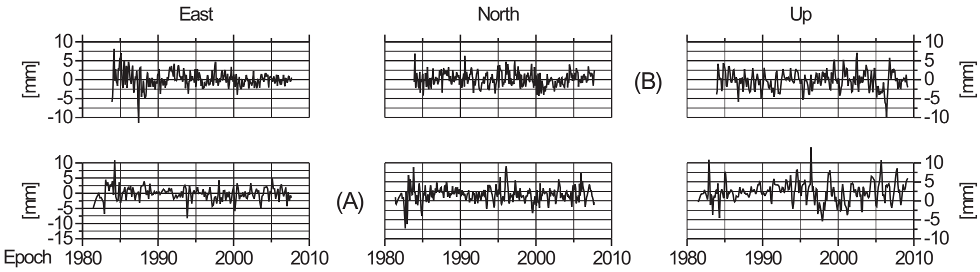

Figure 1: Time series of VLBI sites Wettzell (A) and Westford (B).

2. RESULTS

The smoothed variations of VLBI coordinates are determined in three steps - determination of 0.05-year normal points in the first step, interpolation to equidistant time intervals in the second step, and Fourier approximation with the Least Squares estimation, or Vondrak filtering in the last step. The 11- and 22-year oscillations of the VLBI coordinates are determined by the corresponding harmonics of the Fourier approximation, where the amplitudes are estimated with a level of accuracy of about 0.2 mm. A part of the interannual and decadal natural signals in Earth surface systems can be related to the decadal cycles of solar activity due to solar-terrestrial influences and the interconnection between climatic and weather variations, atmosphere and ocean conditions, hydrological and underground water cycles and others. The comparison between the smoothed time series of VLBI coordinates variations and solar and climatic indices shows an almost exact match of the 11- and 22-year solar and VLBI cycles and good agreement between the interannual VLBI site motions and the solar and climatic indices (Figure 2).

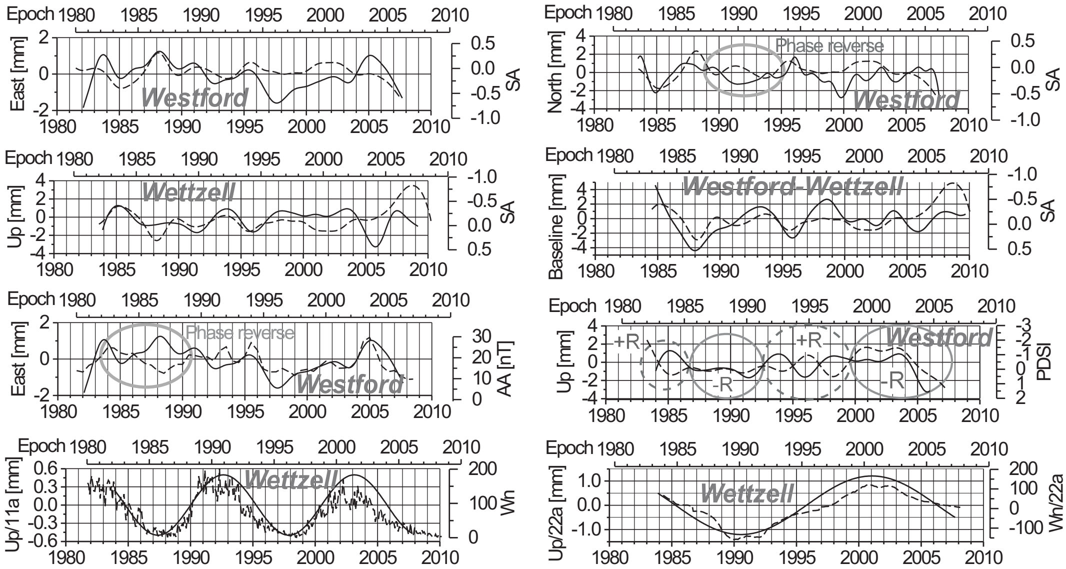

Figure 2: Comparison between the smoothed time series of VLBI sites Wettzell, Westford, the baseline Wettzell-Westford (solid lines) and SA, AA, W_n, W_{n22a}, and PDSI indices (dashed lines).

3. CONCLUSIONS

The decadal oscillations of the non-linear motions of the VLBI sites are correlated with the 11-year and 22-year solar cycles. The smoothed interannual variations of station coordinates and baselines are correlated with the smoothed variations of the equatorial solar asymmetry index SA and the geomagnetic index AA. The ground response to these cycles is not uniform for different sites, somewhere with opposite phases and somewhere without correlation. The climatic variations, expressed by the Palomar Drought Severity Index (PDSI), are connected with the interannual site motions. The smoothed PDSI variations strongly correlate with interanual site oscillations with phase reverse in 5- to 8-year intervals. The interannual and decadal variations of the equatorial solar asymmetry modulate the solar wind and corresponding geomagnetic field changes. The local ground changes are affected by the solar asymmetry and geomagnetic field variations, which is expressed by significant correlation and sudden phase change. The coordinates of individual stations seem to be more sensitive to the solar cycles than the baselines. All these results mean that the solar activity cycles affect crust deformations with dominating local effects and the solar-terrestrial influences show individual revealing for given Earth points.

The most probable interannual and decadal excitations of the local and global crustal deformations are climatic and atmosphere changes on the Earth surface, partially affected by the solar activity cycles, total solar irradiance, solar wind, interplanetary magnetic field and the corresponding response of the Earth's ionosphere. According to the results in Böckmann et al. (2007), the VLBI site motions are common for some colocated GPS and SLR stations, so it is possible to create models of local solar and climatic influences on VLBI, GPS, and SLR station variations.

Acknowledgements. The paper was supported by contract DO02-275 with the Bulgarian NSF

4. REFERENCES

Böckmann S., Artz T., König R., Müller H., Nothnagel A., Panafidina N., Steigenberger P., Thaller D., Tesmer V., 2007, Consistent VLBI, GPS and SLR Time Series of Station Positions and Troposphere Parameters, Geotechnologien Science Report No. 11, Observations of the System Earth from Space, ISSN 1619–7399, pp. 60–63

KG++: SOFTWARE FOR PROCESSING SATELLITE LASER RANGING OBSERVATIONS

V.Ya. CHOLIY[1], V.P. ZHABOROVSKY[2]

[1] Kyiv Shevchenko University
01601, Ukraine, Kyiv, Glushkova str. 2
e-mail: charlie@univ.kiev.ua

[2] Main Astronomical Observatory Ukrainian Academy of Sciences
03127, Ukraine, Kyiv, Zabolotnogo str. 27
zhskyy@gmail.com

ABSTRACT. The software KG++ for processing satellite laser ranging observations is presented. The software architecture, methodology with respect to utilization of models, ordinal differential equations (ODE) integrating procedure and test results are shown and analyzed. The implementation of IERS standard models into the system is demonstrated. The software will be used in the Ukrainian center of Satellite Laser Ranging (SLR) data analysis.

1. INTRODUCTION

The Earth as a planet is characterized by a set of dynamic and geodetic parameters: radius, mass, instantaneous rotation axis, rotation speed, geopotential coefficients, nutation parameters, Love and Shida numbers, etc. To observe and deduce them, different geophysical and astronomical methods are used. Until the end of the seventies the only method applicable for that purpose was astrometric observation of the stars. In the last 40 years new methods, including Very Long Baseline Interferometry (VLBI) of distant radio sources, radio observations of Navigation Satellites, and Satellite Laser Ranging have become available. The latter one is the oldest among these methods - SLR has been used from 1976 until now. The method consists in measuring the distance between terrestrial stations and specially-designed satellites. The distance may be measured with cm precision. If one collects a sufficient amount of observations, any of the listed Earth parameters may be deduced.

The KyivGeodynamics software was created at the Space Geodynamics department of Main Astronomical Observatory (MAO, Kyiv, Ukraine) in the early eighties. Written in an old version of Fortran it is mostly outdated now. The algorithms included in this original software are no more used by the geospatial community and need to be rewritten.

The current version (KG++) isn't a revitalized form of the old KyivGeodynamics, which was used for processing SLR data by the Ukrainian Data Analysis Centre from the time of the MERIT (Measuring of Earth Rotation and Intercomparing of Techniques) project. KG++ is written in C++ from scratch incorporating modern software developing technologies. It uses a plugin approach and it is automatized as much as possible.

The application is cross-platform (tested under Windows XP, Linux-Suse and Mac OS X). It uses its native DBMS (Database Management System) engine which is designed to hold normal points and full-rate SLR data. Simultaneous processing of the data from multiple satellites is possible. Manipulation with different force and transformation models, used in the equation of satellite motion is very user-friendly and intuitive.

2. METHOD

Les us denote with $\vec{R}$ the station geocentric position while $\vec{r}$ represents the satellite geocentric position. The vector between station and satellite reads

$$\vec{\rho} = \vec{r} - \vec{R}. \tag{1}$$

It is convenient to write down $\vec{R}$ in the Earth-based reference frame, but $\vec{r}$ in the space-referred one.

If the transformation matrix between them is denoted as $\mathbb{Q}$, then

$$\vec{\rho} = \vec{r} - \mathbb{Q}\vec{R}. \tag{2}$$

The transformation matrix comprises the position of the instantaneous rotation axis, nutation parameters, tectonics model, etc.

The satellite position $\vec{r}$ is found by integration of the corresponding equation of motion:

$$\frac{d^2\vec{r}}{dt^2} = \vec{F}_{geo} + \vec{F}_{light} + \vec{F}_{planets} + \vec{F}_{others}, \tag{3}$$

where *geo* stands for Earth geopotential force, *light* for direct and indirect radiation pressure, *planets* for influence of Solar system bodies, etc.

The most modern algorithms for calculation of the forces and transformations entering Equations (2) and (3) are collected by the International Earth Rotation and Reference Systems Service in [IERS, 2010]. The calculations are done by cycling according to the scheme in Figure 1 (clockwise from box 1: observations collected by the ObsManager are put into the linear equation system together with the modeled values from the ModelManager and derivatives provided by the Derivator. ρ_o — *observed* distance, ρ_c — *calculated* distance, $\frac{\partial \rho_c}{\partial E_i}$ — derivatives of ρ_c with respect to the estimated parameters, ΔE_i — corrections to model parameters (to be solved for).

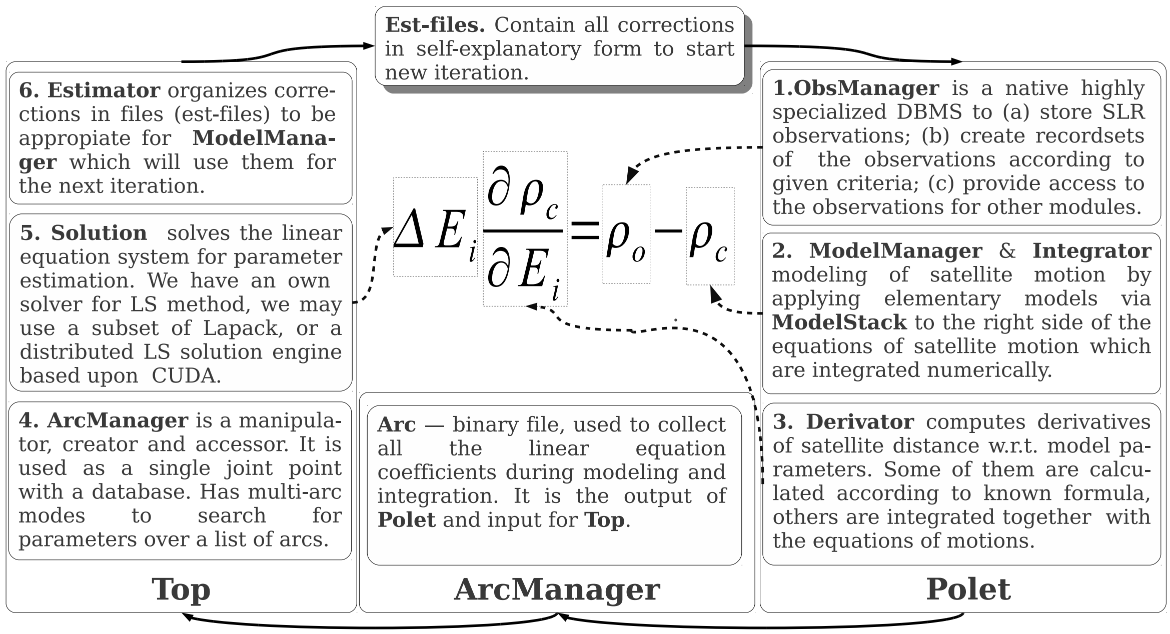

Figure 1: Flowchart of the `KG++`.

The software is based upon a component-oriented architecture, with wide usage of plugins (these are the lightweight software components designed for easy replacement and exchange). Different models are manipulated in the same way: to change the models, one should not recompile code, but instead change the line in the ini-file. The software may integrate many satellites at the same time [Taradiy, 1984], it has a user friendly interface and is well-documented. Serious efforts were made to make the software running under distributed computer environment: our integration subsystem may work under CUDA [NVidia, 2007].

3. REFERENCES

IERS, 2010, "IERS Standards 2010", IERS Conventions Center, 2011, 180 p.

NVidia, 2007, http://nvidia.com/CUDA/

Taradiy V., Tsesis M., ITF Preprints 84-92R, 84-96R, 1984.

ON THE USAGE OF XML FILE FORMAT IN GEODYNAMICS

V.Ya. CHOLIY
Kyiv Shevchenko University
01601, Ukraine, Kyiv, Glushkova str. 2
charlie@univ.kiev.ua

ABSTRACT. We recommend the extended usage of XML data format for the representation of geodynamic observations and processing results. A short introduction to the technology and a simple example for a Consolidated Laser Ranging Data Format (CRD) data file are presented.

TECHNOLOGY

XML = eXtensible Markup Language is the result of a very successful attempt to create a language for standardized text representation of the structured information in data files. XML is a metalanguage: it has no operators, it does not define the algorithms, it does not make calculations. The only purpose of XML is to explain the structure of the files, normally called XML-documents.

Two main features make XML attractive. At first, the document becomes self-explanatory. It itself explains its structure by allowing putting tags into the file. Secondly, the data stay separated from the explanations. Multiple explanations are allowed in the same file. There are two different approaches to make the file self-explanatory: Document Type Declaration (DTD) or XML-scheme. Both of them explain dependencies between data elements of the file and their attributes, value ranges, numbers of tags, etc.

To recognize the internal structure of an XML file and its semantics, specially-designed parsers are used. These are SAX and DOM parsers. To use SAX (Simple Application Programmer Interface or API for XML), the programmer should explain how to process elements of the document. When the parser loads some item, it uses that explanation to do the preprocessing. So, the parser just reacts on loading events. SAX-parsers don't create the internal document structure in memory and don't consume the memory resources. In contrary to SAX, the DOM (Document Object Model) parsers build the document tree. The document components occupy the tree leaves and branchings. The DOM-parser guarantees the access to any of the document elements with DOM-API.

It is possible to process the XML files with specially designed XSLT (eXtensible Stylesheet Language for Transformations). XSLT (written in XML) is a query and transformation language, based upon XML syntax. It is widely used for making transformation of XML files, for example to html, txt or other representations, even to binary ones. It may be used to create reports or just preprocess data, stored in an XML file.

XML is ideal for data storage. There is a tiny difference with respect to the ordinal read/write process. We parse the file during 'read' and serialize it during 'write'. With the standard XML instrumentation, there is no need to write something else. One should just prepare the correct file structure descriprion and put it into the file.

Shortly summarizing:

- the user should concentrate on the data explanation, not on file processing algorithms;
- there is no limitation on the file structure if it is representable as a tree;
- the data may be commented;
- we are able to store text, binary and classified data together in the same file;
- the existing APIs allow effective access;
- there is the possibility to add pre- or post-processing of the data in parsing or serialization.

EXAMPLE

Below, there is a portion of the example CRD file (from Ricklefs R., 2000) followed by its representation in XML syntax.

```
H1 CRD 1 2007 3 20 14
H2 MLRS 7080 24 19 4
H3 LAGEOS2 9207002 5986 22195 0 1
H4 1 2006 11 13 15 25 4 2006 11 13 15 44 40 0 0 0 0 1 0 2 0
C0 0 532.000 std1
60 std1 5 2
11 55504.9728030 0.047379676080 std1 2 120 18 94.0 -1.000 -1.000 -1.0 0.0 0
20 55504.9728030 801.80 282.10 39 1
40 55504.9728030 0 std1 -1 -1 0.000 -913.0 0.0 56.0 -1.000 -1.000 -1.0 3 3 0
11 55988.9809589 0.044893190432 std1 2 120 19 83.0 -1.000 -1.000 -1.0 0.0 0
```

```
<?xml version="1.0" encoding="utf-8"?>
<!-- <!DOCTYPE CrdFile SYSTEM "crd.dtd"> -->
<CrdFile Version="1" Year="2007" Month="3" Day="20" Hour="14">
<Station Name="MLRS" CDPIdentifier="7080" CDPTwoDigot="24" CDPOccupancy="19" TimeScale="4">
<Target Name="LAGEOS2" COSPARId="9207002" SIC="5986" NORAD="22195" TimeScale="0" Type="1">
<Session Type="1" DataReleaseFlag="0" TropoApplied="false" CenterOfMassApplied="false"
      ReceiveAmplApplied="false" StationSysDelayApplied="true"
      SpacecraftSysDelayApplied="false" RangeType="2" DataQuality="0">
<Start Year="2006" Month="11" Day="13" Hour="15" Minute="25" Second="4"/>
<Finish Year="2006" Month="11" Day="13" Hour="15" Minute="44" Second="40"/>
<SystemConfig Type="0" Wavelength="532.000" Id="std1"/>
<Compatibility Id="std1" SCH="5" SCI="2"/>
<Range Moment="55504.9728030" FlightTime="0.047379676080" Id="std1" Event="2"
      NPWindow="120" RawNumber="18" RMS="94.0"/>
<Meteo Moment="55504.9728030" Pressure="801.80" Temperature="282.10" Humidity="39"
      Origin="1"/>
<Calibration Moment="55504.9728030" Type="0" Id="std1" SystemDelay="-913.0"
      DelayShift="0.0" DelayRMS="56.0" CalibrType="3" CalibrShiftType="3" Channel="0"/>
<Range Moment="55988.9809589" FlightTime="0.044893190432" Id="std1" Event="2"
      NPWindow="120" RawNumber="19" RMS="83.0"/>
<Meteo Moment="55988.9809589" Pressure="801.50" Temperature="282.80" Humidity="39"
      Origin="1"/>
```

There is a reference to the “crd.dtd” file in the commented, second line of the XML file. It is a definition of the CRD file with XML syntax. Our recommendations for RINEX, SINEX, CRD, MERIT and some other data file formats will be collected soon on the author’s web page (http://space.univ.kiev.ua/choliy/).

REFERENCES

Ricklefs R., Moore C., 2009, “Consolidated Laser Ranging Data Format CRD v.1.01”.

SOME SYSTEMATIC ERRORS IN AAM AND OAM DATA

D. GAMBIS[1], D. SALSTEIN[2], Ya. CHAPANOV[3]

[1] SYRTE, Observatoire de Paris, CNRS, UPMC
61, Avenue de l'Observatoire, 75014 Paris

[2] Atmospheric and Environmental Research
131 Hartwell Avenue, Lexington, MA 02421, USA

[3] National Institute of Geophysics, Geodesy and Geography of Bulgarian Academy of Sciences
Acad. G. Bonchev Str., Bl.1, Sofia 1113, Bulgaria

e-mail: daniel.gambis@obspm.fr, dsalstei@aer.com, chapanov@clg.bas.bg

ABSTRACT. Atmospheric Angular Momentum (AAM) and Ocean Angular Momentum (OAM) functions excite significant parts of the length of day (LOD) and polar motion variations and provide strong disturbances over the broad band of frequencies with periods from several days to years. The time series of AAM and OAM contain some systematic biases of the mean values for some periods due to unevenly spaced distribution of some observational stations in time. These biases are determined by analyses of the significant linear trends, longer than five years, in the integrated AAM and OAM functions. After estimated biases are removed from the AAM and OAM data, the resulting time series have good consistency in relation to the oscillations with periods from several days to five years. Their application yields a more precise estimation of the periodic terms of the Earth orientation parameters within this band.

1. AAM AND OAM DATA

The AAM and OAM functions for the period 1962.0-now are available via the server of Paris Observatory at http://hpiers.obspm.fr. These functions are based on the data provided by the U.S. National Centers for Environmental Prediction (NCEP) and NASA/JPL for ocean model ECCO JPL. The data in Figure 1 consist of IB-corrected matter terms and motion terms. The high-frequency daily variations are removed by normal points at 0.05 yr, estimated by the Danish method (Kubik, 1982; Kegel, 1987).

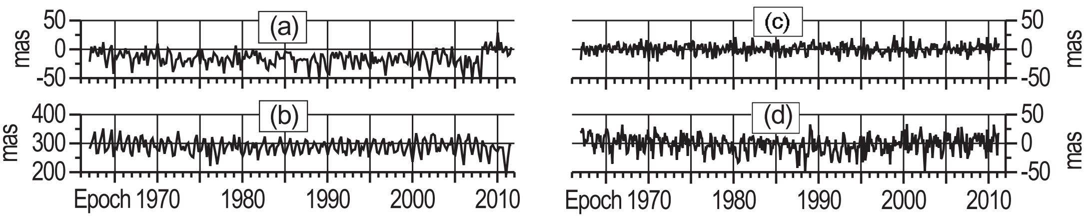

Figure 1: Normal points at 0.05 yr of AAM_x - (a); AAM_y - (b); OAM_x - (c) and OAM_y - (d).

2. AAM AND OAM INTEGRALS

The step-wise systematic biases of the mean in AAM and OAM excitation of LOD are determined in Chapanov and Gambis (2008) by the linear trends in the corresponding excitation functions of UT1. A similar approach is used here. The x and y time series of atmospheric and oceanic excitation of polar motion are integrated (Figure 2). The linear trends with different inclinations correspond to significant biases of the mean values of the AAM and OAM series.

3. SYSTEMATIC ERRORS IN AAM AND OAM

The systematic biases of the mean of x and y AAM and OAM series are illustrated in Figure 3, where the original data are replaced by smoothed time series, determined by Vondrak (1969) filtering. The time interval of each step corresponds to the time intervals of linear trends of the integrated time series from Figure 2. The difference between the maximal and minimal biases of AAM_x is 22.2 mas; AAM_y - 24.2 mas; OAM_x - 3.6 mas and OAM_y - 9.0mas (Table 1).

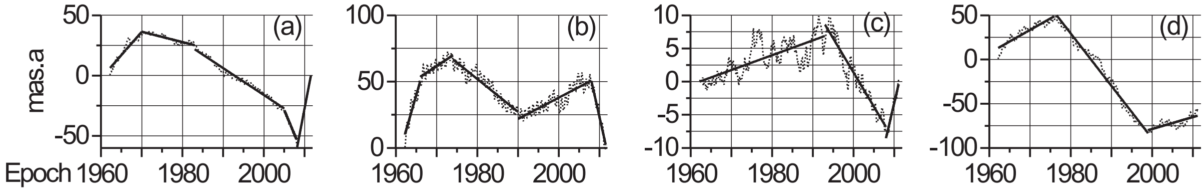

Figure 2: Integrals (in dots) of AAM_x - (a); AAM_y - (b); OAM_x - (c); OAM_y - (d) and linear trends.

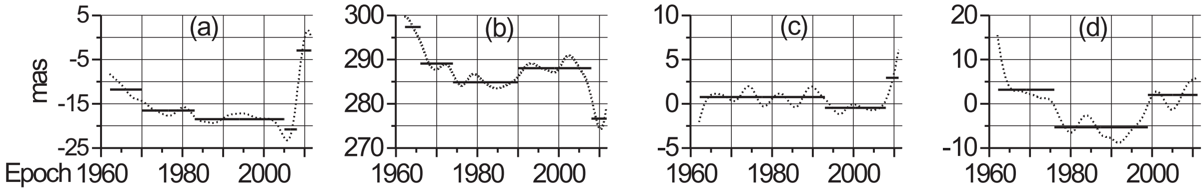

Figure 3: Step-wise biases of smoothed AAM_x - (a); AAM_y - (b); OAM_x - (c) and OAM_y - (d).

4. CONCLUSIONS

The systematic biases of the mean of AAM and OAM excitation functions are determined by a numerical integration of the corresponding normal points of x and y components at 0.05 yr intervals and by a removal of the linear trends from the resulting time series. The AAM time series contain five parts with significant systematic biases and the OAM time series contain three parts. The original AAM and OAM time series reveal step-wise behavior of the mean value due to variable number of used instruments and relatively small systematic deviations from the total mean value for some intervals with duration from 3–15 yr. The maximal effects of the determined biases on the x and y components of AAM variations are 22.2 mas and 24.2 mas, and on the OAM variations 3.6 mas and 9.0 mas. It is possible to improve the quality and accuracy of scientific investigations of Earth Orientation Parameters variations by removing the systematic biases of the mean of AAM and OAM excitation functions.

Time interval	AAM_x	Time interval	AAM_y	Time interval	OAM_x	Time interval	OAM_y
1962.0–1970.0	+4.24	1962.0–1966.0	+11.40	1962.0–1993.0	+0.15	1962.0–1976.0	+4.45
1970.0–1983.0	–0.67	1966.0–1974.0	+2.40	1993.0–2008.0	–0.89	1976.0–1999.0	–4.45
1983.0–2005.0	–2.44	1974.0–1990.0	–2.34	2008.0–2011.7	+2.69	1999.0–2011.7	+3.28
2005.0–2008.0	–7.99	1990.0–2008.0	+1.15				
2008.0–2011.7	+14.20	2008.0–2011.7	–12.83				

Table 1: Systematic biases of excitation due to AAM and OAM for some intervals.

Acknowledgements. The paper was supported by the contract DO02-275 with the Bulgarian NSF. David Salstein was also supported by the US National Science Foundation under Grant ATM-0913780.

5. REFERENCES

Chapanov, Ya. and Gambis D., 2008, "Influence of AAM and OAM on the Universal time variations", AIP. Conf. Proc. Vol. 1043 "Exploring the Solar system and the Universe", Melville, New York, 218-219.

Kegel, J., 1987, "Zur Lokalizierung grober Datenfehler mit Hilfe robuster Ausgleichungsfervahren", Vermessungstechnik, 35, No10, Berlin.

Kubik, K., 1982, "An error theory for the Danish method", ISP Symposium, Comm. III, Helsinki.

Vondrak, J., 1969, "A contribution to the problem of smoothing observational data", Bull. Astron. Inst. Czechosl., 349-355.

ANALYSIS OF THE GEODETIC RESIDUALS AS DIFFERENCES BETWEEN GEODETIC AND SUM OF THE ATMOSPHERIC AND OCEANIC EXCITATION OF POLAR MOTION

B. KOLACZEK, M. PASNICKA, J. NASTULA

Space Research Center Polish Adademy of Sciences
e–mail: kolaczek@cbk.waw.pl

ABSTRACT. Up to now studies of geophysical excitation of polar motion containing AAM (Atmospheric Angular Momentum), OAM (Oceanic Angular Momentum) and HAM (Hydrological Angular Momentum) excitation functions of polar motion have not achieved the total agreement between geophysical and determined geodetic excitation (GAM, Geodetic Angular Momentum) functions of polar motion (Nastula and Kolaczek, 2005; Chen and Wilson, 2005; Brzezinski et al., 2009; Nastula et al., 2011, Gross et al., 2003).

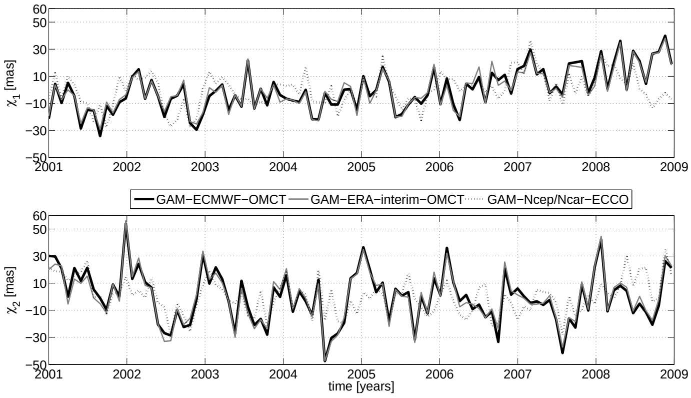

Figure 1: Geodetic residuals for the χ_1 and χ_2 components computed from different models of atmosphere and ocean.

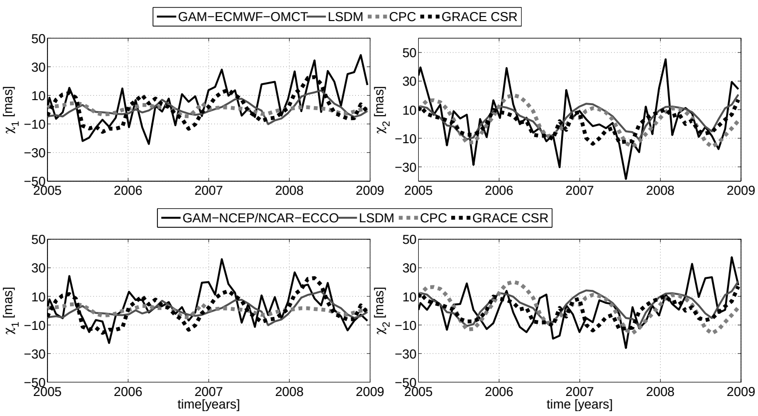

Figure 2: Comparison of geodetic residuals (GAM–ECMWF–OMCT and GAM–NCEP/NCAR–ECCO) in χ_1 and χ_2 components computed from different atmospheric and oceanic models with CPC, LSDM, GRACE CSR hydrological excitations.

Differences between geodetic excitation function of polar motion GAM and joint atmospheric plus oceanic excitation functions named geodetic residuals were computed for different models of AAM and OAM and were analyzed. The obtained geodetic residuals computed for different models of AAM and OAM are different from one model to the other. Standard deviations of the geodetic residuals considered have maxima of the order of over a dozen mas (Figure 1). In the case of geodetic residuals computed with the same OAM models, differences are of the order of several mas only (Figure 1). The results allow to conclude that errors of the OAM are larger than AAM errors.

In Figure 2 geodetic residuals computed for different models of AAM and OAM are compared with variations of different HAM input datasets. Correlation coefficients between the geodetic residuals and different hydrological models HAM are small — they are of the order of 0.1 for the χ_1 and 0.5 for the χ_2 components. It proves that the HAM excitation functions do not explain the considered geodetic residuals. In this situation the HAM excitation functions of polar motion are not able to improve the agreement between geodetic and geophysical excitation functions of polar motion. Other models of geophysical excitation functions have to be improved too.

In order to compare the compatibility between geophysical excitations and geodetic excitation of polar motion, prograde and retrograde components of annual complex polar motion excitation functions were computed for each atmospheric, oceanic and hydrological input dataset. Figure 3 shows that the HAM vectors draw the geophysical excitation closer to that of the GAM.

RESULTS

In these studies we choose the following geophysical models: AAM: ERA – Interim, ECMWF, NCEP/NCAR; OAM: ECCO, OMCT, HAM: LSDM, CPC and sattelite mission GRACE data from CSR (Thomas, 2002; Gross et al., 2003; Salstein et al., 1993).

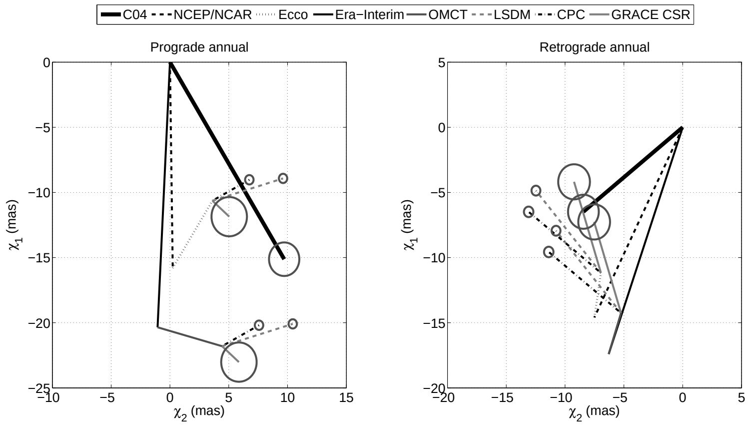

Figure 3: Phasor diagrams of the annual prograde and retrograde oscillation of the geodetic and geophysical excitation of polar motion (analysis done for the period 2001.0–2006.5).

Standard deviations of the considered geodetic residuals shown in Figure 1 have maxima of the order of over a dozen mas. These residuals are different when different OAM models are considered. In the case of geodetic residuals computed with the same OAM models, differences are of the order of several mas only (Figure 1).

To compare these geodetic residuals series with HAM data we choose two models of land hydrology and the HAM obtained from GRACE data (see Figure 2). In the case of the χ_2 component the geodetic residuals GAM-(Era-Interim + OMCT) are greater than the modeled HAM excitations. The geodetic residual GAM-(NCEP/NCAR+ECCO) are comparable with variations of the modeled HAM.

The determined phasor diagrams of geodetic and geophysical excitation functions show that adding successively atmospheric, oceanic and hydrological vectors, the final position becomes closest to the geodetic one but still not the same (Figure 3). Figure 3 shows that the HAM vectors draw the geophysical excitation function vector closer to that of the GAM vector.

REFERENCES

Brzezinski, A., Nastula, J. ,Kolaczek, B., 2009. "Seasonal excitation of polar motion estimated from recent geophysical models and observations", J. Geodyn. 48, 235-240.

Chen, J. and Wilson, C., 2005. "Hydrological excitation of polar motion (1993- 2002)", Geophys. J. Int. 160 (3), 833-839.

Gross, R., Fukumori, I., Menemenlis, D., 2003, "Atmospheric and oceanic excitation of the Earths wobbles during 1980-2000", J. Geophys. Res. 108(B8) (2370).

Nastula, J. and Kolaczek, B., 2005. "Analysis of hydrological excitation of polar motion,. In: Proceedings of the Workshop, Forcing of polar motion in the Chandler frequency band: a contribution to understanding interannual climate variations", Centre European de Geodynamique et de Seismologie, Luxembourg, pp. 149-154.

Nastula, J., Pasnicka, M., Kolaczek, B., 2011, "Comparison of the geophysical excitations of polar motion from the period: 1980.0-2009.0", Acta Geophys. 59 (3), 561-577.

Salstein, D.A., Kann, D.M., Miller, A.J., Rosen, R.D., 1993, "The sub- bureau for atmospheric angular momentum of the international earth rotation service: a meteorological data center with geodetic applications", B. Am. Meteorol. Soc. 74, 67-80.

Thomas, M., 2002, "Ocean induced variations of earth's rotation - results from a simultaneous model of global circulation and tides", Ph.D. thesis, University of Hamburg, Germany.

GEODYNAMIC SIGNALS IN TIME SERIES OF ASTROMETRIC OBSERVATIONS AT BOROWA GORA OBSERVATORY

J. KRYNSKI[1], Y.M. ZANIMONSKIY[2]

[1] Institute of Geodesy and Cartography
27 Modzelewskiego St., 02-679 Warsaw, Poland
e-mail: krynski@igik.edu.pl

[2] Institute of Radio Astronomy of NASU
4 Chervonopraporna St., Kharkiv, 61002, Ukraine
e-mail: zanimonskiy@rian.kharkov.ua

ABSTRACT. Since 1963 astronomical observations are conducted at Borowa Gora Observatory with the use of transit instrument. Instrumental, technological and methodical improvements in acquiring and pre-processing of rotational time observations make the time series inconsistent over the whole period of operation of the instrument. Complex spectral analysis of a long-standing rotational time data series from 1986.0–2010.6 was performed. A number of periodic terms separated from the series investigated were used to create numerical model of the series. The effects of beats observed in the numerical model were discussed. The existence of a distinguished weekly term in the data investigated has been observed. The results obtained were compared with the spectra of EOP from the analysis of IERS data.

1. INTRODUCTION

Although astromertic observations are not used any longer to calculate EOP provided by IERS, they, in contradiction to all space techniques (VLBI, SLR, GNSS, DORIS) contain information on the direction of the plumb line. As such they are of special interest for geodynamic research as well as for classical geodesy that uses surveying instruments oriented with respect to the actual plumb line. Analysis of time series of astrometric was a subject of numerous publications, e.g. (Kruczyk et al., 1999; Gorshkov and Shcherbakova, 2002; Chapanov et al., 2005). The extensive analysis of variations of astronomical longitude with the use of data acquired with transit instrument at the Borowa Gora Geodetic-Geophysical Observatory (BG) of the Institute of Geodesy and Cartography, Warsaw, within the time span 1986.0–2005.5 was performed (Krynski et al., 2005). Extension of the time series of astrometric observations at BG by 20% due to high data quality from last five years makes it much more attractive for the analysis.

2. ASTROMETRIC DATA FROM BOROWA GORA OBSERVATORY

Astrometric observations at BG are conducted since 1963 with the use of transit instrument of Zeiss Jena equipped with photoelectric registration. A long-standing rotational time data series from 1986.0-2010.6, i.e. from last almost 25 years referred to the Hipparcos catalogue is available for complex analysis. Observations cover 1865 nights when either one (481 nights) or two groups of stars were observed. Single determination of rotational time corresponds to a group of stars consisting of 10–11 stars. The differences between mean universal time $UT1^{BG}$ determined at BG and mean universal time $UT1^{BIH}$ of BIH, i.e. the offset of UT1 obtained in BG with respect to that of BIH, are the subject of analysis. Time span of consecutive data in time series investigated varies from 1 day to 167 days (in average 4.82 days). Uncertainty of data (averaged result of observation session of a number of stars) varies from ±0.0034 s to ±0.0155 s (Krynski et al., 2005).

3. SPECTRAL ANALYSIS OF THE OBSERVED TIME SERIES OF THE OFFSET OF UT1 DETERMINED AT BOROWA GORA FROM 1986.0-2010.6

The technique of iterative spectral analysis applied (Box and Jenkins, 1976; Nuttall and Carter, 1982), well suited for the unevenly spaced data. It sequentially eliminates periodic components from the data, till the residuals meet certain criteria of the random process with the quasi-uniform spectral density, like that of the white noise. The results are presented in Figure 1.

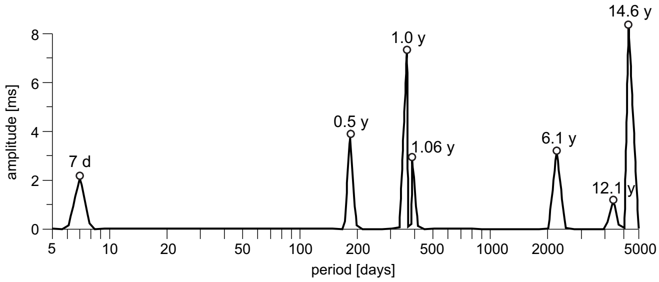

Figure 1: Spectrum of rotational time (UT1 – UTC)^{BG} - (UT1 – UTC)^{BIH} data series

4. SUMMARY AND CONCLUSIONS

Iterative spectral analysis of the observed time series of the offset of UT1 has enabled to allocate seven periodic terms. Available literature signalizes the presence of weekly variations of meteorological parameters, an amount of atmospheric aerosols and storm activity. Corresponding redistribution of moisture changing the moment of inertia of troposphere causes the variations of LOD.

Semi-annual and annual periods may be associated with seasonal redistribution of atmospheric and hydrological masses. The mechanism connecting those seasonal processes with the variations of the direction of the plumb line might be the same as in variations of gravity determined from GRACE data.

Annual term has an adjacent component with period near 387 days. Beat effect of those two terms produces an amplitude modulation of the offset of UT1 with period about 18 years. The consistency of modulation of the offset of UT1 with variations of coordinates of a celestial pole as well as of the difference (UT1 – UTC) is clearly visible. Beat leads to the regular change of phase of annual variations according to changes of amplitude. The largest deviation takes place in the autumn and in the regular way it slides approximately for one month within 18–19 years.

The term with period of 6 years was attempted to be associated with local variations of the direction of the plumb line. 12 year periodic term is rather connected with solar activity. The term with period near 14 years is mentioned in literature but it has not been associated with any physical phenomenon.

Seasonal variations of the refraction can follow the variations due to the weather conditions. Less likely, but still possible are weekly and long-periodic variations of the refraction. Simultaneous observations using different techniques, in particular those including space gravity missions may bring new material that will help to draw more certain conclusions.

Acknowledgements. The research was done in the framework of the statutory project “Problems of geodesy and geodynamics” of the IGiK, Warsaw. The authors acknowledge Mr. M. Moskwinski and dr M. Sekowski from IGiK for providing and pre-processing observational data.

5. REFERENCES

Box, G.E.P., Jenkinsi, G. M., 1976, “Time series analysis, forecasting and control”, Holden Day, San Francisco,

Chapanov, Y., Vondrák, J., Gorshkov, V., Ron, C., 2005, “Six-year cycles of the Earth rotation and gravity”, Reports on Geodesy, No 2(73), WUT, Warsaw, pp. 221-230.

Gorshkov, V., Shcherbakova, N., 2002, “Change of the Pulkovo longitude and longperiodic variations of the Earth rotation”, Izvestia G RN, SPb, 2002, No 216, pp. 430-437.

Hirt, C., Bürki, B., 2006, “Status of Geodetic Astronomy at the Beginning of the 21st Century”, Arbeiten der Fachrichtung Geodäsie und Geoinformatik der Universität Hannover, No 258, pp. 81-99.

Kruczyk, M., Rogowski, J.B., Vondrák, J., 1999, “Preliminary results of astrometric observations in Józefosław”, Reports on Geodesy, No 4(45), WUT, Warsaw, pp. 161166.

Kryński, J., Moskwiński, M., Zanimonskiy, Y.M., 2005, “Analysis of a long-standing series of rotational time determination at Borowa Gora Observatory” (in Polish), Proc. IGiK, T LI, z. 109, pp. 1-30.

Nuttall, A.H., Carter, G.G., 1982, “Spectral Estimation Using Combined Time and Lag Weighting”, Proc. IEEE, Vol. 70, September 1982, pp. 1115-1125.

ON THE IMPACT OF THE GALACTIC ABERRATION ON VLBI-DERIVED PRECESSION MODEL

Z.M. MALKIN
Pulkovo Observatory
Pulkovskoe Ch. 65, St. Petersburg 196140, Russia
e-mail: malkin@gao.spb.ru

ABSTRACT. Corrections to adopted precession rate are usually computed from the linear trends in long-term time series of celestial pole offset (CPO), which are the differences between the measured and the theoretical coordinates of the celestial pole. However, there may be systematic effects in these series influencing obtained result. One of those effects is the Galactic aberration (GA). In this study, we have estimated the impact of GA on the trends in CPO series. A comparison of linear trends in two time series computed with and without modelling of GA has shown that the difference can reach 20 μas/cy, which is substantial for the modern precession model. It was also found that GA influences long-period nutation terms. Thus we can conclude that GA should be included in the VLBI reduction model to avoid these systematic errors.

1. INTRODUCTION

With improvement in the accuracy of astronomical position measurements, the requirements to the accuracy of models used during data processing are also increased. It becomes necessary to take into account finer effects influencing the positions and motions of celestial objects. One of these effects is the Galactic aberration (GA), which is the prevailing part of the acceleration of the Solar system barycenter (SSB) due to its non-linear motion. This effect causes supplement systematic source motions that can influence secular terms in the celestial pole offset (CPO) series, and thus also the precession rate derived from analysis of trends in these series, or from a global VLBI solution.

The impact of GA on VLBI observations (also space astrometric observations) was foreseen many years ago, see e.g., a historical overview in Malkin (2011). However, until recently, the motions of radio sources due to GA were much smaller than the observational accuracy, and the length of highly accurate VLBI observation time series was relatively short to accumulate a significant error from ignoring GA. Thus the inclusion of the GA term in observational models was postponed. In this paper, we show that modeling of GA during the processing of long series of VLBI observations became already substantial. In particular, ignoring corrections of radio source motions for GA directly influences the determination of the precession rate.

2. THE IMPACT OF GA ON SOURCE PROPER MOTIONS

The basic formula for source proper motion caused by GA is given by Kovalevsky (2003)

$$\begin{aligned} \mu_l \cos b &= -A \sin l\,, \\ \mu_b &= -A \cos l \sin b\,, \\ A &= \frac{R_0 \Omega_0^2}{c}\,, \end{aligned} \tag{1}$$

where l and b are the source Galactic coordinates, R_0 is the Galactocentric distance of the SSB, V_0 and Ω_0 are Galactic rotation parameters, c is the speed of light. With the latest estimates of the Galactic rotation parameters, the Galactic aberration constant A = 5.0 μas with an error of several percent, which is sufficient as a good first approximation in order to model the GA effect.

Since GA has not been taken into account so far, its effect is present in all VLBI-derived catalogues of radio source positions, which are thus apparent coordinates. To derive the true coordinates w.r.t. GA influence, the corrections (4) must be subtracted from the catalog positions.

	Series	w/o GA	with GA
		Linear trend, μas/yr	
Variant 1	dX	9.6 ± 0.5	9.7 ± 0.5
	dY	-18.8 ± 0.6	-18.6 ± 0.6
		Linear trend, μas/yr	
Variant 2	dX	3.6 ± 0.8	3.6 ± 0.8
	dY	-14.0 ± 0.8	-14.0 ± 0.8
		Amplitude of 18.6-yr term, μas	
	dX	60.9 ± 5.7	62.6 ± 5.7
	dY	55.5 ± 5.5	54.7 ± 5.5

Table 1: Linear trend and the amplitude of the 18.6-year nutation term in the CPO series

3. THE IMPACT OF GA ON THE PRECESSION RATE

Corrections to the adopted precession rate can be derived directly from analysis of the linear trend in CPO time series dX and dY obtained from individual 24-hour observing sessions. To estimate the impact of GA, we processed 3136 24-hour session observed in 1984–2010, 5.6 million observations in total; 19 of 3136 CPO estimates were excluded from further analysis due to abnormal values or formal errors. After correcting for the Free Core Nutation (FCN), the CPO measurements are interpreted as errors in the adopted precession-nutation model.

Data were processed in two variants: with and without GA modelling. For each variant, dX and dY series were computed. At the next step, the parameters of linear trend in these CPO series were estimated both with and without simultaneous estimation of the parameters of the 18.6-year nutation term. Results of this computation are presented in Table 1.

4. CONCLUSIONS

We have estimated the impact of GA on parameters of precession-nutation model derived from VLBI observations. We found that influence on the linear trends in CPO series, i.e. precession rate, reaches about 0.2 μas/yr. The GA also influences the amplitudes of long-term nutation terms at a μas level, which, in turn causes a change in the linear trend. Notice that modern requirements to the accuracy of the precession model are 1 μas/cy (Capitaine et al. 2003).

Thus, our results indicate that the influence of GA on estimates of precession and nutation parameters is small but not negligible. Therefore, in spite of the fact that the computed effect is smaller than its formal uncertainty, it seems to be already necessary to include the GA correction in standard algorithms for the reduction of the VLBI and observations, as was foreseen may years ago.

More details on this study are given in Malkin (2011).

Acknowledgements. The author is grateful to the organizers of the conference for the travel support.

5. REFERENCES

Capitaine, N., Wallace, P. T., Chapront J., 2003, "Expressions for IAU 2000 precession quantities", A&A, 412, pp. 567–586.

Kovalevsky, J., 2003, "Aberration in proper motions", A&A, 404, pp. 743–747.

Malkin, Z.M., 2011, "The Influence of Galactic Aberration on Precession Parameters Determined from VLBI Observations", Astronomy Reports, 55(9), pp. 810–815.

ACCURACY ASSESSMENT OF THE ERP PREDICTION METHOD BASED ON ANALYSIS OF 100-YEAR ERP SERIES

Z.M. MALKIN[1], V.M. TISSEN[2]
[1]Pulkovo Observatory, St. Petersburg, Russia
e-mail: malkin@gao.spb.ru
[2]Siberian Scientific Research Institute of Metrology (SNIIM), Novosibirsk, Russia
e-mail: tissen@mail.ksn.ru

ABSTRACT. A new method has been developed at the Siberian Research Institute of Metrology (SNIIM) for highly accurate prediction of UT1 and Pole motion (PM). In this study, a detailed comparison was made of real-time UT1 predictions made in 2006–2011 and PM predictions made in 2009–2011 making use of the SNIIM method with simultaneous predictions computed at the International Earth Rotation and Reference Systems Service (IERS), USNO. Obtained results have shown that proposed method provides better accuracy at different prediction lengths.

1. INTRODUCTION

Currently used methods for Earth rotation parameters (ERP, comprising UT1 and polar motion) forecast are mostly based on statistical analysis of time series of observed EOP estimates. Usually, relatively short time series of the 2–6 years length are used to adjust the parameters of prediction model used. Thus these models take into account only short-term variations in Earth's rotation which are not stable enough at decadal time scales. For this reason, such an approach can cause the loss of important information on the long-term behavior of the Earth, which can influence the accuracy of the ERP prediction.

During the last several years, a new method for prediction of Earth rotation parameters (ERP) has been developed at the Siberian Scientific Research Institute of Metrology (SNIIM). It is described in detail in Tissen et al. (2009, 2010). The main distinctive feature of this method is making use of long-time series, up to 100 years, to estimate the trend component in the predicted ERP series. The trend component is modeled as a polyharmonic time series consisting of 20 and more terms with periods from several months to several decades. After removing the trend, the residuals are predicted making use of a modified autoregression technique.

To assess the accuracy of the method, we performed a detailed comparison of real-time ERP predictions computed making use of this method in 2006–2011 with simultaneous predictions computed at the International Earth Rotation and Reference Systems Service (IERS). Results of comparison are shown in the next section.

2. TESTING

The method was tested by means of comparison with the predictions made by the IERS Rapid Service/Prediction Center at USNO. To provide such a comparison, operational ERP series computed daily at USNO were extrapolated at SNIIM soon after appearance of the USNO ERP series in public access. Operationally computed SNIIM predictions were then stored together with the IERS Bulletin A predictions made on the same day. In total, 671 UT1 predictions made from January 2006 till August 2011 and 423 polar motion (PM) predictions made from October 2009 till August 2011 were used in this work. Results of our comparison of SNIIM and USNO predictions are shown in Figure 1.

It should be mentioned, that the frequency of SNIIM predictions gradually increased from about twice a month in 2006 to daily from September 2010 (the beginning of the IERS EOPCPPP campaign). As a consequence, predictions made in different years have different weight in the summary plots presented in Figure 1, especially for UT1. To make a more rigorous and detailed conclusion, a separate comparison was made for each year of data, which confirmed the main results obtained for whole the interval.

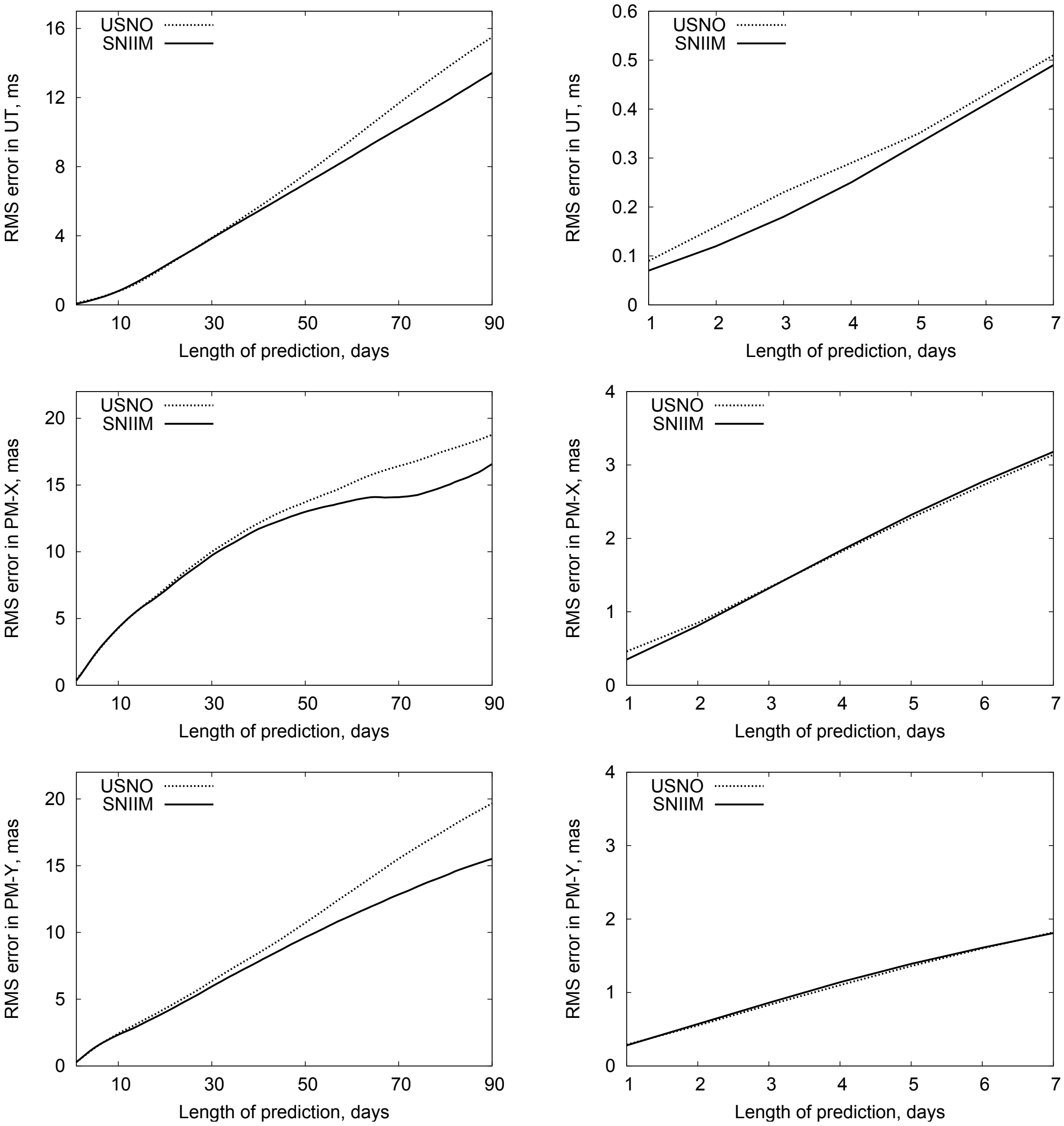

Figure 1: Comparison of the UT1 and polar motion prediction errors made in USNO and SNIIM.

3. CONCLUSIONS

The method of ERP prediction developed at SNIIM has been tested by comparison with the USNO results using 671 UT1 predictions for 2006–2011 and 423 PM predictions for 2009–2011. The SNIIM method has shown the better accuracy for medium-term (up to 3 months) predictions of UT1 and PM. Accuracy of ultra-short-term (several days) PM predictions is practically the same for SNIIM and USNO, but for UT1 prediction SNIIM method showed clear advantage. The latter is especially important for practical applications.

4. REFERENCES

Tissen, V., Tolstikov, A., Balahnenko, A., Malkin, Z. (2009), "High precision prediction of universal time based on 100-year data", Measurement Techniques, 52(2), pp. 1249–1255.

Tissen, V., Tolstikov, A., Malkin, Z., 2010, " UT1 prediction based on long-time series analysis", Artificial Satellites, 45(2), pp. 111–118.

DETECTION OF THE MUTUAL PERIODICAL CHANGES IN THE EARTH RATE OF ROTATION AND THE SOLAR ACTIVITY BY SINGULAR SPECTRUM ANALYSIS

D. MARČETA[1], S. ŠEGAN[1], N. GLIŠOVIĆ[2]

[1] Department of Astronomy, Faculty of Mathematics, University of Belgrade
Studentski trg 16, 11000 Belgrade, Serbia
e-mail: dmarceta@matf.bg.ac.rs, ssegan@matf.bg.ac.rs

[2] Mathematical Institute of the Serbian Academy of Sciences and Arts
Kneza Mihaila 36 , 11000 Belgrade, Serbia
e-mail: natasaglisovic@gmail.com

ABSTRACT. During the examination of regular and irregular changes in the Earth's rate of rotation and solar activity we noticed that there are a lot of repeating matches of the extreme values of these two phenomena in the sense that minimums in one quantity match maximums in the other quantity and vice versa. We used Singular Spectrum Analysis as a modern tool in spectral analysis to detect some harmonics in both phenomena that have very similar periods. The results indicate that there are some periodical changes in these two phenomena that could be connected and some of these periods which are quite long are already identified by some researches of the solar activity.

1. INTRODUCTION

The actual value of the length of day (LOD) originates from some long-term trend with short-term fluctuations between ±3 ms on the time scale of decades. At periods longer than few years, extending to many tens of years, the so-called decadal variations, the sources of excitation for the LOD are more enigmatic. The difficulty is the fact that at these periods many effects may be important, including viscoelastic behavior such as postglacial rebound and exchange of angular momentum with the fluid core. It has become common to invoke the core as the major cause of the decadal LOD changes. Although some climatic forcing of long period LOD changes has been recognized (Hide and Dickey, 1991), it is uncertain at what time scale the atmosphere and ocean become less important than the core. A further difficulty in assessing the atmosphere/ocean role at long periods is that the torques required to cause decadal LOD variations are utterly insignificant when compared with those applied by the atmosphere at shorter time scales.

Some of the recent records of Earth Orientation Parameters (EOP) and algorithms (Vondrák et al, 1998) are considered. The past solutions based on optical astrometry were merged with the combined solutions from the modern techniques (Vondrák and Čepek, 2001). The existing EOP series have been analyzed by many scientists. The most extensive reviews were given in well-known monographs (Munk and MacDonald, 1960; Lambeck, 1980).

By analyzing variation in the LOD and variation in the solar activity, namely number of Sun spots (NSS), some interesting relations were noticed. In Figure 1 are shown 11 years moving averages of these two parameters from 1761–1997 and also the results from the Singular Spectrum Analysis (SSA) (Golyandina et al, 2001) that was applied on these data.

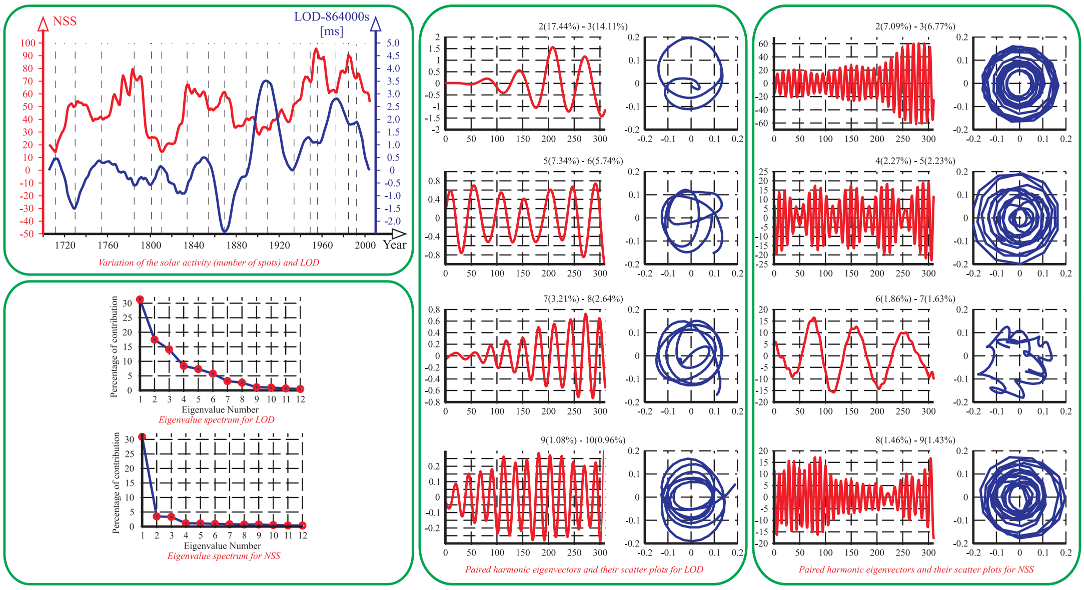

Figure 1: Variation of LOD and NSS and the SSA results

2. RESULTS

The harmonic component 2-3 for LOD has a period of 63 years and its amplitude is modulated with a period of about 178 years. The Amplitude of this component for NSS which has period of 11 years is also modulated with a period of about 178 years. This can be connected with the *Jose cycle* (9 Jupiter/Saturn synodic periods) of the solar activity.

The harmonic component 5-6 for LOD has a period of 47 years and its amplitude is modulated with a period of about 210 years which can be connected with the *de Vries cycle* of the solar activity and also with a period of 84 years which is roughly the period of amplitude modulation of harmonic 6-7 for NSS.

The harmonic term 9-10 has a period of 22 years (two solar cycles) and its amplitude is modulated with a period of about 230 years which can be connected with the *Suess cycle* of the solar activity.

3. CONCLUSIONS

The above analysis shows that the solar activity, directly or indirectly, has a significant influence on the changes in the Earth's rate of rotation. This allows us to use variations in the solar activity to predict changes in the LOD and thus ΔT. This can also be done backward in time to estimate the solar activity based on the historical data of ΔT.

Acknowledgements. This study was supported by the grant awarded by the LOC of Journées 2011

4. REFERENCES

Hide, R. and Dickey, J.O., 1991, "Earth's Variable Rotation", Science, vol. 253, no. 5020, pp. 629 - 637.

Vondrák, J., Pešek, I., Ron, C., Čepek, A., 1998, "Earth orientation parameters 1899.7-1992.0 in the ICRS based on the HIPPARCOS reference frame", Astron. Inst. of the Academy of Sciences of the Czech R., Publ. No. 87.

Vondrák, J. and Čepek, A. 2001, "On the use of the method of combined smoothing to combine EOP data from different techniques", Journées 2000 "Systèmes de référence spatio-temporels", Paris.

Munk, W. H. and MacDonald G. J. F., 1960, "The Rotation of the Earth: A Geophysical Discussion", Cambridge Univ. Press.

Lambeck K., 1980, 'The Earth's Variable Rotation: Geophysical Causes and Consequences", Cambridge Univ. Press.

Golyandina, N., Nekrutkin, V. and Zhigljavsky, A., 2001, "Analysis of Time Series Structure-SSA and Related Techniques", CHAPMAN & HALL/CRC.

NON REGULAR VARIATIONS IN THE LOD FROM EUROPEAN MEDIEVAL ECLIPSES

M.J. MARTINEZ[1], F.J. MARCO[2]

[1] Universidad Politecnica de Valencia
Dept. Matematica Aplicada, Valencia, Spain
e-mail: mjmartin@mat.upv.es

[2] Universidad Jaume I
Dept. Matematicas, Institut de Matematiques i Aplicacions de Castello, Castellon, Spain
e-mail: marco@mat.uji.es

ABSTRACT. The study of ancient eclipses has demonstrated its utility to approximate some astronomical constants, in particular in the field of the Earth's rotation. It is a well known fact that the rate of rotation of the Earth is slowly decreasing in time. There are many possible reasons for this fact, including internal and external mechanisms. The most important external causes are lunar and solar tides. While internal causes can be very diverse: examples of short term effects are changing wind patterns, electromagnetic coupling between the fluid core of the Earth and the lower mantle, while sea-level fluctuations associated with climatic variations are examples of long time effects. In any case, the most important cause is the tidal friction.

The visibility for a solar eclipse depends mainly on the position of the observer on the Earth's surface and on the position of the Moon and Sun in space. If we use the uniform Earth's rotation rate, we realize that the computed eclipse conditions do not correspond with the observed ones, in general. The computed eclipse path will be shifted westwards from the place of observation proportionally to the latitude of the central line of totality (in some cases, annularity). To make the calculations coincide with the observed eclipse, one has to apply a correction corresponding to the angular difference in geographical latitude.

ΔT value is needed not only for the calculation of exact times of an eclipse or occultation, but also for determining the position of the central line or the zone of visibility. A value $\Delta T = 3600$ s is roughly equivalent to a shift of 15° in longitude. Past values of ΔT can be deduced from historical astronomical observations such as ancient eclipses which have been widely studied by F.R. Stephenson [2], [3] who obtained an approximation formula for the values of ΔT in the range between -500 and +1950. This approximation is nowadays widely used in astronomical calculations.

The derived relative error from ΔT obtained from ancient eclipses is quite large, mainly because of the large width of the totality zone and the inaccuracy in the definition of the observational place. A possibility to partially solve these former problems is the analysis of total eclipse records from multiple sites, which could provide a narrow parameter range. In addition, conjunct analysis of these astronomical phenomena is useful for determining a range of ΔT in function of the tidal acceleration of the Moon

1. DETERMINATION OF ΔT AND THE TIDAL ACCELERATION VALUE

In the study of the variation of the Earth rotation using untimed observations of total eclipses, the precision of the ΔT obtained values depends mainly on the width of the totality band and on the precise definition of the observational places. The analysis of the eclipse observed from multiple sites provides a more precise measure for the former value. In addition, there is the possibility of including also the conjunct determination of ΔT and the variation of the tidal acceleration of the lunar motion.

We implicitly assume that the motion of the Moon is accurately known. In fact, this is true if we consider only the period of time covering the last decades, partly as a consequence of the use of modern techniques, such as LLR. Nowadays, we are aware of the existence of two highly correlated quantities: ΔT and the tidal acceleration of the Moon. The usual procedure deals only with the ΔT but in [1], and following the work of other authors ([2], [3] and [4]), we chose three particular eclipses from the XIIIth and XIVth century, all of them observed in Europe and we have obtained the ranges for ΔT for different values of the tidal acceleration. The inclusion in the study of other almost contemporary eclipses should provide an even narrower range of ΔT for each of the values of the tidal acceleration and could help to identify redundant or inconsistent observations.

2. PRELIMINARY RESULT FOR THE XIIIth AND XIVth CENTURIES

In the period between AD500 and the telescopic era numerous Moon and Sun eclipses have been recorded in Europe, especially after AD1000. In most cases, the observations were arranged in a 'professional' way, in the sense that the date and the instant of the day when the eclipse occurred were accurately reported, but in other cases, they were only roughly estimated.

In Figure 1 we can see a preliminary study based on the available data of eclipses observed in Europe between the XIII and the XIV centuries. The period of time covers from 1190 to 1410. The original number of observations from several sources was over 40, but we disregarded all the partial Sun eclipses. A total amount of 25 observations have been collected and analyzed, regarding special attention to those eclipses viewed from multiple sites.

The regression line has been obtained and compared to that obtained by Stephenson, showing a great agreement. However, further computations should be arranged, taking into account other historical data for the epoch, such as occultations or Lunar Eclipses. In addition, the consideration of suitable weights should be considered.

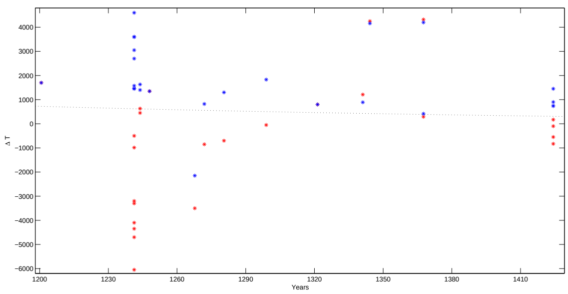

Figure 1: Preliminary study of the available data covering the XIII and the XIVth centuries. The * represent the limit values for the range of the ΔT value at each observational place, the dashed line represents the approximated values obtained by [2] for the ΔT

Acknowledgements. Part of this work was supported by grant P1-1B2009-07 from Fundacio Caixa Castello BANCAIXA.

3. REFERENCES

[1] Martinez M.J., Marco F.J. 1995. Proceedings of the Journees Systemes de Reference Spatio Temporels 2010. pp 213-214

[2] Morrison, L. and Stephenson, F. R., J. Hist. Astron., Vol. 35 Part 3, No. 120, pp 327-336 , 2004.

[3] Stephenson, F.R. Historical Eclipses and Earth Rotation, Cambridge: Cambridge University Press, 1997

[4] Tanikawa K., Soma M. Publ. Astron. Soc. Japan. 56. 879-885. 2004

COMPARISON OF POLAR MOTION EXCITATION FUNCTION DERIVED FROM EQUIVALENT WATER THICKNESS DATA, OBTAINED FROM FILTERED STOKES COEFFICIENTS

T. NAGALSKI
Space Research Center Polish Academy of Sciences
ul. Bartycka 18A, 00-716 Warsaw
e-mail: tnagalski@cbk.waw.pl

ABSTRACT. It is known that the estimates of the Earth's gravity field produced by the Gravity Recovery and Climate Experiment (GRACE) satellite mission can be used to infer changes in equivalent water thickness (EWT). However, inadequately smoothed GRACE satellite mission EWT data contain significant striping and thus ought to be filtered to improve signal to noise ratio. We used Stokes coefficients data from GFZ (GeoForschungsZentrum), JPL (Jet Propulsion Laboratory) and CSR (Center for Space Research), filtered by decorrelation anisotropic filters: DDK3, DDK2 and DDK1 (Kusche et al., 2009) and made available in the ICGEM (International Center for Global Earth Models). To determine gravimetric excitation function of polar motion for the entire globe or selected areas, we convert gravity coefficients into Equivalent Water Thickness fields. To eliminate stripes from the maps of the EWT, one uses anisotropic filters (Kusche et al., 2009) that are smoothing the EWT data. In this study we investigate the influence of decorrelation anisotropic DDK filters used to process the GRACE EWT fields on the determined polar motion gravimetric excitation functions. We investigate the effect of these filters for four regions: 1) entire Earth, 2) ocean area, 3) land area and 4) Tibetan Plateau area (a rectangle bounded by 4 points A(37°N,78°E), B(37°N,102°E), C(28°N,78°E), D(28°N,102°E). Stokes coefficients are made available on the ICGEM web site. The data contain spherical harmonic coefficients delivered by three research centers: CSR, GFZ, JPL. The time span of the data is 2002 - 2010. The time resolution is 30 days. The ICGEM delivers either the raw Stokes coefficients or filtered Stokes coefficients after application of the anisotropic filters.

Computation were based on the following equations: The global and regional gravimetric excitation of polar motion (Eubanks, 1993) is given by

$$\begin{bmatrix} \chi_1 \\ \chi_2 \end{bmatrix} = -\frac{1.098 R_{\oplus}^2}{C-A} \int\int \triangle q(\phi,\lambda,t) sin(\phi) cos(\phi) \begin{bmatrix} \cos(\lambda) \\ \sin(\lambda) \end{bmatrix} dS \ . \tag{1}$$

The function that converts gravity coefficients into maps of Equivalent Water Thickness reads (Chambers, 2008)

$$\triangle q(\phi,\lambda,t) = \frac{R_{\oplus}\rho_{\oplus}}{3\rho_W} \sum_{n=0}^{40} \sum_{m=0}^{n} \frac{(2n+1)}{(1+k_n)} P_{nm}(sin\phi)[\triangle C_{nm}(t) cosm\lambda + \triangle S_{nm}(t) sinm\lambda] \ . \tag{2}$$

χ_1, χ_2 - components of polar motion excitation function
$\triangle q(\phi,\lambda,t)$ - change of water storage in a unit area ($\frac{kg}{m^2}$)
$R_{\oplus}$ - mean Earth radius (6378km)
$\rho_{\oplus}$ - mean density of the Earth ($5517\frac{kg}{m^3}$)
dS - surface area element
C, A - principal moments of inertia
ρ_W - density of fresh water ($1000\frac{kg}{m^3}$)
ϕ, λ, t - latitude, longitude and time
k_n - load Love number of degree n
$P_{nm}(\cdot)$ - fully normalized associated Legendre polynomials degree n and order m

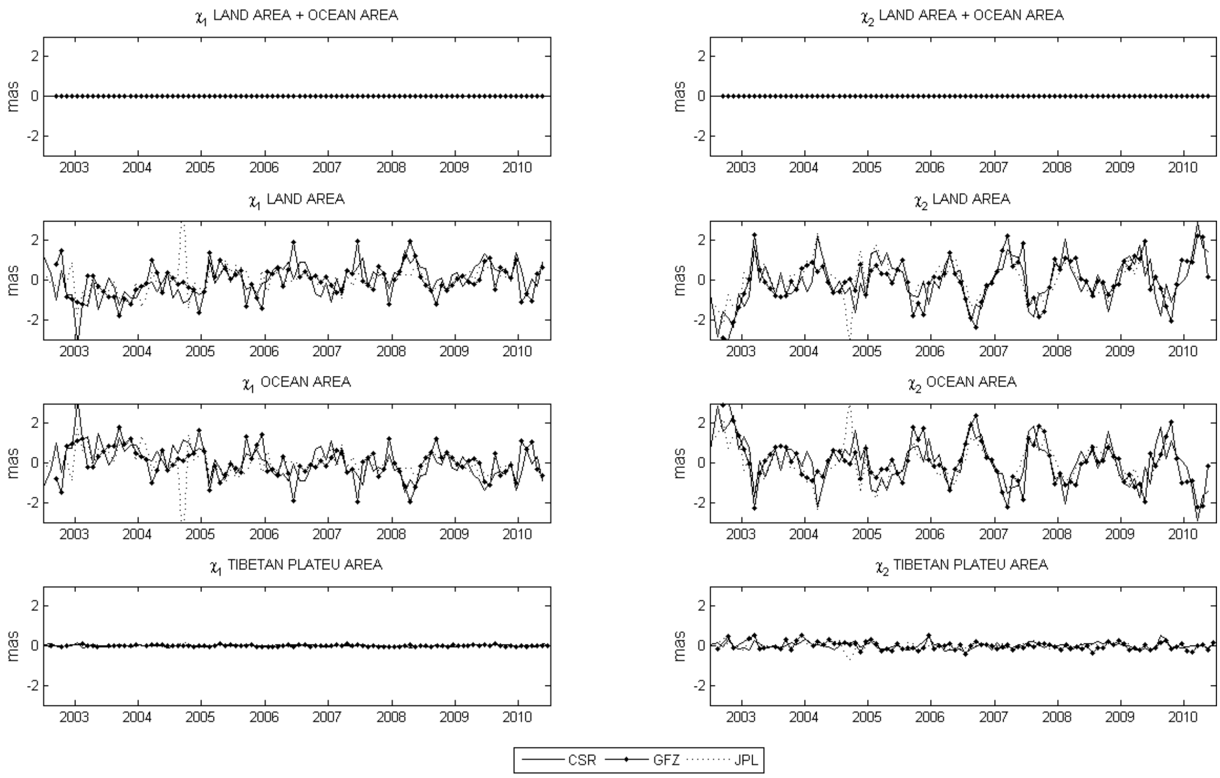

Figure 1: The differences between polar motion excitation computed from Stokes coefficients filtered by DDK3 and DDK2. Coefficients from CSR, GFZ and JPL are processed by the ICGEM. In the subsequent panels there are presented the excitation functions successively for the area of the entire Earth, ocean area, land area and Tibetan Plateau area.

Figure 1 shows comparison of excitation functions from the three research centers CSR, GFZ and JPL at two levels of filtering. In each panel there are plotted the excitation functions from CSR, GFZ and JPL. The analysis shows that the smoothing of Stokes coefficients at two levels of filtering does not affect the excitation function computed for the area of the whole globe. There are significant differences with respect to gravimetric excitation functions determined from filtered data if we take into account smaller areas such as: ocean area, land area or the Tibetan Plateau. Figure 1 also compares the impact of DDK3 and DDK2 filtering. Similar results are seen if we compare DDK1 and DDK2 or DDK1 and DDK3 filtering.

Acknowledgements: The research reported here was supported by the Polish National Science Centre and Information Technology, through project N526157040

REFERENCES

Chambers D. P., 2008, "Converting release-04 gravity coefficients into maps of equivalent water thickness", report, Center for Space Research, University of Texas

Eubanks, T.M., 1993, "Variations in the orientation of the Earth" in "Contributions of Space Geodesy to Geodynamics: Earth Dynamics", Vol. 24, pp. 1-54, eds Smith, D & Turcotte, D., American Geophysical Union, Washington, DC

Kusche J., Schmidt R., Petrovic S., Rietbroek R., 2009, "Decorrelated GRACE Time-Variable Gravity Solutions by GFZ, and their Validation using a Hydrological Model", Journal of Geodesy, Volume 83, Number 10, 903-913, DOI: 10.1007/s00190-009-0308-3

SIMULATION OF THE TIDES OF ANCIENT OCEANS AND THE EVOLUTION OF THE EARTH-MOON SYSTEM

P. NERGE[1], T. LUDWIG[1], M. THOMAS[2], J. JUNGCLAUS[3], J. SÜNDERMANN[4], P. BROSCHE[5]

[1] University of Hamburg, Department of Informatics
e-mail: petra.nerge@informatik.uni-hamburg.de

[2] Helmholtz Centre Potsdam, GFZ German Research Centre for Geosciences

[3] MPI-M Max Planck Institute for Meteorology, Hamburg

[4] University of Hamburg, Institute of Oceanography

[5] University of Bonn, Institute of Astronomy

ABSTRACT. We will simulate the spatial and temporal characteristics of the ocean tides for the present time as well as for a time slice of the Neoproterozoic Era (∼620 Ma b.p.). A focus will be on the transfer of angular momentum between the Earth and the Moon in order to physically simulate the observed increase of day length and the Moon's distance. The numerical results will be validated against geological proxy data of the tidal spectrum of the Australian continental plate.

Subsequently, the evolution of the ocean tides under the influence of the continental drift from present time until the Neoproterozoic will be simulated. Again, a focus will be on the transfer of angular momentum between the Earth and Moon in order to physically explain the dynamical evolution of the Earth-Moon system and, therewith, the increase of day length of about 2 hours as well as the decrease of month length of about 1 day.

Present geodetic and astronomical observations confirm a secular increase of day length of about 2 ms/cy and a lunar recession rate of about 4 cm/year (Williams et al., 2008), which equals a decrease of Earth's rotational energy of about 4×10^{12} W and a mean torque around the Earth's rotational axis of about 5×10^{16} Nm.

The transfer is mainly determined by the ocean tides and is closely interlinked with their resonance characteristics. First model simulations of the M_2 tide for the Permian ocean 250 − 230 Ma b.p. depicted that the angular momentum transfer in the Earth-Moon system was smaller by a factor 2 than at recent time − with comparable tidal amplitudes (Sündermann and Brosche, 1978). Brosche and Hövel (1982) have investigated the angular momentum transfer under the continental drift of the American plates over the last 20 Ma until 10 Ma in the future. Already on this time scale the transfer varies by a factor 2. Comparatively, the deceleration of the Earth's rotation is currently quite high. A variation of the mean tidal torque of about 10% already during the last ten thousand years was evinced by simulations of the M_2 and O_1 tide (Thomas and Sündermann, 1999). Backward simulations of the M_2 tide for 10 topographies of the Precambrian indicate that the angular momentum transfer was almost smaller during the Earth's history than today (Nerge, 1998). If we go backward in time, the Moon approaches the Earth, but it does not reach the Roche limit.

However, there are still considerable deficits in the understanding of Earth's history on the geological time scale. The limited availability of geological proxy data has so far prevented a detailed quantification of the transfer of angular momentum in the Earth-Sun-Moon system far back in the Earth's history. Considering recent paleontological data, and advances in numerical modelling and high performance computing, we will strive to reduce these deficits. First self-consistent geological data on ocean tides, Earth's rotational parameters and orbital elements of the Moon have been provided by the research of Williams (2000) on the sediment layers of South Australia for the Neoproterozoic (∼620 Ma b.p.).

Further, Li, et al. (2008) presented a synthesis of formation (1300 Ma b.p.– 900 Ma b.p.) and breaking up (< 600 Ma b.p.) of the supercontinent Rodinia and devised detailed new paleographical maps for the Neoproterozoic containing the time slice around ∼620 Ma b.p.

Special efforts must be given to the modelling of ephemerides through the Earth-Moon history. A new solution for the computation of the insolation quantities on Earth spanning from -250 Ma to 250 Ma was given by Laskar, et al. (2004), with the evolution of the Earth-Moon semimajor axis of approximately

58.5 Earth radii for 250 Ma b.p., which seems to be in conflict with 58.16 ± 0.30 Earth radii for ∼620 Ma b.p. deduced by Williams (2000); one main source of uncertainty is the evolution of the tidal dynamics and other related factors. However, the most regular components of the orbital solution could still be used over a longer time span.

The simulation of the ocean tides shall be carried out with the three-dimensional Max-Planck-Institute ocean circulation model (Marsland, et al., 2003) forced by the complete lunisolar tidal potential (Thomas, 2001). A curvilinear grid with freely selectable grid poles is utilized by the model. Hence, the resolution can be efficiently increased around Australia for evaluation of our results.

At least 100 years will be the simulation period to also resolve the lunar nodal period of 18.6 years at present. For the time interval back to ∼620 Ma b.p. we plan at least 62 simulations with an interval of 10 Ma. Continuous simulation of the whole interval would require too much computational effort. For the paleogeographical maps, also considering the paleobathymetries, we will base ourselves e.g. on Li, et al. (2008), Müller et al. (2008), Williams et al. (2008) and the Paleomap Project of C.R. Scotese.

The whole work will result in *one* considerably denser reconstruction of tidal dynamics from the Neoproterozoic until the present. Appropriate to the uncertainties in the knowledge of the Earth's history, it will be a first contribution to a statistical treatment of preferably a great many configurations as recommended by Brosche and Sündermann (2011). Astronomers and geodesists could access the energy and angular momentum budgets for the analysis of the evolution of the Earth-Moon system; geologists as well for the analysis of periodic growth features or sedimentary rhythmites.

Acknowledgements. We are grateful for the support from the German Research Foundation through the grant LU 1353/6-1 and the German Climate Computing Center.

REFERENCES

Brosche, P. and Hövel, W., 1982. Tidal friction for times around the presence. In Brosche, P. and Sündermann, J., eds. Tidal Friction and the Earth's Rotation II, Springer Verlag, 175-188.

Brosche, P. and Sündermann, J., 2011. Ozeanschwingungen und Gezeitenreibung – Zur Bewertung von Resonanzkurven. DGG-Mittlg., 1/2011, 43-50.

Laskar, J., Robutel, P., Joutel, F., Gastineau, M., Correia, A. C. M. and Levrard, B., 2004. A long-term numerical solution for the insolation quantities of the Earth. Astron. Astrophys, 428(1), 261-285.

Li, Z.X., Bogdanova, S.V., Collins, A.S., Davidson, A., De Waele, B., Ernst, R.E., Fitzsimons, I.C.W., Fuck, R.A., Gladkochub, D.P., Jacobs, J., Karlstrom, K.E., Lu, S., Natapov, L.M., Pease, V., Pisarevsky, S.A., Thrane, K. and Vernikovsky, V., 2008. Assembly, configuration, and break-up history of Rodinia: A synthesis. Precambrian Res., 160, 179-210.

Marsland, S. J., Haak, H., Jungclaus, J.H., Latif, M. and F. Roeske, 2003. The Max-Planck-Institute global ocean/sea-ice model with orthogonal curvilinear coordinates. Ocean Modell., 5, 91-127.

Müller, D., Sdrolias, M., Gaina, C., Steinberger, B. and Heine, C., 2008. Long-term sea-level fluctuations driven by ocean basin dynamics. Science 319, 1357-1362.

Nerge, P., 1998. Resonanzeigenschaften der globalen Ozeangezeiten für Topographien der Gegenwart und des Proterozoikums Gezeitendrehmoment und die Entwicklung des Systems Erde- Mond während der Erdgeschichte. Diplomarbeit, Institut für Meereskunde, Universität Hamburg, Germany. 117p.

Sündermann, J. and Brosche, P., 1978. The numerical computation of tidal friction for present and ancient oceans. In Brosche, P. and Sündermann, J., eds. Tidal Friction and the Earth's Rotation, Springer Verlag, 125-144.

Thomas, M., 2001. Ozeanisch induzierte Erdrotationsschwankungen – Ergebnisse eines Simultanmodells für Zirkulation und Gezeiten im Weltozean. Dissertation, Universität Hamburg, Fachbereich Geowissenschaften, 129p.

Thomas, M. and Sündermann, J., 1999. Tides and tidal torques of the world ocean since the last glacial maximum. J. Geophys. Res., 104, C2, 3159-3183.

Williams, G.E., 2000. Geological constraints on the precambrian history of earth's rotation and the moon's orbit. Rev. Geophys., 38, 37-59.

Williams, G.E., Gostin, V.A., McKirdy, D.M. and Preiss, W.V., 2008. The Elatina glaciation, late Cryogenian (Marinoan Epoch), South Australia: Sedimentary facies and palaeoenvironments. Precambrian Res., 163, 307-331

Williams, J.D., 2008, DE421 Lunar orbit, physical librations, and surface coordinates, JPL IOM 335-JW,DB,WF-20080314-001, March 14, 2008.

NUTATION AND HIGH PRECISION ASTROMETRY OBSERVATION TECHNIQUES

K. YAO, N. CAPITAINE, S. LAMBERT
SYRTE, Observatoire de Paris, CNRS, UPMC
61, Ave. de l'Observatoire, 75014 Paris, France
e-mail: kunliang.yao@obspm.fr, n.capitaine@obspm.fr, sebastien.lambert@obspm.fr

ABSTRACT. The purpose of this paper is to compare the principles and potentials of the best high accuracy astrometry/geodetic techniques for the determination of the Earth's nutation. Nutation estimation is currently dominated by VLBI observations. The GNSS satellite orbits are not stable celestial references due to the discrepancies in the models for various perturbations and are correlated with Earth's rotation. But the high precision and the high time resolution of the GNSS observations give them the possibility to be used to estimate short-period nutation terms. In this work, based on observations from 2002 to 2010, we make an evaluation of the precision and resolution that can be achieved by each of these techniques for the estimation of the amplitudes of nutation as functions of the period. We report on the accuracy of the IAU 2006/2000 precession-nutation model as compared to VLBI observations and on some preliminary tests for possible GNSS contribution for improving that model.

1. DETERMIMATION OF NUTATION BY VLBI AND GPS

VLBI is currently the most important technique to estimate the Earth rotation angle, ERA, (or length of day, or UT1) as well as precession-nutation; IVS analysis centers currently provide celestial pole offsets, i.e. corrections (dX, dY) to the IAU 2006/2000 precession-nutation model (Wallace & Capitaine, 2006), X, Y being the coordinates of the Celestial intermediate pole (CIP) in the Geocentric Celestial Reference System (GCRS).

GPS is the most important technique to estimate the pole coordinates x_p, y_p, but does not provide celestial pole offsets. However, it has been shown (Rothacher et al. 1999, Weber & Rothacher, 2001) that GPS can contribute to nutation estimation for short term nutations.

In both techniques, the effect of precession-nutation appears through the transformation between coordinates [ITRS] in the International Terrestrial Reference System and [GCRS] in the GCRS by the following equation:

$$[GCRS] = Q(t) * R(t) * W(t) * [ITRS], \tag{1}$$

where Q(t) is a matrix determined by (X, Y), R(t) is a matrix determined by the rotation angle ERA, and W(t) is a matrix determined by (x_p, y_p).

1.1. Analysis of VLBI solutions

We have applied a least-squares method, based on Equation (2), to different VLBI solutions for estimating the largest corrections to nutation :

$$dX + \mathrm{i} * dY = \sum (A_{retro} * e^{retro} + A_{pro} * e^{pro}). \tag{2}$$

The results shown in Table 1 are all consistent for terms with periods greater than 27.6 days, but large discrepancies appear between those corresponding to shorter periods. This implies that VLBI is able to estimate corrections to the IAU 2000 nutation; it can detect a small signal corresponding to the long period nutation terms, but is not efficient for estimating short period terms.

Amplitudes (uas)	solution YAO		bkg00013		iaa2007a		opa2010d	
periods	Real	imag	real	imag	real	imag	real	imag
-6798.4	26.8 ±1.8	-31.1 ±1.8	59.1 ± 2.2	-16.0± 2.2	22.5 ± 2.2	-42.8 ± 2.2	28.5 ± 1.3	-27.2 ± 1.3
6798.4	18.4 ±1.8	-34.8± 1.8	30.3± 2.2	-23.8± 2.2	21.9± 2.2	-35.2± 2.2	24.3± 1.3	-28.6±1.3
-182.6	-11.3± 1.6	5.5± 1.6	-13.3± 2.1	7.9± 2.1	-15.6± 2.1	5.3± 2.1	-11.8± 1.1	6.0± 1.1
-27.6	-15.0± 1.6	-3.4± 1.6	-14.7± 2.1	-4.4± 2.1	-17.7± 2.0	-2.9± 2.0	-14.7± 1.0	-6.8± 1.1
-13.7	-14.9± 1.6	-12.3± 1.6	-9.5± 2.1	-9.1± 2.1	-14.3± 2.0	-10.9± 2.0	-10.6± 1.0	-11.9± 1.0
13.7	-7.6± 1.6	11.5± 1.6	-8.3± 2.1	12.4 ±2.1	6.1± 2.0	-5.9± 2.0	-4.9± 1.0	12.8± 1.0
-9.13	-5.3± 1.8	2.8± 1.8	-7.2± 2.2	3.7± 2.2	-4.3± 2.2	-0.5± 2.2	-5.5± 1.1	0.7± 1.1
7.10	7.0± 1.6	-0.2± 1.6	7.6± 2.1	-1.4± 2.1	6.3 ±2.0	-1.2± 2.0	-2.8± 1.1	0.0± 1.1
6.86	5.1± 1.9	-1.2± 1.9	5.8± 2.4	5.3± 2.4	1.7± 2.3	7.3± 2.3	2.8± 1.2	1.1± 1.2
WRMS (mas)	dX	dY	dX	dY	dX	dY	dX	dY
pre-fit	0.618	0.886	0.177	0.191	0.176	0.217	0.231	0.219
FCN removed	0.604	0.823	0.142	0.140	0.141	0.144	0.181	0.184
post-fit	0.579	0.767	0.122	0.123	0.118	0.121	0.133	0.133

Table 1: Amplitudes of a few nutation terms estimated by least-squares analyses of VLBI solutions and WRMS

1.2. Satellite orbital elements and nutation

By investigating the ITRS satellite position, we can obtain from Equation (1) and (Rothacher & Beutler 1999), the following relations between the $\dot{X}$, $\dot{Y}$, $\dot{\text{ERA}}$ and satellite orbital parameters rates (Ω: ascending node, i: inclination, u_0: argument of latitude at the osculation epoch):

$$\dot{\text{ERA}} = -\dot{\Omega} - \cos i \cdot \dot{u}_0, \quad \dot{X} = -\sin\Omega \cdot \dot{i} + \sin i \cos\Omega \cdot \dot{u}_0, \quad \dot{Y} = \cos\Omega \cdot \dot{i} + \sin i \sin\Omega \cdot \dot{u}_0. \tag{3}$$

Due to strong correlations, the $\dot{X}$, $\dot{Y}$, $\dot{\text{ERA}}$ estimates are affected by the systematic errors in the orbital elements coming from deficiencies in the gravitational and non gravitational forces. Therefore, in order to use Equation (3) with the real GPS satellite orbital elements (see Figure 1), the main sources of perturbations (listed in Table 2) need to be modeled as best precise as possible.

Main sources of perturbation	acceleration magnitude ($m * s^{-2}$)
Non-sphericity of the Earth	$5 * 10^{-5}$
Moon attraction	$5 * 10^{-6}$
Sun attraction	$2 * 10^{-6}$
Direct and indirect Sun radiation pressure	$1 * 10^{-7}$
Relative effect	$3 * 10^{-9}$

Table 2: Perturbation on the GPS satellite orbital elements

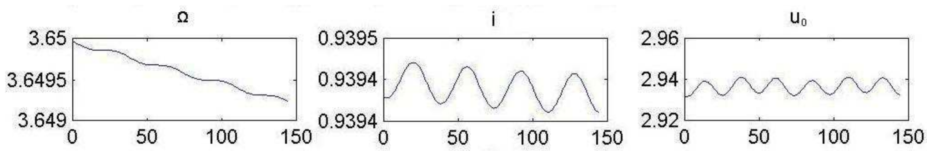

Figure 1: GPS satellite angular orbital elements during 1 day, sample rate: 10 min

The numerical values of the rates of (X, Y) and ERA can be compared with the semi-analytical series for the time derivatives derived from the IAU 2006/2000 model for X and Y (see Yao & Capitaine 2011). This would be a new method to estimate discrepancies in the nutation model. Preliminary tests have been done with GPS observations during a 3-month period in 2011.

2. REFERENCES

Rothacher M., Beutler G., Herring T. A., Weber R., 1999, "Estimation of nutation using the Global Positioning System", Journal of geophysical research, vol. 104, n^{0}B3, pp. 4835–4859.

Wallace, P.T., Capitaine, N., 2006, "Precession-nutation procedures consistent with IAU 2006 resolutions", A&A , 459, pp. 981–985.

Weber, R., Rothacher M., 2001, "A Revised Set of Nutation Amplitudes Calculated From six Years of GPS Data", AGU Meeting 2001, abstract G51C-0252.

Yao, K., Capitaine, N., 2011, "Modeling of the Earth rotation and high precision astrometric observation techniques", Proceedings of the Journées 2010 "Systèmes de Référence Spatio-Temporels", N. Capitaine (ed.), Observatoire de Paris, pp. 227–228.

Session 4:

Celestial mechanics of solar system bodies

Mécanique céleste des corps du système solaire

ANALYTICAL MODELING OF THE RIGID INTERNAL MOTIONS OF A THREE-LAYER CELESTIAL BODY THROUGH HAMILTON'S PRINCIPLE

A. ESCAPA
Department of Applied Mathematics, University of Alicante
PO Box 99, E-03080 Alicante, Spain
e-mail: alberto.escapa@ua.es

ABSTRACT. We describe how to construct an analytical approximated representation of the internal rigid motions of a non–rigid three–layer celestial body by using the Hamilton's principle. This method runs parallel to those employed in the Lagrangian or Hamiltonian formulations of Analytical Dynamics. We also discuss the advantages of this approach with respect to other known treatments that tackle this complex problem.

1. INTRODUCTION

The interior of some bodies of the solar system can be approximately reproduced by a non–rigid three–layer model. This model consists on a solid external layer that encloses a fluid containing a solid body (see Figure 1). Indeed, it is the case of the Earth, but other planets or moons might also present the same structure (see, for example, Grinfeld and Wisdom 2005, Hussmann et al. 2006) like Mercury or some icy moons containing a subsurface ocean (Europa, Titania, etc.).

Although all of these bodies share a similar structure, it is necessary to remark that their physical characteristics can be quite different. This is easily understood if we consider, for example, simple models with homogeneous spherical layers for the Earth, Mercury, Titania, and Europa (Grinfeld and Wisdom 2005, Hussmann et al. 2006). The ratio between the density of the fluid and that of the internal solid layer, ρ_F/ρ_S, is close to 1 in the case of the Earth and Mercury, and relatively small for Europa and Titania. This fact is explained taking into account that for the Earth and Mercury the fluid and the internal solid layer have an almost identical iron composition. In contrast, the fluid layer of the models of the icy bodies Europa and Titania is a subsurface ammonia–water ocean, much less dense than the internal solid layer that is composed of silicate rock (Hussmann et al. 2006).

We can also observe other important differences in the relative mass of each layer depending on the particular body. This is shown in Table 1 for the above mentioned bodies, where we have displayed the values for the ratios m_M/m, m_F/m, and m_S/m, the subscripts M, F, and S referring to the external layer, the fluid, and the internal solid layer, respectively. The symbol m denotes the mass of the body and $m_{M,F,S}$ the mass of the respective layer.

Body	m_M/m	m_F/m	m_S/m	ρ_F/ρ_S
Earth	0.63	0.35	0.02	0.92
Mercury	0.31	0.09	0.60	0.84
Titania	0.38	0.04	0.58	0.29
Europa	0.04	0.04	0.92	0.24

Table 1: Some examples of simple models of three–layer bodies of the solar system.

From the point of view of Dynamics, this system presents an interesting feature: even for the simplest models the solid constituents can perform independent rigid internal motions, that is to say, can make independent rotations and translations around the barycenter of the body. Therefore, for these models there can appear differential rotations, or librations, and translations of the internal solid body with respect to the external solid layer.

The interest in investigating those internal motions relies on the fact that their modeling is essential to determine the evolution of the reference systems attached to each celestial body. At the same time, since the rigid motions are affected by the specific characteristics of the body, their observation can constrain, to some extent, the structure of the body (see, for example, Koot 2011), giving valuable information about its interior. Many times it is not possible to obtain this information by other means.

2. COMMON APPROACHES TO STUDY THE DYNAMICS OF A THREE–LAYER BODY

There exist distinct ways to model the dynamical behavior of the rigid motions of a three–layer body (see, for example, Escapa et al. 2001, Escapa and Fukushima 2011, and references therein), whose geometrical and physical configurations are assumed to be quasi–spherical. Some of them are based on the partial differential equations of Continuous Mechanics, such as the elastic–gravitational normal mode theories developed to study the rigid internal motions of the Earth (see, for example, Smith 1977). However, the intrinsic nature of these normal mode methods, which usually are numerical, does not provide much insight into the evolution of the model and its dependence with the physical characteristics of the body. In addition, to profit all the potential of these approaches it is necessary to have detailed density and rheological parameter profiles within the body, what can present some inconveniences from the perspective of Dynamical Astronomy (see, for example, Dehant et al. 1999), or not to be available for some bodies of the solar system.

Other different approaches consider the vectorial form of the evolution of the linear and angular momentum for each layer taken as a whole subsystem. It is the case, for example, of Mathews et al. (1991) when studying the Earth nutations, of Van Hoolst et al. (2008) when treating the Europa librations, or of Grinfeld and Wisdom (2005) when modeling the differential internal translations of a three–layer body, usually referred as the Slichter modes in the Earth terminology. These formulations require the explicit calculation of the forces and torques exerted by each layer on the remaining ones. For instance, it is necessary to compute the hydrodynamical interactions that the fluid exerts on the adjacent solid layers. Since these methods only focus on a part of the internal motions of the system, the rigid part, they are less complete than those based on Continuous Mechanics. Indeed, in their construction it is necessary to make some *a priori* assumptions that approximate to some degree the fluid flow and the elastic deformation field of its constituents. Nevertheless, they offer some advantages due to its relative simplicity, which often makes possible to obtain a clear representation of the influence of the physical characteristics of the body in its motion. This is mainly due to the fact that the rheology of the body is characterized by a small set of parameters that reflects these properties in an averaged sense such as the moments of inertia, Love numbers, etc. It allows the fitting of some of them to the available observations, what is specially meaningful for astronomic and geodetic purposes.

Yet another possible framework to tackle the dynamics of a three–layer body is by means of the variational principles of Mechanics, starting from Hamilton's principle (in its broader sense) and running parallel to the formulations used in Analytical Dynamics. There have been many investigations that have already employed this kind of methods to study the rotational, or librational, motions of non–rigid celestial bodies composed of one or two layers. This is the case of the Earth (see, for example, Poincaré 1910; Jeffreys and Vicente 1957; Moritz 1982; Kubo 1991; Getino 1995; Getino and Ferrándiz 1995, 2001; Ferrándiz et al. 2004; Escapa 2011), but also of other celestial bodies like, for example, Io (Henrard 2008) or Mercury (Noyelles et al. 2010). These variational formulations have been extended to different three–layer bodies, considering the rotational motions (see, for example, Escapa et al. 2000, 2001, 2002) and also the translational ones (Escapa and Fukushima 2011).

The variational methods present the same advantages and limitations as the vectorial treatments when compared with Continuous Mechanics formulations. However, Hamilton's principle theories have also some important gain with respect to the vectorial approaches. Besides the general benefits over the vectorial mechanics methods (see, for example, Lanczos 1986), the variational theories allow to treat the fluid and solid layers as one single dynamical system. It implies that it is not necessary to compute explicitly the hydrodynamical interactions exerted by the fluid on the solid layers (see, for example, Lamb 1963), what simplifies greatly the construction of the equations of motion. In addition the form of these equations is well suited to apply the analytical and numerical mathematical tools developed in other branches of Celestial Mechanics. It makes possible, for example, the construction of consistent higher order analytical approximated solutions or the study of the couplings among the internal and external rigid motions.

3. ANALYTICAL MODELING TROUGH HAMILTON'S PRINCIPLE

Next, we will briefly describe the necessary steps to determine the rigid internal motions of a three–layer celestial body within a variational framework. To get a more complete description on these topics, we refer the reader to the works by Escapa et al. (2001, 2002), Escapa and Fukushima (2011), and references therein.

Hamilton's principle for holonomic dynamical systems (see, for example, Whittaker 1988) states that the value of a certain integral is stationary in the motion. Explicitly, it holds that

$$\int_{t_0}^{t_1} (\delta\mathcal{T} + \delta\mathcal{W})\ dt = 0, \tag{1}$$

where δ denotes the variation, $\mathcal{T}$ is the kinetic energy of the system, and $\mathcal{W}$ is the work done on the system by the external forces that, in the general situation, are non–conservative. From this equation, and following a known process, one obtains a system of differential equations that determines the motion. These differential equations can adopt diverse forms. From the point of view of Celestial Mechanics and focusing on the study of the dynamics of a three–layer celestial body, the most common and useful forms are those derived from a Lagrangian or a Hamiltonian functions of the system.

Let us recall that if the Lagrangian of the system is given by

$$\mathcal{L} = \mathcal{T} - \mathcal{V}, \tag{2}$$

where $\mathcal{V}$ is the potential energy stemming from the conservative forces acting on the system, the equations of motion in terms of a holonomic set of n generalized coordinates q and its associated velocities $\dot{q}$ are

$$\frac{d}{dt}\left(\frac{\partial\mathcal{L}}{\partial\dot{q}_i}\right) - \left(\frac{\partial\mathcal{L}}{\partial q_i}\right) = \mathcal{Q}_i. \tag{3}$$

Here, $\mathcal{Q}_i$ are the generalized force associated to the coordinate q_i, with $i = 1, ..., n$, included to account for the non–conservative nature of a part of the external interactions.

A related form to these equations is obtained when substituting the generalized velocities $\dot{q}_i$ by n independent linear combination of them ω_i, which define a quasi–coordinates set. This substitution is convenient, for example, in some applications related with the rotation of celestial bodies (see, for example, Moritz 1982, Escapa et al. 2002). By so doing, the equations of motion (see, for example, Whittaker 1988) turn out to be

$$\frac{d}{dt}\left(\frac{\partial\mathcal{L}}{\partial\omega_i}\right) + \sum_{j,\,k} c_{ijk}\omega_j\frac{\partial\mathcal{L}}{\partial\omega_k} - \sum_r \beta_{ri}\frac{\partial\mathcal{L}}{\partial q_r} = \mathcal{Q}_i, \tag{4}$$

where c_{ijk} and β_{ri}, with $i, j, r = 1, ..., n$, are functions of q_i, whose explicit expressions can be derived from the relationship between $\dot{q}$ and ω.

Finally, other important way to implement Hamilton's principle is through the Hamiltonian function of the system. In the case of natural systems (see, for example, Whittaker 1988), it takes the form

$$\mathcal{H} = \mathcal{T} + \mathcal{V}. \tag{5}$$

This function depends on n canonical momenta p_i, with $i = 1, ..., n$, and n canonical conjugated coordinates q_i (not being necessarily a holonomic set of generalized coordinates) that describe the dynamical configurations of the system

$$\begin{aligned}\frac{dp_i}{dt} &= -\frac{\partial\mathcal{H}}{\partial q_i} + \mathcal{Q}_{q_i},\\ \frac{dq_i}{dt} &= \frac{\partial\mathcal{H}}{\partial p_i} - \mathcal{Q}_{p_i}.\end{aligned} \tag{6}$$

The functions $\mathcal{Q}_{p_i}$ and $\mathcal{Q}_{q_i}$ are the canonical generalized forces that must be include in the presence of non–conservative forms. Although sometimes the geometrical or kinematical meaning of a canonical set is not so clear as in the case of the generalized coordinates, the Hamiltonian formalism has been very useful in the field of Celestial Mechanics because of the existence of systematic perturbation methods, such as those based on the Lie series method (Hori 1966), which allows to find an approximation of the solution of the equations of motion.

Regardless the particular formalism that materializes Hamilton's principle, the procedure in which the equations of motion are constructed is quite similar from a formal perspective and can be sequenced as follows:

a) To chose a finite number of generalized coordinates, or canonical variables, that determine the rigid motions of the system. For example, if the solid layers are assumed to be rigid bodies one could take the coordinates of their barycenters to describe their translational motion and some angles, like the Euler ones, to describe their rotational motion. When considering elastic bodies this choice must be adapted by introducing, for example, the concept of Tisserand mean system (see, for example, Escapa 2011). In regard to the fluid, and depending on the particular problem under consideration, the fluid flow can be represented for these purposes by means of a potential motion (see, for example, Escapa and Fukushima 2011), a Poincaré flow (see, for example, Escapa et al. 2001, 2002), etc.

b) To construct the kinetic energy of the system. It is given by the sum of the kinetic energy of its layers

$$\mathcal{T} = \mathcal{T}_M + \mathcal{T}_F + \mathcal{T}_S. \tag{7}$$

In the general situation, and once evaluated the field of the velocities within the body, this computation relies on the modeling of the inertia matrices that depends on the elastic deformation of the layers (see, for example, Getino and Ferrándiz 1995, 2001, Escapa 2011) and also on the deformation of the fluid layer due to the differential motions of the solid constituents (see, for example, Escapa et al. 2001). It is important to underline that in the variational methods the term $\mathcal{T}_F$ is the responsible of modeling the solids–fluid interactions (see, for example, Lamb 1963). So, those interactions are automatically incorporated when constructing the kinetic energy of the system, without the need of computing them separately as it is done in the vectorial treatments.

c) To obtain the potential energy of the system. This function, which has often a gravitational origin, is convenient split into the form

$$\mathcal{V} = \mathcal{V}_{\text{int}} + \mathcal{V}_{\text{ext}}, \tag{8}$$

where $\mathcal{V}_{\text{int}}$ is the internal potential energy of the system, arising from the conservative interactions among the constituents of the non–rigid body. In a similar way, $\mathcal{V}_{\text{ext}}$ is the external potential energy of the system that accounts for the conservative interactions between the body and the external bodies or fields.

d) To compute the generalized, or canonical, forces due to non–conservative forces or torques. These interactions are related with dissipative process usually connected with the rheological properties of the fluid. The construction of these functions requires the evaluation of the virtual work made by the forces, or torques, in a virtual displacement of the system that, depending on the situation, must be expressed in terms of the generalized coordinates, the quasi–coordinates, or the canonical set (see, for example, Getino et al. 2000, Escapa et al. 2002).

e) To form the system of ordinary differential equations that characterize the dynamics of the system. From the expressions of the kinetic energy, the potential energy, and the generalized forces of the system, the computation of the equations of motion is straightforward by applying Equations (3), (4), and (6) depending on the chosen formalism to describe the dynamics of the system.

Once obtained the differential equations of the system, it is necessary to solve them in order to have a quantitative description of the motion. Regrettably, in very few cases it is possible to find an exact analytical solution of this kind of equations. Therefore, bearing in mind the purposes of the investigations one is forced to employ analytical perturbation methods, numerical integration methods, or a combination of both. In this regard, and as it is known from the transformation theory of Dynamics, a convenient choice of the variables used to describe the dynamics of the system can make easier these tasks.

4. DISCUSSION

In the scope of this note, it is not possible to work out in detail the previous procedure for some concrete model. We refer to the reader to the works by Escapa et al. (2001) and Escapa and Fukushima (2011), where he will find two quite different examples of the application of variational methods to the study of the dynamics of three–layer bodies. In the first one, developed within a Hamiltonian formalism, it is investigated the rotational motion of a three–layer Earth model (Figure 1, left side) composed of three nearly spherical, elliptical layers, with common barycenters: an axial–symmetric rigid mantle, an stratified fluid outer core, and an axial–symmetric inner core. For this model the fluid flow is assumed to have uniform vorticity, that is to say, it is considered a Poincaré flow, whereas the solid constituents rotates like rigid bodies. The key point in this case is the construction of the matrix of inertia of the fluid layer, which has a part depending on the rotational variables of the system, since the mantle and the inner core can rotate independently.

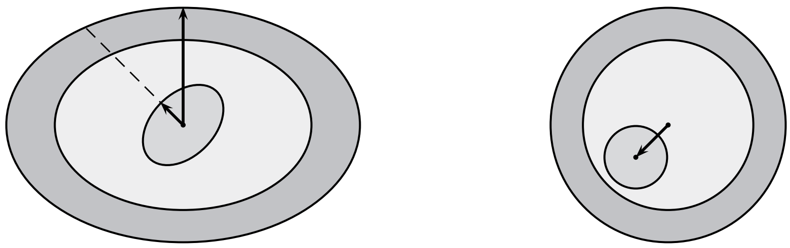

Figure 1: Three–layer models (not scaled) considered in Escapa et al. (2001) and Escapa and Fukushima (2011).

In the second one, constructed within a Lagrangian formalism, it is worked out the internal translational motion of a body differentiated into three homogeneous layers (Figure 1, right side) with spherical symmetry: an external ice-I layer, a subsurface ammonia–water ocean, and a rocky inner core. This is the basic structure of three–layer icy bodies. In contrast to the rotational situation, here the fluid motion is entirely due to the translational motion of the solid rigid layers. It implies that the fluid flow is irrotational and can be derived from a velocity potential. This velocity potential is a solution of the Laplace equation in the fluid domain with the proper boundary conditions.

Both examples lead to analytical solutions, since the equations of motions are linearized around a periodic motion or an equilibrium position. In this way, the rigid motions are characterized by a set of proper frequencies (rotational and translational normal modes) that explicitly depends on some parameter describing the properties of the models like its moments of inertia, masses, and densities. This allows to perform a detailed study of the dependence of those frequencies on the physical characteristics of the model and *vice versa*.

In conclusion, Hamilton's principle formalisms constitute a convenient approach to model the rigid internal motions of a three–layer celestial body. In the variational methods, the dynamics is constructed from the kinetic energy, the potential energy, and the generalized forces of the system, the physical specification of the body being determined by a small set of parameters. One of the main advantages of these treatments relies on the consideration of the solid and fluid layers as forming one single dynamical system. It implies that it is not necessary to compute explicitly the fluid-solids hydrodynamical interactions.

In addition, the form of the differential equations of the motion allows to apply the mathematical tools of Celestial Mechanics, what is specially relevant when one aims at obtaining an analytical approximated description. Moreover, the Hamiltonian formalism is particularly appropriated to construct higher order perturbation solutions in a systematic and consistent way. These kind of solutions can be helpful, for example, to establish standard models, like in the Earth rotation theory case, or to check the numerical codes employed by other treatments.

At any rate, it is important to remark that the intrinsic complexity of the motions of a non–rigid three–layer celestial body makes advisable, if not necessary, to develop different and independent approaches in order to compare the results derived by each of them. It will improve our understanding on the dynamics of these systems.

Acknowledgements. This work has been partially supported by the Spanish projects I+D+I AYA2010-22039-C02-01, AYA2010-22039-C02-02, Generalitat Valenciana project ACOMP/2011/196, Universidad de Alicante project GRE11-08, and by the International Teams program, project 172, of the International Space Science Institute (ISSI) at Bern, Switzerland.

5. REFERENCES

Dehant, V. et al., 1999, Considerations concerning the non–rigid Earth nutation theory, Celest. Mech. Dyn. Astron., 72, 245–310.

Escapa, A., 2011, Corrections stemming from the non–osculating character of the Andoyer variables used in the description of rotation of the elastic Earth, Celest. Mech. Dyn. Astr. , 110, 99–142.

Escapa, A. and Fukushima, T., 2011, Free translational oscillations of icy bodies with a subsurface ocean using a variational approach, AJ, 141, article id. 77.

Escapa, A., Getino, J., and J. M. Ferrándiz, 2000, Free frequencies for a three layered Earth model, in Proceedings of IAU Colloquium 178, edited by S. Dick, D. McCarthy, and B. Luzum, ASP Conference Series, 208, 481–485.

Escapa, A., Getino, J., and J. M. Ferrándiz, 2001, Canonical approach to the free nutations of a three–layer Earth model, J. Geophys. Res., 106, 11387–11397.

Escapa, A., Getino, J., and Ferrándiz, J. M., 2002, Application of Poincaré's formalism to the free nutations of a three–layer Earth model, in Proceedings of the Journées 2001. Ed. N. Capitane, Observatoire de Paris, 239–245.

Ferrándiz, J. M., Navarro, J. F., Escapa, A., and Getino, J., 2004, Precession of the non–rigid Earth: effect of the fluid outer core, AJ, 128, 1407–1411.

Getino, J., 1995, Forced nutation of a rigid mantle–liquid core Earth model in canonical formulation, Geophys. J. Int., 122, 803–814.

Getino, J. and Ferrándiz, J. M., 1995, On the effect of mantle's elasticity on the Earth's rotation, Celest. Mech. Dyn. Astron., 61, 117–180.

Getino, J. and Ferrándiz, J. M., 2001, Forced nutation of a two–layer Earth model, MNRAS, 322, 785–799.

Getino, J., González, A.B., and Escapa, A., 2000, The rotation of a non–rigid, non–symmetrical earth II: free nutations and dissipative effects, Celest. Mech. Dyn. Astron., 76, 1–21.

Grinfeld, P. and Wisdom, J., 2005, Motion of the mantle in the translational mode the Earth and Mercury, Phys. Earth Planet. Int., 151, 77–87.

Henrard, J., 2008, The rotation of Io with a liquid core, Celest. Mech. Dyn. Astron., 101, 1–12.

Hori, G., 1966, Theory of general perturbation with unspecified canonical variables, Publ. Astron. Soc. Jpn., 18, 287–296.

Hussmann, H., Sohl, F., and Spohn, T., 2006, Subsurface oceans and deep interiors of medium–sized outer planet satellites and large trans–neptunian objects, Icarus, 185, 258–273.

Jeffreys, H. and Vicente, R. O., 1957, The theory of nutation and the variation of latitude, MNRAS, 117, 142-161.

Koot, L., 2011, Constraints on the structure and dynamics of the Earth's deep interior inferred from nutation observations, Journées 2011 "Systèmes de référence spatio-temporels", Book of abstracts, 13.

Kubo, Y., 1991, Solution to the rotation of the elastic Earth by method of the rigid dynamics, Celest. Mech. Dyn. Astron., 50, 165–187.

Lamb, H., 1963, Hydrodynamics, 6th edition. Cambridge University Press.

Lanczos, C., 1986, The Variational Principles of Mechanic, 4th edition. Dover Publications.

Mathews, P. M., Buffett, B. A., Herring, T. A., and Shapiro, I. I., 1991, Forced nutations of the Earth: influence of inner core dynamics I . Theory, J. Geophys. Res. 96, 19–42.

Moritz, H., 1982, A variational principle for Molodensky's liquid core problem, Bull. Geod., 56, 381–400.

Noyelles, B., Dufey, J., and Lemaitre, A., 2010, Core–mantle interactions for Mercury, Mon. Not. R. Astron. Soc., 407, 479–496.

Poincaré, H., 1910, Sur la précession des corps deformables, Bull. Astron., 27, 321–356.

Smith, M.L., 1977, Wobble and nutation of the Earth. Geophys. J.R. Astron. Soc., 50, 103–140.

Van Hoolst, T.,Rambaux, N., Karatekin, ., Dehant, V., and Rivoldini, A., 2008, The librations, shape, and icy shell of Europa, Icarus, 195, 386-399

Whittaker, E. T., 1988, A treatise on the Analytical Dynamics of particles and rigid bodies, 4th edition. Cambridge University Press.

PROGRESS REPORT OF THE IAU COMMISSION 4 WORKING GROUP ON EPHEMERIS ACCESS AND THE COMPARISON OF HIGH ACCURACY PLANETARY EPHEMERIDES

J.L. HILTON
U.S. Naval Observatory
3450 Massachusetts Ave., NW, Washington, DC 20392, USA
e-mail: james.hilton@usno.navy.mil

ABSTRACT. In September 2010 IAU Commission 4, Ephemerides, organized a working group to provide a recommendation for a preferred format for solar system ephemerides. The purpose of this recommendation is to provide easy access to a wide range of solar system ephemerides for users. The working group, chaired by Hilton, includes representatives from each of the major planetary ephemeris groups and representatives from the satellite and asteroid ephemeris communities. The working group has tentatively decided to recommend the SPK format developed by the Jet Propulsion Laboratory's Navigation and Ancillary Information Facility for use with its SPICE Toolkit. Certain details, however, must still be resolved before a final recommendation is made by the working group.

An update is also provided to ongoing analysis comparing the three high accuracy planetary ephemerides, DE421, EPM2008, and INPOP10a. The principal topics of this update are: replacing the INPOP08 ephemeris with the INPOP10a ephemeris, making the comparisons with respect to DE421 rather than DE405, and comparing the $TT - TDB$ values determined in EPM2008 and INPOP10a with the Fairhead & Bretagnon (1990, A&A, **229**, 240) model used in DE421 as T_{eph}.

1. THE IAU WORKING GROUP ON EPHEMERIS ACCESS

In September 2010 IAU Commission 4, Ephemerides, organized a working group to provide a recommendation for a preferred format for solar system ephemerides. The members of the working group are J. Hilton (U.S. Naval Observatory, USNO) chair, J.-E. Arlot (Institut de mécanique céleste et de calcul des éphémérides, IMCCE), S. Bell (Her Majesty's Nautical Almanac Office), O. Bratseva (Inst. of Applied Astronomy RAS, IAA), N. Capitaine (Paris Obs.), A. Fienga (IMCCE), W. Folkner (Jet Propulsion Laboratory, JPL), M. Gastineau (IMCCE), E. Pitjeva (IAA), V. Skripnichenko (IAA), and P. Wallace (retired). The membership of the working group includes individuals from the planetary, satellite, and minor planet ephemeris producer and user communities.

The primary objective of the working group is to provide a recommended standard file format and software to give seamless access to the user community of high accuracy planetary and lunar ephemerides. These ephemerides are currently available from IAA in Russia, IMCCE in France, and JPL in the US. Not only must the file format and software be able to handle the positions and velocities of the planets, Moon and Pluto, it must be able to handle ephemerides for the orientation of the Moon and $TT - TDB$, the difference between the Terrestrial Time (TT) and Barycentric Dynamical Time (TDB) timescales.

The format should also be flexible enough to handle asteroids, satellites, and other natural solar system objects. To meet this secondary goal the file format needs to handle arbitrary coordinate origins, highly eccentric orbits, and objects with significant non-gravitational forces. For eccentric orbits and orbits with non-gravitational forces, either the time-segment length or the numerical order of the parameters representing the orbit should vary. An ephemeris with fixed order and time-segment length may be many times larger than one where these parameters are flexible because they must be devised to accurately describe that part of the ephemeris where the greatest change with time occurs. For example: a fixed order ephemeris of N II Nereid can cover with the same accuracy a time-segment at apoapsis that is approximately seven times longer than it can at periapsis. A similar comet Halley ephemeris could have a segment time-segment at apoapsis that is approximately 60 times its periapsis length.

1.1. Existing Formats

The working group started with the four formats in which the high accuracy planetary ephemerides are currently distributed: the CALCEPH format, the Export format, the IAA ephemeris format, and the Spacecraft Planet Kernel (SPK) format. Each format has its strengths and weaknesses as described below.

CALCEPH: The CALCEPH file format and software were designed for use with the Intégrateur Numérique Planétaire de l'Observatoire de Paris (INPOP) ephemerides developed at the IMCCE. Gastineau *et al.* (2011) state that the internal format of the CALCEPH ephemerides is described in Hoffman (1998). Thus, the format of a CALCEPH ephemeris file is similar to the Export format file described below. The main difference is: a CALCEPH file can accept one-dimension ephemerides. The ability to use one-dimension ephemerides allows CALCEPH to elegantly handle the $TT - TDB$ ephemeris. There is also an ASCII version of the INPOP10a ephemeris, which has a significantly different format form the binary version. One reason for the development of INPOP is for use with Gaia; giving CALCEPH a major user. It also means CALCEPH is actively being maintained. To simplify cross-platform use, the CALCEPH software can detect whether the Chebyshev coefficients are stored in big-endian or little-endian order. It is distributed as a linked in library for use with Fortran 77, 95, and 2003 and C with both single and multiple threads. CALCEPH does not currently have a wide user base, however.

Export Format: The Export format was developed by the Solar System Dynamics group at JPL in the 1970s. Since then it has become widely used in the planetary astronomy community. It handles planetary and lunar orbits, lunar orientation, and Earth nutation ephemerides. It evaluates the ephemerides using fixed order Chebyshev polynomials (Newhall 1989). The coefficients for the Chebyshev polynomials are stored in a binary file. The ephemeris reading software, called *testeph.f*, does not detect whether the binary is in big-endian or little-endian order, so the files are distributed in ASCII format and converted to binary by the user with an auxiliary program. The Export format is built around the expectation that the reading software has some *a priori* knowledge of the contents of the ephemeris, such as the reference system and center of each ephemeris. It also assumes that all ephemerides are three dimensional. It packs all of the bodies in the ephemeris into sub-ephemerides with a common time-segment length, making it difficult to use with bodies on highly eccentric orbits. The software is available only in single thread Fortran 77 and has been essentially static for decades. Only minor revisions have been made as necessary. JPL also makes unsupported C and Java versions, written by third parties, available.

IAA Ephemeris Format: The IAA ephemeris format was developed at the IAA for use with its planetary ephemerides at about the same time the Export format was developed. It has been widely available only for the last few years, so it is not well known. It currently handles planetary and lunar orbits and $TT - TDB$ ephemerides. There are plans to include lunar orientation ephemerides in the near future (Yagudina 2011, private communication). Like CALCEPH and the Export format it stores the ephemerides using Chebyshev polynomials of the velocities of the bodies relying on a fixed order for the ephemeris of each planet where the center and reference systems are assumed. Also like the Export format, it assumes all the ephemerides are three-dimensional. However, rather than using a single file, the ephemeris for each body is stored in a separate file. These files can be either in binary or ASCII text format, whichever format is used depends on an initializing function called before starting evaluation. The initializing function stores the entire ephemeris in memory, which allows for fast evaluation, but at the cost of a significant initial delay. The reading software, called *calc_eph* is available in single thread C, Fortran 90, Java, and Pascal. It is actively being maintained by the IAA.

SPK Format: The SPK format is a specialization of the Double precision Array File (DAF) format developed by the Navigation and Ancillary Information Facility (NAIF) at JPL. It was developed for use in the SPICE Toolkit to support spacecraft missions originating at JPL. As such, it has become widely used and is the *de facto* standard in the aerospace community. The SPICE Toolkit is actively maintained by NAIF. The SPK format was developed to handle the position ephemerides of an arbitrary number of solar system bodies each with a specified reference system, center, and three dimensions. The ephemeris can be stored in several different ways including Chebyshev polynomials with fixed or variable time-length segments and as osculating orbital elements. The data in SPK files are stored in binary format, and the SPICE Toolkit is designed to be platform independent. The SPK format was not designed to handle orientation ephemerides, but they may be introduced by including an 'Object ID Number' for each orientation ephemeris. Alternatively, a different specialization of the DAF format called the Planetary

Constants Kernel (PCK) does handle orientation ephemerides. However, the PCK format cannot be used in an SPK file, so this option would require separate files for position and orientation ephemerides. The DAF, and hence the SPK, format is quite complex because it was designed to handle numerous other types of data as well as ephemerides. The SPICE Toolkit is available only in single thread Fortran 77 and may not be optimized for users who want to use it only for ephemeris access.

1.2. Current Status

The working group has tentatively elected to recommend the SPK format subject to meeting the following requirements:

1. There must be a readily available, detailed specification of the appropriate parts of the SPK format for use with ephemeris files,
2. there must be Object ID Numbers added to the SPK format to allow the storage of lunar orientation and $TT - TDB$ ephemerides,
3. a data type must be developed in the SPK format for storage of the IAA ephemerides using the current format of Chebyshev polynomials in their ephemerides,
4. stand alone ephemeris reading software must be made available, and
5. the names and values of the parameters used in the construction of the ephemerides are to be stored in the Comment Area.

The sense of the working group is that it was preferable to store the ephemerides in a single file. Thus, an Object ID Number must be assigned to the current lunar orientation ephemeris. At this time no other solar system object's orientation ephemeris requires an Object ID Number[1].

Storage of the $TT - TDB$ ephemeris as an SPK file also requires the assignment of an Object ID Number. Since the $TT - TDB$ ephemeris is one-dimensional and a PCK ephemeris is expecting three dimensions, there is waste of storage space. That waste, however, is small. Based on the size of the binary $TT - TDB$ ephemeris of IAA's EPM2008, the excess storage is approximately 600 kB for a span of 100 years.

NAIF has agreed to produce both the specification and stand alone ephemeris reading software and will add a new type to handle the IAA style Chebyshev polynomials and required Object ID Numbers for including the lunar orientation and $TT - TDB$ within the SPK ephemeris format.

The Comment Area of an SPK file already will accept any number of records consisting of printable ASCII characters. Thus, meeting the fifth requirement is a matter of discipline on the part of the ephemeris makers.

2. COMPARISON OF THE DE421, EPM2008, AND INPOP10A EPHEMERIDES

This comparison is an extension of the report made at Journées 2010 (Hilton & Hohenkerk 2011). The principle differences between this and the previous report are:

1. The comparisons are made with respect to DE421 rather than DE405,
2. INPOP10a has replaced INPOP08 in the comparisons, and
3. ephemerides of $TT - TDB$ in EPM2008 and INPOP10a are compared to Fairhead & Bretagnon (1990), which is used for $TT - T_{eph}$ in the JPL ephemerides.

2.1. Range, Longitude, and Latitude

The differences between the ephemerides in range, longitude, and latitude are more likely the result of either the inclusion of an important new data set such as the introduction of Galileo observations into INPOP10a or decisions on the part of the ephemeris maker to resolve difficulties such as highly correlated parameters. Ultimately, the one true test of an ephemeris is how well it predicts observations that were not used in its construction.

DE421 has replaced DE405 as the basis for comparison not because DE421 is considered superior to the other ephemerides, but because it is the direct descendent of DE405. The differences between DE421, EPM2008, and INPOP10a are small enough that, if DE405 was used as the basis for comparison the differences with DE405 would tend to dominate over the differences between these three ephemerides.

[1]The Earth's orientation is complex and available from the International Earth Rotation and Reference Frames Service at http://www.iers.org. The orientations of other solar system bodies are poorly known and may be represented as quickly evaluated theories (Archinal et al. 2011).

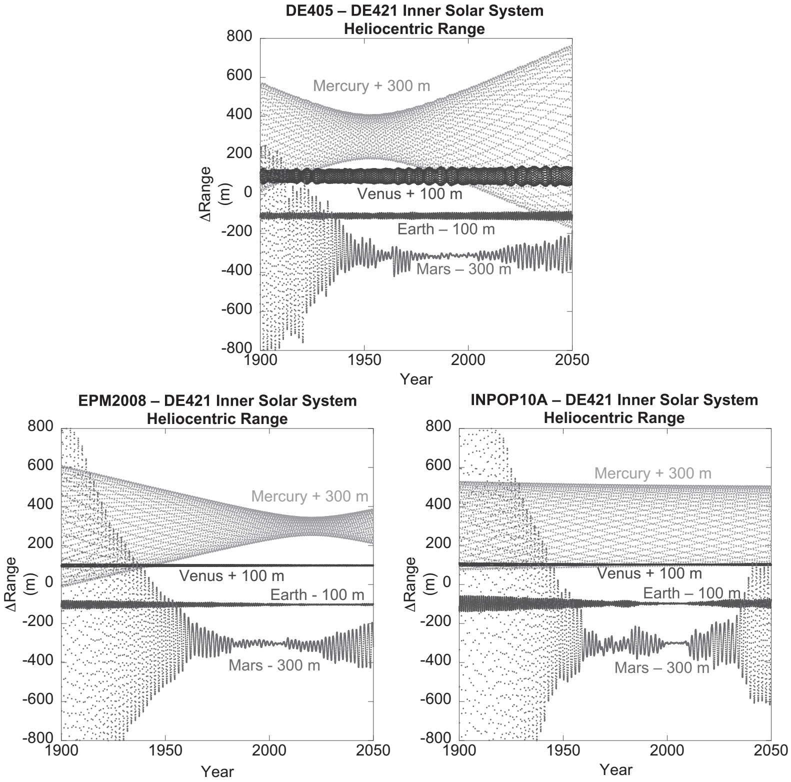

Figure 1: The differences in the heliocentric ranges of the inner solar system planets with respect to DE421.

The Inner Solar System Figure 1 shows the differences in range for the inner solar system planets with respect to DE421. The differences for EPM2008 and INPOP10a for Venus and the Earth are visibly smaller than those for DE405 – DE421.

The distinctive "bowtie" shapes of the DE405 and EPM2008 differences in the range of Mercury are probably the result of a small difference in the mean motion of Mercury in these ephemerides compared to DE421. To account for the size of the differences would require a change in Mercury's mean semimajor axis of 0.6 m for DE405 and 0.4 m for EPM2008. Equivalently, a change in the combined Sun-Mercury mass of 3 parts in 10^{11} for DE405 and 2 parts 10^{11} for EPM2008 would also account for the differences.

The apparently constant envelope for the differences for INPOP10a compared to DE421 is possibly caused by a slight rotation of the ellipse of Mercury's orbit. A rotation of 4 mas, approximately 1.1 km along track, would account for the differences. There is also a small change in the amplitude of the differences with time as in the DE405 and EPM2008 differences. A change of 17 cm in the mean semimajor axis, or 9 parts in 10^{13} in the combined Sun-Mercury mass would account for the rate of change in the differences.

Thus, even such apparently large differences are the result of minute changes in the models used by the different ephemeris makers.

Jupiter and Saturn Figure 2 shows the most dramatic differences between the ephemerides are for Jupiter and Saturn. The differences in the more recent ephemerides with respect to DE405 are so great that the scale for the DE405 – DE421 differences is two orders of magnitude greater than the one used for the EPM2008 – DE421 and INPOP10a – DE421 differences.

The improvement of these two ephemerides are the result of recent spacecraft data. DE405 includes both Galileo and Ulysses data, but is pre-Cassini. Thus, the DE405 – DE421 differences for Jupiter are smaller than those for Saturn. Similarly, INPOP10a's Jupiter ephemeris is superior to that of INPOP08 (Hilton & Hohenkerk 2011) because one of the differences between INPOP08 and INPOP10a is the inclusion Galileo data.

The change with time in the range of Jupiter between EPM2008 and DE421 can be explained by a

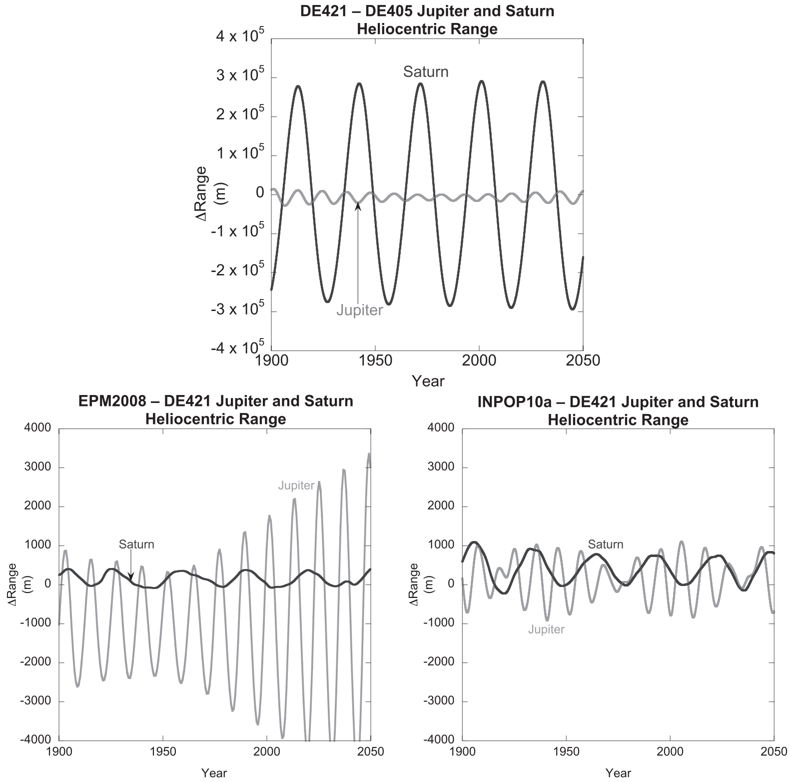

Figure 2: The differences in the heliocentric ranges of Jupiter and Saturn with respect to DE421.

difference in its semimajor axis of approximately 1100 m between the two ephemerides. The approximate mean difference measured from Figure 2 is 900 m. The uncertainty in both the required change in the semimajor axis and the measured offset are on the order of tens to hundreds of meters. Again, a small difference in this one parameter may be responsible for the difference.

2.2. $TT - TDB$

The independent argument for the ephemerides is Barycentric Dynamical Time (TDB), the coordinate time for the barycentric reference system. The realization of this time scale is called T_{eph} in the JPL ephemerides. The value of $TT - T_{eph}$ is determined using the algorithm of Fairhead & Bretagnon (1990), henceforth $F\&B$. Both EPM2008 and INPOP10a determine $TT - TDB$ from the ephemerides themselves using an iterative process. Figure 3 shows the difference in $TT - TDB$ for these two ephemerides with respect to $F\&B$. The points are the differences at 10 day intervals and the lines are five year running averages.

Determination of $TT - TDB$ in both EPM2008 and INPOP10a include the masses and orbits of minor planets not used in $F\&B$. Over a long enough time period there should be no mean difference in the value of $TT - TDB$. However, the orbits of these bodies are non-commensurate, so the timescale over which the differences average out is expected to be orders of magnitude longer than to their orbital periods (2-10 yr for main belt objects and $>$ 170 yr for trans-Neptune objects, TNOs). As a result, the gravitational potential at the barycenter is different than for $F\&B$. And the mean rate of TDB determined using the ephemerides will be somewhat different. Over the period of comparison, the mean difference is approximately linear. The mean slope, determined from a least-squares fit to the five year running average, is 0.12 ns yr^{-1} for EPM2008 and 0.03 ns yr^{-1} for INPOP 10a. The steeper slope for EPM2008 is explained by the inclusion of 20 large TNOs other than Pluto in its model. Hilton & Hohenkerk (2011) give another demonstration of the effect of including the TNOs in EPM2008 on the position heliocenter of with respect to the barycenter. The relatively short periods of approximately 300 main belt objects cause a pseudo-random motion of the heliocenter about its short-term mean position. This motion about the mean position is apparent in the points at 10 day intervals which form envelopes approximately 10 ns wide around the mean slope of each difference. At the current epoch there is an approximately 3-4 ns

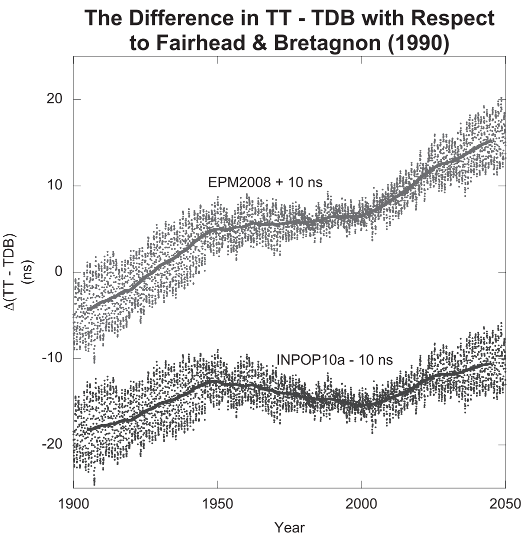

Figure 3: The differences in $TT - TDB$ in EPM2008 and INPOP10a with respect to Fairhead & Bretagnon.

offset between the $F\&B$ value for $TT - TDB$ and those of EPM2008 and INPOP10a.

3. DISCUSSION

The IAU Working Group on Ephemeris Access has tentatively agreed to standardize on SPICE Toolkit's SPK format. NAIF, the group at JPL that maintains the SPICE Toolkit, will assign body identification numbers for $TT - TDB$ and the lunar orientation angles so they may be included in SPK format files. A specification of that format for the fixed length Chebyshev polynomial formats is currently being written. A type to handle the IAA's velocity based Chebyshev polynomials and stand alone SPK file format reading software will be taken care of next. Other details, such as whether to include the SPK Type 14 (Chebyshev polynomials with unequal time steps) for highly eccentric orbits or to develop a type for planetary theories, will be taken up at a later date.

The comparison of the DE421, EPM2008, and INPOP10a is continuing using DE421 as the basis for comparison to remove the larger differences between DE405 and these three ephemerides. The inclusion of Galileo observations in INPOP10a makes this ephemeris a significant improvement over INPOP08. $TT - TDB$ for INPOP10a and particularly EPM2008 show both short term variations and secular slopes compared to the Fairhead & Bretagnon (1990) algorithm used for the same purpose for the JPL ephemerides. These differences are attributed to the inclusion of main belt asteroids and, in EPM2008, 20 trans-Neptunian objects other than Pluto in the determination of $TT - TDB$.

4. REFERENCES

Archinal, B.A. *et al.* 2011, Celest. Mech. Dyn. Astr. , **109**, 101–135

Fairhead, L. & Bretagnon, P. 1990, A&A , **229**, 240–247

Gastineau, M., Laskar, J., Fienga, A., & Manche, H. 2011, CALCEPH Library: Reference Manual v. 1.2.0, (Besançon, FRANCE: CNRS - Observatoire de besançon), 30 pp.[2]

Hilton J.L. & Hohenkerk C.Y. 2011, in The Proceedings of the Journées 2010, N. Capitaine, ed. (Paris: Observatoire de Paris), 77–80

Hoffman, D. 1998, "A Set of C Utility Programs for Processing JPL Ephemeris Data," preprint, (available by file transfer protocol from JPL Solar System Dynamics[3])

Newhall, X X 1989, Celest. Mech. Dyn. Astr. , **45**, 305–310

[2] http://www.imcce.fr/inpop/calceph/calceph.pdf
[3] ftp://ssd.jpl.nasa.gov/pub/eph/planets/C-versions/hoffman/

NEW ADDITIONS TO THE ASTRONOMICAL ALMANAC: ALMANAC DATA FOR DWARF PLANETS

J.M. WERATSCHNIG[1], S.G. STEWART[2], J.L. HILTON[2]

[1] HMNAO, UKHO, Admiralty Way, Taunton, TA1 2DP, UK
e-mail: hmnao@ukho.gov.uk

[2] Astronomical Applications Department, USNO
3450 Massachusetts Ave, NW, Washington, DC 20392-5420, USA
e-mail: susan.stewart@usno.navy.mil, james.hilton@usno.navy.mil

ABSTRACT *The Astronomical Almanac* (AsA) is regarded as a standard publication, therefore any changes to it must reflect current astronomical understanding. Following IAU resolution B5, (1) Ceres, (13340) Pluto, (136108) Haumea, (136199) Eris and (136472) Makemake have been designated dwarf planets. Beginning with the 2013 edition, the AsA will reflect this new classification scheme. New additions with regard to dwarf planets and calculations used to obtain them are discussed in this paper. We also present new definitions and their application for dwarf planets.

1. INTRODUCTION

Section G of the AsA has been restructured to cover "Dwarf Planets and Small Solar System Bodies". We follow the new IAU classification scheme (see IAU Resolution B5 and B6) for solar system bodies throughout this section (and also Section E which deals with planets). This scheme distinguishes between three main types of bodies:

1. Planets: a "planet" is in orbit around the Sun, has sufficient mass for its self-gravity to assume a hydrostatic equilibrium (nearly round) shape, and has cleared the neighbourhood around its orbit.

2. Dwarf Planets: a "dwarf planet" is in orbit around the Sun, and assumes a hydrostatic equilibrium (nearly round) shape, but it has not cleared the neighbourhood around its orbit (and is not a satellite).

3. Small Solar System Bodies: all other bodies, except satellites, in orbit around the Sun.

Data for comets and bright minor planets continue to be given within Section G in the format of previous editions of the AsA. This paper explains the new data which have been added to Section G for dwarf planets. The current list of dwarf planets considered in the AsA follows the list published on the IAU website which includes the following objects: Ceres, Pluto, Haumea, Eris and Makemake. Given that dwarf planets are a new category in solar system nomenclature, new discoveries and reclassifications of known objects are likely. Additionally, ephemerides and estimates of physical properties are subject to change. Thus, the contents and data for these objects are likely to change in the foreseeable future. Table 1 lists the physical properties of the five dwarf planets as published in the 2013 edition of the AsA.

2. CARTOGRAPHIC COORDINATES AND ROTATIONAL ELEMENTS

In order to calculate ephemerides for physical observations of the dwarf planets, we use information provided in the 2009 report of the Working Group for Cartographic Coordinates and Rotational Elements (WGCCRE, Archinal et al., 2011a). At the moment, WGCCRE data are available for Pluto and Ceres. The main change for Pluto in the 2009 WGCCRE report was a change in the definition of poles due to its reclassification. An error was discovered in the 2009 WGCCRE data for Pluto during the preparation of the material for the 2013 AsA. Hence, an erratum was issued for the 2009 WGCCRE (Archinal et al. 2011b). We use these corrected values for Pluto. Dwarf planets and small solar system bodies (minor planets, comets) differ in the scheme used to describe cartographic coordinates and rotational elements

Name	Equ. Radius	Mass	Minimum Geo-centric Distance	Sidereal Period of Rotation	Maximum Angular Diameter	Geometric Albedo	Year of Dis-covery
	km	kg	au	d	′		
Ceres	479.7	9.39×10^{20}	1.5833	0.3781	0.840	0.073	1801
Pluto	1195.0	130.41×10^{20}	28.6031	6.3872	0.110	0.30	1930
Haumea	1000.0	42.00×10^{20}	33.5620	0.1631	0.092	0.73	2004
Eris	1200.0	166.95×10^{20}	37.5984	1.0800	0.088	0.86	2005
Makemake	850.0	–	37.0193	7.7710	0.053	0.78	2005

Table 1: Physical properties of dwarf planets (see AsA (2013))

	Dwarf Planets	Planets
Poles (defined differently for planets and dwarf planets)	Positive or negative pole: the direction follows the right hand rule.	North or south pole, depending on the position (above or below) in regard to the invariable plane of solar system
Cartographic Position of Prime Meridian (Definition is the same for both planets and dwarf planets): Where possible, this is defined by a surface feature, e.g.: • Ceres: (Unnamed) bright spot • Pluto: Sub-Charon point • Mars: Crater Airy-0		

Table 2: Some definitions for dwarf planets and planets from the 2009 WGCCRE report

compared to planets. Pluto's rotation which was described as retrograde while it was listed with the planets, is now a positive value. Table 2 gives the definition of some relevant data in detail.

3. ORBITAL DATA

For Ceres, Pluto and Eris we publish the following data (these objects have been chosen due to historical reasons - Ceres and Pluto are both well known objects, while the discovery of Eris has started the discussion on how a planet/dwarf planet should be defined. In the future, data of more dwarf planets are most likely going to be included in the AsA):

- Osculating elements for Ceres, Pluto and Eris: osculating elements are tabulated for three days per year. The chosen dates are 100 day dates (Table 3 shows an example of this).
- Heliocentric coordinates for Ceres, Pluto and Eris: like the osculating elements, the table is for three 100 day dates per year.
- Astrometric coordinates: are given for Ceres, Pluto and Eris if they have an opposition during the year of the AsA. A daily ephemeris 60 days either side of the opposition date is printed in such a case. Along with the ephemeris data, star charts showing the path of the dwarf planet are provided. The first chart shows an overview of the whole year (plus some overlap), the second chart is a detailed map of the path 60 days either side of the opposition date. Figure 1 shows the charts for Eris for the year 2013.

For Ceres and Pluto, enough observational data are available to also reliably provide the following information:

- Ephemerides for physical observations: are given in an interval of 10 days, and the data are tabulated over the whole year (see Table 4).

Name	Magnitude Parameters		Mean Diameter	Julian Date	Inclination	Long. of Asc. Node	Arg. of Perihelion	Semi-major Axis	Daily Motion	Eccentricity	Mean Anomaly
	H	G			i	Ω	ω	a	n	e	M
			km	245	°	°	°	au	°/d	°	
Ceres	3.34	0.12	952	6400.5	10.594	80.330	72.167	2.768	0.2140	0.076	327.8540426
				6500.5	10.594	80.329	72.259	2.767	0.2141	0.075	349.1710915
				6600.5	10.594	80.328	72.292	2.766	0.2141	0.075	10.5575049

Table 3: Osculating elements, given for the ecliptic and equinox of J2000.0 (Ceres, AsA (2013))

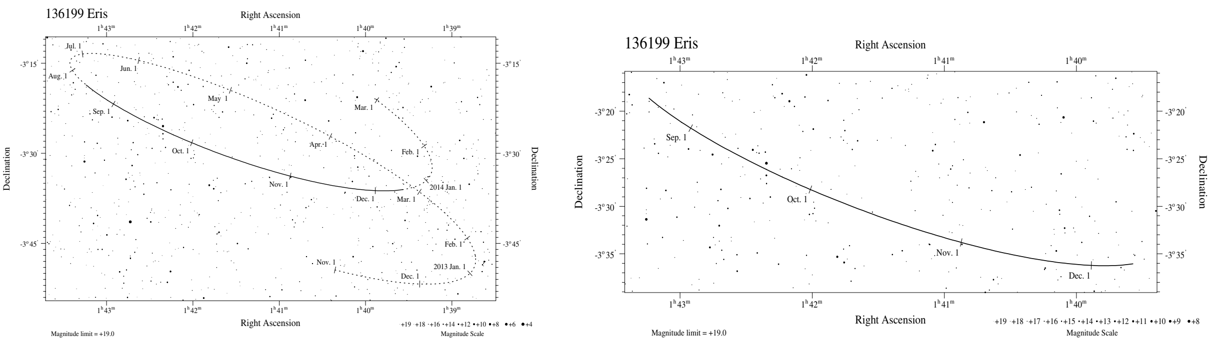

Figure 1: Star charts showing astrometric coordinates for a dwarf planet (in this case, Eris) : the first chart shows the path of the dwarf planet over the whole year, while the second chart is a detailed view of the path 60 days either side of opposition.

Date		Light Time	Visual Magnitude	Phase Angle	L_S	Sub-Earth Point Longitude	Sub-Earth Point Latitude	Positive Pole P.A.
		m		°	°	°	°	°
Jan	-12	277.07	14.2	0.4	59.00	259.40	+ 47.8	235.34
	-2	277.28	14.2	0.1	59.06	139.31	+ 48.1	235.00
	8	277.24	14.2	0.3	59.12	343.23	+ 48.4	234.65

Table 4: Excerpt of the ephemeris for physical observations, for 0^h terrestrial time (Pluto, AsA (2013))

4. CALCULATIONS

Different methods were used to calculate the published data. In detail these included:

- Osculating elements:

  Ceres: the same method and calculations as used for minor planets are applied. The data for Ceres therefore continue seamless from earlier editions, where Ceres is still tabulated with the minor planets.

  Pluto and Eris: the osculating elements for those two objects are calculated using methods as applied by USNO to produce the osculating elements for planets in Section E of the AsA. The mass of all the planets which are inside the orbit of Pluto or Eris is included in the calculations.

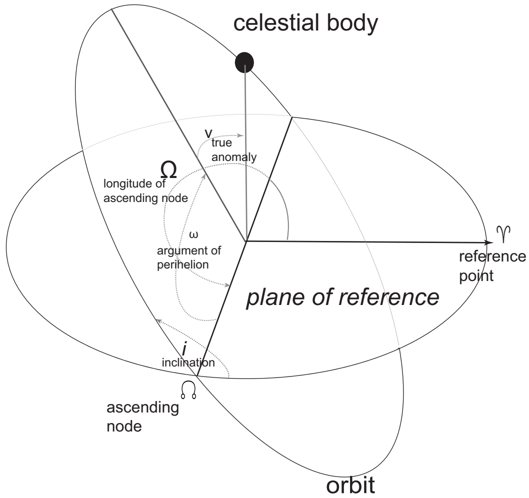

Figure 2: Osculating elements as they are tabulated in the AsA. The value of the true anomaly ν relates to the tabulated mean anomaly M: $\nu = M + (2e - e^3/4)\sin M + (5e^2/4)\sin 2M + (13e^3/12)\sin 3M + ...$

For Pluto we can therefore seamlessly go from the 2012 to the 2013 edition. Figure 2 shows the tabulated elements, Table 3 provides an example for the data as it is tabulated in the AsA.

- Heliocentric coordinates: this table is calculated using HMNAO routines; it is corrected for frame bias.
- Astrometric coordinates: this table is calculated the same way as the astrometric coordinates for minor planets.
- Ephemerides for physical observations: here, we follow the procedures used in Section E for planets to calculate these data for Pluto and Ceres. When looking at overlapping days between 2012 (e.g. from AsA 2012) and 2013 (see Table 4), the table for Pluto very clearly shows the difference which is due to different definitions between planets and dwarf planets - e.g. the position of the pole is 180 degrees shifted, since for dwarf planets the positive pole is tabulated as opposed to the north pole for planets.

5. REFERENCES

Archinal, B.A. et al., 2011a, "Report of the IAU Working Group on Cartographic Coordinates and Rotational Elements: 2009", Celestial Mechanics and Dynamical Astronomy, Volume 109, Issue 2, pp.101-135

Archinal, B.A. et al., 2011b, " Errata to the WGCCRE Report 2009", Celest. Mech. 110, 401, 2011

IAU Resolution B5 and B6, http://www.iau.org/static/resolutions/Resolution_GA26-5-6.pdf

The Astronomical Almanac, 2013, US GPO, Washington

PRECISE ANALYTICAL CALCULATION OF THE EFFECT OF SOLID EARTH TIDES ON SATELLITE MOTION

S.M. KUDRYAVTSEV

M.V. Lomonosov Moscow State University, Sternberg Astronomical Institute
13, Universitetsky Pr., Moscow, 119991, RUSSIA
e-mail: ksm@sai.msu.ru

ABSTRACT. First we obtain accurate analytical series representing the main part of variations of the geopotential coefficients caused by the solid Earth tides. The KSM03 expansion of the Earth tide-generating potential is used as a source. Then we use these series in analytical calculation of the corresponding tidal perturbations in satellite motion. Two geodynamical satellites are considered: low-altitude STARLETTE and high-altitude ETALON-1. The accuracy (r.m.s. error) of analytical calculation of the discussed effect is estimated as 2 cm for STARLETTE over a time interval of 1 month (or some 415 orbits of the satellite) and 1 mm for ETALON-1 over a time interval of 1 year (or some 775 orbits of the satellite).

1. CONVENTIONAL MODEL OF THE SOLID EARTH TIDES

The IERS Conventions (2010) (Petit & Luzum 2010) describe the main effect of the solid Earth tides on the Earth gravitational potential through variations $\Delta\bar{C}^{ST}_{nm}$, $\Delta\bar{S}^{ST}_{nm}$ in instantaneous values of the normalized standard geopotential coefficients

$$\Delta\bar{C}^{ST}_{nm} - i\Delta\bar{S}^{ST}_{nm} = \frac{k_{nm}}{2n+1}\sum_{j=2}^{3}\frac{\mu_j}{\mu_E}\left(\frac{R_E}{r_j}\right)^{n+1}\bar{P}_{nm}\left(\sin\phi_j\right)e^{-im\lambda_j}, \tag{1}$$

where $i \equiv \sqrt{-1}$; k_{nm} are frequency-independent conventional Love numbers; R_E, μ_E are, respectively, the Earth's equatorial radius and gravitational parameter; μ_j, r_j, ϕ_j and λ_j are, respectively, the gravitational parameter, geocentric distance, geocentric latitude and East longitude (from Greenwich) of the Moon ($j = 2$) and Sun ($j = 3$), calculated on the basis of numerical planetary/lunar ephemerides; $\bar{P}_{nm}$ are the normalized associated Legendre functions.

Only the solid Earth tides of degree 2 and 3 by the IERS Conventions (2010) are recommended to be taken into account in accurate propagation of satellite motion. The degree 2 tides also lead to some variations in the degree 4 gravitational coefficients as a consequence of the Earth's ellipticity and the Coriolis force due to the planet rotation

$$\Delta\bar{C}^{ST}_{4m} - i\Delta\bar{S}^{ST}_{4m} = \frac{k^{(+)}_{2m}}{5}\sum_{j=2}^{3}\frac{\mu_j}{\mu_E}\left(\frac{R_E}{r_j}\right)^{3}\bar{P}_{2m}\left(\sin\phi_j\right)e^{-im\lambda_j}, \tag{2}$$

where $m = 0, 1, 2$; and $k^{(+)}_{2m}$ are some small additional parameters characterizing the degree 2 Love numbers (Wahr 1981).

Anelasticity of the Earth's mantle leads to a certain phase lag in the deformational response of the Earth to tidal forces; mathematically it is described by introducing complex values for Love numbers. Another effect of the anelasticity is the frequency dependence of Love numbers (Wahr 1981). In order to account for the latter effect, Eanes et al (1983) suggest to compute some additional corrections to the gravitational coefficients $\bar{C}_{2m}$, $\bar{S}_{2m}$ due to deviations of the frequency dependent degree 2 Love numbers from their nominal values k_{2m}. The IERS Conventions (2010) give these corrections by trigonometric series.

Equations (1)–(2) can be conveniently used in numerical theories of satellite motion, but for use in analytical theories these equations should be developed to harmonic series. The next section presents our results in this field.

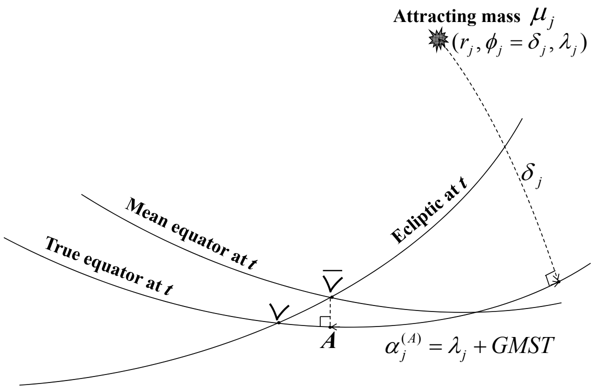

Figure 1: Spherical coordinates used in the KSM03 development of the Earth TGP

2. REPRESENTATION OF THE SOLID EARTH TIDE EFFECT ON GEOPOTENTIAL BY ANALYTICAL SERIES

In order to build compact analytical series representing the main variations in Equations (1)–(2) of the geopotential coefficients due to the solid Earth tides, we use the latest development of the Earth tide-generating potential (TGP), KSM03 (Kudryavtsev 2004). The instantaneous value for the Earth TGP, V, at an arbitrary point P on the Earth's surface at epoch t by the KSM03 development is given as follows

$$\begin{aligned} V(t) &= \sum_{n=2}^{\infty}\left(\frac{r}{R_E}\right)^n \sum_{m=0}^{n} \bar{P}_{nm}(\sin\phi) \\ &\times \left[\bar{C}'_{nm}(t)\cos m\theta^{(A)}(t) + \bar{S}'_{nm}(t)\sin m\theta^{(A)}(t)\right], \end{aligned} \tag{3}$$

where

$$\bar{C}'_{nm}(t) \equiv \frac{1}{2n+1}\sum_j \frac{\mu_j}{R_E}\left(\frac{R_E}{r_j(t)}\right)^{n+1} \bar{P}_{nm}(\sin\delta_j(t))\cos m\alpha_j^{(A)}(t), \tag{4}$$

$$\bar{S}'_{nm}(t) \equiv \frac{1}{2n+1}\sum_j \frac{\mu_j}{R_E}\left(\frac{R_E}{r_j(t)}\right)^{n+1} \bar{P}_{nm}(\sin\delta_j(t))\sin m\alpha_j^{(A)}(t), \tag{5}$$

and $\alpha_j^{(A)}(t)$, $\delta_j(t)$ are, respectively, the instantaneous right ascension and declination of the j^{th} attracting body referred to the true equator of epoch t with the origin point A - that being the projection of the mean equinox of date (Figure 1); r, ϕ are, respectively, the geocentric distance and geocentric latitude of P, and $\theta^{(A)}(t)$ is the local sidereal time at P reckoned from point A. The latter parameter is related to the Earth-fixed East longitude (from Greenwich) λ of point P as

$$\theta^{(A)}(t) = \lambda + GMST, \tag{6}$$

where $GMST$ is Greenwich mean sidereal time as defined by Aoki et al (1982). (In the KSM03 development, Equation (3) is also completed by some additional terms of degree $n = 1$ reflecting the main effect of the Earth's flattening, but these terms are not relevant to the present study.)

The $\bar{C}'_{nm}$, $\bar{S}'_{nm}$ coefficients by the KSM03 development are represented by 2nd-order Poisson series with numerical coefficients; the argument of every series' term is a fourth-order polynomial of time t.

By comparing Equation (1) and Equations (4)–(5) and taking into account the relations $\phi_j = \delta_j$ and $\alpha_j^{(A)}(t) = \lambda_j + GMST$, one can find the following equations linking the original coefficients $\bar{C}'_{nm}$, $\bar{S}'_{nm}$ in the KSM03 development of the Earth TGP and main variations $\Delta\bar{C}^{ST}_{nm}$, $\Delta\bar{S}^{ST}_{nm}$ of the geopotential coefficients due to the solid Earth tides

$$\Delta\bar{C}^{ST}_{nm} = \Delta\bar{C}'_{nm}\cos(m \times GMST) + \Delta\bar{S}'_{nm}\sin(m \times GMST), \quad (7)$$

$$\Delta\bar{S}^{ST}_{nm} = \Delta\bar{S}'_{nm}\cos(m \times GMST) - \Delta\bar{C}'_{nm}\sin(m \times GMST), \quad (8)$$

where

$$\Delta\bar{C}'_{nm} = \frac{R_E}{\mu_E}\left(\Re k_{nm}\bar{C}'_{nm} + \Im k_{nm}\bar{S}'_{nm}\right), \quad (9)$$

$$\Delta\bar{S}'_{nm} = \frac{R_E}{\mu_E}\left(\Re k_{nm}\bar{S}'_{nm} - \Im k_{nm}\bar{C}'_{nm}\right), \quad (10)$$

and $\Re k_{nm}$, $\Im k_{nm}$ are, respectively, the real and imaginary parts of the complex value for the frequency-independent nominal Love number k_{nm}. Equations (9)–(10) are written in general form, but presently only degree 2 nominal Love numbers by the IERS Conventions (2010) are given by complex values (to be used in case of anelastic Earth). From Equation (2) and Equations (4)–(5) one can find the additional changes in the $\Delta\bar{C}'_{4m}$ and $\Delta\bar{S}'_{4m}$ coefficients produced by the degree 2 tides

$$\Delta\bar{C}'_{4m} = \frac{R_E}{\mu_E}k^{(+)}_{2m}\bar{C}'_{2m}, \quad (11)$$

$$\Delta\bar{S}'_{4m} = \frac{R_E}{\mu_E}k^{(+)}_{2m}\bar{S}'_{2m}, \quad (12)$$

where $m = 0, 1, 2$. (In satellite dynamics the direct effect of the degree 4 solid Earth tides on the $\Delta\bar{C}'_{4m}$ and $\Delta\bar{S}'_{4m}$ coefficients, given by Equations (1)–(2), is considered as negligible.)

By using Equations (9)–(12) and the KSM03 harmonic development for the $\bar{C}'_{nm}$, $\bar{S}'_{nm}$ coefficients, we obtained analytical series for $\Delta\bar{C}'_{nm}$ and $\Delta\bar{S}'_{nm}$ for every relevant n and m. The series and their format description are available at http://lnfm1.sai.msu.ru/neb/ksm/solid_tides/SolidTides_Geopotential.zip. The maximum number of Poisson terms in the obtained series is 436 (in case of $\Delta\bar{C}'_{22}$); the maximum error of representing the numerical values for $\Delta\bar{C}'_{nm}$ and $\Delta\bar{S}'_{nm}$ by the analytical series is less than 0.7×10^{-12} (the comparison is done with use of the numerical ephemeris DE423 (Folkner 2010) over 1800–2200).

3. USE OF NEW SERIES IN ANALYTICAL THEORY OF SATELLITE MOTION

The new series for tidal variations of the geopotential coefficients due to the solid Earth tides are used in the author's analytical theory of satellite motion (Kudryavtsev 2002). We studied the effect of the solid Earth tides on motion of two geodetic satellites: low-altitude STARLETTE (the semimajor axis $a = 7335$ km) and high altitude ETALON-1 ($a = 25500$ km). First, we computed positions of those satellites over one month for STARLETTE (or for some 415 orbits of the satellite) and over one year for ETALON-1 (or for some 775 its orbits). Here the 15th-order Everhart's numerical integration method was used. The tide model included both the main part of the solid Earth tides defined by Equations (1)–(2) and the additional corrections accounting for frequency dependence of the degree 2 Love numbers. Positions of the attracting bodies were calculated on the basis of DE423 planetary/lunar ephemerides. The sampled step was chosen equal to 0.1 day for STARLETTE and to 1 day for ETALON-1. Then we assumed these satellites' positions as fictitious observations and processed them with help of the least-mean-square method, where our analytical theory for propagation of the satellite motion was used. The theory employed the new analytical series, Equations (7)–(8), describing the effect of the solid Earth tides, plus the known trigonometric series for corrections to geopotential coefficients, caused by frequency dependence of the degree 2 Love numbers. The tidal perturbations of the first and second order by the analytical theory were calculated.

A comparison of the satellites coordinates obtained by the two methods is done. As a result, the r.m.s. error of analytical calculating the effect of the solid Earth tides with help of the new series is estimated as equal to 2 cm for the STARLETTE satellite (over 1 month), and to 1 mm for the ETALON-1 satellite (over 1 year). For comparison, if one did not take into account the corresponding tidal effect at all, the r.m.s error would be some 13.5 m for STARLETTE and 5.1 m for ETALON-1.

Acknowledgements. Research supported in part by the Russian Foundation for Basic Research under grant no. 10-02-00234-a. A travel grant provided to the author by the LOC of the Journées 2011 is sincerely appreciated.

4. REFERENCES

Aoki, S., Guinot, B., Kaplan, G.H., Kinoshita, H., McCarthy, D.D., Seidelmann, P.K., 1982, "The new definition of Universal Time", A&A, 105, pp. 359–361.

Eanes R. J., Schutz, B., Tapley, B., 1983, "Earth and ocean tide effects on Lageos and Starlette" In: Kuo, J.T. (ed.) Proceed. of the Ninth Intern. Sympos. on Earth tides, E. Sckweizerbart'sche Verlagabuchhandlung, Stuttgart.

Folkner, W.M., 2010, "Planetary ephemeris DE423 fit to Messenger encounters with Mercury", JPL Interoffice Memorandum 343.R-10-001, 15 pp.

Kudryavtsev, S.M., 2002, "Precision analytical calculation of geodynamical effects on satellite motion", Celest. Mech. Dyn. Astr., 82, pp. 301–316.

Kudryavtsev, S.M., 2004, "Improved harmonic development of the Earth tide-generating potential", J. Geodesy, 77, pp. 829–838.

Petit, G., Luzum, B. (eds.), 2010, "IERS Conventions (2010)" (IERS Technical Note 36) Frankfurt am Main: Verlag des Bundesamts für Kartographie und Geodäsie, 179 pp., ISBN 3-89888-989-6.

Wahr, J.M., 1981, "Body tides on an elliptical, rotating, elastic and oceanless Earth", Geophys. J. R. Astron. Soc., 64, pp. 677–703.

CONSTRUCTION OF THE NUMERICAL AND SEMI-ANALYTICAL SOLUTIONS OF THE MOON ROTATION

V.V. PASHKEVICH, G.I. EROSHKIN
Central (Pulkovo) Astronomical Observatory of RAS
Pulkovskoe shosse, 65/1, 196140, St.Petersburg, Russia
e-mail: pashvladvit@yandex.ru, eroshkin@gao.spb.ru

ABSTRACT. In this research the problem of the lunar rotation motion is studied for the Newtonian case over long time intervals. The numerical solution of the Moon rotation is implemented with the quadruple precision of the calculations. The results of the numerical solution of the problem are compared with the composite semi-analytical theory of the Moon rotation (SMR) (Pashkevich and Eroshkin, 2010) with respect to the fixed ecliptic of epoch J2000. The initial conditions of the numerical integration are taken from SMR. The investigation of the discrepancies is carried out by the least squares and spectral analysis methods. All the secular, periodic and Poisson terms, representing the behavior of the residuals, are interpreted as corrections to SMR semi-analytical theory. As a result, the new high-precision Moon Rotation Series (MRS2011) is constructed, which is dynamically adequate to the DE404/LE404 and the DE406/LE406 ephemeris over 418.9, 2000 and 6000 years. The comparison of the new high-precision Moon Rotation solutions of MRS2011 with the solution of MRS2010 (Pashkevich and Eroshkin, 2010), which is dynamically adequate to the DE200/LE200 ephemeris over 418.9 year time interval, is performed. A numerical solution for the Moon rotation is obtained anew with the new initial conditions calculated by means of MRS2011. The discrepancies between the new numerical solution and the semi-analytical solution of MRS2011 do not surpass 20 mas over 418.9 year time interval, 48 mas over 2000 year time interval and 8 arcsec over 6000 year time interval. Thus, the result of the comparison demonstrates a good consistency of MRS2011 series with the DE/LE ephemeris.

1. INTRODUCTION

In the previous research (Pashkevich and Eroshkin, 2010) the high-precision Moon Rotation semi-analytical solutions of MRS2010, dynamically adequate to the DE200/LE200 ephemeris, was constructed over 418.9 year time interval.

The main purposes of this research are the construction of the new high-precision Moon Rotation Series (MRS2011), dynamically adequate to the DE404/LE404 and the DE406/LE406 ephemeris, over long time intervals. The mathematical model of the present investigation is identical to that used by Pashkevich and Eroshkin (2010). The orbital motions of the disturbing bodies are defined by the DE404/LE404 and the DE406/LE406 ephemeris. The dynamics of the rotational motion of the Moon is studied numerically by using Rodrigues-Hamilton parameters over 418.9, 2000 and 6000 years. The high-precision numerical integration method (Belikov, 1990), with a number of modifications (Eroshkin et al., 1993), was applied.

2. ALGORITHMS AND RESULTS

The result of the comparison of the numerical solution and semi-analytical solution SMR is studied by means the iterative algorithm:

1. The numerical solution of the Moon rotation is implemented with the quadruple precision of the calculations. The initial conditions are computed by the semi-analytical theory of the Moon rotation (SMR), which corresponds to the fixed ecliptic J2000.0. The discrepancies between the numerical solution and SMR are obtained in Euler angles over all the investigation time intervals with one day spacing (presented in Figure 1).

2. The investigation of the discrepancies is carried out by the least squares method (LSQ) and by the spectral analysis method (SA) (Pashkevich and Eroshkin, 2010). The secular terms are defined by LSQ. The set of the frequencies of SMR theory is used without a change. Only the coefficients of the periodical terms are improved and the coefficients of the Poisson terms are calculated by LSQ and by SA

(the spectral analysis scheme presented under in this paper). The secular, periodic and Poisson terms representing the new high-precision Moon rotation series MRS2011-i (where i is a number of the iteration) are determined.

3. The numerical solution of the Moon rotation is constructed anew with the new initial conditions, which are calculated by MRS2011-i.

4. Steps 2 and 3 are repeated till the best results for the discrepancies between new numerical solution and new MRS2011-i are obtained.

The spectral analysis scheme of SA is following: The spectrum of the discrepancies between the numerical solution and semi-analytical solution of the (i-1)-th iteration is constructed anew after the removal of every largest residual harmonic from the discrepancies. The set of the frequencies of the semi-analytical solution of the lunar physical libration SMR is used for the power spectrum construction. The amplitudes of the power spectrum are computed by LSQ. Each maximum term of the constructed spectrum is used for the determination of the new coefficients of the periodic and Poisson terms. Every coefficient of the new periodic term equals the sum of the calculated periodic and Poisson terms coefficients of the discrepancies and the coefficients of the corresponding periodic and Poisson terms of the (i-1)-th semi-analytical solution of the lunar physical libration problem. The found new harmonic is removed from the discrepancies and from the used set of the frequencies of SMR. This procedure is performed for every harmonic of the set and is accomplished successively up to the least term of the set. The new periodic and Poisson terms representing the new series MRS2011-i are determined.

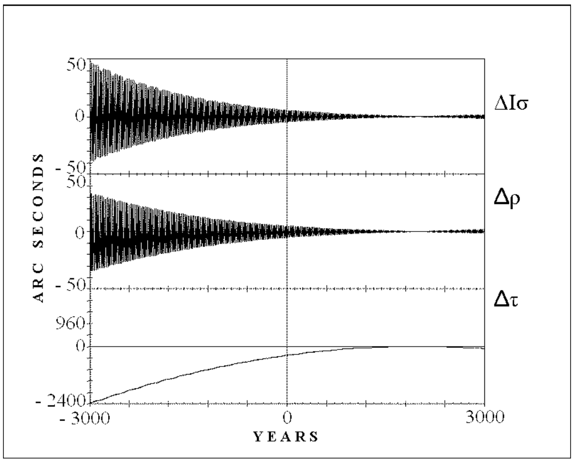

Figure 1: The discrepancies are depicted between the numerical and SMR semi-analytical solutions of the Moon rotation over 6000 years.

At first this investigation is carried out on 418.9 years time interval. The discrepancies between the numerical integration of the lunar rotation and the Moon rotation series SMR (for the DE404/LE404 ephemeris and for the DE406/LE406 ephemeris) are obtained in the perturbing terms of the lunar physical librations (in the longitude $\Delta\tau$, in the inclination $\Delta\rho$ and in the node longitude $\Delta\sigma$, which is multiplied by the mean inclination of the lunar equator to the ecliptic of date I (Newhall and Williams, 1997)) over 418.9 year time interval with one day spacing.

As a result of this research was obtained that the discrepancy between the new numerical and the new MRS2011A-1 semi-analytical solutions of the Moon rotation for the DE406/LE406 ephemeris (presented in Figure 2) and the DE404/LE404 ephemeris are very close to each other after the first iteration of the iterative algorithm. The residuals between the new numerical and the new MRS2011A-1 semi-analytical solutions of the Moon rotation (for the DE406/LE406 ephemeris), after the first iteration of the iterative algorithm, and the residuals between the numerical and MRS2010 (Pashkevich and Eroshkin, 2010) semi-analytical solutions of the Moon rotation (for the DE200/LE200 ephemeris) are also similar. Namely, the periodic and Poisson parts of MRS2011A are very close periodic and Poisson parts of MRS2010, over all time interval of MRS2010, that evidences a good convergency of the iterative algorithm of this investigation.

This investigation is continued on 2000 years time interval. The results of this investigation demonstrate that the residuals between the numerical and MRS2011B-1 semi-analytical solutions of the Moon

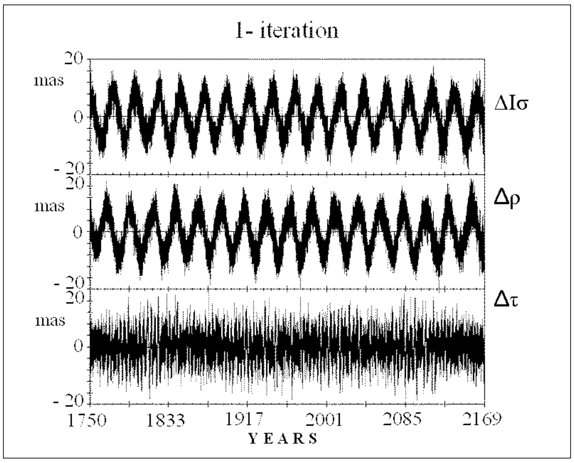

Figure 2: The residuals between the new numerical and the new MRS2011A-1 semi-analytical solutions of the Moon rotation (for the DE406/LE406 ephemeris), after the first iteration of the iterative algorithm.

rotation for the DE404/LE404 ephemeris and the DE406/LE406 ephemeris are very close to each other after the first iteration of the iterative algorithm. Thus, the second iteration is used only for the investigation with the application of the DE406/LE406 ephemeris.

The residuals between the numerical and MRS2011B-2 semi-analytical solutions, after the second iteration, and the residuals between the numerical and MRS2011B-3 semi-analytical solutions (presented in Figure 3), after the third iteration are similar. Then the process of the iterative algorithm is finished at this step.

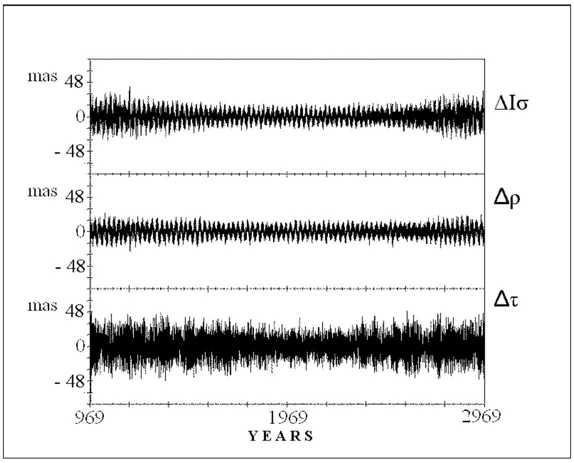

Figure 3: The residuals between the numerical and MRS2011B-3 semi-analytical solutions, after the third iteration of the iterative algorithm.

This investigation is finished at 6000 years time interval only for the DE406/LE406 ephemeris. In Figure 1 the discrepancies are depicted between the numerical and SMR semi-analytical solutions of the Moon rotation over 6000 years. The secular trend in the longitude of the descending node of epoch J2000 of the lunar equator longitude ψ does not surpass 40 arcmin over 6000 years.

Two iterations of the iterative algorithm in the present study were enough. The discrepancies between the numerical and MRS2011C-2 semi-analytical solutions, after the second iteration is presented in Figure 4. The discrepancies in the libration angles decrease after the second iteration and are less than 8 arcsec over 6000 years.

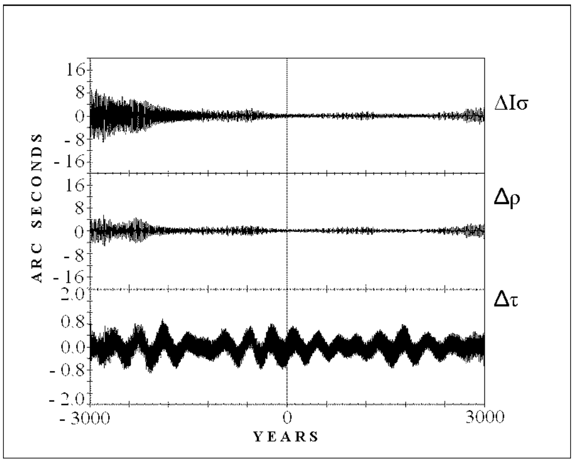

Figure 4: The discrepancies between the numerical and MRS2011C-2 semi-analytical solutions, after the second iteration.

3. CONCLUSION

As the results of this investigation, the new high-precision Moon Rotation Series are constructed: MRS2011A, dynamically adequate to the DE404/LE404 (DE406/LE406) ephemeris, over 418 years, MRS2011B, dynamically adequate to the DE404/LE404 (DE406/LE406) ephemeris, over 2000 years, MRS2011C, dynamically adequate to the DE406/LE406 ephemeris, over 6000 years.

The periodic and Poisson parts of MRS2011A are very close to the periodic and Poisson parts of MRS2010, over all time interval of MRS2010, that evidences a good convergency of the iterative algorithm of this investigation. The new more accurate series MRS2011 includes about 1523 secular, periodical and Poisson terms with the periods from 5.648 days to 84541.30 years. The discrepancies between the numerical solution and MRS2011 do not surpass:

20 mas over 418 year time interval,

48 mas over 2000 year time interval,

8 arcsec over 6000 year time interval.

It means a good consistency of MRS2011 series with the DE/LE ephemeris.

Acknowledgements. The authors are very grateful to Prof. Aleksander Brzeziński, Dr. Wieslaw Kosek for very useful discussions, Prof. Janusz Zielinski, Dr. Miloslawa Rutkowska, Dr. Leszek Jaworski and Dr. Ryszard Sdunek for the grants of financial support. The investigation was carried out at the Central (Pulkovo) Astronomical Observatory of the Russian Academy of Science and the Space Research Centre of the Polish Academy of Science, under a financial support of the Cooperation between the Polish and Russian Academies of Sciences, Theme No 38 and the grants of Polish Academy of Science, No 501-1-95 Dr. Ryszard Sdunek, 501-1-80 Prof. Janusz Zielinski, 123-033-49-17 PECS-98085 EEI Dr. Jaworski Leszek and Dr. Miloslawa Rutkowska.

4. REFERENCES

Belikov M.V., 1990, "Methods of numerical integration with uniform and mean square approximation for solving problems of ephemeris astronomy and satellite geodesy", Manus. Geod., 15, No4, pp.182-200.

Eroshkin G.I., Taibatorov K.A., Trubitsina A.A., 1993, "Constructing the specialized numerical ephemerides of the Moon and the Sun for solving the problems of the Earth's artificial satellite dynamics", ITA RAS, Preprint No 31, (in Russian).

Pashkevich V.V., Eroshkin G.I., 2010, "Application of the spectral analysis for modeling the rotations of the Moon", Artificial Satellites, 45, 4, pp. 153-162.

Newhall X X and Williams J.G., 1997, "Estimation of the lunar physical librations", Celestial Mechanics and Dynamical Astronomy, 66, pp. 21-30.

TAKING INTO ACCOUNT THE PLANETARY PERTURBATIONS IN THE MOON'S THEORY

T.V. IVANOVA
Institute of Theoretical Astronomy of Russian Academy of Sciences
10, Kutuzov quay, St.-Petersburg, 191187, Russia
e-mail: itv@ipa.nw.ru

ABSTRACT. The semi–analytical Moon's theory is treated in the form compatible with the general planetary theory GPT (Brumberg, 1995). The Moon is considered to be an additional planet in the field of eight major planets. Hence, according to the technique of the GPT, the theory of the orbital lunar motion can be presented by means of the series in the evolutionary eccentric and oblique variables with quasi-periodic coefficients in mean longitudes of the planets and the Moon. The time dependence of the evolutionary variables is determined by the trigonometric solution of the autonomous secular system describing the secular motions of the lunar perigee and node with taking into account the secular planetary inequalities. In this paper the right–hand members of the secular system are obtained in the analytical form. All the analytical calculations are performed by the echeloned Poisson series processor EPSP (Ivanova, 2001).

1. EQUATIONS OF LUNAR MOTION

The equations of the Moon's motion in geocentric rectangular coordinates x, y, z are described in the classical form

$$\ddot{x} = \frac{\partial U}{\partial x}\,, \qquad \ddot{y} = \frac{\partial U}{\partial y}\,, \qquad \ddot{z} = \frac{\partial U}{\partial z} \tag{1}$$

with the force function U

$$U = n^2\,\mathrm{a}^2 \left[\frac{\mathrm{a}}{r} + \left(\frac{n_3}{n}\right)^2 \frac{M_s}{M_s + M_3} \sum_{k=1}^{\infty} A_3^{(k-1)} \left(\frac{r}{\mathrm{a}}\right)^{k+1} \left(\frac{\mathrm{a}_3}{r_3}\right)^{k+2} P_{k+1}\left(\omega_3\right) \right.$$

$$\left. + \sum_{i=1, i\neq 3}^{8} \left(\frac{n_i}{n}\right)^2 \frac{M_i}{M_s + M_i} \sum_{k=1}^{\infty} A_i^{(k-1)} \left(\frac{r}{\mathrm{a}}\right)^{k+1} \left(\frac{\mathrm{a}_i}{\Delta_{3i}}\right)^{k+2} P_{k+1}\left(\omega_i\right) \right]. \tag{2}$$

$$M_3 = M_e + M_m, \quad A_i^{(k-1)} = \epsilon_k \left(\frac{\mathrm{a}}{\mathrm{a}_i}\right)^{k-1}, \quad \epsilon_k = \left(\frac{M_m}{M_3}\right)^k + (-1)^{k+1} \left(\frac{M_e}{M_3}\right)^k,$$

$$\Delta_{3i} = \mid \mathbf{r_3} - \mathbf{r_i} \mid, \qquad \omega_3 = \frac{\mathbf{r r_3}}{r\, r_3}, \qquad \omega_i = \frac{\mathbf{r}(\mathbf{r_3} - \mathbf{r_i})}{r\,\Delta_{3i}}\,.$$

Here M_s, M_e, M_m are the masses of the Sun, the Earth and the Moon, respectively. The index i points to the principal planet with number i. a, n, $\mathbf{r}$ are the semi–major axis, mean motion and radius–vector of the Moon, respectively. a_i, n_i, $\mathbf{r_i}$ $(i = 1, 2, \ldots, 8)$ are the same for the major planets. $P_k(\omega_i)$ are the Legendre polynomials. For the Moon, the values both with index 9 and without any indices are used.

Instead of rectangular coordinates $\mathbf{r} = (x, y, z)$ one introduces the dimentionless complex conjugate variables p, q and real variable w, representing deviations from the planar circular motion

$$x + \sqrt{-1}\, y = \mathrm{a}(1 - p) \exp \sqrt{-1}\, \lambda, \quad q = \overline{p}, \quad z = \mathrm{a}\, w, \quad w = \overline{w}\,, \tag{3}$$

λ being the mean longitude of the Moon. Here the bar means a conjugate value. The heliocentric coordinates $\mathbf{r_i} = (x_i, y_i, z_i)$ of the principal planets are subjected to the similar transformation.

In terms of the new variables the equations of lunar motion take the form

$$\ddot{p} + 2\sqrt{-1} n \dot{p} - \frac{3}{2} n^2 (p + q) = n^2 P\,,$$

$$\ddot{w} + n^2 w \qquad\qquad = n^2 W \tag{4}$$

with the right–hand members

$$P = -1 - \frac{1}{2}\,p - \frac{3}{2}\,q + \frac{2}{n^2\,\mathrm{a}^2}\,\frac{\partial U}{\partial q}, \qquad W = w + \frac{1}{n^2\,\mathrm{a}^2}\,\frac{\partial U}{\partial w}\,. \tag{5}$$

2. RIGHT–HAND MEMBERS

The right–hand members can be expressed in the form

$$P = P^{(kep)} + P^{(sol)} + P^{(pla)}\,, \qquad W = W^{(kep)} + W^{(sol)} + W^{(pla)}\,. \tag{6}$$

Here P^{kep} and W^{kep} correspond to the keplerian geocentric lunar motion:

$$P^{kep} = -1 - \frac{1}{2}p - \frac{3}{2}q + (1-p)\frac{\mathrm{a}^3}{r^3}, \qquad W^{kep} = \left(1 - \frac{\mathrm{a}^3}{r^3}\right)\,w\,. \tag{7}$$

P^{sol} and W^{sol} are due to the action of the Sun:

$$P^{(sol)} = \left(\frac{n_3}{n}\right)^2 \frac{M_s}{M_s + M_3} \sum_{k=1}^{\infty} \epsilon_k \left(\frac{\mathrm{a}}{\mathrm{a}_3}\right)^{k-1} P_k{}^{(sol)}\,,$$

$$P_k{}^{(sol)} = (1-p)\left(\frac{r}{\mathrm{a}}\right)^{k-1}\left(\frac{\mathrm{a}_3}{r_3}\right)^{k+2} C_{k-1}^{\frac{3}{2}}(\omega_3) - (1-p_3)\,\zeta_3^{-1}\left(\frac{r}{\mathrm{a}}\right)^{k}\left(\frac{\mathrm{a}_3}{r_3}\right)^{k+3} C_k^{\frac{3}{2}}(\omega_3)\,, \tag{8}$$

$$W^{(sol)} = \left(\frac{n_3}{n}\right)^2 \frac{M_s}{M_s + M_3} \sum_{k=1}^{\infty} \epsilon_k \left(\frac{\mathrm{a}}{\mathrm{a}_3}\right)^{k-1} W_k{}^{(sol)}\,,$$

$$W_k{}^{(sol)} = -w\left(\frac{r}{\mathrm{a}}\right)^{k-1}\left(\frac{\mathrm{a}_3}{r_3}\right)^{k+2} C_{k-1}^{\frac{3}{2}}(\omega_3) + w_3\left(\frac{r}{\mathrm{a}}\right)^{k}\left(\frac{\mathrm{a}_3}{r_3}\right)^{k+3} C_k^{\frac{3}{2}}(\omega_3)\,. \tag{9}$$

P^{pla} and W^{pla} are responsible for the planetary perturbations:

$$P^{(pla)} = \sum_{i=1, i\neq 3}^{8} \left(\frac{n_i}{n}\right)^2 \frac{M_i}{M_s + M_i} \sum_{k=1}^{\infty} \epsilon_k \left(\frac{\mathrm{a}}{\mathrm{a}_i}\right)^{k-1} \left(\frac{\mathrm{a}_i}{\mathrm{a}_{3i}}\right)^{k+2} P_{ik}^{(pla)}\,,$$

$$P_{ik}{}^{(pla)} = (1-p)\left(\frac{r}{\mathrm{a}}\right)^{k-1}\left(\frac{\mathrm{a}_{3i}}{\Delta_{3i}}\right)^{k+2} C_{k-1}^{\frac{3}{2}}(\omega_i) -$$

$$-\left(\frac{r}{\mathrm{a}}\right)^{k}\left[(1-p_3)\,\zeta_3^{-1}\frac{\mathrm{a}_3}{a_{3i}} - (1-p_i)\,\zeta_i^{-1}\frac{\mathrm{a}_i}{a_{3i}}\right]\left(\frac{\mathrm{a}_{3i}}{\Delta_{3i}}\right)^{k+3} C_k^{\frac{3}{2}}(\omega_i)\,, \tag{10}$$

$$W^{(pla)} = \sum_{i=1, i\neq 3}^{8} \left(\frac{n_i}{n}\right)^2 \frac{M_i}{M_s + M_i} \sum_{k=1}^{\infty} \epsilon_k \left(\frac{\mathrm{a}}{\mathrm{a}_i}\right)^{k-1} \left(\frac{\mathrm{a}_i}{\mathrm{a}_{3i}}\right)^{k+2} W_{ik}^{(pla)}\,,$$

$$W_{ik}{}^{(pla)} = -w\left(\frac{r}{\mathrm{a}}\right)^{k-1}\left(\frac{\mathrm{a}_{3i}}{\Delta_{3i}}\right)^{k+2} C_{k-1}^{\frac{3}{2}}(\omega_i) + \left(\frac{r}{\mathrm{a}}\right)^{k}\left(w_3\frac{\mathrm{a}_3}{a_{3i}} - w_i\frac{\mathrm{a}_i}{a_{3i}}\right)\left(\frac{\mathrm{a}_{3i}}{\Delta_{3i}}\right)^{k+3} C_k^{\frac{3}{2}}(\omega_i)\,. \tag{11}$$

Here $\mathrm{a}_{3i} = \max\{\mathrm{a}_3, \mathrm{a}_i\}$, $\quad C_k^{\frac{3}{2}}(\omega_i)$ are Gegenbauer polynomials.
The right–hand members are expanded into the Poisson series in power and exponential variables

$$p,\ q,\ w,\ p_i,\ q_i,\ w_i,\ \zeta_i = \exp\sqrt{-1}\,(\lambda - \lambda_i), \qquad i = 1, 2, \ldots, 8. \qquad (12)\,.$$

The keplerian and solar right–hand members were obtained in (Ivanova, 2011) concerning the determination of the secular indirect planetary perturbations within the frames of the main problem.

In constructing the Moon's theory there is no necessity to have a very accurate theory of motion for the major planets. It is sufficient to use only Keplerian terms, a first–order intermediary and first–order linear theory. Therefore the coordinates of the major planets necessary for the Moon's theory may be presented in the form

$$p_i = \delta p_i^{(0)} + p_{i,0}^{(1)} + \delta p_{i,1}^{(1)}\,, \qquad w_i = w_i^{(0)} + w_{i,1}^{(1)} \tag{13}$$

where the upper indices point out the order of smallness relative to the masses. The second sub-indices are responsible for the orders of the eccentricities and inclinations.

The first parts stand here for the Keplerian terms determined by the literal expansions in powers of the complex Laplace–type variables $a_i, \overline{a}_i, b_i, \overline{b}_i$ propotional to the eccentricity and inclination of the body with number i

$$\delta p_i^{(0)} = \sum p_{klmn}^{(0)}\, a_i^k \overline{a}_i^l b_i^m \overline{b}_i^n\,, \qquad w_i^{(0)} = \sum w_{klmn}^{(0)}\, a_i^k \overline{a}_i^l b_i^m \overline{b}_i^n\,. \tag{14}$$

The coefficients in Equation (14) are numerical constants.

The second part in p_i describes the terms of first order relative to the mass parameter in the intermediate solution

$$p_{i,0}^{(1)} = \sum_{\gamma} p_{i,\gamma}^{(1)}\, \exp \sqrt{-1}\,(\gamma\lambda)\,,$$

$$\gamma = (\gamma_1, \gamma_2, \ldots, \gamma_8), \quad (\gamma\lambda) = \sum_{j=1}^{8} \gamma_j \lambda_j, \quad \sum_{j=1}^{8} \gamma_j = 0\,. \tag{15}$$

And the last parts contain the linear terms in the eccentricities and inclinations taking into account only the first order terms relative to the masses. In explicit form they are expressed by the relations

$$\delta p_{i,1}^{(1)} = \sum_{j=1, j\neq i}^{8} \delta p_{ij,1}^{(1)}, \qquad w_{i,1}^{(1)} = \sum_{j=1, j\neq i}^{8} w_{ij,1}^{(1)}\,, \tag{16}$$

$$\delta p_{ij,1}^{(1)} = c(i,j,0)a_i + d(i,j,0)\overline{a}_i + c(i,j,1)a_j + d(i,j,1)\overline{a}_j\,,$$

$$w_{ij,1}^{(1)} = f(i,j,0)b_i + \overline{f}(i,j,0)\overline{b}_i + f(i,j,1)b_j + \overline{f}(i,j,1)\overline{b}_j$$

with quasi–periodic coefficients c, d and f.
The right–hand members are obtained in a purely analytical form.

3. INTERMEDIARY

In accordance with the general planetary technique the solution of the Moon's equations is represented in the form

$$p = p^{(0)} + \delta p, \qquad w = \delta w \tag{17}$$

where

$$p = p^{(0)}, \qquad w = 0 \tag{18}$$

is a particular planar quasi-periodic solution provided that the major planets move in their intermediate orbits

$$p_i = p_i^{(0)}, \qquad w_i = 0\,.$$

This solution generalizes Hill's variational curve and includes all solar and planetary inequalities independent of the eccentricities and inclinations of all the bodies. The solution is represented by the multiple Fourier series

$$p^{(0)} = \sum_{\gamma} p_{\gamma}\, \exp \sqrt{-1}\,(\gamma\lambda)\,,$$

$$\gamma = (\gamma_1, \gamma_2, \ldots, \gamma_9), \quad (\gamma\lambda) = \sum_{i=1}^{9} \gamma_i \lambda_i, \quad \sum_{i=1}^{9} \gamma_i = 0 \tag{19}$$

in mean longitudes of all the bodies. The coefficients depend on the masses, mean motions and the semi-major axes. The intermediary was obtained up to 14th order relative to small parameters M_i, $\frac{n_i}{n}$, $\frac{\mathrm{a}}{\mathrm{a}_i}$ in (Ivanova, 2011). Its expansion contains about ten thousands terms.

4. DETERMINATION OF δp AND w

The functions $\delta p, w$ satisfy the equations

$$\delta\ddot{p} + 2\sqrt{-1}n\delta\dot{p} + n^2\left[\left(-\frac{3}{2}+K\right)\delta p + \left(-\frac{3}{2}+L\right)\delta q\right] = n^2 P' , \tag{20}$$

$$\ddot{w} + n^2(1+M)w = n^2 W' \tag{21}$$

with the right–hand members of the form

$$P' = P - P^{(0)} + K\delta p + L\delta q, \qquad W' = W + Mw\,. \tag{22}$$

P', W' don't contain the linear terms with respect to the lunar variables δp, δq and w.
$P^{(0)}$ is the right–hand member of the equation for the intermediary,
K, L, M are the functions of the intermediate solution.
δp and w are sought by iterations in the form of power series

$$\delta p = \sum p_{klmn} \prod_{i=1}^{9} a_i^{k_i}\overline{a}_i^{l_i} b_i^{m_i}\overline{b}_i^{n_i}\,, \qquad w = \sum w_{klmn} \prod_{i=1}^{9} a_i^{k_i}\overline{a}_i^{l_i} b_i^{m_i}\overline{b}_i^{n_i} \tag{23}$$

with the initial approximation

$$\delta p = -\frac{1}{2}a_9 + \frac{3}{2}\overline{a}_9\,, \qquad w = b_9 + \overline{b}_9\,. \tag{24}$$

The summation is performed over all the non-negative values of 9-indices k, l, m, n. The coefficients are the functions of the intermediate solution.

The method of δp and w construction is based on the separation of the fast and slowly changing variables by means of a number of the linear and Birkhoff transformations of the variables. The series (23) are in fact not a solution of the equations of the Moon's motion but a transformation to the secular system describing the evolution of the lunar orbit.

5. SECULAR SYSTEM

The time dependence of Laplace-type variables is determined by the solution of the autonomous secular system

$$\dot{\alpha} = \sqrt{-1}\,N\left[A\alpha + \Phi(\alpha,\overline{\alpha},\beta,\overline{\beta})\right], \qquad \dot{\beta} = \sqrt{-1}\,N\left[B\beta + \Psi(\alpha,\overline{\alpha},\beta,\overline{\beta})\right] \tag{25}$$

in slowly changing variables

$$\alpha = (\alpha_1,\ldots,\alpha_9)\ (\alpha_i = a_i \exp -\sqrt{-1}\lambda_i)\,,$$
$$\beta = (\beta_1,\ldots,\beta_9)\ (\beta_i = b_i \exp -\sqrt{-1}\lambda_i)\,. \tag{26}$$

Here $N = diag(n_1,\ldots,n_9)$, A and B are 9×9 matrices of semi-major axes, mean motions and masses of all the bodies under consideration, 9-vectors Φ, Ψ contain only forms of odd degree in slowly changing variables α, $\overline{\alpha}$, β, $\overline{\beta}$ starting with the third degree terms.

To complete this system one should add the equations for the conjugate variables. The right–hand members of the secular system for the Moon are obtained in the purely analytical form but the trigonometric solution of the secular system has the semi–analytical form. It includes terms due to the secular evolution of the lunar perigee and node as well as of that of the major planets.

Now this work is in progress.

6. REFERENCES

Brumberg V., 1995, "Analytical Techniques of Celestial Mechanics", Springer, Heidelberg.
Ivanova T., 2001,"A new echeloned series processor (EPSP)", Celest. Mech. Dyn. Astr. 80, pp. 167–176.
Ivanova T., 2011,"On constructing the analytical Moon's theory", in book of abstracts, JENAM 2011, Saint Petersburg, Russia.

EPM-ERA2011 LUNAR EPHEMERIS AND SELENODYNAMICAL PARAMETERS FROM LLR (1970-2011) DATA

E.I. YAGUDINA, G.A. KRASINSKY, S.O. PROKHORENKO
Institute of Applied Astronomy, Acad. Sci., Russia
10, Kutuzov quay, 191187, St.-Petersburg, Russia
e-mail: eiya@ipa.nw.ru; kra@ipa.nw.ru; prs@ipa.nw.ru

ABSTRACT. The modern Lunar ephemerides are constructed at JPL,USA (DE403,DE405, DE421); in Institute of Celestial Mechanics, France (series of INPOP) and at the Institute of Applied Astronomy RAS in the framework of ERA system (Krasinsky and Vasiliev, 1996). The dynamical model EPM-ERA has been constructed by simultaneous numerical integration of equations of orbital motion of the Moon, major planets, the biggest asteroids, and the lunar rotation. The dissipative effect of lunar rotation was included in the new version of ephemeris with retarded argument under integration of orbital and rotational Lunar motion. The comparison of improved dynamical model was made with 17742 LLR observations (1970-2011) for obtaining selenodynamical parameters. The version has been compared with three versions of the DE ephemerides and French ephemeris INPOP10.

1. INTRODUCTION

The subtle effects in the rotation of the Moon may be studied making use of lunar laser ranging measurements (LLR) provided by regular observational programs started in 1969, when the first reflector was put at the Moon surface. The analysis of the LLR data with applications to lunar rotation is given in (Dickey et al., 1994; Williams et al., 2001; Aleshkina et al.,1996). Unlike the problem of the Earth's rotation no monitoring of rotational parameters of the Moon is yet possible, thus the case of the Moon seems even more complicated then that of the Earth. The small effects to be studied are only detectable if a sophisticated dynamical model both of the orbital and rotational motions of the Moon is constructed by simultaneous integration of equations of motion of the major planets and the Moon (including equations of the lunar rotation). High accuracy of the LLR data requires dynamical theories of the adequate precision. The analysis of LLR data depends not only on a dynamical model but on partial derivatives in respect to a number of parameters many of which also require numerical integration. The comparison of the improved dynamical model was made using 17742 LLR observations (1970-2011). This version has also been processed with three versions of DE ephemerides and French INPOP10 one.

2. THE EPM-ERA DYNAMICAL MODEL

In this paper only a brief summary of the model used is described. The full theory was presented in the paper (Krasinsky G., 2002). The precise dynamical model EPM-ERA has been constructed by simultaneous numerical integration of equations of orbital motion of the Moon, major planets, the biggest asteroids, and the lunar rotation. The potential of the Moon is calculated up to the fourth order of the zonal index, the potential of the Earth includes the second order harmonics C_{20} and C_{22}. Tidal perturbations in the lunar orbital motion, caused by tidal dissipation on the Earth's body, have been computed by the model using a constant lag. Partial derivatives of ranging with respect to dynamical parameters of the orbital and rotational model of the Moon are computed mostly by integrating the variational equations; in a few cases, they have been obtained by integrating the rigorous system of equations with slightly varied values of the parameters under study. In the current version of the EPM-ERA 2011 ephemeris, the model of the tidal perturbations in the rotational motion of the Moon (due to dissipation in the Moon's body) is constructed using retarded argument. The expansion of the retarded function in a power series of delay is used.

3. OBSERVATIONS

In the present analysis, 17742 LLR observations of the time interval 1970-2011 have been included in the processing. They were carried out mainly at McDonald (Texas), where at different times three different sites were activated as the McDonald observatory, MLRS1 and MLRS2; Cerga station (France); a set of two-year observations made at Haleakala Observatory (Hawai) and 915 observations were made at Apache station (mm accuracy). The number of observations at each site is shown in Table 1. LLR analysis of a number of parameters under estimation appears to be strongly correlated and may be reliably estimated because four reflectors could be observed.

Station	Time interval	Number of LLR observations
McDonald	1970 March - 1985 June	3440
MLRS1	1985 January - 1988 January	275
MLRS2	1988 August - 2011 August	3194
HALEAKALA	1989 November - 1990 August	694
CERGA	1985 January - 2011 June	9224
APACHE	2006 August - 2010 November	915
TOTAL	1970 March- 2011 July	17742

Table 1: Distribution of LLR observations

The number of ranging to Apollo 11, 14, 15 and Lunokhod2 are 1819, 1757, 13667, 499 respectively. Unfortunately, such disparity of the distribution deteriorates the reliability of the estimation of a number of selenodynamical parameters. Before 1998, the observations were obtained by the request from observatories, later on they were retrieved from the following FTP servers: "ccdisa.gsfc.nasa.gov/pub/slr", "oca.eugemini.donnees.las_lunes", "http://www.physics.ucsd.edu/~tmurphy/apollo/norm_pts.html" for observations from Apache station. Some observations were obtained by private correspondence.

4. PARAMETERS DETERMINED

In Table 2, a list of parameters under study in the LLR processing are presented. The set of parameters includes the lunar initial coordinates and velocities, libration angles and their velocities, Stokes coefficients of the selenopotential, Lunar Love numbers $k2$, $h2$, $l2$, the angles of tide delay, the coordinates of reflectors, observational stations, etc. All the improved values of dynamical parameters were fed back into the EPM-ERA theory. As lunar rangings are invariant, relative to rotations of the Earth-Moon system as a whole,

N	Parameters estimated
1-6	Lunar orbital state vector for epoch JD 2446000.5
7-12	Eulers angles and their time derivatives for the same epoch
13-18, 22-24	Coordinates of reflectors A11, A14, L2
20	X coordinate for reflector Apollo 15 (A15)
25-42	Coordinates of 6 observational stations
44	Lag of the Earths body tides
48-51	Secular trends in siderial angles of the Earth and Moon
55	Lag of the Moons body tides
52-54, 59-63	Harmonics of lunar potential from C_{20} to S_{33}
56-58	Lunar Love numbers $k2$, $h2$, $l2$
64-65	secular trends of the corrections to the parameters of Earths equator

Table 2: Parameters determined

the whole set of orientation parameters of this system cannot be determined simultaneously. Due to this, the coordinates of the most often observable reflector Apollo15 have been fixed (longitude and latitude). The values of these two parameters were obtained from a simplified solution made at the first step, in which lunar libration was not improved. LLR observations are sensitive to the Earth's gravitational constant GmE. Our experience has shown that the observable effect reduces to scaling of distances and cannot be reliably separated from the corrections to the X coordinates of the reflectors. Thus, the value was not included into the list of estimated parameters.

5. ANALYSIS OF THE RESULTS

The numerical theory EPM-ERA has been compared with the set (17742) of LLR observations and all the parameters listed above have been determined. The corrections to 65 parameters were fed back by several iterations and the result can be seen in Table 3. The number of observations used, post-fit and pre-fit residuals, observational stations and periods of observations at every station are also given in Table 3. Because the EPM-ERA model was improved by the corrections obtained, the post-fit residuals practically coincide with O-C differences computed using the improved model. It is known that the analysis of LLR data not only depends on the dynamical model but on partial derivatives relative to a number of parameters many of which also require numerical integration. Thus, to compare our result with the results obtained using DE or INPOP10 ephemerides, all analogous calculations have been made with mentioned ephemerides using derivatives from EPM-ERA.

Number of observations	WRMS[cm] O-C	WRMS[cm] residuals	Observational stations	Interval of observations
3414	31. 5	31.5	McDonald	19700415.0-19850630.0
275	12.2	12.2	MLRS1	19850301.0-19880127.1
9224	5.4	5.3	CERGA	19840407.2-20110621.2
692	13.6	13.7	Haleakala	19891113.1-19900830.1
2862	6.7	6.7	MLRS2	19880229.0-20110721.1
915	5.2	5.0	Apache	20060407.1-20101030.1
17378	6.6	6.5	Total	19700415.0-20110721.1

Table 3: EPM-ERA ephemeris, statistics of residuals

Because the nominal values of the parameters for DE and INPOP10 ephemerides are not known, the corrections could only be fed back to the coordinates of reflectors and the coordinates of ground stations. Post-fit residuals and the number of the observations used for all the versions of DE ephemerides and INPOP10 are presented in Table 4. The O-C differences are only shown for EPM-ERA ephemeris: in case of EPM-ERA, all the corrections could be fed back, as for DE and INPOP10 ephemerides O-C differences (after feeding back corrections to reflectors and coordinates of ground stations) are big: it is not known what other parameters different from those used EPM-ERA ephemeris had been determined. At the plots of Figures 1 to 5 the residuals for DE ephemerides, INPOP10 and for EPM-ERA2011 are presented.

Ephemerides	Wrms(cm) O-C	Wrms(cm) residuals	Number of observations	Number of deleted observations
DE 403		5.2	17369	373
DE 405		5.6	17379	363
DE 421		5.7	17375	367
INPOP10		5.1	17377	365
EPM-ERA 2011	6.6	6.5	17378	364

Table 4: Statistics of residuals for EPM-ERA ephemeris, compared with DE and INPOP10 ephemerides

6. CONCLUDING REMARKS

The investigation shows that the current accuracy of lunar component of DE (5.4-5.7 cm) and INPOP10 (5.1 cm) ephemerides is a slightly better than that of EPM-ERA2011 (6.5 cm). The source of this discrepancy is due to not complete account of the tidal perturbations in the rotational motion of the Moon. Currently, a test of this part of the model, as well as changes to the integrator process, are under

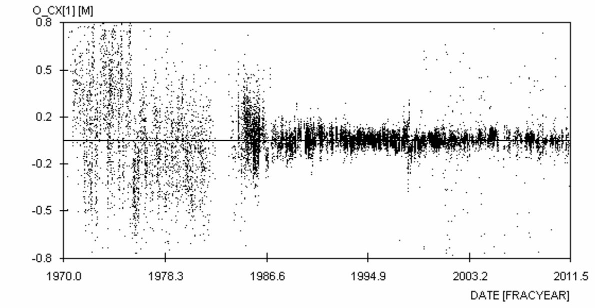

Figure 1: DE403

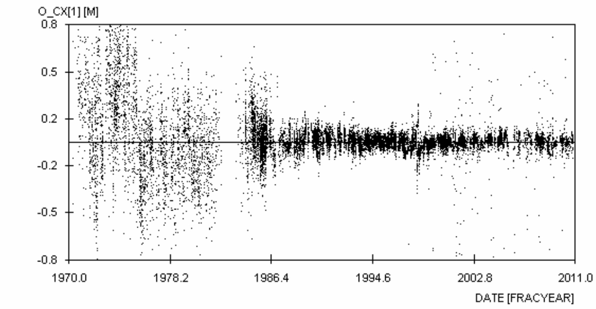

Figure 2: DE405

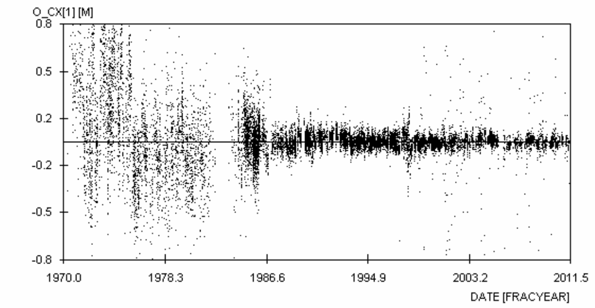

Figure 3: DE421

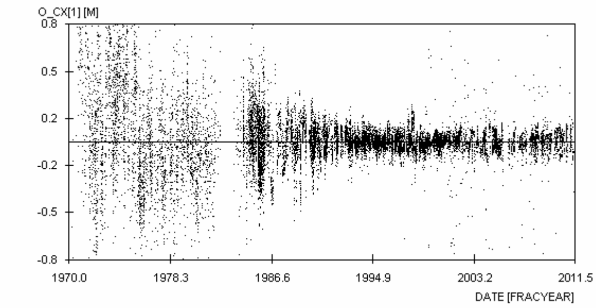

Figure 4: EPM-ERA2011

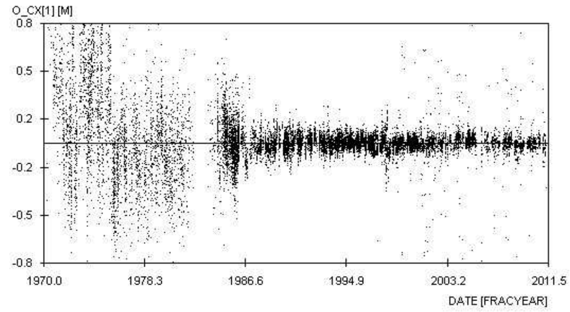

Figure 5: INPOP10

way.

Acknowledgements. The authors would like to thank Williams J. (JPL, USA) and Manche H. (IMCCE, France) for useful advices.

7. REFERENCES

Aleshkina E.Yu., KrasinskyG.A., Vasiliev M.V., 1996, "Analysis of LLR data by the program ERA", Proceedings of IAU Colloquium 165, Poznan, Poland, pp. 228-232.

Dickey J.O. et all., 1994, "Lunar laser Ranging: a continuing legacy of Apollo program". Science, v. 265, pp. 482-490.

Krasinsky G.A., Vasiliev M.V., 1996, "ERA: knowledge base for Ephemeris and dynamical astronomy", Proceedings of IAU Colloquium 165, Poznan, Poland, pp. 239–244.

Krasinsky G.A.,2002, "Selenodynamical parameters from analysis of LLR observations of 1970-2001", Comminications of the IAA RAS, N 148, pp. 1-27.

Williams J.G. et al., 2001, "Lunar rotational dissipation in solid body and molten core". J. Geophys. Res. Planets, 106, pp. 279333-27968.

LUNAR EFFECTS ON CLOSE ENCOUNTERS OF HUNGARIA ASTEROIDS AND NEAR-EARTH ASTEROIDS WITH THE EARTH

A. BAZSÓ, M. GALIAZZO

Institute for Astrophysics, University of Vienna
Türkenschanzstraße 17, A-1180 Vienna, Austria
e-mail: akos.bazso@univie.ac.at, mattia.galiazzo@univie.ac.at

ABSTRACT. The Earth is target to many celestial objects, among them Near Earth Asteroids (NEA) play a significant role. Different dynamical groups have been found, the source of these asteroids is mainly the the main belt, in particular we consider the Hungaria group. group. We carry out a statistical investigation by numerical integration of the motion of real asteroids and their hypothetical clones in a simplified dynamical model of the solar system up to 100 My. In a first part we present integrations of existing Hungaria asteroids to determine which of them could become NEAs. Then the influence of the Moon on the orbits of these NEAs is investigated. The main goal is to find the frequency of close encounters and deflection angles due to them, possible impacts and the strength of deflection by the Moon.

1. INTRODUCTION

The population of Main-Belt Asteroids (MBA) was found by Hirayama (1918) to be clustered into "families" of asteroids, which share similar orbital elements (i.e. semi-major axis a, eccentricity e, inclination i). Later it turned out that the families can also be discriminated by spectroscopic properties. These groups and families originated presumably by collisional break-up of larger objects, a process which is still ongoing in the solar system.

One of these groups is the Hungaria group, named after the biggest object (434) Hungaria, located at the inner edge of the main-belt at approximately 2 AU (astronomical units). The Hungaria group is an interesting case to study the dynamics of MBAs, since it is surrounded by several mean-motion resonances (MMR) and secular resonances (SR). On the outer edge the J4:1 MMR with Jupiter effectively removes asteroids, while the inner edge is shaped by Mars encounters at perihelion, additionally the M3:4 MMR acts inside the orbital parameter region of the Hungarias, and the ν_6 secular resonance limits the maximum inclination of the group's members (Milani et al., 2010).

All these constraints lead to the conclusion, that since the scattering of objects from the Hungaria group preferably happens towards the inner solar system (Galiazzo et al., 2012), there must be an exchange of asteroids between the Hungaria group and the NEAs. The spectra of Enstatite achondrite meteorites (McSween, 1999) studied on Earth give indirect evidence for a link to Hungaria asteroids, as they show similar features like the E-type spectral class to which and approximately 60% of the Hungaria population belongs (Warner et al., 2009).

To confirm this link we started a study on the dynamics of the Hungaria group with the aim to find out more about the evolution to Near-Earth asteroids and their long-time behaviour. The main point is the investigation of close-encounters to the Earth, where also the influence of the Moon needs to be taken into account. Domingos et al. (2004) verified that the orbits of NEAs can be significantly affected by the Moon at low relative velocities. The gravitational influence of the Moon results in a twofold effect: on one hand the Moon can prevent the Earth from collisions, but on the other hand it can enhance the collision rates.

2. DESCRIPTION OF THE MODELS AND METHODS

This study consists of two complementary parts:

1. In the first part from a selection of 200 real asteroids we found 11 Mars-crossing objects that subsequently become NEAs ("escapers", see Table 1 of Galiazzo et al., 2012). These 11 Hungarias

were cloned, i.e. their initial conditions (orbital elements a, e, i) were slightly modified, to enhance the statistics of close encounters. The dynamical model consisted of the planets Venus to Saturn, the integrations were carried out for 100 million years with the Lie N-body integrator (Hanslmeier & Dvorak, 1984; Eggl & Dvorak, 2010), which is capable of treating close encounters accurately by using an adaptive step-size.

In our sample of Hungarias we have chosen objects that fall into the following intervals of osculating elements: $1.78 \leq a[\mathrm{AU}] \leq 2.03$, $0 \leq e \leq 0.19$, $12 \leq i[\mathrm{deg}] \leq 31$. Their typical diameters, based on current observational data, range from $\approx 0.5 - 2.5$ km, which is comparable to the NEA sizes.

The primary goals were to establish the number of close encounters and impacts, the impact probability and relations between different encounter related parameters.

2. The following part concentrates on the NEAs, as we have previously seen that many Hungarias can evolve into orbits typical for NEAs. We investigate each of the three NEA groups in detail by selecting some hundred objects (100 Atens, 200 Apollos, and 300 Amors) and running numerical integrations for 10 million years using the same code as above. The integration time here is shorter than for the Hungarias, since due to their typically smaller semi-major axes the orbital evolution of NEAs is faster, and additionally the median lifetime of NEAs is of the same order as our integration time (Gladman et al., 1997).

   We compare the evolution of NEAs in two models, model 1 (M1) is the spatial elliptic restricted three body problem Sun-Earth-NEA, and model 2 (M2) the spatial restricted four body problem Sun-Earth-Moon-NEA (we always consider the NEAs to be massless). In this way we can compare the results for close encounters without Moon in M1 with those in M2 with the Moon's contribution added.

For each close encounter[1] of every asteroid we collect data like the minimum distance to the Earth, the relative velocities, the time spent inside the lunar orbit, and the magnitude of deviation from the unperturbed orbit during fly-by. The latter is expressed by the "deflection angle", by which we mean the angle formed by the velocity vectors at the time instants of begin and end of the close encounter. The deflection angle depends on the velocity and the minimum distance to Earth, the closer the asteroid approaches the higher the angle gets since the trajectory is strongly influenced.

3. RESULTS

The data for close encounters (see Table 1) are at first glance as expected. The Amor group asteroids with typically relatively large semi-major axes ($a \geq 1.5$ AU) have the fewest encounters with Earth. On the contrary there is a sharp increase for both the Apollos ($a \geq 1$ AU) and Atens ($a < 1$ AU), as both are Earth orbit crossing populations, whereas the Amors only approach Earth at their perihelia. The table also shows that there is a difference in the relative velocities for Amors vs. Apollos/Atens, although the average velocity for Amors (M2) is almost as high as for the other NEA groups. The other velocities do not exhibit such big differences, for each group the values lie within the $1 - \sigma$ interval. Considering the deflection angles it is obvious that a lower relative velocity result in a higher deflection, if the asteroids pass close enough by the Earth or Moon.

The number of close encounters is not given for the Hungarias in Table 1, because the numbers depend strongly on the clones chosen, and that would make an average incomparable. There are even clones completely lacking close encounters, which are derived from an object that itself does have close encounters, thus showing how sensitive the results are with respect to the initial conditions, and that the reliable orbit determination after a close encounter is not trivial. Higher relative velocities for Hungarias in the table are due to the fact, that they first increase their eccentricities to leave the main belt and become Mars crossers, then having Mars encounters further increase the eccentricity. So when they finally evolve into Earth orbit crossing asteroids they quite often have a higher mean eccentricity than other NEAs.

For the deflection angle we find a quite simple relation to the minimal distance. When both are plotted as in Figure 1 a fitting function of the form $y = a/x^b + c$ can be used, where the exponent $b \approx 1$. This fit also holds in the case of NEAs, with the angles being larger, reaching up to more than 90° in extreme

[1]We define a "close encounter" of an asteroid to the Earth, if the mutual distance of the two bodies is less than 0.0025 AU, which is the average lunar distance of 384400 km.

group (model)	total number of encounters	relative velocity [km/s]	deflection angle [deg]	duration [days]
Amors (M1)	296	10.5	6.77	0.54
Amors (M2)	315	14.0	7.71	0.36
Apollos (M1)	10789	14.7	1.83	0.43
Apollos (M2)	12558	13.5	2.06	0.46
Atens (M1)	25258	14.4	1.45	0.44
Atens (M2)	26425	15.1	1.37	0.42
Hungarias (M1)	—	20.3	0.8	0.35
Hungarias (M2)	—	20.1	12.8	0.34

Table 1: Summary of the close encounter count with direct comparison between the two models M1/M2 for NEAs (The numbers for Hungaria escapers are not given, see text for explanation). For every group the total (absolute) number of encounters within 0.0025 AU is shown, first for model 1 where there is no influence by the Moon, and second for model 2 including the additional gravitational effect caused by the Moon. Also shown are the averaged values for the relative velocity, deflection angles and durations, i.e. the time elapsed between entering and exiting the region inside 0.0025 AU.

cases where there would be an impact. The scattering of points in the plot is a natural consequence of the variation in encounter velocity, which itself depends on the osculating elements (eccentricity, inclination) at the given time. Apart from the values shown in the table, when considering all the clones, the duration of close encounters seems to be shorter (or at most similar) in the case of model 1 (without Moon), while the deflection angles are systematically larger in model 2 (with Moon).

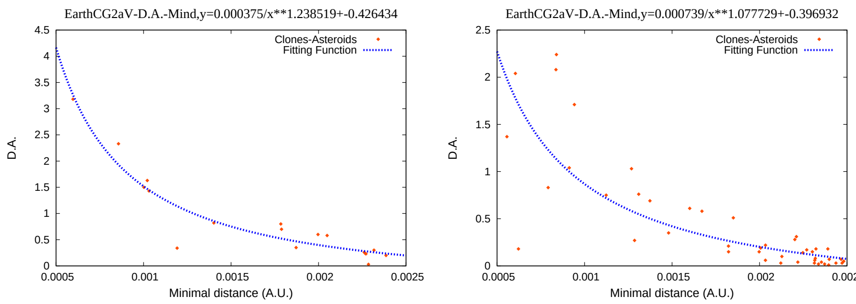

Figure 1: Dependence of the deflection angle on the minimal distance to Earth for close encounters with velocities less than 11.2 km/s. Every point in the plot corresponds to a separate close encounter event. The left figure shows the case for a Hungaria asteroid without the Moon, on the right the same object with the Moon.

In the integrations the majority of close encounters takes place at a rather large distance, so most of the time only "shallow encounters" occur. This behaviour is well visible in Figure 2, where the highest fraction of events (around 70%) falls into the right-most bin, representing minimal encounter distances just below the lunar distance. Here qualitatively no difference between Hungarias and NEAs is found, in any case one can observe a linear trend in these log-log plots (minimal distance vs. number).

For the two selected Hungaria asteroids shown in the left part of Figure 2 there were no impacts, so the minimal distances are well above the "critical" value of 6400 km, while for the NEAs the figures show several cases with impacts, that fall either into the bin at 3.5 or 3.8. It is also visible that the fraction (relative number of cases) is systematically higher for the lowest distance bins in model 2 (including the Moon) compared to model 1. When computing the impact probability P_c for the Hungarias using the method of Dvorak & Pilat-Lohinger (1999) we get for M1 $P_{c,1} = 9.7 \times 10^{-8}$/year, and for M2 $P_{c,2} = 1.1 \times 10^{-8}$/year. Here we see that the impact probability is higher without the Moon.

4. CONCLUSIONS

Considering the data presented we argue, that the Moon does have a non-negligible effect on close

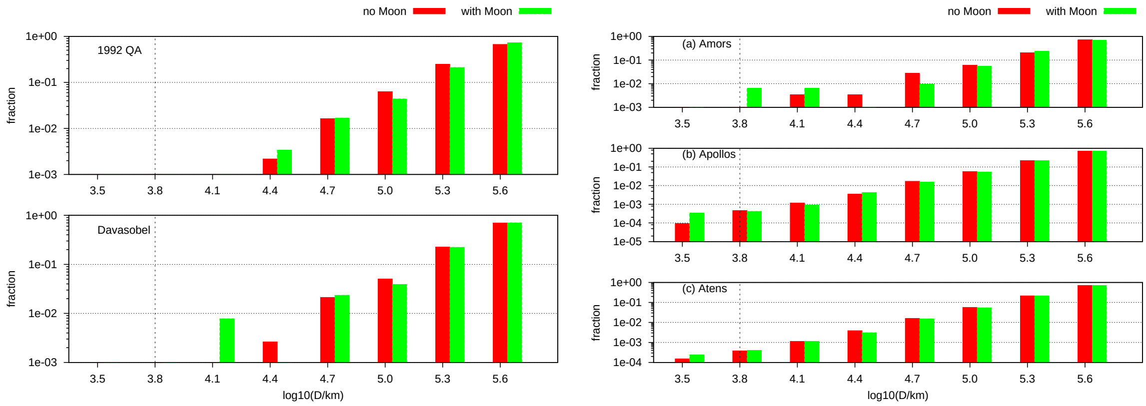

Figure 2: Histograms for the distribution of the distances for two selected Hungarias (left) and the NEA groups (right). The bars represent the fraction of cases (number per bin normalised by the total number of close encounters) for the distance D being lower than a certain value. The red (left) resp. right (green) bars indicate model 1 resp. model 2. Note that the distance is on a logarithmic scale, i.e. the plot range corresponds to an interval of $3200 < D < 400000$ km. The vertical lines at 3.8 indicate the collision distance of approximately one Earth radius, $D = 10^{3.8} \approx 6300$ km.

encounters of both Hungarias and Near Earth asteroids. We have shown that there are distinct differences whether or not the Moon's gravitational influence is taken into account. The number of close encounters is similar in both models, and is only comparable for objects belonging to the same group of NEAs. Although the absolute numbers depend on the arbitrary choice of the limit distance (for a larger value of 0.01 AU instead of 0.0025 AU the number of close encounters increases by an order of magnitude at least), a normalisation still gives good results. The deflection angles and impact probabilities indicate that in the Moon's presence incoming asteroids are more effectively scattered, which is why the first values are higher and the latter lower. The interesting shift of minimal encounter distances to lower values in model 2 gives rise to additional questions, that we need to tackle in future work. We will continue our work to better understand the role of the Moon, but we are aware that we need more data to draw decisive conclusions.

5. REFERENCES

Domingos, R. C., Winter, O. C., Neto, E. V., 2004, "Collisions with the Earth: the Moon's contribution", Advances in Space Research, 33, pp. 1534–1538

Dvorak, R. and Pilat-Lohinger, E., 1999, "On the dynamical evolution of the Atens and the Apollos", Planetary and Space Science, 47, pp. 665–677

Eggl, S. and Dvorak, R., 2010, "An Introduction to Common Numerical Integration Codes Used in Dynamical Astronomy", In: Lecture Notes in Physics, Berlin Springer Verlag, 790, J. Souchay & R. Dvorak (Eds.), pp. 431–480

Galiazzo, M., Bazsó, Á., Dvorak, R., 2012, "The Hungaria Asteroids: resonances, close encounters and impacts with terrestrial planets", Planetary and Space Science, submitted

Gladman, B. J., Migliorini, F., Morbidelli, A., Zappala, V., Michel, P., Cellino, A., Froeschle, C., Levison, H. F., Bailey, M., Duncan, M., 1997, "Dynamical lifetimes of objects injected into asteroid belt resonances", Science, 277, pp. 197–201

Hanslmeier, A. and Dvorak, R., 1984, "Numerical Integration with Lie Series", A&A , 132, pp. 203–208

Hirayama, K., 1918, "Groups of asteroids probably of common origin", AJ , 31, pp. 185–188

McSween, H. Y., 1999, "Meteorites and their parent planets", Cambridge University Press, Cambridge, UK, pp. 168.

Milani, A., Knežević, Z., Novaković, B., Cellino, A., 2010, "Dynamics of the Hungaria asteroids", Icarus, 207, pp. 769–794

Warner, B. D., Harris, A. W., Vokrouhlický, D., Nesvorný, D., Bottke, W. F., 2009, "Analysis of the Hungaria asteroid population", Icarus, 204, pp. 172–182

ON THE STABILITY OF EARTH'S TROJANS

C. LHOTKA[1], L.Y. ZHOU[2], R. DVORAK[3]
[1] Département de Mathématique
Rempart de la Vierge 8, B-5000 Namur, Belgium
email: clhotka@fundp.ac.be
[2] Departement of Astronomy, Nanjing University
Nanjing, 210093, China
[3] Institute for Astronomy, University of Vienna
Türkenschanzstraße 17, A-1180 Vienna, Austria

ABSTRACT. The gas giants Jupiter and Neptune are known to host Trojans, and also Mars has co-orbiting asteroids. Recently, in an extensive numerical investigation ([8]) the possibility of captures of asteroids by the terrestrial planets and even the Earth into the 1:1 mean motion resonance (MMR) was studied. The first Earth Trojan has been observed ([2]) and found to be in a so-called tadpole orbit closed to the Lagrange point L_4. We did a detailed study of the actual orbit of this Trojan 2010 TK7 including the study of clone orbits, derived an analytical mapping in a simplified dynamical system (Sun+Earth+massless asteroid) and studied the phase space structure of the Earth's Lagrange points with respect to the eccentricities and the inclinations of a large number of fictitious Trojans. The extension of stable zones around the Lagrange points is established with the aid of dynamical mappings; the known Trojan 2010 TK7 finds himself inside an unstable zone.

1. INTRODUCTION

Trojan asteroids move in the same orbits as their host planets, but around 60 degrees ahead or 60 degrees behind them close to the so-called Lagrange points L_4 or L_5. Up to now we observe Trojans of Jupiter (about 4000), of Neptune (7) and also of Mars (3) but the other planets still seem to lack of such a companion (e.g. [9]). Although in the original paper of the first confirmed discovery of a Trojan asteroid ([2]) a dynamical study has been undertaken we extended it to a more detailed investigation. We make use of a dynamical symplectic mapping of the Sun-Earth Trojan model and of extensive numerical integrations of fictitious Trojans in the full model of our Solar system. With this approach we were able to obtain a deeper understanding of the dynamical aspects of the first confirmed Earth Trojan asteroid 2010 TK_7 as well as the stability of Earth Trojan asteroids in general.

2. THE REAL ORBIT OF 2010 TK_7

The orbit of the asteroid 2010 TK_7 is numerically simulated to obtain a direct estimation of its orbital stability and its origin. After some test runnings and comparisons between different numerical codes, we choose the *Mercury6* integrator package ([1]) to make our simulations in this part. For the initial conditions of 2010 TK_7, we adopt the data listed in the AstDyS website[1]. Specifically, at epoch JD2455800.5, the semi-major axis $a = 1.00037\,\mathrm{AU}$, eccentricity $e = 0.190818$, inclination $i = 20^\circ.88$, ascending node $\Omega = 96^\circ.539$, perihelion argument $\omega = 45^\circ.846$ and the mean anomaly $M = 217^\circ.329$. Since the errors are unavoidable in the observation and orbital determination, we simultaneously simulate the evolution of a cloud of 100 clone orbits within the error bars. These clone orbits are generated using the covariance matrix listed in the AstDyS website. Two dynamical models are applied. In one model, we include the Sun and eight planets from Mercury to Neptune and the Earth is placed in the barycenter of the Earth-Moon system and its mass is replaced by the combined mass of the system. In the other model however, the Earth and the Moon are treated separately. Hereafter the former and later models are denoted by EMB and E+M, respectively. In two dynamical models, we integrate the nominal and clone

[1]http://newton.dm.unipi.it

orbits both forward (to future) and backward (to past) for 1 million years. During the integration, we check the resonant angle $\delta\lambda = \lambda - \lambda_{\rm EMB}$ (the difference between the mean longitude of the asteroid and the barycenter of the Earth-Moon system). At the start of integration ($t = 0$), the $\delta\lambda$ librates around 60° since 2010 TK$_7$ is on a tadpole orbit around L_4 right now. But it may leave this region in both backward and forward integrations. We record the moment t_1 when $\delta\lambda$ reaches 180° for the first time, and the moment t_2 when $\delta\lambda$ attains 360°. So t_1 and t_2 are the time when an asteroid escapes from the L_4 tadpole region and from the 1:1 MMR. Figure1 summarizes the distribution of t_1 and t_2.

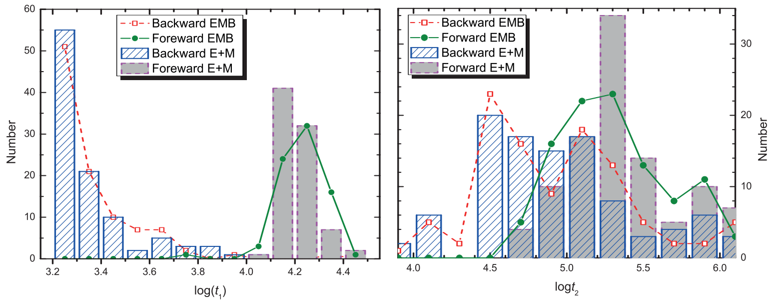

Figure 1: The time when clone asteroids escape from the L_4 region (t_1) and from the 1:1 MMR (t_2).

From the distribution of t_1 and t_2, we conclude that the two models EMB and E+M are consistent with each other, they do not make considerable differences. It is more or less a natural consequence of the Earth and the Moon being a close binary. From Figure 1, we can also conclude that 2010 TK$_7$ is a temporal Earth Trojan. In fact the nominal orbit will leave the L_4 region in about 17000 years, while most of the clone orbits will escape in ~ 15000 years. The results of backward integration show that most of the clones became L_4 Earth Trojans only about 1700 years ago, just as the nominal orbit did. As for the time they leave the 1:1 MMR, it is $\sim 4.0 \times 10^4$ years in the past and $\sim 2.5 \times 10^5$ years in the future. The total time for this object being in the 1:1 MMR with the Earth is less than $\sim 3.0 \times 10^5$ years.

3. THE ANALYTICAL MAPPING

The most basic dynamical model behind the motion of 2010 TK$_7$ takes the form:

$$H = H_{\rm Kep} + T + \mu' R(a, e, i, \omega, \Omega, M, M'; P') \ . \tag{1}$$

Here H_{Kep} defines the motion of the asteroid around the Sun and $\mu' R$ gives the potential of the Earth with mass μ'. Here M' denotes the mean anomaly of the Earth. R is time dependent due to the presence of M', we therefore extend the phase space with T (assuming, that the mean motion n' of the Earth is equal to one). Moreover, we denote by P' the orbital parameters of the Earth $P' = (a', e', i', \omega', \Omega')$. In the further discussion we use the modified Delaunay variables $\lambda_1 = M + \omega + \Omega$, $\lambda_2 = -\omega - \Omega$, $\lambda_3 = -\Omega$ and their conjugated momenta $\Lambda_1 = \sqrt{a}$, $\Lambda_2 = \sqrt{a}(1 - \sqrt{1 - e^2})$, $\Lambda_3 = 2\sqrt{a}\sqrt{1 - e^2}\sin^2(i/2)$ and similar for the orbital parameters of the Earth. Moreover, we write $\Lambda = (\Lambda_1, \Lambda_2, \Lambda_3)$ and $\lambda = (\lambda_1, \lambda_2, \lambda_3)$ in short. The aim of this section is to investigate the role of P' on the mean orbit of the asteroid 2010 TK$_7$. For this reason we will make use of a symplectic mapping based on the averaged Hamiltonian ([6]):

$$\tilde{H} = -\frac{1}{2\Lambda_1^2} + \frac{1}{2\pi}\int_0^{2\pi} \mu' R\,(\Lambda, \tau, \lambda_2, \lambda_3, \lambda_1'; P')\, {\rm d}\lambda_1' \ , \tag{2}$$

where $\tau = \lambda_1 - \lambda_1'$ is the resonant angle (which is also related to $\delta\lambda$ of the previous section). Thus, the average over the fast angle λ_1' defines the mean dynamics close to the $1:1$ MMR. To shorten notation we will write $\lambda = (\tau, \lambda_2, \lambda_3)$ from now on. Based on Equation (2) we define a transformation from state $(\lambda^{(k)}, \Lambda^{(k)})$ to $(\lambda^{(k+1)}, \Lambda^{(k+1)})$ via the generating function:

$$W_{P'} = W_{P'}\left(\lambda^{(k)}, \Lambda^{(k+1)}; P'\right) = \lambda^{(k)} \cdot \Lambda^{(k+1)} + 2\pi\tilde{H}\left(\lambda^{(k)}, \Lambda^{(k+1)}; P'\right) \ .$$

Based on it the mapping from time k to $k+1$ is given by:

$$\lambda_j^{(k+1)} = \frac{\partial W_{P'}}{\partial \Lambda_j^{(k+1)}} \ , \quad \Lambda_j^{(k)} = \frac{\partial W_{P'}}{\partial \lambda_j^{(k)}} \quad \text{with } j = 1, 2, 3 \ . \tag{3}$$

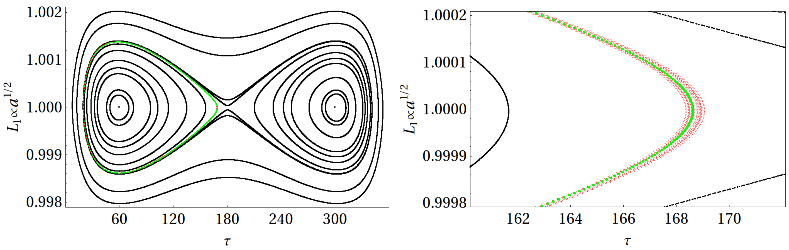

Figure 2: Dynamics in the (τ, Λ_1)-plane. Left: varying τ within 0 and 360°. Right: $P' = const$ (green) vs. $P' = P'_k$ (red). See text.

The system (Equation 3) describes the time-evolution of the mean orbital elements of the asteroid at times $t = 2\pi k$. In physical units the time step corresponds to 1 Earth-year. We iterate the mapping for initial conditions provided in [2] in the case of i) fixed orbital parameters of the Earth $P' = const$ and ii) time varying parameters $P' = P'_k$. To obtain P' and P'_k we integrate the equations of motion of the full Solar system and maintain Earth's orbital elements, say $P'(t)$, at discrete times $P'_k = P'(k[years])$. A typical phase portrait is provided in Figure 2 (left): we see the fixed points of the mapping L_4, L_3, L_5 situated along $a = 1$ and located at $\tau = 60°, 180°, 300°$, respectively. The stable pair is surrounded by small librational curves, while seperatrix-like motion originates from the unstable fixed point. The effect of the time variation of P' can be seen in Figure 2 (right). While for constant P' the motion getting close to L_3 remains on a thin curve for long times (green), the motion for time varying P'_k covers a wider range in the phase space and eventually reaches the tadpole regime of motion around L_5 (red). The effect of the additional perturbations therefore may explain the jumping of the Trojan from one to another stable equilibrium as well as a possible trapping of the asteroid in the horse-shoe regime of motion.

4. DYNAMICAL MAPS OF THE L_4 REGION

We integrated the orbits of thousand of fictitious Trojans in the L_4 region and we established how extended is this zone with respect to the semi-major axis and to the inclination. We included the planets Venus, Earth, Mars and the two giant planets Jupiter and Saturn in our dynamical model [2]; the Earth and Moon system was regarded as one 'planet' situated in their barycenter [3] and the fictitious asteroids were taken as massless bodies. The integration method used in this section was the very fast and precise Lie-code with an automatic step size control already used extensively in our former studies (e.g. [5], [4], [3], [9]) and the integration time was set to up to 10^8 years. In Figure 3 we show the results of this numerical study: on the one hand we checked the libration around the Lagrange point L_4 [4] and on the other hand the eccentricity is quite a sensitive marker for stable and unstable orbits in the Trojan zone. In the respective Figure 3 (left graph) the amplitude of the libration angle is given by different colors. One can see that around the center ($a = 1$) there is a dark black region extending up to an inclination of about 15° which means that the Trojans are suffering only from small oscillations around L_4. More to the edge with larger and smaller initial semi-major axes of the fictitious body these oscillations increase in amplitude up to about 40°, then, on both sides with respect to the semi-major axes the orange color indicates that from the tadpole orbits just around one Lagrange point the orbits developed into horseshoes around both libration points; but they are still stable. We can see another stable window between an initial inclination of $25° < i < 40°$ and another small one for $i \sim 50°$. Whereas this small window disappears for integration $T > 10^7$ years, the larger stable window remains. We studied it with another tool namely by checking the orbital eccentricity. It turned out that any value of $e > 0.3$ leads to an escape from the stable region; we therefore plotted in Figure 3 (right graph) the corresponding values. It is interesting to see that now on the edge to the unstable region on both sides of the Lagrange point very stable (almost circular) orbits survive which are marked by dark blue inside the 'blue' window extending between 0.997 AU $< a <$ 1.003 AU.

[2]test computations for the complete system with the eight planets did not qualitatively change the picture
[3]all involved planets are regarded as point masses
[4]in many studies (e.g. [7]) the symmetry of both equilibria was shown

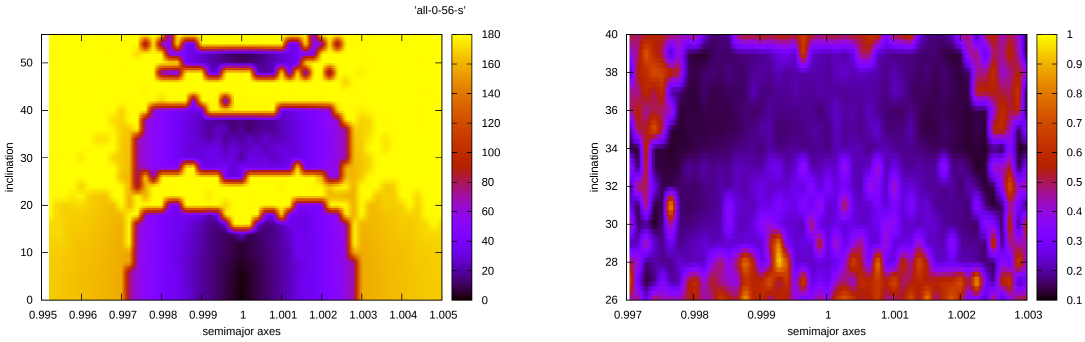

Figure 3: Dynamical map of the L_4 region. Left: the libration amplitudes of the fictitious Trojans; tadpole orbits are inside the red line in dark blue and violet close to the center, horseshoe orbits are in orange, escapers in light yellow. Right: maximum eccentricity of the Trojans within 10^7 years of integration; stable orbits are shown in dark blue, escaping orbits are marked from orange to yellow.

5. CONCLUSIONS

In this study we confirm that the recently discovered Earth Trojan 2010 TK_7 is a temporarily captured asteroid, which is stable only for several thousand years. In its actual orbit it is in a tadpole orbit around L_4, but it is a jumping Trojan changing its orbit between tadpole around one or the other equilibrium point and horseshoe orbits; but then it escapes from the stable region. This dynamical behaviour is observed in backward as well in forward integration and well confirmed by all three methods used in the paper. Two main stable regions were found. One for low inclined orbits ($i < 15°$) and one for $25° < i < 40°$. Surprisingly is that the Trojan discovered by recent observations is in none of these stable regions but well inside an unstable zone! But we may be able in future to observe many more of these companions of the Earth.

Acknowledgements. ZLY thanks the financial support by the National Natural Science Foundation of China (No. 10833001, 11073012, 11078001).

6. REFERENCES

[1] Chambers, J., 1999, "A hybrid symplectic integrator that permits close encounters between massive bodies", MNRAS , 304, 793–799.
[2] Connors, M., Wiegert, P., Veillet, C., 2011, "Earth's Trojan asteroid", Nature, Vol.475, 481-483.
[3] Dvorak, R., Bazsó, A., Zhou, L.-Y., 2010, "Where are the Uranus Trojans?", Celest. Mech. Dyn. Astr. 107, 1–15.
[4] Dvorak, R., Lhotka, Ch., Schwarz, R., 2008, "The dynamics of inclined Neptune Trojans", Celest. Mech. Dyn. Astr. 102, 97–110.
[5] Dvorak, R., Pilat-Lohinger, E., Schwarz, R., Freistetter, F, 2004, "Extrasolar Trojan Planets close to habitable zones", A&A 426, L37–L40.
[6] Lhotka, C., Efthymiopoulos, C., Dvorak, R., 2008, "Nekhoroshev stability at L4 or L5 in the elliptic-restricted three-body problem - application to Trojan asteroids" MNRAS 384, 1165–1177.
[7] Nesvorný, D., Dones, L., 2002, "How Long-Lived Are the Hypothetical Trojan Populations of Saturn, Uranus, and Neptune?", Icarus 160, 271–288.
[8] Schwarz, R., Dvorak, R., 2011, "On the Capture of Asteroids by Venus, Earth and Mars into the 1:1 Mean Motion Resonance", Celest. Mech. Dyn. Astr. (submitted)
[9] Zhou, L.Y., Dvorak, R., Sun, Y.S., 2011, "The dynamics of Neptune Trojans - II. Eccentric orbits and observed objects", MNRAS 410, 1849–1860.

WHERE ARE THE SATURN TROJANS ?

H. BAUDISCH, R.DVORAK
Institute for Astronomy, University of Vienna
Türkenschanzstraße 17, A-1180 Vienna, Austria
e-mail: helmut.baudisch@chello.at, e-mail: dvorak@astro.univie.ac.at

ABSTRACT. The gas giants Jupiter and Neptune are known to host Trojan asteroids but up to now no asteroids have been found around the libration points of Uranus and Saturn. With the aid of numerical integrations we checked the stability of fictitious bodies in the 1:1 Mean Motion Resonance with Saturn. Former studies show that around the Lagrange points the bodies escape quite fast whereas a stable ring survives for million of years. Using the results of our investigation in different dynamical models we could show that Jupiter is responsible for the unstable hole around the equilateral equilibrium points.

1. INTRODUCTION

The Lagrange points in the restricted three body problem (built up of two massive bodies – called primary bodies – on circular orbits and a third massless one) mark positions where the centrifugal forces are in equilibrium with the combined gravitational forces exerted by the Sun and a planet. The astronomer Joseph Louis Lagrange (1736 – 1813) was the first who predicted that these points of equilibrium exist. Whereas the points L_1 to L_3 (on the connecting line between the massive bodies) are unstable, the equilibrium points L_4 and L_5 (building an equilateral triangle with the two primaries) are stable[1]. In a rotating coordinate system - the primaries on the x-axes – they are located 60° ahead respectively behind the planet. Consequently the massless body is in a 1:1 Mean Motion Resonance (MMR) and one speaks of coorbital motion. Because of the stability of the two equilateral Lagrange points the area close by allows stable motion and in fact many asteroids are found coorbiting the planet Jupiter (3191 respectively 1743) Neptune (six respectively two) and Mars (one respectively three). Even the Earth has one Trojan close to L_4 (Connors et al, 2011). But why are there no Trojans of Saturn, the second planet in size? Many studies deal with this question for the gas-giants like Baudisch (2010), Dvorak et al (2008), Dvorak et al (2010), Holman and Wisdom (1993), Innanen and Mikkola (1989), Téger (2000), Nesvorný and Dones (2002), Zhou et al (2009) and Zhou et al (2011).

In Figure we show a schematic picture of the restricted problem Sun-Saturn (left graph) and the stable zone around L_4 which is a longitudinal stretched region; we show also the real libration motion of a fictitious Trojan around the Lagrange point L_4 (right picture). One can distinguish two well separated periods namely a large one covering the whole stable region and a small one with many loops.

2. DESCRIPTION OF THE MODELS AND METHODS

To check the stability of Trojans around Saturn we use the results of extensive numerical integrations of a great number of orbits of fictitious massless bodies in the region around L_4. The restricted problem is not a realistic model to answer this question and consequently no analytic approaches (compare Lhotka et al., 2008) can be used for this problem. Five different dynamical models were used: SJUN: all planets of the outer Solar System, SJN: without Uranus, SJU: without Neptune, SUN: without Jupiter, SJ: only with Jupiter as perturber.

In the region around L_4 we equally distributed for a grid with initial conditions the fictitious Trojans and varied the semimajor axes a and the angular distance to the Lagrange point. In additional runs the initial inclination of the fictitious Trojan with respect to the plane of motion of Saturn was set to several values $i < 10°$. As integration method we choose the Lie-integration, a well established tool of computercode to integrate the orbits of Solar System bodies with an automatic stepsize control (Dvorak et al., 2008). We emphasize that for this kind of investigation only point masses were taken for the

[1] depending on the mass ratio μ of the primaries which should be $\mu < 1/27$

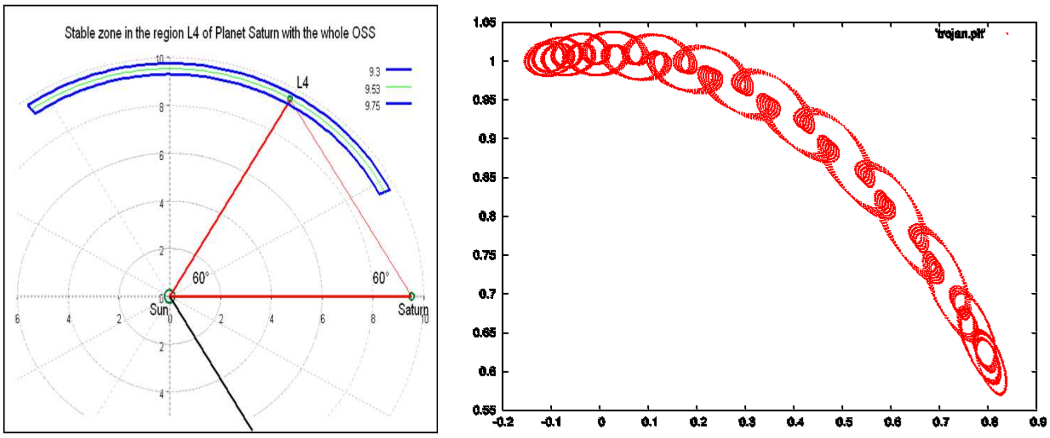

Figure 1: Schematic view of the Sun-Saturn system and the stable region around the Lagrange point L_4 in a rotating coordinate system $x-y$ measured in AU (left picture). Motion of a massless body in the Sun-Jupiter system in the rotating coordinate system; distances measured in units of the semimajor axis of Jupiter (right picture)

planets and no other than the gravitational forces were taken into account.

3. RESULTS

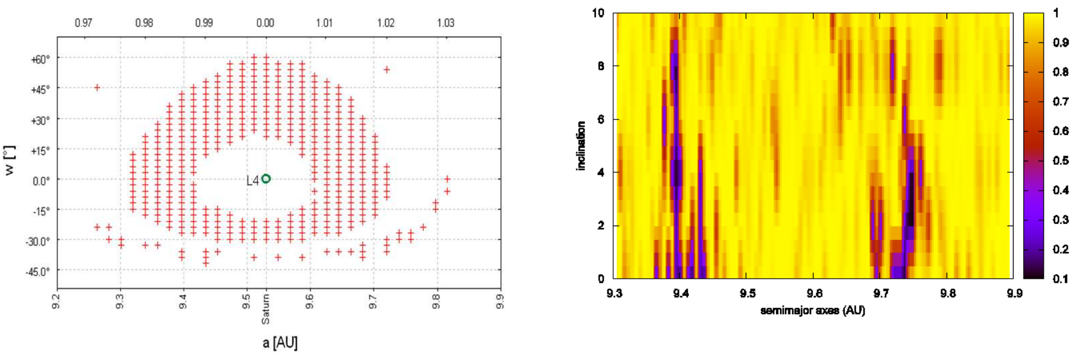

Figure 2: Stable ring (marked by crosses) around the Lagrange point L_4 of Saturn in the model of the outer Solar System after an integration time of 10^6 years semimajor axes versus the elongation around the equilibrium point (left picture). Cut through the equilibrium point L_4 for different initial semimajor axes versus different inclinations for the Trojan integrated for 10^8 years (right picture)

An interesting feature, namely a stable ring around the Lagrange point is visible in Figure (left picture). Close to the equilibrium point the fictitious Trojans escape rather fast, which can be seen in more detail in Figure : on the left graph we plotted the escape times for a cut where we were fixing the semimajor axes ($a = a_{Saturn}$) and varying the initial angular distance to the Lagrange point; on the right graph we fixed the angular distance and just varied the semimajor axis. Comparing the results it is evident that the longer integration time of 10^7 years does not change qualitatively the ring structure with respect to the shorter integration time. In additional runs we changed the integration time to 10^8 years for the cuts where we varied the semimajor axes but we also changed the initial inclination up to $10°$ (Figure , right graph). Here we can see that even for the plane problem which we treated in the former runs almost no orbits are stable for such a long integration time – the stable ring disappeared! Only some scattered points of stability with orbits of small eccentricity survived (dark blue colors). That means that no Trojans of Saturn can be on stable orbits for the life time of our Solar System. They cannot have

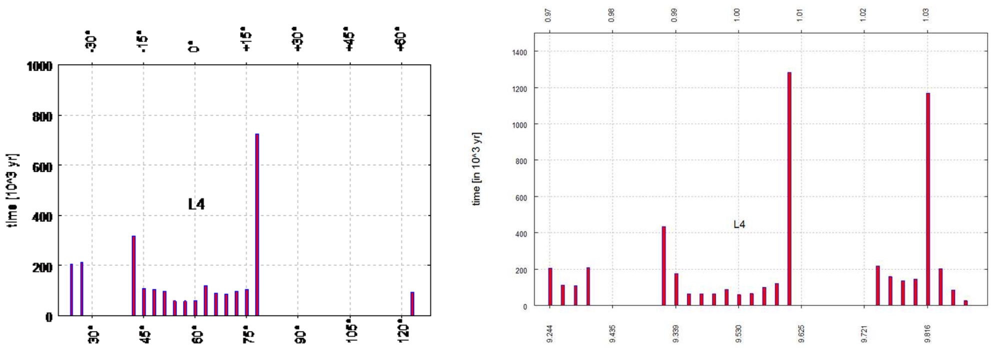

Figure 3: Escape times after an integration time of 10^7 years for cuts through $a = a_{Saturn}$ (left graph) and when the elongation δ is constant (right graph)

formed "in situ" together with their planet like for Jupiter (Robutel et al., 2005) and Neptune (Zhou et al., 2009, Zhou et al., 2011) Trojans.

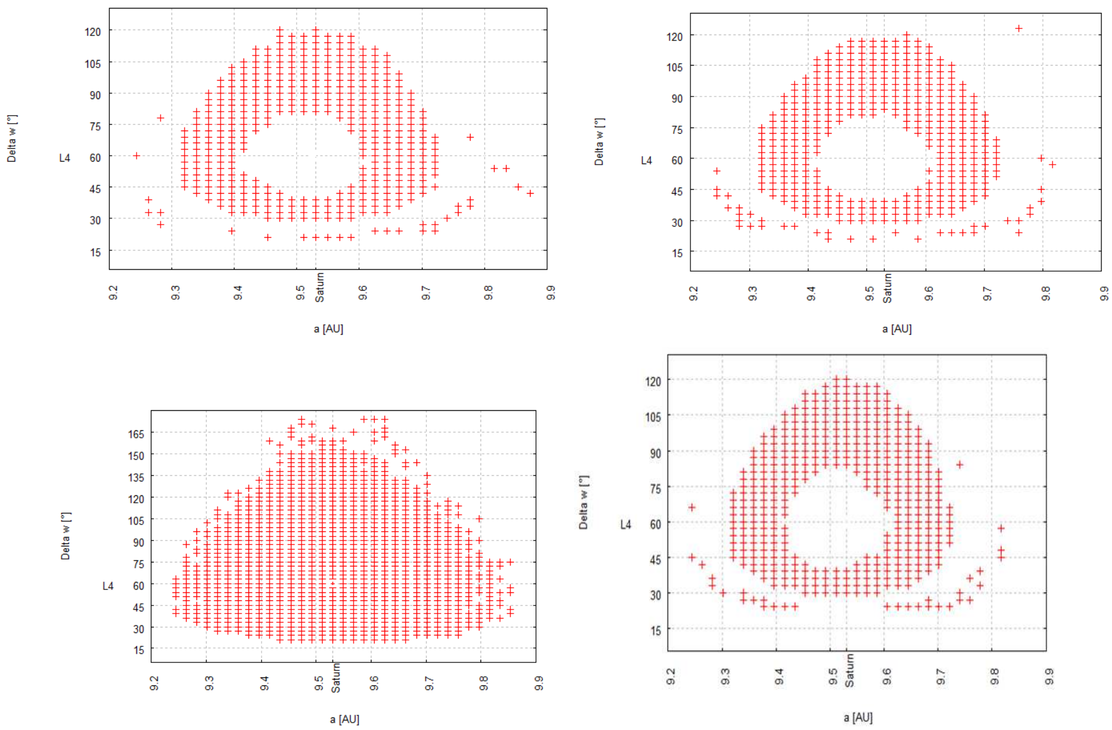

Figure 4: Stable regions for 4 different dynamical models semimajor axis versus elongation from L_4: SJU (upper left), SJN (Upper right), SUN (lower left) and SJ (lower right); for details see text

But what caused the unstable hole? Therefore we investigated different fictive dynamical systems described in Chapter 2. In Figure (upper left) we show the results for a system without Neptune (SJU) and in the same figure (upper right) the results for the dynamical system without Uranus (SJN). Even eliminating Uranus and Neptune, which means a system with only Saturn and Jupiter (SJ) (lower right), we always see nearly the same picture with an unstable hole close to the Lagrange point itself. But the integration without Jupiter (SUN), (lower left graph), shows that the hole is no more here, but a significantly larger stable region around L_4 is visible. With the whole OSS (model SJUN, Figure 2, left picture) the situation is nearly identical with a system with only Saturn and Jupiter.

4. CONCLUSIONS

The influence of Uranus and Neptune as perturbing planets of Trojan asteroids of Saturn is insignificant. The planet Jupiter is solely responsible for the hole of instability for short time integrations ($T < 10^7$) compared to the age of the planetary system. On the long term scale this planet also destabilizes the whole region around the Saturnian libration points. If we find in the future Trojans of Saturn, these Trojans could only be captured asteroids, in orbits in the 1:1 MMR for a short time. However, up to the present day, no Trojans of Saturn have been found. Are they too small for our current instruments or are possible captures too short with respect to the time they stay in the vicinity of L_4 and L_5? The question remains thrilling!

5. REFERENCES

Baudisch, H., 2010, "Investigation on the stability of the Trojans of Saturn around L4 (and L5)", Masterthesis at the Institute of Astronomy, p.95.

Connors, M., Wiegart, P., Veillet, C., 2011, "Earth's Trojan asteroids", Nature 475, 481-483.

Dvorak, R., Bazsó, A., Zhou, L.-Y., 2010, "Where are the Uranus Trojans?", Celest. Mech. Dyn. Astr. 107, 1-15.

Dvorak, R., Lhotka, Ch., Schwarz, R., 2008, "The dynamics of inclined Neptune Trojans", Celest. Mech. Dyn. Astr. 102, 97-110.

Holman, M., Wisdom, J., 1993 "Dynamical stability in the Outer Solar System and the delivery of short period comets", AJ , 105, 5, 1987-1999.

Innanen, K., Mikkola, S., 1989, "Studies on Solar System Dynamics I: The stability of Saturnian Trojans", AJ , 97, 3, 900-908.

Lhotka, C., Efthymiopoulos, C.,Dvorak, R., 2008, "Nekhoroshev stability at L4 or L5 in the elliptic-restricted three-body problem - application to Trojan asteroids" MNRAS 384, 1165-1177.

Nesvorný, D., Dones, L., 2002, "How Long-Lived Are the Hypothetical Trojan Populations of Saturn, Uranus, and Neptune?", Icarus 160, 271-288.

Robutel, P., Gabern, F., Jorba, A., 2005, "The Observed Trojans and the Global Dynamics Around The Lagrangian Points of the Sun Jupiter System", Celest. Mech. Dyn. Astr. 92, 53-69.

Téger, F., 2000, "On the stability of Lagrangian points L4 and L5 of Saturn, Proceedings of the 2nd Austrian Hungarian Workshop", 31-38.

Zhou, L.Y., Dvorak, R., Sun, Y.S., 2009, "The dynamics of Neptune Trojans - I. The inclined orbits", MNRAS 398, 1217-1227.

Zhou, L.Y., Dvorak, R. Sun, Y.S., 2011, "The dynamics of Neptune Trojans - II. Eccentric orbits and observed objects", MNRAS 410, 1849-1860.

EFFECTS OF ASTEROIDS ON THE ORBITAL MOTIONS OF TERRESTRIAL PLANETS

S. ALJBAAE, J. SOUCHAY
Observatoire de Paris - SYRTE
e-mail: safwan.aljbaae@obspm.fr

ABSTRACT. The perturbations from the largest ∼300 asteroids which were taken into account in the ephemerides DE403 (Standish et al. 1995), EPM98 (Pitjeva 2001), and INPOP08 (Fienga et al. 2009) are a major problem in the construction of theses ephemeris. Therefore, it looks important to evaluate of the individual effects of largest asteroids of the solar system on the orbits of the terrestrial planets (Mercury, Venus, Earth and Mars) because these effects could reach a few kilometers in several decades in the case of Mars. This is the purpose of this work. For that our methodology consists in several stages:

- ⋆ A numerical integration of the orbits of the planets at short and long time scales with and without the disturbing asteroid from which we want to know the effects.
- ⋆ A determination of the signal representing the effects, by simple substraction.
- ⋆ The analysis of the signal by the method of FFT (Fast Fourier Transform);
- ⋆ The adjustment of the signal by a set of sinusoids determined in the previous step.

We analyze in detail the influences of 43 among the largest asteroids on the six orbital elements a, e, i, Ω, $\tilde{\omega}$ and λ of Mercury, Venus, the EMB (Earth-Moon barycenter) and Mars. In addition we study their influence on two fundamental parameters: the distance and the orientation vector from the EMB to each of the terrestrial planets. This type of study is interesting in many fields, such as planetary ephemerides, as well as space navigation, to understand better the effects of each asteroid taken individually on the terrestrial planets. Note that this type of study is a continuation of previous ones (Williams, 1984; Mouret et al. 2009).

1. INTRODUCTION

The motion of a given planet around the Sun can be considered at first approximation as a Keplerian motion perturbed by the other planets and the small bodies of the solar system. Each of these perturbations must be treated either analytically or numerically, and can be measured as a change of the planet's osculating orbital elements ($a, e, i, \Omega, \varpi = \Omega + w$ and $L = \varpi + M$) determined from the perturbing function $\Re$, according to the Lagrange formula. The corresponding analytical developments of the perturbing function $\Re$ as a function of the orbital elements of the two bodies considered are particularly complex. On the contrary it is easy to use the numerical integration (Runge-Kutta of the 12th order), in computing the 9-body problem (without asteroids), then of the 10-body problem (with the given asteroid). Then we determine the effect of the asteroid considered on each orbital parameter of the planet studied by simple subtraction of the two signals. We focus our efforts in performing the frequency analysis of the data, using fast Fourier transform (FFT) to determine the leading frequencies. At last we carry out a nonlinear regression in which the differential data are modeled by the least-square method following an equation of the type: $F(t) = a_o + a_1 t + a_2 t^2 + \sum_{i=1}^{N} A_i \sin(f_i t) + B_i \cos(f_i t) + C_i t \sin(f_i t) + D_i t \cos(f_i t)$

We have also calculated the individual effects of the leading asteroids on the Earth-Moon distance, showing that they are quite larger than the level of precision of the LLR (Lunar Laser Ranging), and the individual influences of each asteroid on the distance from the EMB to each terestial planet and their orientation vector as seen from the EMB, which are very important parameters in space navigation and astrometry. Below, we present below an example of our results which consists in tables with the Fourier and Poisson components for the perturbations of the orbital elements of each terrestrial planet due to each asteroid, and the corresponding curves (the initial signal, the adjustment determined by our FFT analysis and the residuals). In each case (planet, astroid, orbital element) we find that our fit is satisfactory, since the post-fit residuals are significantly lower than the original signal.

2. RESULTS

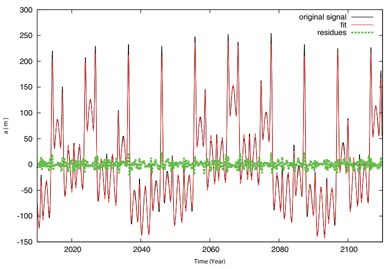

Figure 1: Influence of Ceres on Mars semi major axis (in red)

BIAS : 0.137559 $\times 10^{+2}$
LINEAR : -0.377681 $\times 10^{-2}$
T^2 : 0.333290 $\times 10^{-5}$

PERIOD (Day)	PERIOD (Year)	SIN $\times 10^0$	COS $\times 10^0$	$\times 10^0$	T SIN $\times 10^{-4}$	T COS $\times 10^{-4}$	$\times 10^{-3}$	amplitud $\times 10^1$	Asteroid
27960.94	76.55	2.644	2.158	3.413	0.291	- 3.054	0.432	0.563	1_ Ceres
16191.36	44.33	- 54.282	- 53.165	75.981	67.182	62.329	8.815	5.757	1_ Ceres
4886.42	13.38	- 1.227	9.966	10.042	2.164	- 13.844	1.958	0.691	1_ Ceres
3754.72	10.28	15.277	57.810	59.794	- 9.105	- 0.557	0.079	5.954	1_ Ceres
3047.01	8.34	- 16.680	- 0.495	16.687	7.171	0.221	0.031	1.542	1_ Ceres
1877.01	5.14	24.877	16.008	29.582	- 20.336	- 10.365	1.466	2.495	1_ Ceres
1251.31	3.43	8.691	- 0.233	8.694	- 10.205	0.628	0.089	0.671	1_ Ceres
1161.51	3.18	6.924	- 12.634	14.407	6.635	2.299	0.325	1.484	1_ Ceres
887.06	2.43	3.562	- 39.634	39.793	14.293	19.194	2.714	3.622	1_ Ceres
717.51	1.96	- 5.645	- 11.862	13.136	9.587	5.867	0.830	1.149	1_ Ceres
687.06	1.88	- 3.017	- 0.612	3.078	1.168	- 1.459	0.206	0.304	1_ Ceres
602.38	1.65	- 4.163	- 2.346	4.779	6.308	0.588	0.083	0.316	1_ Ceres
580.76	1.59	- 43.229	24.966	49.921	- 13.036	- 34.487	4.877	4.935	1_ Ceres
502.95	1.38	- 11.922	15.858	19.840	- 7.375	- 15.356	2.172	1.844	1_ Ceres
443.53	1.21	- 0.836	8.157	8.199	- 5.500	- 8.805	1.245	0.669	1_ Ceres
408.23	1.12	11.695	- 37.093	38.893	- 56.454	184.861	26.143	1.956	1_ Ceres
396.66	1.09	1.263	2.717	2.996	- 3.399	- 2.282	0.323	0.215	1_ Ceres
387.17	1.06	19.798	0.132	19.798	- 3.570	24.294	3.436	2.008	1_ Ceres
350.98	0.96	9.686	- 4.009	10.483	- 0.729	12.473	1.764	0.962	1_ Ceres
320.97	0.88	3.050	- 3.512	4.652	0.594	5.911	0.836	0.402	1_ Ceres
314.71	0.86	4.284	2.959	5.207	- 5.783	3.139	0.444	0.473	1_ Ceres
AMPLITUDE	Before= 409.294276				After= 57.641405				

Table 1: Influence of Ceres on Mars' semi major axis. Decomposition in Fourier and Poisson series

	asteroide	Δa [m]	$\Delta e \times a_{Mars}$	Δi ["] $\times 10^{-6}$	$\Delta\Omega$ ["] $\times 10^{-6}$	$\Delta\varpi$ ["] $\times 10^{-6}$	$\Delta\lambda$ ["] $\times 10^{-6}$
1	Ceres	385.99973	1018.25341	837.97915	37190.92552	16391.84563	19419.20264
2	Pallas	193.24460	413.14399	441.88830	12173.16362	3700.64524	18125.33458
3	Juno	29.79749	47.96241	35.77520	869.55154	430.40624	3198.86497
4	Vesta	404.55975	1636.34551	586.32212	8301.55218	14585.61346	64574.80064
6	Hebe	61.28165	319.84333	74.70642	1275.36428	2971.28411	4854.97680
7	Iris	63.86719	135.36684	10.91732	972.29642	1218.83655	1869.09102
8	Flora	22.17044	65.30294	27.75361	131.25152	362.96686	2024.49401
9	Metis	66.42932	218.60586	11.70010	876.90488	2098.95546	2956.91830
10	Hygiea	40.41443	244.13825	38.31212	1254.45965	2798.38321	2998.78852
11	Parthenope	7.79214	51.54678	7.89198	42.35986	505.50615	464.19872
13	Egeria	11.49283	23.51995	6.00169	1626.31059	361.99825	619.36587
14	Irene	12.16370	21.63927	13.84427	483.07604	271.56248	1050.89770
15	Eunomia	22.84708	71.25421	64.06555	1315.85795	470.31980	2029.37351
16	Psyche	6.99493	21.21170	9.41352	229.74675	161.67922	645.65713
17	Thetis	2.17981	7.78699	2.12143	5.41765	68.21111	219.80180
18	Melpomene	6.50754	13.38326	14.99738	180.46621	105.09344	119.62906
19	Fortuna	25.64017	117.05157	1.45028	241.74259	1004.49811	6000.85764
20	Massalia	43.15692	87.96440	0.52064	92.24314	785.42295	2598.67141
21	Lutetia	4.85095	36.77710	0.95140	13.72545	290.94054	488.24872
22	Kalliope	2.24835	8.23317	3.41134	335.01872	66.82759	193.40492
24	Themis	8.29007	35.55968	0.45115	40.77149	263.71602	2145.45218
28	Bellona	13.00662	27.20348	20.89924	241.43927	481.31076	666.97955
29	Amphitrite	14.75650	49.64686	21.15240	273.76387	582.36206	1189.20823
31	Euphrosyne	5.12241	22.00394	5.49823	240.62689	302.94482	359.52655
45	Eugenia	7.74860	23.94010	19.99905	233.45638	290.71744	267.90582
46	Hestia	17.96786	63.84851	10.11392	600.04503	585.88586	1087.43324
47	Aglaja	0.56693	1.52783	0.98627	13.06890	14.46588	3.34039
48	Doris	2.88513	13.51154	4.41259	192.22558	143.69507	293.43395
49	Pales	1.36624	6.58591	0.74581	33.42004	44.87418	46.59249
52	Europa	6.43481	26.91968	13.23229	69.31637	342.50298	1296.25556
65	Cybele	2.39575	7.49899	3.32215	76.06273	71.36757	325.08383
87	Sylvia	1.35168	3.38215	3.47084	213.27108	43.60731	26.55712
88	Thisbe	4.08374	12.87875	6.41856	289.82627	119.82741	613.18320
90	Antiope	0.42065	2.01203	0.04924	0.74104	18.39564	53.38957
107	Camilla	1.45676	3.18390	5.05085	147.73203	63.08296	17.97039
111	Ate	144.29700	397.32342	171.68672	4215.37702	5169.29002	31583.25731
121	Hermione	0.65030	1.99023	0.94898	52.20717	20.46184	138.98339
130	Elektra	2.82965	10.37911	10.78122	110.47445	115.07394	132.25069
165	Loreley	6.50281	27.76875	28.27952	465.04322	345.34894	231.09589
189	Phthia	0.06564	0.31375	0.02352	2.13209	3.13691	8.40850
243	Ida	0.02475	0.03559	0.00574	0.31220	0.46578	2.44193
253	Mathilde	0.11630	0.19786	0.12028	4.48961	2.69194	8.82521
283	Emma	0.35806	1.11882	1.04708	16.94125	9.49715	9.82103

Table 2: Influence of each asteroid on each Mars orbital parameter: peak-to-peak amplitude for a 100 yr time interval

Mercury asteroide	EMB-Mercury $\times \frac{\Delta M}{M}$	Venus asteroide	EMB-Venus $\times \frac{\Delta M}{M}$	Mars asteroide	EMB-Mars $\times \frac{\Delta M}{M}$
46_ Hestia	694.01010	46_ Hestia	1164.60600	111_ Ate	12258.22000
111_ Ate	390.65110	111_ Ate	389.29540	46_ Hestia	2484.66100
3_ Juno	77.53379	3_ Juno	141.34980	19_ Fortuna	1485.34900
165_ Loreley	61.31650	165_ Loreley	84.56231	24_ Themis	1291.46300
88_ Thisbe	35.62771	18_ Melpomene	70.40396	3_ Juno	1221.21800
6_ Hebe	32.65011	88_ Thisbe	65.21992	6_ Hebe	1109.21300
18_ Melpomene	25.56851	28_ Bellona	49.60696	9_ Metis	1058.72800
52_ Europa	23.19845	6_ Hebe	47.85985	29_ Amphitrite	676.18000
19_ Fortuna	19.74131	52_ Europa	28.09674	52_ Europa	529.57310
28_ Bellona	18.67213	2_ Pallas	26.95967	88_ Thisbe	374.38660
9_ Metis	12.18488	13_ Egeria	26.70767	20_ Massalia	349.37370
65_ Cybele	11.15585	45_ Eugenia	26.37660	8_ Flora	342.20010
2_ Pallas	10.79248	29_ Amphitrite	26.10475	165_ Loreley	311.62700
20_ Massalia	10.47764	20_ Massalia	23.69739	14_ Irene	263.50100
48_ Doris	10.30252	7_ Iris	23.64386	28_ Bellona	261.16760
47_ Aglaja	9.39728	10_ Hygiea	23.34137	7_ Iris	236.89170
24_ Themis	8.70575	24_ Themis	21.92538	4_ Vesta	226.52210
16_ Psyche	8.32899	65_ Cybele	16.96635	2_ Pallas	189.73690
29_ Amphitrite	8.32330	14_ Irene	14.22438	48_ Doris	189.62930
7_ Iris	7.55930	4_ Vesta	13.51992	13_ Egeria	185.14450
14_ Irene	7.49308	19_ Fortuna	12.13824	10_ Hygiea	168.26760
10_ Hygiea	7.24384	9_ Metis	10.88285	15_ Eunomia	165.01150
31_ Euphrosyne	5.37681	1_ Ceres	9.52207	16_ Psyche	152.56800
15_ Eunomia	4.74114	16_ Psyche	9.44188	65_ Cybele	144.84320
4_ Vesta	4.70565	49_ Pales	9.38891	45_ Eugenia	129.93130
13_ Egeria	3.79465	48_ Doris	6.92858	31_ Euphrosyne	86.37314
8_ Flora	3.65469	130_ Elektra	4.64705	18_ Melpomene	66.79982
45_ Eugenia	2.95697	8_ Flora	4.34414	21_ Lutetia	42.14033
49_ Pales	2.60837	31_ Euphrosyne	3.12844	1_ Ceres	39.82367
189_ Phthia	2.25191	22_ Kalliope	2.01498	17_ Thetis	32.21822
130_ Elektra	1.70296	11_ Parthenope	1.97254	11_ Parthenope	19.60792
243_ Ida	1.47892	107_ Camilla	1.92639	130_ Elektra	16.72673
121_ Hermione	1.36178	15_ Eunomia	1.87222	121_ Hermione	14.81428
11_ Parthenope	0.98616	47_ Aglaja	1.65449	49_ Pales	10.80631
253_ Mathilde	0.94971	189_ Phthia	1.37761	22_ Kalliope	9.68023
21_ Lutetia	0.90056	121_ Hermione	0.83037	189_ Phthia	7.42760
22_ Kalliope	0.56491	21_ Lutetia	0.77383	47_ Aglaja	4.95920
17_ Thetis	0.55424	17_ Thetis	0.55975	107_ Camilla	2.31888
283_ Emma	0.52483	283_ Emma	0.52277	90_ Antiope	1.03507
107_ Camilla	0.47895	243_ Ida	0.25822	253_ Mathilde	0.87222
90_ Antiope	0.28519	87_ Sylvia	0.20355	87_ Sylvia	0.50908
1_ Ceres	0.14139	253_ Mathilde	0.18701	283_ Emma	0.14407
87_ Sylvia	0.09770	90_ Antiope	0.10771	243_ Ida	0.07351

Table 3: Uncertainty of the EMB-Mercury, EMB-Venus and EMB-Mars distance due to the asteroid masses inaccuracy

3. REFERENCES

J.G. Williams, 1984, Determining Asteroid Masses from Perturbations on Mars, ICARUS, 57, 1-13

E.M. Standish, Newhall, Williams, J.G., Folkner, W.M., 1995, JPL Planetary and lunar ephemerides, DE403/LE403. Interoffice Memorandum, IOM 314.10-127

E.V. Pitjeva, 2001, Modern numerical ephemerides of planets and the importance of ranging observations for their creation, Celestial mechanics and dynamical astronomy, 80, 249271

A. Fienga, Laskar, J., Morley, T., Manche, H., Kuchynka, P., Le Poncin-Lafitte, C., Budnik, F., Gastineau, M., and Somenzi, L., 2009, INPOP08, a 4-D planetary ephemeris: From asteroid and time-scale computations to ESA Mars Express and Venus Express contributions, A&A, 507, 1675-1686

S. Mouret, Simon, J.L., Mignard, F., and Hestroffer, D., 2009, The list of asteroids perturbing the Mars orbit to be seen during future space missions, A&A, 508, 479-489

THE INVARIABLE PLANE OF THE SOLAR SYSTEM: A NATURAL REFERENCE PLANE IN THE STUDY OF THE DYNAMICS OF SOLAR SYSTEM BODIES

D. SOUAMI[1,2], J. SOUCHAY[2]
[1] Université Pierre et Marie Curie
75252 Paris cedex 5, France
[2] SYRTE : UMR 8630 - Observatoire de Paris, CNRS UPMC
61 Avenue de lObservatoire, 75014 Paris, France
e-mail: damya.souami@obspm.fr, jean.souchay@obspm.fr

ABSTRACT. In this work we determine the orientation of the invariable plane of the solar system. The idea of using the invariable plane as a reference frame in the study of the dynamics of solar system bodies goes back at least to Laplace.
Using numerical planetary ephemerides : INPOP10a, DE405, DE406 over their available time span we have computed the orientation of the invariable plane for different epochs considering a time step of one day. This leads us to find a good agreement between the different values obtained, and can be considered as a good test of the ephemerides. The relativistic effects up to the first post-newtonian order were included through an effective mass, the so-called Tolmann-mass. Our results are considered as a confirmation and an improvement of the results obtained in Burkhardt (1982).

1. INTRODUCTION

The aim of this paper is to investigate the characteristics of the invariable plane and to define its orientation with respect to the ecliptic and the equator. The notion of the invariable plane was introduced by Pierre Simon Lalplace in his "Oeuvres Complètes". He introduced what seemed to be the natural reference plane when studying the motion of planets, asteroids, comets ...

2. DEFINITION OF THE INVARIABLE PLANE

Let us consider the solar system as an isolated system so that its total angular momentum vector is constant with respect to both spatial and time coordinates. The invariable plane of the solar system is defined as the plane perpendicular to its total angular momentum and passing through its barycentre. Being fixed, it provides a permanent natural reference plane, whereas the ecliptic alters with time. Thus the invariable plane should be considered as the *natural reference plane* when studying the dynamics of solar system bodies.

Let us consider the following 10-body system : the Sun, Pluto and all the eight planets, the Earth being replaced by the Earth-Moon Barycentre (EMB). Disregarding the rotation of all the ten bodies constituting the system; the total orbital angular momentum of a the system is:

$$\mathbf{L_{tot}} = \sum_{j=1}^{N} m_j \mathbf{r_j} \otimes \dot{\mathbf{r}}_\mathbf{j} \tag{1}$$

m_j, $\mathbf{r_j}$, $\dot{\mathbf{r}}_\mathbf{j}$ are respcetively the mass, the barycentric position vector and barycentric velocity vector of the j^{th} body.

The relativistic effects being taken into account up to the first order in the post-Newtonian approximation, in Equation (1) m_j is replaced by an effective mass (the so-called Tolmann-Mass) m_j^*, given by Equation (2) (see Standish & al. 1976)

$$m_j^* = m_j . \Big[1 + \frac{\dot{\mathbf{r}}_\mathbf{j}^\mathbf{2}}{2c^2} - \frac{1}{2c^2} \Big(\sum_{k \neq j} \frac{G m_k}{|\mathbf{r_k} - \mathbf{r_j}|} \Big) \Big] \tag{2}$$

The components of the angular momentum ($\mathbf{L}$) are given as a function of the inclination (i) and the node (Ω) of the invariable plane.

$$\begin{aligned} L_1 &= \mathbf{L} \cdot \sin\Omega \cdot \sin i \\ L_2 &= -\mathbf{L} \cdot \cos\Omega \cdot \sin i \\ L_3 &= \mathbf{L} \cdot \cos i \end{aligned} \tag{3}$$

The primary constants for both the DE and the INPOP10a ephemeris are respectively given in (Standish, 1998) and (Fienga & al. 2010).

Numerical ephemeris	Times-span (JD)	Time-span	Number of days
INPOP10a	2076569.0 – 2826520.0	03 May 973 - 25 Aug 3026	749951
DE405	2305424.5 – 2524624.5	09 Dec 1599 to 31 Jan 2200	219200
DE406	625360.50 – 2816848.5	23 Feb -3001 to March 2nd, 3000	2191488

Table 1: Numerical ephemeris time span.

3. RESULTS

Using Equations (1) – (3), we have computed for each ephemeris the orientation of the invariable plane with respect to both the ICRS and the ecliptic-equinox of J2000.

	DE405 / DE406		INPOP10a		Burkhardt, 1982	
	Ecliptic	Equator	Ecliptic	Equator	Ecliptic	Equator
i at J2000	$1°34'43''.33124$	$23°0'31''.98231$	$1°34'43''.31903$	$23°0'31''.97914$	$1°35'13''.86$	$23°0'22''.11$
Ω at J2000	$107°34'56''.17914$	$3°51'9''.45913$	$107°34'56''.47403$	$3°51'9''.42191$	$107°36'30''.8$	$3°52'23''.7$

Table 2: Orientation of the invariable plane at the epoch J2000.

Ephemeris	DE405		DE406		INPOP10a	
	Ecliptic	Equator	Ecliptic	Equator	Ecliptic	Equator
minimal i	$1°34'43''.33115$	$23°0'31''.98185$	$1°34'43''.33064$	$23°0'31''.97992$	$1°34'43''.31883$	$23°0'31''.97657$
maximal i	$1°34'43''.33129$	$23°0'31''.98321$	$1°34'43''.33148$	$23°0'31''.99351$	$1°34'43''.32005$	$23°0'31''.98120$
minimal Ω	$107°34'56''.14530$	$3°51'9''.45884$	$107°34'55''.76351$	$3°51'9''.45769$	$107°34'56''.38804$	$3°51'9''.41993$
maximal Ω	$107°34'56''.19574$	$3°51'9''.45968$	$107°34'56''.26643$	$3°51'9''.46523$	$107°34'56''.57119$	$3°51'9''.42587$

Table 3: Orientation of the invariable plane over the ephemeris time span (See Table 1).

4. CONCLUSIONS

We have determined the orientation of the invariable plane with respect to both ICRS and equinox-ecliptic J2000. The small differences observed in the computed values are due to the use of numerical ephemerides with different primary parameters. Thus we are conditioned by the precision of the ephemerides. Nevertheless we observe a good agreement between the DE405 and INPOP10a ephemeris. We think that such a determination of the invariable plane is of fundamental interest in the topic of solar system studies. These results will be refined by taking into account the effects of the largest asteroids.

5. REFERENCES

Burkhardt, G. 1982. On the invariable plane of the solar system,vol. 106, pages 133-136.

A. Fienga, H. Manche, P. Kuchynka, J. Laskar, and M. Gastineau. November 2010. Planetary and Lunar ephemerides, INPOP10A. ArXiv e-prints.

De Laplace, P. S.Oeuvres compètes de Laplace, vol. 11, pages 548 - 553.

E. M. Standish, Jr., M. S. W. Keesey, and X. X. Newhall. February 1976 JPL Development Ephemeris number 96.

Standish, E M. 1998. JPL planetary and lunar ephemerides, DE405/LE405.

AVERAGING IN THE N-BODY PROBLEM WITH THE LIE-SERIES METHOD IN STANDARD OSCULATING ELEMENTS

I. TUPIKOVA
Lohrmann Observatory, Institute for Planetary Geodesy
Mommsenstr. 13, 01062 Dresden, Germany

ABSTRACT. A new method allowing to average the equations of motion in the N-body problem in a set of standard osculating elements with the usage of all the standard expansions of perturbing functions is proposed. The main idea is to double the number of variables and to conduct an averaging in a corresponding extended phase space. The additional variables disappear from the final results and transformation formulae. Once obtained, the averaged equations of motion can be applied in semi-analytical schemes for numerical integration as well as for further dynamical studies.

Only exceptional cases of celestial mechanical problems allow a construction of a precise analytical solution. As a rule, these are the model problems which allow to get an idea about the global behavior of a solution but are not precise enough to get the real positions of celestial objects. As an alternative, a series of methods to obtain an analytical solution in an approximate way has been elaborated (Le Verrier, Gauss, Lindstedt, Hamilton, Jacobi, Poincaré, Hori, Deprit and others) and successfully applied for solar system ephemerides, satellite and asteroid theories. Due to the presence of numerous resonances, not even a formal convergence can be guaranteed in most cases. The semi-analytical approach can then be applied based on the idea going back to Poincaré's statement that the short-periodic perturbations do not play a significant role in the long-term dynamics. The main problem of going beyond the first order approximation is not only the immense size of analytical calculations but also due to the fact that the differential equations of the N-body problem do not allow a canonical representation in standard osculating elements of the orbits. The two known possibilities to deal with a single Hamiltonian are:
1. The Jacobi Hamiltonian formalism (Jacobi, 1842), where the position and velocity of a planet m_1 are given in a reference frame with origin in m_0; position and velocity of m_2 are given in a reference frame with origin in the barycenter of m_1 and m_0, etc. Due to this hierarchical structure, no general expression for the perturbing function exists.
2. The Poincaré reduction (Laskar & Robutel, 1995) where the angular variables and the corresponding momenta are defined in two different reference systems. This approach necessarily introduces non-osculating elements in the expansions. Both of these methods require the introduction of generalized orbital elements instead of standard osculating elements (Beaugé et al., 2007). We propose here a way to use the advantages of a canonical formalism in standard osculating elements. To conduct the transformation, the Lie-series method has been chosen. This method gives the solution and the transformation formulae in explicit form and (in contrast to Poincaré's method) avoids the appearance of mixed terms.

In fact, every differential equation can be written in canonical form with the help of some additional variables. To give an idea, let us consider the equations of motion of two bodies a and b around a central body in some system of osculating canonical elements

$$\frac{\partial x_i^a}{\partial t} = \frac{\partial R^a}{\partial x_{i+3}^a}, \quad \frac{\partial x_{i+3}^a}{\partial t} = -\frac{\partial R^a}{\partial x_i^a}; \quad \frac{\partial x_i^b}{\partial t} = \frac{\partial R^b}{\partial x_{i+3}^b}, \quad \frac{\partial x_{i+3}^b}{\partial t} = -\frac{\partial R^b}{\partial x_i^b}. \tag{1}$$

These equations can be written as one canonical system after introducing additional variables $\mathbf{Y} = (\mathbf{y}^a, \mathbf{y}^b)$ conjugate to $\mathbf{X} = (\mathbf{x}^a, \mathbf{x}^b)$ in the $2 * 2 * 6$ dimensional phase space as

$$\frac{\partial \mathbf{X}}{\partial t} = \frac{\partial F}{\partial \mathbf{Y}}, \quad \frac{\partial \mathbf{Y}}{\partial t} = -\frac{\partial F}{\partial \mathbf{X}}, \tag{2}$$

with the Hamiltonian

$$F = \sum_{i=1}^{3} \left(y_i^a \frac{\partial}{\partial x_{i+3}^a} - y_{i+3}^a \frac{\partial}{\partial x_i^a} \right) R^a + \sum_{i=1}^{3} \left(y_i^b \frac{\partial}{\partial x_{i+3}^b} - y_{i+3}^b \frac{\partial}{\partial x_i^b} \right) R^b .$$

For the extended canonical system in Equation (2) we can apply a conservative Lie-series transformation to obtain a new Hamiltonian averaged according to a chosen scheme up to the desired order in the small parameter of the problem (mass of the perturbing body relative to the mass of the central body). With a special choice of generating function S, the resulting formulae do not contain the additional variables and represent in fact the averaged system in Equation (1) in standard mean osculating elements. The averaged equations of motion cannot principally built a canonical system but have a compact quasi-canonical form expressed through the Poisson brackets. For the case of three fully interactive bodies up to second order in the small parameter they can be written in the following form (the upper index (1) marks the new elements): for body a

$$\frac{\partial x_i^{(1),a}}{\partial t} = \frac{\partial < R_0^a + R_1^a + R_2^a >_{\mathrm{s}}}{\partial x_{i+3}^{(1),a}} + \frac{1}{2} < \left[\left\{ \frac{\partial (R_1^a + < R_1^a >_{\mathrm{s}})}{\partial x_{i+3}^{(1),a}}, S_1^b \right\}^b + \left\{ R_1^b + < R_1^b >_{\mathrm{s}}, \frac{\partial S_1^a}{\partial x_{i+3}^{(1),a}} \right\}^b \right] >_{\mathrm{s}},$$

$$\frac{\partial x_{i+3}^{(1),a}}{\partial t} = \frac{\partial < R_0^a + R_1^a + R_2^a >_{\mathrm{s}}}{\partial x_i^{(1),a}} - \frac{1}{2} < \left[\left\{ \frac{\partial (R_1^a + < R_1^a >_{\mathrm{s}})}{\partial x_i^{(1),a}}, S_1^b \right\}^b + \left\{ R_1^b + < R_1^b >_{\mathrm{s}}, \frac{\partial S_1^a}{\partial x_i^{(1),b}} \right\}^b \right] >_{\mathrm{s}}$$

and for body b

$$\frac{\partial x_i^{(1),b}}{\partial t} = \frac{\partial < R_0^b + R_1^b + R_2^b >_{\mathrm{s}}}{\partial x_{i+3}^{(1),b}} + \frac{1}{2} < \left[\left\{ \frac{\partial (R_1^b + < R_1^b >_{\mathrm{s}})}{\partial x_{i+3}^{(1),b}}, S_1^a \right\}^a + \left\{ R_1^a + < R_1^a >_{\mathrm{s}}, \frac{\partial S_1^b}{\partial x_{i+3}^{(1),b}} \right\}^a \right] >_{\mathrm{s}}$$

$$\frac{\partial x_{i+3}^{(1),b}}{\partial t} = \frac{\partial < R_0^b + R_1^b + R_2^b >_{\mathrm{s}}}{\partial x_i^{(1),b}} - \frac{1}{2} < \left[\left\{ \frac{\partial (R_1^b + < R_1^b >_{\mathrm{s}})}{\partial x_i^{(1),b}}, S_1^a \right\}^a + \left\{ R_1^a + < R_1^a >_{\mathrm{s}}, \frac{\partial S_1^b}{\partial x_i^{(1),b}} \right\}^a \right] >_{\mathrm{s}} .$$

Here $< f_i >_{\mathrm{s}}$ stands for the secular part of f which is of order i in the small parameter and the indices at the Poisson brackets denotes in which elements they should be calculated. The terms on the right side are principally new: they visualize in an unexpectedly simple form the fact that the osculating elements do not build a canonical set in the N-body problem. The algorithm can be applied to an arbitrary number of interacting bodies and extended to further approximations. In case of mean-motion resonances the resonant terms should be preserved in the averaged equations of motion for further numerical integration or qualitative dynamical studies.

The simplified form of the algorithm has already been applied to the problem of asteroid motion in the gravitational field of fully interacting perturbing bodies (Tupikova, 2009). It was shown that in the case when only the equations for a massless body have been averaged, they still keep the canonical form at least to order three in the small parameter. Our method revealed also some important new terms that were missed in those theories where not the whole system of differential equations of motion of all the bodies involved has been treated simultaneously in the same algorithm, but an already simplified model for the system of perturbing bodies has been inserted into the equations of asteroid motion.

REFERENCES

Jacobi C. G. J., 1842, “Vorlesungen über Dynamik”, Reimer Verlag, Berlin.

Laskar J., Robutel, P., 1995, “Stability of the planetary three-body problem. I. Expansion of the planetary Hamiltonian”, Celest. Mech. Dyn. Astr. , 62, pp. 193–217.

Beaugé C., Ferraz-Mello S., Mitchenko T. A. , 2007, “Planetary masses and orbital parameter from radial velocity measurements”, AJ , 131, pp. 2299–2313.

Tupikova, I., 2009,“About averaging procedures in the problem of asteroid motion”, Celest. Mech. Dyn. Astr. , 104, 1–2, pp. 129–144.

Session 5:

Space observations and dedicated missions for geodesy and astronomy

Observations spatiales et missions dédiées la géodésie et l'astronomie

GOCE: ITS PRINCIPLES AND SCIENCE

R. RUMMEL, T. GRUBER, W. YI, A. ALBERTELLA
Institute of Astronomical and Physical Geodesy (IAPG)
Technische Universität München, 80290 Munich, Germany
e-mail: rummel@bv.tum.de

ABSTRACT. GOCE is the first satellite mission with a gravity gradiometer. It is very successful in delivering the global geoid and gravity anomaly field with rather high spatial resolution. The gradiometer measurements are based on the principle of differential accelerometry. It is the centre piece of a sensor system comprising in addition GPS, star tracking, angular control by magnetic torquing, drag free control in flight direction by ion thrusting and calibration via shaking with cold gas thrusters. Gravity field sensitivity is enhanced by the satellite's extremely low orbit altitude of only 265 km. GOCE science and application is primarily about "dynamic topography". In geophysics dynamic topography is referred to as that part of surface deformation which is not in isostatic balance but supported by vertical stresses at the base of the lithosphere. Gravity and geoid anomalies reflect the gravitational effect of dynamic topography. In oceanography dynamic topography is the deviation of the actual mean ocean surface, as measured by satellite altimetry, from the geoid which is the hypothetical ocean surface at rest. The uses of mean dynamic ocean topography range from ocean circulation studies via mass and heat transport in the oceans to the unification of height systems and levelling by GPS. Full exploitation of GOCE requires its combination with GRACE and with satellite laser ranging and GPS. The considered measurements and techniques must all refer consistently to the same set of geodetic standards such as those defined by the IERS.

1. INTRODUCTION

GOCE (Gravity and steady-state Ocean Circulation Explorer), the first mission of ESA's living planet programme, has been launched on March 17, 2009 (Journal of Geodesy, 2011). Its mission objectives are the determination of the geoid with an accuracy of 1-2 cm and gravity anomalies with 1 mGal, both with a spatial resolution of 100 km half-wavelength, which corresponds to a spherical harmonic expansion up to degree and order (d/o) 200. GOCE is the first satellite equipped with a gravity gradiometer instrument. Here we will summarize the principles of the gradiometer and of the entire sensor system. This description is followed by a short report about GOCE's performance. We will then talk about GOCE and GRACE and about IERS-standards. Finally a short account will be given of the state-of-the-art of science and application and some conclusions will be drawn.

2. PRINCIPLES

The core instrument of GOCE is a three axis gravity gradiometer, consisting of six accelerometers with very high sensitivity. The measurement principle is differential accelerometry. The measurements are taken in the gradiometer instrument reference frame with x pointing approximately in flight direction, z pointing towards the Earth and y completing a right-handed coordinate triad. Each accelerometer measures the sum of gravitational gradients, centrifugal accelerations (containing squares of angular velocities) and Euler angular accelerations. The contribution due to angular accelerations is isolated by separating the 3×3 matrix of acceleration differences into its symmetric and skew-symmetric part. Integration over time of the angular accelerations, and combination with the angular measurements of the star trackers on board, yields the angular velocities about the axes of the instrument. The GOCE gradiometer measures the gradient components V_{xx}, V_{yy}, V_{zz}, and V_{xz} with high precision and the components V_{xy} and V_{yz} with much lower precision. The gradiometer instrument is made to measure the medium to short spatial scales of the gravity field very well. At long wavelengths the accelerometers of the gradiometer instrument exhibit rather complex coloured noise behaviour. This part is therefore derived from the orbit as determined by high-low tracking using GPS. The sensor system comprises star

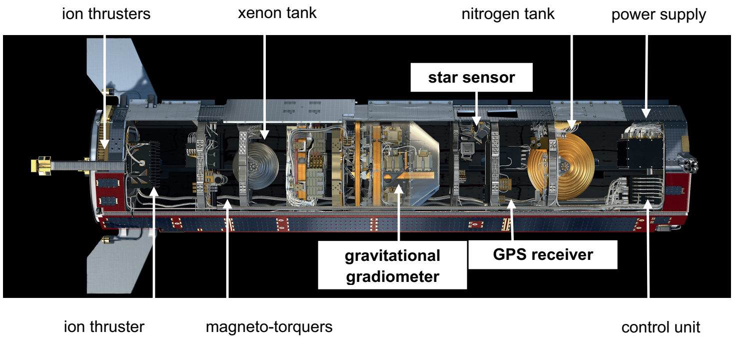

Figure 1: Gravitational field sensor system of GOCE, (source: ESA).

tracking, angular control by magnetic torquers and drag free control in flight direction, cf. Figure 1. The star tracking provides the orientation of the spacecraft with a precision of a few arc seconds relative to the celestial reference frame. In addition, it is combined with accelerometer data for angular rate reconstruction. The common mode accelerations along the three axes of the accelerometers serve as control signal for the drag free control in flight direction. The latter allows maintaining an orbit altitude as low as 265 km. The extremely low orbit altitude was chosen in order to enhance the gradiometric signal as well as the gravity related orbit perturbations. The mean orbit is almost circular and sun-synchronous with an inclination of 96.5°. This implies that the two polar areas with an opening angle of 6.5° are left without data. For more details it is referred to Rummel & Gruber (2010), Rummel et al., (2011) or to the GOCE special issue of Journal of Geodesy (vol. 85, no.11, 2011).

3. PERFORMANCE

On November 1, 2009 the first measurement cycle started. Since then the mission is in continuous operation with so far three major interruptions, from February 12 to March 2 and from July 2 to September 25, 2010 due to problems with the processor units and from January 1 to January 21, 2011 because of a software problem of the GPS receiver. Data flow and level-1 and level-2 processing are nominal. Currently, i.e. as of spring 2012, 1.5 years of mission data have been processed. All instruments work well. Only the noise level of the measured gradients in z-direction is somewhat higher than specified. More specifically, while the noise level of the components V_{xx} and V_{yy} is close to the predefined requirement, it is almost twice as high for V_{zz} and V_{xz} for reasons still not understood. A very powerful test of the gradiometer performance is the Laplace condition, i.e. the condition that the sum of the three diagonal gradient components V_{xx}, V_{yy} and V_{zz} has to be zero, in theory. In reality it gives the combined noise level of these three components. Power spectral densities of the gradiometer performance based on the Laplace condition show that the noise behaviour is essentially white in the measurement band from $5 \cdot 10^{-3}$ Hz to 0.1 Hz. The noise level is increasing proportionally to 1/frequency below the measurement band. Currently a first re-processing of all level-1B data is underway, with improved processing of the orientation quaternions from star tracking and of the angular rate reconstruction (Stummer et al, 2011). This will primarily improve the determination of the long spatial scales of the gravity field.

One measurement cycle takes about 61 days, usually followed by a calibration. The calibration signal is generated by a set of cold gas thrusters. So far, the High level Processing Facility (HPF), responsible for the level-2 processing (orbits and gravity field models), has produced three releases of GOCE gravity models (two months, six months and 12 months) together with their variance-covariance information. Three alternative processing concepts have been pursued; compare (Pail et al., 2011). All models have maximum d/o between 210 and 250. They are listed in Table 1. Also two combined GRACE/GOCE models GOCO01s and GOCE02s have been published (Pail et al., 2010).

4. GOCE, GRACE AND IERS-STANDARDS

It should be understood that intrinsically GRACE models are superior to GOCE models at low degrees and orders, say below d/o 100, at d/o between 100 and 140 the fields are of comparable quality

Model	Data	D/O	Characteristics
DIR1	2 Months	240	Direct Approach: Prior model (combined) plus GOCE orbits & gradiometry
DIR2	6 Months	240	Direct Approach: Prior model (GRACE-only) plus GOCE orbits & gradiometry
DIR3	1 Year	240	Direct Approach: Prior model (GRACE-only normals) plus GOCE gradiometry
TIM1	2 Months	224	Time-Wise Approach: Pure GOCE (kin. orbits & gradiometry)
TIM2	6 Months	250	Time-Wise Approach: Pure GOCE (kin. orbits & gradiometry)
TIM3	1 Year	250	Time-Wise Approach: Pure GOCE (kin. orbits & gradiometry)
SPW1	2 Months	210	Space-Wise Approach: GRACE low d/o plus GOCE gradiometry
SPW2	6 Months	240	Space-Wise Approach: Pure GOCE (kin. orbits & gradiometry)

Table 1: GOCE gravity models produced by HPF and released by ESA (Nov. 2011). D/O is the highest degree of the series of spherical harmonic coefficients (source: Th. Gruber)

and above d/o 140 GOCE is more accurate than GRACE. This can also be seen from a contribution analysis as shown in Figure 2. The great sensitivity of GRACE at lower degrees and orders is the reason for its capability to measure the small temporal gravity variations due to mass changes of ice, ocean and continental hydrology; it will be rather difficult to recover temporal variations from GOCE data. The cumulative geoid error of release-3 models is about 4-5 cm. It will go down to 2 to 3 cm by the end of 2012, the extended mission period.

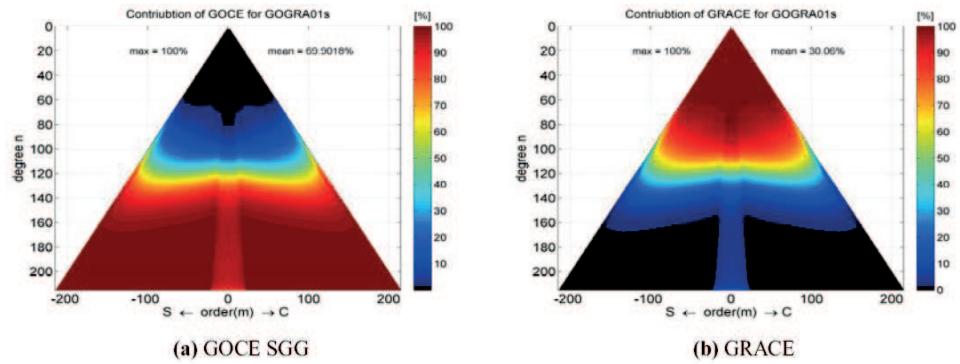

Figure 2: Percentage of the contribution of (a) GOCE (70%) being superior to GRACE from d/o 120 upwards and (b) GRACE (30%) dominating up to d/o 120 and) in a combined field. The relative weights are derived from variance component estimation, (source: W. Yi, 2012).

However, also gravity field models based solely on GRACE exhibit some weakness at very low degree and orders. Therefore it is advisable to combine GRACE measurements with time series of satellite laser tracking to satellites, such as LAGEOS 1 and 2, Stella, Starlette etc. Thus, the issue of the consistent use of standards and of compatibility of the included techniques has to be addressed. A geoid accuracy of 1 to 2 cm corresponds to about 1 ppb relative to the Earth's radius; a gravity accuracy of 1 mGal corresponds to 1 ppm w.r.t. gravity itself. Thus, GOCE, GRACE and satellite laser tracking and GPS have to be consistent at this level of relative precision. Furthermore, the combined use of geometric information (positions of individual points or the shape of the ocean's surface) and gravity/geoid information will require a global consistency of these two independent "worlds" at the level of a few ppb. GOCE gravity field analysis is based on GOCE standards, Gruber et al. (2009). They are almost but not exactly identical to the IERS-standards 2003, McCarthy & Petit (2004). The same is true for GRACE. Thus, combination of GOCE, GRACE, satellite laser ranging and GPS require adaptation in order to achieve perfect agreement of these data in terms of the applied fundamental constants and reductions, tide models and models of geophysical fluids. Combination of geometry with gravity and geoid goes one step further. It requires, in addition, full consistency in terms of permanent tides, GIA models, loading models etc. Also the question of how to deal with the three "degree equal one"-terms is of concern, as discussed e.g. in Wahr et al. (1998). This is a field that still needs intensive consideration, also before the background of the objectives of the Global Geodetic Observing System, compare Plag & Pearlman (2009).

5. SCIENCE AND APPLICATIONS

The main fields of GOCE application are geodesy, solid Earth physics and oceanography. The common denominator of the science objectives of GOCE is "dynamic topography".

Discovering the connection between processes observed on the Earth or in space and their internal dynamics is an essential goal in **solid Earth physics**. In good approximation the Earth is in isostatic balance. Dynamic topography in geophysics means the deformation of the surface of the Earth, not in isostatic balance but supported by the vertical stresses at the base of the lithosphere that are generated by flow in the mantle below. Comparison of the geoid or gravity anomaly signal as measured by GOCE with an Earth model in hydrostatic equilibrium predominantly reflects dynamic topography. The geoid or gravity anomaly signal generated by topographic masses in isostatic balance is generally much smaller. Research activities in solid Earth physics related to GOCE are just starting now.

At the end of 2012 approximately 16 measurement cycles will be completed, leading to an improvement by a factor of four compared with the first two-month models. EGM2008 combines ITG-GRACE03s (up to d/o 120) with gravity anomalies based satellite altimetry in all ocean areas and terrestrial Δg on land. Comparison with the GOCE models shows significant differences in those areas of the Earth where our expectation is, that in EGM2008 terrestrial gravity anomalies are either missing or sparse or inaccurate. These are Antarctica and parts of South America, Africa, Himalaya and SE-Asia. While the RMS-differences at d/o 180 between the GOCE release-3 fields and EGM2008 in terms of geoid height are between 3.5 cm and 5 cm in regions with good terrestrial gravity data (Australia, Europe and USA) they vary between 25 cm and 35 cm in South America, Africa and Himalaya and are about 11 cm in Antarctica (no terrestrial data are included there in EGM2008).

In **oceanography**, dynamic topography is defined as the deviation of the actual mean ocean surface from the geoid. Here the GOCE geoid serves as equilibrium surface, an idealization of the world's oceans at complete rest. The actual ocean surface is measured from space by radar altimetry. It is the first time that dynamic ocean topography is available from space with great detail and precision and without the use of oceanographic in-situ data.

For ocean studies the point of departure is geodetic dynamic ocean topography (DOT) with high spatial resolution, as derived from satellite altimetry and a GOCE geoid model. Taking the difference between the altimetric mean sea surface height h and geoid height N from GOCE implies the recovery of a rather small quantity, i.e. of dynamic ocean topography, from two much larger quantities. Furthermore, each the two quantities is delivered by its own satellite platform and measurement system. Also, their mathematical representation is fundamentally different: while altimetric heights are sampled along the ground tracks of the satellite as a densely spaced series of individual measurements, geoid heights are computed from a spherical harmonic representation of a gravity model which is derived by least squares adjustment from a large global data set of gradiometer measurements. Thus, consistency between altimetric sea surface heights h and geoid heights N is of utmost importance. A precondition is that h and N refer to the same coordinate system, reference ellipsoid and permanent tide system, see e.g. Hughes & Bingham (2008), Bingham et al. (2008). This is straightforward, in principle. However, it is less trivial to get the two quantities also spectrally consistent due to their completely different mathematical representation, as explained above. Various strategies exist, see e.g. Bingham et al. (2008), Albertella & Rummel (2009), Bosch & Savcenko (2010). In particular in coastal zones spectral consistency is difficult to achieve. Various models of altimetric mean sea surfaces exist, e.g. Hernandez & Schaeffer (2000), Andersen & Knudsen (2009) or Dettmering & Bosch (2010). They may differ in terms of the used time period, starting epoch, orbits, processing strategy, reduction models, treatment of sea ice and coastal zones, repeat cycles and selection of altimetric satellites. Criteria are needed as a guideline for sensible intercomparison, validation experiments with in-situ data, and for various oceanographic applications.

In Figure 3 a DOT is shown for the area of the Antarctic Circumpolar Current (ACC) with three spatial resolutions, up to d/o 60, 120, and 180. The DOT is thereby filtered with a Gauss-filter. There is the possibility to compare geodetic DOT-models with available ocean data and oceanic DOT models

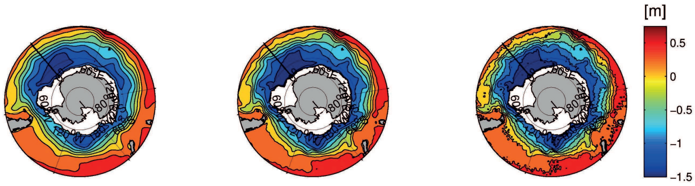

Figure 3: Mean dynamic ocean topography (DOT) of the Antarctic Circumpolar Current from a multi-year and multi-mission altimetric mean sea surface and the geoid computed using a GOCE-only gravity model based on six months of data up to d/o=60, 120 and 180 applying a Gauss-filter (from left to right). Units are meters.

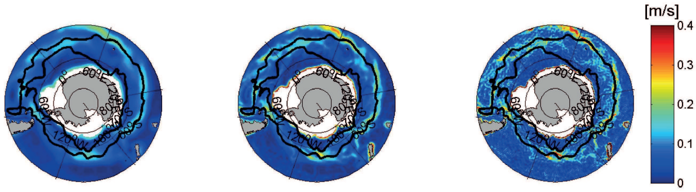

Figure 4: Geostrophic velocities as derived from the DOT of Figure 3 and also for d/o=60, D/O=120 and D/O180 (from left to right). Also shown are the fronts derived from oceanographic in-situ data. Units are meters per second.

such as Rio et al. (2007), Maximenko et al. (2009). GOCE based DOT-models with high spatial resolution are getting available just now, e.g. Le Traon et al. (2011) or Bingham et al. (2011). Geodetic mean topography is the point of departure for studies of surface ocean circulation, geostrophic velocities, assimilation into numerical ocean models, mass and heat transport. In geodesy it is the key to a global unification of height systems.

The effect of the high spatial resolution of GOCE will be especially important when computing geostrophic velocities and consequently in investigations of ocean mass and heat transport. Geostrophic velocities are a vector field on the Earth sphere, essentially the curl of the surface gradient field of the mean dynamic topography, or in other words a first spatial derivative. This leads to an amplification of smaller scales relative to the longer scales. In other words smaller spatial scales get a higher weight relative to the long spatial scales, cf. Janjic et al. (2012). Figure 4 shows the geostrophic velocities computed from the DOT model of Figure 3 for the area of the ACC, again up to d/o= 60, 120, and 180. The figure includes the fronts as derived from oceanographic in-situ data.

6. CONCLUSIONS

GOCE is a geodetic satellite mission. It demonstrates the value of gradiometry for global gravity field and geoid determination. More specifically, spatial scales typically between 80 km and 200 km will become much more consistent and accurate. Applications of gravity and geoid models in geophysics, oceanography and geodesy require an extremely high level of consistency and accuracy over the entire spectrum of spatial scales, or degrees and orders of a corresponding spherical harmonic series expansion. This will only be attainable if GOCE is combined with GRACE and with satellite laser ranging and GPS. It will require joint processing based on one common set of geodetic standards. Earth-fixed and celestial reference system, normal gravity, the attraction of sun, moon and planets, the effect of geophysical fluids, loading, tectonic motion and post-glacial re-adjustment must be dealt with consistently. Modern space geodesy is delivering essential Earth and climate variables. Geodesy will reach its full potential in Earth system science if Earth rotation, geometry and gravity/geoid can be analyzed in one unified system.

Acknowledgements. The work of R. Rummel and W. Yi is supported by the Institute for Advanced Study,

Technische Universität München.

7. REFERENCES

Albertella, A., R. Rummel (2009): On the Spectral Consistency of the Altimetric Ocean and Geoid Surface, A One-dimensional Example, J Geod 83: 805-815, DOI 10.1007/s00190-008-02999-5.

Andersen,O.B., P. Knudsen (2009) DNSC08 mean sea surface and mean topography models, J. Geophys. Res., 114, C11001.

Bingham, R. J., P. Knudsen, O. Andersen, and R. Pail (2011), An initial estimate of the North Atlantic steady-state geostrophic circulation from GOCE, Geophys. Res. Lett., 38, L01606, doi:10.1029/2010GL045633.

Bingham RJ, Haines K, Hughes CW. (2008) Calculating the Ocean's Mean Dynamic Topography from a Mean Sea Surface and a Geoid. Journal of Atmospheric and Oceanic Technology 2008, 25(10), 1808-1822.

Bosch W., R. Savcenko (2010) On estimating the dynamic ocean topography a profile approach; in: Mertikas (ed.) Gravity, Geoid and Earth Observation, IAG Symposia, 135, 247-252, Springer.

Dettmering D., Bosch W. (2010): Envisat radar altimeter calibration by multi-mission crossover analysis. Proceedings of the ESA Living Planet Symposium, Bergen, Norway, ESA Publication SP-686 (CD-Rom).

Gruber, Th., O. Abrikosov and U. Hugentobler: GOCE Standards, ESA-Technical Note, GO-TN-HPF-GS-0111, 2009.

Hernandez, F., P. Schaeffer (2000) Altimetric Mean Sea Surfaces and gravity Anomaly Maps Intercomparisons, CLS, AVI-NT-011-5242-CLS.

Hughes CW, Bingham RJ. (2008) An Oceanographer's Guide to GOCE and the Geoid. Ocean Science, 4(1), 15-29.

Janjic, T., J. Schröter, R. Savcenko, W. Bosch, A. Albertella, R. Rummel, O. Klatt (2012) Impact of combining GRACE andGOCE gravity data on ocean circulation estimates, Ocean Sci, 8, 65-79. doi: 10.5194/os-8-65-2012

Journal of Geodesy (2011) Special Issue: GOCE-The gravity and Steady-state Ocean Circulation Explorer (guest editor: R. Rummel), 85(11) 747-884.

Le Traon, P.Y., P. Schaeffer, S. Guinehut, M.H. Rio, F. Hernandez, G. Larnicol, J.M. Lemoine (2011) Mean Ocean dynamic Topography from GOCE and Altimetry, ESA SP686

Maximenko, N., P. Niiler, M.-H. Rio, O. Melnichenko, L. Centurioni, D. Chambers, V. Zlotnicki, and B. Galperin (2009): Mean dynamic topography of the ocean derived from satellite and drifting buoy data using three different techniques journal. J. Atmos. Ocean. Tech., 26 (9), 19101919.

McCarthy D.D., G. Petit (eds.) (2004) IERS Conventions (2003), IERS Technical Note 32, 127 pages, Verlag des Bundesamts für Kartographie und Geodäsie, Frankfurt am Main

Pail, R., et al. (2010), Combined satellite gravity field model GOCO01S derived from GOCE and GRACE, Geophys. Res. Lett., 37, L20314, doi:10.1029/2010GL044906.

Pail, R., et al. (2011) First GOCE gravity field models derived by three different approaches, J Geod 85(11) 819-843. doi:10.1007/s00190-011-0467-x

Plag, H.-P., M. Pearlman (eds.) (2009) Global Geodetic Observing System Meeting the Requirements of a Global Society on a Changing Planet in 2020, Springer, Heidelberg. DOI 10.1007/978-3-642-02687-4

Rio, M.-H., P.-M. Poulain, A. Pascual, E. Mauri, G. Larnicol, and R. Santoleri, (2007): A Mean Dynamic Topography of the Mediterranean Sea computed from altimetric data, in-situ measurements and a general circulation model., J. Mar. Sys.

Rummel, R. W. Yi, C. Stummer (2011) GOCE Gravitational Gradiometry, Journal of Geodesy, 85(11), 777-790. DOI 10.1007/s00190-011-0500-0.

Rummel, R., T.Gruber (2010): Gravity and steady-state ocean circulation explorer GOCE, in: Flechtner, F. et al. (eds.) System Earth via Geodetic-Geophysical Space Techniques, (Advanced technologies in Earth sciences), p.203-212, Springer, Berlin Heidelberg.

Stummer, C., T. Fecher, R. Pail (2001) Alternative method for angular rate determination within the GOCE gradiometer processing, J Geod 85(9) 585-596. DOI 10.1007/s00190-011-0461-3

Wahr, J., M. Molenaar and F. Bryan (1998) Time variability of the Earth's gravity field: hydrological and oceanic effects and their possible detection using GRACE, J Geoph. Res. 103(B12), 30,205-30,229.

Yi, W. (2012) The Earth's gravity field from GOCE, dissertation, Fakultät für Bauingenieur- und Vermessungswesen, Technische Universität München.

THE FUTURE GLOBAL VLBI2010 NETWORK OF THE IVS

H. HASE[1], D. BEHREND[2], C. MA[3], B. PETRACHENKO[4], H. SCHUH[5], A. WHITNEY[6]

[1] Bundesamt für Kartographie und Geodäsie
Sackenrieder Str. 25, 93444 Bad Kötzting, Germany
e-mail: hayo.hase@bkg.bund.de

[2] NVI, Inc./NASA Goddard Space Flight Center
Code 698.2, Greenbelt, MD 20770, USA
e-mail: dirk.behrend@nasa.gov

[3] NASA Goddard Space Flight Center
Code 698.2, Greenbelt, MD 20770, USA
e-mail: chopo.ma@nasa.gov

[4] Natural Resources Canada
Geodetic Survey Division, 615 Booth Street,
Fourth Floor, Ottawa, ON, K1A 0E0, Canada
e-mail: bill.petrachenko@nrc-cnrc.gc.ca

[5] Vienna University of Technology, Institute of Geodesy and Geophysics
Gusshausstrasse 27-29, 1040 Vienna, Austria
e-mail: harald.schuh@tuwien.ac.at

[6] MIT Haystack Observatory
Off Route 40, Westford, MA 01886, USA
e-mail: awhitney@haystack.mit.edu

ABSTRACT. The VLBI2010 concept was developed by the International VLBI Service for Geodesy and Astrometry (IVS) in order to create the next generation VLBI system needed to meet the goals of the Global Geodetic Observing System (GGOS) of the International Association of Geodesy (IAG). Global measurement goals of 1 mm position error and 0.1 mm/year site velocity error require new radio telescope designs, new VLBI receiving and recording systems, new concepts for data transmission and correlation, as well as updated software for scheduling, data analysis, and archiving. In December 2010, the IVS VLBI2010 Project Executive Group (V2PEG) conducted a survey among existing IVS network stations to measure awareness of VLBI2010 and to learn about modernization plans towards VLBI2010; the results of this survey indicate that most of the IVS network stations are already planning the transition to VLBI2010 capabilities. The survey indicated that up to 20 new radio telescopes at 17 sites with VLBI2010 compliance could become operational by 2017; a sufficient number of VLBI2010-compatible radio telescopes should be available by 2014–15 to support initial VLBI2010 operations.

1. INTRODUCTION

The Directing Board (DB) of the International VLBI Service for Geodesy and Astrometry (IVS) established the VLBI2010 Project Executive Group (V2PEG) in early 2009 to provide strategic leadership to the VLBI2010 project and guide the transition from the VLBI2010 development phase to the VLBI2010 implementation phase. V2PEG is also the primary point of contact for VLBI2010-related questions from institutions that are interested either to upgrade existing VLBI operations to VLBI2010 compatibility or to build new compatible systems. The V2PEG has also been involved at different levels to help expedite administrative processes concerning the setup of VLBI2010 radio telescope projects, including the proof-of-concept project.

In 2010, V2PEG conducted a survey among existing IVS network stations in order to:

- gather information about individual VLBI2010 plans,
- trigger VLBI2010 discussion at the network station level,

- solicit input on what the V2PEG can do to provide the best support to individual VLBI2010 projects.

The survey addressed 31 IVS network stations, all of which replied. Subsequently, the survey results were re-distributed back to the IVS network stations in January 2011, which are also available at the IVS Web site (Hase et al., 2011).

2. VLBI2010

In the first decade of this millennium the IVS established two working groups to define the outline of VLBI2010. Working Group 2 "Product Specifications and Observing Programs" got the task to define the VLBI2010 measurement goals and to propose corresponding observing programs. The Working Group 2 report (Schuh et al., 2003) was completed in 2002, describing the future demands of the service products. Several products, such as station coordinates, episodic events, Earth rotation velocity, rotational pole position, nutational parameters, as well as geophysical properties of the ionosphere and troposphere, demand continuous seven days per week observation. The follow-up IVS Working Group 3 "VLBI 2010" was created in September 2003. It examined current and future requirements for VLBI geodetic systems, including all components from antenna to analysis, and published a report with recommendations for a new generation of systems. The final report was presented in 2005 (Niell et al, 2005). The main characteristics of the future VLBI2010 system can be identified as follows:

- continuous observations in 30 s slew-track cycles,
- fast radio telescopes of $\geq$ 12-meter reflector class with kinematic parameters of either a single 12-meter diameter antenna with very high slew rates, e.g. 12 deg/s in azimuth, or a pair of 12-meter diameter antennas, each with more moderate slew rates, e.g. 5 deg/s in azimuth (Petrachenko et al., 2009),
- wideband feed, 2–14 GHz (later 2–18 GHz),
- digital baseband converter,
- high-data-rate sampling data acquisition, $\geq$ 8 Gbps,
- broadband connectivity for e-transfer and e-VLBI,
- distributed remote controlled continuous operation of the VLBI network,
- software correlator,
- automated production process including analysis.

3. GLOBAL GEODETIC OBSERVING SYSTEM

The International Association of Geodesy (IAG), within the International Union of Geodesy and Geophysics (IUGG), contributes with the Global Geodetic Observing System (GGOS) to the Global Earth Observing System of Systems (GEOSS). GEOSS is an outcome of the Group on Earth Observation (GEO) which is composed of 87 nations plus the European Commission and 64 participating organizations (as of December 2011). The envisaged goals of GGOS are:

- 1 mm position accuracy, 0.1 mm/year velocity accuracy,
- continuous observations for time series of station positions and Earth orientation parameters,
- turnaround time to initial geodetic products of less than 24 hours.

The realization of GGOS calls on the IVS community to improve its performance to VLBI2010 standards.

4. IVS NETWORK STATION SURVEY

The survey consisted of six questions (see detailed questions in the analysis report Hase et al., 2011):

1. Specify plan to upgrade your site to full VLBI2010 capability.
2. Do you plan to acquire a new radio telescope that fully meets the VLBI2010 recommendations?
3. Do you plan to continue operating your existing legacy radio telescope in the future?
4. What is the best estimate of the year in which your VLBI2010 capability will become operational?
5. At what stage are you in the planning process?
6. What support do you need from the IVS?

The answers received were, of course, based on best estimates of the availability of resources to build new systems. However, the average of optimistic and pessimistic estimates gives a first clue to the future development of the VLBI2010 network. Summarizing the results:

- By 2013, a sufficient number of VLBI2010 compatible radio telescopes will be available for significant, but not full-time, VLBI2010 operations (Figure 1).
- By 2017, approximately 20 new radio telescopes at 17 sites operated by IVS network station institutions will be available for full-time VLBI2010 observations (Figure 2). Additional new stations may also join if approved and constructed.
- Even in 2017, the American/Pacific region will still lack presence of VLBI2010 network stations, though a 10-station NASA network covering some of this area may eventually be built.
- Through at least 2015, observations by a large number of legacy S/X-band telescopes will still be supported for data continuity, astrometry and space applications (Figure 3).
- Many network stations need technical consultation about VLBI2010, as well as support letters to be successful with the administration and funding level.

Table 1 shows detailed IVS station-by-station projections through 2017 according to survey results. The stations marked with an asterisk (*) are planning very fast radio telescopes that are compliant with the proposed VLBI2010 slewing rate and observation mode. Stations marked with two asterisks (**) will follow the twin telescope concept, which consists of two VLBI2010 radio telescopes at one location. Stations marked with a plus (+) will be VLBI2010 compliant except that only a single antenna with a ∼5 deg/sec azimuth slew rate is currently planned. Legacy stations upgrading to VLBI2010 receivers and data systems are unmarked. Stations marked with a minus (-) will continue to operate with S/X-band only. The indicated year is an estimate for operational capability for the IVS.

The upgrade list according to Table 1 constitutes a snaphot as of January 2011. In order to capture changes in plans and to be more concise, the V2PEG intends to contact the IVS network stations again about a year after the original survey requesting updated information. In early March 2012 a VLBI2010 workshop about technical specifications of the station hardware will be held in Wettzell, Germany. Station managers and technical staff are encouraged to participate in this workshop in order to advance the effort to establish a more powerful global VLBI network.

5. CONCLUSION

A highly capable VLBI2010 network will be implemented within this decade; new broadband 2–14 GHz observation modes will come into regular operation from 2014/2015 onwards with full operation by about 2017. The current S/X operation mode will be maintained in parallel at a number of legacy stations for data continuity, astrometry and space applications.

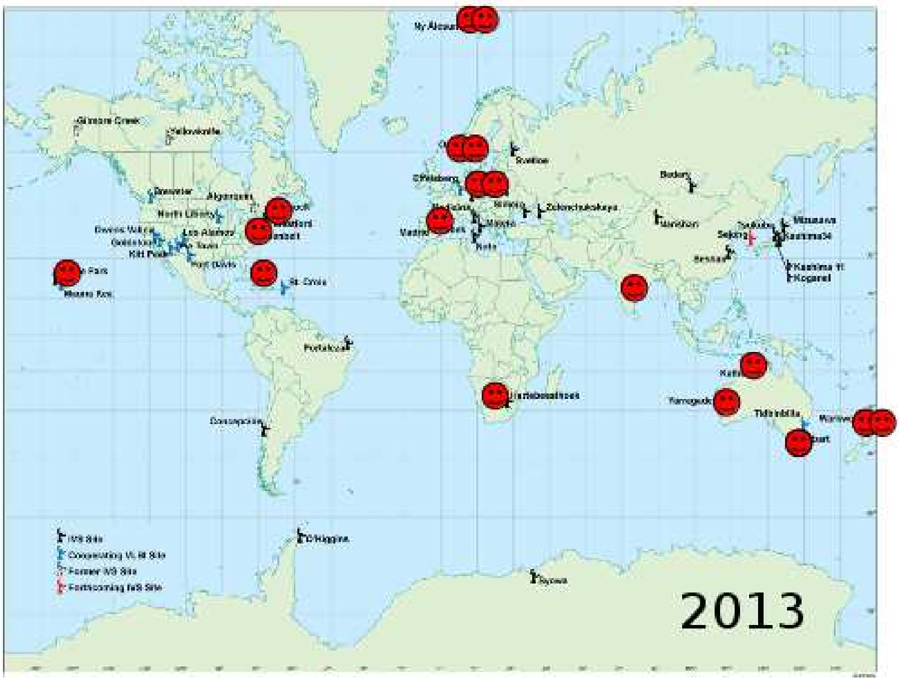

Figure 1: Prediction for 2013: Approximately 13 stations will be available, allowing significant, but not full-time, VLBI2010 observations.

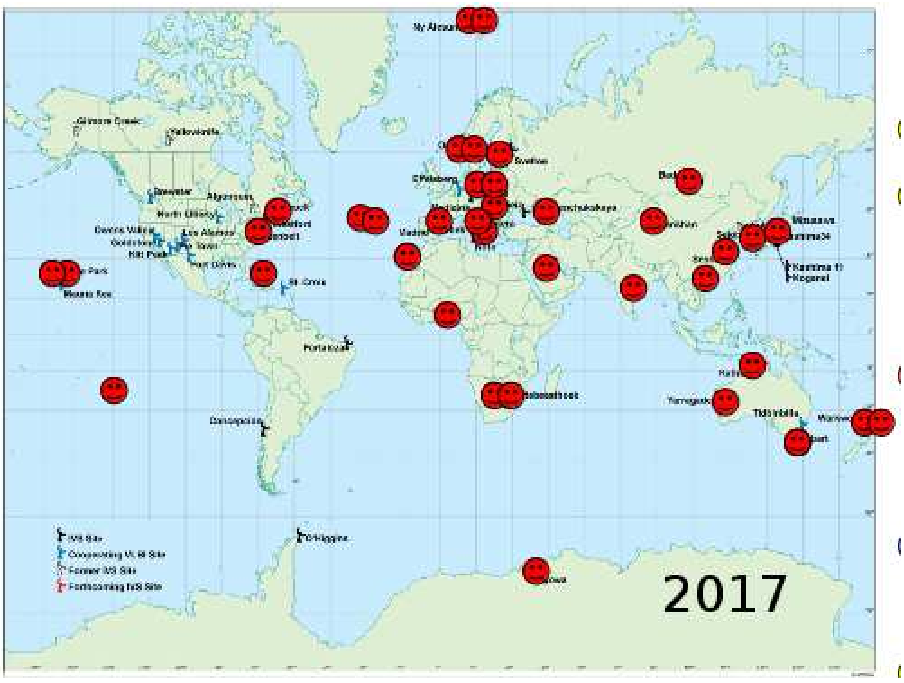

Figure 2: Prediction for VLBI2010 observations in 2017: Approximately 20 stations will be available for full-time observations. Additional sites in Tahiti, Nigeria, Saudi-Arabia and India may join the IVS network if funding is approved.

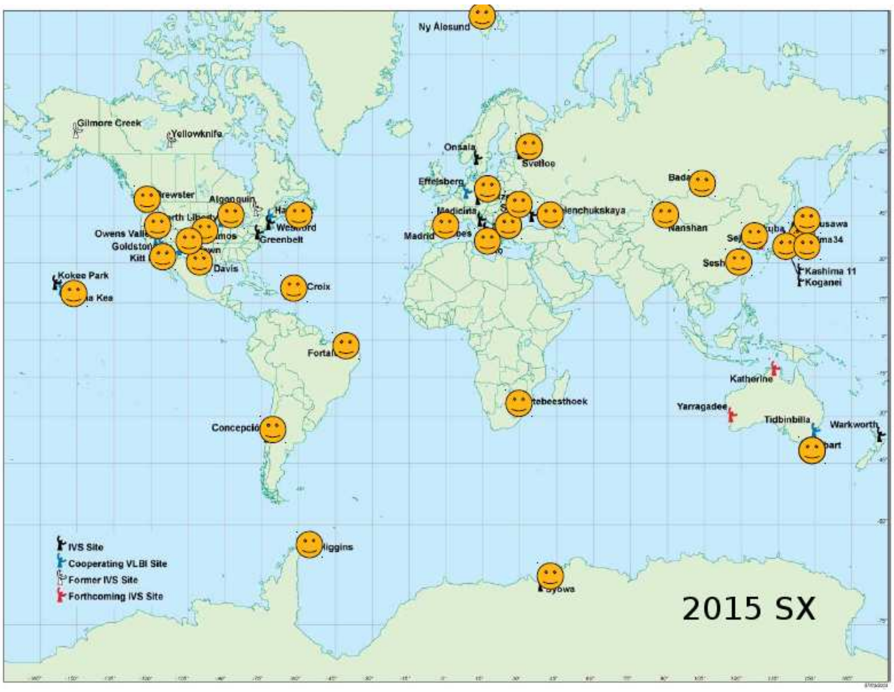

Figure 3: Prediction for S/X observations in 2015: IVS will still utilize existing global S/X network stations for some time to support data continuity, astrometry and space applications.

6. REFERENCES

Hase, H., Behrend, D., Ma, C., Petrachenko, W., Schuh, H., Whitney, A., 2011, "Network Station Survey 2010, Analysis", IVS Document `http://ivscc.gsfc.nasa.gov/technology/vlbi2010-docs/ns-survey2010.pdf`.

Schuh, H., Charlot, P., Hase, H., Himwich, E., Kingham, K., Klatt, C., Ma, C., Malkin, Z., Niell, A., Nothnagel, A., Schlüter, W., Takashima, K., Vandenberg, N., 2003, "IVS Working Group 2 for Product Specification and Observing Programs, Final Report", IVS Document `http://ivscc.gsfc.nasa.gov/about/wg/wg2/IVS_WG2_report_130202-letter.pdf`.

Niell, A., Whitney, A., Petrachenko, B., Schlüter, W., Vandenberg, N., Hase, H., Koyama, Y., Ma, C., Schuh, H., Tuccari, G., 2005, "VLBI2010 – A Vision for Geodetic VLBI, Current and Future Requirements for Geodetic VLBI Systems", IVS Document `http://ivscc.gsfc.nasa.gov/about/wg/wg3/IVS_WG3_report_050916.pdf`.

Petrachenko, B., Niell, A., Behrend, D., Corey, B., Böhm, J., Charlot, P., Collioud, A., Gipson, J., Haas, R., Hobiger, T., Koyama, Y., MacMillan, D., Malkin, Z., Nilsson, T., Pany, A., Tuccari, G., Whitney, A., Wresnik, J., 2009, "Design Aspects of the VLBI2010 System: Progress Report of the IVS VLBI2010 Committee", NASA/TM-2009-214180, 58 pp.

network station	country	year	project name
Hobart+	Australia	2010	AuScope
Warkworth+	New Zealand	2010	
Yarragadee+	Australia	2011	AuScope
Katherine+	Australia	2011	AuScope
Wettzell**	Germany	2011	TTW
Westford+	U.S.A.	2011	POC
Greenbelt+	U.S.A.	2011	POC
Kashima34	Japan	2013	
Koganei11	Japan	2013	
Yebes*	Spain	2013	RAEGE
Onsala**	Sweden	2013	
Badary*	Russia	2014	
Zelenchukskaya+	Russia	2014	
Matera*	Italy	2014	
Santa Maria*	Portugal	2014	RAEGE
Fortaleza	Brazil	2014	
Kokee Park*	U.S.A.	2014	
Sejong22	Korea	2015	
Gran Canaria*	Spain	2015	RAEGE
Hartebeesthoek*	South Africa	2015	
Tsukuba32	Japan	2016	
Tsukuba*	Japan	2016	
Sheshan*	China	2016	
Hainan*	China	2016	
Flores*	Portugal	2016	RAEGE
Ny Ålesund**	Norway	2017	
Arecibo+	Puerto Rico	2017?	
VERA-	Japan	n.a.	
Simeiz	Ukraine	n.a.	
Svetloe	Russia	n.a.	
Medicina	Italy	n.a.	
Noto	Italy	n.a.	
Syowa	Antarctica	n.a.	
O'Higgins	Antarctica	n.a.	
TIGO	Chile	n.a.	
VLBA-	U.S.A.	n.a.	

Table 1: Details of the projected schedule of VLBI2010-station construction through 2017 (see text for details).

ESTIMATION OF THE GROUND-SPACE INTERFEROMETER PARAMETERS DURING RADIOASTRON MISSION

V.E. ZHAROV[1], I.A. GIRIN[2], V.I. KOSTENKO[2], S.F. LIKHACHEV[2]
[1] Lomonosov Moscow State University, Sternberg Astronomical Institute
Universitetskij prospect, 13, Moscow
e-mail: vladzh2007@yandex.ru
[2] Astro Space Center of Lebedev Physical Institute of RAS
84/32 Profsoyuznaya st., Moscow
e-mail: vkostenko@asc.rssi.ru

ABSTRACT. The model of motion of the space radio telescope (SRT) was developed for calculation of the interferometer delay and other parameters to ensure the proper work of the Astro Space Center correlator during the Radioastron mission. The ARIADNA package was used as base for correlation process. This package was used for estimation of the ground-space interferometer parameters too.

1. INTRODUCTION

The RadioAstron project is an international collaborative mission to launch a satellite carrying a 10-meter space radio telescope (SRT) on the elliptical orbit around the Earth. The aim of the mission is to create the ground-space VLBI to observe the radio sources with high angular resolution. The orbit of the SRT has an apogee altitude of about 330 000 km, a period of 8–9 days, and an eccentricity of about 0.9. The ground-space VLBI observations at a standard radio astronomical wavelength set of 1.35, 6, 18, and 92 cm with such orbit would provide information about structure of the galactic and extragalactic radio sources at microarcsecond level.

Our goal is to use the ground-space VLBI observations for the solution of some astrometric problems such as study of the defining sources structures and their variations, connection of the ICRF and dynamical system based on the pulsar timing, by means of measuring the ground telescopes coordinates relative to the center of mass of the Earth.

The key for solution of these problems is the reconstruction of the SRT precise orbit. A model of motion of the SRT was developed for calculation of the interferometer delay and other parameters to ensure the proper work of the Astro Space Center correlator. The ARIADNA package was used as base for correlation process.

2. MODELLING OF THE SRT TRAJECTORY

In order to model the SRT trajectory the ARIADNA package was transformed significantly and was named as ORBITA [1]. Main difference of new package from the ARIADNA package is calculation of the SRT motion parameters.

The orbital elements of the SRT are chosen to maximize their evolution by weak gravitational perturbations from the Moon and the Sun [2]. Such an evolution provides a possibility to observe many radio sources, located on the sky at directions close to the orbit plane, to start their study with moderate angular resolution.

The initial elements of orbit were established: apogee height $H_a = 333455$ km; perigee height $H_p = 578$ km; longitude of ascending node $\Omega = 342.2°$; ascending node-perigee angle $\omega = 302.0°$; inclination of the orbit $i = 51.4°$; eccentricity $e = 0.93$. Initial rotation period is about 8.32 days.

From the ballistic point of view the SRT is a difficult object. The pressure of solar radiation produces different effects on the different elements of the spacecraft construction. As a result, a force-moment appears around the spacecraft center of mass. The reaction-wheel system is used to keep spacecraft orientation constant. Long-run effects of force-moments lead to a permanent increase of angular momentum that requires unloading the momentum of the spinning reaction wheels by switching the gas engines on.

Such operations result in perturbations of the motion of the SRT center of mass. Estimations show that the velocity changes caused by such perturbation can achieve values of 1–5 mm/s.

Ballistic navigation information (vector of state of spacecraft, range and radial velocity measured by ground tracking stations, etc.) used in the ORBITA package is distributed by the Keldysh Institute of Applied Mathematics. It is named for this study as "reference".

We had not real noisy signals received by the ground telescope and SRT. So at the first stage of work the reference trajectory of the SRT (really unknown) was used for calculation of the vectors of state $\mathbf{X_S}, \dot{\mathbf{X}}_\mathbf{S}, \ddot{\mathbf{X}}_\mathbf{S}$ beginning from t_0 to moment of observation t_j $(j = 0, 1, 2, ..)$. Then the digitized noisy signal (bit sequence) $x(t_j)$ for the terrestrial telescope was generated. Similar signal $y(t_j)$ for the SRT was generated by shifting the bit sequence $x(t_j)$ on calculated delay, fringe frequency and adding the phase drift due to relativistic effects. Test of correlation (calculation of delay, fringe frequency and phase by the ORBITA software for reference trajectory of the SRT) was done according to the diagram in Figure 1a.

For the second test the "model" trajectory of the SRT was generated. Numerical integration of the differential equations was used. We consider that this trajectory is known and can be reconstructed on base of known forces. The vector of state for time t_0 was taken from the "reference" orbit. Because the forces acting on the SRT in the ORBITA package differ from ones and used for calculation of the reference trajectory the "model" trajectory will go away from it. The vectors of state $\mathbf{X^m_S}, \dot{\mathbf{X}}^\mathbf{m}{}_\mathbf{S}, \ddot{\mathbf{X}}^\mathbf{m}{}_\mathbf{S}$ for moments of observation t_j $(j = 0, 1, 2, ..)$ are known and used for calculation of delay, fringe frequency and phase as apriori parameters for correlator. Method of generation of the signal and correlation test for this stage are shown in Figure 1b.

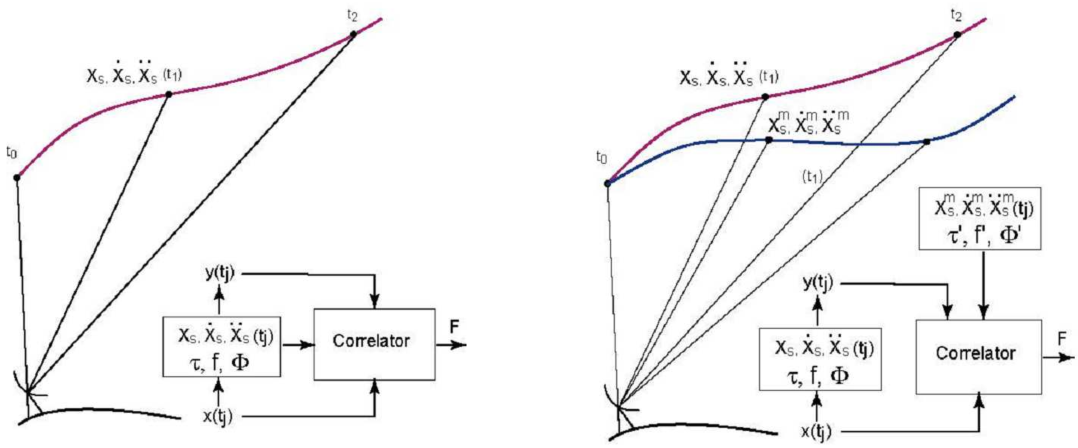

Figure 1: Method of the correlator test a) for the reference trajectory of the SRT and b) for the reference and "model" trajectories.

Two stages of simulation allow to estimate the effect of uncertainty of the vectors of state $\mathbf{X^m_S}, \dot{\mathbf{X}}^\mathbf{m}{}_\mathbf{S}, \ddot{\mathbf{X}}^\mathbf{m}{}_\mathbf{S}$ for different moments of observation t_j on coherent time of integration. Uncertainty means here the differences $|\mathbf{X_S} - \mathbf{X^m_S}|, |\dot{\mathbf{X}}_\mathbf{S} - \dot{\mathbf{X}}^\mathbf{m}{}_\mathbf{S}|, |\ddot{\mathbf{X}}_\mathbf{S} - \ddot{\mathbf{X}}^\mathbf{m}{}_\mathbf{S}|$ that will increase with t_j because trajectories will go away.

The last stage of simulation is connected with estimation of such parameters of the ground-space VLBI as sensitivity and its dependence from the integration time. Such estimation can be done by adding independent noise signals with known amplitude for each bit sequences $x(t_j)$ and $y(t_j)$. Varying signal-to-noise ratio and uncertainty of the vectors of state $\mathbf{X^m_S}, \dot{\mathbf{X}}^\mathbf{m}{}_\mathbf{S}, \ddot{\mathbf{X}}^\mathbf{m}{}_\mathbf{S}$ one can estimate sensitivity of the ground-space interferometer for different ground telescopes. As example the cross-correlation function for SRT – Simeiz interferometer is shown in Figure 2.

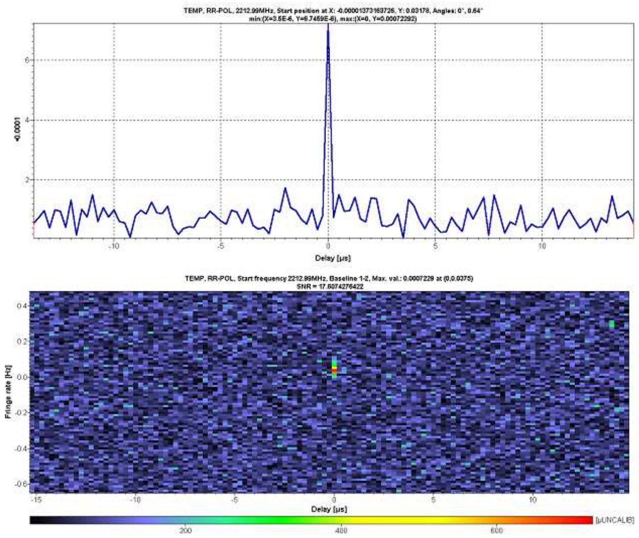

Figure 2: Modelled interferometer pattern for SRT – Simeiz VLBI.

3. CONCLUSION

It was shown that the key for success of the Radioastron mission is the reconstruction of the SRT precise orbit. A model of motion of the SRT was developed for calculation of the interferometer delay and other parameters to ensure the proper work of the Astro Space Center correlator. The ARIADNA/ORBITA package was used as base for correlation process. To study the parameters of the ground-space interferometer two noisy signals "received" by the ground telescope and SRT were emulated. At first, the position and velocity of the SRT were varied relative to the known (reference) trajectory and then the signal to noise ratio (SNR) was changed. The Correlation of signals gives us the possibility to estimate such parameters of the ground-space VLBI as sensitivity and its dependence from the integration time, the coherence time and dependence from the SNR and the SRT position errors. It was shown that to ensure the mission success, the different methods of SRT orbit control have to be developed and applied.

The first observations were made on November 15, 2011 at 18 cm wavelength [3]. The quasar 0212+735 was observed and fringes were found on December 8, 2011 between the space radio telescope and the following ground based radio telescopes: the 32-meter Russian "Quasar" antennas at Svetloe, Zelenchukskaya, and Badary of the Institute of Applied Astronomy, Russian Academy of Sciences, the 64-meter Ukranian antenna at Evpatoria, the State Space Agency of Ukraine, and the Max-Planck-Institute for Radio Astronomy 100-meter antenna at Effelsberg, Germany.

This result confirmed estimates based on our simulations.

4. REFERENCES

[1] Zharov, V.E. Modelling of observations on the ground-space interferometer during Radioastron mission. Private communication (in Russian), 2011.

[2] http://www.asc.rssi.ru/radioastron/documents/rauh/en/rauh.pdf

[3] http://www.asc.rssi.ru/radioastron/news/newsl/en/newsl_10_en.pdf

LARES: A NEW ASI MISSION TO IMPROVE THE MEASUREMENT OF LENSE-THIRRING EFFECT WITH SATELLITE LASER RANGING

E.C. PAVLIS[1], I. CIUFOLINI[2], A. PAOLOZZI[3]

[1] Goddard Earth Science and Technology Center, University of Maryland
Baltimore County, USA
e-mail: epavlis@umbc.edu

[2] Dip. Ingegneria dell'Innovazione, Università del Salento and INFN Sezione di Lecce
Via Monteroni, 73100 Lecce, Italy

[3] Scuola di Ingegneria Aerospaziale, Sapienza Università di Roma, Italy

ABSTRACT. LARES, Laser Relativity Satellite, is a spherical laser-ranged satellite, passive and covered with retroreflectors. It will be launched with ESA's new launch vehicle VEGA (ESA-ELV-ASI-AVIO) in early 2012. Its orbital elements will be: inclination $70° \pm 1°$, semi-major axis 7830 km and near zero eccentricity. Its weight is about 387 kg and its radius 18.2 cm. It will be the single known most dense body orbiting Earth in the solar system, and the non-gravitational perturbations will be minimized by its very small 'cross-section-to-mass' ratio. The main objective of the LARES satellite is a test of the frame-dragging effect, a consequence of the gravitomagnetic field predicted by Einstein's theory of General Relativity. Together with the orbital data from LAGEOS and LAGEOS 2, it will allow a measurement of frame-dragging with an accuracy of a few percent.

1. INTRODUCTION

Einstein's theory of General Relativity (GR) states that the gravitational field is locally 'unobservable' in free-falling frames and in these local inertial frames the laws of physics are those of Special Relativity (Weinberg 1972, Misner, Thorne and Wheeler 1973, Ciufolini and Wheeler 1995). The axes of the non-rotating local inertial frames are determined by free-falling, torque-free gyroscopes. According to GR, gravitation is the curvature of spacetime. One of several tests of GR concerns dragging of inertial frames and gravitomagnetism. The free-falling gyroscopes are dragged by the flow and rotation of nearby matter, such as a spinning mass, i.e., their orientation changes with respect to the distant stars: this is the "dragging of inertial frames" or "frame-dragging", as Einstein called it in a letter to Ernst Mach (Einstein 1913). Mach thought that centrifugal and inertial forces are due to rotations and accelerations with respect to all the masses in the Universe (Mach's principle). In GR the inertial and centrifugal forces are due to our accelerations and rotations with respect to the local inertial frames. Frame-dragging phenomena, which are due to mass currents and mass rotation, can be described as gravitomagnetism (Thorne, Price and Macdonald 1986, Ciufolini and Wheeler 1995) because of a formal analogy of electrodynamics with the general theory of relativity, in the weak field and slow motion approximation (see Figure 1).

In General Relativity, a torque-free spinning gyroscope defines an non-rotating axis relative to the local inertial frames, however, the orbital plane of a test particle is also a kind of large gyroscope that is affected by GR effects. The LAGEOS (LAser GEOdynamics Satellite) experiment measured the frame-dragging effect on the orbital plane of the two LAGEOS satellites (Ciufolini and Pavlis, 2004), and LARES (LAser RElativity Satellite) will test this effect with improved accuracy by observing the orbital plane's precession for LARES and two LAGEOS satellites. The Gravity Probe B space experiment tested frame-dragging of small gyroscopes. The frame-dragging effect on an orbiting test-particle is represented by the rate of change of its angular momentum vector. This is also known as the Lense-Thirring effect, that is, the precession of the nodes of a planet, moon or satellite described by the rate of change of its nodal longitude: $\dot{\Omega}^{L-T} = \frac{2GJ}{c^2 a^3 (1-e^2)^{3/2}}$, where Ω is the longitude of the nodal line of the satellite, J is the angular momentum of the central body, a the semi-major axis of the orbiting test-particle, e its orbital eccentricity, G the gravitational constant and c the speed of light. The Lense-Thirring effect is $\cong$31 mas/yr on the node of LAGEOS (Ciufolini, 1986) and $\cong$31.5 mas/yr on the node of LAGEOS 2.

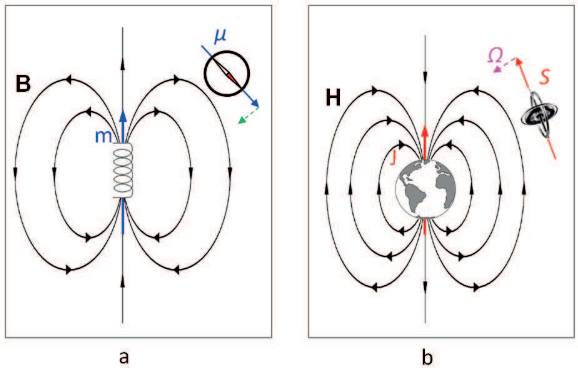

Figure 1: Frame-dragging and the gravitomagnetic analogy in GR with electrodynamics. In (a) the magnetic field B generated by a magnetic dipole m and a test magnetic dipole μ, that is, a magnetic needle, which tends to be aligned along B. In (b) the gravitomagnetic field H generated by the spin J of a central body and frame dragging $\dot{\Omega}$ of a test gyroscope S

2. SATELLITE LASER RANGING, THE GRACE GRAVITY MODELS AND LARES

Satellite Laser Ranging (SLR), a geodetic technique with a precision of a few millimeters, has already proven to be a powerful technique for fundamental physics experiments. With the recent development of the high resolution and high accuracy gravity models from the GRACE mission (Pavlis, 2002), the limitations due to the Newtonian effects' errors were overcome. Frame-dragging was initially measured in 2004–2010, using the two LAGEOS satellites, with an accuracy of about 10% (Ciufolini and Pavlis, 2004; Ciufolini et al. 2010b) and, in 2011, the Gravity Probe B team reported a measurement of frame-dragging with accuracy of about 20% (Everitt et al. 2011). The measurement of frame-dragging was possible despite the much larger error in the dominant first even zonal harmonic J_2 thanks to the approach described in (Ciufolini, 1989), that eliminates the influence of that error. This approach can be extended to eliminate the influence of additional even zonal harmonics as additional orbits become available and provide additional independent data. This is exactly where LARES is entering the picture. The addition of LARES data will allow us to eliminate the error due to the uncertainty in the next even zonal harmonic, J_4.

Studies at the University of Salento, Sapienza University of Rome, University of Maryland, BC, GFZ Potsdam/Munich, and at the Center for Space Research of the University of Texas at Austin have confirmed the accuracy of the measurement of the Lense-Thirring effect using the LAGEOS and LAGEOS 2 orbital data. However, for a measurement of the Lense-Thirring effect accurate to 1%, it will be necessary to use the LARES satellite together with the LAGEOS satellites, in order to eliminate the error from the present day uncertainty in J_4.

3. THE LARES EXPERIMENT

ASI's LARES space experiment is based on the launch of the laser-ranged satellite LARES (LAser RElativity Satellite), using ESA's new launch vehicle VEGA. LARES will have an altitude of about 1450 km, orbital inclination of about $70° \pm 1°$ and near zero eccentricity. The LARES satellite together with the LAGEOS (NASA) and LAGEOS 2 (NASA and ASI) satellites and using the GRACE-derived Earth's gravity field models will allow a measurement of Earth's gravitomagnetic field and of the Lense-Thirring effect with an uncertainty of a few percent (Ciufolini et al., 2010a; 2011). The design of LARES was dictated by the need of reducing the surface perturbations such as thermal and atmospheric drag at an altitude of 1450 km. The body of LARES was thus designed as a solid piece in contrast to the LAGEOS satellites (Paolozzi, Ciufolini and Vendittozzi, 2011). Reduction of sub-components reduces contact conductance that in turn cause temperature gradients on the surface of the satellite. To reduce the effect of surface perturbations further, a non-typical material for aerospace constructions has been chosen: a tungsten alloy (Paolozzi et al. 2009a). The density of the chosen non-magnetic alloy was 18000

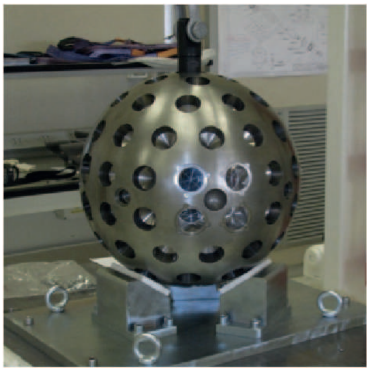

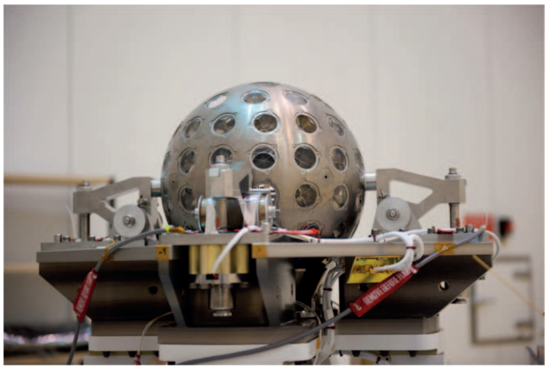

Figure 2: Left: The LARES satellite on the assembly line, with the retroreflectors being installed. Right: LARES mounted on the interface with the payloads pallet, prior to its mounting on the rocket

kg/m^3 that brought the overall density of the satellite (including the cavities for the retro-reflectors) just over 15000 kg/m^3. This resulted in a cross-section-to-mass ratio that is about 2.7 times better than the LAGEOS design. Roughly speaking, this number is a reduction factor to be applied to the uncertainties of the non-gravitational perturbations. The high density will make LARES the object with the highest mean density in the solar system.

In spite of its small dimensions (radius of 182 mm) the total mass is still 387 kg. Being in principle a test particle, like the LAGEOS satellites, LARES is spherical and completely passive, carrying 92 evenly distributed Cube Corner Reflectors (CCRs). The optical quality of the CCR material is extremely uniform and isotropic (Suprasil 311). The surface quality of the three back faces is 1/10th of the light wavelength while for the front face 1/8th, resulting in a quality of the reflected waveform of 1/4th of the wavelength. To compensate for the satellite motion the CCR dihedral angles of all the three back faces have been offset by an amount that is between 1 and 2 arcseconds. This procedure is well known for space CCRs and it is required to modify the Far Field Diffraction Pattern (i.e. the power distribution expected on the ground) so that the maximum power will be shifted from the center of the pattern by the amount the satellite travelled during the laser pulse flight. The distribution of the CCRs was organized on parallels, symmetrically disposed with respect to the equatorial circle. This distribution will allow an easier satellite spin axis determination from ground station telescopes using sun glints: when the direction Sun-CCR front face and the direction ground observer-CCR front face will agree with the laws of reflection a sun glint will be recorded. Estimation of the spin axis of the satellite will help estimating the thermal thrust vector perturbation. In the equatorial region of LARES there are no CCRs but eight cavities used for handling and for interfacing with the separation system. Four of the handling holes will be covered with tungsten alloy caps before launch, to slightly improve the surface-to-mass ratio. The other four cavities required for the separation system of the satellite will remain as such after the separation (right part of Figure 2). However the size (volume and depth) of those cavities have been minimized so that the estimated effect on the orbit is negligible. The minimization of the cavity size was possible by tightening the manufacturing tolerances at the technological limit possible today (Paolozzi et al. 2009b). Design and main tests of the LARES satellite and its separation system (Paolozzi et al. 2009c, Paolozzi et al. 2011) have been performed at Sapienza University. The construction of the Mechanical Ground Support Equipment and some prototypes were the responsibility of the universities. Launch is foreseen at the beginning of 2012[1].

4. CONCLUSIONS

ASI's mission LARES, a new design of laser-ranged-satellite, is ready and awaiting launch from Kouru, in early 2012, on ESA's new launch vehicle VEGA. LARES, together with the two LAGEOS satellites and the Earth gravity field models from the GRACE mission, will test Einstein's theory of General Relativity by measuring the frame-dragging effect with an accuracy of a few percent. Furthermore, simulations indicate that the addition of LARES to the current geodetic targets used for the development of the

[1]LARES was successfully launched on 10:00 UTC Feb. 13, 2012.

ITRF will make a significant contribution towards the future accuracy goals for the ITRF as set by GGOS (Pavlis et al., 2009).

Acknowledgements. Erricos Pavlis gratefully acknowledges the support of NASA Grant NNX09AU86G; Ignazio Ciufolini and Antonio Paolozzi gratefully acknowledge the support of the Italian Space Agency (ASI) Grants I/043/08/0 and I/016/07/0.

5. REFERENCES

Ciufolini, I., Measurement of the Lense-Thirring drag on high-altitude laser-ranged artificial satellites, Phys. Rev. Lett. 56, 278-281 (1986).

Ciufolini, I., A comprehensive introduction to the Lageos gravitomagnetic experiment: from the importance of the gravitomagnetic field in physics to preliminary error analysis and error budget, Int. J. Mod. Phys. A 4, 3083-3145 (1989).

Ciufolini I., Paolozzi A., Pavlis E. C., Ries J. C., Koenig R. and Matzner R., The LARES Relativity Experiment, in: General Relativity and John Archibald Wheeler, I. Ciufolini and R. Matzner eds. (Springer, 2010a) 467-492.

Ciufolini I., Paolozzi A., Pavlis E. C., Ries J. C., Koenig R., Matzner R., Sindoni G., and Neumayer H., Testing Gravitational Physics with Satellite Laser Ranging, European Physics Journal Plus 126 72 (2011).

Ciufolini, I., and Pavlis, E. C., A confirmation of the general relativistic prediction of the Lense-Thirring effect, Nature 431 958-960 (2004).

Ciufolini I., Pavlis E. C., Ries J. C., Koenig R., Sindoni G., Paolozzi A. and Neumayer H., Test of Gravitomagnetism with the LAGEOS and GRACE Satellites, in: General Relativity and John Archibald Wheeler, I. Ciufolini and R. Matzner eds. (Springer, 2010b) 371-434.

Ciufolini, I., and Wheeler, J. A. Gravitation and Inertia (Princeton Univ. Press, Princeton, New Jersey, 1995).

Einstein, A., Letter to Ernst Mach. Zurich, 25 June 1913, in ref. (Misner, Thorne and Wheeler 1973) p. 544.

Everitt, C. W. F., et al. Gravity Probe B: Final Results of a Space Experiment to Test General Relativity, Phys. Rev. Lett. 106 221101 (2011).

Misner, C. W., Thorne, K. S., and Wheeler, J. A., 1973 Gravitation (Freeman, San Francisco).

Paolozzi A., I. Ciufolini, F. Felli, A. Brotzu, D. Pilone (2009a). Issues on LARES Satellite material, IAC Proceedings 2009, Daejeon, Republic of Korea, 12-16 Oct. 2009, p. 1-7.

Paolozzi A., I. Ciufolini, C. Vendittozzi, F. Passeggio, L. Caputo, G. Caputo (2009b) Technological challenges for manufacturing LARES Satellite, IAC Proceedings 2009, Daejeon, Republic of Korea, 12-16 October 2009, p. 1-6.

Paolozzi A., I. Ciufolini, I. Peroni, C. Paris, M. Ramiconi, F. M. Onorati, L. Acquaroli (2009c) Testing the LARES separation system breadboards, IAC Proceedings 2009, Daejeon, Republic of Korea, 12-16 October 2009, p. 1-6.

Paolozzi A., Ciufolini I., Vendittozzi C., Engineering and scientific aspects of LARES satellite, Acta Astronautica 69, 127-134, 2011.

Pavlis, E.C., Geodetic Contributions to Gravitational Experiments in Space, in Recent Developments in General Relativity, Genoa 2000, R. Cianci, et al., eds. (Springer-Verlag, Milan, 2002) 217-233.

Pavlis, E. C. et al., (2009), "The goals, achievements, and tools of modern geodesy", in GGOS2020: The Global Geodetic Observing System, H.- P. Plag and M. Pearlman(eds.) Chapter 2, pp. 24-62, GGOS/IAG, Springer-Verlag, New York.

Thorne, K. S., Price, R. H., and Macdonald, D. A., 1986 The Membrane Paradigm (Yale Univ. Press, NewHaven).

Weinberg, S., 1972 Gravitation and Cosmology: Principles and Applications of the General Theory of Relativity (Wiley, New York).

THE AUSCOPE VLBI PROJECT

J.E.J. LOVELL[1], J.N. MCCALLUM[1], S.S. SHABALA[1], J.M. DICKEY[1], C.S. WATSON[2], O.A. TITOV[3], S.J. TINGAY[4], C. REYNOLDS[4] J.S. MORGAN[4]

[1] School of Mathematics and Physics, University of Tasmania,
Private Bag 37, Hobart, 7001, Australia
e-mail: Jim.Lovell@utas.edu.au

[2] School of Geography and Environmental Studies, University of Tasmania,
Private Bag 76, Hobart, 7001, Australia

[3] Geoscience Australia, P.O. Box 378, Canberra, ACT 2601, Australia

[4]International Centre for Radio Astronomy Research, Curtin University,
GPO Box U1987, Perth, WA 6845, Australia

ABSTRACT. The AuScope VLBI array, consisting of three new 12-meter radio telescopes in Australia dedicated to geodesy, has recently commenced operations. The telescopes at Hobart (Tasmania), Katherine (Northern Territory) and Yarragadee (Western Australia) are co-located with other space geodetic techniques including Global Navigation Satellite Systems (GNSS) and gravity infrastructure, and in the case of Yarragadee, Satellite Laser Ranging facilities. This new facility will make significant contributions to improving the densification of the International Celestial Reference Frame in the southern hemisphere, and subsequently, improve the International Terrestrial Reference Frame through the improved ability to detect and mitigate systematic error. Improvements to both the ICRF and ITRF, as well as the simultaneous densification of the GNSS network across Australia will enable the improved measurement of intraplate deformation across the Australian tectonic plate.

1. INTRODUCTION

In 2006 the National Cooperative Research Infrastructure Strategy (NCRIS) initiated program 5.13, "Structure and Evolution of the Australian Continent", which is funded by the Department of Innovation, Industry, Science and Research (DIISR) and managed by AuScope Ltd. (www.auscope.org.au). A major component of this project was the establishment of a national geospatial framework to provide an integrated spatial positioning system spanning the whole continent. Total federal funding for this undertaking is AUD$15.8M, together with AUD$21M from Universities, State Governments and Geoscience Australia. The infrastructure that was funded to achieve this improvement to the geospatial framework included:

- three 12-meter radio telescopes and a software correlator
- about 100 GNSS receivers
- upgrade of existing SLR facilities
- an absolute gravimeter and three tidal gravimeters
- improved computing facilities

As part of this effort, the University of Tasmania (UTAS) has constructed three new radio telescopes, located near Hobart (Tasmania), Yarragadee (Western Australia), and Katherine (Northern Territory). UTAS is responsible for construction and operation of three new VLBI sites (Figure 1). A software correlator has been developed at Curtin University of Technology.

These new telescopes will double the number of IVS stations in the Southern Hemisphere. They will allow the extension of astrometric VLBI solutions to radio sources south of declination -40 deg, an area of the sky that has been severely under-sampled by the existing array because so few telescopes are available in the south. The AuScope telescopes are intended to observe for 180 days per year, increasing

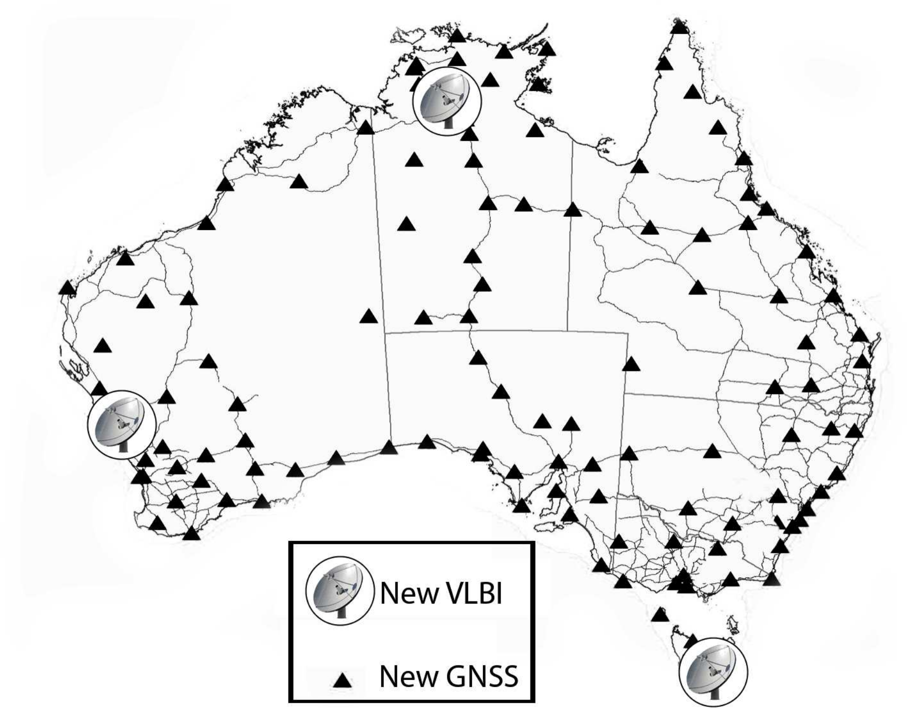

Figure 1: The geographical distribution of VLBI and GNSS infrastructure for AuScope. From West to East, the new VLBI stations are at Yarragadee, Katherine and Hobart. An additional ~100 GNSS receivers will be distributed across the continent.

the number of geodetic VLBI observations in Australia by a factor of nine. The AuScope telescopes closely follow the International VLBI Service VLBI2010 specification for the next generation of telescopes for geodesy (Petrachenko et al., 2009) or provide an upgrade path to meet the specification where it is not currently possible to do so.

2. INFRASTRUCTURE

Each AuScope VLBI observatory is equipped with a 12.1 m diameter main reflector designed and constructed by COBHAM Satcom, Patriot Products division. The telescope specifications include: 0.3 mm of surface precision (RMS), fast slewing rates (5 deg/s in azimuth and 1.25 deg/s in elevation), and acceleration (1.3 deg/s/s). All three sites are equipped with dual polarization S and X-band feeds from COBHAM with room temperature receivers, developed at UTAS by Prof. Peter McCulloch. The receiver systems cover 2.2 to 2.4 GHz at S-band and 8.1 to 9.1 GHz at X-band. System Equivalent Flux Densities (SEFDs) are 3500 Jy in both bands. Data digitisation and formatting is managed by the Digital Base Band Converter (DBBC) system from HAT-Lab, and data are recorded using the Conduant Mark5B+ system. Each site is equipped with VCH-1005A Hydrogen maser time and frequency standards from Vremya-CH.

Observatory sites were selected to satisfy two main criteria: good geographical coverage over the Australian continent and co-location with existing geodetic techniques. The new Hobart telescope is co-located with the existing 26 m telescope to preserve the more than 20 year VLBI time series at the site. Midway between the 26 m and 12 m telescopes is the HOB2 GNSS installation which has been a core site of the International GNSS Service (IGS) since its conception. A hut capable of housing a mobile gravimeter is also co-located on the site. The Yarragadee telescope provides a far western point on the continent and is co-located with multiple existing geodetic techniques including SLR, GNSS, DORIS and gravity. The Katherine site is new and provides a central longitude, northern site. The telescope at Katherine is co-located with a new GNSS site that forms part of the AuScope GNSS network.

AuScope also includes funding for a software correlator, the Curtin University Parallel Processor for Astronomy (CUPPA), a 20 node beowulf computing cluster. Each node consists of a server class PC with dual quad-core processors, 8 GB of RAM and 1 TB of internal hard disk storage. Additionally, the cluster incorporates external mass storage and a total disk pool of 100 TB is available to the cluster. CUPPA is networked internally with standard 1 GbE (two ports per node) and with a 10 GbE connection to iVEC, the eastern Australian state supercomputing centre. In order to process AuScope data, three Mark5B+ VLBI data recorder/playback units were acquired for CUPPA. For VLBI correlation, CUPPA runs the DiFX software correlator (Deller et al 2007) . DiFX has a global user and developer community and is used for astronomical and geodetic correlation at major facilities in the US, Germany and Australia, as well as minor facilities in Australia, New Zealand, the US and Italy.

3. PROJECT STATUS

Construction of the first AuScope telescope at Hobart was completed in 2009 and officially opened at the IVS General Meeting on February 9 2010. Following a period of commissioning, testing and debugging, the Hobart telescope made its first successful IVS observation in October 2010. Construction and commissioning at the other two sites continued in parallel. Yarragadee made its first successful IVS observation in May 2011 and, following a successful full-network fringe check on June 8 2011, correlated at CUPPA. All three telescopes participated in an IVS observation for the first time on June 16 2011.

All three observatories were designed and constructed to be remotely controlled and monitored to keep operating costs at a minimum. Operation of the AuScope VLBI array is being carried out from a dedicated operations room on the Sandy Bay campus of the University of Tasmania.

At present, the AuScope VLBI facility has sufficient operational funds for ∼70 observing days per year, usually consisting of two AuScope telescopes observing as part of the IVS network. Unfortunately operational funds are not presently sufficient to support correlation at CUPPA.

The three AuScope stations have shown good geodetic results since they started operations. The geodetic position accuracy varies around 5 to 10 mm with a tendency to decrease with time as improvements are made to hardware and operational procedures. In August 2011, the AUSTRAL02 IVS observing session was undertaken, comprising the three AuScope stations and the 64 m radio telescope at Parkes. The AUSTRAL sessions are focussed on improving the celestial and terrestrial reference frame in the southern hemisphere. For all three AuScope stations, the accuracy was 6 to 9 mm for the height components and 2 to 3 mm for the horizontal components. This corresponds to a factor of two improvement compared to standard IVS observations typically involving two Australian stations. The recent AUSTRAL03 session (November 2011), which includes the three AuScope telescopes and Warkworth, was recorded with a higher data rate than AUSTRAL02 (1 Gbps compared to 256 Mbps), therefore permitting more observations and better sky coverage, and will hopefully act as a demonstration of the benefits of the advantages of higher data rates and smaller, faster moving telescopes.

4. GEODETIC RESEARCH AT THE UNIVERSITY OF TASMANIA

Space geodetic tools including Global Navigation Satellite Systems (GNSS), Satellite Laser Ranging (SLR) and Very Long Baseline Interferometry (VLBI) are key to the realisation of modern celestial and terrestrial reference frames that underpin the study of both astronomical and Earth based phenomena. "Environmental space geodesy", or the use of space geodetic tools applied to global climate change and sea level studies, crustal strain and seismic deformation, and surface expression of hydrologic loading, is an active theme area of research at UTAS between the School of Maths and Physics and the School of Geography and Environmental Studies. With the completion of the AuScope telescope array, a high priority for research and development within this theme area is geodetic VLBI and its contribution to improving the reference frame. A specific focus of this theme area includes the investigation of systematic errors that currently limit individual space geodetic techniques and therefore their combination in the process of realising the terrestrial reference frame. A specific outcome of the new AuScope telescope array will therefore be the further characterisation and mitigation of systematic error sources within geodetic VLBI and GNSS data analyses.

Areas of activity include automated monitoring of the 26 and 12 m telescopes to better understand thermally induced deformation, source structure and motion studies, network effects, and from a GNSS perspective, investigations into the mitigation of spurious energy at harmonics of the GPS draconitic year in coordinate time series. These are some of a number of sources of systematic error that bias the ITRF and hence limit geophysical interpretation from space geodetic data.

The UTAS Mt. Pleasant Observatory is one of only three radio telescopes in the Southern Hemisphere that contribute regularly to the IVS. The new AuScope telescope array in combination with a new 12 m telescope at Warkworth, New Zealand (Gulyaev & Natusch 2010), will more than double the coverage of the IVS in the Southern Hemisphere. Improved spatial and temporal coverage across the Southern Hemisphere offers significant potential for both improved astrometric and geodetic VLBI. Specifically, improved estimates of intra-plate crustal strain and far field Earthquake deformation will be possible, as well as the further investigation of hydrological loading signals that will dominate the northern telescope site at Katherine. Combined with analyses of GNSS data, the AuScope VLBI and GNSS arrays provide a unique opportunity to address different systematic error contributions to both space geodetic techniques.

By achieving key improvements to systematic error contributions in specific space geodetic analysis techniques, we aim to work towards an improved definition of the terrestrial reference frame (TRF). This will be accomplished through the generation of a TRF based on multiple observational techniques that has an improved handling of effects including non-linear site motion induced by earthquakes, quasi-periodic motion of the crust induced by hydrological loading, and spurious hardware-related offsets in global navigational satellite system (GNSS) measurements. Each of these previously mentioned signals are visible in the time series at the Hobart GNSS site, HOB2, and clear opportunity exists to make significant improvement across these areas.

5. REFERENCES

Deller, A. T., Tingay, S. J., Bailes, M. & West, C. 2007, "DiFX: A Software Correlator for Very Long Baseline Interferometry Using Multiprocessor Computing Environments", PASP, 119, 318

Gulyaev, S., Natusch, T., 2010 "New Zealand 12-m VLBI Station", International VLBI Service for Geodesy and Astrometry 2009 AnnualReport, NASA/TP 2010-215860. Eds.: D. Behrend and K. D. Baver, pp. 138-141.

Petrachenko, B. et al., 2009, "Design Aspects of the VLBI2010 System. Progress Report of the IVS VLBI2010 Committee." NASA/TM-2009-214180, June 2009.

Discussion:

On future IAU recommendations and organization

Recommandations pour l'UAI et pour son organisation

ON FUTURE IAU RECOMMENDATIONS AND ORGANIZATION

D.D. MCCARTHY
U.S. Naval Observatory
3450 Massachusetts Ave., NW, Washington, DC 20392, USA
e-mail: dennis.mccarthy@referencesystems.info

ABSTRACT. Following the presentations presented above, a brief discussion period addressed issues related to nomenclature, the draft resolution regarding the definition of the astronomical unit, recommendations for standardizing access to ephemerides, requirements for new working groups and the future of the Journées.

1. NOMENCLATURE

Participants discussed the possible formation of a Division I standing committee for nomenclature, which would address solely the issues of proper standardization of definitions and descriptions of technical terms related to fundamental astronomy. It was suggested that such a group might be composed of a limited number of subject-matter experts and instituted by the Division Organizing Committee with members proposed by Commission Presidents and the chair appointed by the Division President in consultation with the members of the Standing Committee. The membership as well as the group's continued existence would be reviewed by the Division at each General Assembly, but it is assumed that it would continue as a quasi-permanent activity and could be augmented with other subject matter experts upon recommendation by the chair of the Standing Committee and the approval of the Division Organizing Committee.

Such a committee would be expected to address, for example, the issues regarding clarifying nomenclature that were raised earlier in the meeting. These included suggestions regarding clear nomenclature for the current precession and nutation models as proposed by George Kaplan or nomenclature issues regarding the application of zonal tide corrections to the UT1 Earth orientation parameter. The consensus was that such a group would indeed be helpful but the specific details of its formation should await the details of the proposed reorganization of the structure of the IAU.

2. ASTRONOMICAL UNIT

The details of a proposed resolution regarding the definition of the astronomical unit to be presented at the IAU 2012 General Assembly were discussed at length. Participants agreed that a clear modern definition of the astronomical unit was required but there was need for further discussion regarding the specific details of that definition. There was general agreement that the astronomical unit be re-defined to be a conventional unit of length to be used with all time scales (including TCB, TDB, TCG, and TT), and that the Gaussian gravitational constant k be deleted from the system of astronomical constants. Participants also felt that the value of the heliocentric gravitation constant be determined observationally. This discussion and subsequent electronic correspondence among the participants resulted in the final draft resolution to be proposed at the 2012 IAU General Assembly (see Appendix 1).

3. ACCESS TO EPHEMERIDES

Following the earlier report of the IAU Commission 4 Working Group on Standardizing Access to Ephemerides, whose goal is to facilitate the use of ephemerides, there was discussion regarding the recommendation to work toward using the SPICE format developed of JPL.

4. WORKING GROUP ON ICRS

Participants discussed the need for a new Division I working group concerned with the mathematical models to be used in the future definition of the International Celestial Reference System. The group would deal with systematic effects in the definition and realization of the ICRS due to differences in modeling such effects as aberration, lensing, etc. It would be expected to report its recommendations at the 2015 IAU General Assembly and be composed of members who are actively concerned with the realization of the ICRS (e.g. GAIA and IVS).

5. WORKING GROUP ON ENSEMBLE PULSAR TIME

There was general agreement that a Division I Working Group devoted to the topic of creating a time scale based on pulsar observations would be very useful to establish the long-term stability of time scales. That group would be expected to coordinate observing efforts and standardize analysis procedures. The goal would be to work toward an ensemble pulsar time and to report at the 2015 General Assembly on the feasibility of such a project. Members would be expected to come from Commissions 4 and 31.

6. JOURNÉES AS A MEETING OF IAU DIVISION I ?

There was considerable discussion on the proposal to work toward making future Journées meetings a means to organize a scientific meeting of IAU Division 1 members between meetings of the IAU General Assembly. There was general agreement on the principle but concerns were expressed regarding the funding necessary for the meeting.

APPENDIX 1 - IAU 2012 RESOLUTION PROPOSAL

Re-definition of the astronomical unit of length

The XXVIII General Assembly of International Astronomical Union,
noting

1. that the International Astronomical Union (IAU) 1976 System of Astronomical Constants specifies the units for the dynamics of the solar system, including the day ($D = 86400$ s), the mass of the Sun, M_S, and the *astronomical unit of length* or simply the *astronomical unit* whose definition[i] is based on the value of the Gaussian gravitational constant,
2. that the intention of the IAU 1976 definition of the astronomical unit was to provide accurate relative distances in the solar system when absolute distances could not be estimated with high accuracy.
3. that, to calculate the heliocentric gravitation constant, GM_S, in Système International (SI) units[ii], the Gaussian gravitational constant k, is used, along with an astronomical unit determined observationally,
4. that the IAU 2009 System of astronomical constants (IAU 2009 Resolution B2) retains the IAU 1976 definition of the astronomical unit, by specifying k as an "auxiliary defining constant" with the numerical value given in the IAU 1976 System of Astronomical Constants,
5. that the value of the astronomical unit compatible with Barycentric Dynamical Time (TDB) in Table 1 of the IAU 2009 System (149 597 870 700 m $\pm$ 3 m), is an average (Pitjeva and Standish 2009) of recent estimates for the astronomical unit defined by k,
6. that the TDB-compatible value for GM_S listed in Table 1 of the IAU 2009 System, derived by using the astronomical unit fit to the DE421 ephemerides (Folkner et al. 2008), is consistent with the value of the astronomical unit of Table 1 to within the errors of the estimate; and

[i] The IAU 1976 definition is: "The astronomical unit of length is that length (A) for which the Gaussian gravitational constant (k) takes the value of 0.017 202 098 95 when the units of measurements are the astronomical unit of length, mass and time. The dimensions of k^2 are those of the constant of gravitation (G), i.e., $L^3M^{-1}T^{-2}$. The term "unit distance" is also for the length A."

[ii] using the equation $A^3k^2/D^2 = GM_\mathrm{S}$ where A is the astronomical unit and D the time interval of one day, and k the Gaussian gravitational constant

considering

1. the need for a self-consistent set of units and numerical standards for use in modern dynamical astronomy in the framework of General Relativity,
2. that the accuracy of absolute distance measurements provided by modern observations makes the use of relative distances unnecessary,
3. that modern planetary ephemerides can provide GM_{S} directly in SI units and that this quantity may vary with time,
4. the need for a unit of length approximating the Sun-Earth distance, and
5. that various symbols are presently in use for the astronomical unit,

recommends

1. that the astronomical unit be re-defined to be a conventional unit of length equal to 149 597 870 700 m exactly, as adopted in IAU 2009 Resolution B2,
2. that this definition of the astronomical unit be used with all time scales (including TCB, TDB, TCG, and TT),
3. that the Gaussian gravitational constant k be deleted from the system of astronomical constants,
4. that the value of the heliocentric gravitation constant, GM_S, be determined observationally in SI units, and
5. that the unique symbol "au" be used for the astronomical unit.

REFERENCES

Capitaine, N., Guinot, B., Klioner, S., 2011, Proposal for the re-definition of the astronomical unit of length through a fixed relation to the SI metre, Proceedings of the Journées 2010 Systèmes de référence spatio-temporels, N. Capitaine (ed.), pp. 20–23

Fienga, A., Laskar, J., Morley, T., Manche, H., Kuchynka, P., Le Poncin-Lafitte, C., Budnik, F., Gastineau, M., Somenzi, L., 2009, INPOP08: a 4D-planetary ephemeris: From asteroid and time-scale computations to ESA Mars Express and Venus Express contributions, A&A 507, 3, 1675

Fienga, A., Laskar, J., Kuchynka, P., Manche, H., Desvignes, G., Gastineau, M., Cognard, I., Theureau, G., 2011, INPOP10a and its applications in fundamental physics, Celest. Mech. Dyn. Astr., Volume 111, on line edition (http://www.springerlink.com/content/0923-2958).

Folkner W.M., Williams J.G., Boggs D.H., 2008, Memorandum IOM 343R-08-003, Jet Propulsion Laboratory

International Astronomical Union (IAU), Proceedings of the Sixteenth General Assembly, Transactions of the IAU, XVIB, p. 31, pp. 52–66, (1976).

International Astronomical Union (IAU), Proceedings of the Twenty Seventh General Assembly," Transactions of the IAU, VXVIIB, p. 57, pp. 6: 55-70 (2010).

Klioner S., 2008, Relativistic scaling of astronomical quantities and the system of astronomical units, A&A 478, 951

Klioner, S. A., Capitaine, N., Folkner, W. M., Guinot, B., Huang, T.-Y., Kopeikin, S. M., Pitjeva, E. V., Seidelmann, P. K., Soffel, M. H., "Units of relativistic time scales and associated quantities", in Relativity in Fundamental Astronomy: Dynamics, Reference Frames, and Data Analysis, Proceedings of the IAU Symposium, Volume 261, p. 79-84

Luzum, B., Capitaine, N., Fienga, A., Folkner, W., Fukushima, T., Hilton. J., Hohenkerk, C., Krasinsky, G., Petit, G., Pitjeva, E., Soffel, M., Wallace, P., 2011, "The IAU 2009 system of astronomical constants: the final report of the IAU Working Group on Numerical Standards for Fundamental Astronomy," Celest. Mech. Dyn. Astr. , doi: 10.1007/s10569-011-9352-4

Pitjeva, E.V. and Standish, E.M., 2009, "Proposals for the masses of the three largest asteroids, the Moon-Earth mass ratio and the astronomical unit," Celest. Mech. Dyn. Astr. 103, 365, doi: 10.1007/s10569-009-9203-8

Standish, E.M., 2004, The Astronomical Unit now, in Transits of Venus, New views of the Solar System and Galaxy, Proceedings of the IAU Colloquium 196, D. W. Kurtz ed., 163

TOWARD AN IAU 2012 RESOLUTION FOR THE RE-DEFINITION OF THE ASTRONOMICAL UNIT OF LENGTH

N. CAPITAINE
SYRTE, Observatoire de Paris, CNRS, UPMC,
61, avenue de l'Observatoire, 75014 – Paris, France
e-mail: n.capitaine@obspm.fr

ABSTRACT. This contribution to the Journées 2011 discussion concerns the draft Resolution proposal to the IAU 2012 General Assembly for a re-definition of the astronomical unit. That proposal is based on the paper by Capitaine et al. (2011) and on subsequent discussions within the IAU Working Group on "Numerical Standards for Fundamental astronomy", either by e-mail, or during the WG meeting after the Journées 2010 in Paris. The purpose is to re-define the astronomical unit (of length) as a fixed number of SI metres through a defining constant; that constant should be, for continuity reason, the value for the current best estimate of that quantity in metres as adopted by IAU 2009 Resolution B2 (i.e 149 597 870 700 m). After recalling the properties of the IAU 1976 astronomical unit and its status in the IAU 2009 System of astronomical constants, we explain the main reasons for a change; we present and discuss the proposed new definition. One important consequence is that the heliocentric gravitational constant, GM_S, would cease to have a "fixed" value in astronomical units and will have to be determined experimentally. This would be compliant with modern dynamics of the solar system as it would let possible variations of GM_S appear directly. Moreover, this would avoid an unnecessary deviation from the Système International d'Unités (SI) and should be used with all the time scales (including TCB, TDB, TCG and TT). This draft IAU Resolution proposal is submitted for discussion to IAU Division 1 and, more widely, to the astronomical community.

1. THE IAU 1976 DEFINITION OF THE ASTRONOMICAL UNIT

The International Astronomical Union (IAU) 1976 System of Astronomical Constants specifies the units for the dynamics of the solar system; this includes the day (D = 86400 s), the mass of the Sun, M_S, and the astronomical unit of length (i.e. the astronomical unit), the definition of which is based on the value of the Gaussian gravitational constant.

The IAU 1976 definition is: "The astronomical unit of length is that length (A) for which the Gaussian gravitational constant (k) takes the value of 0.01720209895 when the units of measurements are the astronomical units of length, mass and time. The dimensions of k^2 are those of the constant of gravitation (G), i.e., $L^3M^{-1}T^{-2}$. The term "unit distance" is also for the length A."

The aim of the above definition was to provide accurate relative distances (expressed in astronomical units) in the solar system, when absolute distances could not be estimated with high accuracy. The consequences were the following:

- the Gaussian gravitational constant k was a "defining constant" of the IAU 1976 System, with the value $k = 0.017\ 202\ 098\ 95$ from Gauss (1809),
- the value of the astronomical unit in metres was determined observationally, i.e. fitted to a planetary ephemeris with a certain uncertainty; note that, the "primary constant" in the IAU 1976 System was the light time τ_A for unit distance while the unit distance, $A = c\tau_A$ was a "derived constant",
- the value in SI units of the heliocentric gravitational constant (or Sun mass parameter), GM_S, had to be derived from k, along with the adopted value for the astronomical unit in metres, using the formula: $GM_\mathrm{S} = A^3k^2/D^2$ (1); it was a "derived constant" of the IAU 1976 System,
- the use of Equation (1), made the value of the astronomical unit of mass in SI dependent on the value of the astronomical unit of length.

2. THE IAU 2009 SYSTEM OF ASTRONOMICAL CONSTANTS

The IAU 2009 System of astronomical constants adopted by IAU 2009 Resolution B2 retained the IAU 1976 definition of the astronomical unit. The Gaussian gravitational constant, k, is listed in the IAU 2009 System (see Table 1) as an "auxiliary defining constant" (with its IAU 1976 numerical value) that has to be used to define the astronomical unit and its relationship with GM_S.

Constant	Description	Value	Uncertainty
		Auxiliary Defining Constants	
k	Gaussian gravitational constant	$1.720209895 \times 10^{-2}$	
Constant	Description	Value	Uncertainty
		Other Constants	
au	Astronomical unit	$1.49597870700 \times 10^{11}$ m (TDB compatible)	3 m (TDB compatible)
		Body Constants	
GM_S	Heliocentric gravitational constant	$1.32712442099 \times 10^{20}$ m^3s^{-2} (TCB-compatible)	1.0×10^{10} m^3s^{-2} (TCB-compatible)
		$1.32712440041 \times 10^{20}$ m^3s^{-2} (TDB-compatible)	1.0×10^{10} m^3s^{-2} (TDB-compatible)

Table 1: Extract of the IAU 2009 System of Astronomical Constants (from Luzum et al., 2011).

The IAU 2009 value of the astronomical unit (cf. Table 1) has been taken from Pitjeva & Standish (2009); it is an average of recent estimates for the astronomical unit defined by k. The value is compatible with Barycentric Dynamical Time (TDB). There was no accepted definition for the TCB-compatible value of the au at the time of the adoption of the IAU 2009 system.

The IAU 2009 value for GM_S (cf. Table 1) has been taken from Folkner et al. (2008); the TDB-compatible value was derived from Equation (1) by using the astronomical unit (as defined by k) fit to the DE421 ephemerides and is consistent with the IAU 2009 value of the au to within the errors of the estimate. The fact that the IAU 2009 GM_S value was not directly obtained from Equation (1) by using the IAU 2009 au value shows that the historical definition of the au is no more appropriate for being used with modern solar system ephemerides.

3. MODERN CONTEXT

Due to the huge improvement achieved in solar system ephemerides during the last decade, the definition and status of the au need to be re-considered. This was discussed recently by Klioner (2008), Capitaine & Guinot (2009) and Capitaine et al. (2011).

First, it should be noted that there is a need for a self-consistent set of units and numerical standards for use in modern dynamical astronomy in the framework of General Relativity. Therefore, the definition of the astronomical unit should be adapted to comply with this new context. If the historical status of the au were to be kept, it would be necessary to extend its definition to General Relativity. However, each of the considered options for such an extension would give rise to some difficulties in its application, so that extending the current definition of the astronomical unit to the relativistic framework would be very confusing.

Second, the accuracy of absolute distance measurements provided by modern observations in the solar system (ranging to planets, spacecraft observations, Very Long Baseline Interferometry (VLBI), etc.,) makes the use of relative distances (which was the reason for the historical definition of the au) unnecessary.

Third, modern planetary ephemerides (e.g. INPOP08, DE423, EPM2008) can now determine the solar mass parameter, GM_{Sun}, directly in SI units and this quantity may vary with time. The direct estimation of $GM_{\rm Sun}$ has been first tested in the INPOP08 ephemerides (Fienga et al., 2009). The decrease of that quantity is expected to be detectable in a near future, i.e. when the accuracy has been improved by a factor 10. With the current definition of the *au*, the time dependence of $GM_{\rm Sun}$ leads to time-dependent astronomical units for length and mass; the use of such units to measure possible time variations of the solar mass parameters would be a non-sense.

These make clear that the IAU 1976 definition of the *au* currently appears as an intermediate unit only used for historical purposes and has to be changed. It it necessary to note, that although the definition of the au has to be revised, there is still a need (especially for expressing the distances in the solar system) for a unit of length approximating the Sun-Earth distance.

Another point that should be mentioned is that various symbols are presently in use for the astronomical unit and that adopting a new definition would give the opportunity to give an IAU recommendation for the symbol to be used.

4. DEFINING THE ASTRONOMICAL UNIT AS A FIXED NUMBER OF SI METRES

The proposal is to re-define the astronomical unit to be a conventional unit of length, i.e. astronomical unit = L_A metres exactly, L_A being a defining number; the defining number should be, for continuity reason, the value for the current best estimate of the astronomical unit in metres as adopted by IAU 2009 Resolution B2.

The Resolution proposal is based on the paper by Capitaine et al. (2011) and on subsequent discussions within the IAU Working Group on "Numerical Standards for Fundamental astronomy", either by e-mail, or during the WG meeting after the Journées 2010 in Paris.

Note that the Bureau International des Poids et Mesures (BIPM) Consultative Committee for Units (CCU) declared its support to move to a fixed relationship to the SI metre through a defining number determined by continuity (CCU 2009).

This new definition would change the status of the astronomical unit, which will limit its role to that of a unit of length of "convenient" size for some applications. The consequences will be as follows:

- k will not have a role any more; it should be deleted from the IAU System of astronomical constants,
- the experimental determination of the astronomical unit in SI unit will be abandoned,
- the SI value of $GM_{\rm Sun}$ will be determined experimentally.

This new definition would have the advantages of:

- being a great simplification for the users of the astronomical constants,
- letting possible variations of the mass parameter of the Sun ($GM_{\rm Sun}$) to appear directly, and
- avoiding an unnecessary deviation from the SI,
- being in accordance with the adopted way (Klioner et al. 2009) to use the SI units for the relativistic time scales and associated quantities (i.e. so that, for distances in astronomical units, the TDB-compatible value is $(1 - L_B)\times$ the TCB-compatible value, $1 - L_B$ being the defining conversion factor between TCB and TDB).

5. THE DRAFT IAU 2012 RESOLUTION PROPOSAL

The draft Resolution proposal that is currently submitted to Division I recommends:

1. that the astronomical unit be re-defined to be a conventional unit of length equal to 149 597 870 700 m exactly, as adopted in IAU 2009 Resolution B2,

2. that this definition of the astronomical unit be used with all time scales (including TCB, TDB, TCG, and TT),

3. that the Gaussian gravitational constant k be deleted from the system of astronomical constants,

4. that the value of the heliocentric gravitation constant, $GM_{\rm Sun}$, be determined observationally in SI units, and

5. that the unique symbol, *au*, be used for the astronomical unit.

6. CONCLUDING REMARKS

A revision of the definition and status of the astronomical unit have been shown to be necessary in order to make the system of astronomical constants best compliant with modern dynamical astronomy.

This is recommended in a draft Resolution proposal to the IAU 2012 General Assembly that re-defines the astronomical unit as a fixed number of SI metres through a defining constant.

The new definition will change the status of the astronomical unit of length, with a number of advantages as compared to the historical definition (still in use in the IAU 2009 System of astronomical constants) that have been discussed in the previous sections.

This proposal is submitted to the astronomical community before being proposed to be adopted at the next IAU GA (2012).

7. REFERENCES

Capitaine, N., Guinot, B., 2009, "The astronomical units", Proceedings of the "Journées 2008 Systèmes de référence spatio-temporels", M. Soffel and N. Capitaine (eds.), Lohrmann-Observatorium and Observatoire de Paris, pp 73–74.

Capitaine, N., Guinot, B., Klioner, S., 2011, "Proposal for the re-definition of the astronomical unit of length through a fixed relation to the SI metre", Proceedings of the "Journées 2010 Systèmes de référence spatio-temporels", N. Capitaine (ed.), pp. 20–23.

CCU 2009: Report of the 19th meeting (26-28 May 2009) to the International Committee for Weights and Measures (`http://www.bipm.org/en/committees/cc/ccu/publications_cc.html`).

Fienga, A., Laskar, J., Morley, T., Manche, H., Kuchynka, P., Le Poncin-Lafitte, C., Budnik, F., Gastineau, M., Somenzi, L., 2009, "INPOP08: a 4D-planetary ephemeris: From asteroid and time-scale computations to ESA Mars Express and Venus Express contributions", A&A 507, 3, 1675–1686.

Folkner W.M., Williams J.G., Boggs D.H., 2008, Memorandum IOM 343R-08-003, Jet Propulsion Laboratory.

Gauss, C.F., "Theory of the Motion of the Heavenly Bodies Moving About the Sun in Conic Sections", Boston: Little, Brown, and Company, p. 2, (1809).

International Astronomical Union (IAU), "Proceedings of the Sixteenth General Assembly," Transactions of the IAU, XVIB, p. 31, pp. 52–66, (1976).

International Astronomical Union (IAU), "Proceedings of the Twenty-Seventh General Assembly," Transactions of the IAU, XXVIIB, (2009).

Klioner S., 2008, "Relativistic scaling of astronomical quantities and the system of astronomical units", A&A 478, 951–95.

Klioner, S. A., Capitaine, N., Folkner, W. M., Guinot, B., Huang, T.-Y., Kopeikin, S. M., Pitjeva, E. V., Seidelmann, P. K., Soffel, M. H., "Units of relativistic time scales and associated quantities", in Relativity in Fundamental Astronomy: Dynamics, Reference Frames, and Data Analysis, Proceedings of the IAU Symposium, Volume 261, p. 79-84.

Luzum, B., Capitaine, N., Fienga, A., Folkner, W., Fukushima, T., Hilton. J., Hohenkerk, C., Krasinsky, G., Petit, G., Pitjeva, E., Soffel, M., Wallace, P., 2011, "The IAU 2009 system of astronomical constants: the final report of the IAU Working Group on Numerical Standards for Fundamental Astronomy," Celest. Mech. Dyn. Astr. 110, 4, pp. 293–304.

Pitjeva, E.V., Standish, E.M., 2009, "Proposals for the masses of the three largest asteroids, the Moon-Earth mass ratio and the astronomical unit," Celest. Mech. Dyn. Astr. 103, pp. 365–372.

NOMENCLATURE FOR THE CURRENT PRECESSION AND NUTATION MODELS

S.E. URBAN, G.H. KAPLAN
U.S. Naval Observatory
3450 Massachusetts Ave., NW, Washington, DC 20392, USA
e-mail: sean.urban@usno.navy.mil, george.kaplan@usno.navy.mil

ABSTRACT. For much of the last decade, the latest and best adopted precession and nutation theories were described as the IAU 2000A Precession-Nutation Model, a phrase taken from IAU 2000 Resolution B1.6. Since the adoption of a new precession theory by the IAU in 2006, that phrase has gradually been abandoned without an agreed-upon replacement. The situation is complicated not just by the new precession theory, but by the availability of an adjusted IAU 2000A nutation model that is often not distinguished in print from the original. New agreed-upon nomenclature is required to avoid confusion.

1. PROBLEMS

There are two main problems that have recently emerged, both of which can be addressed with consistent nomenclature. Problem one: the term "IAU 2000A precession-nutation model" is now an ambiguous name. There are several algorithms used for precession and nutation over the past decade that could have a reasonable claim to be part of the IAU 2000A precession-nutation model. These include the following.

For Precession:

P1: Corrections to $\Delta\psi$ and $\Delta\epsilon$, linear with respect to time, on top of the Lieske et al. (1977) precession formulation. This was the precession solution in Mathews, Herring, and Buffett (2002) referred to in IAU 2000 resolution B1.6. This is consistent with what is stated in the IERS Conventions (2010) section 5.2.1 (IERS 2010).

P2: The interim IERS precession expressions given in the IERS Conventions (2003) (IERS 2004). They are provided in the IERS Conventions (2003) in section 5.5.2 as "Precession Developments Compatible with the IAU2000A Model" under the general heading of section 5.5, "IAU 2000A and IAU 2000B Precession and Nutation Model".

P3: Capitaine et al. (2003) P03 precession, recommended by the IAU Working Group on Precession and the Ecliptic and adopted by the IAU in 2006. This is the culmination of the search for a new complete precession theory that began shortly after the 2000 General Assembly. It is now the IAU recommended model.

For Nutation:

N1: The MHB nutation series. This is the series presented in Mathews, Herring, and Buffett (2002) referred to in IAU 2000 resolution B1.6.

N2: The MHB nutation series with corrections for P03 precession. The small additional corrections are from Wallace and Capitaine (2006) and are needed for the IAU adopted nutation and precession to be consistent at the highest levels of precision.

Problem two: groups are now using their own, often different names for precession-nutation models. This leads to confusion for software developers incorporating "IAU precession-nutation", for users that need to understand the data they are using, and for people trying to clearly document their work. Some example of different terminology include the following.

- IERS 2010 uses "IAU 2006/2000A".

- For nutation, IERS 2010 recommends N2 be designated "IAU $2000A_{R06}$."
- Standards of Fundamental Astronomy (SOFA) uses "00A" suffix for the combination of P1 and N1.
- SOFA uses "06A" suffix for the combination of P3 and N2.
- The Astronomical Almanac uses only P3 for precession but both N1 and N2 for nutation. These are termed "IAU 2006" precession and "IAU 2000A" nutation. There are no different designations between the two nutation models, but rather the differences are described within the text.
- The Explanatory Supplement to The Astronomical Almanac (Urban and Seidelmann 2012) uses "IAU 2006/2000A" for the combination of P3 and N1, and "IAU $2006/2000A_R$" for P3 and N2, when a distinction is needed.
- Use of the name "IAU 2000A" precession-nutation is dwindling.

2. GOAL

The goal of this discussion is to agree on standard nomenclature to unambiguously define which algorithms are being used. Emphasis should include accommodating names currently or recently in use, if practical.

3. PROPOSALS AND DISCUSSION

Four proposals were put forward in order to foster discussion. They included using "IAU 2000A" precession-nutation as either a generic name to any pair of precession-nutation algorithms described earlier or as a specific name for P1 + N1. Also, the proposals included "IAU 2006/2000A" precession-nutation being the specific name of P3 + N1, and "IAU $2006/2000A_{R06}$" being the specific name of P3 + N2. Any combination of models not explicitly defined should be described within the document in which they appear.

Due to another set of nomenclature items (see McCarthy, this issue), discussion on the four proposals was effectively shelved. Instead, the participants agreed that an IAU Division I "standing committee" should be formed to deal with these and future nomenclature issues.

4. REFERENCES

IERS, 2004, "IERS Conventions (2003)", McCarthy, D.D. and Petit, G. (Editors), Verlag des Bundesamts für Kartographie und Geodäsie, Frankfurt am Main.

IERS, 2010, "IERS Conventions (2010)", Petit, G. and Luzum, B. (Editors), Verlag des Bundesamts für Kartographie und Geodäsie, Frankfurt am Main.

Lieske, J.H., Lederle, T., Fricke, W. and Morando, B., 1977, "Expressions for the Precession Quantities Based upon the IAU (1976) System of Astronomical Constants", A&A 58, pp. 1–16.

Mathews, P.M., Herring, T.A., and Buffett, B.A., 2002, "Modeling of nutation and precession: New nutation series for nonrigid Earth and insights into the Earth's interior", J. Geophys. Res. (Solid Earth), 107(B4), doi:10.1029/2001JB000390.

Urban, S.E. and Seidelmann P.K. (Editors), 2012, "The Explanatory Supplement to The Astronomical Almanac", 3rd edition, in press.

Wallace, P.T. and Capitaine, N., 2006, "Precession-nutation procedures consistent with IAU 2006 resolutions", A&A 459, pp. 981–985.

STANDARDIZING ACCESS TO EPHEMERIDES

J.L. HILTON
U.S. Naval Observatory
3450 Massachusetts Ave., NW, Washington, DC 20392, USA
e-mail: james.hilton@usno.navy.mil

1. DISCUSSION

As reported in Hilton (2012), the IAU Working Group on Ephemeris Access has tentatively agreed to standardize on the SPICE Toolkit's Spacecraft and Planet Kernel (SPK) format. The Navigation and Ancillary Information Facility (NAIF), the group at JPL that maintains the SPICE Toolkit, has agreed to assign body identification numbers for $TT - TDB$ and the lunar orientation angles so they may be included in SPK format files. A type to handle the Russian Institute of Applied Astronomy's velocity-based Chebyshev polynomials and stand alone SPK file format reading software are being addressed. A specification of the file format for fixed length Chebyshev polynomial formats is also currently being written. Other details, such as whether to include the SPK Type 14 (Chebyshev polynomials with unequal time steps) for highly eccentric orbits or to develop a type for planetary theories, may be extensions to this initial package of ephemeris file format and software.

The purpose of this recommendation is not only to have a common format for the ephemeris files, but to make available software to evaluate the ephemeris files without requiring the user to have any knowledge of the details of the ephemeris structure. Therefore, both the software and format are required to be flexible enough to handle a variety of applications and formats. The file format and software should also be extensible to additional ephemeris formats. The SPK format and software are both designed around this concept.

The primary discussion on this recommendation was that the working group had not taken into account the possibility that an ephemeris might be stored as a planetary theory. This is true. Such a possibility has not been discussed by the working group. The software and file format, however, are structured in a manner that would allow such a format to be added at a later date.

The working group also recognizes that there will be those users with requirements that will compel the development of their own reading software. Thus, a widely available file format specification is required. Hilton, in consultation with C. Acton[1], is drafting a specification of those parts of the SPK format required for the ephemerides of solar system bodies from the SPICE Toolkit documentation and software comments.

Finally, the author suggested that the use of the ephemeris file format and software should not be formalized as an IAU recommendation. That is, he suggested that its use not be compelled by the imposition of a recommendation. This suggestion has not been formally discussed by the working group, but has arisen from informal one-on-one talks between Hilton and other members of the working group. Instead, the availability of the software and ephemerides would be advertised, likely through a working group report. Other possible places to advertise its availability are: the IAU Commission 4 web site, the web and ftp sites of the three producers of high accuracy planetary ephemerides.

2. REFERENCES

Hilton J.L. 2012, in The Proceedings of the Journées 2011, N. Capitaine, ed. (Paris: Observatoire de Paris), in this volume

[1]Manager of the NAIF Group at JPL.

POSTFACE

JOURNÉES 2013 SYSTÈMES DE RÉFÉRENCE SPATIO-TEMPORELS
"Scientific developments based on high accurate space-time reference frames"
Observatoire de Paris (France), 16-18 September 2013

Scientific Organizing Committee
N. Capitaine, France (Chair); A. Brzeziński, Poland; V. Dehant, Belgium; A. Escapa, Spain; C. Hohenkerk, UK; Cheng-Li Huang, China; I. Kumkova, Russian Federation; D.D. McCarthy, USA; M. Soffel, Germany; J. Souchay, France; J. Vondrák, Czech R.; Ya. Yatskiv, Ukraine

Local Organizing Committee
Chair: N. Dimarcq (SYRTE, Observatoire de Paris)

Conference location : Observatoire de Paris, Paris, France

Scientific objectives
The Journées 2013 "Systèmes de référence spatio-temporels", with the sub-title "Scientific developments based on high accurate space-time reference frames", will be organized at Paris Observatory, from 16 to 18 September 2013. These Journées will be the twenty-second conference in this series whose main purpose is to provide a forum for advanced discussion in the fields of space and time reference systems, Earth rotation, astrometry and time.

During the latest IAU General Assembly, big progresses have been reported in JD7 "Space-time reference systems for future research", and also Division 1 meetings, regarding theoretical aspects of reference systems, requirements on space-time reference systems for future space missions, advanced dynamical models for the solar system, time and frequency transfer, Earth rotation modelling, astrometric catalogues, ephemerides, atomic time, pulsar-based timescale, etc.

Some of those issues have appeared as being essential for future scientific discussions. In addition, proposals for new working groups have been made (on ICRS, UTC, pulsar time, nomenclature, Earth rotation modelling, ...) that are quite relevant to the field of the Journées.

The scientific programme of the Journées 2013 will include sessions on the scientific developments in geodesy, astronomy and astrophysics based on high accurate reference frames and time scales. In addition, there will be presentations and discussions related to the new IAU Division A Working Groups that have been established at the 28th IAU GA.

Contact : Journées 2013, Nicole Capitaine, SYRTE, Observatoire de Paris,
61, avenue de l'Observatoire, 75014, Paris, France;
phone : 33 1 40 51 22 31; fax : 33 1 40 51 22 91; e-mail : n.capitaine@obspm.fr (Subject: Journees 2013), or see the web page of the Journées 2013 at: `http://syrte.obspm.fr/journees2013/` (that will be regularly updated).